

POST-FIRE DAMAGE AND CORROSION IN STRUCTURAL STEELS:
CHARACTERIZATION AND PREVENTION

A Dissertation
Submitted to the Graduate Faculty
of the
North Dakota State University
of Agriculture and Applied Science

By

Hizb Ullah Sajid

In Partial Fulfillment of the Requirements
for the Degree of
DOCTOR OF PHILOSOPHY

Major Program:
Civil Engineering

August 2021

Fargo, North Dakota

North Dakota State University
Graduate School

Title

POST-FIRE DAMAGE AND CORROSION IN STRUCTURAL STEELS:
CHARACTERIZATION AND PREVENTION

By

Hizb Ullah Sajid

The Supervisory Committee certifies that this *disquisition* complies with North Dakota State University's regulations and meets the accepted standards for the degree of

DOCTOR OF PHILOSOPHY

SUPERVISORY COMMITTEE:

Ravi Kiran Yellavajjala

Chair

Dinesh R. Katti

Mijia Yang

Dante Battocchi

Michael D. Engelhardt

Approved:

December 10, 2021

Date

Xuefeng (Micheal) Chu

Department Chair

ABSTRACT

Steel structures frequently experience extreme service conditions such as fire accidents, corrosion, etc., resulting in significant deterioration, reduced service life, and increased maintenance cost. Almost 0.5 million structural fire accidents are reported annually in the U.S., inflicting a considerable toll on infrastructure. Similarly, corrosion-induced deterioration is the leading cause of premature failure in infrastructure and costs \$22.6 billion in infrastructure maintenance annually. The bridge infrastructure vulnerability to these extreme service conditions is compounded by the aging bridge inventory (42% of the 617,000 bridges in the U.S. are 50 years or older). To improve the resilience and the “C-” infrastructure grade, it is vital to understand the material-scale damages and mechanisms induced by such extreme service conditions and develop efficient mitigation strategies. This dissertation adopts a two-prong approach to understand and predict the material-scale damage after exposure to fire accidents in steel structures and mitigate corrosion damage in steel/RC structures. Specifically, it aims to improve our current understanding of the post-fire mechanical behavior of steels and propose a microstructure-based approach for forensic analysis of fire-affected steel structures in phase-I. It further aims to mitigate corrosion in steel/RC structures by employing agriculturally-derived non-toxic materials and surface treatments in phase-II.

Post-fire mechanical and microstructural investigations conducted in phase-I revealed that stress concentrations and fire-extinguishing methods significantly affect the post-fire mechanical behavior of structural steels, and post-fire steel microstructure can be utilized to accurately estimate the mechanical strength of structural steels without the knowledge of fire temperatures. The outcomes of phase-I of this dissertation can lead to accurate forensic fire investigations and usability determination of the fire-affected steel structures. The results

obtained from phase-II of this dissertation revealed the role of surface treatments in improving the corrosion resistance and validated the performance of the agriculturally-derived materials such as corn-derived inhibitors and soy-protein coatings in lowering the corrosion damage in structural steels and embedded rebars by up to 90% without compromising the integrity of cement-based materials. These outcomes will lead to mitigating corrosion-induced deterioration in aging and new infrastructure. Overall, the outcomes of this dissertation contribute to improving infrastructure resilience and reducing maintenance costs.

ACKNOWLEDGMENTS

In the name of Almighty Allah, the most merciful and the most beneficial. Thanks to Almighty Allah for giving me the strength to complete this scholarly work and enabling me to make a scholarly contribution in the service of society, science, and engineering.

Ph.D. is a long journey and I would like to express my sincere gratitude and appreciation to my Ph.D. advisor and mentor, Dr. Ravi Kiran Yellavajjala who guided and supported me throughout my Ph.D. journey at NDSU and whose mentorship played an instrumental role in the completion of this dissertation. I am thankful to Dr. Ravi Kiran Yellavajjala for his confidence and belief in my abilities. I am also thankful for his constant encouragement and endless proofreading hours on my research papers that helped shaped me into an active researcher and helped this dissertation turned into reality. His dedication will continue to serve as a source of inspiration for me in the years to come.

I am highly thankful to my dissertation committee members Dr. Michael Englehardt (CAEE UT Austin), Dr. Mijia Yang (CEE, NDSU), Dr. Dinesh Katti (CEE, NDSU), and Dr. Dante Battocchi (CPM, NDSU) for their encouragement, helpful comments, and support that played a critical role in the successful completion of the dissertation.

I am highly thankful to Mr. Shannon Viestenz (Late) (IME, NDSU), Dr. Xiaoning Qi (CPM, NDSU), Mr. Gregory Strommen (Research Park, NDSU), and Dr. Chunju Gu (CPM, NDSU) for their assistance during my experimental work. I would also like to express my gratitude to the current and past members of the DAMS research group at CEE, particularly to Dayakar Naik Lavadiya, for their support and help. Special thanks go to the Pakistani Students community and Friends at NDSU who always made me feel at home.

This dissertation would not have been possible without the endless encouragement and support of my brothers Sikandar Sajid and Saif Ullah Sajid and the constant prayers and support of my parents. They endured my absence and remained steadfast and supportive throughout this journey and for that, I am forever grateful.

In the end, I would like to thank the anonymous reviewers whose comments and feedback greatly improved the quality of my scholarly work.

DEDICATION

To my beloved mom and dad.

TABLE OF CONTENTS

ABSTRACT.....	iii
ACKNOWLEDGMENTS	v
DEDICATION	vii
LIST OF TABLES	xvi
LIST OF FIGURES	xix
LIST OF ABBREVIATIONS.....	xxxii
LIST OF SYMBOLS	xxxvi
1. INTRODUCTION	1
1.1. Background	1
1.2. Fire Damage in Steel Structures.....	2
1.3. Corrosion Damage in Steel and RC Structures	5
1.4. Existing Literature.....	10
1.4.1. Fire-Damage in Steel Structures: In-Fire Damage in Structural Steels.....	10
1.4.2. Fire-Damage in Steel Structures: Post-Fire Damage in Structural Steels	11
1.4.3. Corrosion Damage Mitigation in Steel and RC Structures	13
1.5. Limitations of Existing Literature	16
1.5.1. Stress Concentration in Steel Structures is Ignored	17
1.5.2. Limitations of Current Post-Fire Approaches	18
1.5.3. Limitations of Existing Corrosion Prevention Techniques in Steel and RC Structures.....	19
1.6. Problem Statement and Research Objectives	22
1.7. Organization of Dissertation	24
1.8. References	27
2. INFLUENCE OF STRESS CONCENTRATION AND COOLING METHODS ON POST-FIRE MECHANICAL BEHAVIOR OF ASTM A36 STEELS	37

2.1. Introduction	37
2.2. Experimental Procedure	40
2.2.1. Finite Element Analyses of Test Specimens	40
2.2.2. Heating and Cooling of Test Specimens	44
2.2.3. Post-Fire Mechanical Tests	45
2.3. Results and Discussions	46
2.3.1. Visual Observation	46
2.3.2. Post-Fire Load Displacement Curves	50
2.3.3. FE Analysis and Stress Triaxialities of Post-Fire Specimens	65
2.3.4. Elastic Modulus	69
2.3.5. Yield Strength.....	73
2.3.6. Ultimate Tensile Strength.....	79
2.3.7. Ductility.....	84
2.3.8. SEM Analysis.....	89
2.4. Conclusions	95
2.5. References	97
3. INFLUENCE OF HIGH STRESS TRIAXIALITY ON MECHANICAL STRENGTH OF ASTM A36, ASTM A572 AND ASTM A992 STEELS	103
3.1. Introduction	103
3.2. Experimental Study and Finite Element Modeling	104
3.3. Results and Discussion.....	109
3.4. Conclusions	113
3.5. References	113
4. POST-FIRE MECHANICAL BEHAVIOR OF ASTM A572 STEELS SUBJECTED TO HIGH STRESS TRIAXIALITIES	116
4.1. Introduction	116

4.2. Experimental Procedure	120
4.2.1. Test Specimens	121
4.2.2. Post-Fire Mechanical Tests	124
4.3. Results and Discussion.....	126
4.3.1. Post-Fire Load Displacement Curves	126
4.3.2. Finite Element Analysis of Post-Fire Specimens	134
4.3.3. Stress Triaxialities of Post-Fire Specimens.....	137
4.3.4. Elastic Modulus.....	140
4.3.5. Yield Strength.....	144
4.3.6. Ultimate Tensile Strength.....	151
4.3.7. Ductility.....	155
4.3.8. Discussion on Residual Strength Factors for Structural Steels	159
4.4. Conclusions	164
4.5. References	166
5. MICROSTRUCTURE-MECHANICAL PROPERTY RELATIONSHIPS FOR POST-FIRE STRUCTURAL STEELS	175
5.1. Introduction	175
5.2. Experimental Procedure	179
5.2.1. Test Specimens	179
5.2.2. Characterization of Microstructure of Post-fire Test Specimens	180
5.3. Results and Discussion.....	182
5.3.1. Post-Fire Microstructure.....	183
5.3.2. Post-Fire Microstructure and Mechanical Properties	191
5.3.3. Predictive Models	201
5.4. Conclusions	207
5.5. References	209

6. INFLUENCE OF CORROSION AND SURFACE ROUGHNESS ON WETTABILITY OF ASTM A36 STEELS	215
6.1. Introduction	215
6.2. Experimental Procedure	220
6.2.1. Specimen Preparation	220
6.2.2. Contact Angle Test	221
6.2.3. Accelerated Corrosion Test	222
6.2.4. Surface Roughness Test	224
6.3. Results and Discussions	227
6.3.1. Contact Angle and Corrosion	227
6.3.2. Contact Angle and Surface Roughness Due to Corrosion.....	235
6.3.3. Contact Angle and Surface Roughness of Bare Steel	238
6.3.4. Surface Roughness and Corrosion.....	243
6.3.5. Surface Roughness, Wettability and Surface Energies	244
6.3.6. SEM and EDS Analysis.....	246
6.4. Predictive Equations.....	250
6.5. Conclusions	252
6.6. References	253
7. EMPLOYING CORN DERIVED PRODUCTS TO REDUCE THE CORROSIVITY OF PAVEMENT DEICING MATERIALS	264
7.1. Introduction	264
7.2. Experimental Procedure	271
7.2.1. Test Specimens	271
7.2.2. Corrosion Tests.....	273
7.2.3. Corrosion Products Characterization.....	276
7.3. Results and Discussion.....	276

7.3.1. Accelerated Corrosion Tests.....	277
7.3.2. Potentiodynamic Polarization Tests	280
7.3.3. Tafel Extrapolation Results	283
7.3.4. Corrosion Inhibition Mechanism of Polyols	288
7.3.5. Surface Characterization Results.....	293
7.4. Conclusions	299
7.5. References	300
8. IMPROVING THE WETTABILITY OF STRUCTURAL STEELS BY EMPLOYING IONIC LIQUIDS	310
8.1. Introduction	310
8.2. Experimental Procedure	315
8.2.1. Preparation of Ionic Liquids Solutions.....	315
8.2.2. Ionic Liquid Surface Treatment.....	317
8.2.3. Contact Angle.....	318
8.2.4. Surface Free Energy	320
8.3. Results and Discussion.....	322
8.3.1. Water Contact Angle.....	322
8.3.2. Discussion on Water Contact Angle of RTIL-treated Steel Surfaces	326
8.3.3. Diiodomethane Contact Angle	328
8.3.4. Surface Free Energy	332
8.4. Conclusions	333
8.5. References	335
9. IMPROVING THE ICE-MELTING CAPACITY OF TRADITIONAL DEICERS	356
9.1. Introduction	356
9.2. Experimental Work	360
9.2.1. Ice Melting Capacity Tests.....	360

9.2.2. Skid Resistance Tests	362
9.2.3. Viscosity Tests.....	363
9.2.4. Dissolved Oxygen (DO) Tests.....	365
9.3. Results and Discussions	366
9.3.1. Ice Melting Capacity	366
9.3.2. Comparison of Ice Melting Capacities of Liquid Deicers.....	370
9.3.3. Skid Resistance.....	373
9.3.4. Viscosity	375
9.3.5. Dissolved Oxygen Test Results.....	376
9.4. Conclusions	377
9.5. References	379
10. A SURVEY ON THE EFFECTS OF DEICING MATERIALS ON PROPERTIES OF CEMENT-BASED MATERIALS.....	385
10.1. Introduction	385
10.2. Deicers-induced Deterioration Mechanisms in Concrete.....	388
10.2.1. Physical Deterioration	388
10.2.2. Chemical Deterioration	393
10.3. Experimental Techniques for Characterizing Physical and Chemical Deterioration.....	396
10.3.1. Materials Selection and Mix Design	397
10.3.2. Deicer Selection.....	397
10.3.3. Deicer Exposure Methods	400
10.3.4. Deicer-induced Deterioration Tests.....	402
10.4. A Critical Review of Previous Literature.....	406
10.4.1. Scaling.....	406
10.4.2. Compressive Strength.....	416
10.4.3. Mass Change	424

10.5. Conclusions	429
10.6. Recommendations and Future Research Directions.....	430
10.7. References	432
11. EFFECT OF AGRO-DERIVED CORROSION INHIBITORS ON THE PROPERTIES OF PORTLAND CEMENT MORTAR.....	447
11.1. Introduction	447
11.2. Experimental Procedure	451
11.2.1. Test Specimens.....	452
11.2.2. Corrosion Inhibitors Included Deicers Exposure Conditions.....	452
11.2.3. Physical Characterization: Mass Change, Scaling, and Compressive Strength	453
11.2.4. Chemical Characterization: XRD and SEM, and EDS Analysis	454
11.3. Results and Discussions	455
11.3.1. Scaling	455
11.3.2. Mass Change	460
11.3.3. Compressive Strength.....	462
11.3.4. Chemical Characterization: XRD, SEM, and EDS Analysis	464
11.3.5. Performance Comparison with the Literature and Discussion	471
11.4. Conclusions	472
11.5. References	474
12. SOY-PROTEIN AND POLYOL-BASED COATINGS FOR MITIGATING CORROSION IN REINFORCED CONCRETE STRUCTURES	480
12.1. Introduction	480
12.2. Coatings for Steel Rebars and the Potential of Soybean-Based Coating Material.....	483
12.3. Experimental Procedure	485
12.3.1. Soy Protein Isolate.....	485
12.3.2. Synthesis of Soy-Based Coatings.....	486

12.3.3. Physical and Chemical Characterization Tests.....	487
12.3.4. Corrosion Performance Characterization	489
12.4. Results and Discussion.....	492
12.4.1. Visual Brittleness of Cured Soy Protein Coatings	492
12.4.2. Viscosities of Soy Protein Coatings	493
12.4.3. Abrasion Resistance of Soy Protein Coatings.....	494
12.4.4. FTIR Results.....	495
12.4.5. Corrosion Performance Characterization	496
12.5. Conclusions	499
12.6. References	500
13. SUMMARY, OUTCOMES, AND FUTURE DIRECTIONS.....	507
13.1. Summary and Outcomes	507
13.2. Future Recommendation	510
13.2.1. Post-Fire Damage Characterization and Multi-Scale Modeling	510
13.2.2. Post-Fire Damage Models for Inclusion in Building Standards.....	510
13.2.3. Residual Mechanical Properties Prediction for Steels with Variable Grain Sizes.....	511
13.2.4. Long-Term Field Performance of Polyol-Mixed Salt Brine Deicers	512
13.2.5. Mixing Polyol Additives in Other Deicers	512
13.2.6. Inclusion of Traditional and Novel Materials in Bio-Based Coatings	513

LIST OF TABLES

<u>Table</u>	<u>Page</u>
2.1. Geometric details of test specimens.....	41
2.2. Mechanical properties of ASTM A36 steel.	44
2.3. Post-fire yield strength of test specimens.	74
2.4. Post-fire ultimate tensile strength of test specimens.....	80
2.5. Post-fire ductility of test specimens.....	85
3.1. Chemical composition of ASTM A36, A572, and A992 structural steels.....	105
3.2. Experimental material properties of structural steels (obtained from un-notched test specimens) and comparison with ASTM standards.	107
4.1. Post-fire mechanical tests conducted on different types of steels.....	119
4.2. Geometric details of test specimens.....	122
4.3. Chemical composition of ASTM A572 steel.....	123
4.4. Mechanical properties of ASTM A572 steel.	124
4.5. Post-fire elastic modulus of test specimens.	142
4.6. Post-fire yield strength of test specimens.	148
4.7. Post-fire yield strength residual factors of test specimens.....	148
4.8. Post-fire ultimate tensile strength of test specimens.....	153
4.9. Post-fire ultimate tensile strength residual factors of test specimens.	155
4.10. Post-fire ductility of test specimens.....	157
4.11. Post-fire ductility residual factors of test specimens.	159
4.12. Predictive models for strength residual strength factors for different structural steels.....	162
5.1. Chemical composition of ASTM A36, A572, and A992 structural steels.....	178
5.2. Post-fire yield strength of structural steel specimens (R = residual factor).....	192

5.3.	Post-fire ultimate tensile strength of structural steel specimens (R = residual factor).....	197
5.4.	Post-fire ductility of structural steel specimens (R = residual factor).	198
5.5.	Existing microstructure-property relationship models for yield strength.	206
6.1.	Testing conditions for ISO 14993 accelerated corrosion test.	223
6.2.	Contact angles of set-A test specimens before corrosion exposure.....	228
6.3.	Contact angles of set-A test specimens after corrosion exposure.....	231
6.4.	Rate of corrosion in different set-A test specimens.....	235
6.5.	Surface roughness of representative set-A test specimens after corrosion exposure.....	237
6.6.	Surface roughness of representative set-B test specimens polished to different grit sizes.....	239
6.7.	Contact angles of set-B test specimens polished to different grit sizes.	239
6.8.	Surface free energies of test specimens.	246
7.1.	Chemical and physical properties of maltitol, mannitol, and sorbitol.	271
7.2.	Chemical composition of ASTM A572 steel.....	273
7.3.	Polarization parameters obtained from Tafel extrapolation.....	286
7.4.	Calculated thermodynamic parameters from the Langmuir isotherm.	292
8.1.	The purity and presence of impurities in the ILs.	316
8.2.	Chemical composition of ASTM A572 high strength low alloy steel.....	318
8.3.	Surface tension (polar and dispersive components) of the probing liquids (adapted from ref. [161]).	320
9.1.	Freezing points of salt brine containing bio-based additives [33].	360
9.2.	Average BPN values of the pavement surface before and after the treatment with deicer solution.	374
9.3.	The viscosity of deicer solutions (20.3°C). (S. No. 6-11 values are obtained from ref. [19].	376
9.4.	Three-day Dissolved Oxygen test of river water mixed with various deicers.....	377

10.1.	Studies focused on scaling damages on concrete due to deicer exposure.	407
10.2.	Scaling rating description.	412
11.1.	Experimental scheme.	454
11.2.	Description of the visual rating of scaling damage in cement mortar specimens.	460

LIST OF FIGURES

<u>Figure</u>	<u>Page</u>
1.1 Structural fires in the U.S. (Source: NFPA 2020).	3
1.2 Fire statistics in the United States (1978-2015): (a) average structural fire losses and (b) number of structural fire accidents.	4
1.3 Fire accidents in buildings and bridges.....	4
1.4 Examples of corroded reinforced concrete structures in the U.S. Midwest region: (a,b) corroded rebars, excessive delamination, and spalling in the RC columns of a railroad bridge, and (c) delamination, spalling and corroded rebar in a pump house in a powerhouse.	6
1.5 Bridge bearing failure reasons.	6
1.6 Typical corrosion damages observed in the transportation infrastructure: (a) brake line and fender corrosion, (b) exhaust system corrosion [29], (c) steel rebar corrosion [30], and (d) gusset plate corrosion [31]......	9
1.7 Factors affecting corrosion rates in structural steels.....	9
1.8 Elevated temperature mechanical properties residual factors for structural steels.	11
1.9 Post-fire mechanical properties residual factors for structural steels.	13
1.10 Sources of stress concentration in steel structures.....	17
1.11 Stress concentration leading to failure of a steel girder.....	18
1.12 Surface oxide colors after exposure of steels to different elevated temperatures [84]......	19
1.13 Dissertation flowchart.....	26
2.1 Average losses per structural fire in USD in the US from 1978-2015.	40
2.2 The number of structural fire accidents reported in the US between 1978-2015.	40
2.3 Geometric details of typical test specimens (all dimensions are in mm).....	41
2.4 (a) Applied boundary conditions, (b) typical C-notch, (c) typical U-notch, (d) typical V-notch.....	42
2.5 (a) Strain hardening curve of SPR test specimen, (b) experimental and FE load-displacement curve of SPR test specimen.	43

2.6.	Initial stress triaxiality profiles of test specimens.....	44
2.7.	Specimens placed inside an electric furnace for heating.	45
2.8.	Typical uniaxial tension test setup.....	46
2.9.	Schematic of oxidation layers formed on iron substrate beyond 700 °C after 24 hours.....	48
2.10.	Specimens after being subjected to different temperatures and cooling regimes.	49
2.11.	Load-displacement curves of specimen SPR-AC (RT-700 °C).....	51
2.12.	Load-displacement curves of specimen SPR-AC (800-1000 °C).....	51
2.13.	Load-displacement curves of specimen SPR-WC (RT-700 °C).....	52
2.14.	Load-displacement curves of specimen SPR-WC (800-1000 °C).....	52
2.15.	Load-displacement curves of specimen CN1-AC (RT-700 °C).	53
2.16.	Load-displacement curves of specimen CN1-AC (800-1000 °C).	53
2.17.	Load-displacement curves of specimen CN1-WC (RT-700 °C).	54
2.18.	Load-displacement curves of specimen CN1-WC (800-1000 °C).	54
2.19.	Load-displacement curves of specimen CN2-AC (RT-700 °C).	55
2.20.	Load-displacement curves of specimen CN2-AC (800-1000 °C).	55
2.21.	Load-displacement curves of specimen CN2-WC (RT-700 °C).	56
2.22.	Load-displacement curves of specimen CN2-WC (800-1000 °C).	56
2.23.	Load-displacement curves of specimen CN3-AC (RT-700 °C).	57
2.24.	Load-displacement curves of specimen CN3-AC (800-1000 °C).	57
2.25.	Load-displacement curves of specimen CN3-WC (RT-700 °C).	58
2.26.	Load-displacement curves of specimen CN3-WC (800-1000 °C).	58
2.27.	Load-displacement curves of specimen UN1-AC (RT-700 °C).....	59
2.28.	Load-displacement curves of specimen UN1-AC (800-1000 °C).....	59
2.29.	Load-displacement curves of specimen UN1-WC (RT-700 °C).....	60
2.30.	Load-displacement curves of specimen UN1-WC (800-1000 °C).	60

2.31.	Load-displacement curves of specimen VN1-AC (RT-700 °C).....	61
2.32.	Load-displacement curves of specimen VN1-AC (800-1000 °C).....	61
2.33.	Load-displacement curves of specimen VN1-WC (RT-700 °C).....	62
2.34.	Load-displacement curves of specimen VN1-WC (800-1000 °C).....	62
2.35.	Load-displacement curves of specimen VN2-AC (RT-700 °C).....	63
2.36.	Load-displacement curves of specimen VN2-AC (800-1000 °C).....	63
2.37.	Load-displacement curves of specimen VN2-WC (RT-700 °C).....	64
2.38.	Load-displacement curves of specimen VN2-WC (800-1000 °C).....	64
2.39.	Strain hardening curves of un-notched test specimens.....	66
2.40.	Maximum stress triaxialities of post-fire test specimens at 1.35±0.05% strain: a) CN1, b) CN2, c) CN3, d) UN1, e) VN1, and f) VN2.....	68
2.41.	Average stress triaxialities of post-fire test specimens at 1.35±0.05% strain: a) CN1, b) CN2, c) CN3, d) UN1, e) VN1, and f) VN2.....	69
2.42.	Residual factors of specimen SPR under different cooling regimes: a) elastic modulus, b) yield strength, c) ultimate tensile strength, d) fracture strain, and e) uniform strain.....	71
2.43.	Elastic modulus residual factors of post-fire test specimens: a) CN1, b) CN2, c) CN3, d) UN1, e) VN1, and f) VN2.....	72
2.44.	Yield strength residual factors of post-fire test specimens: a) CN1, b) CN2, c) CN3, d) UN1, e) VN1, and f) VN2.....	76
2.45.	Microstructure of ASTM A36 steel at room temperature (RT).....	77
2.46.	Microstructure of ASTM A36 steel after air-cooling from 900 °C to RT.....	77
2.47.	Microstructure of ASTM A36 steel after water-cooling from 900 °C to RT.....	77
2.48.	Average stress triaxiality versus yield strength of post-fire test specimens: a) CN1, b) CN2, c) CN3, d) UN1, e) VN1, and f) VN2.....	79
2.49.	Ultimate tensile strength residual factors of post-fire test specimens: a) CN1, b) CN2, c) CN3, d) UN1, e) VN1, and f) VN2.....	82
2.50.	Average stress triaxiality versus ultimate tensile strength of post-fire test specimens: a) CN1, b) CN2, c) CN3, d) UN1, e) VN1, and f) VN2.....	84

2.51.	Fracture strain residual factors of post-fire test specimens a) CN1, b) CN2, c) CN3, d) UN1, e) VN1, and f) VN2.....	88
2.52.	Uniform strain residual factors of post-fire test specimens a) CN1, b) CN2, c) CN3, d) UN1, e) VN1, and f) VN2.....	89
2.53.	SEM analysis of specimen SPR-RT.	92
2.54.	SEM analysis of specimen SPR-900-AC.....	92
2.55.	SEM analysis of specimen SPR-900-WC.....	93
2.56.	SEM analysis of specimen VN1-RT.....	93
2.57.	SEM analysis of specimen VN1-900-AC.	94
2.58.	SEM analysis of specimen VN1-900-WC.	94
3.1.	Geometric details of axisymmetric test specimens (all dimensions are in mm.).....	105
3.2.	Engineering stress-strain curves of un-notched and notched test specimens.	107
3.3.	(a) Initial stress triaxiality profiles, (b) stress triaxiality profiles at ultimate load.....	108
3.4.	Strain hardening curves of un-notched test specimens used in finite element analysis.....	108
3.5.	(a) Applied boundary and loading conditions, (b) typical C-notch mesh, (c) typical U-notch mesh, and (d) typical V-notch mesh.	109
3.6.	Average initial stress triaxiality versus yield strength.	111
3.7.	Average ultimate stress triaxiality versus ultimate tensile strength.....	112
4.1.	Geometric details of typical test specimens (all dimensions are in mm.).....	122
4.2.	Initial stress triaxiality profiles of test specimens.....	123
4.3.	Heating of test specimens inside an electric furnace.	125
4.4.	Typical heating and cooling profile of test specimens.....	125
4.5.	Uniaxial tension test setup and extensometer mounted on the test specimen.....	125
4.6.	Load-displacement curves of specimen SPR-AC.	127
4.7.	Load-displacement curves of specimen SPR-AC.	128
4.8.	Load-displacement curves of specimen CN1-AC.....	128

4.9.	Load-displacement curves of specimen CN1-WC.....	129
4.10.	Load-displacement curves of specimen CN2-AC.....	129
4.11.	Load-displacement curves of specimen CN2-WC.....	130
4.12.	Load-displacement curves of specimen CN3-AC.....	130
4.13.	Load-displacement curves of specimen CN3-WC.....	131
4.14.	Load-displacement curves of specimen UN1-AC.	131
4.15.	Load-displacement curves of specimen CN4-WC.....	132
4.16.	Load-displacement curves of specimen VN1-AC.	132
4.17.	Load-displacement curves of specimen VN1-WC.	133
4.18.	Load-displacement curves of specimen VN2-AC.	133
4.19.	Load-displacement curves of specimen VN2-WC.	134
4.20.	(a) Test specimen, (b) finite element model and applied boundary conditions, (c) typical C-notch mesh.	136
4.21.	(a) Strain hardening curve of SPR test specimen, (b) experimental and FE load-displacement curve of SPR test specimen.	136
4.22.	Strain hardening curves of un-notched test specimens.	137
4.23.	Maximum stress triaxialities of post-fire test specimens at $1.35\pm 0.05\%$ strain: a) CN1, b) CN2, c) CN3, d) UN1, e) VN1, and f) VN2.	139
4.24.	Average stress triaxialities of post-fire test specimens at $1.35\pm 0.05\%$ strain: a) CN1, b) CN2, c) CN3, d) UN1, e) VN1, and f) VN2.	140
4.25.	Residual factors of specimen SPR under different cooling regimes: a) elastic modulus, b) yield strength, c) ultimate tensile strength, and d) ductility.....	143
4.26.	Elastic modulus residual factors of post-fire test specimens: a) CN1, b) CN2, c) CN3, d) UN1, e) VN1, and f) VN2.....	144
4.27.	Yield strength residual factors of post-fire test specimens: a) CN1, b) CN2, c) CN3, d) UN1, e) VN1, and f) VN2.....	149
4.28.	Microstructure of ASTM A572 Gr. 50 steel at room temperature.	150
4.29.	Microstructure of ASTM A572 gr. 50 steel after air-cooling from 900 °C to room temperature.	150

4.30.	Microstructure of ASTM A572 Gr. 50 steel after water-cooling from 900 °C to room temperature.	151
4.31.	Ultimate tensile strength residual factors of post-fire test specimens: a) CN1, b) CN2, c) CN3, d) UN1, e) VN1, and f) VN2.	154
4.32.	Ductility residual factors of post-fire test specimens: a) CN1, b) CN2, c) CN3, d) UN1, e) VN1, and f) VN2.	158
4.33.	Comparison of yield strength residual factors of structural steels.	163
4.34.	Comparison of ultimate tensile strength residual factors of structural steels.	164
5.1.	The crystal structures of (a) ferrite (body-centered cubic), (b) austenite (face-centered cubic, and (c) cementite (orthorhombic). Adapted from (Vander Voort 2004).	178
5.2.	Geometric details of a typical cylindrical test specimen's (a) gauge section, and (b) cross-section. (all dimensions are in mm.).	180
5.3.	Typical epoxy mounted metallographic specimen with locations where micrographs are extracted for microstructural analysis.	182
5.4.	Iron-Iron Carbide phase diagram for hypoeutectoid steels (0.022-0.76% C).	182
5.5.	Microstructure of reference steel specimens evaluated at room temperature: (a) ASTM A36, (b) ASTM A572 Gr. 50, and (c) ASTM A992.	185
5.6.	Post-fire air-cooled microstructures of structural steel specimens corresponding to different target temperatures (500-700 °C).	186
5.7.	Post-fire air-cooled microstructures of structural steel specimens corresponding to different target temperatures (800-1000 °C).	187
5.8.	Fractions of ferrite and pearlite in AC steels: (a) A36, (b) A572, and (c) A992.	188
5.9.	Ferrite grain and pearlite colony size in AC steels: (a) A36, (b) A572, and (c) A992.	188
5.10.	Post-fire yield strength (YS), ultimate tensile strength (UTS) and evolution of (a) ferrite volume fraction (VF), (b) pearlite VF, (c) ferrite grain size (GS) and (d) pearlite colony size (CS) of ASTM A36 steel specimens corresponding to different target temperatures.	193
5.11.	Post-fire yield strength (YS), ultimate tensile strength (UTS) and evolution of (a) ferrite volume fraction (VF), (b) pearlite VF, (c) ferrite grain size (GS) and (d) pearlite colony size (CS) of ASTM A572 steel specimens corresponding to different target temperatures.	194

5.12.	Post-fire yield strength (YS), ultimate tensile strength (UTS) and evolution of (a) ferrite volume fraction (VF), (b) pearlite VF, (c) ferrite grain size (GS) and (d) pearlite colony size (CS) of ASTM A992 steel specimens corresponding to different target temperatures.	195
5.13.	Post-fire ductility and evolution of (a) ferrite volume fraction (VF), (b) pearlite VF, (c) ferrite grain size (GS) and (d) pearlite colony size (CS) of ASTM A36 steel specimens corresponding to different target temperatures.	199
5.14.	Post-fire ductility and evolution of (a) ferrite volume fraction (VF), (b) pearlite VF, (c) ferrite grain size (GS) and (d) pearlite colony size (CS) of ASTM A572 steel specimens corresponding to different target temperatures.	200
5.15.	Post-fire ductility and evolution of (a) ferrite volume fraction (VF), (b) pearlite VF, (c) ferrite grain size (GS) and (d) pearlite colony size (CS) of ASTM A992 steel specimens corresponding to different target temperatures.	201
5.16.	Yield strengths of test specimens obtained from experiments and multivariate linear regression-based models for (a) ASTM A36, (b) ASTM A572, and (c) ASTM A992.....	203
5.17.	Comparison of the proposed model for ASTM A36 steel with the existing microstructure-property relationship for yield strength.	204
5.18.	Comparison of the proposed model for ASTM A572 Gr. 50 steel with the existing microstructure-property relationship for yield strength.	204
5.19.	Comparison of the proposed model for ASTM A992 steel with the existing microstructure-property relationship for yield strength.	205
6.1.	(a) Typical specimen during contact angle test, (b) Contact angle measurement.	218
6.2.	Illustration of wetting on rough surfaces (a) Wenzel state, (b) Cassie-Baxter state.	220
6.3.	Optical goniometer for contact angle test.	222
6.4.	Specimens placed at 20° angle inside salt spray chamber.	224
6.5.	Stylus profiler for measuring surface roughness of corroded specimens.	226
6.6.	Non-contact optical profiler for measuring surface roughness of uncorroded specimens.	227
6.7.	Typical images of water droplets on surfaces of specimens before corrosion.	229
6.8.	Optical micrographs for specimens during initial phase of corrosion.	230
6.9.	Variation in contact angle of specimens subjected to different corrosion durations.	232

6.10.	Corrosion exposure time in hours versus contact angle in degrees.	233
6.11.	Corrosion exposure versus rate of corrosion.	235
6.12.	Surface roughness profiles of specimens subjected to different corrosion durations.....	237
6.13.	Surface roughness versus contact angle of test specimens subjected to corrosion.	237
6.14.	Surface roughness profiles of test specimens polished using 120 and 400 grit sizes.....	240
6.15.	Surface roughness profiles of test specimens polished to grit sizes equal to or finer than 800 grit size.....	240
6.16.	3D surface profiles of test specimens polished to different grit sizes.....	241
6.17.	Typical images of water droplets on specimen’s surfaces polished to different grit sizes.....	242
6.18.	Surface roughness versus contact angle of test specimens polished to different grit sizes.....	243
6.19.	Visual comparison of corrosion on surfaces of most and least polished test specimens after 4 hours corrosion exposure (figure not to scale).....	244
6.20.	Surface free energy of test specimens at different surface roughness.	246
6.21.	SEM micrographs of test specimen S4 (subjected to 4 hours corrosion).	248
6.22.	SEM micrographs of test specimen S16 (subjected to 16 hours corrosion).	248
6.23.	EDS analysis of specimen S4 (subjected to 4 hours corrosion).....	249
6.24.	EDS analysis of specimen S16 (subjected to 16 hours corrosion).....	249
6.25.	EDS analysis of specimen S16 at goethite location.....	249
6.26.	Comparison of proposed equations for low surface roughness with test data.	251
6.27.	Comparison of proposed equations for medium surface roughness with test data.	251
6.28.	Comparison of proposed equations for high surface roughness with test data.	252
7.1.	Annual salt (<i>NaCl</i>) consumption in the US for roadway deicing during the 1940-2014 period (data source: US Geological Survey).	266

7.2.	Typical corrosion damages observed in the transportation infrastructure: (a) brake line and fender corrosion, (b) exhaust system corrosion [78] (c) steel rebar corrosion [79], and (d) gusset plate corrosion [80].	267
7.3.	Specimens for corrosion tests: (a) cylindrical specimens for visually observing corrosion in a highly corrosive environment, and (b) steel plates for PD tests.	272
7.4.	Typical cylindrical specimen subjected to flowing deicing media (23.0% <i>NaCl</i> brine + polyol) inside an environmental chamber at 30 °C temperature and 100% relative humidity conditions.	275
7.5.	Typical corrosion cell with steel plate as working electrode (WE) (exposed area: 7.07 cm ²), saturated calomel electrode as reference electrode (RE) and stainless steel wire mesh as counter electrode (CE).	276
7.6.	The visual appearance of ASTM A572 steel specimens exposed to the traditional deicing solution (23% <i>NaCl</i> brine).	278
7.7.	Visual appearance of ASTM A572 steel specimens exposed to deicing solution containing 0.5%, 1.0%, 2.0% and 3.0% sorbitol.	278
7.8.	Visual appearance of ASTM A572 steel specimens exposed to deicing solution containing 0.5%, 1.0%, 2.0% and 3.0% mannitol.	279
7.9.	Visual appearance of ASTM A572 steel specimens exposed to deicing solution containing 0.5%, 1.0%, 2.0% and 3.0% maltitol.	280
7.10.	Schematic polarization curve of a typical test specimen.	282
7.11.	Potentiodynamic polarization curves of ASTM A572 steel specimens in deicing solution (23% <i>NaCl</i> brine) in the absence and presence of various polyols concentrations (0.5%, 1.0%, 2.0%, and 3.0%).	283
7.12.	Corrosion current densities of ASTM A572 steel specimens as a function of polyols concentration in deicing solution.	287
7.13.	Corrosion inhibition efficiencies of polyols as a function of polyols concentration in deicing solution.	287
7.14.	Corrosion rates in ASTM A572 steels as a function of polyols concentrations in deicing solution.	288
7.15.	Langmuir adsorption isotherm plots for steel specimens in brine solution containing various concentrations of polyols in deicing solution.	292
7.16.	SEM micrographs of corroded steel surfaces corresponding to (a) 23% wt. sodium chloride deicing solution, (b) 3.0% wt. sorbitol in deicing solution, (c) 3.0% wt. mannitol in deicing solution, and (d) 3.0% wt. maltitol in deicing solution.	294

7.17.	EDS analysis of corroded steel surfaces corresponding to 23% wt. sodium chloride deicing solution.....	295
7.18.	EDS analysis of corroded steel surfaces corresponding to (a) 3.0% wt. sorbitol in deicing solution, (b) 3.0% wt. mannitol in deicing solution, and (c) 3.0% wt. maltitol in deicing solution.	296
7.19.	XRD patterns for phases present in the corrosion products formed on steel specimens in the absence and presence of 3.0% wt. polyol corrosion inhibitors in ref. deicing solution (23% wt. <i>NaCl</i>).	298
8.1.	Reasons for bridge support bearing replacement (adopted from [4]).	311
8.2.	Illustration of contact angle (θ_c) of a probing liquid on a solid surface formed at the intersection of the three interfacial tensions (γ_{SL} , γ_{SV} , γ_{LV}).....	312
8.3.	Molecular structures of ionic liquids used in this study.	317
8.4.	Water Contact angle results for 1% IL+Ethanol (exposure duration: 30 minutes) at different time intervals.....	324
8.5.	Water Contact angle results for 1% IL+Ethanol (exposure duration: 4 hours) at different time intervals.....	324
8.6.	Water Contact angles for 1% IL+Ethanol (exposure duration: 30 minutes) at different time intervals.....	325
8.7.	Water Contact angles for 1% IL+Ethanol (exposure duration: 4 hours) at different time intervals.....	325
8.8.	Diiodomethane contact angles for 1% IL+Ethanol (exposure duration: 30 minutes) at different time intervals.....	330
8.9.	Diiodomethane contact angles for 1% IL+Ethanol (exposure duration: 4 hours) at different time intervals.....	331
8.10.	Diiodomethane Contact angle results for 1% IL+Ethanol (exposure duration: 30 minutes) at different time intervals.....	331
8.11.	Diiodomethane Contact angle results for 1% IL+Ethanol (exposure duration: 4 hours).	332
8.12.	Average surface free energies (polar and dispersive components) of untreated and RTIL-treated steel specimens.	333
9.1.	Test setup for conducting ice melting tests.....	361
9.2.	British Pendulum Tester for measuring skid resistance of pavement surface.	363

9.3.	Viscosity test set up.	365
9.4.	Benchtop Dissolved Oxygen Meter.	366
9.5.	Percent decrease in weight of ice cube with an increase in the concentration of (a) sorbitol, (b) mannitol, and (c) maltitol, in the 23.3% wt. NaCl deicer at various low temperatures.	368
9.6.	Percent decrease in the weight of ice cube immersed in (a) 23.3% wt. NaCl brine+sorbitol, (b) 23.3% wt. NaCl brine+mannitol, and (c) 23.3% wt. NaCl brine+maltitol solutions when compared to the traditional deicing solution (23.3% wt. NaCl brine), at different low temperatures.	369
9.7.	A comparison of the performance of the ice melting capacity of different deicers when compared to 23.3% NaCl salt brine deicer at -10°C and -12.2°C.	372
9.8.	A comparison of the performance of the ice melting capacity of different deicers when compared to 23.3% NaCl salt brine deicer at -20°C and -17.77°C.	372
9.9.	Skid resistance test on the PCC surface for all four optimal combinations of polyol and brine.	374
9.10.	Reduction in average BPN value for various combinations of bio-based deicing solutions and salt brine deicer (brine).	375
10.1.	Mechanism of scaling due to hydrostatic pressure. (a) water in the concrete pore before freezing; (b) hydrostatic pressure by ice in the concrete pores after freezing where the capillary pores leave space to the increased ice volume (c) scaling of the surface particle due to hydrostatic pressure.	391
10.2.	Mechanism of osmotic pressure development.	391
10.3.	Backscattered electron images of (a) cement matrix (b) air void in cement paste matrix indicating the formation of crystals of Friedel’s salt (shown by green circles), ettringite (shown by orange circles), and Ca-oxy (shown by blue circles). (adopted from Ref. [23]).	395
10.4.	XRD spectra of concrete specimens after 180 days of deicing solution exposure indicate the formation of brucite (B, occurring at around 40° and 51.5°) and other products. (adopted from Ref. [24]).	395
10.5.	The number of peer-reviewed publications (journal articles, reports, and proceedings) on different types of deicers in the period 1980-2021. The data is obtained from the Scopus database using the following search query: deicing/deicer/anti-icing and “name of deicer”.	400
10.6.	The variation of scaling rating with the number of F-T cycles for different studies ([5] [35] [49] [72] [71] [68] [76]).	411

10.7.	The variation of scaling rating with the number of W-D cycles for different studies.	414
10.8.	Change in concrete compressive strength under F-T cycles in deicing solution.....	421
10.9.	Concrete compressive strength trends observed under W-D cycles in deicing solution.....	423
10.10.	Mass variation with the increase in F-T cycles.....	427
10.11.	Mass variation with the increase in W-D cycles.....	428
11.1.	Experimental protocol for wet-dry exposure cycles and typical OPC mortar specimen after 28 days of curing.	453
11.2.	Visual appearance of cement mortar specimens after 0-40 W-D exposure cycles.....	458
11.3.	Visual appearance of cement mortar specimens after 0, 50-90 W-D exposure cycles.....	459
11.4.	Visual observation-based scaling rating assigned to the OPC mortar specimens after exposure to W-D cycles of NaCl salt brine deicer with and without polyol corrosion inhibitors.	460
11.5.	Mass change observed in the cement mortar specimens with respect to the number of W-D cycles of NaCl salt brine deicer with and without polyol corrosion inhibitors (note: negative mass change means mass gain).....	462
11.6.	Compressive strength of cement mortar after exposure to W-D exposure cycles of NaCl salt brine deicer with and without polyol corrosion inhibitors.....	463
11.7.	XRD spectra of cement mortar specimens after exposure to 60 W-D cycles of NaCl deicing solution in the absence and presence of polyol corrosion inhibitors.....	465
11.8.	SEM micrographs of cement mortar specimens after exposure to 60 W-D cycles of NaCl deicing solution in the absence and presence of polyol corrosion inhibitors.	468
11.9.	SEM micrograph and EDS spectra of cement mortar specimens after exposure to 60 W-D cycles of tap water.	469
11.10.	EDS spectra of cement mortar specimens after exposure to 60 W-D cycles of NaCl deicing solution in the absence and presence of polyol corrosion inhibitors.....	470
11.11.	A comparison of compressive strength deterioration of cement mortar and concrete caused by different corrosion inhibitors and deicers.....	472

12.1.	Examples of corroded reinforced concrete structures in the U.S. Midwest region: (a,b) corroded rebars, excessive delamination, and spalling in the RC columns of a railroad bridge (MN, USA), and (c) delamination, spalling and corroded rebar in a pump house in a powerhouse (WY, USA).....	482
12.2.	Typical workflow for each soy protein coating formulation trial.....	487
12.3.	Falling Sand Abrasion Tester for determining the abrasion resistance of the soy protein-coated steel panels.....	489
12.4.	Viscosity test setup.	489
12.5.	Schematic of macrocell corrosion test setup.....	491
12.6.	Uncoated (control) rebars and 10% and 15% soy protein-coated rebar specimens.....	491
12.7.	Rapid macrocell corrosion test specimens preparation (uncoated and coated rebars embedded in cement mortar).	492
12.8.	Visual brittleness of soy protein coatings with different concentrations of sorbitol.	493
12.9.	Viscosities of soy protein coatings with different concentrations of sorbitol.....	494
12.10.	Abrasion resistance of soy protein coatings with different concentrations of sorbitol.	495
12.11.	FTIR spectra of soy protein coatings with different concentrations of sorbitol.	496
12.12.	Potentiodynamic polarization curves of (a) 10% SPI coated steel panels and (b) 15% SPI coated steel panels, with 30% (w/w% of SPI) sorbitol as a plasticizer.	498
12.13.	Corrosion rates obtained from rapid macrocell corrosion tests for uncoated rebars and soy protein-coated rebars that are embedded in Portland cement mortar.	499

LIST OF ABBREVIATIONS

HSS	High Strength Steel.
VHSS	Very High Strength Steel.
UHSS	Ultra High Strength Steel.
AISC	American Institute of Steel Construction.
ASCE	American Society of Civil Engineers.
BS5950.....	British Standard 5950.
AS4100	Australia Standard 4100.
CECS.....	China Association for Engineering Construction Standardization.
EC3	Eurocode 3.
ASTM	American Society for Testing and Materials.
CIA.....	Cooling-in-Air.
CIW.....	Cooling-in-Water.
CIB	Cooling-in-Blanket.
AC.....	Air-cooled.
WC	Water-cooled.
CN.....	Circular Notch.
UN.....	U-shaped Notch.
VN.....	V-shaped Notch.
CAX4	4-node, First-order, Axisymmetric Solid Element.
CNC	Computer Numeric Control.
CRSI.....	Concrete Reinforcing Steel Institute.
RC	Reinforced Concrete.
ACI.....	American Concrete Institute.

AASHTOAmerican Association of State Highway Officials.

FBEFusion Bonded Epoxy.

ElDuctility.

YSYield Strength.

UTSUltimate Tensile Strength.

SPRReference Specimen.

PLCPortevin-Le Chatelier Effect.

RTRoom Temperature.

FCCFace-Centered Cubic.

BCCBody-Centered Cubic.

MVCMicrovoid Coalescence.

SEMScanning Electron Microscopy.

EDSEnergy Dispersive X-ray Spectroscopy.

FTIRFourier Transform Infrared.

PHMSA.....Pipeline and Hazardous Materials Safety
Administration.

CSH.....Calcium Silicate Hydrate.

MSH.....Magnesium Silicate Hydrate.

SCESaturated Calomel Electrode.

WEWorking Electrode.

CECounter Electrode.

XRDX-ray Diffraction.

IE.....Inhibition Efficiency.

CRCorrosion Rate.

EWEquivalent Weight.

RTIL.....Room Temperature Ionic Liquids.

IL.....	Ionic Liquid.
SFE.....	Surface Free Energy.
CCM.....	Complex Chloride Mineral.
DO.....	Dissolved Oxygen.
IMC.....	Ice Melting Capacity.
SHRP.....	Strategic Highway Research Program.
BPN.....	British Pendulum Number.
SPI.....	Soy Protein Isolate.
NC.....	Normal Concrete.
AC.....	Air Entrained Concrete.
ACA.....	Air Entrained Concrete with Air-Cooled Blast Furnace Slag (ACBFS) Aggregate.
AOFA.....	Air Entrained Concrete with Fly Ash as a Partial Replacement of OPC with ACBFS Aggregate.
AOSA.....	Air Entrained Concrete with Slag Cement as a Partial Replacement of OPC with ACBFS Aggregate.
AOFSA.....	Air Entrained Concrete with Fly ash and Slag cement as partial replacement of OPC with ACBFS Aggregate.
AOD.....	Air Entrained Concrete with Dolomite Aggregate.
AOFD.....	Air Entrained Concrete with Fly Ash as a Partial Replacement of OPC with Dolomite Aggregate.
AOSD.....	Air Entrained Concrete with Slag Cement as a Partial Replacement of OPC with Dolomite Aggregate.
AOFSD.....	Air Entrained Concrete with Fly Ash and Slag Cement as a Partial Replacement of OPC with Dolomite Aggregate.

NLFSPC.....	Non-Latex Modified Fly Ash, Slag, Polypropylene Fiber, and Cellulose Micro-Type Fiber Reinforced Concrete.
LFSPC.....	Latex Modified Fly Ash, Slag, Polypropylene Fiber, and Cellulose Micro-Type Fiber Reinforced Concrete.
ALP.....	Air Entrained Limestone-Portland Cement Concrete.
AC30.....	Air Entrained C30 Type Concrete.
AC50.....	Air Entrained C50 Type Concrete.
AP.....	Air Entrained Paste.
ACCA.....	Air Entraining with Curing in Air.
ACW.....	Air Entraining with Curing in Water.
AAC.....	Alkali Aluminosilicate Cement Concrete.
AAAC.....	Air Entrained Alkali Aluminosilicate Cement Concrete.
FC.....	Fly Ash Concrete.
FA.....	Fly Ash.
HPC.....	High-Performance Concrete
NCW.....	Normal Concrete with Curing in Water.
SF.....	Silica Fume.
Salt A.....	80% NaCl + 20% CaCl ₂ .
Salt B.....	70% NaCl + 25% MgCl ₂ + 5% CaCl ₂ .

LIST OF SYMBOLS

T_{σ}	Stress triaxiality.
E_T	Elastic modulus corresponding to a target temperature “T”.
$E_{20,SPR}$	Elastic modulus of un-notched test specimen at room temperature.
$E_{T,CN1}$	Elastic modulus of CN1 specimen corresponding to a target temperature “T”.
F_y	Yield strength corresponding to 0.2% strain offset.
$F_{y,T}$	Yield strength corresponding to a target temperature “T”.
$F_{y,20,SPR}$	Yield strength of un-notched test specimen at room temperature.
$F_{y,T,CN1}$	Yield strength of CN1 specimen corresponding to a target temperature “T”.
F_u	Ultimate tensile strength.
$F_{u,T}$	Ultimate tensile strength corresponding to a target temperature “T”.
$F_{u,20,SPR}$	Ultimate tensile strength of un-notched test specimen at room temperature.
$F_{u,T,CN1}$	Ultimate tensile strength of CN1 specimen corresponding to a target temperature “T”.
El	Ductility or elongation.
El_T	Ductility corresponding to a target temperature “T”.
$El_{20,SPR}$	Ductility of un-notched test specimen at room temperature.
$El_{T,CN1}$	Ductility of CN1 specimen corresponding to a target temperature “T”.
$T_{\sigma,max}^i$	Maximum initial stress triaxiality.
T_{avg}^i	Average initial stress triaxiality.

T_{avg}^u	Average stress triaxiality evaluated at strain corresponding to ultimate load.
σ_y	Average yield strength corresponding to 0.2% strain offset.
σ_u	Average ultimate tensile strength.
Fe_3C	Iron carbide.
SiC	Silicon carbide.
$\alpha-Fe$	Ferrite.
$\gamma-Fe$	Austenite.
N_f	Free nitrogen content.
S_p	Pearlite spacing in micrometers.
d_α	Ferrite grain size in millimeters.
g_F	Ferrite grain size in micrometers.
c_p	Pearlite colony size in micrometers.
θ_c	Contact angle.
R_a	Roughness average.
R_q	Root mean square roughness.
R_z	Mean surface depth.
R_t	Maximum peak to valley height.
$\alpha-FeOOH$	Goethite structure.
$\gamma-FeOOH$	Lepidocrocite structure.
γ_s	Surface free energy of solids.
γ_l	Surface tension of liquids.
γ_{ls}	Interfacial tension between solid and liquid surface.
$NaCl$	Sodium chloride.

$CaCl_2$	Calcium chloride.
$MgCl_2$	Magnesium chloride.
CH_3COOK	Potassium acetate.
CH_3COONa	Sodium acetate.
$CaMg_2(CH_3COO)_6$	Calcium magnesium acetate.
$KHCO_2$	Potassium formate.
$FeCl_2$	Ferrous chloride.
$NaOH$	Sodium hydroxide.
E_{corr}	Corrosion potential.
E_{pit}	Pitting potential.
i_{corr}	Corrosion current density.
β_a	Anodic Tafel slope.
β_c	Cathodic Tafel slope.
i_{corr}^o	Corrosion current density in the absence of corrosion inhibitor.
i_{corr}^{inh}	Corrosion current density in the presence of corrosion inhibitor.
ρ	Density of steel.
n_i	Valence of the <i>i</i> th element of the steel alloy.
f_i	Fraction of the <i>i</i> th element of the steel alloy.
W_i	Atomic weight of the <i>i</i> th element of the steel alloy.
C_{inh}	Corrosion inhibitor concentration.
K_{ads}	Standard adsorption equilibrium constant.
ΔG_{ads}^o	Standard free energy of adsorption.
R	Universal gas constant.

$[EMIM][AlCl_4]$	1-ethyl-3-methylimidazolium tetrachloroaluminate.
$[BMIM][PF_6]$	1-butyl-3-methylimidazolium hexafluorophosphate.
$[EMIM][BF_4]$	1-ethyl-3-methylimidazolium tetrafluoroborate.
$[HMIM][Br]$	1-hexyl-3-methylimidazolium bromide.
$[HMIM][PF_6]$	1-hexyl-3-methylimidazolium hexafluorophosphate.
$[BMIM][NTf_2]$	1-butyl-3-methylimidazolium bis(trifluoromethylsulfonyl)imide.
$[DPMIM][NTf_2]$	1,2-dimethyl-3-propylimidazolium bis(trifluoromethylsulfonyl)imide.
γ_{sv}^p	Polar component of surface free energy.
γ_{sv}^d	Dispersive component of surface free energy.
W_{sl}	Work of adhesion.
W_{ss}	Work of cohesion for the solid.
W_{ll}	Work of cohesion for the liquid.
θ_o	Apparent contact angle of a water droplet.
M	Torque.
η	Viscosity.
τ	Shear stress.
R_i	Radius of the swindle.
L	Length of the swindle.
ω	Angular velocity.

1. INTRODUCTION

This chapter discusses the background and motivation of the research conducted in this dissertation. The problem statement and goals are also discussed and the main research objectives of this dissertation are outlined. The chapter-wise organization of this dissertation is provided at the end of this chapter.

1.1. Background

Steel structures undergo a variety of damage mechanisms during service conditions that eventually lead to local or global failure of steel structures. This includes ductile or brittle fracture, fatigue damage, local and global buckling of members, corrosion damage, and metallurgical degradation of structural steel components. These damage modes can either initiate on their own or as a consequence of another damage mode. Among these damage and failure modes, corrosion damage is widely recognized as a major damage phenomenon that is encountered in almost all types of steel structures regardless of the loading and service conditions. Apart from the corrosion damage, metallurgical degradation is another damage mechanism that occurs when steel structures undergo microstructural changes due to exposure to elevated temperatures in fire accidents. Metallurgical degradation during fire damage leads to local and global buckling and instabilities and thus compromises the integrity of a steel structure.

Both fire damage and corrosion damage, although generally occurs non-simultaneously, have similar deteriorating repercussions for steel and reinforced concrete (RC) structures. Both fire and corrosion damage modes result in a significant degradation in material properties and cause progressive deterioration in steel and RC structures. The degradation in material properties compromises the functionality of the structural members either instantaneously (e.g. in the case of fire damage) or over an extended period (e.g. in the case of corrosion damage). This

eventually leads to a reduction in the overall load-carrying capacity of the members and may result in the progressive collapse of the structure. While the fire-induced damages require instantaneous repairs, the corrosion damage is linked to more frequent and costly maintenance throughout the service life of a steel or reinforced concrete (RC) structure. This dissertation aims to quantify the fire-induced material degradation in steel structures. This dissertation further aims to mitigate the corrosion damage in steel and reinforced concrete structures by utilizing agriculturally derived low-cost and non-toxic materials. The importance and implication of fire damage in steel structures and corrosion damage in steel and RC structures are discussed in the next section.

1.2. Fire Damage in Steel Structures

Structural steels that include mild steels, high strength steels (HSS), high strength low alloy steels (HSLA), and very high strength steels (VHSS) are among the most popularly used building materials in the United States (US). High thermal conductivity and low specific heat make structural steels vulnerable to fire accidents [1]. Fire accidents are very common and according to the National Fire Protection Agency (NFPA) 2020 report, one structural fire is reported every 64 seconds in the US [2]. In total, 481,500 structural fire accidents were reported in 2019 that accounted for 37% of total fire accidents in the US (see Figure 1.1) [2]. These structural fires resulted in 2,980 civilian deaths, 13,900 civilian injuries, and \$12.3 billion in property damages in 2019 alone. Figure 1.2 illustrates average losses per structural fire in US Dollars and the number of structural fire accidents reported in the US between 1978 and 2015.

Fire accidents are common in both buildings and bridges (see Figure 1.3). Bridge fire accidents in the past have resulted in severe damage and even collapse of entire bridge spans [3, 4]. In addition to arson and wildfires, bridge fires are commonly caused by vehicular accidents

that usually involve trucks and tankers carrying highly flammable liquids or gas fuels [4, 5]. A survey conducted by the New York Department of Transportation (NYDOT) in 2008 revealed that fire accidents caused nearly three times more bridge collapses when compared to earthquakes, which highlights the high incidence rate of bridge fire accidents [6]. When compared to steel buildings, steel bridges are particularly vulnerable to fire hazards due to the lack of fire protection [7, 8]. High strength low alloy (HSLA) steels are commonly used in the construction of bridges due to their conformity to ASTM A709 bridge steel specifications [9, 10]. Among HSLA steels, ASTM A572 Gr. 50 [11] has become the primary choice of steel grade for the construction of bridges due to its improved strength, ductility, and weldability characteristics that result in increased structural efficiency [9]. Despite excellent mechanical properties, HSLA structural steels remain vulnerable to degradation in mechanical properties when subjected to fires for extended durations due to their high conductivity and low specific heat. Recent fire accidents in bridges [12, 13] have further highlighted the importance of understanding the behavior of ASTM A572 and other structural steels during fire and post-fire conditions.

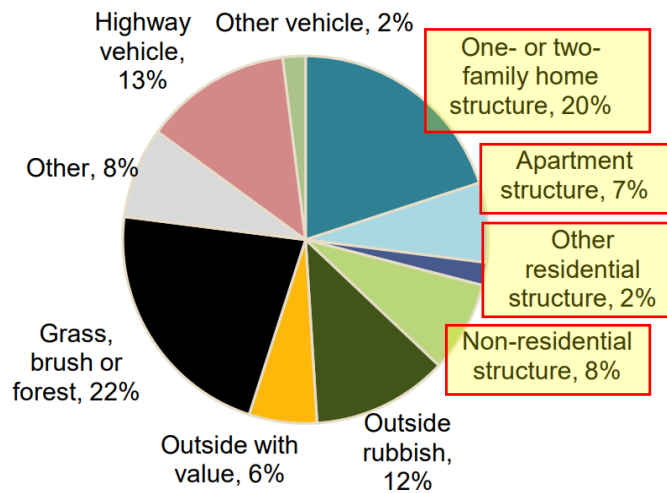


Figure 1.1. Structural fires in the U.S. (Source: NFPA 2020).

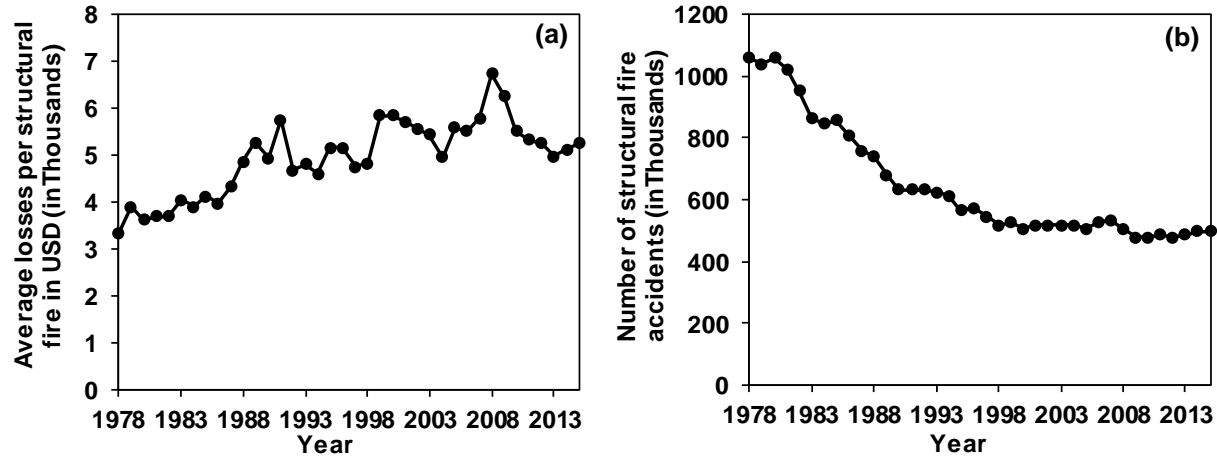


Figure 1.2. Fire statistics in the United States (1978-2015): (a) average structural fire losses and (b) number of structural fire accidents.



FutureHAUS lab, Virginia (2017)
(Credit: The Roanoke Star News)



Railroad bridge fire, Pennsylvania (2018)
(Source: Fox News)



Plasco building, Tehran (2017)
(Credit: Antonio Bilotta)



Windsor Tower, Madrid (2005)
(Credit: New Steel Construction)

Figure 1.3. Fire accidents in buildings and bridges.

1.3. Corrosion Damage in Steel and RC Structures

Corrosion is widely recognized as a primary deterioration mechanism in steel and reinforced concrete (RC) structures. Corrosion-induced damage poses a significant threat to the safety and integrity of both inland and offshore infrastructure. Corrosion-induced degradation in transportation infrastructure is largely driven by deicers-supplied chloride ions that initiate and accelerate corrosion processes. The U.S. has approximately 617,000 bridges and almost 42% of these bridges are 50 years or older. Around 9% of bridges in the U.S. are deemed structurally deficient whereas 1 in 3 bridges in the U.S. requires repair or replacement (ASCE 2021 Infrastructure Card). Corrosion remains one of the primary causes of deterioration and structural deficiency in older bridges. According to one study, about 70-90% of the premature damages in RC structures are attributed to corrosion. Some examples of deicer-induced corrosion damage in RC structures in the U.S. Midwest region are provided in Figure 1.4. Many studies, including a survey (see Figure 1.5), have pointed out corrosion as one of the main deterioration mechanisms that lead to a reduction in functionality and service life of metallic support bearings in bridges, which result in frequent maintenance and repairs. The corrosion problem in metallic support bearings is further exacerbated by exposure to deicing salts, rainwater, ineffective lubrication, excretes from animals, and leakages in the superstructure that allow the flow of deicing salts, dirt, and rainwater towards the bearings. The direct maintenance and replacement cost of bearings accounts for about 7% of the entire bridge maintenance budget. The annual direct cost of infrastructure corrosion in the U.S. is estimated to be \$22.6 billion, which includes \$13.6 billion of bridge corrosion. The indirect annual cost of corrosion-incurred traffic delays and loss of productivity is estimated to be 10 times higher than the direct cost of corrosion. Americans lost 6.9 billion hours and 3.1 billion gallons of fuel due to traffic delays resulting in a cumulative

loss of \$160 billion in 2014 alone [14]. The steel structures present along the pavements and the automobiles undergo higher corrosion in the presence of chloride ions in the surrounding environment. In 2010, the annual cost of automobile corrosion due to deicing salt alone was estimated to be \$11.7 billion [15]. Every ton of deicing salt applied on pavements is estimated to cost damages ranging from \$803 to \$3,341/ton to transportation infrastructure, automobiles, and environment [16].

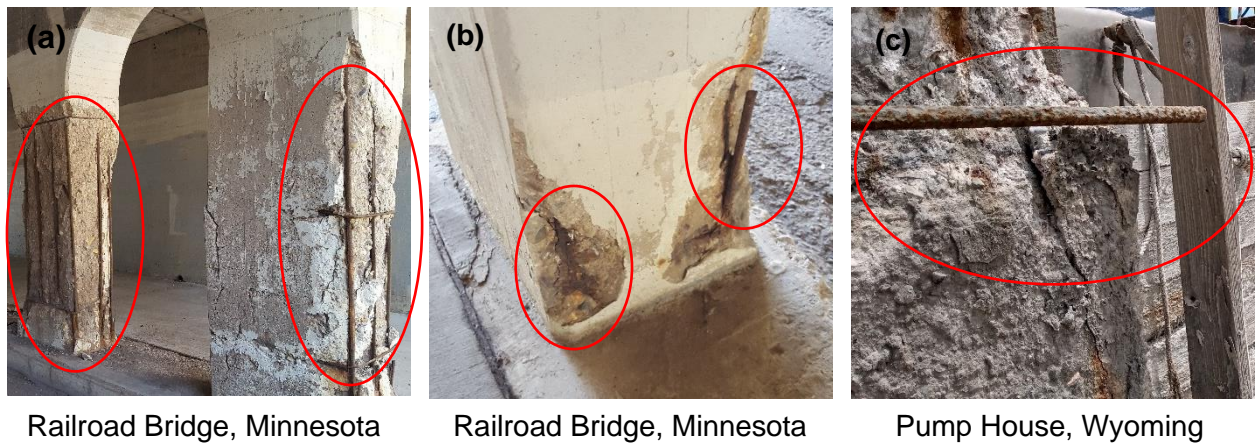


Figure 1.4. Examples of corroded reinforced concrete structures in the U.S. Midwest region: (a,b) corroded rebars, excessive delamination, and spalling in the RC columns of a railroad bridge, and (c) delamination, spalling and corroded rebar in a pump house in a powerhouse.

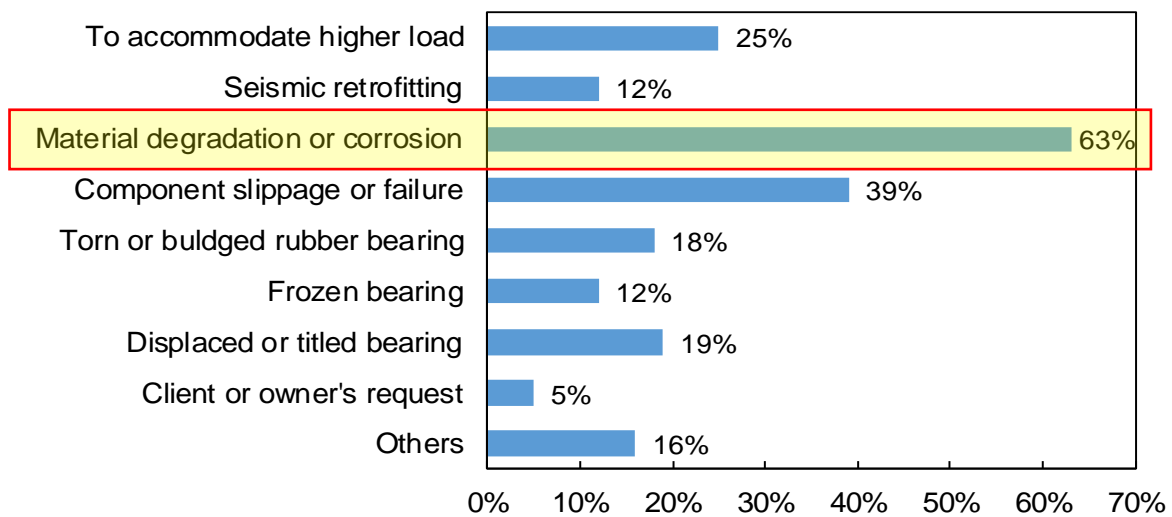


Figure 1.5. Bridge bearing failure reasons.

The corrosion damage in steel and RC structures is manifested in the form of a reduction in flexural and shear capacities of the members and connections, stress concentrations, and brittle fracture failure of components due to localized corrosion. Corrosion deterioration induces progressive weakening of structure over time, diminishing safety levels, and an overall reduction in the capacity and functionality of the structure. In the past, damage due to corrosion has resulted in severe damage and even collapse of both inland and offshore structures causing huge loss of life and property [17–20]. According to the Pipeline and Hazardous Materials Safety Administration (PHMSA) statistics, about 17% of pipeline accidents that occurred in the United States in the past 20 years are caused by corrosion-induced failures [21]. Corrosion is recognized as one of the primary contributing factors in 20% of all refinery accidents that occurred in European Union countries in the past 30 years [18]. In the aviation industry, over 20% of accidents that resulted in human injury are caused by corrosion failures [22]. The total cost of corrosion-related damages in 2016 is estimated to be 2.5 trillion USD globally [23]. The United States [24] and other major economies [22] regularly spend huge amounts of money on repairs and maintenance associated with corrosion damages.

Corrosion initiation in steel requires the steel surface to be covered with water or moisture, which can serve as an electrolyte and facilitate the migration of ions [25]. The moisture content that is needed to complete the corrosion reactions can be supplied by rain, fog, or relative humidity of the environment [26]. Even in the absence of deicers, the corrosion reactions can proceed at a slow rate given the above requirements are fulfilled and there is a certain critical level of humidity in the environment [27]. When deicers are applied on the pavements, the salt particles get deposited on steel structures such as bridges that are present in the vicinity. These salt particles affect the rate of corrosion in steel in numerous ways. Firstly, due to the

hygroscopic nature of salts, they absorb moisture from the air and hence the corrosion reactions proceed even at relatively lower humidity levels. Secondly, the presence of chloride ions increases the conductivity of water and hence results in faster corrosion rates. Thirdly, chloride ions can deteriorate the protective oxide layer that might be present on the surface of some steels [27]. All these factors lead to an increase in the rate of corrosion and hence faster deterioration of steels. When compared to granular salt deicers, salt brines are observed to be even more corrosive [28]. The application of pavement deicers typically causes corrosion in bridge decks, steel bridges, and automobiles, as illustrated in Figure 1.6. Apart from environmental exposure conditions (humidity, temperature, and presence of chloride or other corrosion accelerating ions), the corrosion rates are also influenced by the surface characteristics of the steel (such as surface roughness that can render the surface of the steel as hydrophilic or hydrophobic) and the metallurgical heterogeneities (such as the presence of vacancies and impurities in the microstructure, and distribution of grain boundaries), as depicted in Figure 1.7.

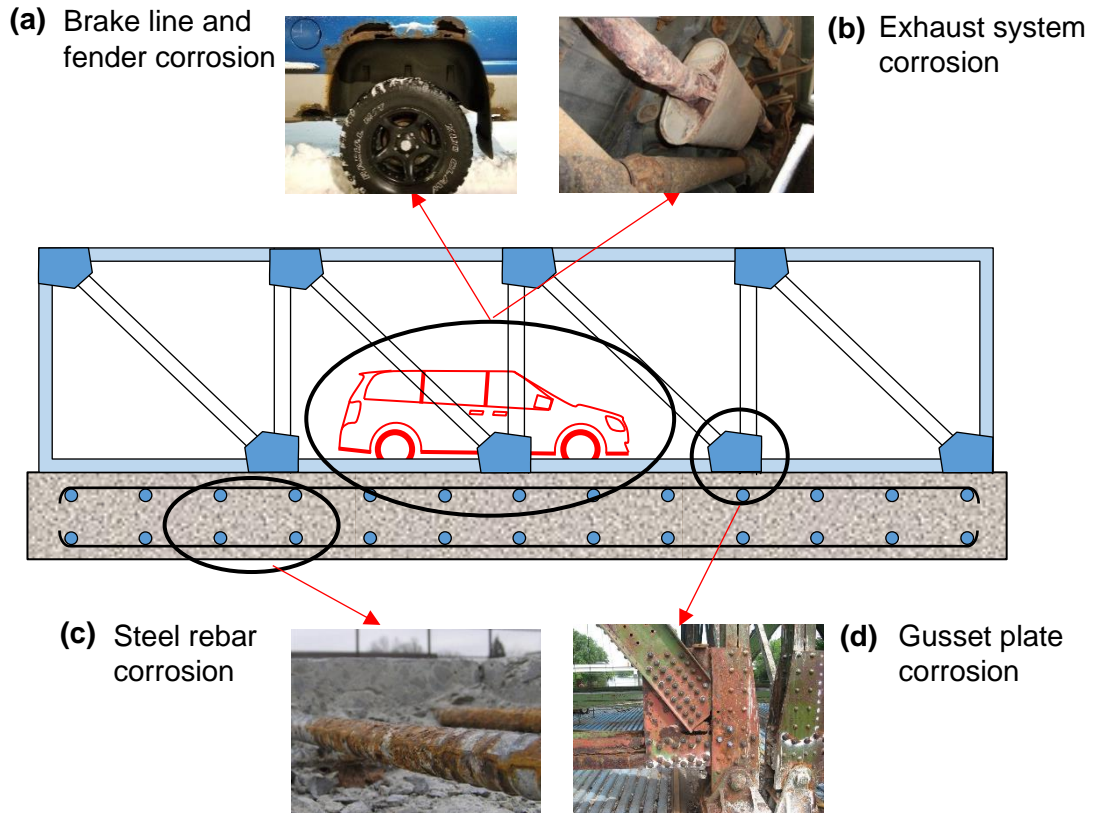


Figure 1.6. Typical corrosion damages observed in the transportation infrastructure: (a) brake line and fender corrosion, (b) exhaust system corrosion [29], (c) steel rebar corrosion [30], and (d) gusset plate corrosion [31].

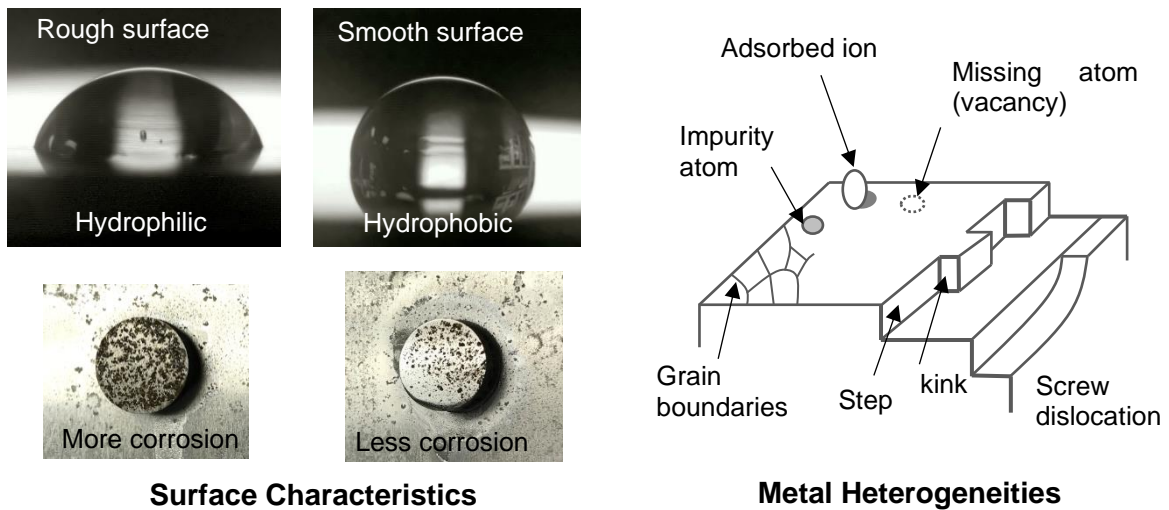


Figure 1.7. Factors affecting corrosion rates in structural steels.

1.4. Existing Literature

This section briefly summarizes the goals and results of the existing literature that addresses the fire damage in steel structures and corrosion damage in steel and RC structures. In the case of fire damage in steel structures, the state-of-the-art review presented in the next section mostly focuses on understanding the in-fire and post-fire mechanical behavior of structural steels. It further explains the current approaches that are used for evaluating post-fire damage in structural steels in terms of loss in mechanical properties. The corrosion damage review section aims to identify the most common corrosion mitigation techniques that are currently used in the steel and RC construction industry. The limitations of the existing literature and research needs are discussed in the subsequent sections.

1.4.1. Fire-Damage in Steel Structures: In-Fire Damage in Structural Steels

The in-fire damage in structural steels is usually quantified in terms of loss in mechanical properties of structural steels. In recent years, a significant amount of research has been conducted to investigate the mechanical properties of various types of structural steels during fire. The in-fire mechanical properties of structural steels can help in designing a steel structure that can provide the intended performance in a fire accident. Specifically, in-fire mechanical properties of structural steels are required in the performance-based fire design of steel structures. To this end, researchers have investigated the in-fire properties of mild steels and high strength low alloy steels and have proposed residual factors that can be used to estimate the in-fire mechanical properties of structural steels [32-41]. Moreover, current design standards and codes such as AISC [42], ASCE [43], BS5950 [44], AS 4100 [45], EC3 [46] and CECS200 [47] have specified residual factors for estimating elevated temperature mechanical properties of structural steels (see Figure 1.8).

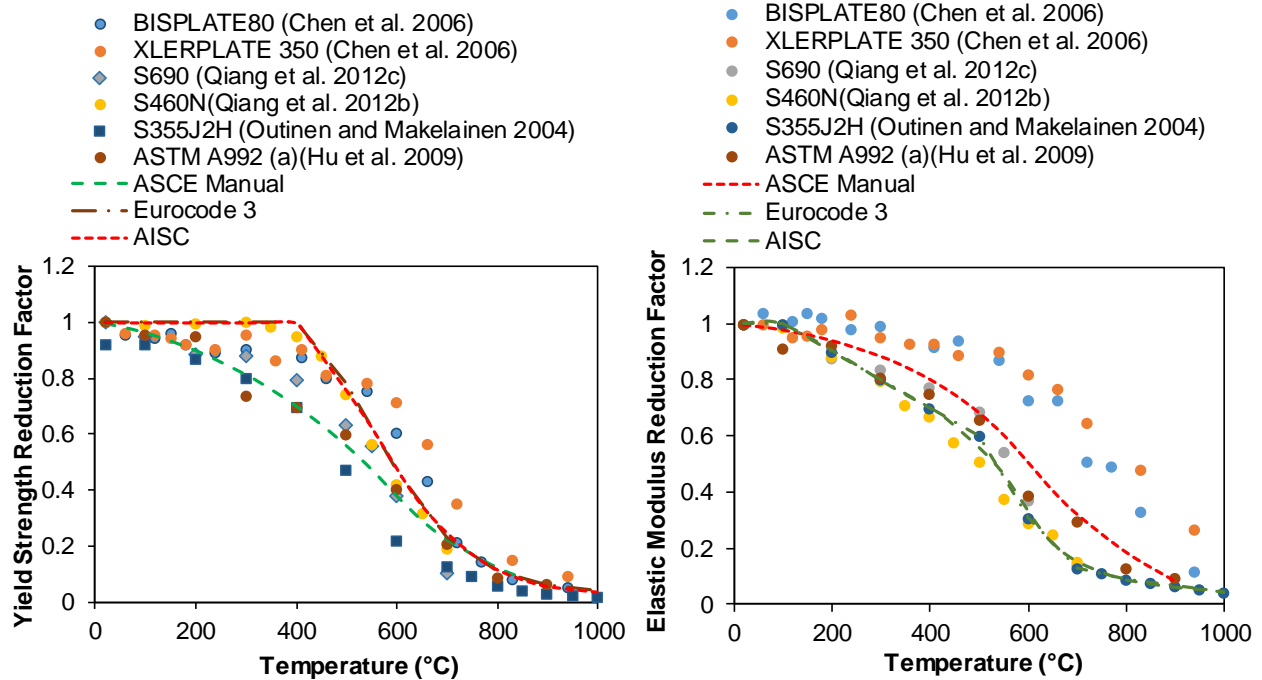


Figure 1.8. Elevated temperature mechanical properties residual factors for structural steels.

1.4.2. Fire-Damage in Steel Structures: Post-Fire Damage in Structural Steels

Steel members may experience severe degradation in strength properties due to exposure to elevated temperatures and hence may prevent immediate occupancy or use after fire accidents. Post-fire mechanical properties of structural steels are required to determine the usability of a steel structure after a fire accident [48]. In general, buildings codes allow the use of steel structures subjected to fire if there is no obvious distortion in steel members [49]. Post-fire performance of structural steels is critical in determining the residual capacity and subsequent usability of steel structures after the fire is extinguished. To this end, post-fire mechanical behavior has been reported for various structural steels that include mild steels (Q235, Q345 [50]), high strength steels (S355J2H [40], Grade 350, Grade 800 [51, 52], Q420 [50], Q460 [53], S460NL, S690QL [54], S690RQT [41], Q690 [55, 56], ASTM A992 [57], ASTM A572 [58], GLG460, GLG550, GLG650, GLG835 [59]), very high strength steels (S960QL [60], Grade 1200 [51, 52]), S690RQT [41], cold-formed steels [61, 62], cast steels (G20Mn5N, G20Mn5QT

[63]) and stainless steels [64, 65]. In these studies, the evaluation of the post-fire performance of structural steels is achieved by subjecting post-fire steel specimens to uniaxial tension tests. Typical test specimens were prepared and tested in accordance with ASTM E8 [66] or ISO standard (GB/T 228.1-2010 [67]) depending on the type of structural steel and the country in which the structural steel is used. For post-fire tests, specimens are first heated to a target temperature and maintained at the target temperature for a certain period to achieve uniform temperature throughout the test specimens. Specimens are then cooled down to room temperature using different cooling methods, namely: cooling-in-air (CIA), cooling-in-water (CIW), and cooling-in-blanket (CIB). In the case of CIA, the specimens are cooled by placing them outside the furnace or inside the furnace (with the furnace door kept open) after leaving the specimens at the target temperature for a specified time. In the case of CIW, the specimens are either placed in water or a water-jet is applied to cool down the specimens to room temperature. In the case of CIB, specimens are kept in a ceramic fiber blanket until they are cooled down to room temperature. Residual factors are computed based on one of three cooling methods, as discussed above. The residual factor is defined as the ratio of the value of a specific mechanical property after being cooled down from an elevated target temperature to its value at room temperature. Thus, a high residual factor indicates a lower level of degradation in a mechanical property and vice versa. The post-fire residual factors that are currently available in the literature are summarized in Figure 1.9.

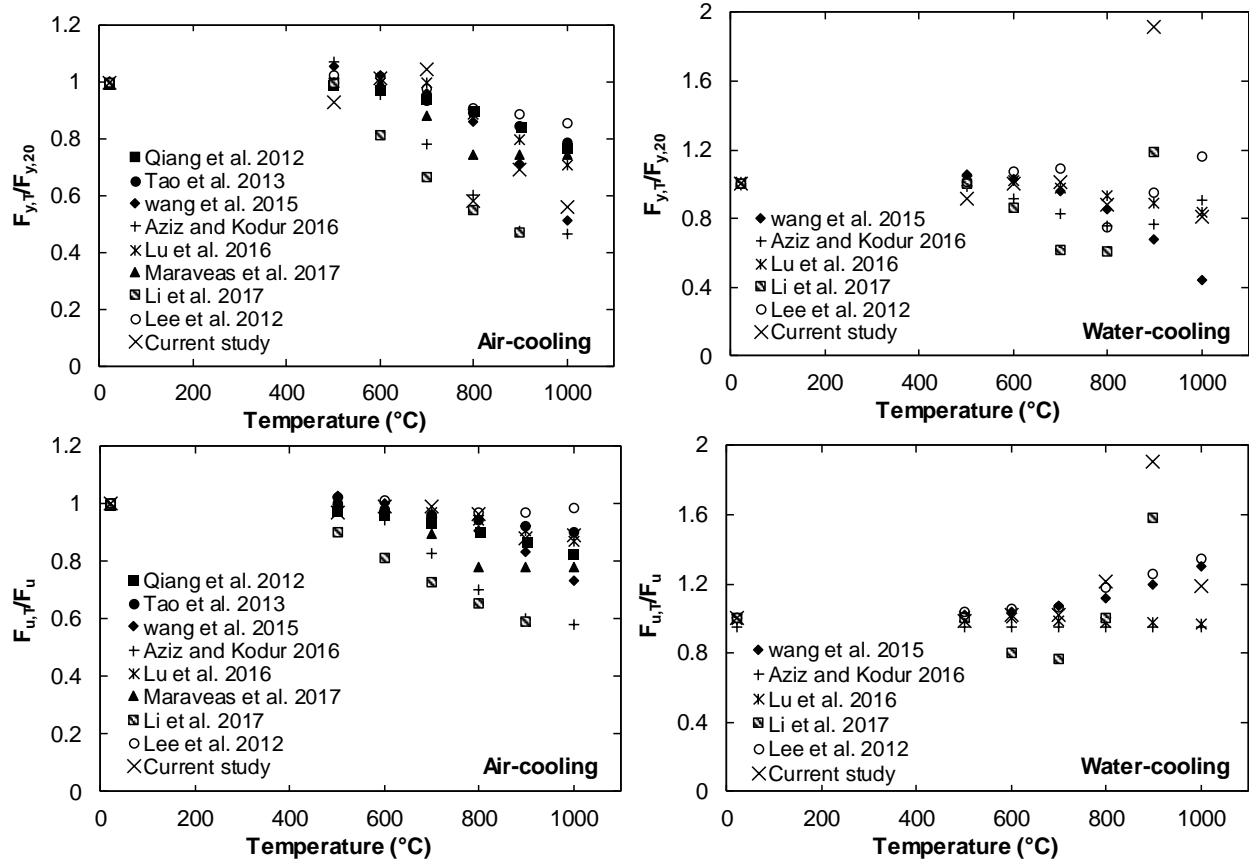


Figure 1.9. Post-fire mechanical properties residual factors for structural steels.

1.4.3. Corrosion Damage Mitigation in Steel and RC Structures

There are four common ways of combating corrosion in steel and RC structures and the choice of these techniques depending on the cost, the severity level of the corrosion, and the type of structure. Each of these techniques has implications for the design of new structures and the maintenance of old structures. These include 1) coating of steel surfaces with anti-corrosive coating materials, 2) the usage of corrosion inhibitors, 3) adopting corrosion allowance for a steel member in the design stage, and 4) using corrosion-resistance stainless steel or weathering steel. The most relevant existing literature on these corrosion mitigation techniques is discussed in the following subsections.

1.4.3.1. Coating of steel surfaces with corrosion-resistant coatings

The usage of coating materials that effectively separate the steel from the corrosive media is by far the most common corrosion protection technique in the construction industry. The rebar coating industry currently uses four types of coating technologies that are recognized by ASTM International and Concrete Reinforcing Steel Institute (CRSI). These include epoxy-coated rebars (ASTM A775, A884, A934), galvanized rebars (ASTM A767), dual-coated rebars (ASTM A1055), and vinyl-coated rebars (ASTM A933) [68]. Among these coatings, epoxy-coating is most widely used in North America. Approximately 10% of all reinforcing bars in North America are estimated to be coated. Similarly, around 74,097 bridge decks use epoxy-coated rebars whereas 1,072 bridge decks utilized galvanized rebars. Galvanized steels commonly employ a zinc layer which is deposited either using hot dipping, electroplating, or spraying and usually conforms to ASTM A767. Recently, epoxy coatings and bio-based coatings that incorporate additives such as graphene [69], carbon nanotubes [70], silica [71], and nano clay [72] have been investigated for their corrosion protection performance in rebars and structural steels.

1.4.3.2. Usage of corrosion inhibitors

Corrosion inhibitors are commonly used to protect rebars and structural steels against chloride-induced corrosion. Corrosion inhibitors are added to the corrosive media (e.g. salt brine deicers) in small quantities and they inhibit corrosion through the adsorption mechanism. Corrosion inhibitors are commonly categorized as 1) inorganic inhibitors (or passivators), 2) organic inhibitors, and 3) vapor-phase inhibitors [73]. The choice of using either organic or inorganic inhibitors is influenced by many factors such as the cost of inhibitor, toxicity, efficiency, etc. In recent years, research efforts have intensified to develop low-cost

environment-friendly organic inhibitors. To this end, various compounds have been developed and tested for their corrosion inhibition performance which includes agriculture-based products, plant extracts, and different ionic liquids among other compounds [74-78].

The corrosion inhibitors that are commonly used in RC structures can be divided into two categories: 1) admixed corrosion inhibitors, and 2) migratory corrosion inhibitors. Admixed corrosion inhibitors are used as an additive in fresh concrete and they help protect the rebar from corrosion by delaying the corrosion inhibition and propagation phases and stabilizing the passive layer present on the steel surface. On the other hand, migratory corrosion inhibitors are used in hardened concrete and they serve to re-passivate the rebar. The most commonly used corrosion inhibitors in concrete include nitrite-based inhibitors (such as calcium nitrite), amines, phosphate-based inhibitors (such as sodium monofluoro phosphate), and other organic inhibitors. Recently, ionic liquids have been explored as potential inhibitor candidates for RC materials.

1.4.3.3. Corrosion allowance for structural steels

Corrosion allowance refers to the additional thickness of sections included during the design stage of steel members for the anticipated corrosion thickness loss in the members. If the corrosion rates are known for the service life of a steel or RC bridge, the corrosion allowance (amount of section thickness loss) can be used to accommodate the future thickness loss due to corrosion. Adopting corrosion allowance is particularly useful in the case of weathering steels wherein uniform corrosion is expected [79]. For this purpose, usually, the thickness of members is increased at the design stage, e.g., for a 38 mm weathering steel, a 0.8 mm increase in thickness can be adopted based on stress calculations [79].

1.4.3.4. Corrosion-resistant metallic and polymeric materials

Corrosion-resistance metallic materials can be used to protect components from corrosion in highly corrosive environments. To this end, stainless steels have been used in many mechanical and biomedical applications (such as stents and dental implants) due to their superior corrosion resistance owing to the presence of high chromium content in the stainless steels. Using stainless steel instead of low carbon structural and reinforcing steels is another way of protecting infrastructure from corrosion. Some studies have explored the usage of stainless structural steel in structural applications. Currently, the American Institute of Steel Construction (AISC) is working towards the development of guidelines for fabrication, erection, and design of stainless structural members. Apart from stainless steel, other materials that have been investigated in the structural application include carbon nanotubes and polymeric materials.

1.5. Limitations of Existing Literature

As noticed from the literature review provided in the previous sections, a significant amount of research work has been conducted to evaluate the fire damage in steel structures in terms of loss in post-fire mechanical properties. Moreover, several corrosion mitigation technologies are available for preventing and mitigating corrosion in steel and RC structures. While the existing literature significantly improved our understanding of fire and corrosion damage, many limitations need to be addressed. The limitations associated with the usage of existing post-fire residual factors and post-fire mechanical properties prediction approaches are discussed in the next section. Moreover, the limitations that exist with the usage of current corrosion prevention techniques in steel and RC structures are also discussed in the next section.

1.5.1. Stress Concentration in Steel Structures is Ignored

The accuracy and reliability of post-fire residual factors are vital when estimating the residual capacity of steel structures for post-fire use. Although residual factors for elastic modulus, yield strength, ultimate tensile strength, and ductility of various structural steels exist in the literature, current post-fire residual factors are based on exposure to elevated temperatures alone and do not incorporate the influence of stress concentration, an important phenomenon that is frequently observed in steel members. Stress concentration in steel members usually results from pitting corrosion [80, 81] and other geometric discontinuities (e.g., welds, sharp corners, etc.) in steel members, as illustrated in Figure 1.10. Stress concentration can be quantified in terms of stress triaxiality (T_σ), which is defined as the ratio of hydrostatic stress to Von Mises stress. Higher stress triaxiality indicates a higher level of stress concentration. Studies conducted in the past have demonstrated that the presence of high stress triaxiality significantly influences the strength and ductility of structural steels [82, 83]. Moreover, stress concentration can lead to abrupt failure of steel components, as shown in Figure 1.11 wherein a steel girder suffered brittle failure due to the stress concentration generated by the presence of hole in the flange section.

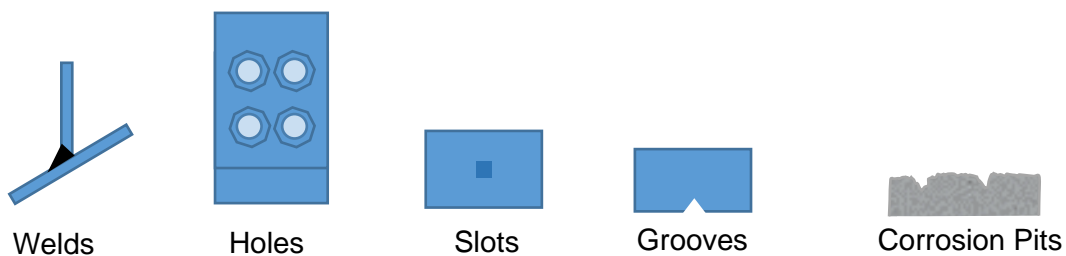


Figure 1.10. Sources of stress concentration in steel structures.

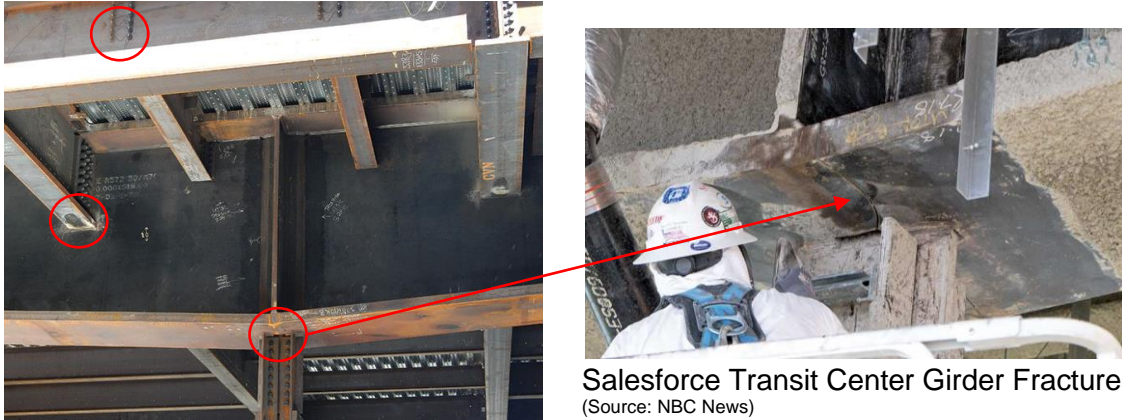


Figure 1.11. Stress concentration leading to failure of a steel girder.

1.5.2. Limitations of Current Post-Fire Approaches

Post-fire mechanical properties are important for evaluating the residual capacity of a steel structure after a fire accident. Owing to the importance of these properties in evaluating the performance of steel structures after the fire, extensive research has been carried out on structural steels worldwide (as discussed in Section 1.4.1 and Section 1.4.2) and as a result of these investigations, it has become possible to conveniently predict the mechanical properties of structural steels that are subjected to fire accidents as a function of elevated temperature. All the existing residual factors that are currently available in the literature require the temperature reached during a fire accident to be known. However, the temperatures developed during a fire accident are seldom known. Several approaches can be used for evaluating fire temperatures. The fire temperature values can be assessed from the melting of metallic materials (steels) in a fire accident. However, the melting temperatures of metallic materials are usually too high to reach in a fire accident. Another approach to determine the fire temperatures is to use the surface oxidation colors [84] (see Figure 1.12). Different oxide products are formed on steel surfaces at different fire temperatures and hence these colors can be used as an indication of a particular fire temperature. However, this approach is highly subjective. Moreover, the surface oxide colors

change rapidly due to ensuing corrosion that happens in steel members after extinguishing the fire. The smoke and burning colors further complicate achieving a stable oxide color on the steel surface. Finally, fire sensors can be used to aid in knowing the fire temperature values. However, the common fire sensors are only meant to sense high temperatures and do not provide the high temperatures that are reached during fire accidents. While sophisticated fire sensors are available, however, it is not practical to install costly fire sensors throughout a building or bridge. To summarize, in the absence of fire temperature, the existing post-fire residual factors could not be used for predicting post-fire mechanical properties of structural steels and subsequent usability of a fire-affected steel structure.

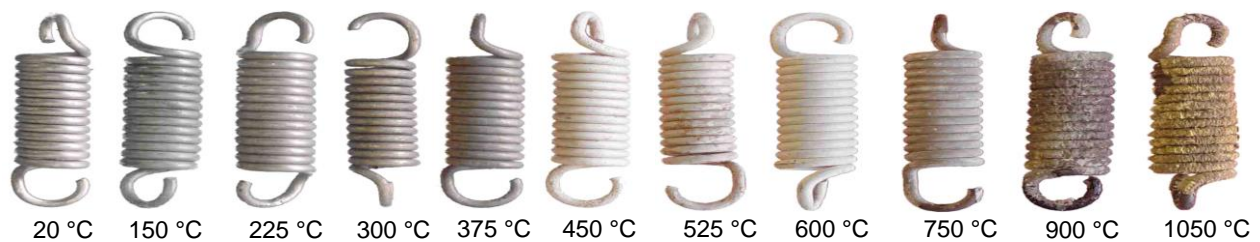


Figure 1.12. Surface oxide colors after exposure of steels to different elevated temperatures [84].

1.5.3. Limitations of Existing Corrosion Prevention Techniques in Steel and RC Structures

Each of the existing corrosion protection technology that is currently available for steel and RC bridges has limitations and negative implications for the design of new steel and RC structures and the maintenance of old structures. These limitations are listed below.

1. While the epoxy coatings are relatively inexpensive, there are three main disadvantages of using the currently available epoxy-coated rebars. First, epoxy coatings are prone to damage before placement in concrete. This major weakness of epoxy-coated rebars is now widely recognized in the construction industry. The selective damage in epoxy coated rebars can lead to localized corrosion in rebars instead of uniform corrosion, which could be more devastating for loaded rebar. Secondly, epoxy coatings reduce the

bond strength between concrete and rebars by 10 to 50% which reduces the composite action of a reinforcing bar in concrete. The reduction in bond strength of the epoxy-coated rebars, therefore, mandates the need of increasing the development length by up to 50% as per the American Concrete Institute (ACI) 318-14 specification. Similarly, American Associate of State Highway Officials (AASHTO) specifications for bridges require a 15-50% increase in the development length. Hence, one limitation of the epoxy coating is compensated by a drastic increase in the material cost. Thirdly, the epoxy coating materials are made of constituents that are declared carcinogenic by environmental protection agencies. The most commonly used epoxy coatings in the construction industry (fusion bonded epoxy (FBE) coatings) are highly toxic. The safety datasheet of the 3M-supplied FBE rebar coatings noted category 1A for carcinogenicity and category 2 for reproductive toxicity.

2. Apart from the epoxy-coated rebars, the galvanized rebars also have a fair share of disadvantages associated with their usage. In the presence of fresh concrete, the zinc layer of the galvanized coatings rapidly corrodes until the concrete gets hardened. This leads to a drastic reduction in the thickness of the galvanized coatings as well as an increase in the porosity of the concrete due to hydrogen evolution cathodic reactions [85]. To avoid this problem, ASTM A676 requires pretreatment of the galvanized rebars with chromate. The pretreatment inhibits chemical reactions between the fresh concrete and the zinc layer. However, the additional cost of pretreatment and the carcinogenic nature, and the environmental concerns of chromates are widely known which limits the usage of zinc-cladded galvanized rebars.

3. While many inorganic and organic inhibitors effectively inhibit corrosion of steel in corrosive media, their toxicity and cost limit their practical application. Many inorganic inhibitors have compounds (such as chromates and phosphates, etc.) that are toxic and are declared carcinogenic by environmental protection agencies [86, 87]. In recent years, research efforts have intensified to develop low-cost environment-friendly organic inhibitors. To this end, various compounds have been developed and tested for their corrosion inhibition performance that include agriculture-based products, plant extracts, and different ionic liquids among other compounds [74-78]. However, many of these products are either too expensive or cannot be produced in bulk scale for pavement deicing applications and rebars. The ionic liquids corrosion inhibitors that are increasingly being investigated for steels are too costly and impractical to use in steel and RC structures.
4. High initial dosages of admixed and migratory corrosion inhibitors are required to stabilize the rebar passivation layer and delay the initiation and propagation of chloride-induced corrosion. Such corrosion inhibitors are mostly effective in the early stage of usage and are no more effective once the chloride concentration in the concrete pore solution increases. Moreover, the negative impacts of admixed and migrating corrosion inhibitors on the properties of fresh and hardened concrete (e.g. increase in the hydration time, the interaction of corrosion inhibitors with the cement hydration products, and aggravation of the alkali-aggregate reactions, etc.) are well established. More importantly, many existing corrosion inhibitors are observed to reduce the compressive strength of concrete. To counter the negative effects of the corrosion inhibitors, further additives need to be added to the concrete which increases the cost of the concreting.

5. While stainless structural steels present an attractive alternative to combat corrosion, they are too costly to use in large-scale structures. Moreover, the American Institute of Steel Construction (AISC) has yet to approve standards for the design, fabrication, and erection of stainless structural steels, and thus their usage is limited by the absence of design standards for stainless steel structural members.
6. Using corrosion allowance at the steel design stage for corrosion protection requires that thickness loss of steel members over the entire service life of the structure be known. Currently, many empirical models exist in the literature predicting the mass/thickness loss. However, due to the complex nature of corrosion, many of these models are based on short-term corrosion tests that usually do not translate to long-term corrosion loss in steel structures. As a result, no unified corrosion thickness loss model exists for structural and reinforcing steels, and thus AISC, ACI, and AASHTO design codes do not provide guidance on corrosion allowance.

1.6. Problem Statement and Research Objectives

From the literature review, it is evident that significant efforts have been invested in understanding and quantifying the fire damage in steel structures in terms of loss in the post-fire mechanical properties. While these investigations have significantly advanced the state-of-the-art, two important questions remained to be answered in the post-fire damage in steel structures. First, the influence of stress concentrations that arise due to abrupt changes in structural geometry has yet to be addressed. Secondly, while post-fire residual factors are available in the literature for many kinds of structural steels, their reliable and accurate usage cannot be realized due to the absence of the primary variable (temperature) that is needed for predicting the post-fire mechanical properties of structural steels after fire accidents. Thirdly, most of the current

design codes do not provide post-fire residual factors for estimating the mechanical properties of structural steels after a fire accident. Only British Codes (BS5950) provides residual yield strength factors but they are only applicable for mild steels and they grossly overestimate the post-fire yield strength of structural steels that are commonly used in the construction industry.

While corrosion prevention technologies have advanced in other fields, the advancement in the construction industry is relatively incremental due to the large-scale nature of the steel and RC structures. It is evident from the literature review that new corrosion protection materials are needed that have adequate strength, minimal toxicity, and limited effect on the bond strength between the concrete and rebars. Due to the large-scale nature of RC structures, it is more economic and practical to reduce the corrosivity of the deicing materials to which RC and steel structures are frequently exposed rather than using standalone corrosion prevention technologies (such as admixed and migratory corrosion inhibitors). Finally, most of the existing corrosion inhibitors, though highly effective, cannot be used in RC structures as these inhibitors are either too expensive or cannot be produced in bulk-scale.

This dissertation aims to address these limitations. Specifically, this dissertation has three overarching goals. Firstly, it aims to understand the influence of stress concentration and cooling methods on the post-fire mechanical behavior of structural steels over a wide range of temperatures and thus obtain more accurate post-fire residual factors for commonly used structural steels. Secondly, it aims to understand the metallurgical aspects of the post-fire structural steels and develop a microstructural approach towards predicting the post-fire mechanical properties of structural steels that are commonly used in buildings and bridges. Lastly, this dissertation aims to develop a non-toxic and cost-effective solution for mitigating

chloride-induced corrosion in steel and RC structures. The specific objectives of this dissertation are as follows:

1. To determine the influence of stress concentration and fire-extinguishing methods on the post-fire mechanical behavior of structural steels.
2. To evaluate the post-fire mechanical behavior of structural steels from microstructure when fire temperature values are not known.
3. To investigate the effectiveness of steel surface modification techniques in mitigating the corrosion in structural steels.
4. To determine the effectiveness and optimal concentrations of corn-derived polyols for reducing the corrosivity of pavement deicing materials.
5. To investigate the influence of corn-derived corrosion inhibitors on the properties of cement materials.
6. To synthesize and evaluate the performance of soy protein-based coatings for mitigating corrosion in RC structures.

1.7. Organization of Dissertation

For achieving the objectives of this study, the research work is divided into two phases. The phase-1 of this dissertation focuses on post-fire damage in structural steels and it aims to achieve objective-1 and objective-2 of this dissertation. The research phase-2 focuses on developing corrosion mitigation techniques that are feasible for large-scale RC and steel structure applications. The research phase-2 aims to achieve objective-3, objective-4, objective-5, and objective-6 of this dissertation. Each research phase has further individual research tasks that are outline in the following dissertation chart (see Figure 1.13). The dissertation flowchart illustrates the research tasks that have already been completed and published, the research tasks

that are completed and are currently under peer-review, and the research tasks that are completed and the manuscript writing is currently in progress. The methodology associated with the individual research tasks is provided in the subsequent chapters. The research work conducted herein is summarized in peer-reviewed journal papers that are provided in the form of dissertation chapters.

Dissertation chapter-2, chapter-3, and chapter-4 are dedicated to objective-1 of this dissertation, which aims to investigate the influence of stress concentration and fire-extinguishing methods on post-fire mechanical properties of structural steels. Chapter-5 is focused on evaluating the post-fire mechanical behavior of structural steels from microstructure when fire temperature values are not known (objective-2). Chapter-6 and Chapter-8 summarize the investigations that are aimed at corrosion prevention through surface modification (objective-3). Chapter-7 discusses the efficacy of agriculturally-derived corrosion inhibitors in reducing the corrosivity of traditional deicing materials (objective-4). Chapter-9, Chapter-10, and Chapter-11 are dedicated to determining the impacts of agriculturally-derived corrosion inhibitors on the ice melting capacity of the traditional salt brine deicer, skid resistance of pavement, and properties of Portland cement mortar (objective-5). Chapter-12 discusses objective-6 which aims to synthesize bio-based coating material for mitigating corrosion in RC structures. The outcomes and scientific contributions of this dissertation, and the future directions are summarized in Chapter-13 of this dissertation.

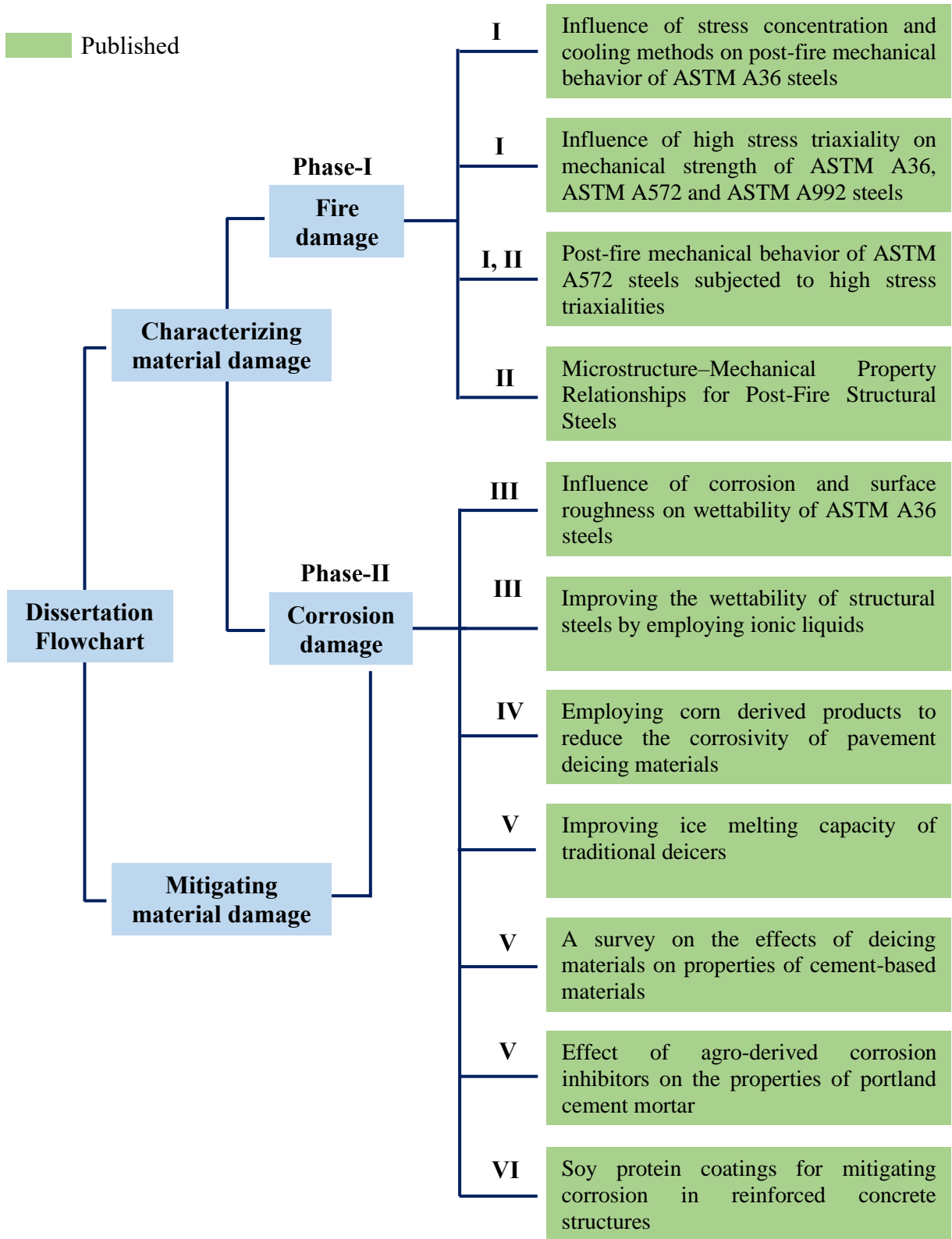


Figure 1.13. Dissertation flowchart.

1.8. References

- [1] V. Kodur, M. Dwaikat, R. Fike, High-Temperature Properties of Steel for Fire Resistance Modeling of Structures, *Journal of Materials in Civil Engineering*, 22 (2010) 423-434.
- [2] H.J. Haynes, Fire loss in the United States during 2015, National Fire Protection Association. Fire Analysis and Research Division, 2016.
- [3] M. Garlock, I. Paya-Zaforteza, V. Kodur, L. Gu, Fire hazard in bridges: Review, assessment and repair strategies, *Engineering Structures*, 35 (2012) 89-98.
- [4] V. Kodur, L. Gu, M. Garlock, Review and assessment of fire hazard in bridges, *Transportation Research Record: Journal of the Transportation Research Board*, (2010) 23-29.
- [5] G. Peris-Sayol, I. Paya-Zaforteza, S. Balasch-Parisi, J. Alós-Moya, Detailed Analysis of the Causes of Bridge Fires and Their Associated Damage Levels, *Journal of Performance of Constructed Facilities*, 31 (2017) 04016108.
- [6] V. Kodur, L. Gu, M.E.M. Garlock, Review and Assessment of Fire Hazard in Bridges, *Transportation Research Record*, 2172 (2010) 23-29.
- [7] Fire Protection of Steel Bridges and the Case of the MacArthur Maze Fire Collapse, in: TCLEE 2009.
- [8] I. Payá-Zaforteza, M.E.M. Garlock, A numerical investigation on the fire response of a steel girder bridge, *Journal of Constructional Steel Research*, 75 (2012) 93-103.
- [9] W.J. Wright, Steel bridge design handbook: Bridge steels and their mechanical properties, in, Federal Highway Administration, Report # FHWA-IF-12-052 - Vol. 1, 2012.

- [10] ASTM International, ASTM A709/A709M Standard Specification for Structural Steel for Bridges, in, ASTM International, West Conshohocken, PA, 2017.
- [11] ASTM International, Standard Specification for High-Strength Low-Alloy Columbium-Vanadium Structural Steel, in, ASTM International, West Conshohocken, PA, 2015.
- [12] B. Jansen, Atlanta bridge collapse shows how fire defeats concrete, steel, in: USA Today, March 31, 2017.
- [13] L. Blest, Fire continues to burn on Enola Low Grade Trail bridge; Cause still under investigation, in: LancasterOnline, April 13, 2018.
- [14] ASCE, America's Infrastructure Report Card 2017, American Society of Civil Engineers, (2019).
- [15] D.L. Kelting, Review of effects and costs of road de-icing with recommendations for winter road management in the Adirondack Park, Report No. AWI2010-01, Adirondack Watershed Institute, (2010).
- [16] X. Shi, L. Fay, Z. Yang, T.A. Nguyen, Y. Liu, Corrosion of deicers to metals in transportation infrastructure: Introduction and recent developments, Corrosion Reviews, 27 (2009) 23-52.
- [17] P.R. Roberge, Corrosion Engineering, McGraw-Hill New York, NY, USA., 2008.
- [18] M.H. Wood, A.V. Arellano, L. Van Wij, Corrosion-Related Accidents in Petroleum Refineries: Lessons learned from accidents in EU and OECD countries, JRC Sci. Policy Reports, EUR. 26331 (2013).
- [19] J. Bhandari, F. Khan, R. Abbassi, V. Garaniya, R. Ojeda, Modelling of pitting corrosion in marine and offshore steel structures—A technical review, J. Loss Prev. Process Ind. 37 (2015) 39–62.

- [20] R.W. Poston, J.S. West, Investigation of the Charlotte Motor Speedway Bridge Collapse, in: Struct. Congr., ASCE, 2005.
- [21] L. Naik, Dayakar, R. Kiran, Data Mining and Equi-Accident Zones for US Pipeline Accidents, J. Loss Prev. Process Ind. (Manuscript under Rev. (2017)).
- [22] S. Lv, Q. Mu, X. Gao, T.S. Srivatsan, Influence of morphology of corrosion on fracture initiation in an aluminum alloy, Mater. Des. 45 (2013) 96–102.
- [23] G. Koch, J. Varney, N. Thompson, O. Moghissi, M. Gould, J. Payer, International Measures of Prevention, Application, and Economics of Corrosion Technologies Study, NACE Int. IMPACT Rep. (2016).
- [24] E. Ghali, V.S. Sastri, M. Elboudjaini, Corrosion prevention and protection: practical solutions, John Wiley and Sons, 2007.
- [25] E. McCafferty, Introduction to Corrosion Science, Springer Science & Business Media, 2010.
- [26] P.A. Schweitzer, Fundamentals of corrosion: mechanisms, causes, and preventative methods, CRC press, 2009.
- [27] Z. Ahmad, E. Institution of Chemical, Principles of corrosion engineering and corrosion control, (2006).
- [28] W.A. Nixon, J. Xiong, Investigation of materials for the reduction and prevention of corrosion on highway maintenance equipment, IIHR Technical Report No. 472, Iowa Highway Research Board, (2009).
- [29] X. Shi, Y. Li, S. Jungwirth, Y. Fang, N. Seeley, E. Jackson, Identification and laboratory assessment of best practices to protect DOT equipment from the corrosive effect of chemical deicers, in, Washington State Department of Transportation, 2012.

- [30] N. Gucunski, A. Maher, B. Basily, H. La, R. Lim, H. Parvardeh, S. Kee, Robotic platform robot for condition assessment of concrete bridge decks using multiple nde technologies, HDKBR INFO Magazine, 3 (2013) 5-12.
- [31] R.E. Mateega, Rehabilitation of Historic Holmes Street Bridge, in: STRUCTURE Magazine, 2013, pp. 3.
- [32] E.M. Aziz, Response of fire exposed steel bridge girders, in, Michigan State University, Ann Arbor, 2015, pp. 321.
- [33] V. Kodur, M. Dwaikat, R. Fike, High-Temperature Properties of Steel for Fire Resistance Modeling of Structures, Journal of Materials in Civil Engineering, 22 (2010) 423-434.
- [34] V. Kodur, E. Aziz, M. Dwaikat, Evaluating Fire Resistance of Steel Girders in Bridges, Journal of Bridge Engineering, 18 (2013) 633-643.
- [35] G. Hu, M.A. Morovat, J. Lee, E. Schell, Elevated Temperature Properties of ASTM A992 Steel, in: Structures Congress 2009, American Society of Civil Engineers, 2009, pp. 1067-1076.
- [36] W. Cai, M.A. Morovat, M.D. Engelhardt, True stress-strain curves for ASTM A992 steel for fracture simulation at elevated temperatures, Journal of Constructional Steel Research, 139 (2017) 272-279.
- [37] J. Lee, M.A. Morovat, G. Hu, M.D. Engelhardt, E.M. Taleff, Experimental investigation of mechanical properties of ASTM A992 steel at elevated temperatures, Engineering Journal-American Institute of Steel Construction, 50 (2013) 249-272.
- [38] M.A. Morovat, A.H.E. Ghor, E.G. Hantouche, Time-Dependent Response of Flush Endplate Connections to Fire Temperatures, Journal of Structural Engineering, 144 (2018) 04018023.

- [39] M. Memari, H. Mahmoud, B. Ellingwood, Stability of Steel Columns Subjected to Earthquake and Fire Loads, *Journal of Structural Engineering*, 144 (2018) 04017173.
- [40] J. Outinen, P. Mäkeläinen, Mechanical properties of structural steel at elevated temperatures and after cooling down, *Fire and materials*, 28 (2004) 237-251.
- [41] S. Chiew, M. Zhao, C. Lee, Mechanical properties of heat-treated high strength steel under fire/post-fire conditions, *Journal of Constructional Steel Research*, 98 (2014) 12-19.
- [42] American Institute of Steel Construction (AISC), AISC 360-05-specification for structural steel buildings, ANSI/AISC, Chicago, (2005).
- [43] American Society of Civil Engineers (ASCE), Structural Fire Protection, ASCE committee on fire protection, Manual No. 78, (1992).
- [44] British Standards Institute (BSI), Structural use of steelwork in building, Part 8: Code of practice for fire resistant design, British Standard Institution, (1990).
- [45] A.S. AS, AS4100: Steel structures, Standards Australia, NSW, Australia, (1998).
- [46] European Committee for Standardization, EN 1993-1-2, Eurocode 3: Design of Steel Structures-Part 1-2: General rules structural fire design, in, Bruxelles, Belgique, 2005.
- [47] China Association for Engineering Construction Standardization CECS200, Chinese technical code for fire safety of steel structure in buildings, in, China Plan Press, Beijing, China, 2006.
- [48] D. Glassman Jonathan, E.M. Garlock Maria, Post-Fire Strength Assessment of Steel Bridges Based on Residual Out-of-Plane Web Deformations, Structures Congress 2014.
- [49] R.H. Tide, Integrity of structural steel after exposure to fire, *Engineering Journal-American Institute of Steel Construction*, 35 (1998) 26-38.

- [50] J. Lu, H. Liu, Z. Chen, X. Liao, Experimental investigation into the post-fire mechanical properties of hot-rolled and cold-formed steels, *Journal of Constructional Steel Research*, 121 (2016) 291-310.
- [51] F. Azhari, A. Heidarpour, X.-L. Zhao, C.R. Hutchinson, Mechanical properties of ultra-high strength (Grade 1200) steel tubes under cooling phase of a fire: an experimental investigation, *Construction and Building Materials*, 93 (2015) 841-850.
- [52] F. Azhari, A. Heidarpour, X.-L. Zhao, C.R. Hutchinson, Post-fire mechanical response of ultra-high strength (Grade 1200) steel under high temperatures: Linking thermal stability and microstructure, *Thin-Walled Structures*, 119 (2017) 114-125.
- [53] W. Wang, T. Liu, J. Liu, Experimental study on post-fire mechanical properties of high strength Q460 steel, *Journal of Constructional Steel Research*, 114 (2015) 100-109.
- [54] X. Qiang, F.S. Bijlaard, H. Kolstein, Post-fire mechanical properties of high strength structural steels S460 and S690, *Engineering Structures*, 35 (2012) 1-10.
- [55] G.-Q. Li, H. Lyu, C. Zhang, Post-fire mechanical properties of high strength Q690 structural steel, *Journal of Constructional Steel Research*, 132 (2017) 108-116.
- [56] C. Siwei, J. Shaokun, G. Houzuo, C. Huixuan, L. Yifeng, L. Kang, Mechanical and ductile fracture performances of high strength structural steel Q690 after a fire: experimental investigation, *Procedia Engineering*, 210 (2017) 496-503.
- [57] J. Lee, M.D. Engelhardt, E.M. Taleff, Mechanical Properties of ASTM A 992 Steel After Fire, *Engineering Journal (Chicago)*, 49 (2012) 33-44.
- [58] [20] E.M. Aziz, V.K. Kodur, Effect of temperature and cooling regime on mechanical properties of high-strength low-alloy steel, *Fire and Materials*, 40 (2016) 926-939.

- [59] Z. Chen, J. Lu, H. Liu, X. Liao, Experimental study on the post-fire mechanical properties of high-strength steel tie rods, *Journal of Constructional Steel Research*, 121 (2016) 311-329.
- [60] X. Qiang, F.S. Bijlaard, H. Kolstein, Post-fire performance of very high strength steel S960, *Journal of Constructional Steel Research*, 80 (2013) 235-242.
- [61] S. Gunalan, M. Mahendran, Experimental investigation of post-fire mechanical properties of cold-formed steels, *Thin-Walled Structures*, 84 (2014) 241-254.
- [62] H.-T. Li, B. Young, Residual mechanical properties of high strength steels after exposure to fire, *Journal of Constructional Steel Research*, 148 (2018) 562-571.
- [63] J. Lu, H. Liu, Z. Chen, L. Bisby, Experimental investigation of the residual mechanical properties of cast steels after exposure to elevated temperature, *Construction and Building Materials*, 143 (2017) 259-271.
- [64] Z. Tao, X.-Q. Wang, M.K. Hassan, T.-Y. Song, L.-A. Xie, Behaviour of three types of stainless steel after exposure to elevated temperatures, *Journal of Constructional Steel Research*, (2018).
- [65] X. Gao, X. Zhang, H. Liu, Z. Chen, H. Li, Residual mechanical properties of stainless steels S30408 and S31608 after fire exposure, *Construction and Building Materials*, 165 (2018) 82-92.
- [66] ASTM, ASTM E8/E8M Standard Test Methods for Tension Testing of Metallic Materials, in, ASTM International, 2016.
- [67] E. ISO, Metallic materials—tensile testing—part 1: method of test at room temperature, European committee for standardization, Brussels, 2009, (2009).

- [68] D. McDonald, Current Status of Coated Reinforcing Steel, in, Structure Magazine. <https://www.structuremag.org/?p=7545>. Accessed on July 7th, 2021, 2014.
- [69] S. Nandhini, M. Devasena, Review on graphene oxide composites, International Journal of Nanomaterials and Nanostructures, 2 (2016) 24-30.
- [70] Y. Cubides, H. Castaneda, Corrosion protection mechanisms of carbon nanotube and zinc-rich epoxy primers on carbon steel in simulated concrete pore solutions in the presence of chloride ions, Corrosion Science, 109 (2016) 145-161.
- [71] A. Afshar, S. Jahandari, H. Rasekh, M. Shariati, A. Afshar, A. Shokrgozar, Corrosion resistance evaluation of rebars with various primers and coatings in concrete modified with different additives, Construction and Building Materials, 262 (2020) 120034.
- [72] N. Sharma, S. Sharma, S.K. Sharma, R. Mehta, Evaluation of corrosion inhibition and self healing capabilities of nanoclay and tung oil microencapsulated epoxy coatings on rebars in concrete, Construction and Building Materials, 259 (2020) 120278.
- [73] R.W. Revie, H.H. Uhlig, Inhibitors and Passivators, in: Corrosion and Corrosion Control, 2008, pp. 303-316.
- [74] O.S. Shehata, L.A. Korshed, A. Attia, Green Corrosion Inhibitors, Past, Present, and Future, in: Corrosion Inhibitors, Principles and Recent Applications, IntechOpen, 2017.
- [75] C. Verma, E.E. Ebenso, M. Quraishi, Ionic liquids as green and sustainable corrosion inhibitors for metals and alloys: an overview, Journal of Molecular Liquids, 233 (2017) 403-414.
- [76] M. Honarvar Nazari, M.S. Shihab, L. Cao, E.A. Havens, X. Shi, A peony-leaves-derived liquid corrosion inhibitor: protecting carbon steel from NaCl, Green Chemistry Letters and Reviews, 10 (2017) 359-379.

- [77] Y. Abboud, O. Tanane, A.E. Bouari, R. Salghi, B. Hammouti, A. Chetouani, S. Jodeh, Corrosion inhibition of carbon steel in hydrochloric acid solution using pomegranate leave extracts, *Corrosion Engineering, Science and Technology*, 51 (2016) 557-565.
- [78] M. Honarvar Nazari, E.A. Havens, A. Muthumani, X. Shi, Effects of processed agro-residues on the performance of sodium chloride brine anti-Icer, *ACS Sustainable Chemistry & Engineering*, 7 (2019) 13655-13667.
- [79] P. Albrecht, T.T. Hall Jr, Atmospheric corrosion resistance of structural steels, *Journal of materials in civil engineering* 15, no. 1 (2003): 2-24.
- [80] R. Wang, R. Ajit Sheno, A. Sobey, Ultimate strength assessment of plated steel structures with random pitting corrosion damage, *Journal of Constructional Steel Research*, 143 (2018) 331-342.
- [81] S. Xu, H. Wang, A. Li, Y. Wang, L. Su, Effects of corrosion on surface characterization and mechanical properties of butt-welded joints, *Journal of Constructional Steel Research*, 126 (2016) 50-62.
- [82] R. Kiran, K. Khandelwal, A micromechanical model for ductile fracture prediction in ASTM A992 steels, *Engineering Fracture Mechanics*, 102 (2013) 101-117.
- [83] R. Kiran, K. Khandelwal, Experimental studies and models for ductile fracture in ASTM A992 steels at high triaxiality, *Journal of Structural Engineering*, 140 (2013) 04013044.
- [84] M. Boniardi, C. Andrea, In-depth approach to fire investigations: microstructural analysis of metallic materials, *Fire and Materials* 39(6) (2015): 600-618.
- [85] Z.Q. Tan, M.H. Carolyn, Effect of surface condition on the initial corrosion of galvanized reinforcing steel embedded in concrete, *Corrosion Science* 50(9) (2008): 2512-2522.
- [86] V.S. Sastri, *Green corrosion inhibitors: theory and practice*, John Wiley & Sons, 2012.

- [87] A.S.H. Makhlof, 1 - Current and advanced coating technologies for industrial applications, in: A.S.H. Makhlof, I. Tiginyanu (Eds.) Nanocoatings and Ultra-Thin Films, Woodhead Publishing, 2011, pp. 3-23.

2. INFLUENCE OF STRESS CONCENTRATION AND COOLING METHODS ON POST-FIRE MECHANICAL BEHAVIOR OF ASTM A36 STEELS¹

This chapter discusses the combined influence of stress concentration and cooling methods on post-fire mechanical properties of ASTM A36 steels. The contents of this chapter have been published in Sajid, H.U. and Kiran, R., 2018. Influence of stress concentration and cooling methods on the post-fire mechanical behavior of ASTM A36 steels. *Construction and Building Materials*, 186, pp.920-945.

2.1. Introduction

Structural steels that include mild steels, high strength steels (HSS), and very high strength steels (VHSS) are one of the most popularly used building materials in the United States (US). High thermal conductivity and low specific heat make structural steels vulnerable to fire accidents [1]. Fire accidents are very common and according to National Fire Protection Agency (NFPA) 2016 report, one structural fire is reported every 63 seconds in the US [2]. In total, 501,500 structural fire accidents were reported in 2015 that accounted for 37% of total fire accidents in the US [2]. These structural fires resulted in 2,685 civilian deaths, 13,000 civilian injuries, and \$10.3 billion in property damages in 2015 alone. Figure 2.1 and Figure 2.2 illustrate average losses per structural fire in US Dollars and the number of structural fire accidents, respectively reported in the US between 1978 and 2015. To ensure safety against fire accidents, structural steel members must satisfy the fire resistance rating specified in buildings codes. Current design standards such as AISC [3], ASCE [4], BS5950 [5], AS 4100 [6], EC3 [7], and CECS200 [8] have also specified residual factors for estimating elevated temperature mechanical

¹ This chapter was co-authored by H.U. Sajid and R. Kiran. H.U. Sajid had the primary responsibility of preparing the specimens, conducting all tests, and drafting this chapter. R. Kiran supervised the research and revised this chapter.

properties of structural steels. As a general rule, the reuse of structural steel after fire exposure is recommended if there is no obvious distortion in the structural members [3, 5, 9].

After the World Trade Center tragedy, a significant amount of research has been conducted by many researchers to investigate the mechanical properties of various types of structural steels during-fire and post-fire scenarios. Post-fire performance of structural steels is critical in determining the residual capacity and subsequent usability of steel structures after the fire is extinguished. To this end, post-fire mechanical behavior has been reported for various structural steels that include mild steels (Q235, Q345 [10]), high strength steels (S355J2H [11], Grade 350, Grade 800 [12, 13], Q420 [10], Q460 [14], S460NL, S690QL [15], S690RQT [16], Q690 [17, 18], ASTM A992 [19], ASTM A572 [20], GLG460, GLG550, GLG650, GLG835 [21]), very high strength steels (S960QL [22], Grade 1200 [12, 13]), S690RQT [16], cold-formed steels [23, 24], cast steels (G20Mn5N, G20Mn5QT [25]) and stainless steels [26, 27]. In these studies, evaluation of the post-fire performance of structural steels is achieved by subjecting post-fire steel specimens to uniaxial tension tests. Typical test specimens were prepared and tested in accordance with ASTM E8 [28] or ISO standard (GB/T 228.1-2010 [29]) depending on the type of structural steel and the country in which the structural steel is used. For post-fire tests, specimens are first heated to a target temperature and maintained at the target temperature for a certain period of time to achieve uniform temperature throughout the test specimens. Specimens are then cooled down to room temperature using different cooling methods, namely: cooling-in-air (CIA), cooling-in-water (CIW), and cooling-in-blanket (CIB). In the case of CIA, the specimens are cooled by placing them outside the furnace or inside the furnace (with the furnace door kept open) after leaving the specimens at the target temperature for a specified time. In the case of CIW, the specimens are either placed in water or a water-jet is applied to cool down the

specimens to room temperature. In the case of CIB, specimens are kept in a ceramic fiber blanket until they are cooled down to room temperature. Residual factors are computed based on one of three cooling methods, as discussed above. The residual factor is defined as the ratio of the value of a specific mechanical property after being cooled down from an elevated target temperature to its value at room temperature. Thus, a high residual factor indicates a lower level of degradation in a mechanical property and vice versa.

The accuracy and reliability of residual factors are vital when estimating the residual capacity of steel structures for post-fire use. Although residual factors for elastic modulus, yield strength, ultimate tensile strength, and ductility of various structural steels exist in the literature, the combined influence of stress concentration and cooling method on residual factors is not yet investigated. Stress concentrations are caused by geometric discontinuities like holes, welds, sharp corners, etc. that are commonly observed in steel structures. Stress concentration is quantified by a dimensionless parameter referred to as stress triaxiality (T_σ). Stress triaxiality is defined as the ratio between hydrostatic stress and von Mises stress. Higher stress triaxiality indicates a higher level of stress concentration. High stress triaxialities are found to have an adverse effect on the ductility of structural steels [30, 31-33]. With this, the residual factors for ASTM A36 steel for various stress triaxialities and cooling methods are investigated in this paper. The rest of the paper is organized as follows: Section 2.2 describes the finite element analysis and experimental procedures (heating and cooling procedure and uniaxial tensile testing of test specimens). Section 2.3 describes test results obtained from uniaxial tensile testing of post-fire specimens and effects of cooling method and stress triaxiality on elastic modulus, yield strength, ultimate tensile strength, and ductility of ASTM A36 steel. In addition to this, the influence of stress concentration and cooling method on fracture initiation and propagation

mechanisms is also discussed in Section 2.3. Important conclusions of this study are summarized in Section 2.4.

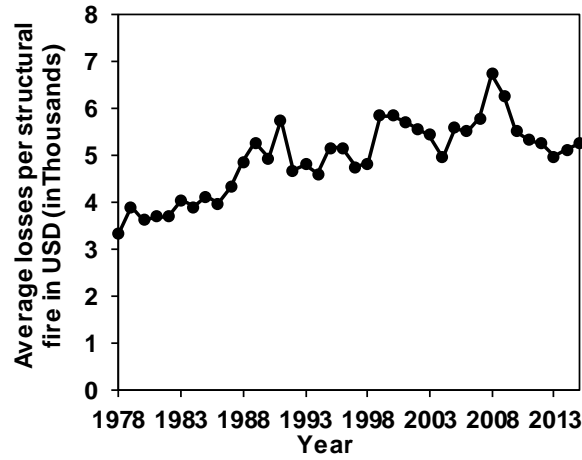


Figure 2.1. Average losses per structural fire in USD in the US from 1978-2015.

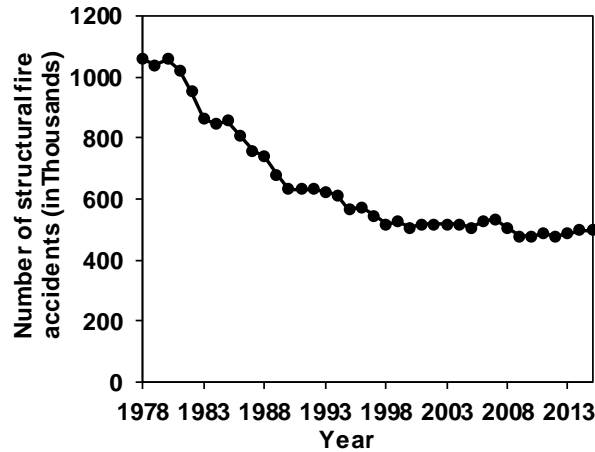


Figure 2.2. The number of structural fire accidents reported in the US between 1978-2015.

2.2. Experimental Procedure

In this section, the details about finite element analysis of test specimens, heating, and cooling procedures, and uniaxial tension test protocols are provided.

2.2.1. Finite Element Analyses of Test Specimens

In this study, six axisymmetrically notched test specimens are chosen to generate a range of high stress triaxialities. The notched geometries are categorized into three classes based on

notch shape, namely: C-notch, U-notch, and V-notch. Geometries of these test specimens and dimensions of the notches are provided in Figure 2.3 and Table 2.1, respectively.

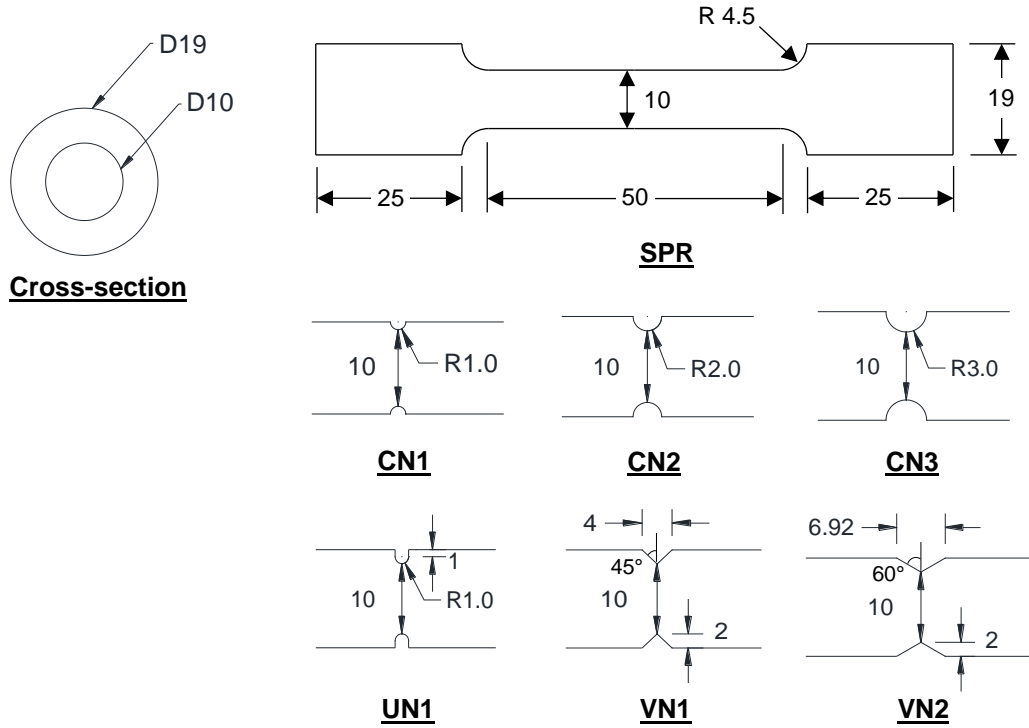


Figure 2.3. Geometric details of typical test specimens (all dimensions are in mm).

Table 2.1. Geometric details of test specimens.

Specimen ID	Notch type	Radius, R (mm)	Depth, D (mm)	Angle, θ (degrees)
SPR	-	-	-	-
CN1	C	1	-	-
CN2	C	2	-	-
CN3	C	3	-	-
UN1	U	1	-	-
VN1	V	-	2	45
VN2	V	-	2	60

Non-linear finite element analysis (FEA) is conducted to obtain the distribution of stress triaxialities across the critical cross-sections of test specimens. Finite element analyses are conducted using commercial FEA software ABAQUS® [34]. Both notched and un-notched test specimens are modeled using four noded bilinear axisymmetric CAX4 elements that are

available in the ABAQUS® element library. Geometric non-linearity is considered and the J_2 plasticity model is used as a constitutive model. The boundary conditions along with typical meshes used for notches are shown in Figure 2.4. The true stress-strain curve obtained from uniaxial tensile tests of un-notched test specimens is used as the hardening curve for the J_2 plasticity model (see Figure 2.5(a)). The actual experimental test protocol for mechanical testing will be discussed in Section 2.2.3. The load-displacement curves obtained from finite element analysis and uniaxial tensile test are compared to check the adequacy of the finite element model, as shown in Figure 2.5(b).

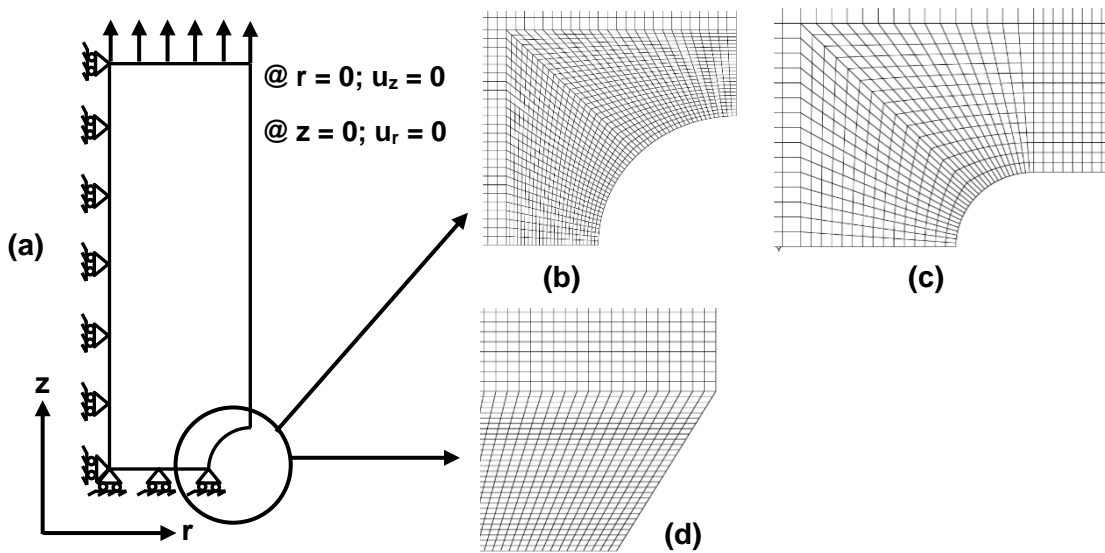


Figure 2.4. (a) Applied boundary conditions, (b) typical C-notch, (c) typical U-notch, (d) typical V-notch.

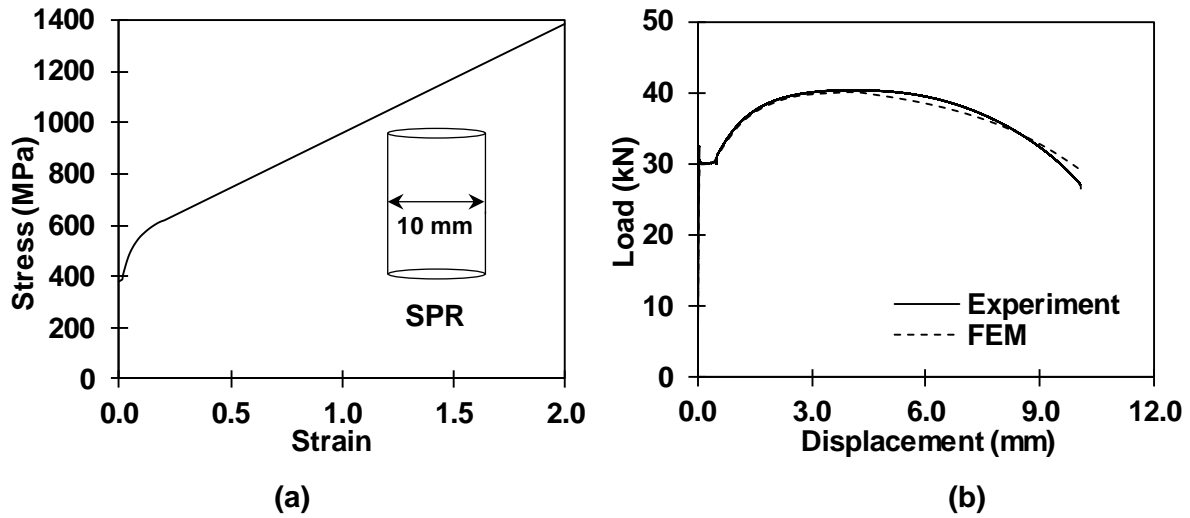


Figure 2.5. (a) Strain hardening curve of SPR test specimen, (b) experimental and FE load-displacement curve of SPR test specimen.

Based on finite element analysis results, stress triaxiality distribution across the critical cross-section (least cross-sectional areas) is obtained for each notched specimen and provided in Figure 2.6. The maximum initial stress triaxialities across the critical cross-section of the notched specimens range from 0.33 to 1.15. Maximum initial stress triaxiality across the notch cross-section refers to the maximum spatial triaxiality observed at $1.35 \pm 0.05\%$ strain. The notched and un-notched specimens are machined from a 19 mm ASTM A36 bar stock using a computer numeric control (CNC) lath machine with a tolerance level of ± 0.025 mm. The mechanical properties of ASTM A36 steel obtained from the uniaxial tensile test are provided in Table 2.2.

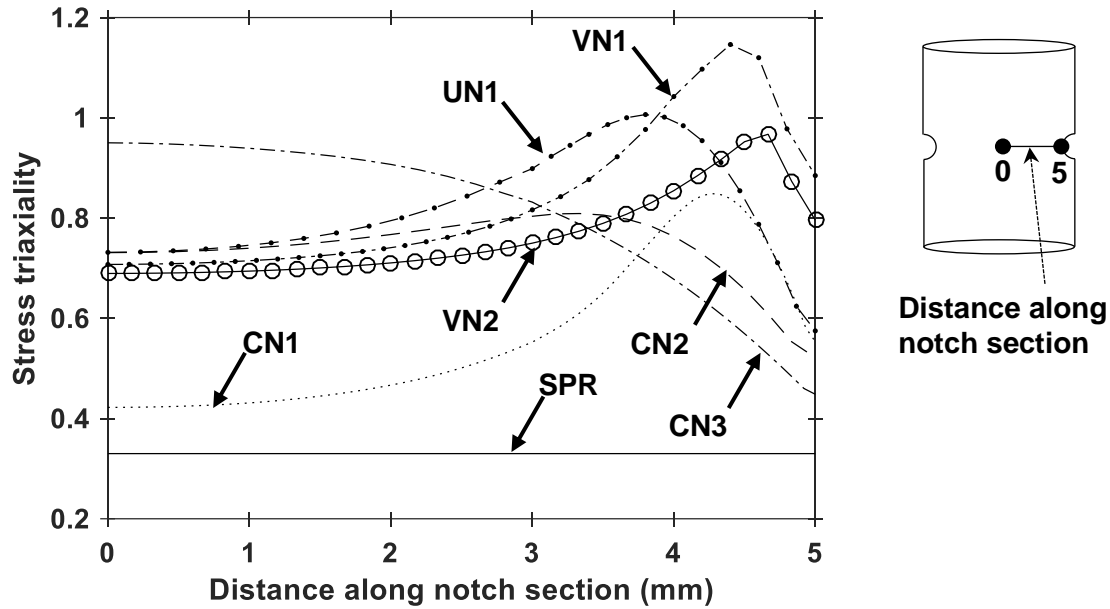


Figure 2.6. Initial stress triaxiality profiles of test specimens.

Table 2.2. Mechanical properties of ASTM A36 steel.

Yield strength (MPa)	Ultimate tensile strength (MPa)	Elongation in 25-mm gauge length (mm)
384	514	40

2.2.2. Heating and Cooling of Test Specimens

In this study, the post-fire mechanical behavior of ASTM A36 steels is evaluated by subjecting the test specimens to the following target temperatures: 20 °C (room temperature), 500 °C, 600 °C, 700 °C, 800 °C, 900 °C, and 1000 °C. Temperature between 20 °C and 500 °C are not studied herein as previous studies have revealed that post-fire mechanical properties of mild steel and other types of structural steels are almost unaffected when cooled from temperatures ranging between 20 °C and 500 °C [10, 20, 35]. The specimens are heated to a target temperature inside an electric furnace with a maximum heating temperature of 1200 °C (see Figure 2.7).

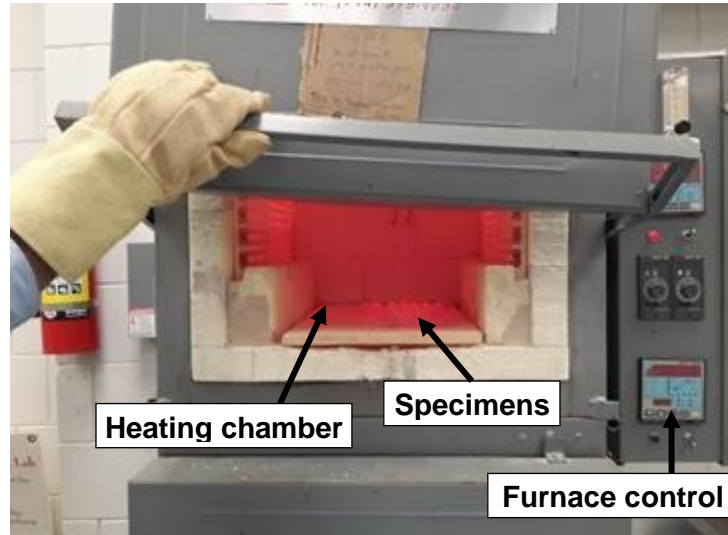


Figure 2.7. Specimens placed inside an electric furnace for heating.

A constant heating rate of $10\text{ }^{\circ}\text{C}/\text{min}$ ($\pm 2\text{ }^{\circ}\text{C}/\text{min}$) is used to achieve the target temperatures. The specimens are kept at the target temperature for a period of 1 hour to ensure uniform distribution of temperature across the test specimen. The temperature inside the furnace is recorded and displayed on the furnace screen via two thermocouples located inside the furnace. After 1 hour of exposure to the target temperature, the specimen is removed from the furnace and cooled down to room temperature using two cooling methods, namely air-cooling (AC) and water-cooling (WC). In the air-cooling method, the heated specimen is placed in an open tray and is left to cool down to room temperature. In the water-cooling method, the heated specimen is immediately placed in a water bath at room temperature for quenching. 14 specimens are heated simultaneously in a single batch. Out of these 14 specimens, 7 specimens are air-cooled and the other 7 specimens are water-cooled.

2.2.3. Post-Fire Mechanical Tests

Uniaxial tensile tests are conducted on air-cooled and water-cooled specimens to evaluate the post-fire mechanical behavior of test specimens using a servo-hydraulic MTS 810 system, with a maximum loading capacity of 300 kN. A displacement rate of 0.02 mm/sec is applied and

extension within the 25 mm gauge portion is measured using an Epsilon Model 3542 contact extensometer. A typical uniaxial tension test setup is shown in Figure 2.8. In total, 91 specimens are tested in this study which includes one room temperature test and 12 residual tests after air-cooling or water-cooling from 6 different temperature conditions (500 °C, 600 °C, 700 °C, 800 °C, 900 °C, and 1000 °C) for each geometry (SPR, CN1, CN2, CN2, CN3, UN1, VN1, and VN2). Moreover, a single test is performed for a particular temperature and cooling condition.

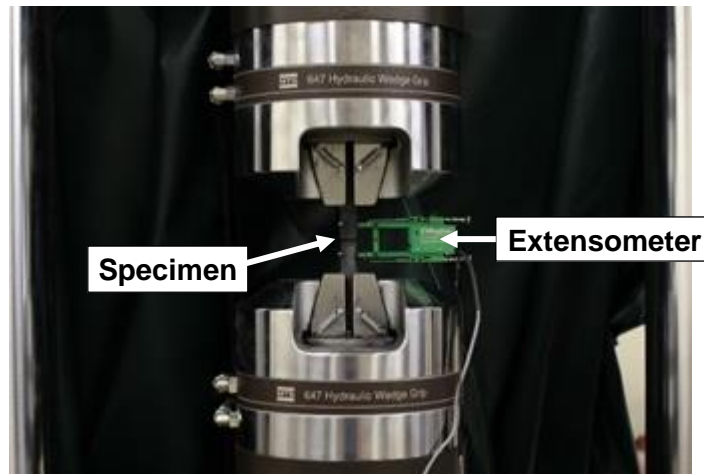


Figure 2.8. Typical uniaxial tension test setup.

2.3. Results and Discussions

In this section, the experimental results obtained from post-fire tensile tests, scanning electron microscopy (SEM) studies on fractured surfaces, and finite element analysis results of post-fire specimens are presented. These results are analyzed to describe the effects of stress triaxiality and cooling methods on post-fire mechanical properties of ASTM A36 steels.

2.3.1. Visual Observation

All specimens are heated to a target temperature and then cooled down to room temperature using the procedures discussed in Section 2.2.2. Oxidation in structural steels occurs at a very slow rate at room temperature. The oxidation rate increases when steel is subjected to high temperatures. The oxidation at high temperatures results in different oxidation products that

form oxide layers on the iron substrate. Below 570 °C, the oxidation layers consist of two oxide products: outer hematite (Fe_2O_3) and inner magnetite (Fe_3O_4) [36]. When steel is subjected to a temperature exceeding 570 °C, a third oxidation product, wüstite (FeO), is formed beneath the magnetite layer [37]. A schematic representation of these oxide layers is shown in Figure 2.9. Wüstite is more stable as the temperature increases beyond 570 °C. However, after cooling down below 570 °C, the wüstite layer decomposes into magnetite and iron [37]. After cooling down from high temperatures, the oxide layers formed as a result of high-temperature exposure can peel off resulting in surface roughness.

The visual appearances of test specimens that are subjected to high target temperatures and then cooled down to room temperature, using air-cooling and water-cooling methods, are shown in Figure 2.10. It can be observed that all post-fire specimens experience considerable change in their color due to high-temperature oxidation, or due to atmospheric corrosion after exposure to fire during the cooling process. Significant corrosion is observed in water-cooled specimens as compared to air-cooled specimens. In the water-cooling method, contact of the specimen with water facilitates electro-chemical reaction causing atmospheric corrosion. In addition to this, beyond 600 °C the surface roughness of test specimens is observed to increase due to peeling of the Wüstite layer. An increase in surface roughness of structural steels is found to increase the rate of corrosion in a recent study [38]. A higher amount of corrosion observed in the case of water-cooled specimens is observed to increase with the target temperatures and this can be directly attributed to the increase in surface roughness caused by peeling of the oxidation layer.

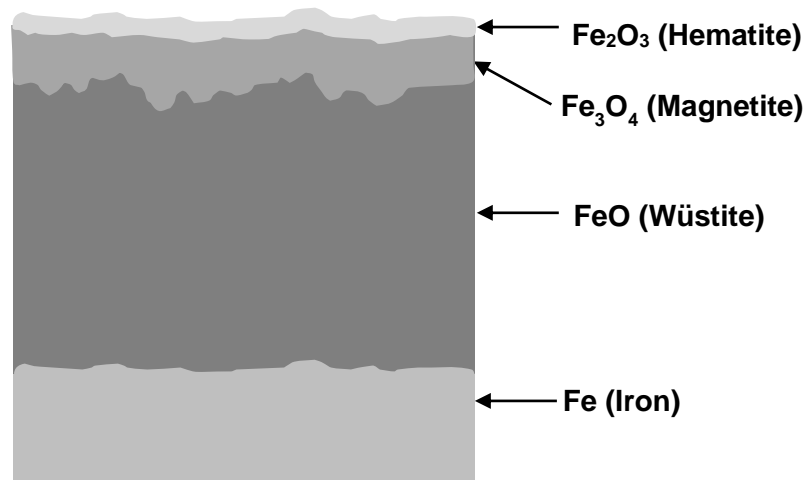


Figure 2.9. Schematic of oxidation layers formed on iron substrate beyond 700 °C after 24 hours.



Figure 2.10. Specimens after being subjected to different temperatures and cooling regimes.

2.3.2. Post-Fire Load Displacement Curves

Post-fire load-displacement curves of each test specimen, obtained from experiments and finite element analyses, for different target temperatures are presented in Figure 2.11 to Figure 2.38. In this section, only experimental post-fire load-displacement curves are discussed, and FEA results will be discussed in Section 2.3.3. As observed in these figures, the load-displacement behavior of ASTM A36 steels is more or less the same when cooled from 600 °C, using both air-cooled and water-cooled methods. Beyond 700 °C, a considerable change in load-displacement curves is observed for both un-notched and notched specimens.

In the case of un-notched air-cooled test specimens (SPR-AC), there is a defined yield plateau for all target temperatures, as shown in Figure 2.11 and Figure 2.12. However, the size of the yield plateau decreases at higher temperatures of 900 °C and 1000 °C. In the case of un-notched water-cooled test specimens (SPR-WC), yield plateau exists in specimens exposed to temperatures up to 700 °C. Beyond 700 °C, the yield plateau disappears in SPR-WC specimens, as shown in Figure 2.13 and Figure 2.14. On the contrary, notched specimens (CN1, CN2, CN3, UN1, VN1, and VN2) do not exhibit a well-defined yield plateau, particularly beyond 700 °C, in both air-cooled and water-cooled cases. At higher temperatures (800 °C, 900 °C, and 1000 °C), minor serrations are observed in the load-displacement curves of notched air-cooled specimens having high triaxialities. These include CN2-AC (Figure 2.20), UN1-AC (Figure 2.28), VN1-AC (Figure 2.31 and Figure 2.32), and VN2-AC (Figure 2.36). These serrations occurred at around 1 mm overall displacement. These serrations might have been the result of the Portevin-Le Chatelier (PLC) effect, which occurs in some materials at the onset of plastic deformation under elevated temperatures [39-41]. However, such types of serrations at room temperature were previously reported for other types of steels.

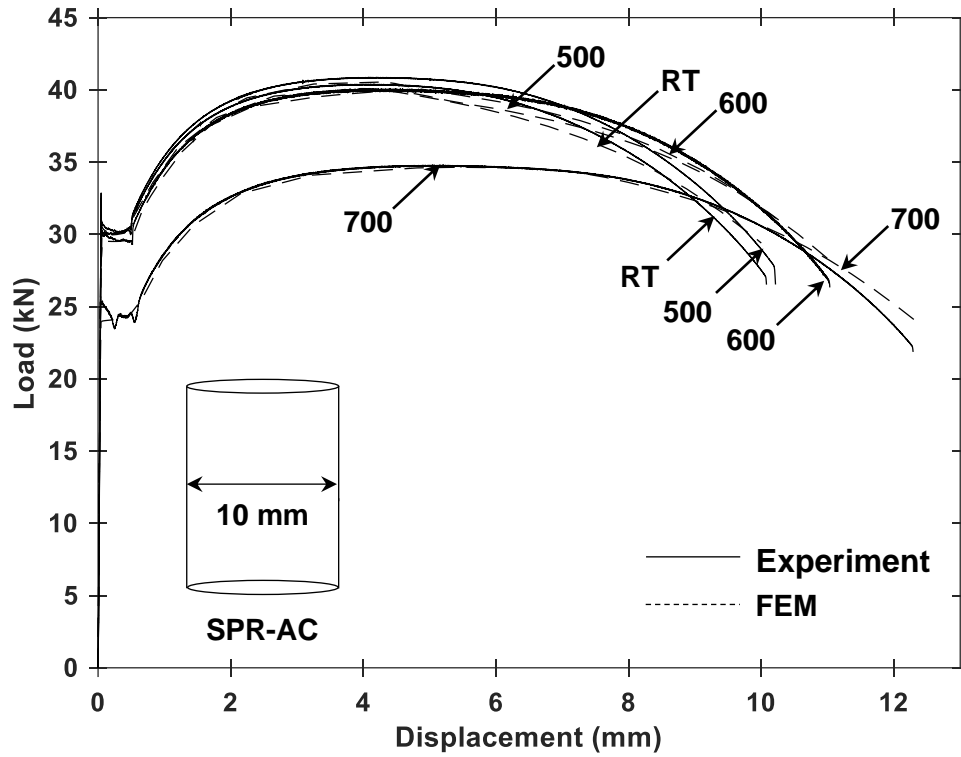


Figure 2.11. Load-displacement curves of specimen SPR-AC (RT-700 °C).

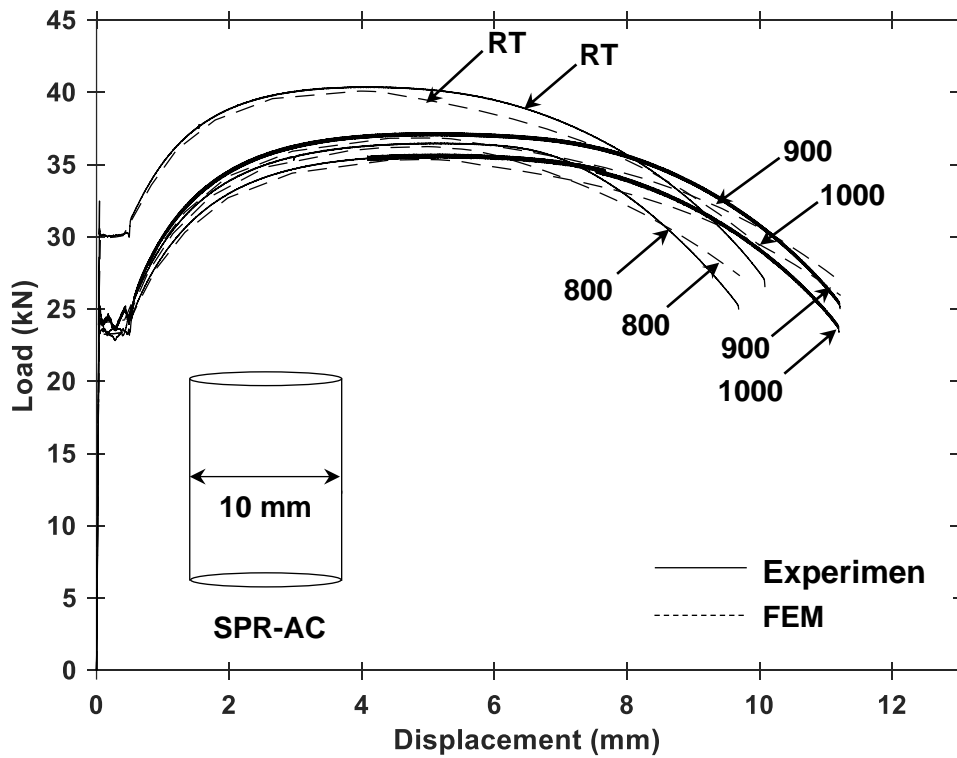


Figure 2.12. Load-displacement curves of specimen SPR-AC (800-1000 °C).

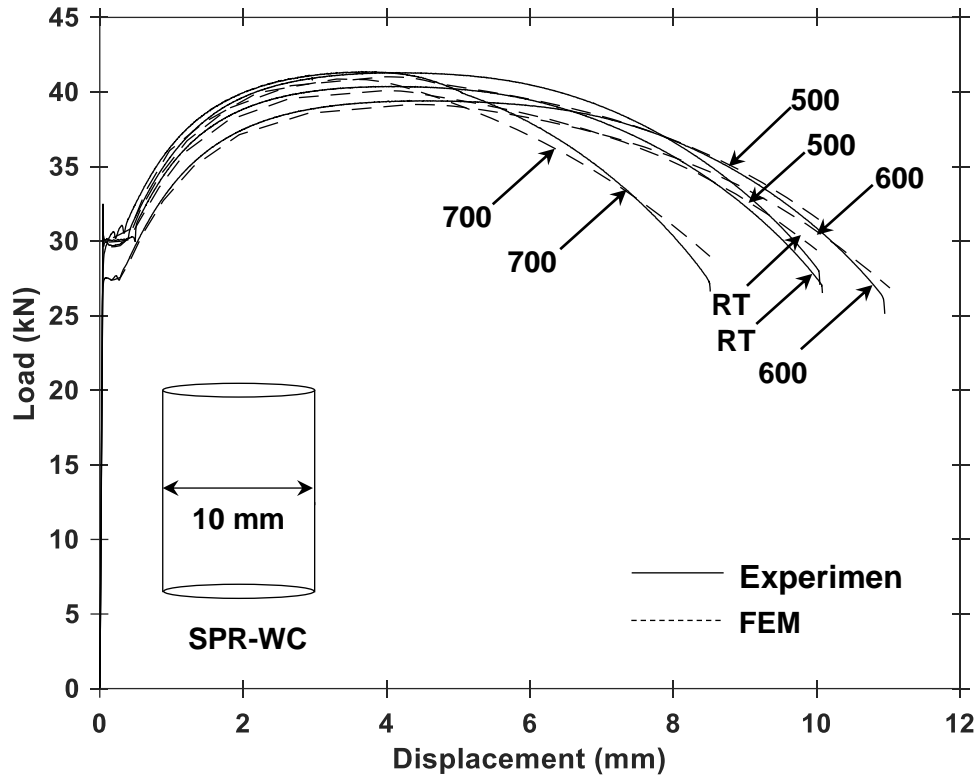


Figure 2.13. Load-displacement curves of specimen SPR-WC (RT-700 °C).

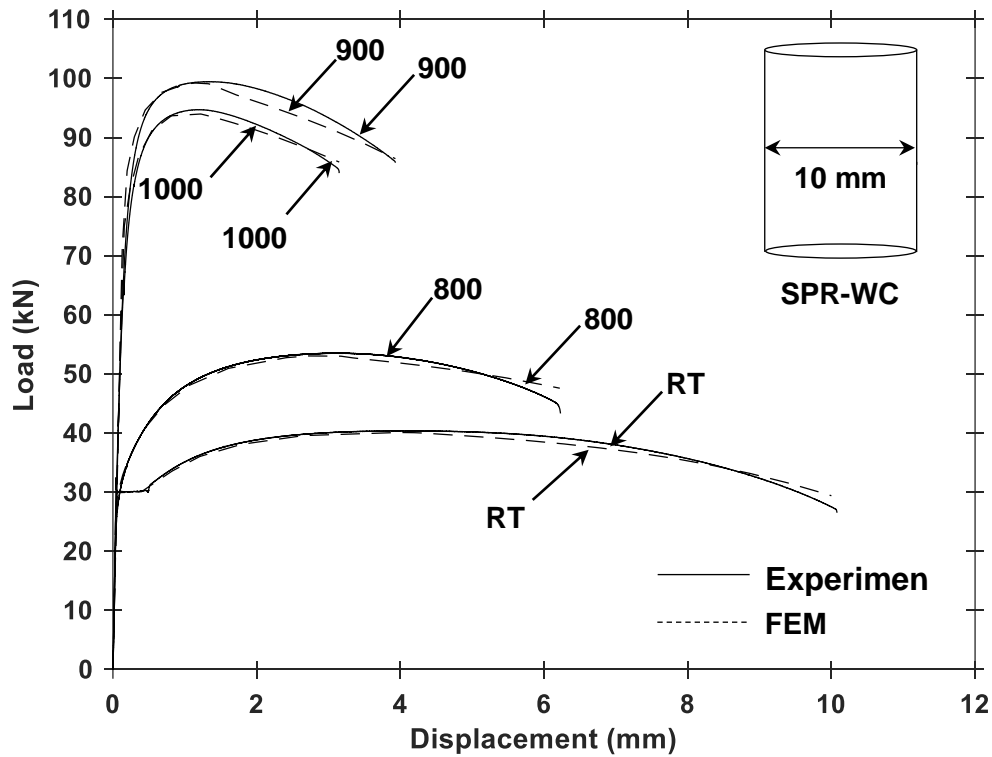


Figure 2.14. Load-displacement curves of specimen SPR-WC (800-1000 °C).

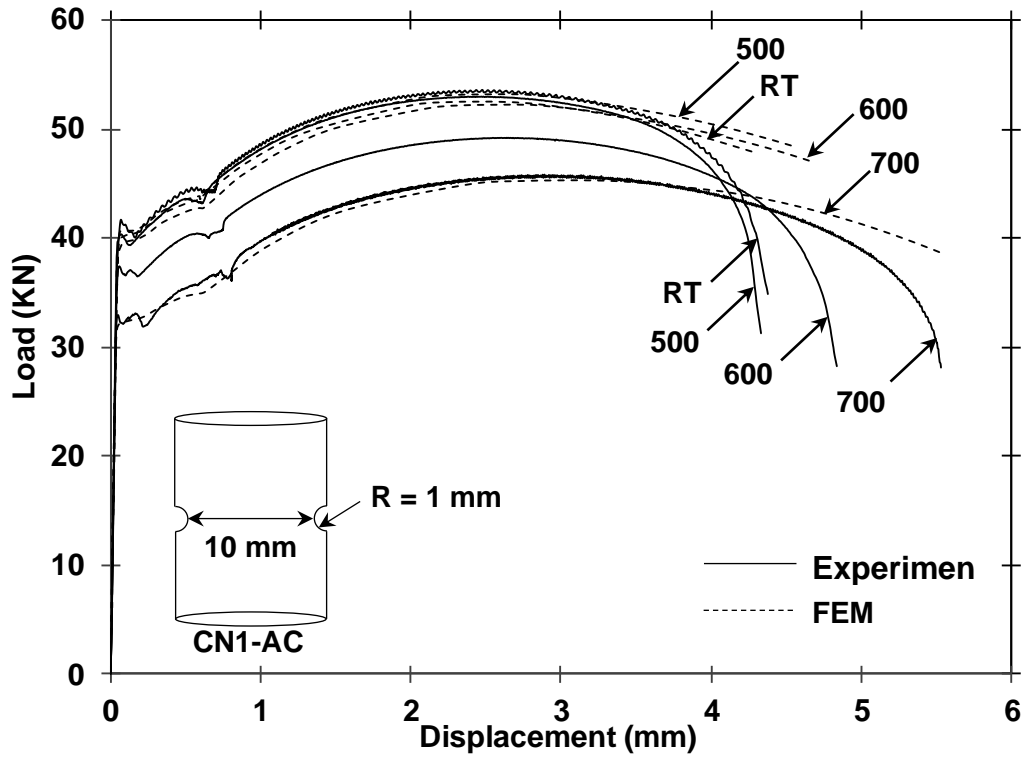


Figure 2.15. Load-displacement curves of specimen CN1-AC (RT-700 °C).

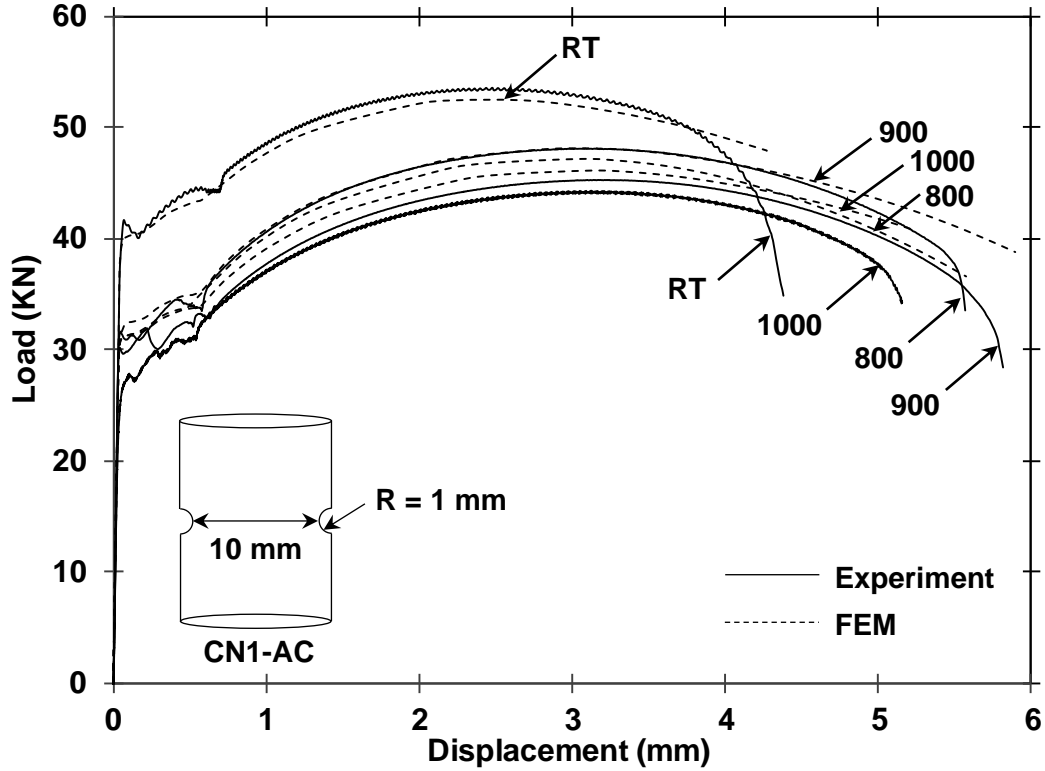


Figure 2.16. Load-displacement curves of specimen CN1-AC (800-1000 °C).

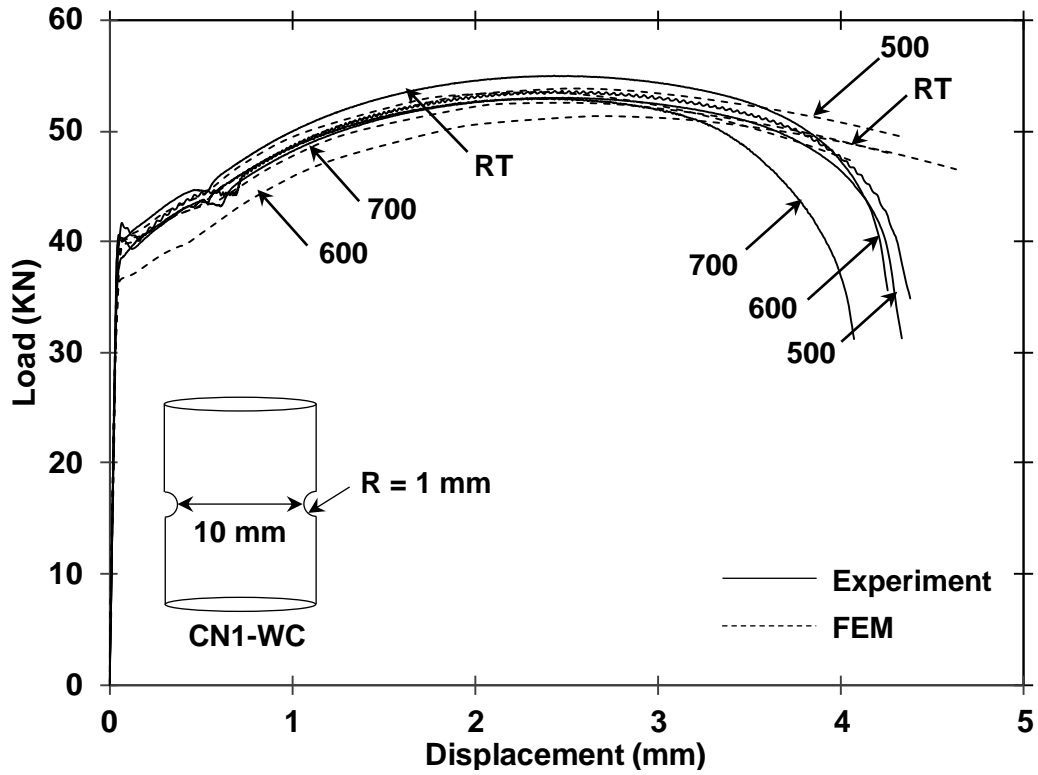


Figure 2.17. Load-displacement curves of specimen CN1-WC (RT-700 °C).

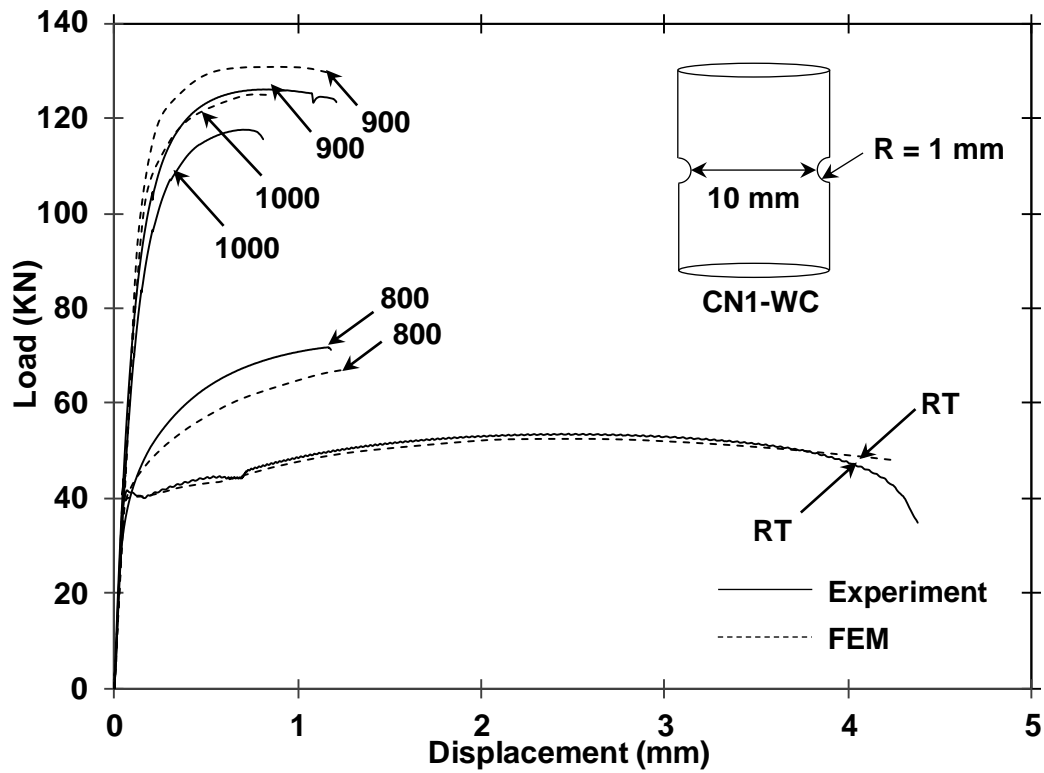


Figure 2.18. Load-displacement curves of specimen CN1-WC (800-1000 °C).

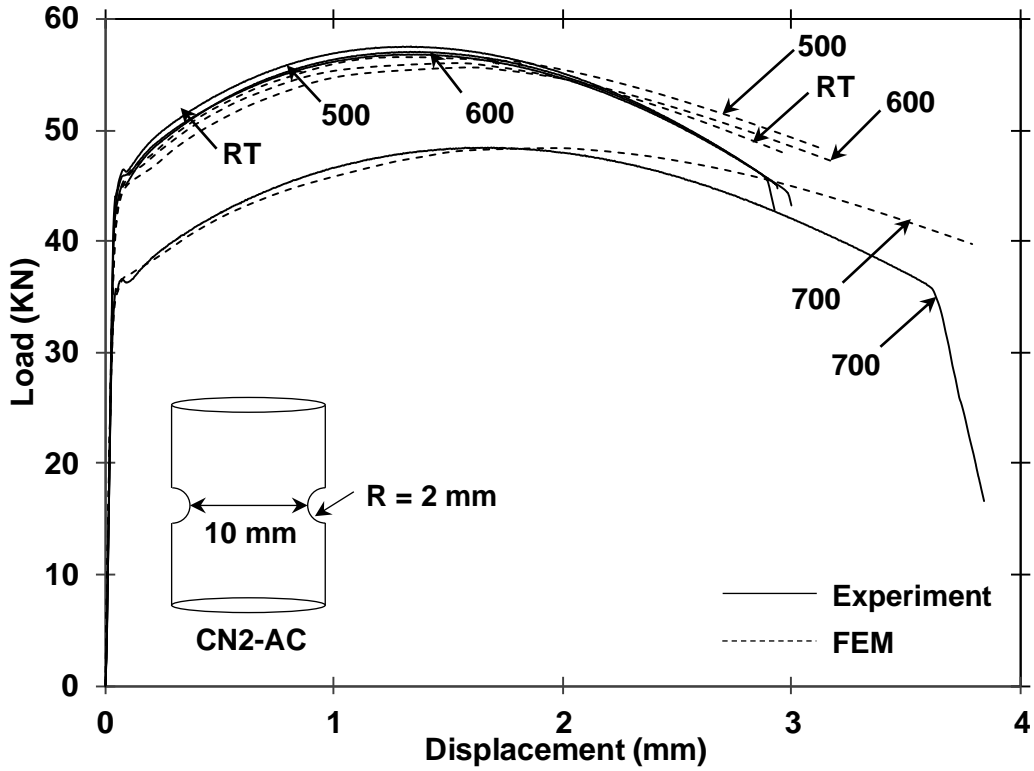


Figure 2.19. Load-displacement curves of specimen CN2-AC (RT-700 °C).

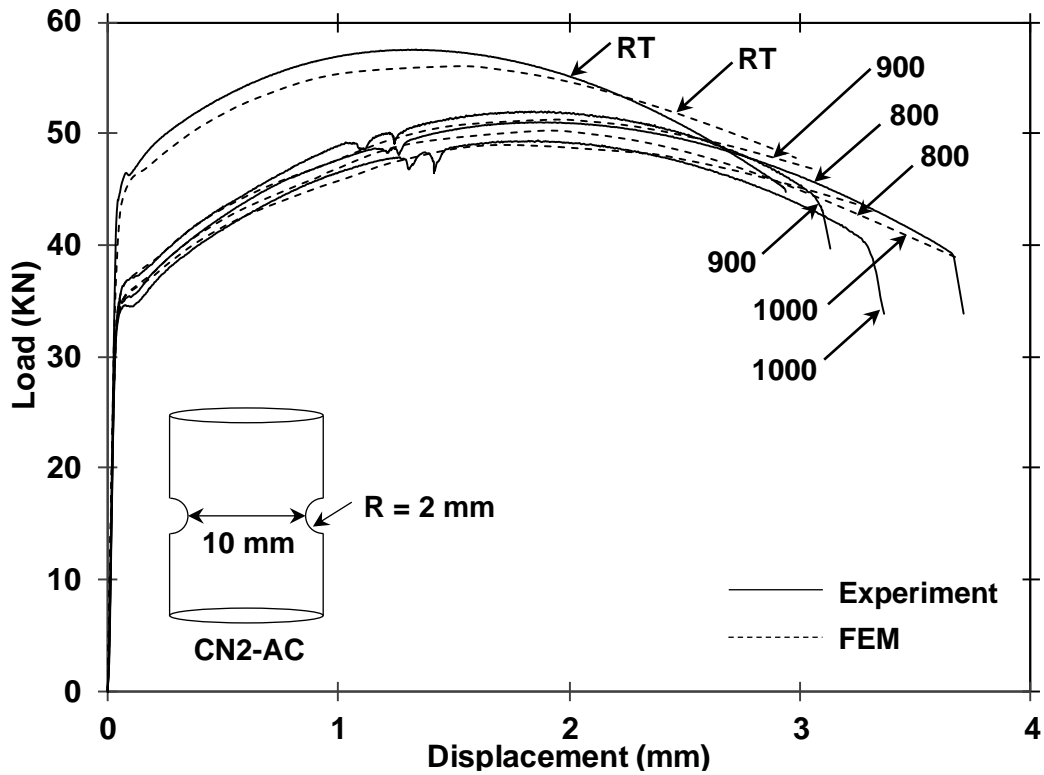


Figure 2.20. Load-displacement curves of specimen CN2-AC (800-1000 °C).

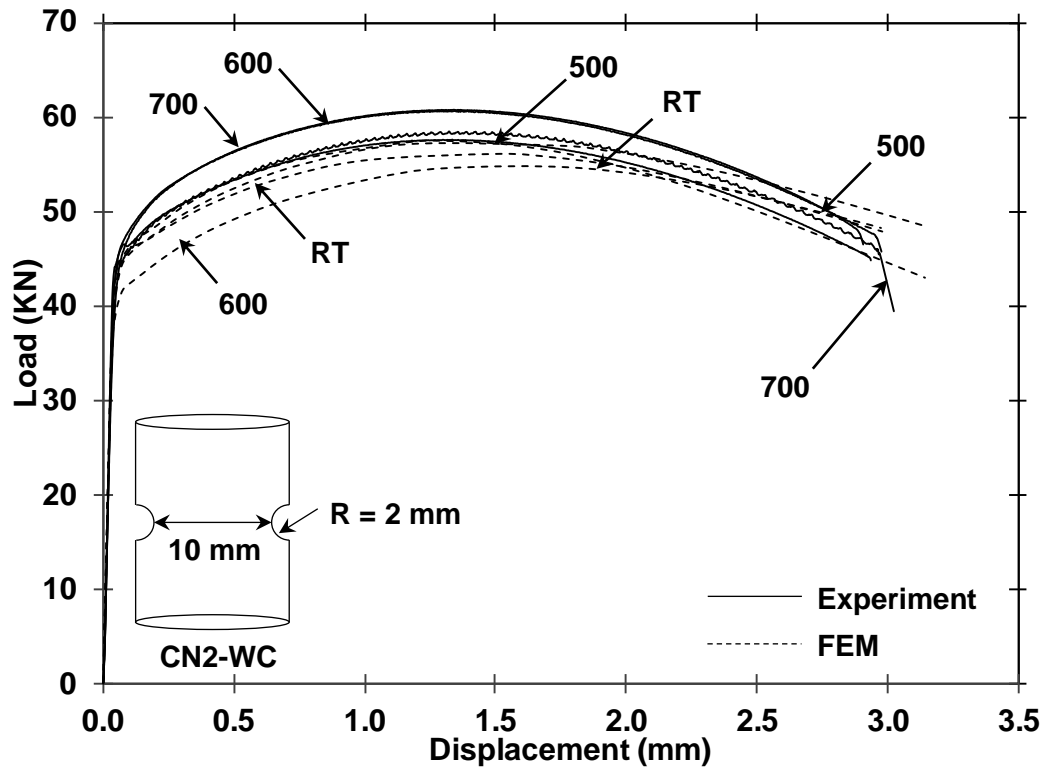


Figure 2.21. Load-displacement curves of specimen CN2-WC (RT-700 °C).

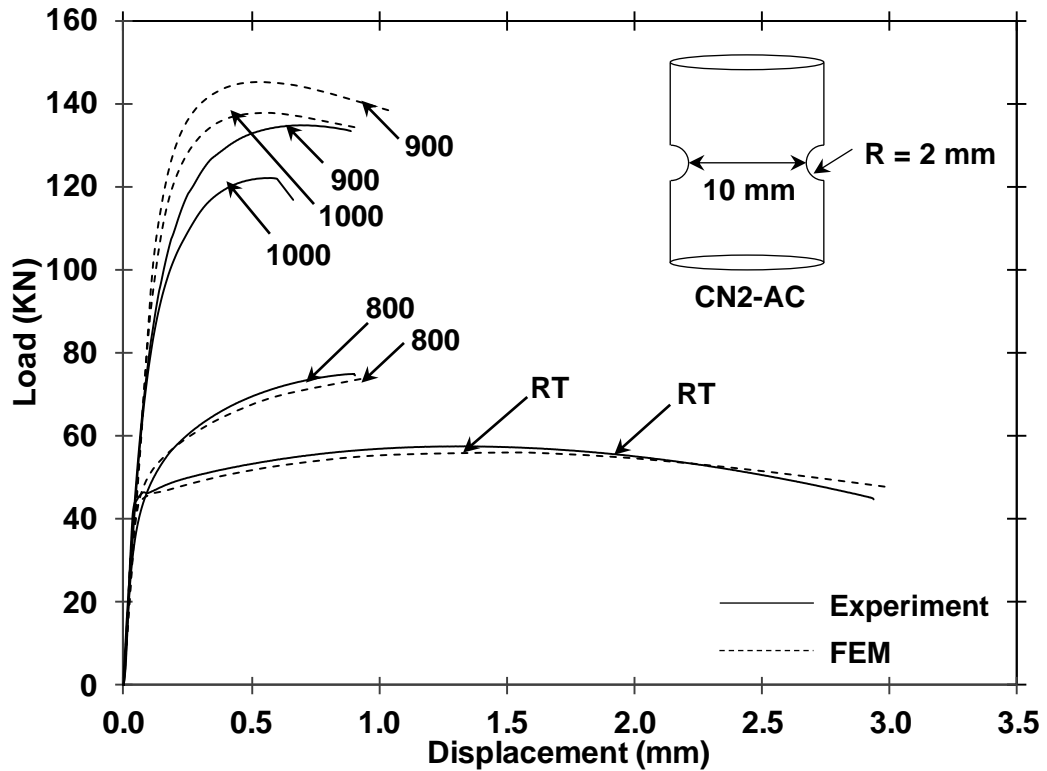


Figure 2.22. Load-displacement curves of specimen CN2-WC (800-1000 °C).

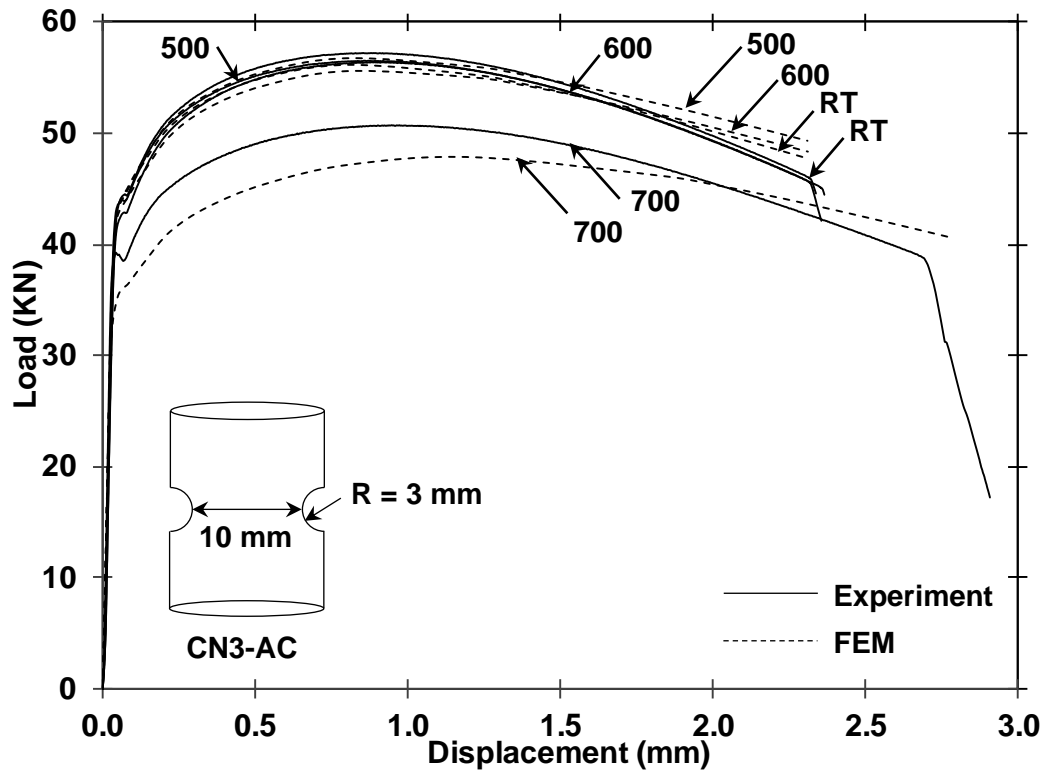


Figure 2.23. Load-displacement curves of specimen CN3-AC (RT-700 °C).

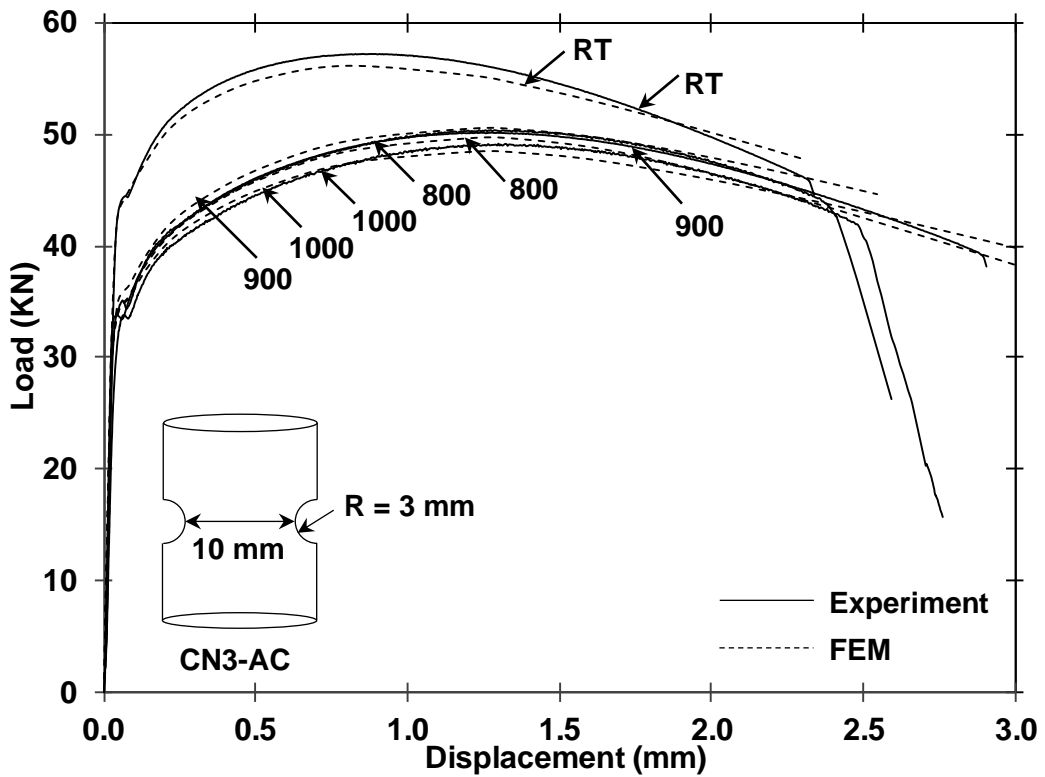


Figure 2.24. Load-displacement curves of specimen CN3-AC (800-1000 °C).

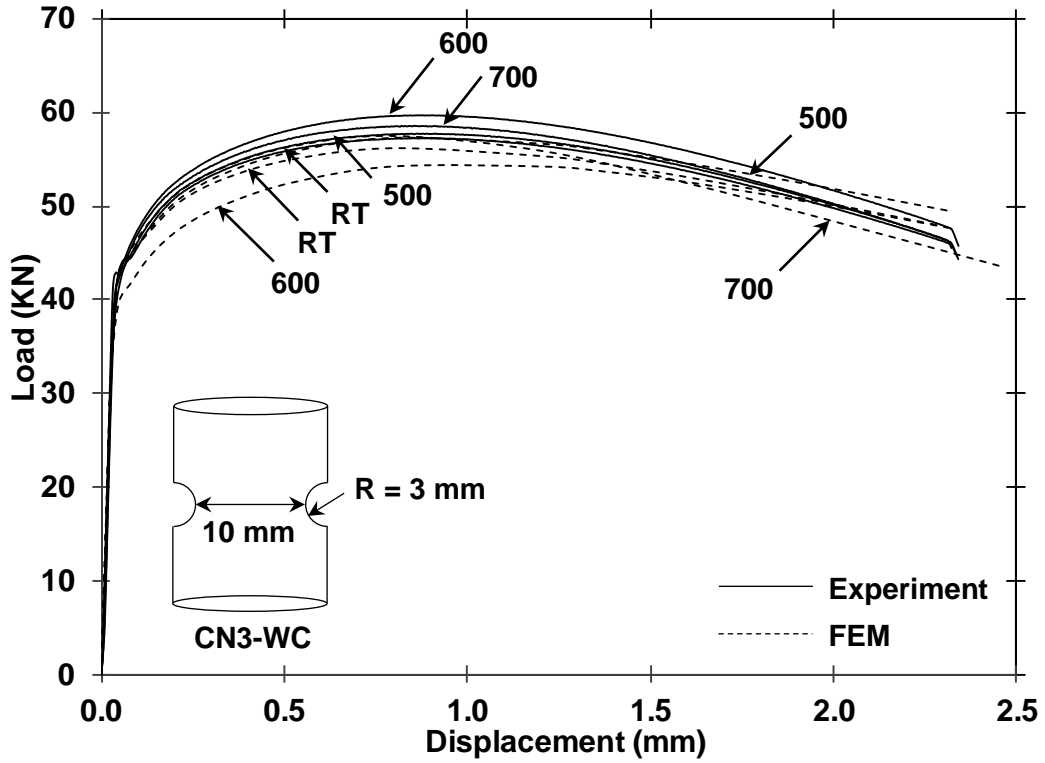


Figure 2.25. Load-displacement curves of specimen CN3-WC (RT-700 °C).

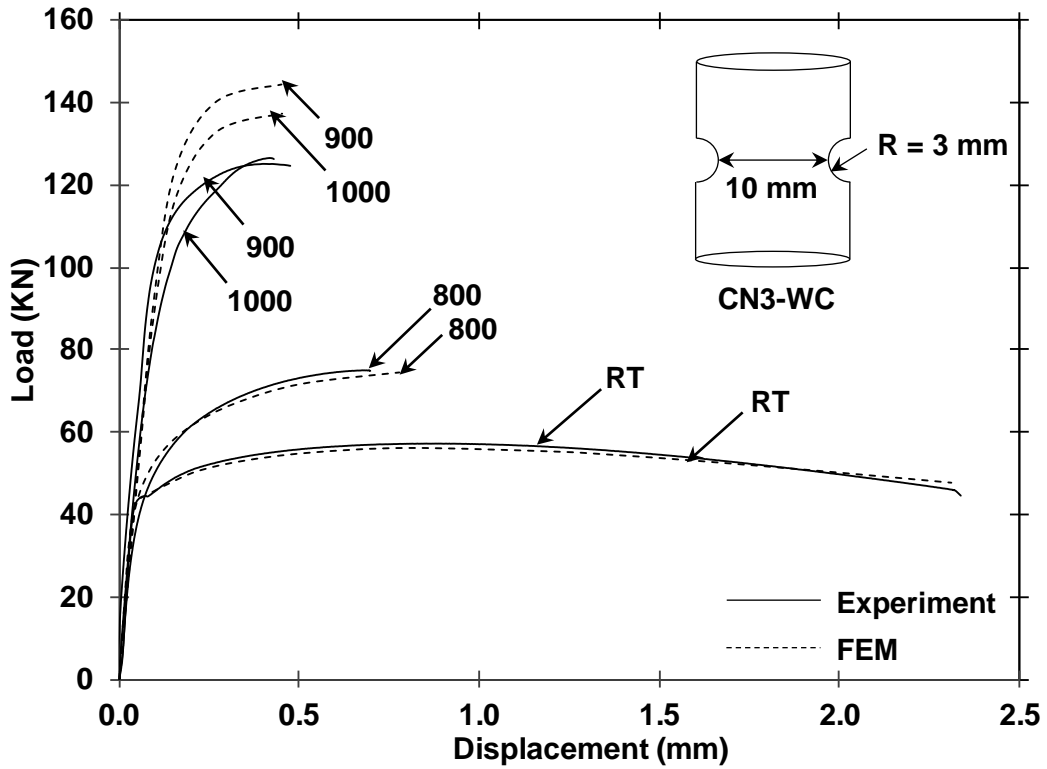


Figure 2.26. Load-displacement curves of specimen CN3-WC (800-1000 °C).

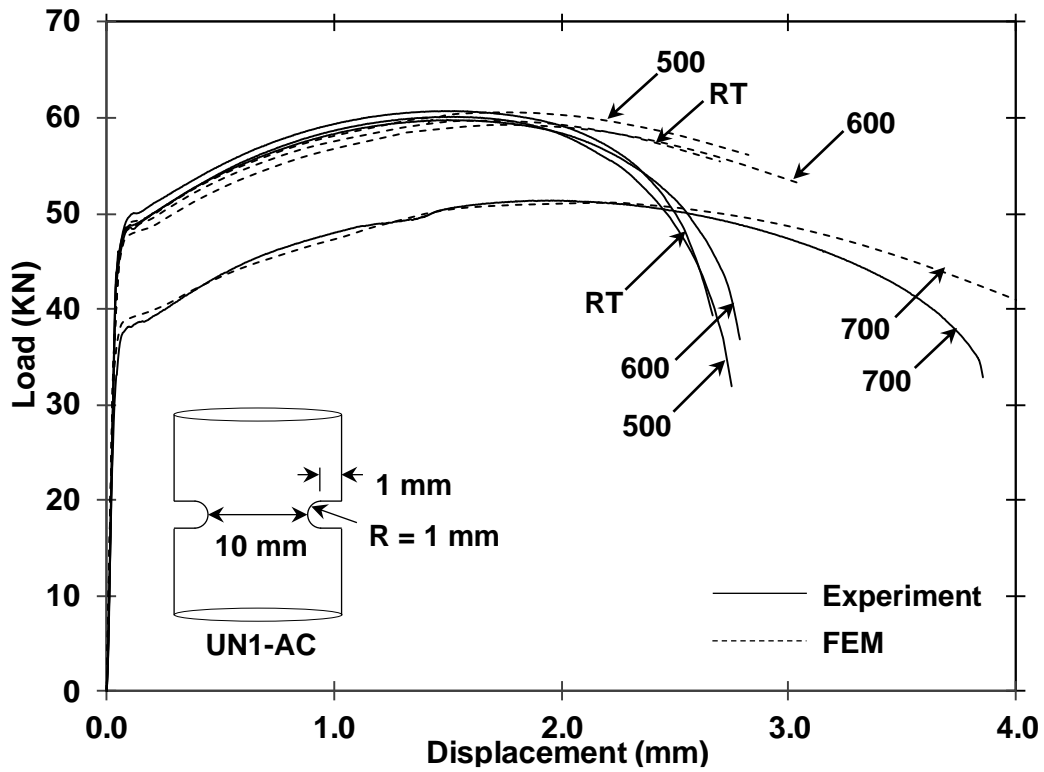


Figure 2.27. Load-displacement curves of specimen UN1-AC (RT-700 °C).

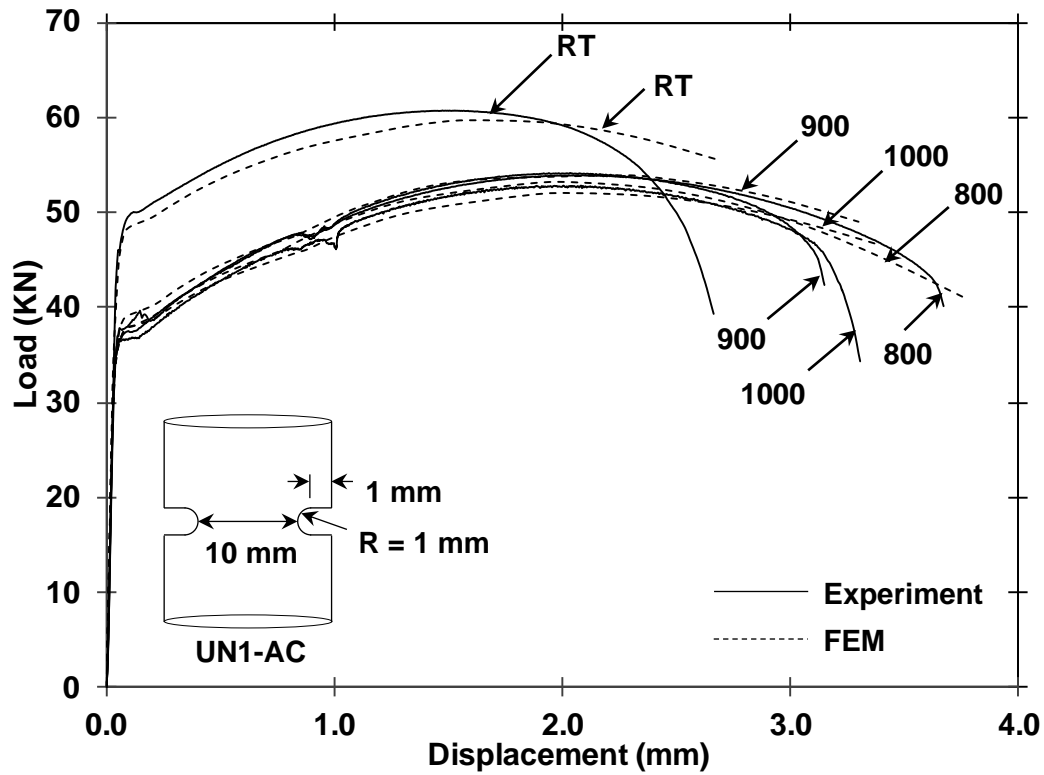


Figure 2.28. Load-displacement curves of specimen UN1-AC (800-1000 °C).

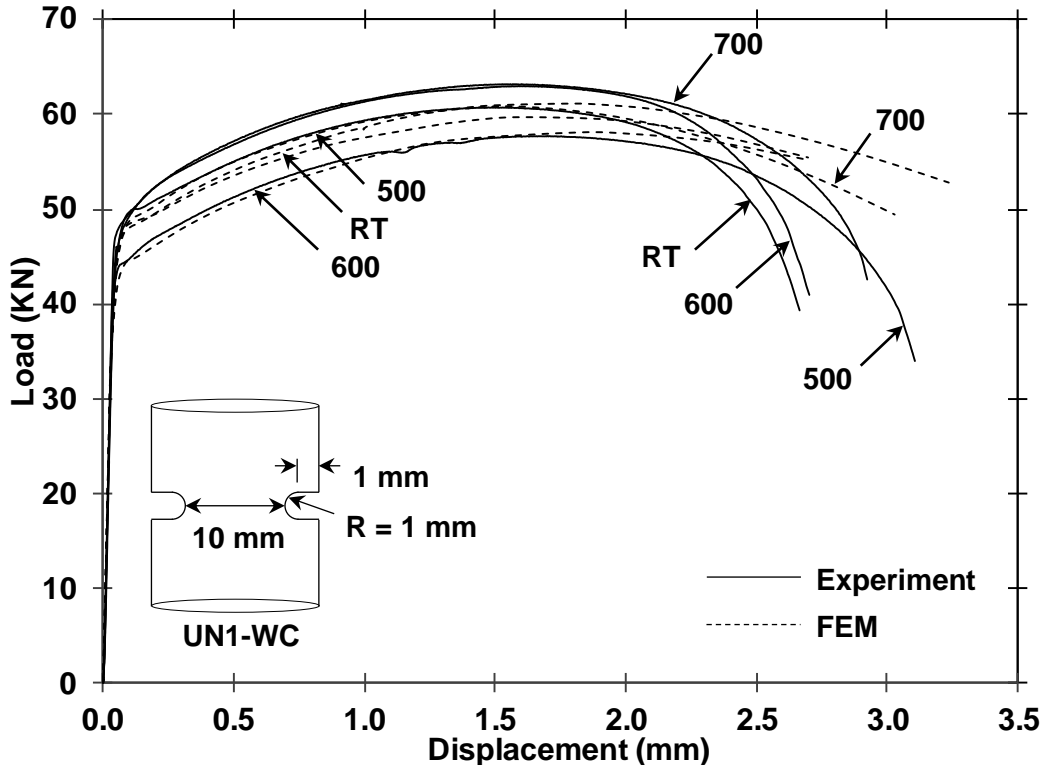


Figure 2.29. Load-displacement curves of specimen UN1-WC (RT-700 °C).

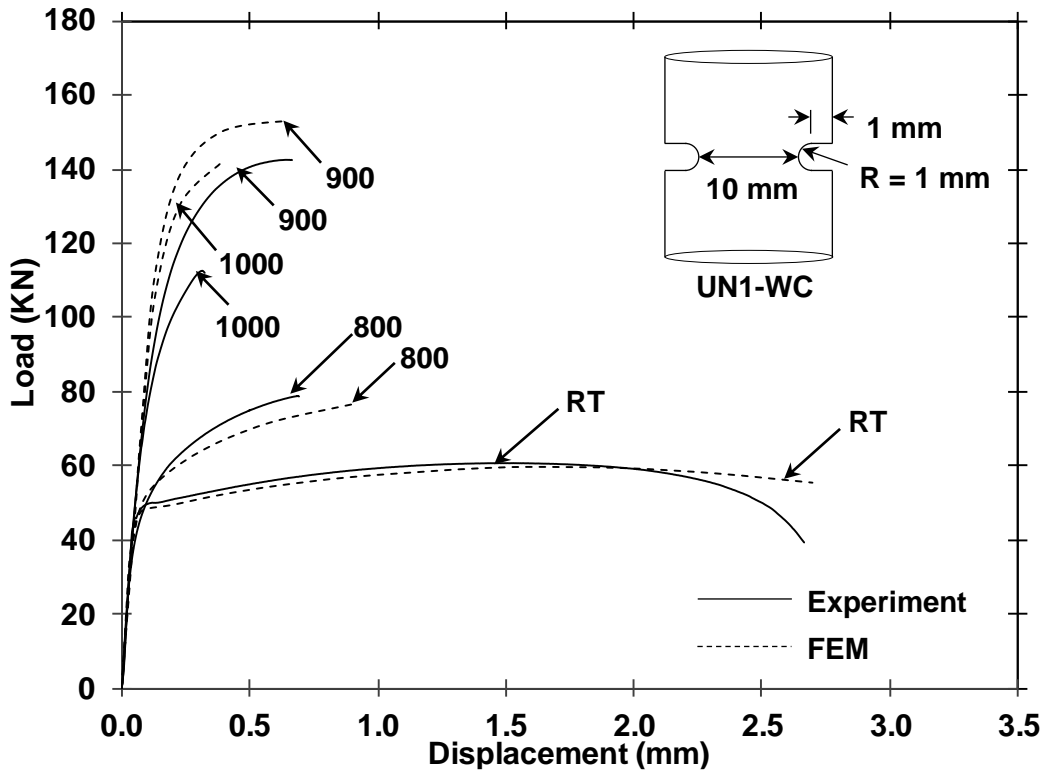


Figure 2.30. Load-displacement curves of specimen UN1-WC (800-1000 °C).

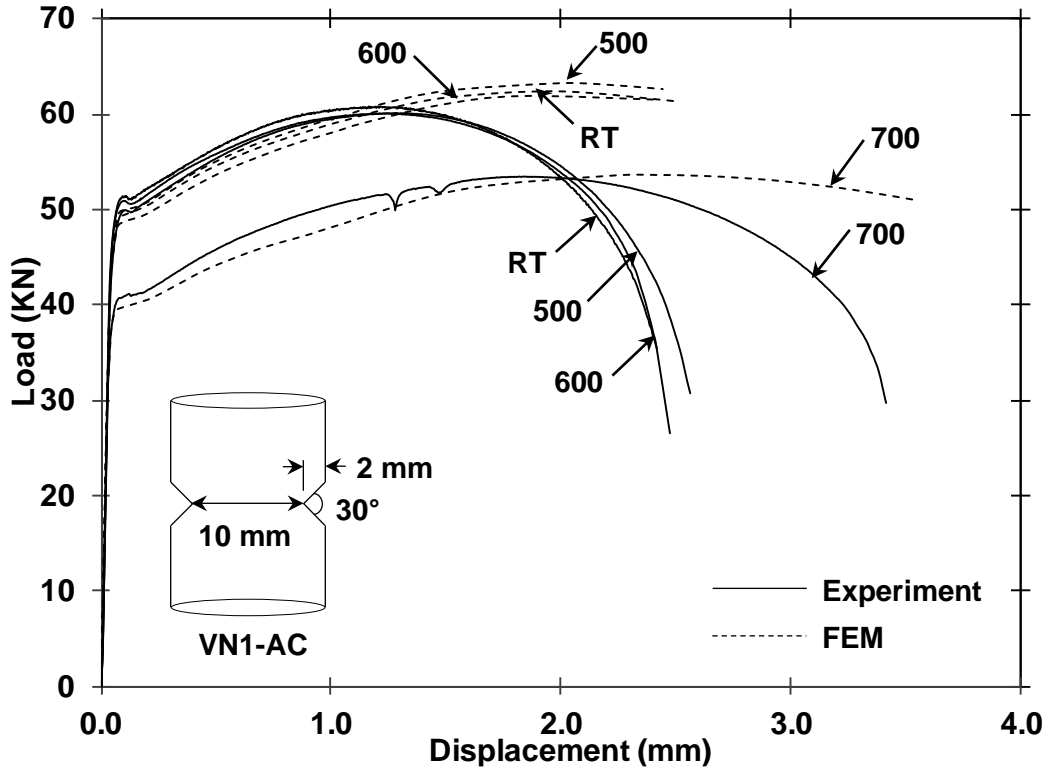


Figure 2.31. Load-displacement curves of specimen VN1-AC (RT-700 °C).

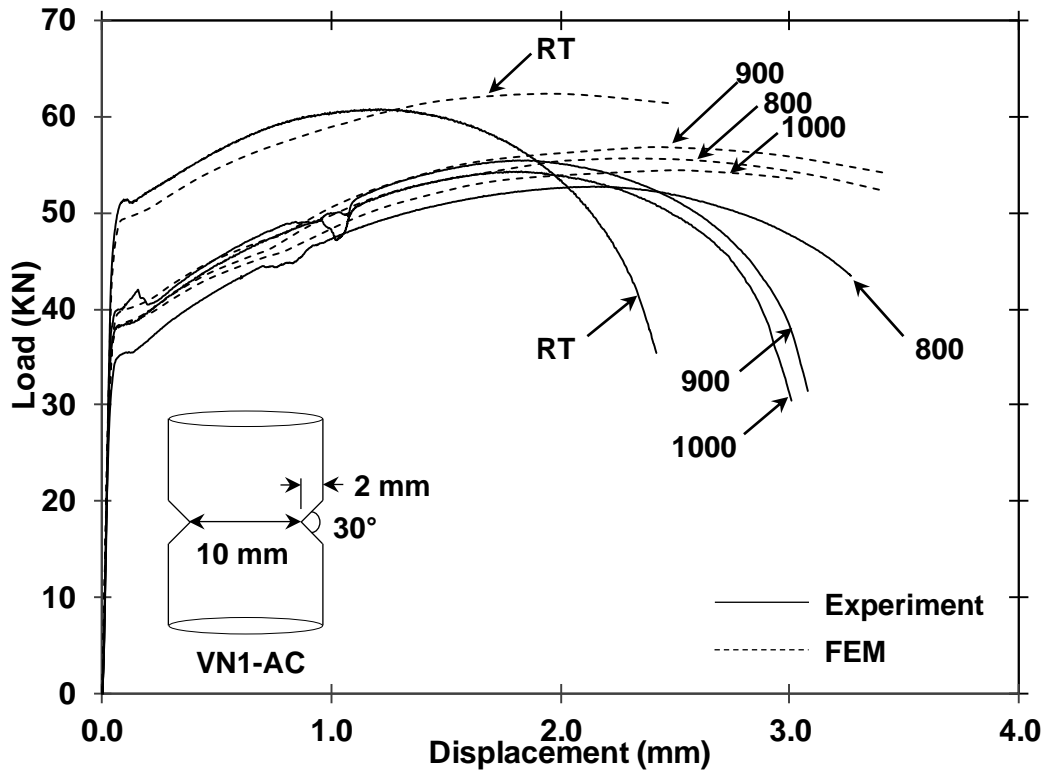


Figure 2.32. Load-displacement curves of specimen VN1-AC (800-1000 °C).

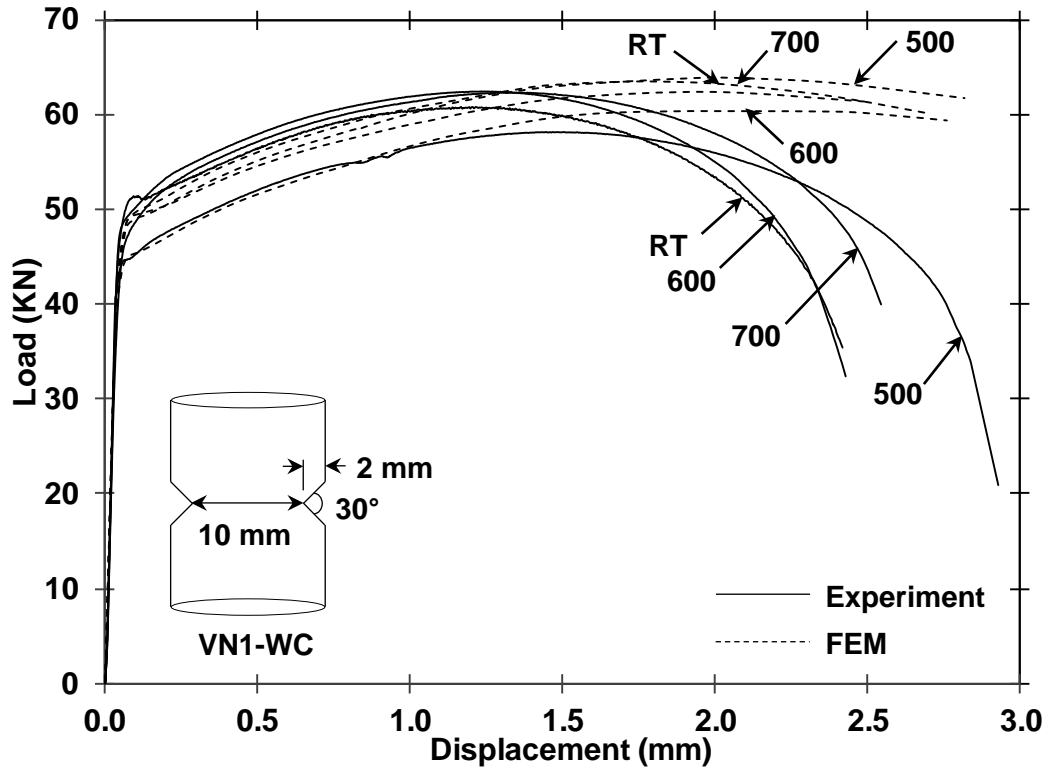


Figure 2.33. Load-displacement curves of specimen VN1-WC (RT-700 °C).

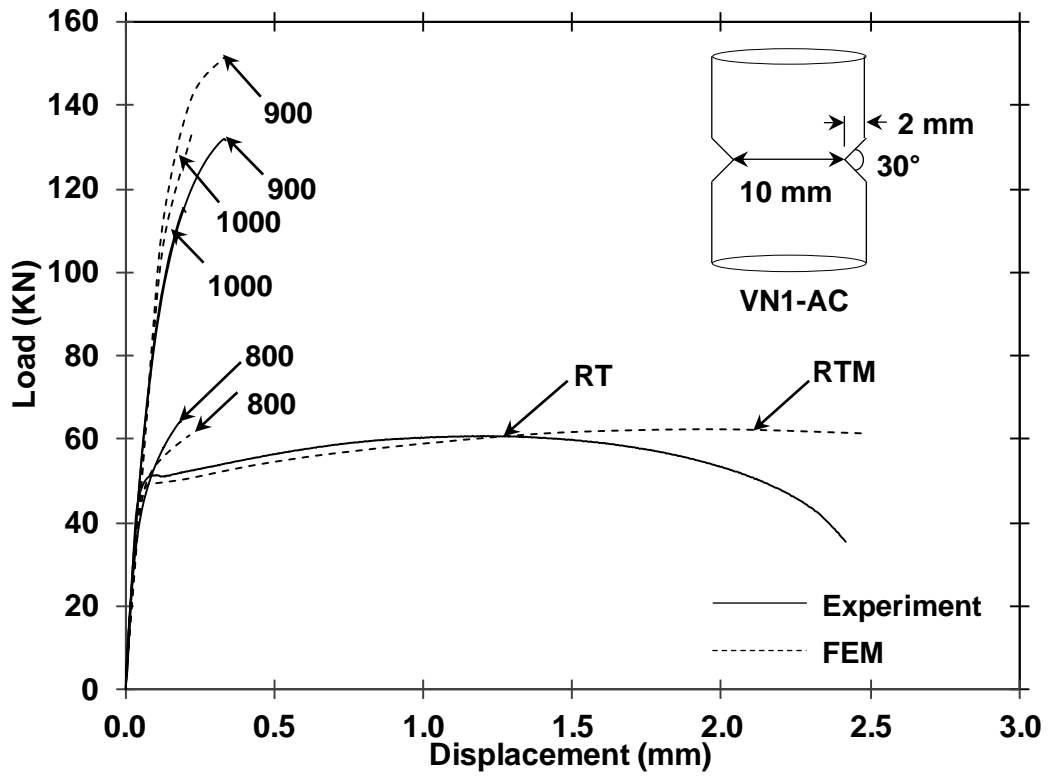


Figure 2.34. Load-displacement curves of specimen VN1-WC (800-1000 °C).

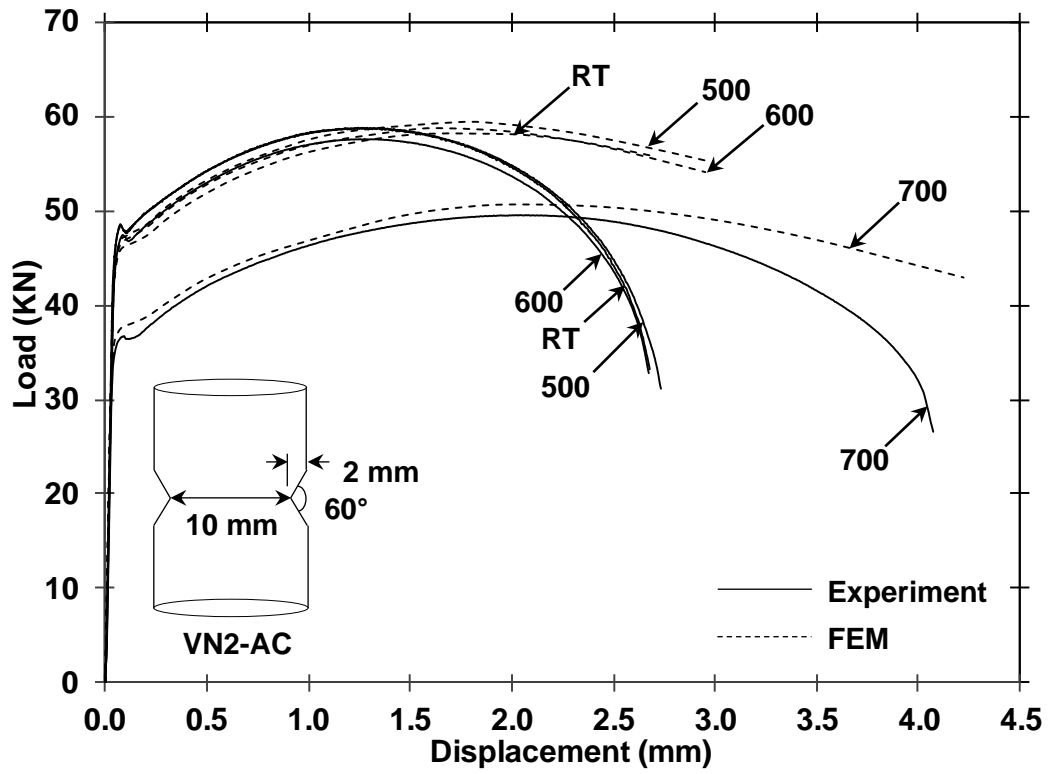


Figure 2.35. Load-displacement curves of specimen VN2-AC (RT-700 °C).

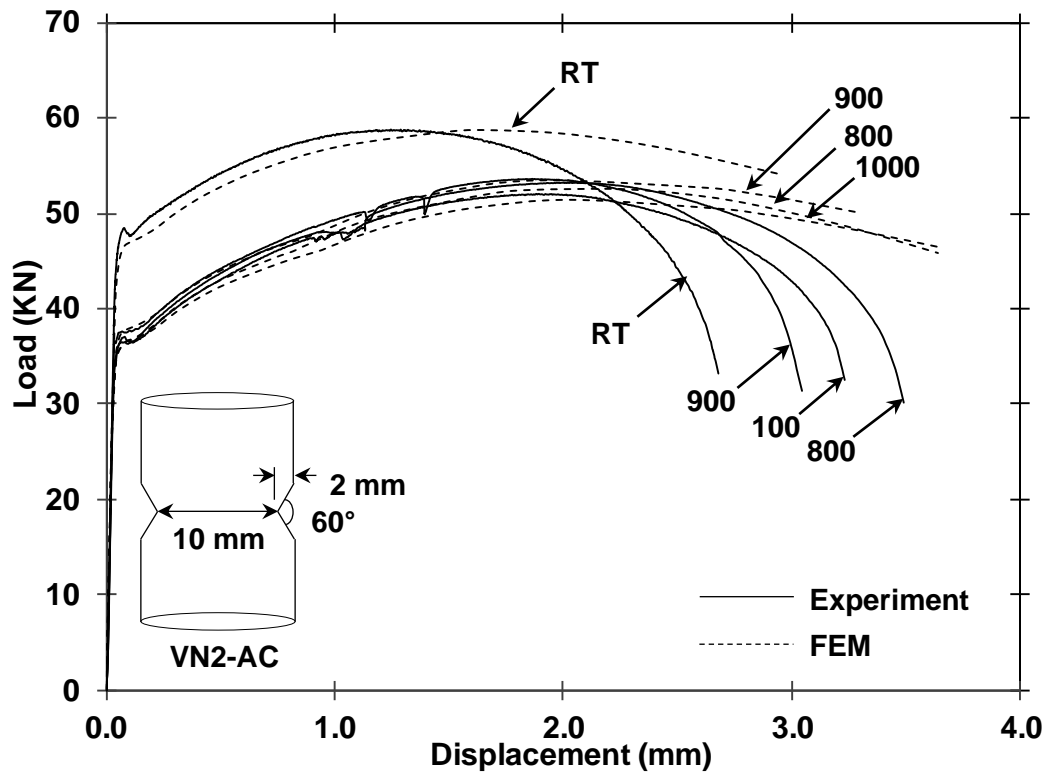


Figure 2.36. Load-displacement curves of specimen VN2-AC (800-1000 °C).

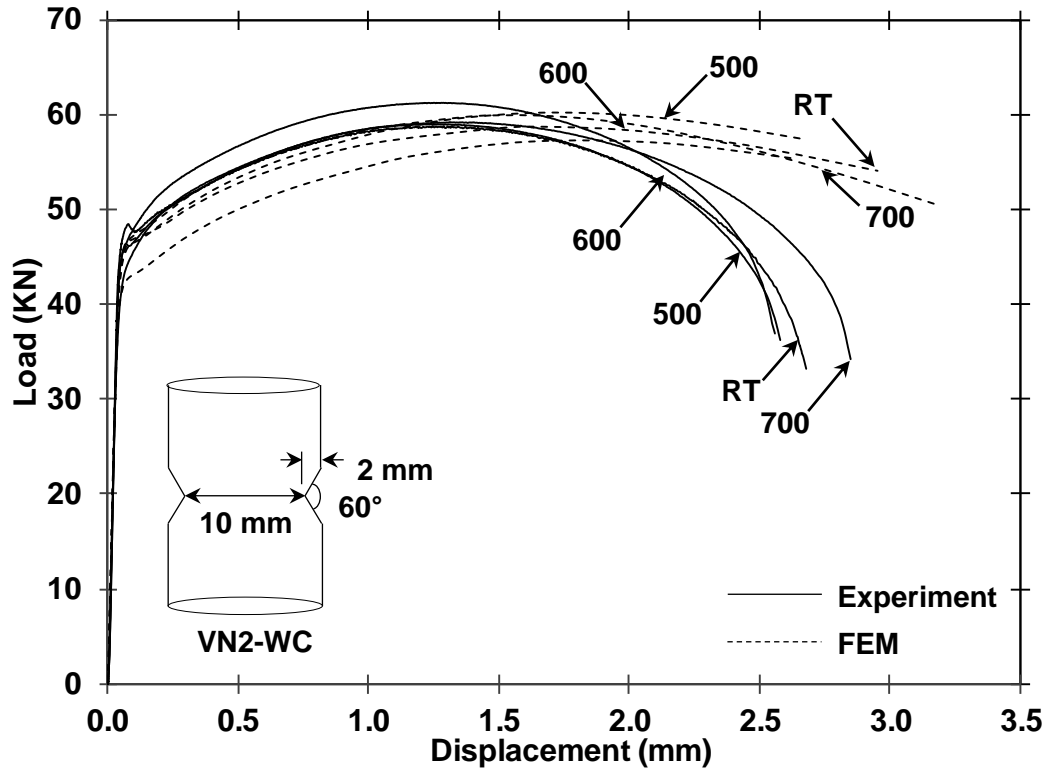


Figure 2.37. Load-displacement curves of specimen VN2-WC (RT-700 °C).

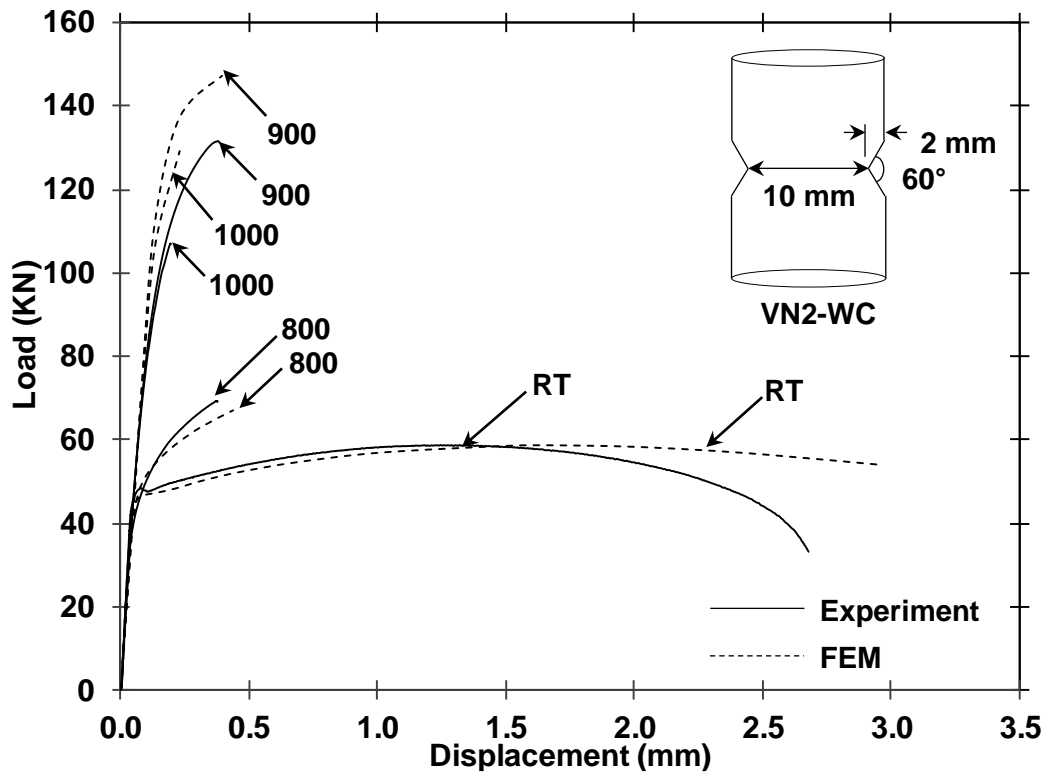


Figure 2.38. Load-displacement curves of specimen VN2-WC (800-1000 °C).

2.3.3. FE Analysis and Stress Triaxialities of Post-Fire Specimens

Non-linear finite element analysis (FEA) is conducted to obtain the stress triaxiality distributions within the critical cross-sections of post-fire test specimens corresponding to different target temperatures and cooling methods. The FEA procedure is discussed in Section 2.2.1. To define the post-fire plastic behavior of notched test specimens, strain hardening curves obtained from uniaxial tensile tests of un-notched test specimens corresponding to different target temperatures are utilized, as shown in Figure 2.39. The load-displacement curves obtained from non-linear finite element analyses are presented along with the experimental load-displacement curves in Figure 2.11 to Figure 2.38. For both notched and un-notched air-cooled test specimens, load-displacement curves obtained from finite element analysis matched reasonably well with those obtained from uniaxial tensile tests until maximum load, except for CN1-600-AC and CN3-700-AC specimens. In the case of CN1-600-AC and CN3-700-AC, about 10% deviation is noticed between experimental and FEM load-displacement curves. Experimental load-displacement curves for air-cooled specimens exhibited rapid degradation in load as compared to FEM results as specimens approached fracture. This difference in experimental and FEM results can be partly attributed to the inadequacy of the J_2 plasticity model to simulate the material softening triggered by void initiation and growth mechanisms [42]. In the case of un-notched water-cooled specimens, FEM results match fairly well with the experimental results until ultimate load, for all target temperatures. For water-cooled notched specimens, experimental load-displacement curves matched well with FEM results until 800 °C. Beyond 800 °C, the FEM-based load-displacement curves did not match well with the experimental results. For temperatures beyond 800 °C, the difference between FEM and experimental load-displacement curves increased as the specimen approaches fracture. An

elastoplastic stress-induced phase transformation model may alleviate this discrepancy [43]. However, such a material model is not used in this study as it falls outside the scope of the current work.

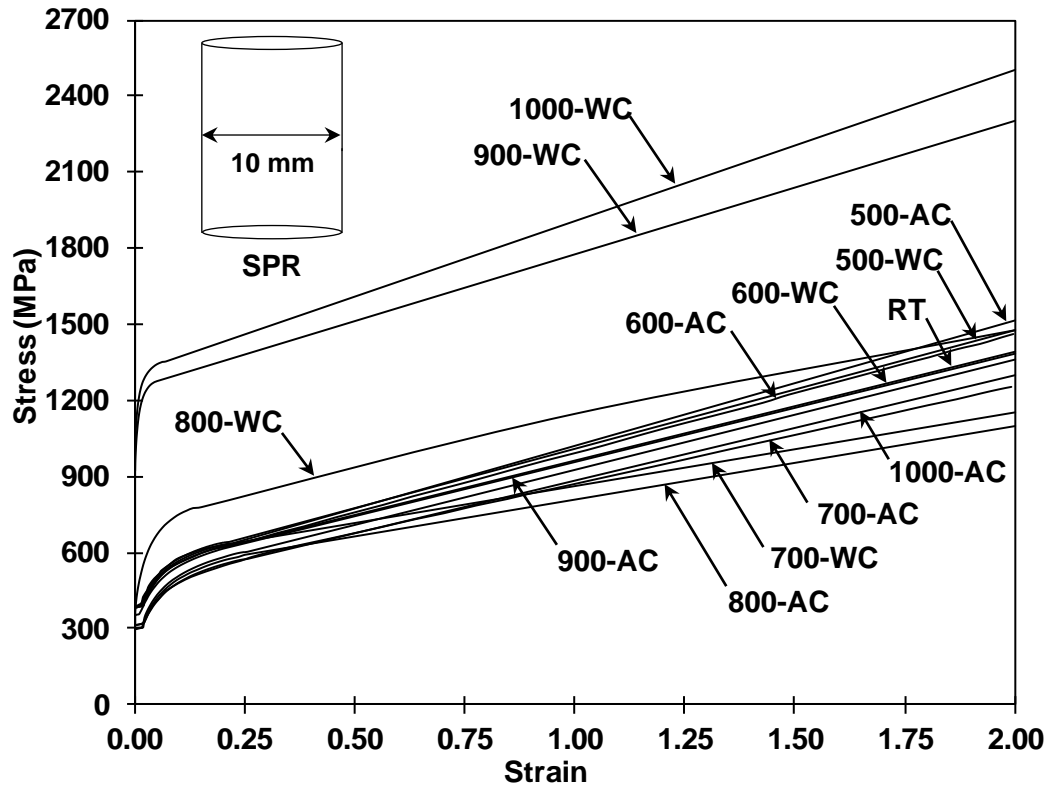


Figure 2.39. Strain hardening curves of un-notched test specimens.

To investigate the relationship between stress triaxialities and cooling methods, maximum and average initial stress triaxialities (spatially averaged over the notch cross-section) corresponding to different temperatures and cooling methods are evaluated and the results are presented in Figure 2.40 and Figure 2.41, respectively. These triaxialities are determined at $1.35 \pm 0.05\%$ strain. It is observed that in almost all notched specimens both maximum and average triaxialities remain unchanged until 700 °C. Beyond 700 °C, AC notched specimens experienced a slight reduction in average stress triaxialities (up to 7%) and maximum stress triaxialities (up to 15%). However, beyond 700 °C, the average stress triaxialities of WC

specimens increases up to 10% whereas maximum stress triaxialities increase by up to 18%. Even a slight reduction or increase in stress triaxiality can alter the ductility in structural steels [30, 44, 45]. As discussed in the previous section, notched WC specimens experienced almost complete loss in ductility (up to 98%) when compared to ductility to un-notched RT specimens. The higher decrease in ductility of notched water-cooled specimens can therefore be partly attributed to an increase in stress triaxiality. Further investigations are required to establish a quantitative relationship between triaxiality and ductility of WC specimens. This is not pursued in this manuscript.

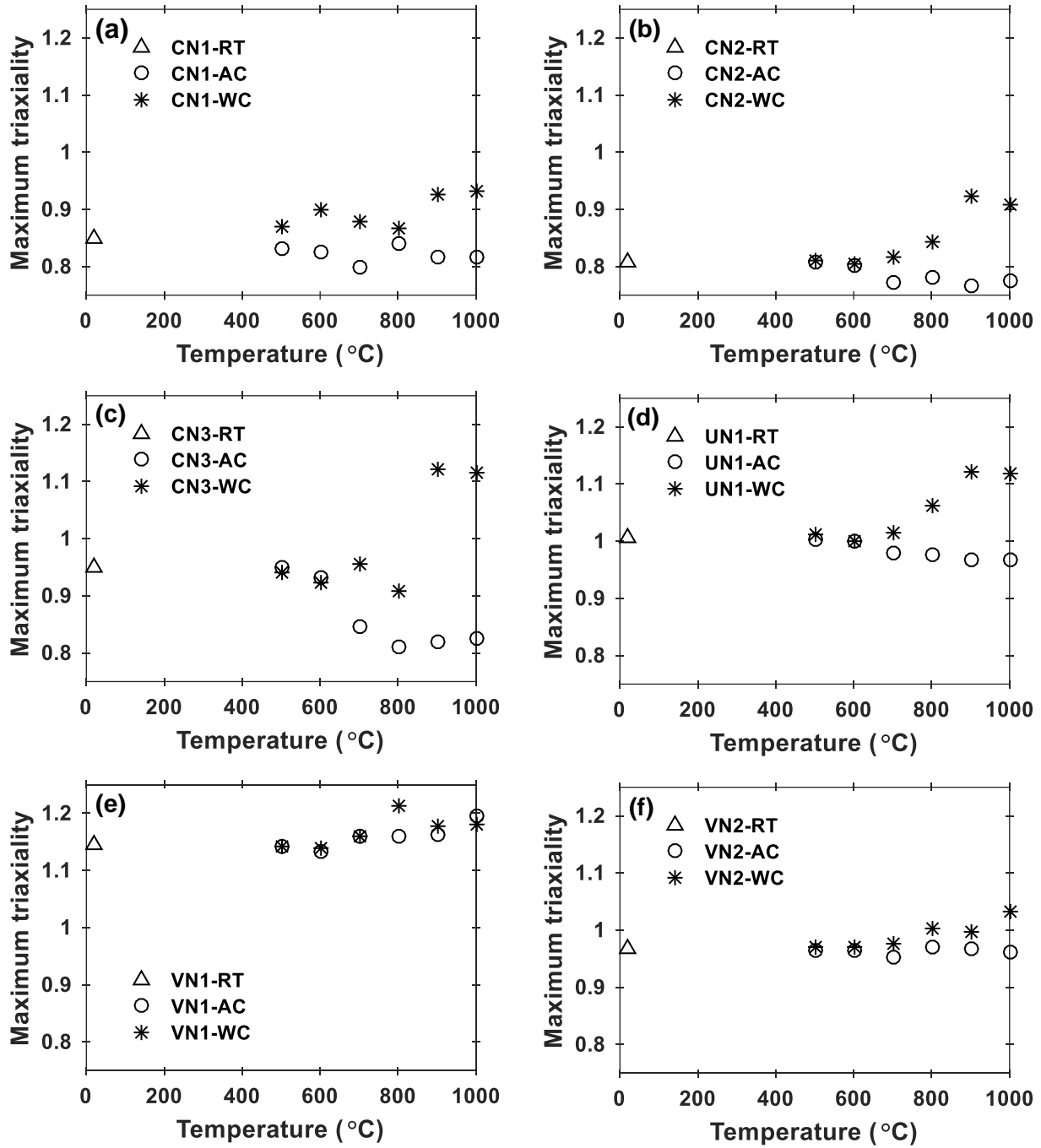


Figure 2.40. Maximum stress triaxialities of post-fire test specimens at 1.35±0.05% strain: a) CN1, b) CN2, c) CN3, d) UN1, e) VN1, and f) VN2.

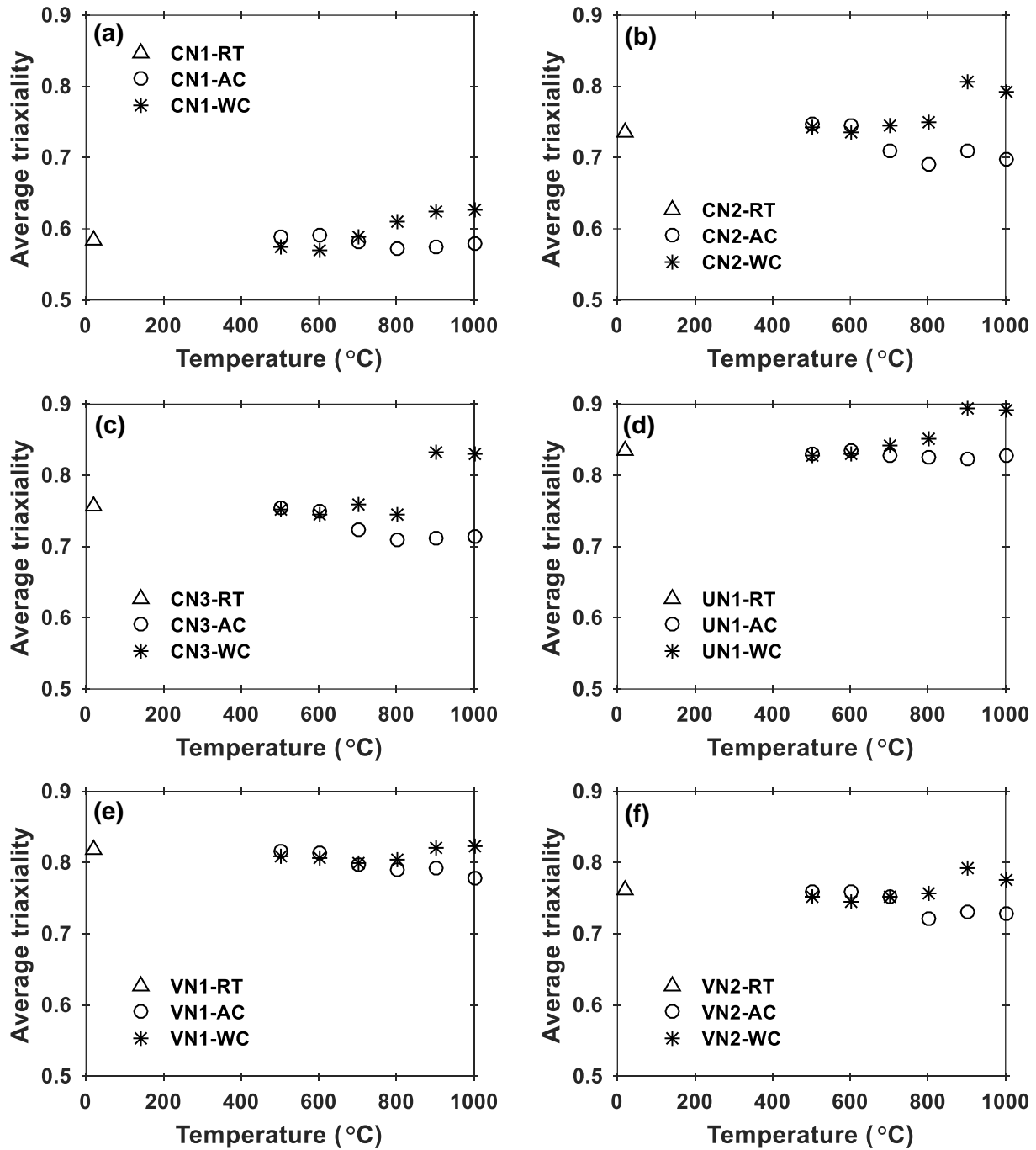


Figure 2.41. Average stress triaxialities of post-fire test specimens at $1.35 \pm 0.05\%$ strain: a) CN1, b) CN2, c) CN3, d) UN1, e) VN1, and f) VN2.

2.3.4. Elastic Modulus

The post-fire elastic modulus of test specimens is determined based on the initial slope of the elastic portion of post-fire engineering stress-strain curves. The elastic modulus residual

factors at different target temperatures and stress triaxialities for un-notched and notched specimens are presented in Figure 2.42(a) and Figure 2.43, respectively. Elastic modulus residual factor is defined as the ratio of elastic modulus of a test specimen of a particular geometry that has been subjected to a target temperature (E_T) to the elastic modulus of the un-notched test specimen at room temperature ($E_{20,SPR}$). For instance, the elastic modulus residual factor of the CN1 test specimen corresponding to a target temperature 'T' is defined as $E_{T,CN1}/E_{20,SPR}$. As observed in Figure 2.42(a), the majority of SPR-AC and SPR-WC specimens experienced only minor reduction in elastic modulus and remained within 10% (as shown by the shaded portion in Figure 2.42(a)) of the RT elastic modulus, irrespective of the target temperature. Post-fire elastic modulus residual factors of notched test specimens (CN1, CN2, CN3, UN1, VN1, and VN2) are presented in Figure 2.43. As observed in Figure 2.43, the elastic modulus of room temperature RT notched specimens increased with an increase in stress triaxiality. The specimens with the highest triaxialities (UN1-RT and VN1-RT) exhibited up to a 78% increase in elastic modulus when compared to the un-notched RT elastic modulus. With the increase in temperature, the post-fire elastic modulus of almost all notched specimens experienced a further increase or decrease of up to 10% in their RT elastic modulus (as shown by the shaded portion in Figure 2.43). However, a few WC specimens (CN1-1000-WC, CN2-1000-WC, and VN2-900-WC) specimens exhibited up to 15% reduction in elastic modulus when compared to the elastic modulus of RT notched specimens. In contrast, CN3-AC and CN3-WC specimens exhibited a further increase of 20% in their RT elastic modulus when cooled from 700 °C.

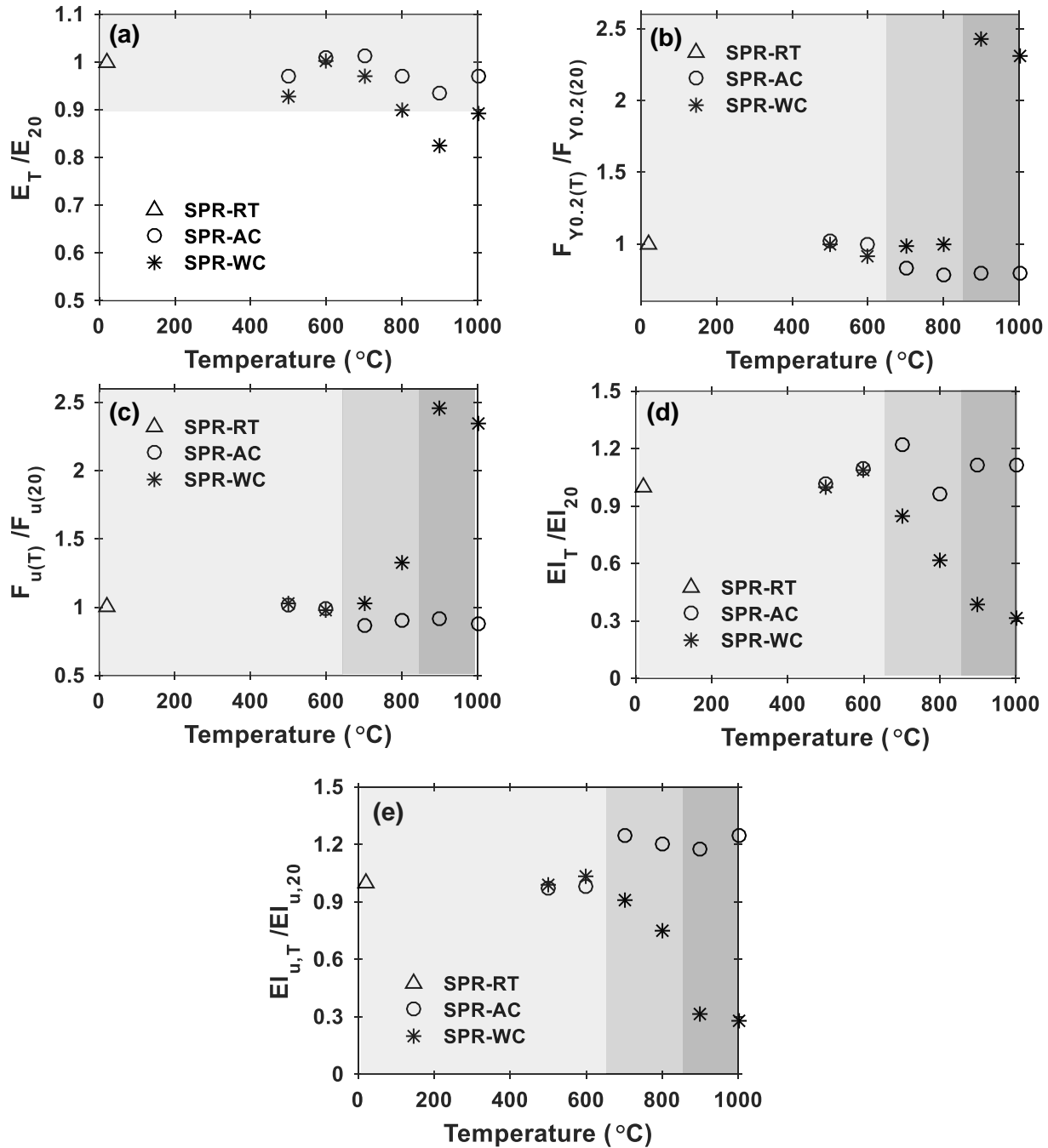


Figure 2.42. Residual factors of specimen SPR under different cooling regimes: a) elastic modulus, b) yield strength, c) ultimate tensile strength, d) fracture strain, and e) uniform strain.

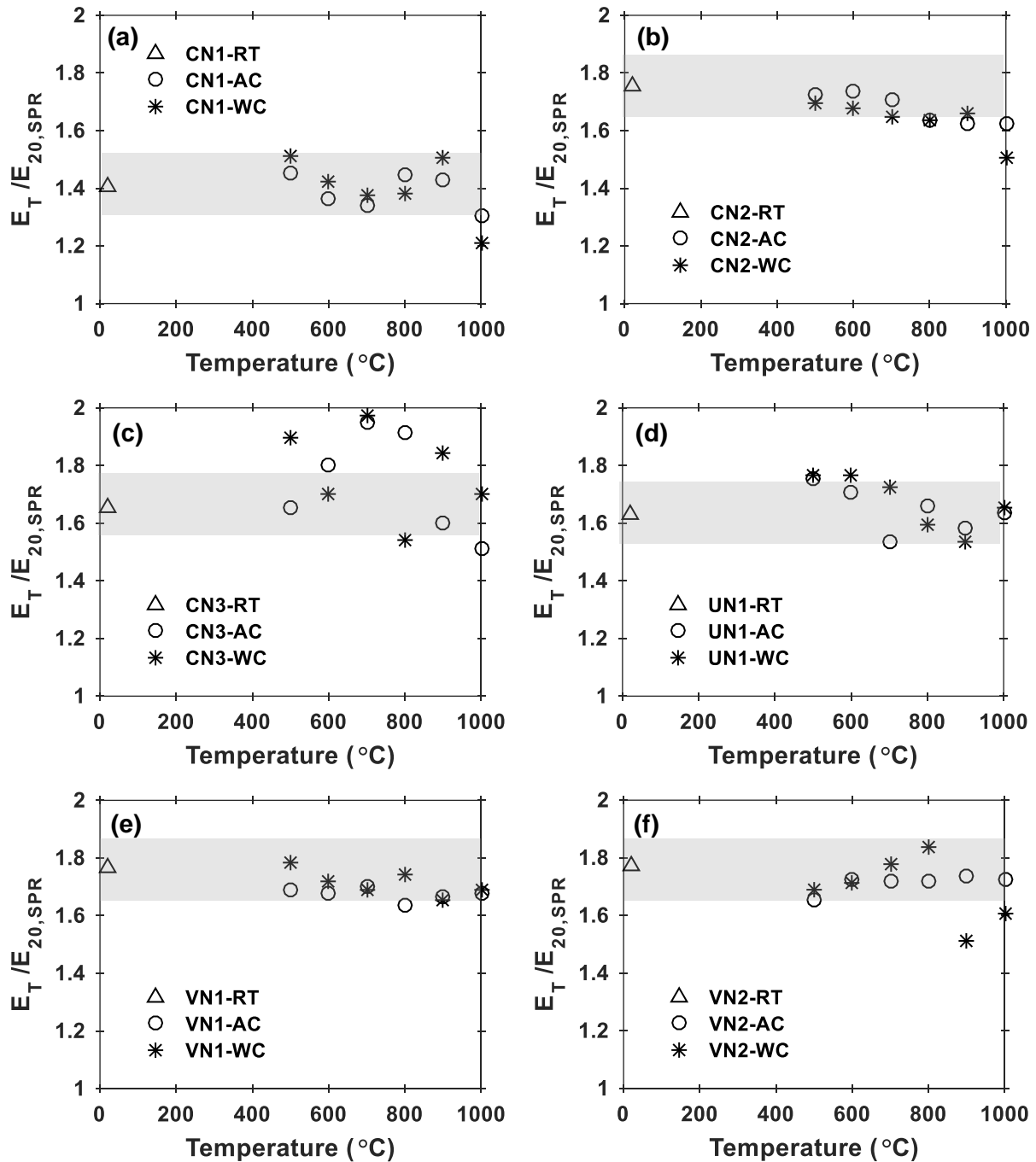


Figure 2.43. Elastic modulus residual factors of post-fire test specimens: a) CN1, b) CN2, c) CN3, d) UN1, e) VN1, and f) VN2.

It is evident from the above discussion that notched specimens experience a major increase in elastic moduli due to an increase in stress triaxiality. Minor differences between elastic moduli of notched RT specimens and post-fire notched specimens (within 10-15%)

indicate that exposure to high temperature does not play a considerable role in altering the elastic moduli of post-fire ASTM A36 steels. The relatively unchanged elastic modulus of steel specimens after exposure to different temperatures can be attributed to the fact that elastic modulus depends on interatomic distances and bonding energy and is relatively uninfluenced by phase changes and grain size changes induced by heat treatment [31]. The few exceptions, where more than 10% change in elastic modulus is observed, can be attributed to material heterogeneities.

At this juncture, it is important to note that the elastic modulus is a material property and should remain invariant irrespective of the cooling methods and triaxiality. The increase in the elastic modulus reported in this section is strongly tied to the definition of the elastic modulus used in this study. A more appropriate way to measure the elastic modulus is by evaluating it from the diametrical strain versus stress and not from the longitudinal strain versus stress curves. However, in the present work, the residual elastic moduli at different temperature levels are extracted from longitudinal strain versus stress curves considering the procedures suggested by ASTM E111 [85] that are usually adopted by structural engineers.

2.3.5. Yield Strength

The strength corresponding to 0.2% engineering strain is taken as the post-fire yield strength of test specimens [31]. The post-fire yield strength values of test specimens are provided in Table 2.3. In addition, yield strength residual factors of un-notched and notched test specimens corresponding to different target temperatures are presented in Figure 2.42(b) and Figure 2.44, respectively. Yield strength residual factor is defined as the ratio of yield strength of test specimen of a particular geometry that has been subjected to a target temperature ($F_{y,T}$) to yield strength of un-notched test specimen at room temperature ($F_{y,20,SPR}$). For instance, the yield

strength residual factor of the CN1 test specimen corresponding to a target temperature ‘T’ is defined as $F_{y,T,CN1}/F_{y,20,SPR}$.

Table 2.3. Post-fire yield strength of test specimens.

Temperature (°C)	Cooling method	Yield strength (MPa)						
		SPR	CN1	CN2	CN3	UN1	VN1	VN2
20	-	383.92	525.21	590.91	572.54	628.50	653.52	610.16
500	AC	389.41	508.49	576.36	556.33	619.11	635.80	609.46
	WC	381.25	510.69	574.77	578.50	565.12	569.55	587.72
600	AC	380.72	466.27	584.19	566.37	620.43	651.57	600.66
	WC	350.45	513.93	607.10	594.19	626.68	631.86	602.91
700	AC	319.35	411.01	463.42	498.01	480.52	516.01	463.86
	WC	378.55	494.60	597.11	580.99	620.41	613.36	572.64
800	AC	300.79	392.29	448.29	441.13	476.30	452.52	471.35
	WC	384.70	522.34	602.69	641.81	634.57	672.25	623.67
900	AC	306.42	378.95	469.57	439.84	481.32	505.85	477.35
	WC	934.39	1121.34	1167.41	1408.84	1271.86	1270.60	1276.74
1000	AC	303.82	348.16	442.48	427.19	466.14	486.83	463.97
	WC	884.75	1082.43	1158.81	1239.09	1077.15	1281.07	1190.81

The influence of triaxiality on yield strength is inferred by comparing the yield strengths of notched RT specimens with un-notched RT specimen (SPR). From Table 2.3, it is clear that the yield strength in the notched RT specimens increased by almost 70% (VN1-notch) and this increase can be attributed to an increase in triaxiality of notched specimens when compared to the un-notched specimen (SPR RT) [47]. The influence of temperature on the yield strength of air-cooled specimens is determined by comparing the yield strengths of SPR AC specimens with the yield strength of SPR RT specimen. The yield strength of SPR specimens remained more or less the same when air-cooled from 600 °C. However, beyond 600 °C (up to 1000 °C), up to 20% degradation in yield strength is observed in SPR AC specimens. This can be attributed to the increase in the average ferrite grain size in the ASTM A36 steel microstructure [48, 49]. At room temperature, the ASTM A36 steel microstructure primarily consists of ferrite (α -iron) and

pearlite, as shown by bright and dark areas in Figure 2.45. Pearlite consists of alternating layers of ferrite (Fe) and cementite (Fe_3C). The presence of cementite imparts hardness to the pearlite. When steel specimens are heated to temperatures beyond 650 °C, ferrite undergoes a polymorphic transformation from body-centered cubic (BCC) to face-centered cubic (FCC) crystal structure, referred to as austenite (γ -iron). Upon cooling slowly (air-cooling) to room temperature, the austenite is transformed back to a relatively uniform and coarse-grained ferrite and pearlite phase, as shown in Figure 2.46. This transformation results in a relatively higher ferrite grain size as evident from Figure 2.46. The decrease in yield strength of AC specimens can be attributed to the increase in grain size of the softer ferrite phase when specimens are air-cooled (slowly cooled) after exposure to high temperatures.

The influence of water cooling on yield strength can be obtained by comparing the yield strengths of SPR WC specimens with the yield strength of SPR RT specimen. There is no significant change in yield strength up to a temperature of 800 °C in the case of WC SPR specimens. However, the SPR specimens water-cooled from temperatures beyond 800 °C, exhibited about 143% higher yield strength when compared to the RT SPR specimen. This can be attributed to the formation of the martensite phase in WC specimens that are exposed to temperatures 900 °C and 1000 °C. When steel specimens are heated to temperatures beyond 860 °C, the ferrite phase fully transforms into the austenite phase. Upon rapid cooling (water-cooling), the austenite phase undergoes diffusionless transformation to a metastable phase, called martensite, as shown in Figure 2.47. Martensite microstructure has a body-centered tetragonal crystal structure and possesses high strength and low ductility [49-52]. The increase in yield and ultimate tensile strength of water-cooled specimens can therefore be attributed to the formation of martensite in these specimens. In a nutshell, the yield strength in AC samples exposed to very

high temperatures is found to decrease due to the increase in grain size, and the yield strength in WC samples exposed to very high temperatures is found to increase significantly due to the formation of harder martensite phase, as discussed above.

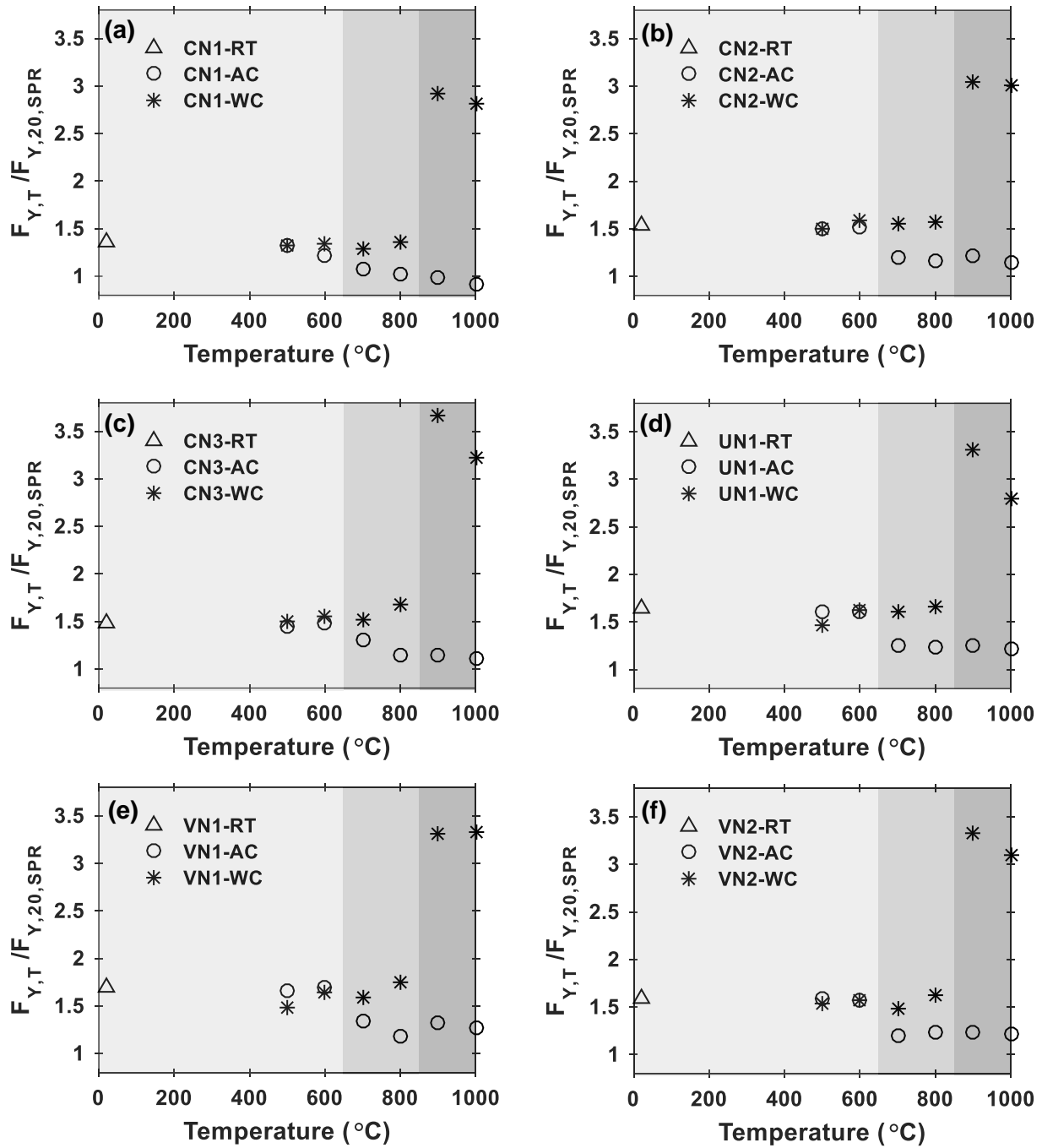


Figure 2.44. Yield strength residual factors of post-fire test specimens: a) CN1, b) CN2, c) CN3, d) UN1, e) VN1, and f) VN2.

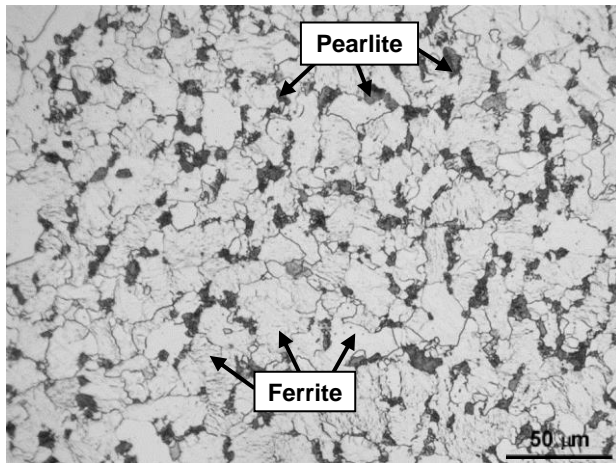


Figure 2.45. Microstructure of ASTM A36 steel at room temperature (RT).

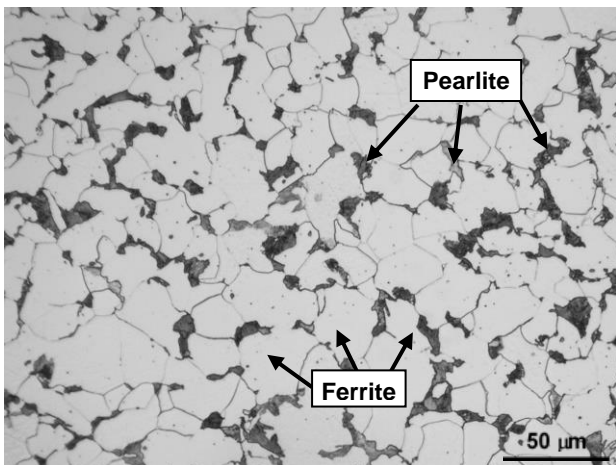


Figure 2.46. Microstructure of ASTM A36 steel after air-cooling from 900 °C to RT.

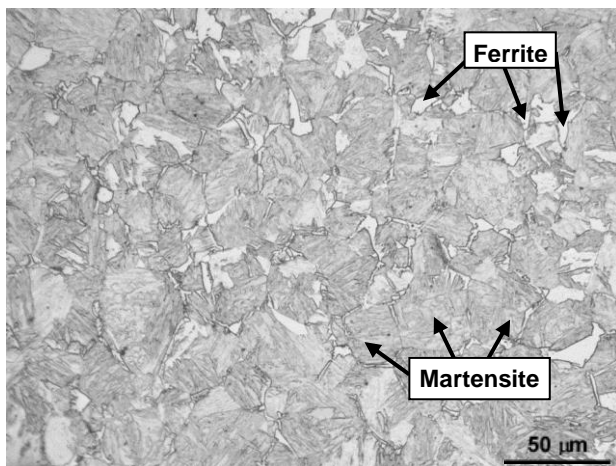


Figure 2.47. Microstructure of ASTM A36 steel after water-cooling from 900 °C to RT.

The combined influence of triaxiality and high temperatures on the yield strength of AC specimens can be obtained by examining the yield strengths of notched AC specimens. The yield strength of all the AC notched specimens is observed to decrease with an increase in temperature, which is also observed in the case of un-notched specimens. No significant decrease in yield strength is noticed in individual AC notched specimens when compared to the SPR RT specimen. However, AC notched specimens experienced up to 33% reduction in yield strength when compared to notched RT specimens. Notwithstanding this observation, the yield strength of AC notched specimens is found to be higher than the yield strength of SPR RT specimen. From this, it is clear that the strengthening caused by high triaxialities dominated the weakening caused by the increase in the grain size leading to a net gain in yield strengths in the case of notched AC samples. The combined influence of triaxiality and high temperatures on the yield strength of WC specimens can be obtained by examining the yield strengths of notched WC specimens. Unlike the AC notched specimens, the yield strength in the case of WC notched specimens is observed to increase with the increase in temperature. This increase is specifically significant for specimens that are cooled from 900 °C and 1000 °C. This increase in yield strength can be attributed to the formation of a stronger martensite phase when water-cooled from high temperatures [49] (see Figure 2.47) and an increase in average stress triaxiality of WC notched specimens, as shown in Figure 2.48 [47]. Overall, elevated temperatures are found to have only a positive effect on the yield strength in the case of notched specimens irrespective of the cooling method.

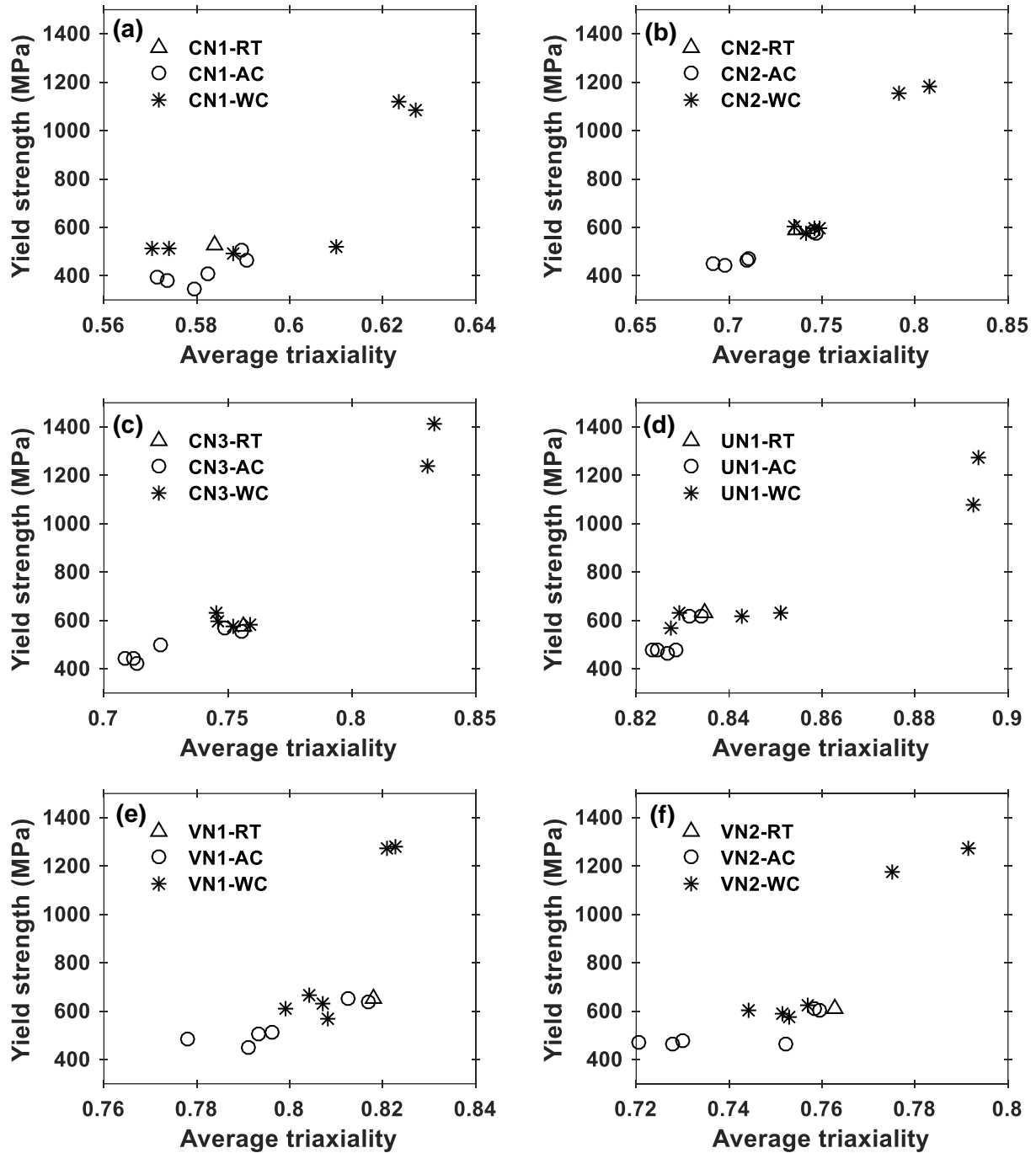


Figure 2.48. Average stress triaxiality versus yield strength of post-fire test specimens: a) CN1, b) CN2, c) CN3, d) UN1, e) VN1, and f) VN2.

2.3.6. Ultimate Tensile Strength

The maximum stress in the engineering stress-strain curve is taken as the ultimate tensile strength of a test specimen in this study. The post-fire ultimate tensile strength values of test

specimens are provided in Table 2.4. In addition, ultimate tensile strength residual factors of un-notched and notched test specimens corresponding to different target temperatures are presented in Figure 2.42(c) and Figure 2.49, respectively. Ultimate tensile strength residual factor is defined as the ratio of ultimate tensile strength of test specimen of a particular geometry that has been subjected to a target temperature ($F_{u,T}$) to ultimate tensile strength of un-notched test specimen at room temperature ($F_{u,20,SPR}$). For instance, the ultimate tensile strength residual factor of CN1 test specimen corresponding to a target temperature ‘T’ is defined as

$$F_{u,T,CN1}/F_{u,20,SPR}$$

Table 2.4. Post-fire ultimate tensile strength of test specimens.

Temperature (°C)	Cooling method	Ultimate tensile strength (MPa)						
		SPR	CN1	CN2	CN3	UN1	VN1	VN2
20	-	514.59	681.70	734.17	728.80	770.81	775.41	749.43
500	AC	520.63	674.38	729.34	719.62	769.10	767.28	750.14
	WC	526.44	691.14	740.58	738.90	734.04	738.87	749.00
600	AC	510.82	626.05	722.39	718.86	763.05	768.76	731.68
	WC	502.40	700.75	773.43	758.44	802.81	790.27	776.11
700	AC	443.49	585.04	616.06	647.28	651.14	678.71	628.26
	WC	527.18	673.15	771.54	744.12	803.80	790.75	753.74
800	AC	465.00	611.80	648.77	640.58	687.12	675.42	679.44
	WC	681.91	911.30	958.79	954.05	1002.62	817.00	886.62
900	AC	474.18	576.21	665.06	642.01	687.87	702.89	682.42
	WC	1266.95	1604.23	1717.21	1595.24	1815.47	1680.81	1676.72
1000	AC	455.33	566.72	630.78	624.99	671.69	691.42	662.35
	WC	1206.62	1497.68	1554.53	1613.01	1434.12	1468.81	1364.02

The influence of triaxiality on ultimate tensile strength is inferred by comparing the ultimate tensile strengths of notched RT specimens with un-notched RT specimens. From Table 2.4, it is clear that the ultimate tensile strength in the notched RT specimens increased by almost 50% (VN1-notch) and this increase can be attributed to increase in triaxiality of notched specimens when compared to the un-notched specimen (SPR) [47]. The influence of temperature

on the ultimate tensile strength of air-cooled specimens can be determined by comparing the ultimate tensile strength of SPR AC specimens with ultimate tensile strength of SPR RT specimen. SPR AC specimens almost completely retained ultimate tensile strength when air-cooled from 600 °C. Beyond 600 °C (up to 1000 °C), up to 14% degradation in ultimate tensile strength is observed in SPR AC specimens, which can be attributed to the increase in the average ferrite grain size in the ASTM A36 steel microstructure [48, 49]. The influence of water cooling on ultimate tensile strength can be obtained by comparing the ultimate tensile strengths of SPR WC specimens with ultimate tensile strength of SPR RT specimen. No considerable change in ultimate tensile strength is observed when SPR specimens are water-cooled from temperatures up to 700 °C. However, the SPR WC specimens exhibited significant increase in ultimate tensile strength when water-cooled from temperatures beyond 700 °C. Specifically, SPR specimen water-cooled from 900 °C exhibited about 146% higher ultimate tensile strength when compared to the RT SPR specimen. This increase in ultimate tensile strength is very close to the amount of increase observed in yield strength of SPR specimen water-cooled from 900 °C (143%) and can be attributed to the formation of stronger martensite phase in WC specimens that are exposed to temperatures of 900 °C and 1000 °C. In summary, the ultimate tensile strength in AC samples exposed to very high temperatures is found to decrease due to the increase in grain size and the ultimate tensile strength in WC samples exposed to very high temperatures is found to increase significantly due to the formation of harder martensite phase.

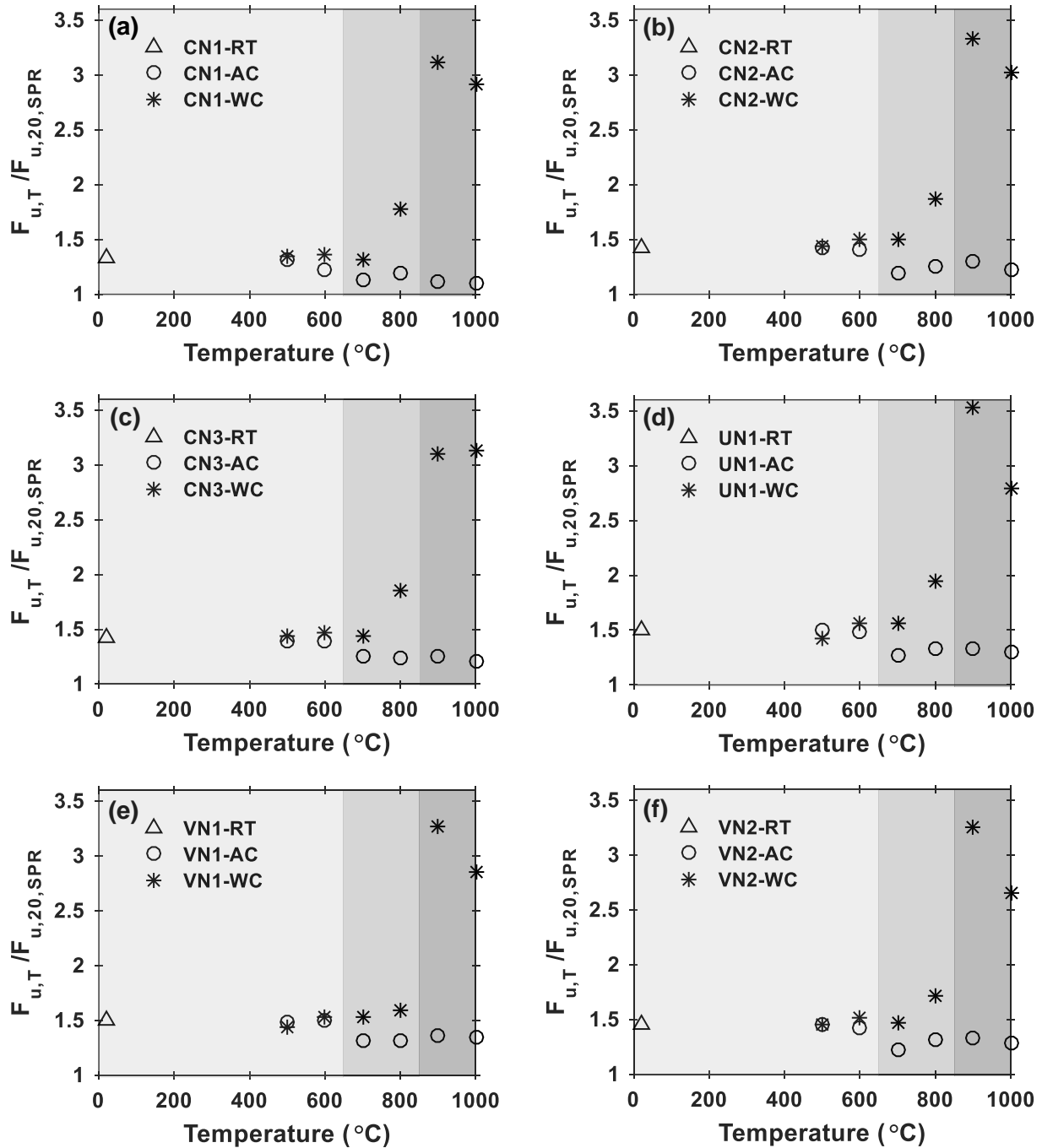


Figure 2.49. Ultimate tensile strength residual factors of post-fire test specimens: a) CN1, b) CN2, c) CN3, d) UN1, e) VN1, and f) VN2.

The combined influence of triaxiality and high temperatures on ultimate tensile strength of AC specimens can be obtained by examining the ultimate tensile strengths of notched AC specimens. AC notched specimens experienced decrease in ultimate tensile strength with

increase in temperature, which is also observed in the case of un-notched specimens. AC notched specimens exhibited up to 17% decrease in ultimate tensile strength when compared to corresponding RT notched specimen. However, the ultimate tensile strength of AC notched specimens remained higher than ultimate tensile strength of SPR RT specimen. This observation shows that the strengthening caused by high triaxialities dominated the weakening caused by increase in the grain size leading to net increase in ultimate tensile strengths in the case of notched AC samples. The combined influence of triaxiality and high temperatures on ultimate tensile strength of WC specimens can be obtained by examining the ultimate tensile strengths of notched WC specimens. Contrary to AC notched specimens, the ultimate tensile strength in the case of WC notched specimens is observed to increase with the increase in temperature, particularly at 900 °C and 1000 °C. Notched specimens that are water-cooled from 900 °C exhibited up to 252% increase in ultimate tensile strength when compared to SPR RT specimen. The significant increase in ultimate tensile strength in notched specimens can be attributed to the presence of high stress triaxiality (see Figure 2.50) and formation of stronger martensite phase when water-cooled from high temperatures. These results suggest that both yield strength and ultimate tensile strength follow similarly increase in trend in case of WC notched specimens. To summarize, high temperatures are found to have only a positive influence on the ultimate tensile strength of notched specimens irrespective of the cooling method.

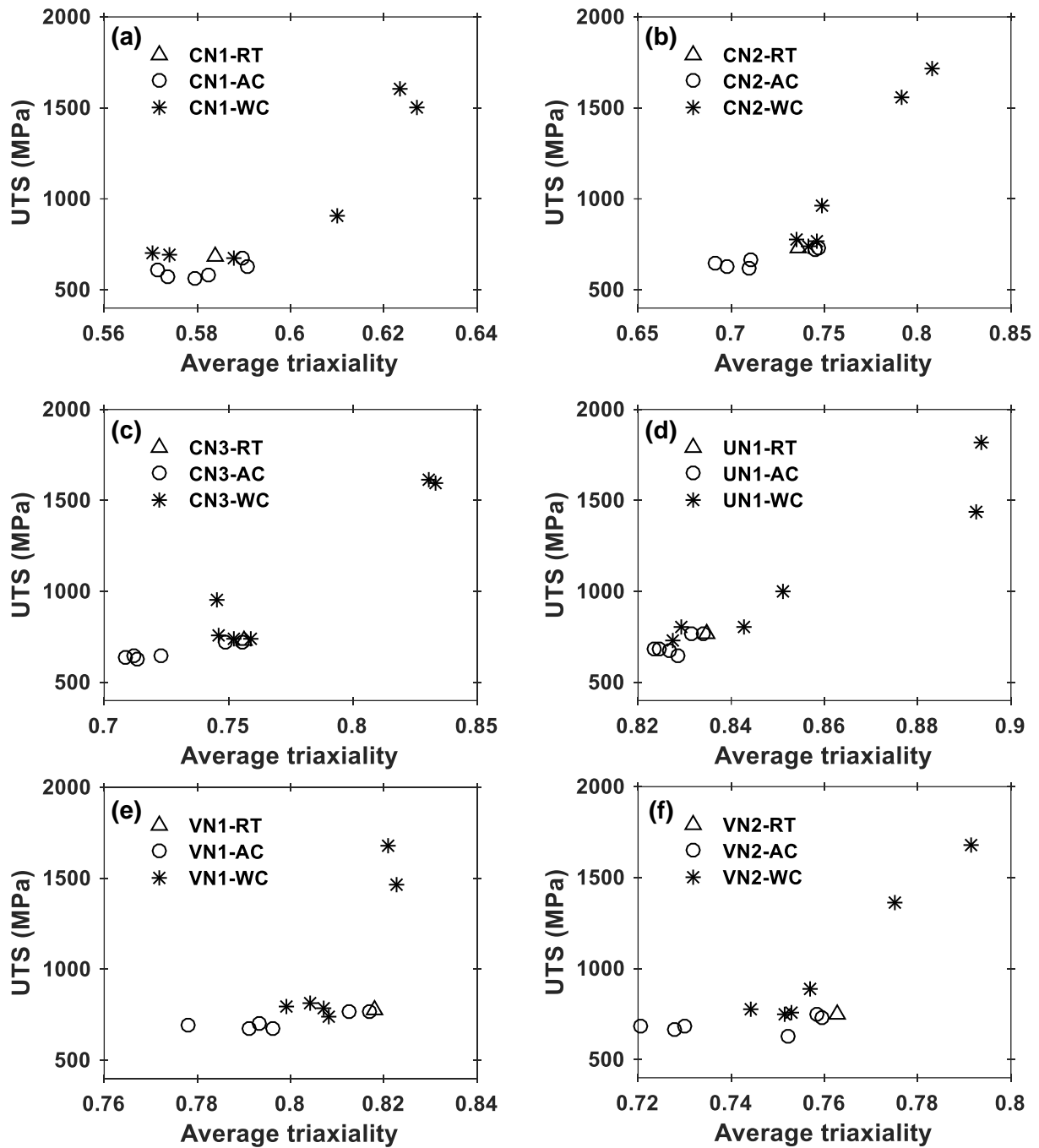


Figure 2.50. Average stress triaxiality versus ultimate tensile strength of post-fire test specimens: a) CN1, b) CN2, c) CN3, d) UN1, e) VN1, and f) VN2.

2.3.7. Ductility

Ductility of structural steel is defined as the ability of structural steel to undergo plastic deformation before fracture. Post-fire ductility values of test specimens are determined based on

the fracture strain of post-fire engineering stress-strain curves and are provided in Table 2.5. Moreover, ductility residual factor, which is defined as the ratio of ductility of test specimen of a particular geometry that has been subjected to a target temperature (El_T) to ductility of un-notched test specimen at room temperature ($El_{20,SPR}$), of each test specimen is provided in Figure 2.42(d) and Figure 2.51, respectively.

Table 2.5. Post-fire ductility of test specimens.

Temperature (°C)	Cooling method	Ductility (%)						
		SPR	CN1	CN2	CN3	UN1	VN1	VN2
20	-	40.31	17.57	11.75	9.35	10.66	9.67	10.72
500	AC	40.86	17.33	11.70	9.42	10.99	10.26	10.94
	WC	40.17	16.53	12.10	9.29	12.42	11.31	10.32
600	AC	44.13	19.35	11.99	9.47	11.14	9.90	10.70
	WC	43.99	17.02	11.63	9.37	10.81	9.71	10.23
700	AC	49.22	22.13	15.36	11.64	15.41	13.66	16.29
	WC	34.06	16.29	11.91	9.37	11.69	10.18	11.40
800	AC	38.77	22.27	14.83	11.62	14.70	13.07	13.96
	WC	24.92	4.72	3.63	2.79	2.77	0.75	1.50
900	AC	44.85	23.26	12.52	10.37	12.60	12.32	12.18
	WC	15.73	4.84	3.56	1.90	2.66	1.35	1.54
1000	AC	44.83	20.62	13.45	11.05	13.23	12.03	12.93
	WC	12.60	3.24	2.66	1.72	1.30	0.81	0.77

To evaluate the influence of triaxiality on ductility, the ductility of notched RT specimens and un-notched RT specimen are compared. As evident from Table 2.5, notched RT specimens exhibited up to 76% decrease in ductility (CN3-RT and VN1-RT), which can be attributed to the higher stress triaxiality in notched specimens when compared to un-notched specimen (SPR) [30, 53]. The influence of temperature on ductility of air-cooled specimens is determined by comparing the ductility of SPR AC specimens with ductility of SPR RT specimen. Similar to the observation made in case of yield strength and ultimate tensile strength, SPR specimens do not exhibit considerable change when in ductility when air-cooled from 600 °C. However, beyond

600 °C (up to 1000 °C), SPR AC specimen experienced up to 22% increase in ductility, which can be attributed to the increase in the ferrite grain size. The influence of water cooling on ductility can be obtained by comparing the ductility of SPR WC specimens with ductility of SPR RT specimen. SPR WC specimens do not experience considerable change in ductility when cooled from temperatures up to 600 °C. However, SPR specimens water cooled from temperatures beyond 600 °C, exhibited about 69% lower ductility when compared to the RT SPR specimen. This can be attributed to the formation of brittle martensite phase in WC specimens that are exposed to temperatures 900 °C and 1000 °C, as discussed in Section 2.3.5. In summary, the ductility of AC samples exposed to very high temperatures is found to increase due to the increase in grain size and the ductility of WC samples exposed to very high temperatures is found to decrease significantly due to the formation of brittle martensite phase.

The combined influence of triaxiality and high temperatures on ductility of AC specimens can be obtained by examining the ductility of notched AC specimens. AC notched-specimens exhibited only minor increase in ductility with increase in temperature. In fact, the ductility of AC notched specimens remained much lower than ductility of SPR RT specimen. This clearly indicates that the adverse effect of high stress triaxiality on ductility dominated the increase in ductility caused by increase in the grain size. As a result, net reduction in ductility is observed in the case of notched AC samples. The combined influence of triaxiality and high temperatures on ductility of WC specimens can be obtained by examining the ductility of notched WC specimens. Unlike the AC notched specimens, WC notched specimens experienced decrease in ductility with the increase in temperature. When water-cooled from 900 °C and 1000 °C temperatures WC notched specimens exhibited up to almost 98% loss in ductility when compared to ductility of SPR RT specimen. This significant reduction in ductility of WC notched

specimens can be attributed to the presence of high triaxiality and formation of brittle martensite phase when notched specimens are water-cooled from high temperatures, as discussed in Section 2.3.3 and Section 2.3.5, respectively. These results indicate that in the case of air-cooling, elevated temperatures only marginally affect the ductility of notched specimens whereas high stress triaxiality adversely affects the ductility of notched specimens. However, in the case of notched WC specimens, both high stress triaxiality and elevated temperatures adversely affect the ductility of specimens.

Beyond necking, the strain in the critical cross-section becomes non-uniform and the extensometers that are employed to measure the longitudinal strains do not capture this non-uniformness. Hence, it is meaningful to study the influence of cooling methods and triaxiality on uniform strains corresponding to the ultimate tensile strength (at the initiation of necking). The uniform strains corresponding to different cooling methods and triaxiality levels are provided in Table 2.6. The residual uniform strain factors for un-notched SPR specimens and notched specimens are provided in Figure 42(e) and Figure 2.52, respectively. As observed in Figure 2.42(e), the influence of cooling methods on uniform strain is almost similar to the influence of cooling methods on fracture strain. Until 600 °C, un-notched AC and un-notched WC specimens did not exhibit any considerable change in uniform strain. When subjected to temperatures beyond 600 °C, un-notched AC specimens exhibited 25% increase in uniform strain whereas un-notched WC specimens experienced 72% reduction in uniform strain. Uniform strain residual factors for post-fire notched specimens are presented in Figure 2.52. As observed in Figure 2.52, the increasing trend in uniform strain of notched AC specimens that are air-cooled from temperatures beyond 600 °C is quite similar to the increasing trend observed in fracture strain of notched AC specimens. Notched specimens exhibited almost similar decreasing trend in both

uniform strain and fracture strain when water-cooled from temperatures beyond 600 °C. In summary, the influence of elevated temperatures, cooling methods and triaxiality on both fracture strain and uniform strain in ASTM A36 steels is found to be almost similar.

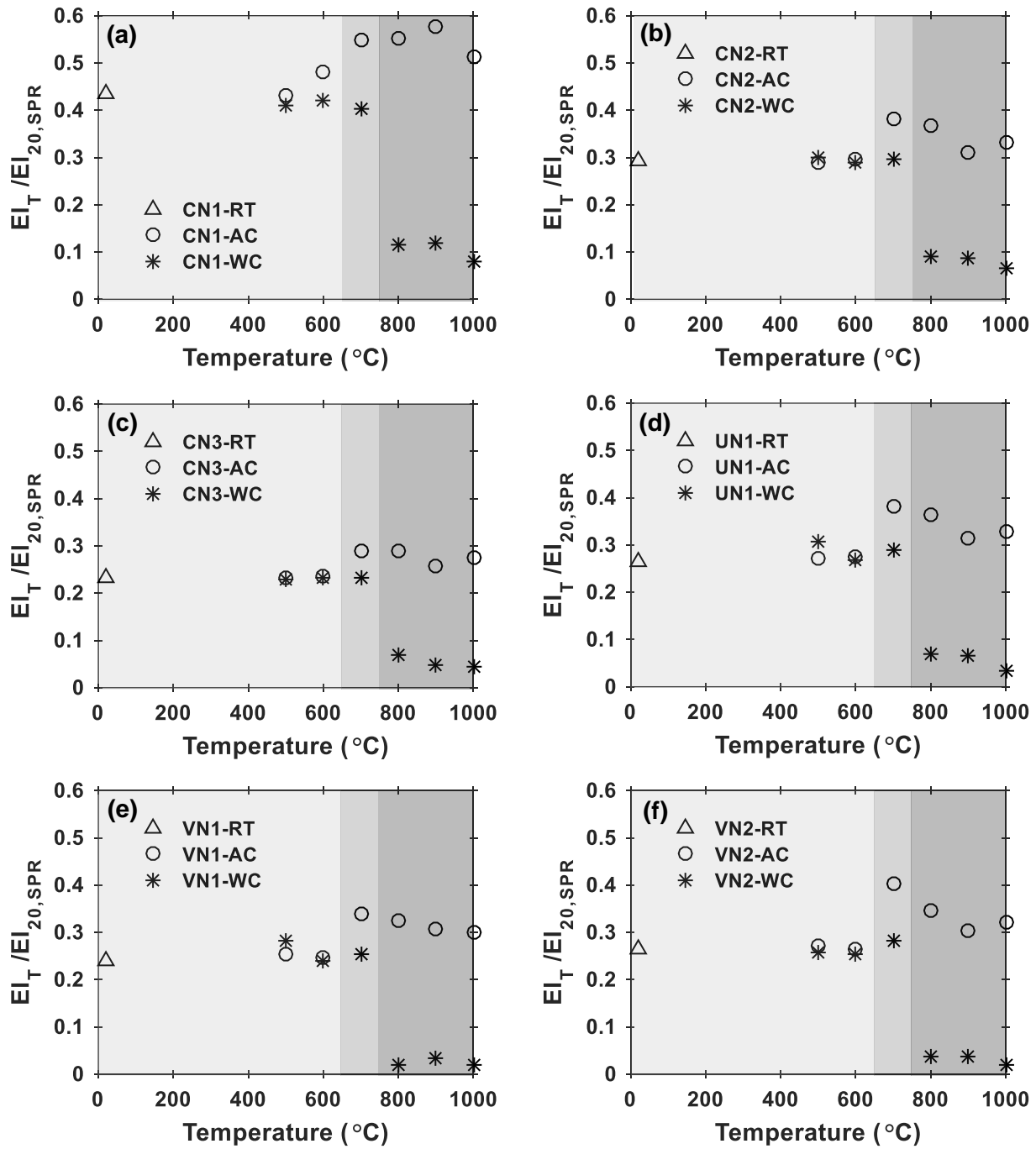


Figure 2.51. Fracture strain residual factors of post-fire test specimens a) CN1, b) CN2, c) CN3, d) UN1, e) VN1, and f) VN2.

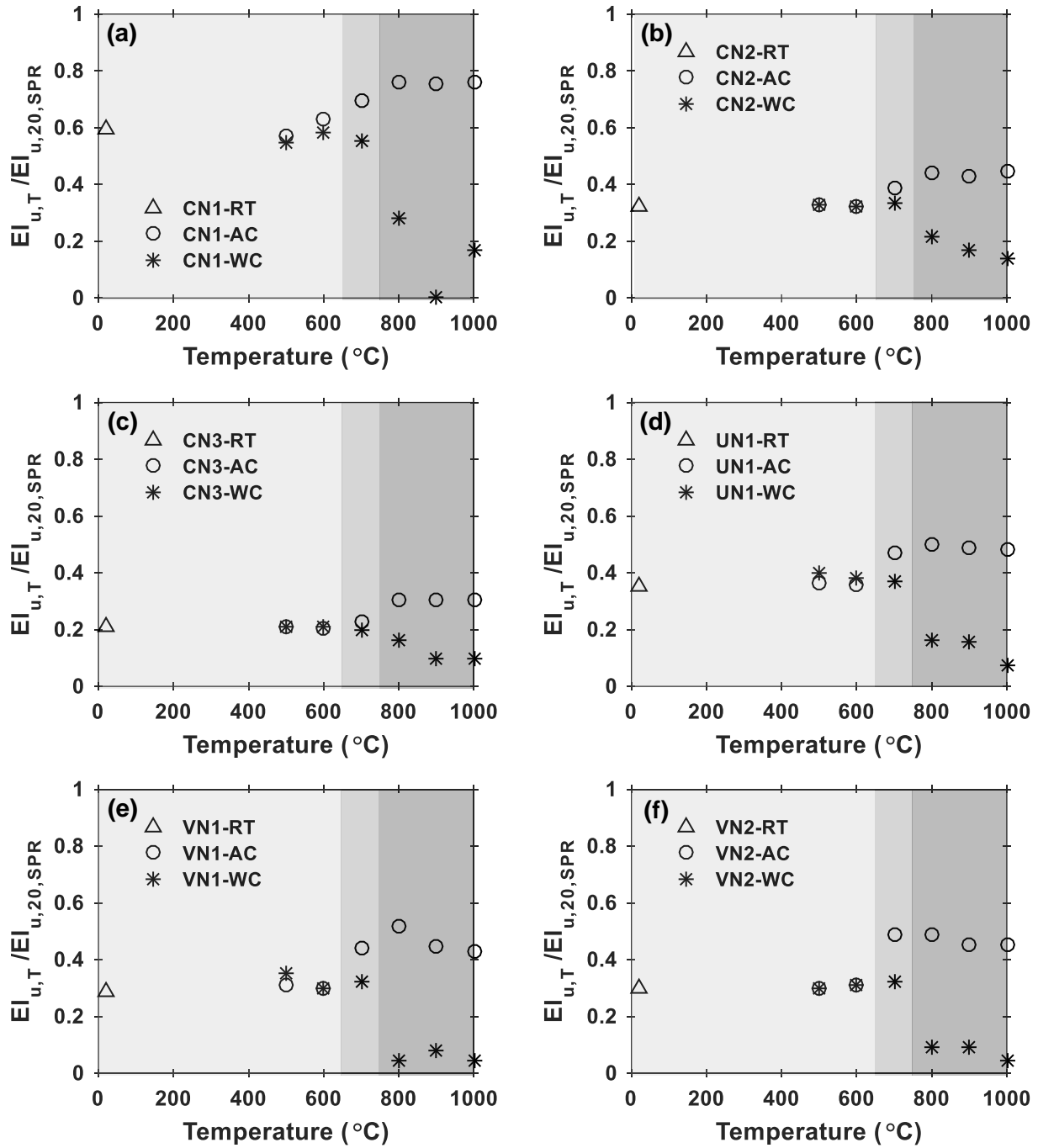


Figure 2.52. Uniform strain residual factors of post-fire test specimens a) CN1, b) CN2, c) CN3, d) UN1, e) VN1, and f) VN2.

2.3.8. SEM Analysis

Scanning Electron Microscope (SEM) analyses of fracture surfaces are conducted in this study to understand the combined influence of cooling methods and stress triaxiality on fracture

initiation and propagation mechanisms in ASTM A36 steels in a post-fire scenario. To this end, SEM analyses are conducted on un-notched (SPR) and notched (VN1) specimens subjected to room temperature (RT) and 900 °C (both AC and WC). SPR and VN1 specimens have the lowest and highest maximum initial stress triaxialities, respectively (SPR-0.33 and VN1-1.15) among all the specimens considered. As discussed in the previous sections, at 900 °C, the mechanical properties of test specimens experienced a significant change in tensile strength and ductility for both AC and WC scenarios. For this reason, the fracture mechanisms in SPR and VN1 specimens at RT and 900°C (both AC and WC) are investigated in this study.

The ductile fracture mechanism in structural steels occurs in three stages: nucleation, growth, and coalescence of microvoids [54]. Microvoids emerge from the debonding or breaking of impurities in the metal matrix. The nucleated microvoids continue to grow in the plastically deforming metal matrix under the influence of stress triaxiality. Finally, adjacent microvoids merge together leading to the coalescence of microvoids. The location where the coalescence of microvoids first occurs is referred to as the microvoid coalescence (MVC) zone [55]. MVC marks the fracture initiation in structural steel. Fracture in structural steels can propagate either as a ductile fracture or brittle fracture [54]. When observed under a microscope, the ductile fracture is characterized by micron-scale cup and cone features (spherical dimples) that are normal to the loading axis, and the brittle fracture is characterized by river-like patterns on the fracture surface.

The SEM micrographs acquired for representative test specimens are provided in Figure 2.53 to Figure 2.58. In light of the above discussion, the following two discrete fracture zones are analyzed in these micrographs: MVC zone and, cleavage fracture zone. SEM micrographs are taken at five distinct locations along a straight line lying on the diameter of the macroscopic

fracture surface (see Figure 2.53). The MVC zone in SPR-RT is characterized by ductile fracture as shown by the presence of microscopic cups and cones (see Figure 2.53). The cleavage fracture zone is characterized by river wave-like patterns. However, the extent of the cleavage fracture zone is found to be much lesser when compared to the MVC zone in the case of SPR-RT specimen. Similarly, microscopic cup and cones and river-like patterns in MVC and cleavage zones, respectively are found on the fracture surface of SPR-900-AC as shown in Figure 2.54. Once again, the extent of MVC (cup and cones) is found to be higher when compared to cleavage fracture in SPR-900-AC specimen. In contrast, the fracture surface of SPR-900-WC, as shown in Figure 2.55, consisted of a larger cleavage fracture region when compared to the MVC region explaining the lower ductility of this specimen when compared to SPR-RT and SPR-AC specimens. Figure 2.55(4) illustrates the transition zone between MVC and cleavage zones.

The SEM micrographs of VN1-RT specimen are presented in Figure 2.56. As observed in Figure 56, the cleavage fracture zone at the center of the specimen is more pronounced when compared to the MVC zone in the periphery. Also, the extent of cleavage fracture zone is found to be larger in the case of VN1-RT specimen when compared to SPR-RT specimen explaining the low fracture strain in VN1-RT. The cleavage fracture zone in VN1-RT specimen is shown in Figure 2.56(2). Figure 2.56 (4) shows the transition from cleavage fracture to MVC zone (ductile fracture) in VN1-RT specimen. VN1-900-AC specimen also exhibited a similar pattern of cleavage fracture in the center and MVC zone at the periphery, as shown in Figure 2.57. However, in this case, a larger MVC zone is observed when compared to VN1-RT specimen signifying the higher ductility of VN1-900-AC specimen. Micrographs of VN1-900-WC specimen are shown in Figure 2.58. From Figure 2.58, the cleavage zones can be observed in almost all micrographs, regardless of their location on the fracture surface. The presence of large

cleavage fracture zones serves as an explanation for the extreme reduction of ductility in the case of VN1-900-WC specimen when compared to other specimens.

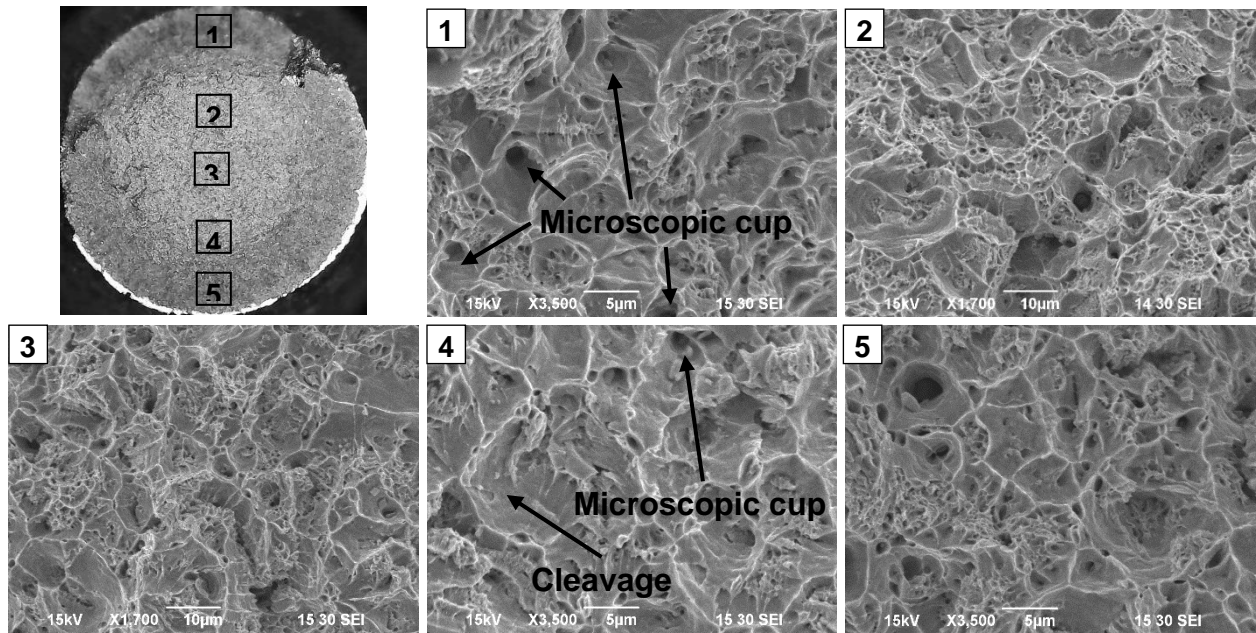


Figure 2.53. SEM analysis of specimen SPR-RT.

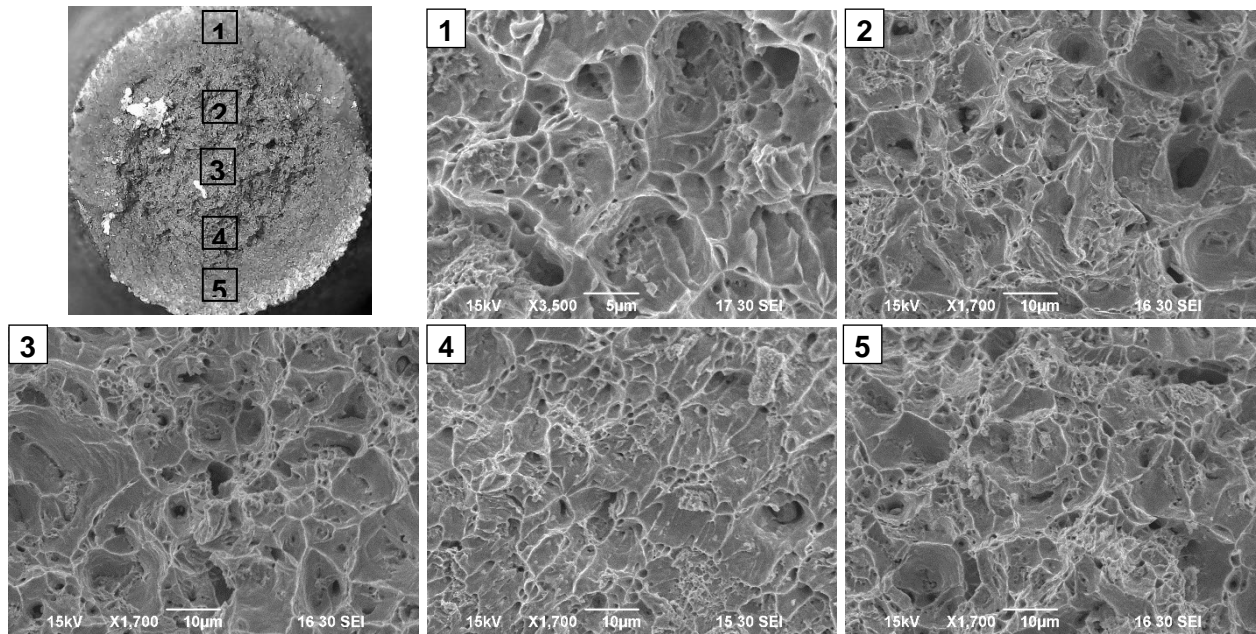


Figure 2.54. SEM analysis of specimen SPR-900-AC.

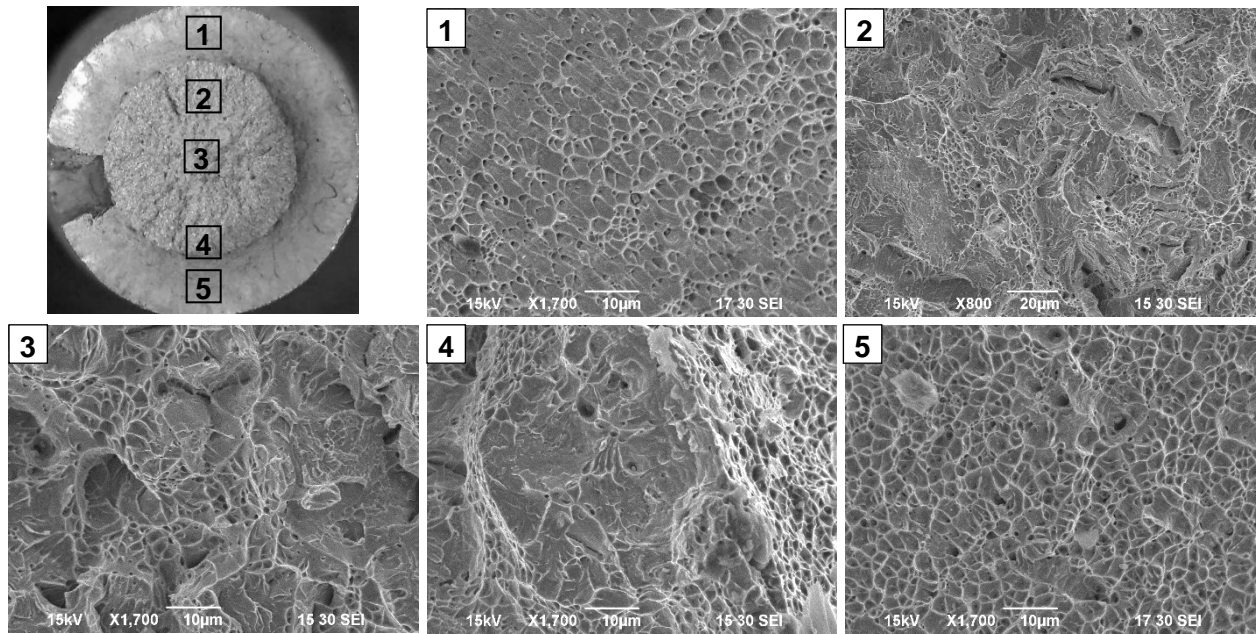


Figure 2.55. SEM analysis of specimen SPR-900-WC.

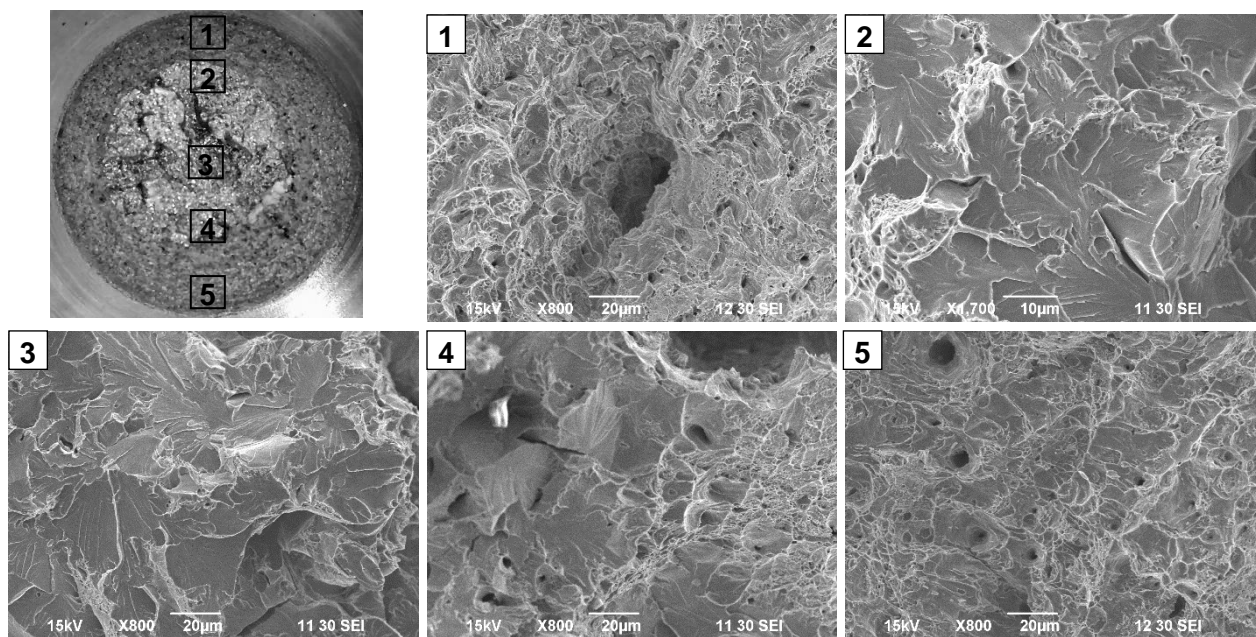


Figure 2.56. SEM analysis of specimen VN1-RT.

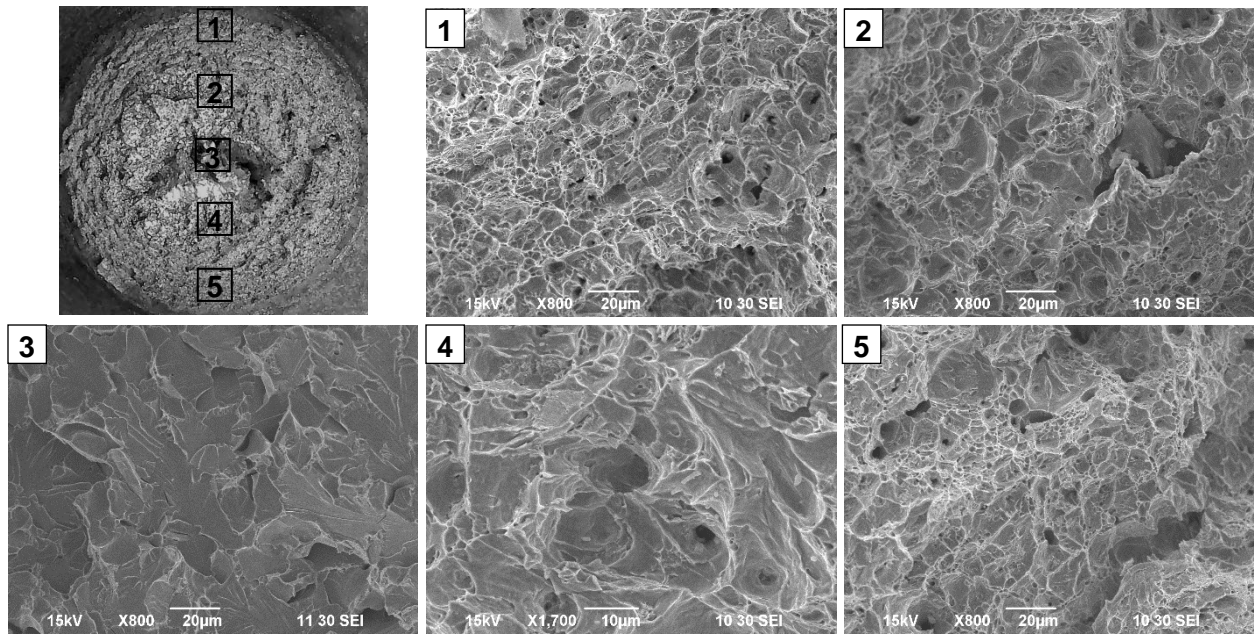


Figure 2.57. SEM analysis of specimen VN1-900-AC.

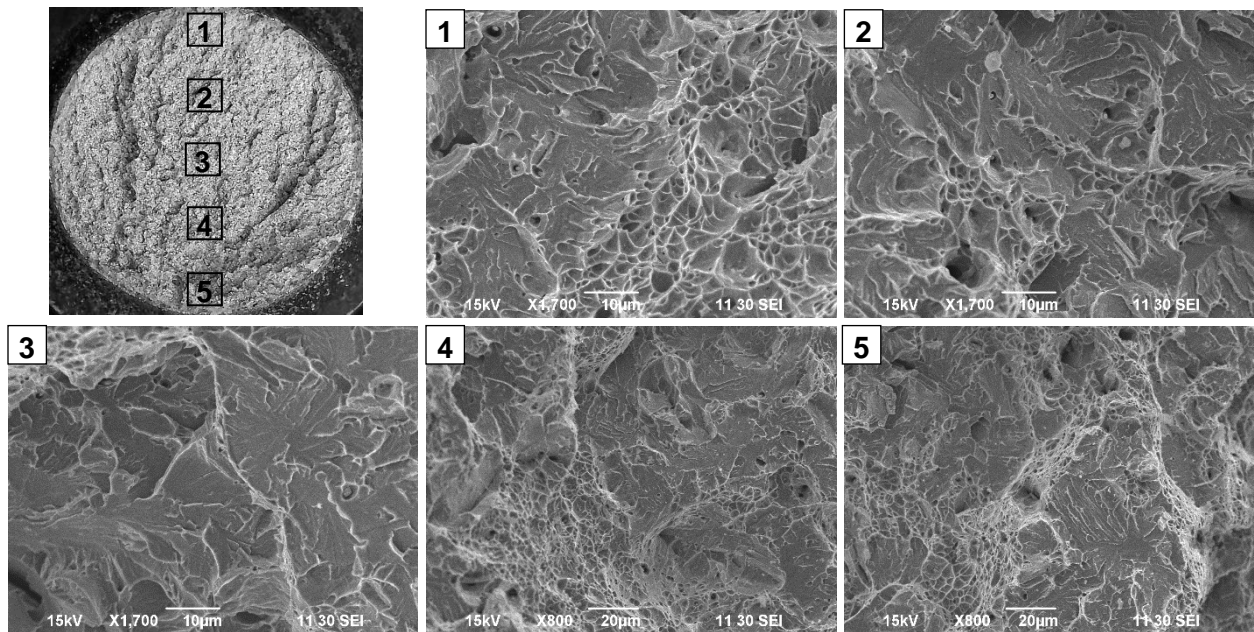


Figure 2.58. SEM analysis of specimen VN1-900-WC.

From the above discussion, it is clear that the specimens with higher ductilities processed larger MVC zones. Specimens with high triaxialities (notched specimens) processed larger cleavage fracture zones when compared to specimens with lower triaxialities (un-notched

specimens) exhibiting low ductilities. Air-cooled specimens processed larger MVC zones when compared to RT and WC specimens and exhibited higher ductilities. Large cleavage fracture zones are found in the case of notched (high triaxiality) WC specimens that processed very low ductilities. In essence, the magnitude of the triaxiality and cooling process is found to influence the extent of MVC and cleavage fracture zones on the fracture surfaces, which can be correlated to the ductility of steel. The development of a quantitative relationship between the size of MVC and cleavage fracture zones with the fracture strains falls outside the scope of this work.

2.4. Conclusions

Following are important conclusions drawn from this study:

1. Post-fire elastic modulus of ASTM A36 steels remained within 10% of the room temperature elastic modulus when specimens are heated up to 1000 °C, regardless of the cooling method.
2. The presence of high stress triaxiality leads to an increase in yield strength and ultimate tensile strength and reduction in ductility of notched specimens at room temperature.
3. Post-fire mechanical properties (yield strength, ultimate tensile strength, and ductility of ASTM A36 steels) remained almost unaffected when specimens are either air-cooled or water-cooled from temperatures up to 600 °C. Up to 600 °C, mechanical properties of ASTM A36 steels are primarily affected by stress triaxiality alone.
4. Cooling method influences the tensile behavior of ASTM A36 steels that are exposed to high temperatures. Post-fire yield strength and ultimate tensile strength of un-notched specimens decreased by up to 20% when air-cooled from temperatures beyond 600 °C due to the formation of coarse-grained ferrite. In contrast, post-fire yield strength and ultimate tensile strength of un-notched specimens increased by up to 146% when water-

cooled from temperatures beyond 800 °C due to the formation of martensite microstructure.

5. Air-cooling of un-notched ASTM A36 specimens from high temperatures resulted in up to a 40% increase in ductility. On the other hand, water-cooled un-notched specimens exhibited up to 76% decrease in ductility when cooled from temperatures beyond 800 °C.
6. Cooling method influences the post-fire stress triaxiality of ASTM A36 steels, which in turn affects the strength and ductility properties of ASTM A36 steels. Initial stress triaxialities of water-cooled notched specimens are observed to increase with target temperature and a slight reduction in initial stress triaxiality with an increase in target temperatures is noticed in the case of air-cooled notched specimens.
7. Combined effect of water-cooling and high stress triaxiality lead to a significant increase of up to 252% in yield strength and ultimate tensile strength of notched specimens that are water-cooled from temperatures beyond 800 °C. For the same target temperatures, notched WC specimens exhibited up to 98% loss in ductility when compared to un-notched RT specimen.
8. Larger cleavage fracture zones are observed in the case of notched specimens when compared to un-notched specimens and this observation serves as one of the possible explanations for the observed lower ductility of notched specimens. Larger micro-void zones are observed in the case of air-cooled specimens when compared to water-cooled specimens explaining the higher ductility of air-cooled specimens when compared to water-cooled specimens.

A number of major fire accidents in steel structures were reported in the last year alone, which resulted in loss of both life and property. Fire accidents that resulted in the collapse of

Atlanta bridge in 2017 [56] and substantial damage in Enola Low Grade Trail bridge [57] are some examples where the deterioration in the mechanical properties of construction materials resulted in the loss of overall structural integrity. The results of this study can be used to estimate the residual load-carrying capacity of steel structures exposed to fire accidents.

2.5. References

- [1] V. Kodur, M. Dwaikat, R. Fike, High-Temperature Properties of Steel for Fire Resistance Modeling of Structures, *Journal of Materials in Civil Engineering*, 22 (2010) 423-434.
- [2] H.J. Haynes, Fire loss in the United States during 2015, National Fire Protection Association. Fire Analysis and Research Division, 2016.
- [3] American Institute of Steel Construction (AISC), AISC 360-05-specification for structural steel buildings, ANSI/AISC, Chicago, (2005).
- [4] American Society of Civil Engineers (ASCE), Structural Fire Protection, ASCE committee on fire protection, Manual No. 78, (1992).
- [5] British Standards Institute (BSI), Structural use of steelwork in building, Part 8: Code of practice for fire resistant design, British Standard Institution, (1990).
- [6] A.S. AS, AS4100: Steel structures, Standards Australia, NSW, Australia, (1998).
- [7] European Committee for Standardization, EN 1993-1-2, Eurocode 3: Design of Steel Structures-Part 1-2: General rules structural fire design, in, Bruxelles, Bélgica, 2005.
- [8] China Association for Engineering Construction Standardization CECS200, Chinese technical code for fire safety of steel structure in buildings, in, China Plan Press, Beijing, China, 2006.
- [9] R.H. Tide, Integrity of structural steel after exposure to fire, *Engineering Journal-American Institute of Steel Construction*, 35 (1998) 26-38.

- [10] J. Lu, H. Liu, Z. Chen, X. Liao, Experimental investigation into the post-fire mechanical properties of hot-rolled and cold-formed steels, *Journal of Constructional Steel Research*, 121 (2016) 291-310.
- [11] J. Outinen, P. Mäkeläinen, Mechanical properties of structural steel at elevated temperatures and after cooling down, *Fire and Materials*, 28 (2004) 237-251.
- [12] F. Azhari, A. Heidarpour, X.-L. Zhao, C.R. Hutchinson, Mechanical properties of ultra-high strength (Grade 1200) steel tubes under cooling phase of a fire: an experimental investigation, *Construction and Building Materials*, 93 (2015) 841-850.
- [13] F. Azhari, A. Heidarpour, X.-L. Zhao, C.R. Hutchinson, Post-fire mechanical response of ultra-high strength (Grade 1200) steel under high temperatures: Linking thermal stability and microstructure, *Thin-Walled Structures*, 119 (2017) 114-125.
- [14] W. Wang, T. Liu, J. Liu, Experimental study on post-fire mechanical properties of high strength Q460 steel, *Journal of Constructional Steel Research*, 114 (2015) 100-109.
- [15] X. Qiang, F.S. Bijlaard, H. Kolstein, Post-fire mechanical properties of high strength structural steels S460 and S690, *Engineering Structures*, 35 (2012) 1-10.
- [16] S. Chiew, M. Zhao, C. Lee, Mechanical properties of heat-treated high strength steel under fire/post-fire conditions, *Journal of Constructional Steel Research*, 98 (2014) 12-19.
- [17] G.-Q. Li, H. Lyu, C. Zhang, Post-fire mechanical properties of high strength Q690 structural steel, *Journal of Constructional Steel Research*, 132 (2017) 108-116.
- [18] C. Siwei, J. Shaokun, G. Houzuo, C. Huixuan, L. Yifeng, L. Kang, Mechanical and ductile fracture performances of high strength structural steel Q690 after a fire: experimental investigation, *Procedia Engineering*, 210 (2017) 496-503.

- [19] J. Lee, M.D. Engelhardt, E.M. Taleff, Mechanical Properties of ASTM A 992 Steel After Fire, *Engineering Journal (Chicago)*, 49 (2012) 33-44.
- [20] E.M. Aziz, V.K. Kodur, Effect of temperature and cooling regime on mechanical properties of high-strength low-alloy steel, *Fire and Materials*, 40 (2016) 926-939.
- [21] Z. Chen, J. Lu, H. Liu, X. Liao, Experimental study on the post-fire mechanical properties of high-strength steel tie rods, *Journal of Constructional Steel Research*, 121 (2016) 311-329.
- [22] X. Qiang, F.S. Bijlaard, H. Kolstein, Post-fire performance of very high strength steel S960, *Journal of Constructional Steel Research*, 80 (2013) 235-242.
- [23] S. Gunalan, M. Mahendran, Experimental investigation of post-fire mechanical properties of cold-formed steels, *Thin-Walled Structures*, 84 (2014) 241-254.
- [24] H.-T. Li, B. Young, Residual mechanical properties of high strength steels after exposure to fire, *Journal of Constructional Steel Research*, 148 (2018) 562-571.
- [25] J. Lu, H. Liu, Z. Chen, L. Bisby, Experimental investigation of the residual mechanical properties of cast steels after exposure to elevated temperature, *Construction and Building Materials*, 143 (2017) 259-271.
- [26] Z. Tao, X.-Q. Wang, M.K. Hassan, T.-Y. Song, L.-A. Xie, Behaviour of three types of stainless steel after exposure to elevated temperatures, *Journal of Constructional Steel Research*, (2018).
- [27] X. Gao, X. Zhang, H. Liu, Z. Chen, H. Li, Residual mechanical properties of stainless steels S30408 and S31608 after fire exposure, *Construction and Building Materials*, 165 (2018) 82-92.

- [28] ASTM, ASTM E8/E8M Standard Test Methods for Tension Testing of Metallic Materials, in, ASTM International, 2016.
- [29] E. ISO, Metallic materials—tensile testing—part 1: method of test at room temperature, European committee for standardization, Brussels, 2009, (2009).
- [30] R. Kiran, K. Khandelwal, Experimental studies and models for ductile fracture in ASTM A992 steels at high triaxiality, *Journal of Structural Engineering*, 140 (2013) 04013044.
- [31] K.K. Chawla, M. Meyers, *Mechanical behavior of materials*, Prentice Hall, 1999.
- [32] H. Kuwamura, K. Yamamoto, Ductile crack as trigger of brittle fracture in steel, *Journal of Structural Engineering*, 123 (1997) 729-735.
- [33] B. Schafer, R. Ojdrovic, M. Zarghamee, Triaxiality and fracture of steel moment connections, *Journal of Structural Engineering*, 126 (2000) 1131-1139.
- [34] Dassault-Systèmes, ABAQUS/standard analysis user's manual, Dassault Systèmes Simulia, Providence, RI., 2016.
- [35] Z. Tao, X.-Q. Wang, B. Uy, Stress-Strain Curves of Structural and Reinforcing Steels after Exposure to Elevated Temperatures, *Journal of Materials in Civil Engineering*, 25 (2013) 1306-1316.
- [36] J.D. Colwell, D. Babic, A Review of Oxidation on Steel Surfaces in the Context of Fire Investigations, *SAE Int. J. Passeng. Cars - Mech. Syst.*, 5 (2012) 1002-1015.
- [37] N. Birks, G.H. Meier, F.S. Pettit, *Introduction to the high temperature oxidation of metals*, Cambridge University Press, 2006.
- [38] H.U. Sajid, R. Kiran, Influence of corrosion and surface roughness on wettability of ASTM A36 steels, *Journal of Constructional Steel Research*, 144 (2018) 310-326.

- [39] J.F. Bell, The Portevin-le Chatelier Effect, in: J.F. Bell (Ed.) The Physics of Large Deformation of Crystalline Solids, Springer Berlin Heidelberg, Berlin, Heidelberg, 1968, pp. 174-193.
- [40] G.E. Dieter, D.J. Bacon, Mechanical metallurgy, McGraw-hill New York, 1986.
- [41] G. Krauss, Martensite in steel: strength and structure, Materials Science and Engineering: A, 273-275 (1999) 40-57.
- [42] R. Kiran, K. Khandelwal, Gurson model parameters for ductile fracture simulation in ASTM A992 steels, Fatigue & Fracture of Engineering Materials & Structures, 37 (2014) 171-183.
- [43] S. Chatterjee, H.K.D.H. Bhadeshia, Transformation induced plasticity assisted steels: stress or strain affected martensitic transformation?, Materials Science and Technology, 23 (2007) 1101-1104.
- [44] J.W. Hancock, A.C. Mackenzie, On the mechanisms of ductile failure in high-strength steels subjected to multi-axial stress-states, Journal of the Mechanics and Physics of Solids, 24 (1976) 147-160.
- [45] W. Li, F. Liao, T. Zhou, H. Askes, Ductile fracture of Q460 steel: Effects of stress triaxiality and Lode angle, Journal of Constructional Steel Research, 123 (2016) 1-17.
- [46] ASTM International, ASTM E111-17 Standard Test Method for Young's Modulus, Tangent Modulus, and Chord Modulus, in, ASTM International, West Conshohocken, PA, 2017.
- [47] H.U. Sajid, R. Kiran, Influence of high stress triaxiality on mechanical strength of ASTM A36, ASTM A572 and ASTM A992 steels, Construction and Building Materials, 176 (2018) 129-134.

- [48] F. Javidan, A. Heidarpour, X.-L. Zhao, C.R. Hutchinson, J. Minkkinen, Effect of weld on the mechanical properties of high strength and ultra-high strength steel tubes in fabricated hybrid sections, *Engineering Structures*, 118 (2016) 16-27.
- [49] W.D. Callister, D.G. Rethwisch, *Materials Science and Engineering: An Introduction*, Wiley, 2010.
- [50] C.R. Brooks, *Principles of the heat treatment of plain carbon and low alloy steels*, ASM international, 1996.
- [51] J. Wang, P.J. van der Wolk, S. van der Zwaag, Determination of martensite start temperature in engineering steels part I. Empirical relations describing the effect of steel chemistry, *Materials transactions, JIM*, 41 (2000) 761-768.
- [52] D.A. Porter, K.E. Easterling, M. Sherif, *Phase Transformations in Metals and Alloys*, (Revised Reprint), CRC Press, 2009.
- [53] R. Kiran, K. Khandelwal, A micromechanical model for ductile fracture prediction in ASTM A992 steels, *Engineering Fracture Mechanics*, 102 (2013) 101-117.
- [54] T.L. Anderson, *Fracture Mechanics: Fundamentals and Applications*, Third Edition, Taylor & Francis, 2005.
- [55] J. Toribio, A fracture criterion for high-strength steel notched bars, *Engineering Fracture Mechanics*, 57 (1997) 391-404.
- [56] B. Jansen, Atlanta bridge collapse shows how fire defeats concrete, steel, in: *USA Today*, March 31, 2017.
- [57] L. Blest, Fire continues to burn on Enola Low Grade Trail bridge; Cause still under investigation, in: *LancasterOnline*, April 13, 2018.

3. INFLUENCE OF HIGH STRESS TRIAXIALITY ON MECHANICAL STRENGTH OF ASTM A36, ASTM A572 AND ASTM A992 STEELS²

This chapter discusses the influence of high stress triaxiality on the mechanical strength of ASTM A36, ASTM A572, ASTM A992 steels. The contents of this chapter have been published in Sajid, H.U. and Kiran, R., 2018. Influence of high stress triaxiality on the mechanical strength of ASTM A36, ASTM A572, and ASTM A992 steels. *Construction and Building Materials*, 176, pp.129-134.

3.1. Introduction

In service conditions, structural steels are routinely subjected to stress concentrations that arise from geometric discontinuities like holes, sharp corners, welds, etc. that are commonly observed in steel structures. Stress concentration is quantified by a dimensionless parameter referred to as stress triaxiality ($T\sigma$). Stress triaxiality is defined as the ratio between hydrostatic stress and von Mises stress. Higher stress triaxiality aggravates the growth of microvoids in the steel matrix [1], which in turn accelerates ductile fracture initiation in steels [2]. High stress triaxiality thus leads to a reduction in ductility of steels [3]. Experimental and numerical studies on high strength low alloy structural steels (ASTM A992) have confirmed the adverse effects of stress triaxiality on the ductility of structural steels [4, 5]. However, the quantitative relationships between stress triaxiality and yield strength and ultimate tensile strength of structural steels that are important design parameters in structural design [6] are not currently addressed. Past studies conducted on different alloys and stainless steels have reported an increase in tensile strength with an increase in stress concentration [7-9]. An unanticipated increase in yield strength and

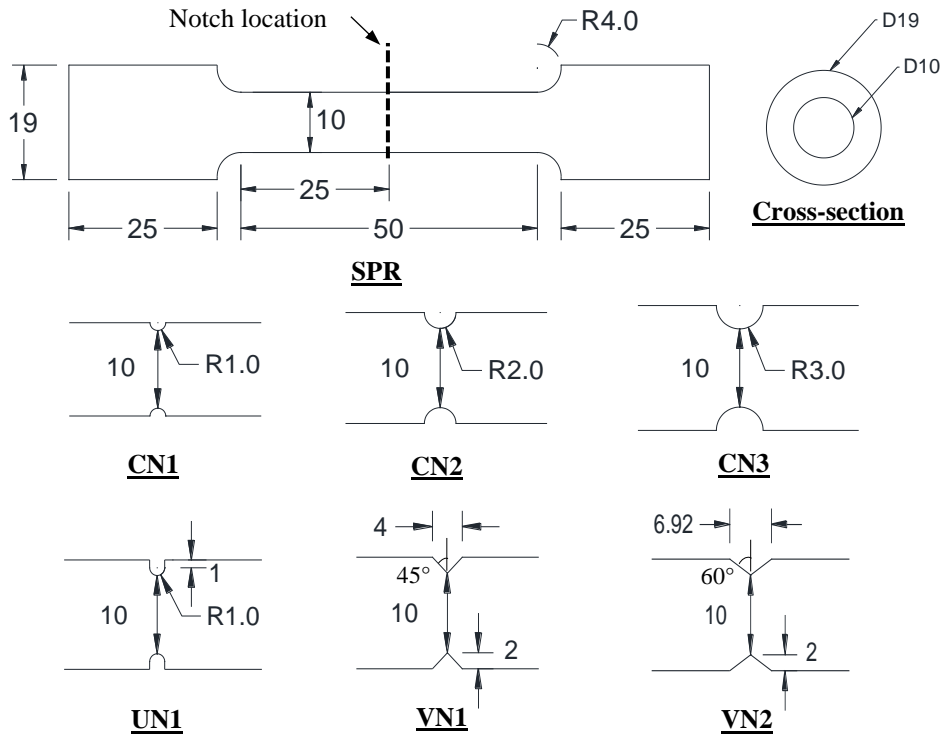
² This chapter was co-authored by H.U. Sajid and R. Kiran. H.U. Sajid had the primary responsibility of preparing the specimens, conducting all tests, and drafting this chapter. R. Kiran supervised the research and revised this chapter.

ultimate tensile strength of structural steels may lead to unintended consequences in structural systems. For instance, stronger beams cause the failure of columns leading to the global collapse of the structure (strong beam-weak column). Components like reduced beam sections, seismic fuse components should fail at pre-designed loads to protect the overall integrity and to avoid progressive collapse of the structure. It is, therefore, important to account for the increased yield strength and ultimate tensile strength due to high triaxiality in the design stage of steel structures [10]. With this objective in mind, the current study aims to establish a quantitative relationship between stress triaxiality, yield strength, and ultimate tensile strength of structural steels (at a material level) that are widely used in the construction industry. In this study, a mild steel (ASTM A36 [11]) along with two high strength low alloy (HSLA) steels (ASTM A572 [12] and ASTM A992 [13]) are investigated. ASTM A36 and ASTM A992 are predominantly used in the construction of steel buildings in the United States whereas ASTM A572 steels are typically used in the construction of bridges [14-16]. ASTM A992 is currently the most common and preferred grade of structural steel used for wide flange shapes in the United States [16, 17].

3.2. Experimental Study and Finite Element Modeling

Preliminary finite element analyses are conducted by choosing different geometries of notched tension specimens to generate a range of stress triaxialities. Based on the results obtained from the preliminary study, six axisymmetrically notched tension specimens are selected. These test specimens are classified as CN (circular-notched specimens), UN (U-notched specimens), and VN (V-notched specimens). The reference un-notched test specimens are labeled as SPR (reference un-notched test specimen). Detailed geometric illustrations of the un-notched and notched specimens are provided in Figure 3.1. The chemical composition of all the three steels used in this study as specified by the manufacturer is summarized in Table 3.1. In

total, 42 test specimens are tested as a part of this experimental study. These specimens are machined using a computer numerically controlled (CNC) lathe machine with a tolerance of ± 0.025 mm.



SPR = Reference un-notched test specimen, **CN** = C-notch, **UN** = U-notch, **VN** = V-notch

Figure 3.1. Geometric details of axisymmetric test specimens (all dimensions are in mm.).

Table 3.1. Chemical composition of ASTM A36, A572, and A992 structural steels.

Chemical composition (%)	ASTM A36	ASTM A572 Gr. 50	ASTM A992
Carbon (C)	0.1500	0.0500	0.1000
Manganese (Mn)	0.6900	1.3400	0.9300
Phosphorous (P)	0.0180	0.0110	0.0160
Sulphur (S)	0.0040	0.0040	0.0440
Silicon (Si)	0.1800	0.1500	0.1900
Copper (Cu)	0.2400	0.2800	0.2500
Chromium (Cr)	0.1500	0.1900	0.1400
Nickle (Ni)	0.0880	0.1300	0.0900
Molybdenum (Mo)	0.0195	0.0400	0.0200
Vanadium (V)	0.0048	0.0830	0.0010
Titanium (Ti)	0.0012	0.0010	—
Niobium (Nb)	0.0024	0.0030	0.0210
Iron (Fe)	98.4521	97.7180	98.1980

The load-displacement behavior of all the test specimens is obtained by conducting uniaxial tension tests using a servo-hydraulic MTS 793 system at a displacement rate of 0.02 mm/sec. An Epsilon Model 3542 contact extensometer with a 1-inch gage length is used to record the strains. The total load and elongation in the gage length are obtained at a sampling rate of 99 Hz, for both un-notched and notched test specimens. Engineering stress-strain curves of un-notched and notched test specimens are provided in Figure 3.2. Near-perfect repeatability of load-displacement curves is obtained for all the un-notched and notched test specimens. For the sake of clarity, a stress-strain curve of only one representative specimen is provided for each un-notched and notched test specimen. Mechanical properties of test specimens evaluated from experimental stress-strain curves are provided in Table 3.2. Non-linear finite element analysis is conducted to obtain stress triaxiality profiles across critical cross-section at two different loading stages: a) initial stage of loading (corresponding to $1.35 \pm 0.5\%$ engineering strain), and b) ultimate load (strain corresponding to maximum stress in engineering stress-strain curve), as shown in Figure 3.3. Maximum initial stress triaxiality ($T_{\sigma,max}^i$) ranges from 0.33 to 1.15. Finite element analyses are conducted using ABAQUS® finite element modeling software. All test specimens are modeled using four noded bilinear axisymmetric CAX4 elements and geometric nonlinearity is considered. J_2 plasticity model is used as the constitutive model. For all steels, the true stress-strain curves obtained from the corresponding SPR specimens are used as the strain hardening curves in the J_2 plasticity model and are provided in Figure 3.4. The applied boundary conditions and loading along with some typical finite element meshes used in the vicinity of the notches are provided in Figure 3.5.

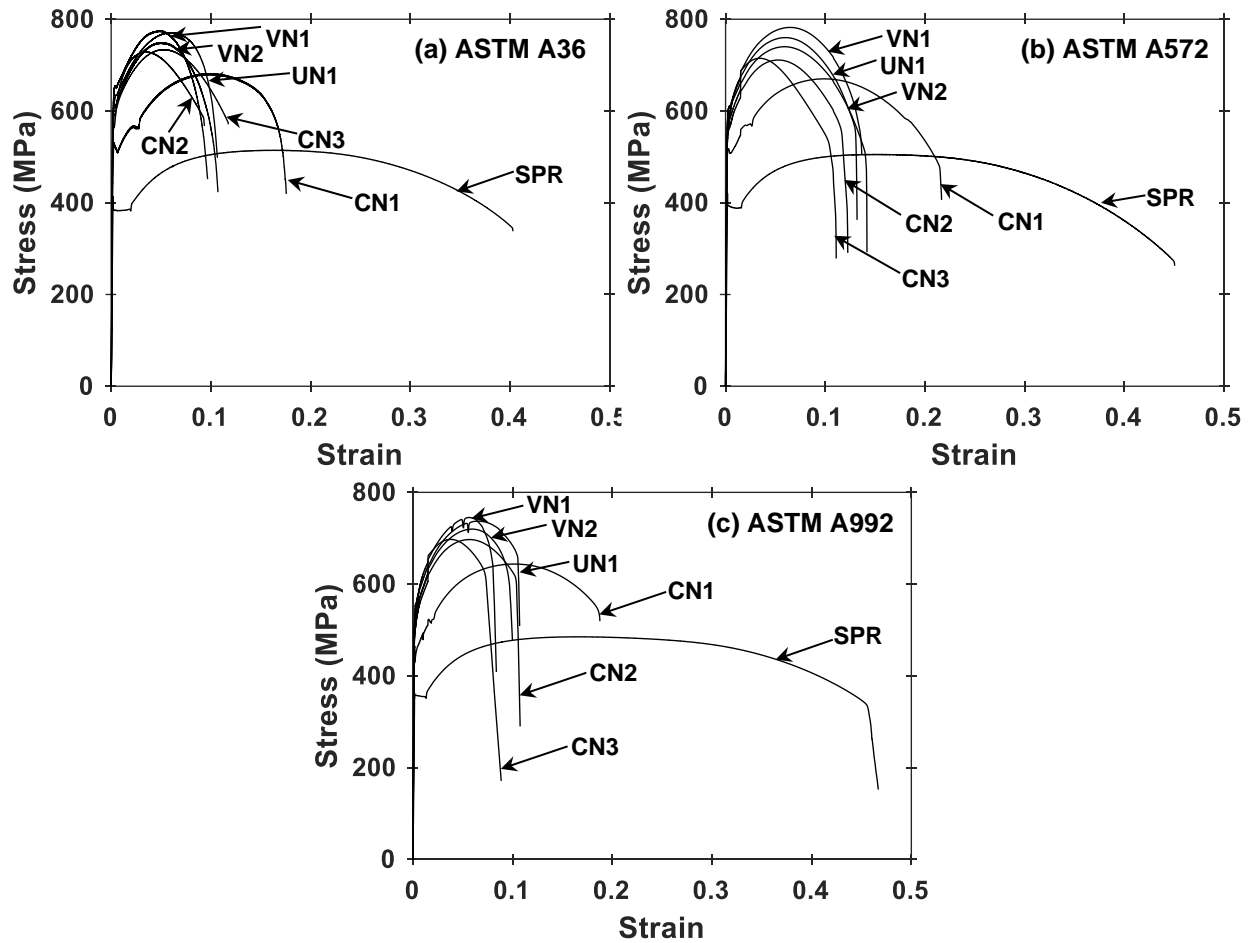


Figure 3.2. Engineering stress-strain curves of un-notched and notched test specimens.

Table 3.2. Experimental material properties of structural steels (obtained from un-notched test specimens) and comparison with ASTM standards.

Steel type	Material property	ASTM specification	Experimental result
ASTM A36	Min. yield strength (MPa)	250	386.48
	Tensile strength (MPa)	400-550	517.09
	Min. elongation over 2" length (%)	23	40.65 (over 1" length)
ASTM A572 Gr. 50	Min. yield strength (MPa)	345	389.15
	Min. tensile strength (MPa)	450	502.40
	Min. elongation over 2" length (%)	21	44.81 (over 1" length)
ASTM A992	Yield strength (MPa)	345-450	354.46
	Min. tensile strength (MPa)	450	484.47
	Min. elongation over 2" length (%)	21	45.07 (over 1" length)
	Max. yield to tensile strength ratio	0.85	0.74

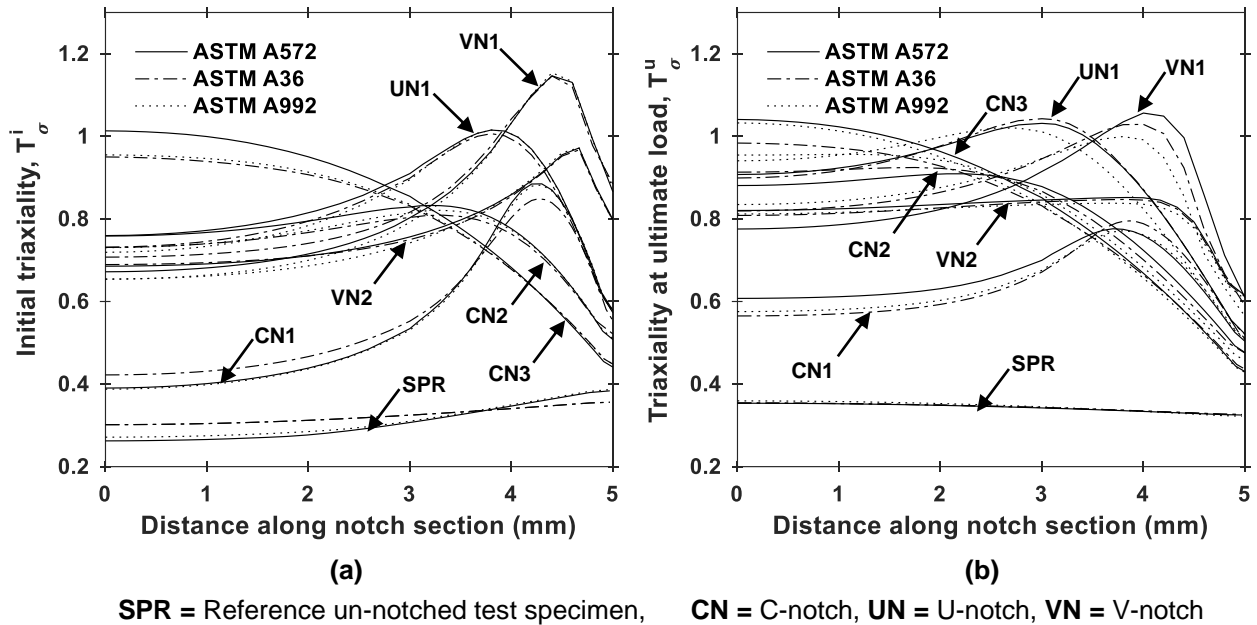


Figure 3.3. (a) Initial stress triaxiality profiles, (b) stress triaxiality profiles at ultimate load.

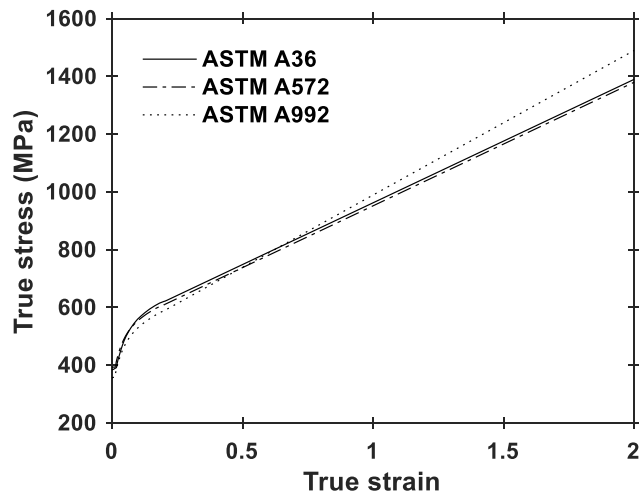


Figure 3.4. Strain hardening curves of un-notched test specimens used in finite element analysis.

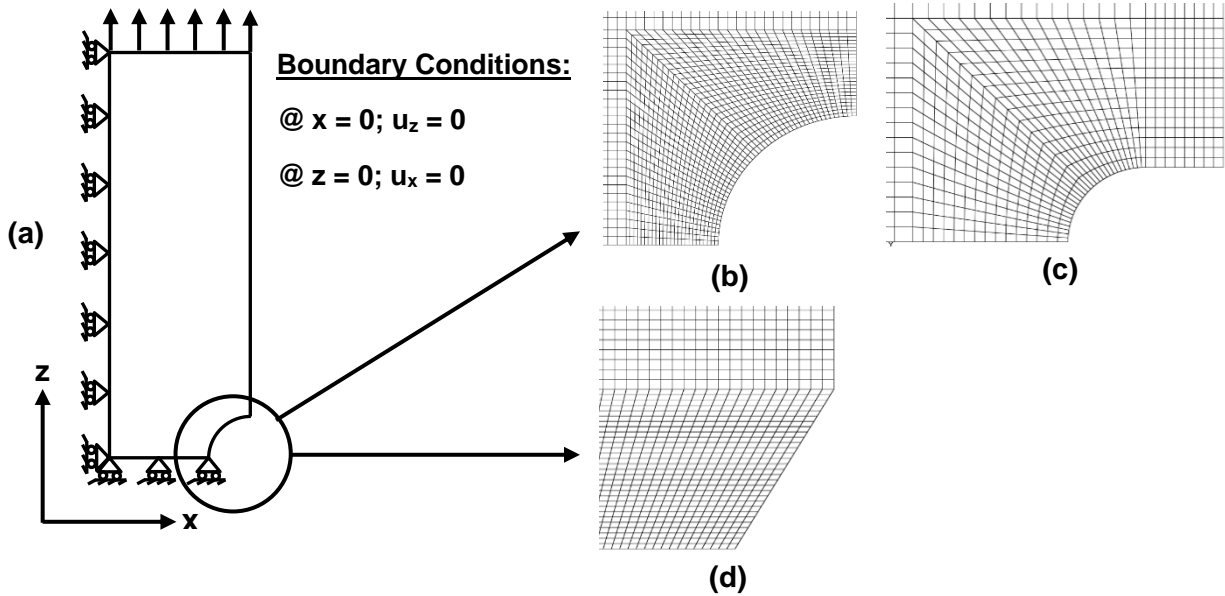


Figure 3.5. (a) Applied boundary and loading conditions, (b) typical C-notch mesh, (c) typical U-notch mesh, and (d) typical V-notch mesh.

3.3. Results and Discussion

In this section, stress-strain curves, yield strength (σ_y) and ultimate tensile strength (σ_u) obtained from uniaxial tensile tests are discussed. Using engineering stress-strain curves, the yield strength of each test specimen is determined based on the 0.2% strain offset method [18]. The maximum engineering stress is taken as the ultimate tensile strength of steel. As observed in Figure 3.2, stress-strain curves of notched specimens are characterized by a significant reduction in ductility and increase in ultimate tensile strength as compared to un-notched specimens, for all three types of steels. A well-defined yield plateau is observed in un-notched specimens which diminishes in the case of notched specimens with high stress triaxiality. It is observed that all notched specimens exhibited a substantial increase in both yield strength and ultimate tensile strength as compared to un-notched steel specimens. Among notched steel specimens, the highest yield strength and ultimate tensile strength are exhibited by specimens with the highest average initial and average ultimate triaxialities (UN1 and VN1), respectively. In the case of

ASTM A36 steel, the yield strength of notched specimens increased by as much as 70% as compared to un-notched steel specimens. Both ASTM A572 and A992 steels exhibited an almost similar increase (up to 57% and 60%, respectively) as compared to un-notched specimens. The ultimate tensile strength of notched specimens made of all three steels exhibited an almost similar increase (ASTM A36-51%, ASTM A572-54%, ASTM A992-53%) when compared to the ultimate tensile strength of corresponding un-notched specimens.

Average yield strength (σ_y) of (two) test specimens for a given geometry is plotted as a function of spatially averaged initial triaxiality (T_{avg}^i), as shown in Figure 3.6. The spatially averaged initial triaxiality (T_{avg}^i) is evaluated by averaging the triaxiality over the critical cross-section of the notched test specimen at a total strain of $1.35 \pm 0.5\%$. The average ultimate tensile strength (σ_u) of two test specimens for a given geometry is plotted against spatially averaged triaxiality evaluated at a strain corresponding to ultimate load (T_{avg}^u), as shown in Figure 3.7.

Triaxiality is dependent on the shape of the notch and material properties. The notches in the test specimens may undergo significant shape change before the ultimate tensile strength is achieved. This shape change in the notch is accounted for by choosing T_{avg}^u which is obtained by evaluating the spatial average of triaxiality across the critical cross-section at the strain corresponding to ultimate tensile strength. From Figure 3.6, it is clear that the yield strength increases linearly with an increase in stress triaxiality for all three steels. Similarly, the ultimate tensile strength is observed to increase linearly with an increase in stress triaxiality, for all three types of steels, as shown in Figure 3.7. Based on experimental and finite element results, the following predictive equations are proposed to estimate yield strength and ultimate tensile strength as a function of spatially averaged initial stress triaxiality and spatially averaged ultimate stress triaxiality, respectively.

ASTM A36 Steel:

$$\sigma_y = 498.59 T_{avg}^i + 218.28 \quad (3.1)$$

$$\sigma_u = 482.50 T_{avg}^u + 351.26 \quad (3.2)$$

ASTM A572 steel:

$$\sigma_y = 407.33 T_{avg}^i + 266.41 \quad (3.3)$$

$$\sigma_u = 489.10 T_{avg}^u + 334.41 \quad (3.4)$$

ASTM A992 steel:

$$\sigma_y = 403.75 T_{avg}^i + 227.78 \quad (3.5)$$

$$\sigma_u = 473.96 T_{avg}^u + 323.57 \quad (3.6)$$

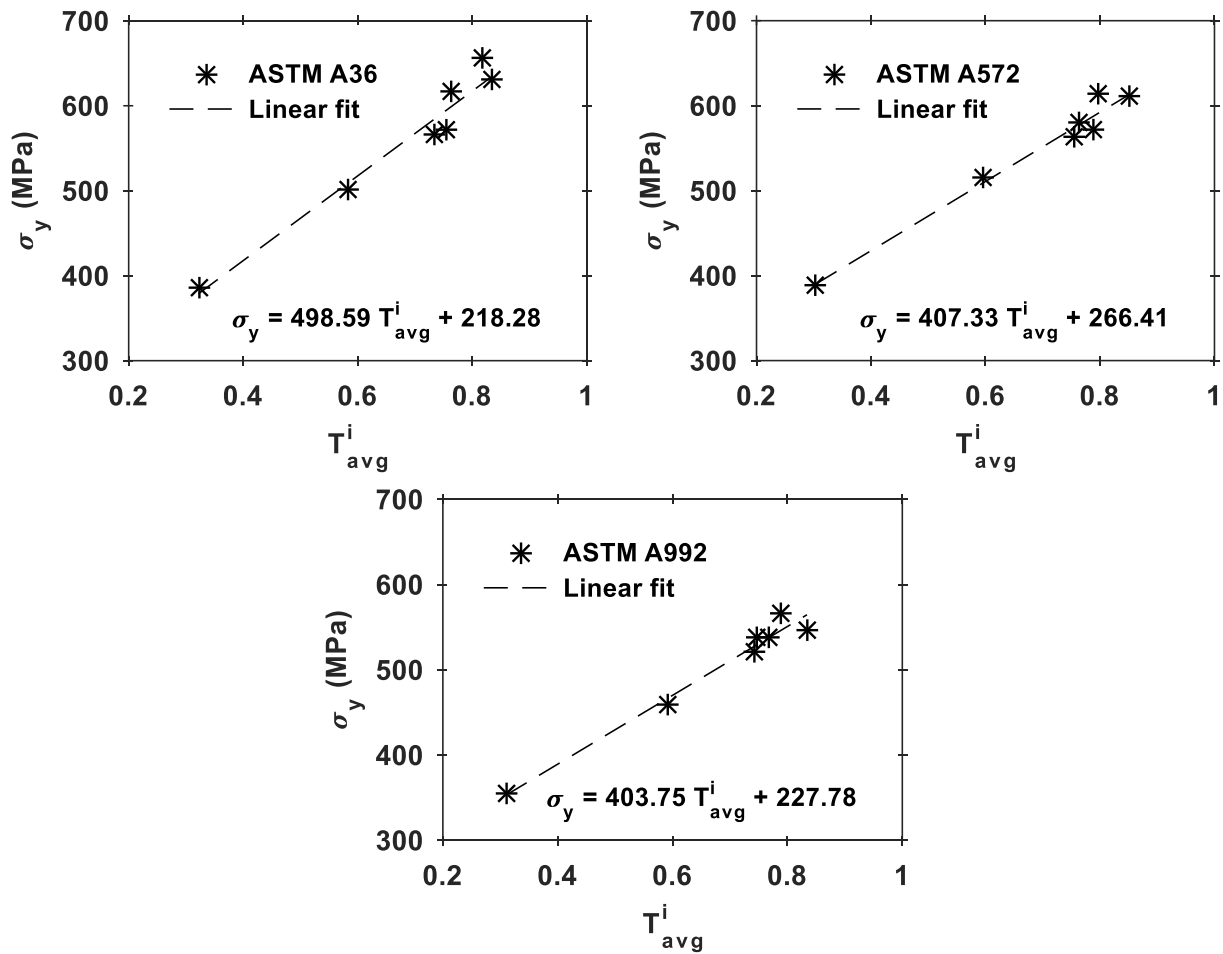


Figure 3.6. Average initial stress triaxiality versus yield strength.

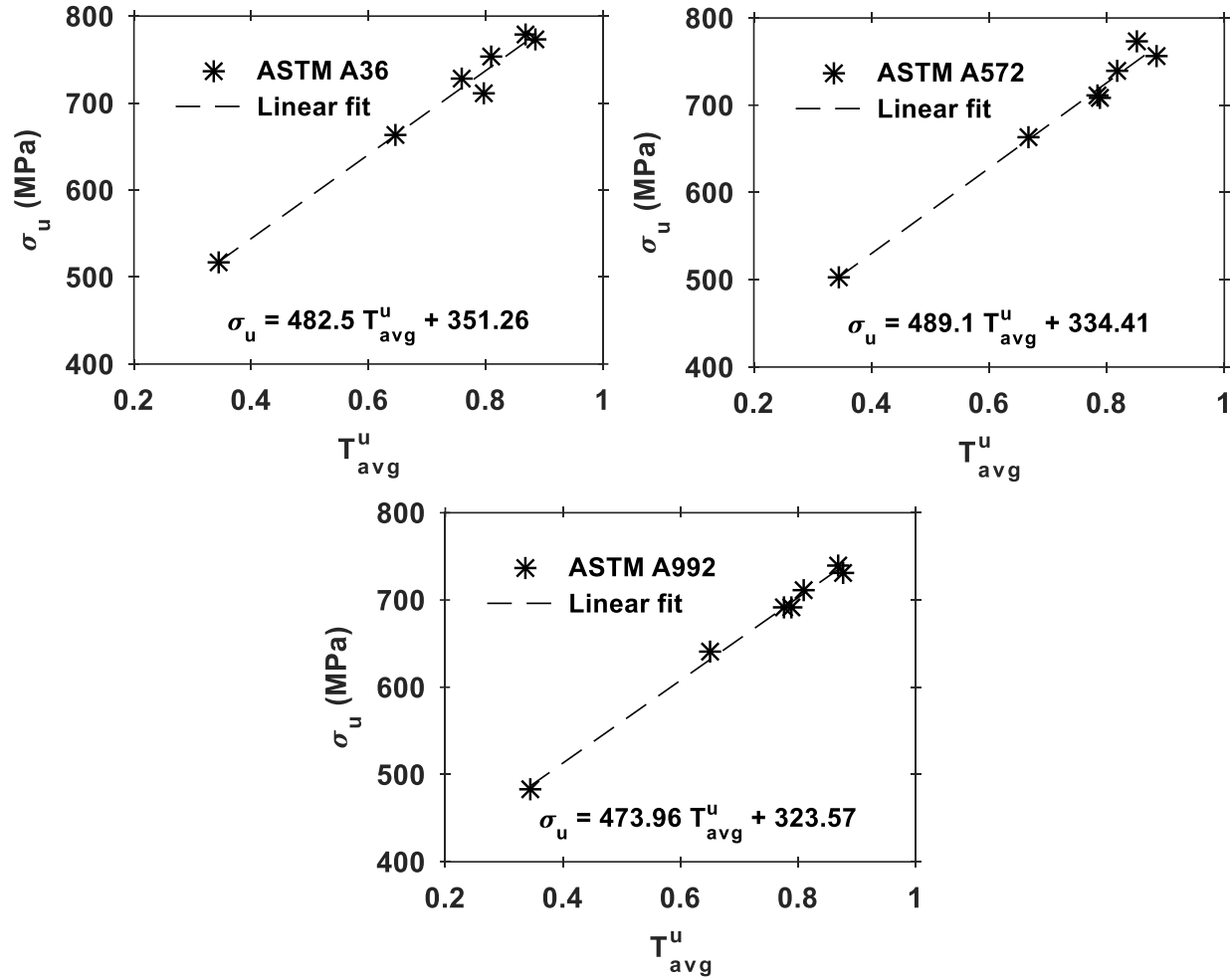


Figure 3.7. Average ultimate stress triaxiality versus ultimate tensile strength.

The authors hypothesize that the strain localization in the vicinity of the notch leads to high strain hardening which ultimately results in increased yield strength and ultimate tensile strength. An increase in the yield strength with an increase in triaxiality is also reported for AISI 1080 steel and Al T6061 alloys [9, 19]. Currently, there is no clear consensus on the exact cause for the increase in yield strength/ ultimate tensile strength of notched specimens and further microscale experimentation is needed to investigate the root cause behind this phenomenon.

3.4. Conclusions

Following are important conclusions drawn from this study:

1. The yield strength of structural steels increased linearly with an increase in stress triaxiality. About 70% increase in yield strength is observed in ASTM A36 steel when the triaxiality is changed from $T_{avg}^l = 0.32$ to $T_{avg}^l = 0.84$. For a similar change in triaxiality, ASTM A572 and ASTM A992 recorded a 57% and 60% increase in yield strength, respectively.
2. The ultimate tensile strength of structural steels also increased linearly with an increase in stress triaxiality. An increase up to 54% in ultimate tensile strength is observed for all the three structural steels considered in this study when the T_{avg}^u is increased from 0.34 to 0.88.

3.5. References

- [1] R. Kiran, K. Khandelwal, A micromechanical model for ductile fracture prediction in ASTM A992 steels, *Engineering Fracture Mechanics*, 102 (2013) 101-117.
- [2] T.L. Anderson, *Fracture Mechanics: Fundamentals and Applications*, Third Edition, Taylor & Francis, 2005.
- [3] A.M. Agogino, Notch effects, stress state, and ductility, *Journal of Engineering Materials and Technology*, 100 (1978) 348-355.
- [4] R. Kiran, K. Khandelwal, Experimental studies and models for ductile fracture in ASTM A992 steels at high triaxiality, *Journal of Structural Engineering*, 140 (2013) 04013044.
- [5] R. Kiran, K. Khandelwal, A triaxiality and Lode parameter dependent ductile fracture criterion, *Engineering Fracture Mechanics*, 128 (2014) 121-138.

- [6] American Institute of Steel Construction (AISC), AISC 360-05-specification for structural steel buildings, ANSI/AISC, Chicago, (2005).
- [7] W.D. Jenkins, W.A. Willard, Effect of temperature and notch geometry on the tensile behavior of a titanium alloy, NBS J ENG INSTRUM, 73 (1966) 5-11.
- [8] J. Ganesh Kumar, M. Nandagopal, P. Parameswaran, K. Laha, M. Mathew, Effect of notch root radius on tensile behaviour of 316L (N) stainless steel, Materials at High Temperatures, 31 (2014) 239-248.
- [9] X. Lei, C. Li, X. Shi, X. Xu, Y. Wei, Notch strengthening or weakening governed by transition of shear failure to normal mode fracture, Scientific reports, 5 (2015) 10537.
- [10] American Institute of Steel Construction, Manual of steel construction, 13th Edition, AISC, Chicago, 2005.
- [11] ASTM International, A36/A36M-14 Standard Specification for Carbon Structural Steel, in, ASTM International, West Conshohocken, PA, 2014.
- [12] ASTM International, Standard Specification for High-Strength Low-Alloy Columbium-Vanadium Structural Steel, in, ASTM International, West Conshohocken, PA, 2015.
- [13] ASTM International, Standard Specification for Structural Steel Shapes, in, ASTM International, West Conshohocken, PA, 2015.
- [14] R. Bjorhovde, Development and use of high performance steel, Journal of Constructional Steel Research, 60 (2004) 393-400.
- [15] E.M. Aziz, V.K. Kodur, Effect of temperature and cooling regime on mechanical properties of high-strength low-alloy steel, Fire and Materials, 40 (2016) 926-939.
- [16] K. Gustafson, P. SE, Evaluation of existing structures, Modern Steel Construction, 47 (2007) 41.

- [17] G. Hu, M.A. Morovat, J. Lee, E. Schell, Elevated Temperature Properties of ASTM A992 Steel, in: Structures Congress 2009, American Society of Civil Engineers, 2009, pp. 1067-1076.
- [18] ASTM International, ASTM A6/A6M-17a Standard Specification for General Requirements for Rolled Structural Steel Bars, Plates, Shapes, and Sheet Piling, in, ASTM International, West Conshohocken, PA, 2017.
- [19] H.J. L., V.R. P., H.R. W., Deformation and Fracture Mechanics of Engineering Materials, 5th Edition, John Wiley and Sons, 2012.

4. POST-FIRE MECHANICAL BEHAVIOR OF ASTM A572 STEELS SUBJECTED TO HIGH STRESS TRIAXIALITIES³

This chapter discusses the post-fire mechanical behavior of ASTM A572 high strength low alloy steels that are subjected to high stress triaxialities. The contents of this chapter have been published in Sajid, H.U. and Kiran, R., 2019. Post-fire mechanical behavior of ASTM A572 steels subjected to high stress triaxialities. *Engineering Structures*, 191, pp.323-342.

4.1. Introduction

Bridge fire accidents in the past have resulted in severe damage and even collapse of entire bridge spans [1, 2]. In addition to arson and wildfires, bridge fires are commonly caused by vehicular accidents that usually involve trucks and tankers carrying highly flammable liquids or gas fuels [2, 3]. A survey conducted by the New York Department of Transportation (NYDOT) in 2008 revealed that fire accidents caused nearly three times more bridge collapses when compared to earthquakes, which highlights the high incidence of bridge fire accidents [4]. When compared to steel buildings, steel bridges are particularly vulnerable to fire hazards due to the lack of fire protection [5, 6]. High strength low alloy (HSLA) steels are commonly used in the construction of bridges due to their conformity to ASTM A709 bridge steel specifications [7, 8]. Among HSLA steels, ASTM A572 Gr. 50 [9] has become the primary choice of steel grade for the construction of bridges due to its improved strength, ductility, and weldability characteristics which result in increased structural efficiency [7]. Despite excellent mechanical properties, HSLA structural steels remain vulnerable to degradation in mechanical properties when subjected to fires for extended durations due to their high conductivity and low specific

³ This chapter was co-authored by H.U. Sajid and R. Kiran. H.U. Sajid had the primary responsibility of preparing the specimens, conducting all tests, and drafting this chapter. R. Kiran supervised the research and revised this chapter.

heat. Recent fire accidents in bridges [10, 11] have further highlighted the importance of understanding the behavior of ASTM A572 steels during fire and post-fire conditions. A significant number of studies were conducted in recent years to understand the in-fire and post-fire behavior of structural steels. Researchers have investigated the in-fire properties of mild steels and high strength low alloy steels and have proposed residual factors that can be used to estimate the in-fire mechanical properties of structural steels [12-21]. Elevated temperature residual factors for different steels are also specified in various building codes [22-26].

Steel members may experience severe degradation in strength properties due to exposure to elevated temperatures and hence may prevent immediate occupancy or use after fire accidents. Post-fire mechanical properties of structural steels are required to determine the usability of a steel structure after a fire accident [27]. In general, buildings codes allow the use of steel structures subjected to fire provided if there is no obvious distortion in steel members [28]. In general, post-fire residual factors are used to evaluate the mechanical properties of structural steels that are subjected to fire and cooled down to room temperature. The post-fire residual factor is defined as the ratio of a given mechanical property of steel exposed to a target elevated temperature to that specific mechanical property evaluated at room temperature. Post-fire residual factors are typically determined by subjecting steel specimens to different target temperatures, cooling them down to room temperature, and subsequently subjected them to uniaxial tension test. In this regard, residual mechanical properties have been explored for various types of steels that include mild steels [20, 29-31], high strength steels [21, 31-37], very high strength steels [38, 39], cold-formed, and cast steels [40, 41] and stainless steels [42]. More details about the type of steels and post-fire test protocols are summarized in Table 4.1. These studies have revealed that both exposures to elevated temperatures and cooling methods

influence the post-fire mechanical properties of steels. The results produced in these studies have greatly improved the understanding of residual mechanical properties of steels after a fire accident. Current post-fire residual factors that are available in the literature are based on exposure to elevated temperatures alone and do not incorporate the influence of stress concentration, an important phenomenon that is frequently observed in steel members. Stress concentration in steel members usually results from pitting corrosion [43, 44] and other geometric discontinuities (e.g., welds, sharp corners, etc.) in steel members. Stress concentration can be quantified in terms of stress triaxiality (T_σ), which is defined as the ratio of hydrostatic stress to Von-Mises stress. Studies conducted in the past have revealed that the presence of high stress triaxiality significantly influences the strength and ductility of structural steels [45-48]. Hence, it is important to consider the influence of high stress triaxiality when determining the residual mechanical properties of structural steels that are exposed to elevated temperatures. This study aims to quantify the combined influence of high stress triaxiality and cooling methods on post-fire mechanical properties of ASTM A572 Gr. 50 steels. To this end, residual mechanical properties of ASTM A572 steels are reported for various stress triaxialities, temperatures, and cooling conditions in this paper. The remaining paper is organized as follows: Section 4.2 explains the detailed experimental and finite element analyses procedure adopted in this study. In Section 4.3, the results obtained from uniaxial tension tests and finite element analyses are discussed. Specifically, the influence of high stress triaxiality and cooling methods on elastic modulus, yield strength, ultimate tensile strength, and ductility of ASTM A572 steel is discussed. Section 4.4 provides the important conclusions that are drawn from this study.

Table 4.1. Post-fire mechanical tests conducted on different types of steels.

Reference	Steel Type/Properties F_y = yield strength (MPa) F_u = ultimate tensile strength (MPa) El = elongation (%)	Temperature (°C)	Heating rate (°C/min) and target time (min)	Cooling Method
Outinen and Mäkeläinen 2004 [20]	S355J2H ($F_y \geq 355$, $F_u = 510$ -680, $El \geq 22$)	334, 369, 498, 532, 569, 602, 611, 617, 643, 658, 674 and 710	-Rate = 20	-Furnace-cooling
Ding et al. 2006 [74]	Q235 ($F_y \geq 235$, $F_u = 375$ -500, $El \geq 23$)	200, 300, 400, 500, 700 and 1000	Target t = 60, 120, 180 (for 200-700 °C) and 120 (for 1000 °C)	-Air-cooling
Qiang et al. 2012 [34]	S460NL ($F_y \geq 460$, $F_u = 540$ -720, $El \geq 17$) S690QL ($F_y \geq 690$, $F_u = 770$ -940, $El \geq 14$)	300, 400, 500, 600, 650, 700, 750, 800, 850, 900 and 1000	-Rate = 10 -Target t = 10	-Air-cooling
Lee et al. 2012 [35]	A992 ($F_y = 345$ -450, $F_u \geq 450$, $El \geq 21$)	200, 300, 400, 500, 600, 700, 800, 900 and 1000	-Heating time = 30 -Target t = 60 -Thermocouples attached to samples	-Blanket-cooling -Air-cooling -Water-cooling
Qiang et al. 2013 [39]	S960QL ($F_y = 960$, $F_u = 980$ -1150, $El = 10$)	300, 400, 500, 600, 650, 700, 750, 800, 850, 900 and 1000	-Rate = 10 -Target t = 10	-Air-cooling
Chiew et al. 2014 [21]	S690RQT (HSS) ($F_y \geq 690$, $F_u = 790$ -930, $El \geq 15$)	400, 600, 800, 900 and 1000	-Time to reach target temperature = 30 min.	-Air cooled inside furnace with furnace door open
Gunalan and Mahendran 2014 [41]	G300 ($F_y \geq 350$, $F_u = 366$, $El \geq 33$) G500 ($F_y \geq 663$, $F_u = 668$, $El \geq 5$) G550 ($F_y \geq 664$, $F_u = 664$, $El \geq 1$ -2)	300, 400, 500, 550, 600, 650, 700, 750 and 800	-Rate = 10-20 -Target t = 50-60	-Air-cooling -Water-cooling
Wang et al. 2015 [32]	Q460 ($F_y \geq 460$, $F_u = 550$ -720, $El \geq 17$)	300, 400, 500, 600, 700, 800 and 900	-Rate = 15 -Target t = 20	-Air-cooling -Water-cooling
Azhari et al. 2015 [38]	Grade 1200 (UHSS) Grade 800 (HSS) Grade 350 (mild steel)	150, 300, 450 and 600	-Target t = 20 -Cooling rate = 10 °C/min and 20 °C/min	-Air-cooling

Table 4.1. Post-fire mechanical tests conducted on different types of steels (continued).

Reference	Steel Type/Properties F_y = yield strength (MPa) F_u = ultimate tensile strength (MPa) El = elongation (%)	Temperature (°C)	Heating rate (°C/min) and target time (min)	Cooling Method
Lu et al. 2016 [29]	Q235 ($F_y \geq 235$, $F_u = 375$ -500, $El \geq 23$) Q345 ($F_y \geq 345$, $F_u = 470$ -630, $El \geq 20$) Q420 ($F_y \geq 420$, $F_u = 520$ -680, $El \geq 19$)	100, 200, 300, 400, 500, 600, 700, 800, 900, and 1000	-Rate = 15 -Target t = 30	-Air-cooling -Water-cooling using water jet spray
Aziz and Kodur 2016 [36]	ASTM A572 Gr. 50 ($F_y \geq 345$, $F_u \geq 450$, $El \geq 21$)	400, 500, 600, 700, 800 and 1000	-Rate = 10 -Target t = 120	-Air-cooling -Water-cooling
Choi and Chung 2016 [75]	SN400 (MS) ($F_y \geq 235$ MPa) SM520 (MS) ($F_y \geq 355$ MPa) SM570 (HSS) ($F_y \geq 440$ MPa) (Korean Steels)	100, 200, 300, 400, 500, 600, 700, 800 and 900	-Rate = 10 -Target t = 10	-Air-cooling
Chen et al. 2016 [37]	GLG460 ($F_y \geq 460$ MPa) GLG550 ($F_y \geq 550$ MPa) GLG650 ($F_y \geq 650$ MPa) GLG835 ($F_y \geq 835$ MPa)	100, 200, 300, 400, 500, 600, 650, 700, 750, 800, 850, 900, and 1000	-Rate = 15 -Target t = 30	-Air-cooling -Water-cooling using water jet spray
Li et al. 2017 [33]	Q690 ($F_y \geq 690$, $F_u = 770$ -940, $El \geq 14$)	300, 400, 500, 600, 700, 800 and 900	-Rate = 5-20 -Target t = 10	-Air-cooling -Water-cooling
Azhari et al. 2017 [76, 77]	Grade 1200 (UHSS) Grade 800 (HSS) Grade 350 (mild steel)	300, 470, 540, 600, 650, 700, 750 and 800	-Rate = 20 -Target t = 20 -Thermocouples attached to samples	-Air-cooling -Water-cooling
Lu et al. 2017 [40]	G20Mn5N G20Mn5QT (Commonly used structural cast steels in China)	100, 200, 300, 400, 500, 600, 650, 700, 750, 800, 850, 900, and 1000	-Rate = 10 -Target t = 30	-Air-cooling -Water-cooling using water jet spray
Sajid and Kiran 2018 [30]	ASTM A36 ($F_y \geq 250$, $F_u = 400$ -550, $El \geq 23$)	500, 600, 700, 800, 900 and 1000	-Rate = 10 -Target t = 60	-Air-cooling -Water-cooling

4.2. Experimental Procedure

This section provides details about the test specimens, heating and cooling methods, and experimental protocols adopted for post-fire uniaxial tension tests.

4.2.1. Test Specimens

Steel specimens are machined from ASTM A572 Gr. 50 steel plates to obtain post-fire mechanical properties of ASTM A572 steels under the influence of high stress triaxiality. Various levels of stress triaxialities are achieved by introducing notches of different shapes and sizes in the test specimens. Geometric details of test specimens (notched and un-notched) and notch dimensions are provided in Figure 4.1 and Table 4.2, respectively. The stress triaxiality profiles along the critical cross-section (minimum cross-section) of test specimens are determined by conducting non-linear finite element analyses (FEA). FEA procedure adopted in this study will be discussed in Section 4.3.2. Using FEA, initial stress triaxiality profiles across critical cross-sections of test specimens are obtained and are illustrated in Figure 4.2 (see Section 4.3.2 for more details). The maximum initial stress triaxialities of test specimens ranged from 0.34 (SPR specimen) to 1.18 (specimen VN1). Maximum initial stress triaxialities of test specimens are evaluated at $1.35 \pm 0.05\%$ engineering strain. The chemical composition of ASTM A572 Gr. 50 steels as specified by the manufacturer is provided in Table 4.3. Room temperature mechanical properties of ASTM A572 steels are determined by performing uniaxial tension tests on un-notched test specimens and are summarized in Table 4.4.

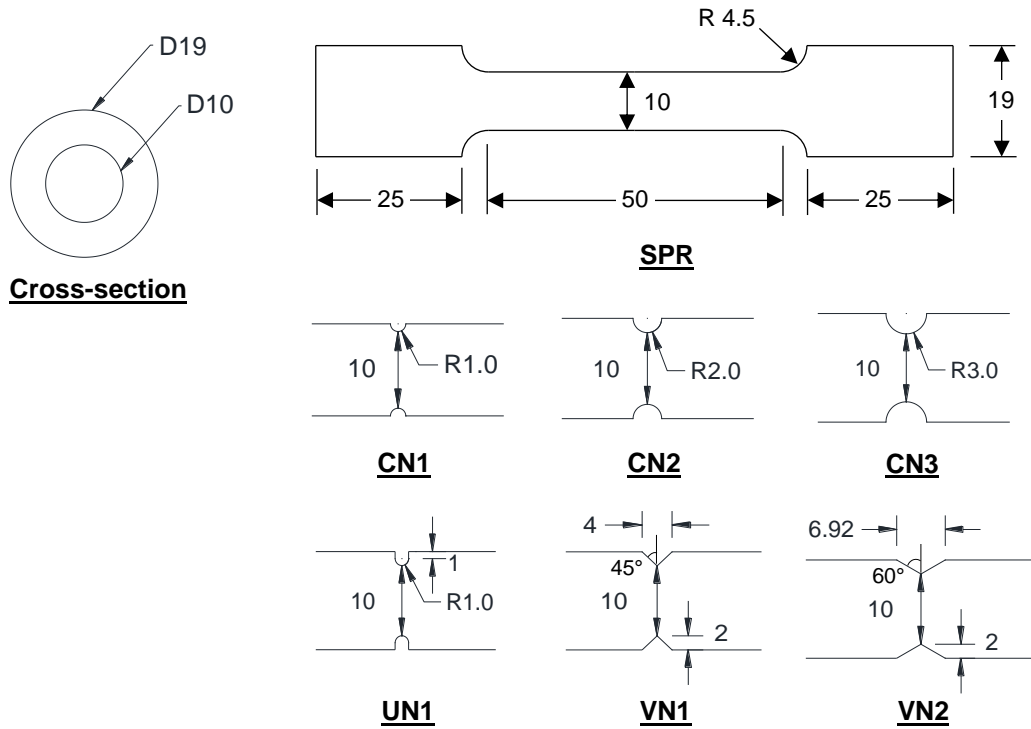


Figure 4.1. Geometric details of typical test specimens (all dimensions are in mm).

Table 4.2. Geometric details of test specimens.

Specimen ID	Notch type	Radius, R (mm)	Depth, D (mm)	Angle, θ (degrees)
SPR	-	-	-	-
CN1	C	1	-	-
CN2	C	2	-	-
CN3	C	3	-	-
UN1	U	1	-	-
VN1	V	-	2	45
VN2	V	-	2	60

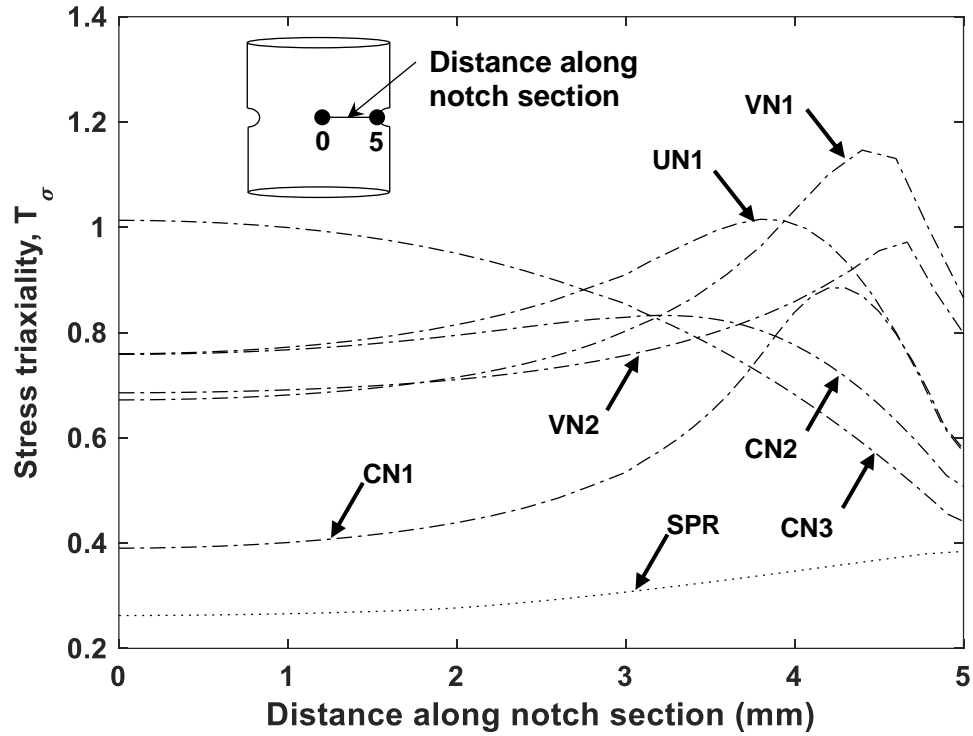


Figure 4.2. Initial stress triaxiality profiles of test specimens.

Table 4.3. Chemical composition of ASTM A572 steel.

Element	Composition (%)
Carbon (C)	0.0500
Manganese (Mn)	1.3400
Phosphorous (P)	0.0110
Sulphur (S)	0.0040
Silicon (Si)	0.1500
Copper (Cu)	0.2800
Chromium (Cr)	0.1900
Nickle (Ni)	0.1300
Molybdenum (Mo)	0.0400
Vanadium (V)	0.0830
Titanium (Ti)	0.0010
Niobium (Nb)	0.0030
Iron (Fe)	97.7180

Table 4.4. Mechanical properties of ASTM A572 steel.

Yield strength (MPa)	Ultimate tensile strength (MPa)	Elongation in 25-mm gauge length (mm)
389	503	45

4.2.2. Post-Fire Mechanical Tests

Test specimens are exposed to temperatures between 500 °C and 1000 °C at 100 °C intervals (500 °C, 600 °C, 700 °C, 800 °C, 900 °C, and 1000 °C). Test specimens are heated at a rate of 10 ± 2 °C/min in an electric furnace (see Figure 4.3) and the heating rate is monitored via two thermocouples located inside the furnace. Each test specimen is subjected to one of the above-mentioned target temperatures for 1 hour to ensure uniform temperature distribution across the test specimens. In the next step, the specimens are cooled down slowly to room temperature using air-cooling (by placing specimens outside the furnace) and rapidly using water-cooling (by placing specimens in a water bath at room temperature). The heating and cooling profiles adopted in this study are illustrated in Figure 4.4. Post-fire mechanical properties of test specimens are then obtained by performing uniaxial tension tests using an MTS 809 servohydraulic system. All test specimens are tested at a constant displacement rate of 1.2 mm/min. The elongation within the 25-mm gauge length is obtained using an epsilon model 354 contact extensometer, as shown in Figure 4.5. The epsilon model 3542 contact extensometer used in this study has a maximum fixed strain error of ± 0.0001 in./in. and meets the ASTM B-1 accuracy requirement as specified in ASTM E83 [49]. For a given test specimen geometry, 13 uniaxial tension tests are conducted which include one room temperature test (reference test), six air-cooled and six water-cooled elevated temperature tests. In total, 91 specimens are tested as part of this study.

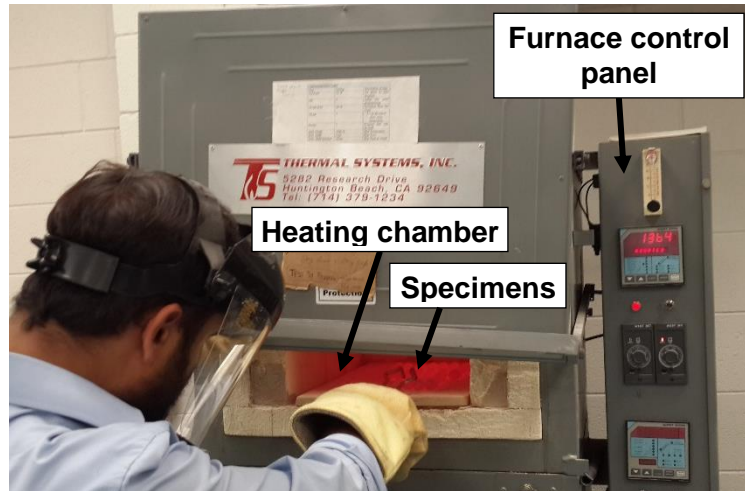


Figure 4.3. Heating of test specimens inside an electric furnace.

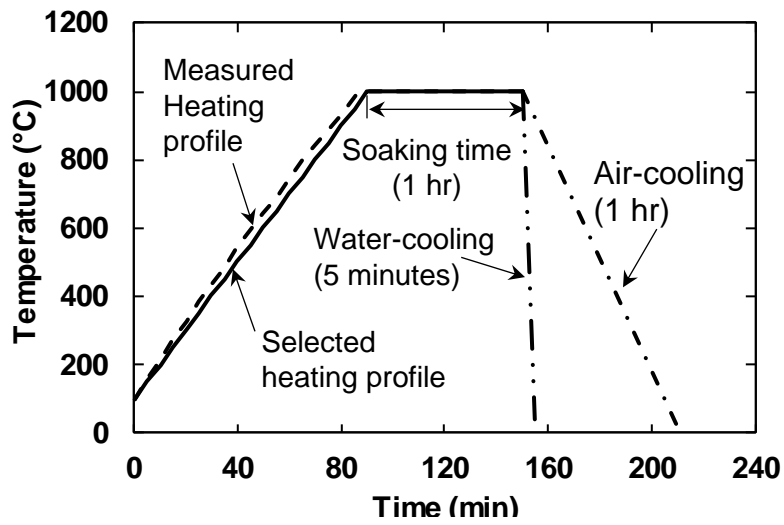


Figure 4.4. Typical heating and cooling profile of test specimens.

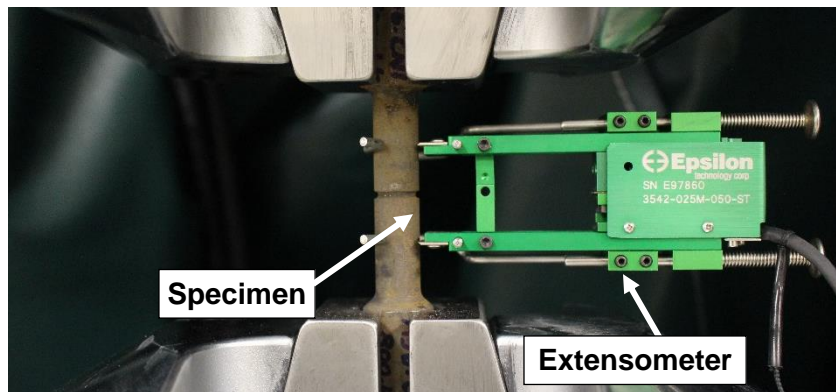


Figure 4.5. Uniaxial tension test setup and extensometer mounted on the test specimen.

4.3. Results and Discussion

In this section, the results obtained from uniaxial tension tests and non-linear finite element analyses are discussed.

4.3.1. Post-Fire Load Displacement Curves

In this section, the experimental load-displacement behavior of post-fire test specimens is discussed. The experimental and FEA-based load-displacement curves of test specimens are provided in Figure 4.6 to Figure 4.19. The FEA procedure and FEA-based load-displacement curves will be discussed in Section 4.3.2. As observed in Figure 4.6 to Figure 4.19, ASTM A572 steels do not exhibit a noticeable change in load-displacement behavior after exposure to temperatures up to 600 °C, irrespective of the cooling method. When exposed to temperatures beyond 600 °C, a considerable change in load-displacement behavior is observed in both cooling methods. The change in mechanical properties will be discussed in Section 4.3.4 through Section 4.3.7. A well-defined yield plateau is observed in un-notched test specimens that are cooled from temperatures up to 600 °C. However, such a yield plateau is not observed when un-notched specimens are cooled from temperatures beyond 600 °C. Unlike un-notched specimens, notched specimens do not exhibit a well-defined yield plateau regardless of temperature and cooling method. Minor serrations (sudden jumps) are observed in experimental load-displacement curves of the following specimens: CN2-1000-AC (see Figure 10), UN1-1000-AC (see Figure 4.14), and VN2-1000-AC (see Figure 4.18), which might have occurred due to a phenomenon referred to as Portevin-Le Chatelier (PLC) effect [50, 51]. PLC effect and the associated unstable plastic flow is observed in some metals as they undergo plastic deformation under certain strain rates and temperatures [51, 52]. This can be attributed to the unstable dislocation motion due to the

transient interaction between diffusing solute atoms and dislocations [52-54]. Such types of serrations were previously reported in mild steels [30].

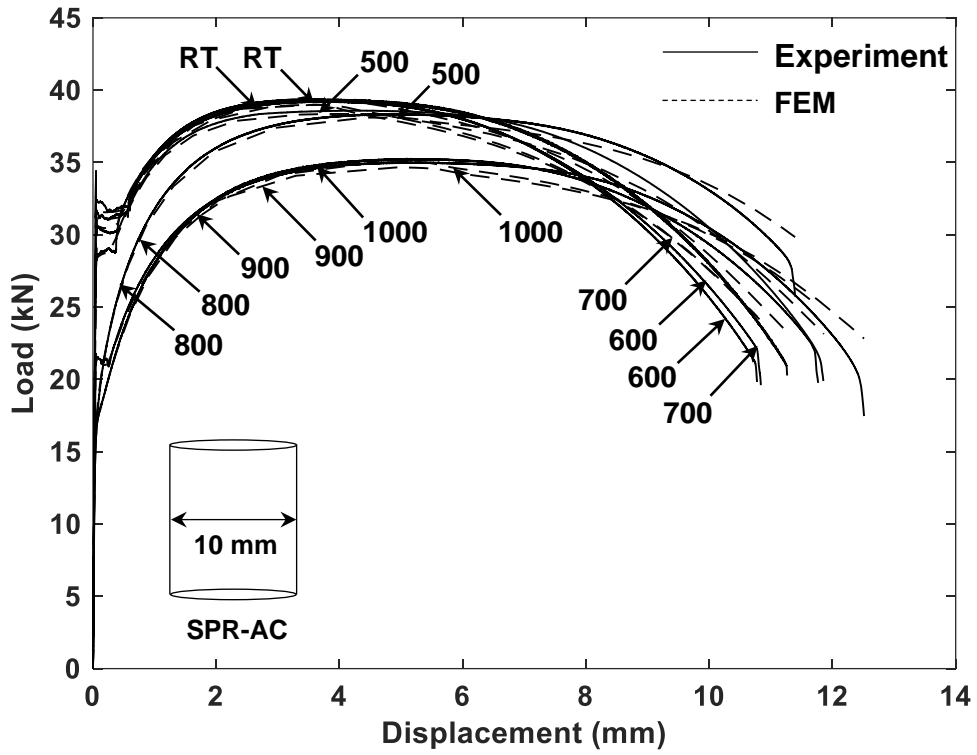


Figure 4.6. Load-displacement curves of specimen SPR-AC.

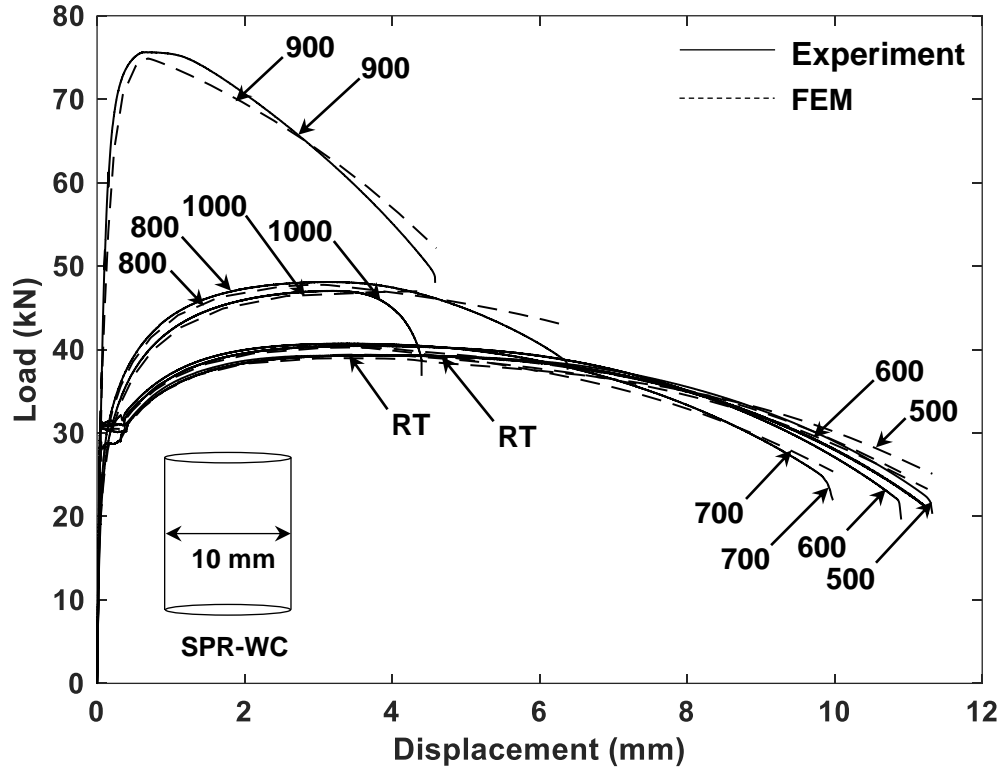


Figure 4.7. Load-displacement curves of specimen SPR-AC.

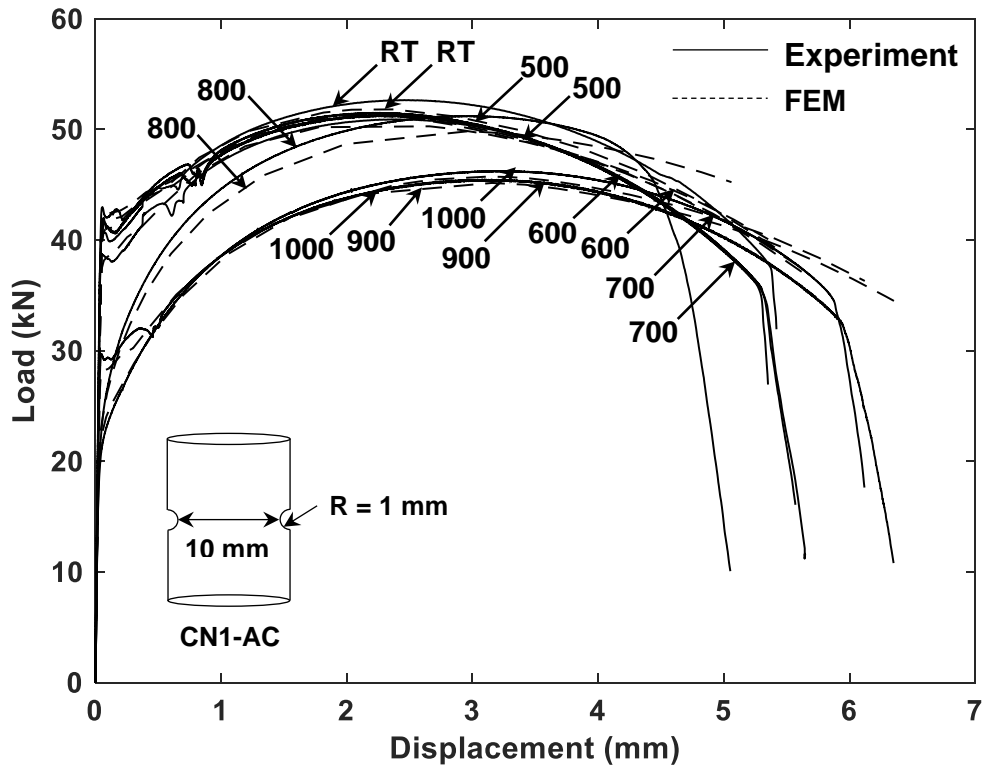


Figure 4.8. Load-displacement curves of specimen CN1-AC.

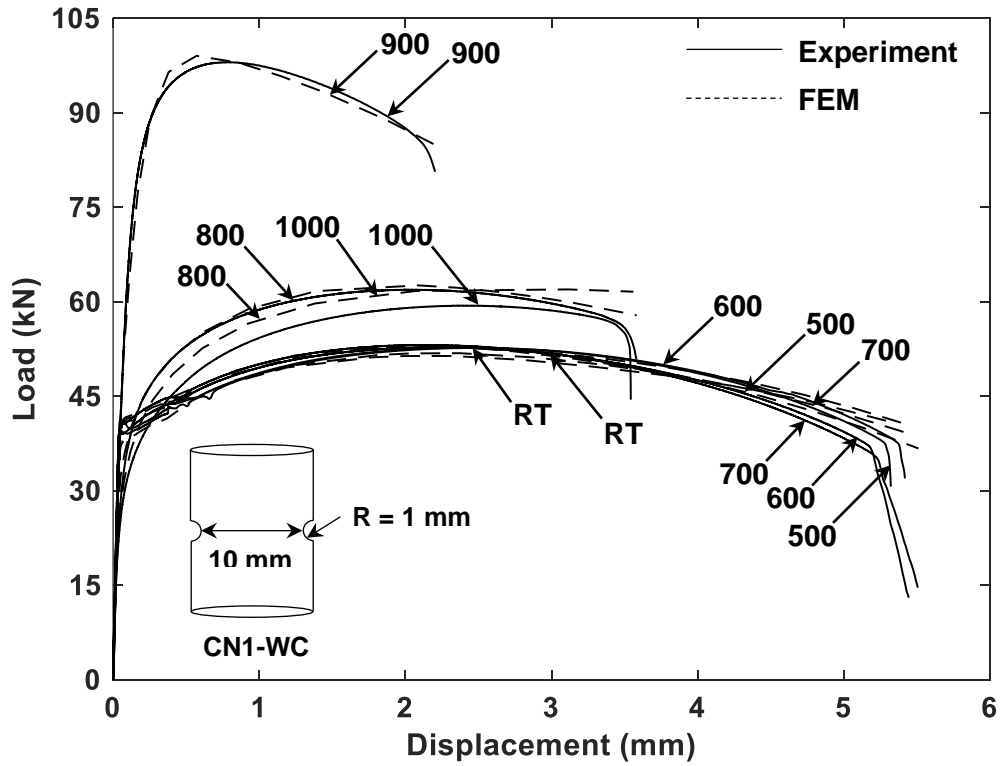


Figure 4.9. Load-displacement curves of specimen CN1-WC.

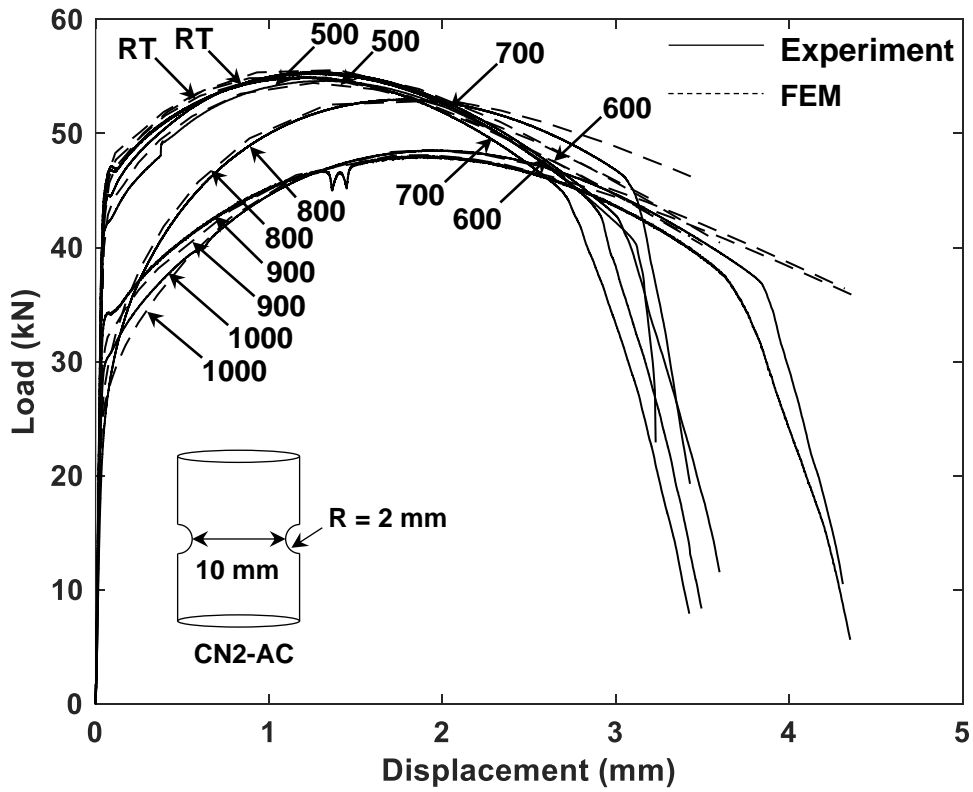


Figure 4.10. Load-displacement curves of specimen CN2-AC.

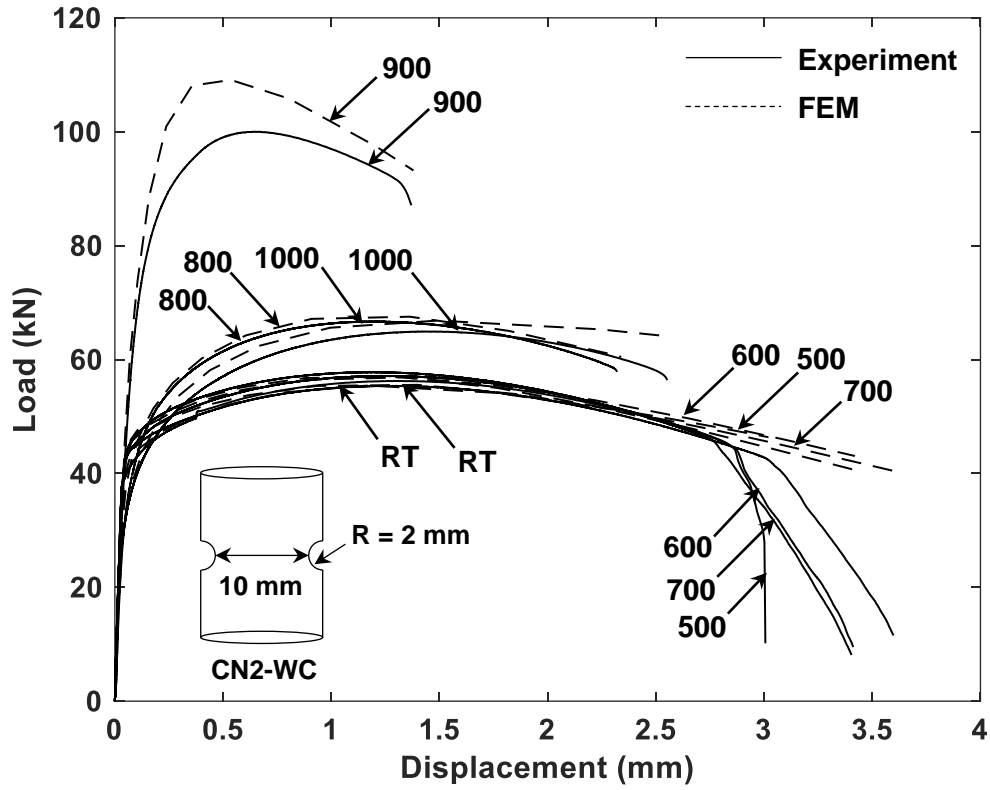


Figure 4.11. Load-displacement curves of specimen CN2-WC.

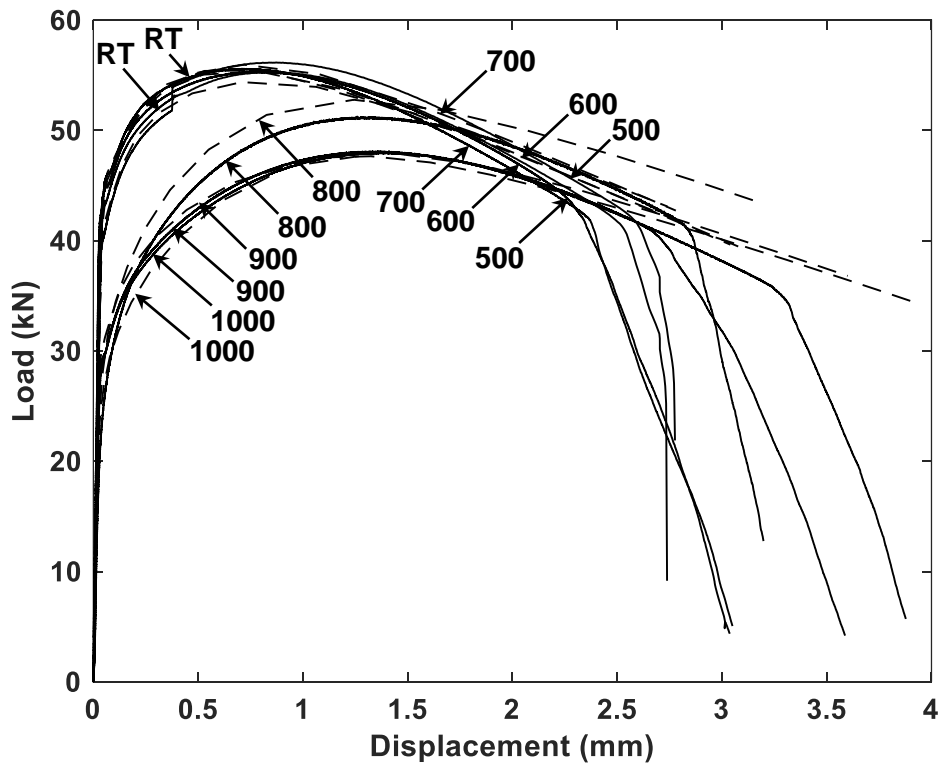


Figure 4.12. Load-displacement curves of specimen CN3-AC.

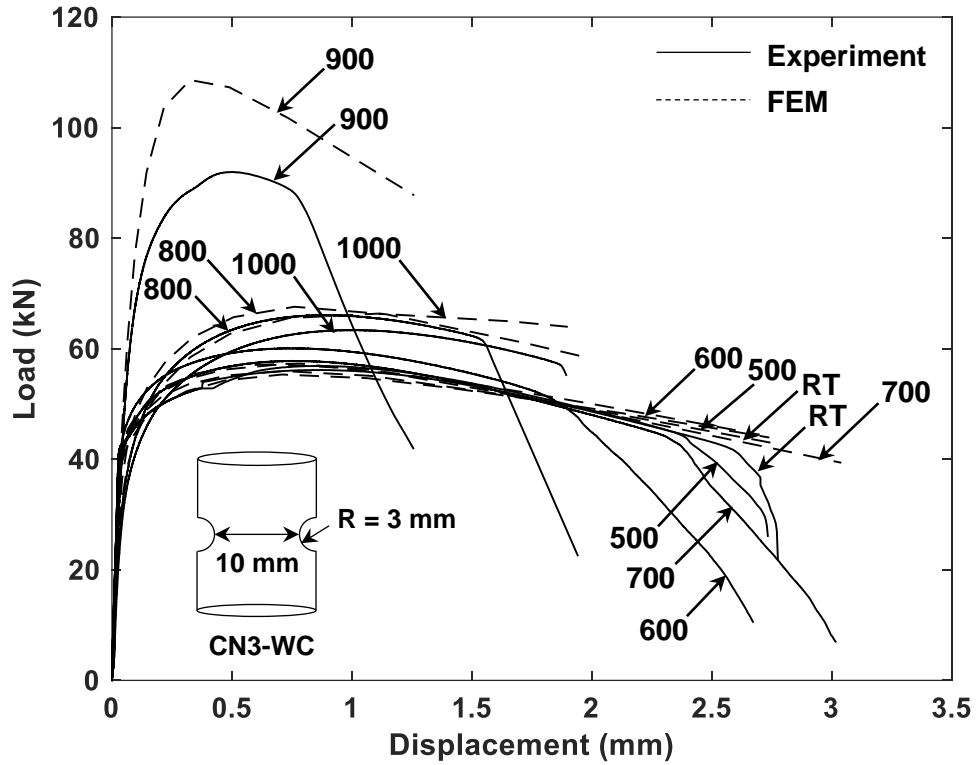


Figure 4.13. Load-displacement curves of specimen CN3-WC.

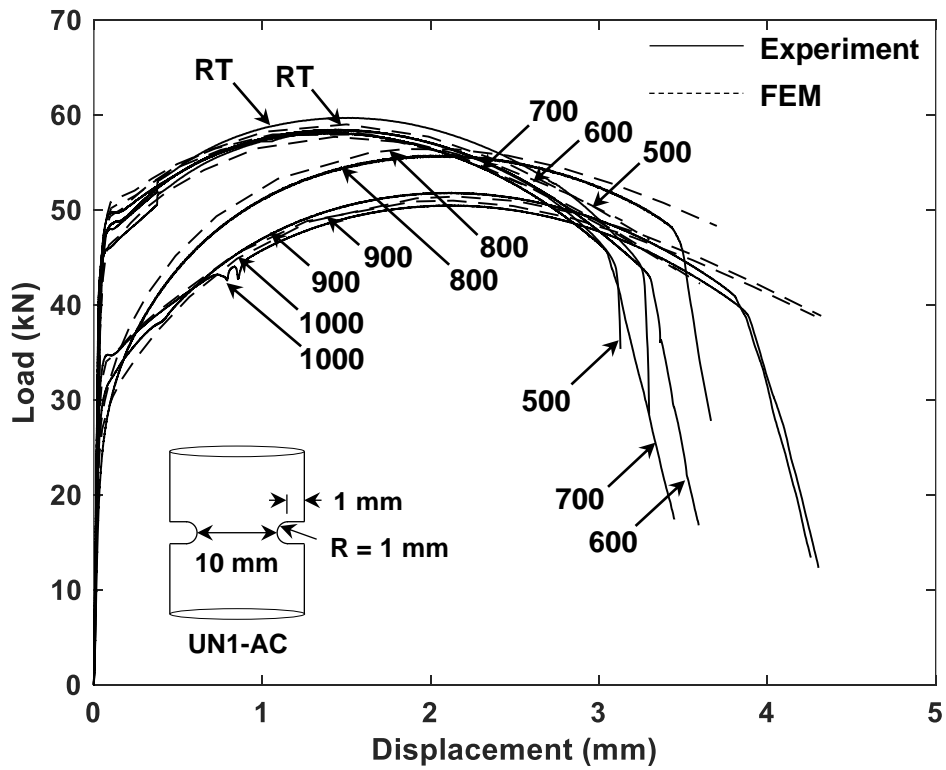


Figure 4.14. Load-displacement curves of specimen UN1-AC.

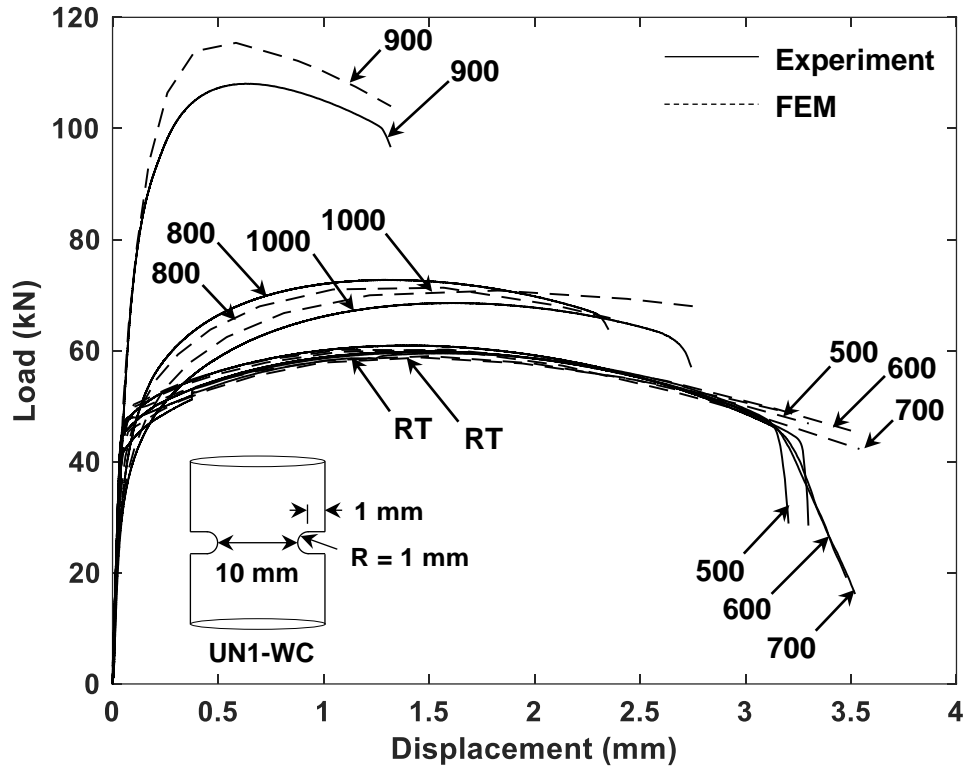


Figure 4.15. Load-displacement curves of specimen CN4-WC.

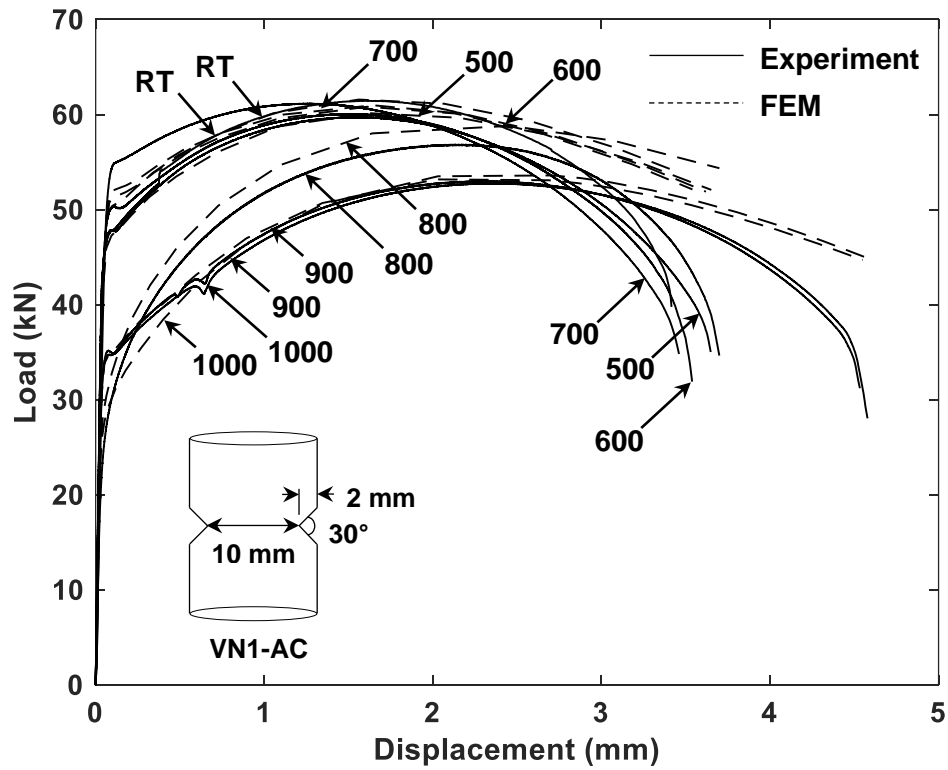


Figure 4.16. Load-displacement curves of specimen VN1-AC.

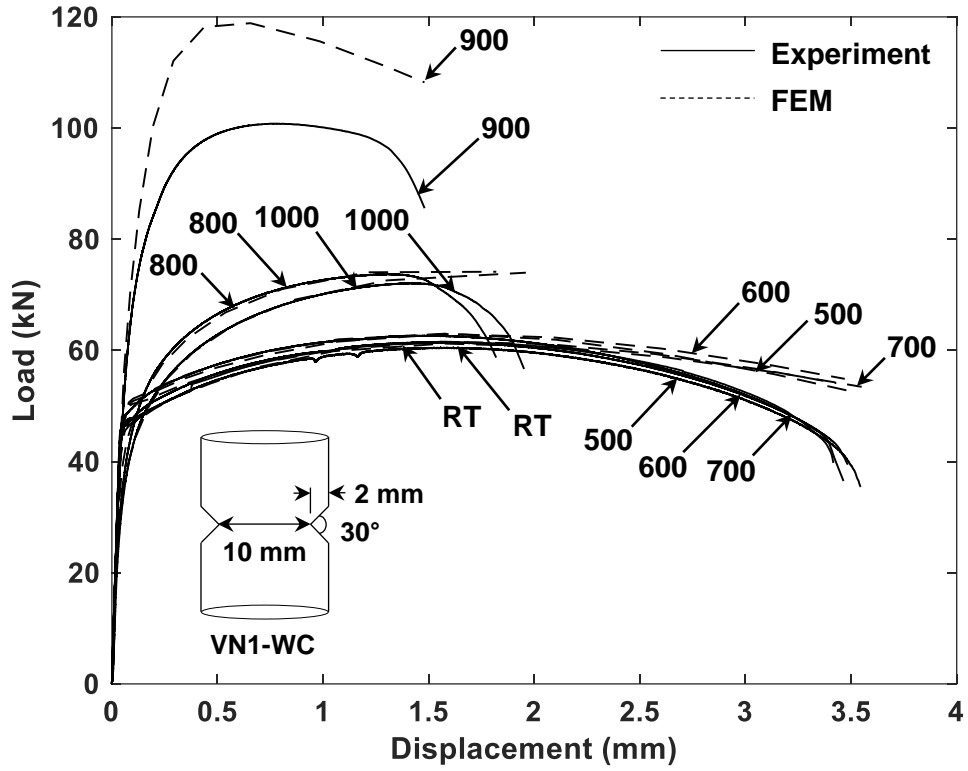


Figure 4.17. Load-displacement curves of specimen VN1-WC.

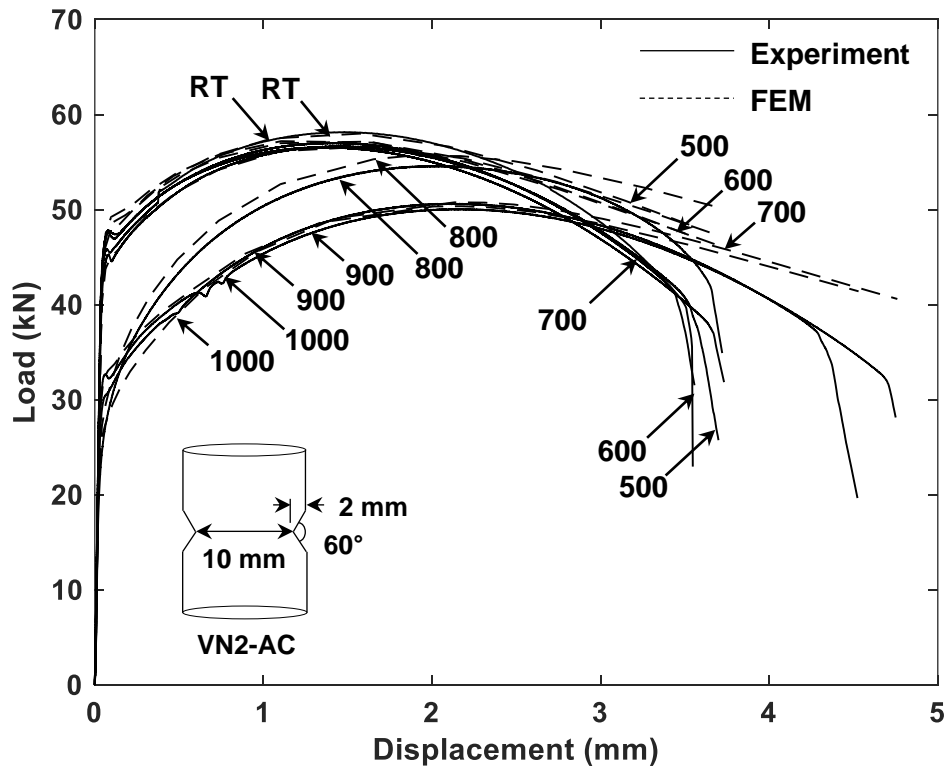


Figure 4.18. Load-displacement curves of specimen VN2-AC.

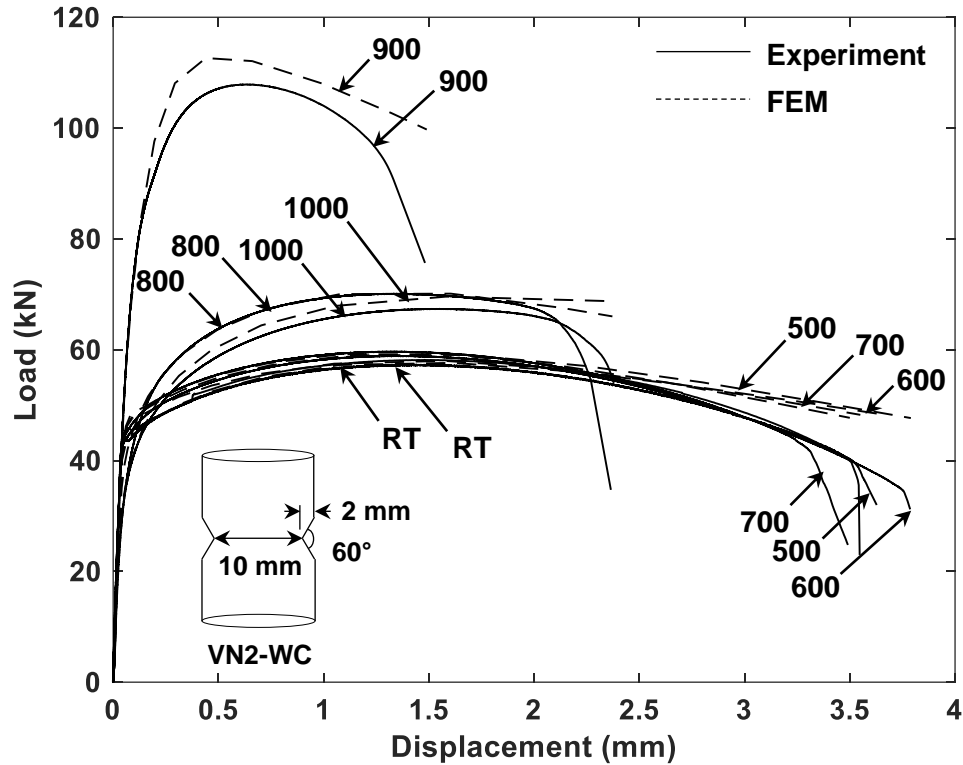


Figure 4.19. Load-displacement curves of specimen VN2-WC.

4.3.2. Finite Element Analysis of Post-Fire Specimens

In this study, non-linear finite element analyses are conducted to obtain stress triaxiality distribution in a given test specimen as a result of exposure to different target temperatures and cooling methods. FEA of test specimens is conducted using ABAQUS® [55] software package. Test geometries are modeled using axisymmetric four noded bilinear CAX4 elements. Geometric nonlinearity is considered in the model. The boundary conditions adopted in the model, and the typical mesh of a C-shaped notch are provided in Figure 4.20. The rate-independent finite strain J2 plasticity model is used as the constitutive model in this study. J2 plasticity model is commonly used for steels and other metals [56]. To calibrate the J2 plasticity model in ABAQUS®, both elastic and plastic material properties are obtained from uniaxial tension test results of un-notched test specimens. This includes the elastic modulus, identifying the onset of yielding in steel, and the true stress-strain relationship in the strain hardening region. An iterative

trial and error procedure is performed to calibrate the hardening curve parameters to obtain a load-displacement curve that agrees well with the experimental load-displacement curve. The calibrated strain hardening curves of the room temperature un-notched specimen and post-fire un-notched specimens for all temperatures and cooling methods are provided in Figure 4.21(a) and Figure 4.22, respectively. The calibrated material properties obtained from un-notched specimens are subsequently used to simulate the load-displacement behavior of notched specimens that are subjected to different target temperatures and cooling methods. As observed in Figure 4.6 to Figure 4.19, with the exception of few specimens (CN2-900-WC, CN3-900-WC, and VN1-900-WC), FEA-based load-displacement curves matched reasonably well with the experimental load-displacement curves. The difference between the FEA and experimental load-displacement results of these WC notched specimens can be attributed to the inadequacy of the J_2 plasticity model to simulate the softening behavior of the steel that is triggered by void initiation and growth mechanisms when steel approaches fracture. If temperature-sensitive constitutive models [57-61] are employed, the necessity of recalibration of the constitutive model at every elevated temperature can be avoided. However, this approach is not adopted in this study as the finite element models are solely used to evaluate the stress triaxiality and not to predict the mechanical properties.

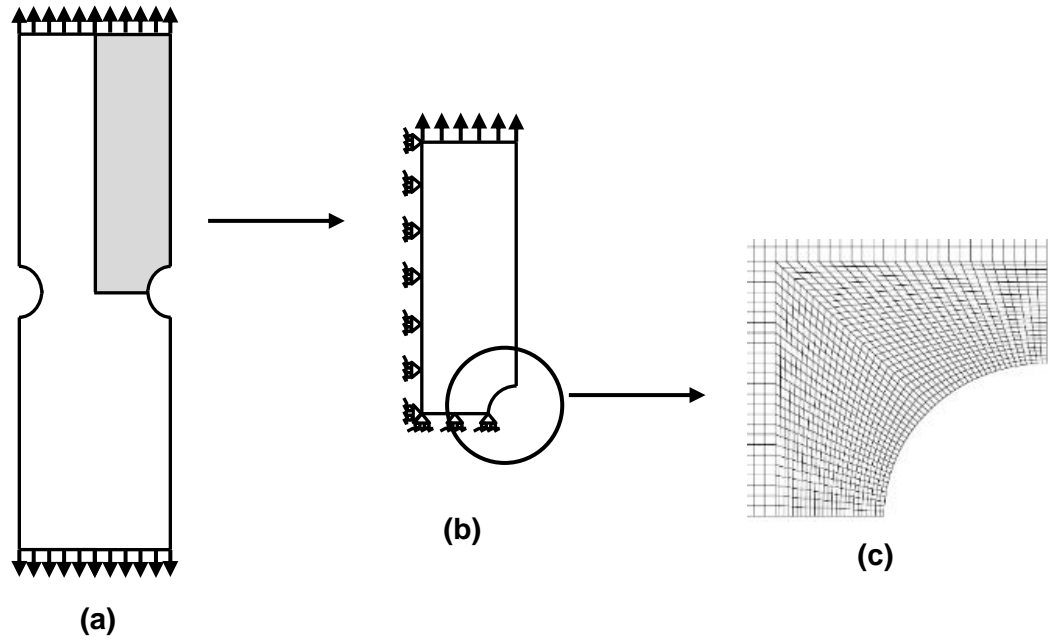


Figure 4.20. (a) Test specimen, (b) finite element model and applied boundary conditions, (c) typical C-notch mesh.

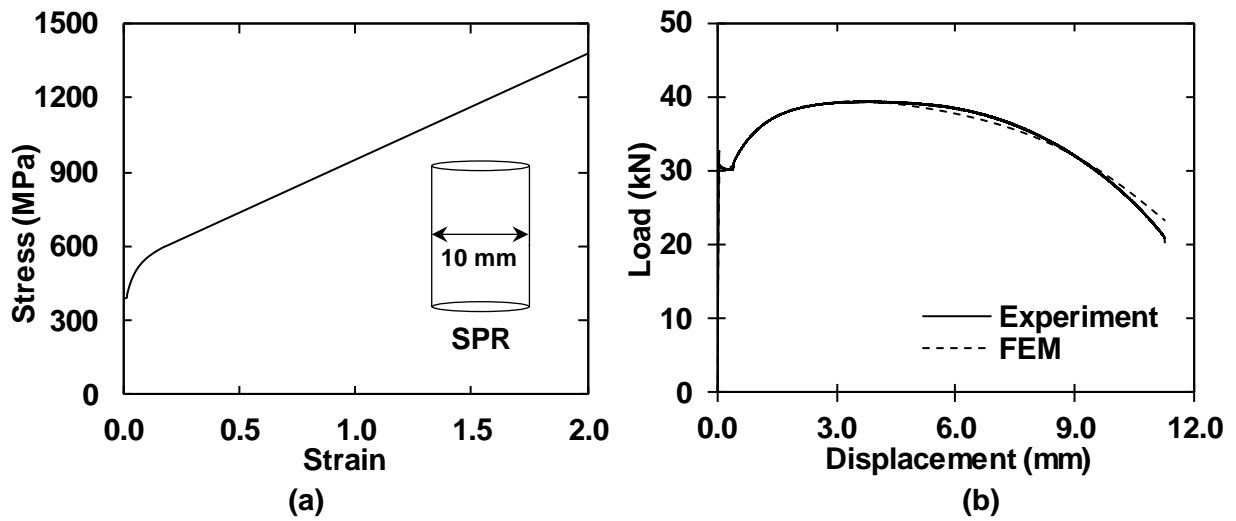


Figure 4.21. (a) Strain hardening curve of SPR test specimen, (b) experimental and FE load-displacement curve of SPR test specimen.

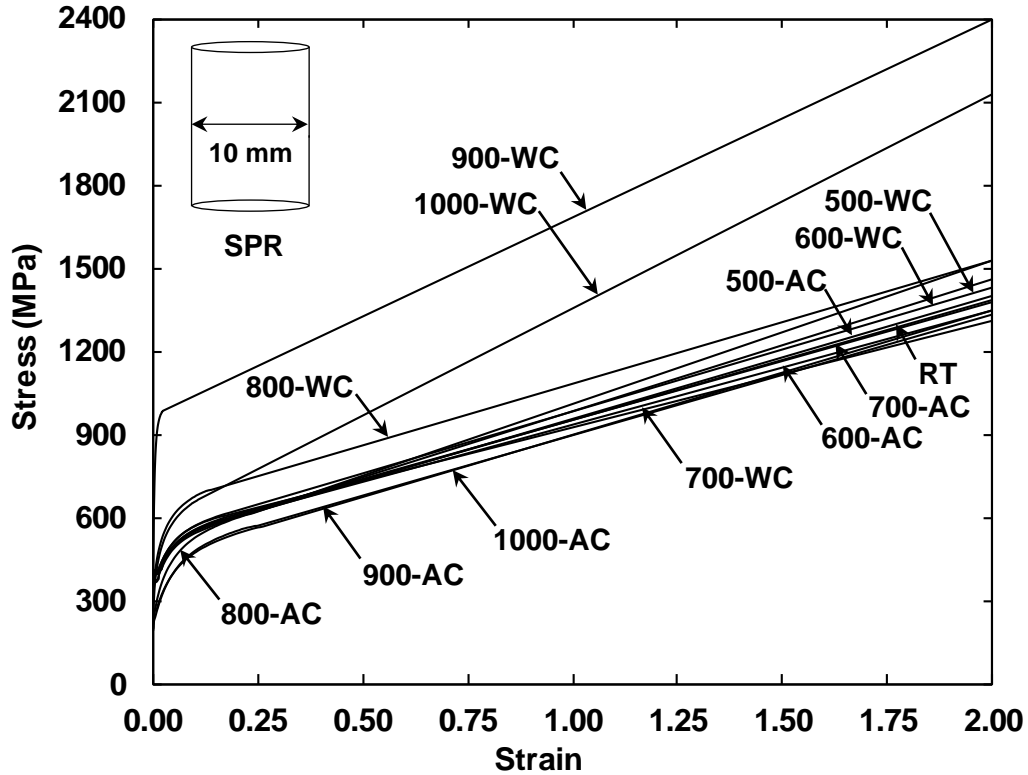


Figure 4.22. Strain hardening curves of un-notched test specimens.

4.3.3. Stress Triaxialities of Post-Fire Specimens

To investigate the change in stress triaxiality distribution in a given test specimen as a result of exposure to different target temperatures and cooling methods, post-fire stress triaxialities are determined using non-linear FEA. Detailed FEA procedure is discussed in the previous section (Section 4.3.2). To this end, maximum initial stress triaxialities and average initial stress triaxialities (average of initial stress triaxialities across critical cross-section) are determined for post-fire notched test specimens and compared with stress triaxialities of corresponding RT notch specimen. Both maximum initial stress triaxialities and average initial stress triaxialities are evaluated at $1.35 \pm 0.05\%$ engineering strain and are provided in Figure 4.23 and Figure 4.24, respectively. In this study, stress triaxialities are determined at $1.35 \pm 0.05\%$ engineering strain as at this strain value, the specimens are beyond the elastic range and have not

experienced considerable plastic deformation and hence the triaxiality would not evolve significantly due to the shape change in specimens. As observed in Figure 4.23 and Figure 4.24, maximum and average stress triaxialities of the majority of notched test specimens remain almost unchanged when specimens are either air-cooled or water-cooled after exposure to temperatures up to 700 °C. A slight decrease (up to 9%) is observed in the average initial stress triaxiality of test specimens when specimens are air-cooled after exposure to temperatures beyond 900 °C. On the other hand, the average and maximum stress triaxialities of specimens that are water-cooled from 900 °C, are observed to increase by up to 9% and 13%, respectively. It is well established that any change in stress triaxiality, albeit minor, can alter the strength and ductility of structural steels [47, 62, 63]. Hence, the change in strength and ductility of ASTM A572 steels that are exposed to high temperatures can be partly attributed to temperature-induced changes in stress triaxialities.

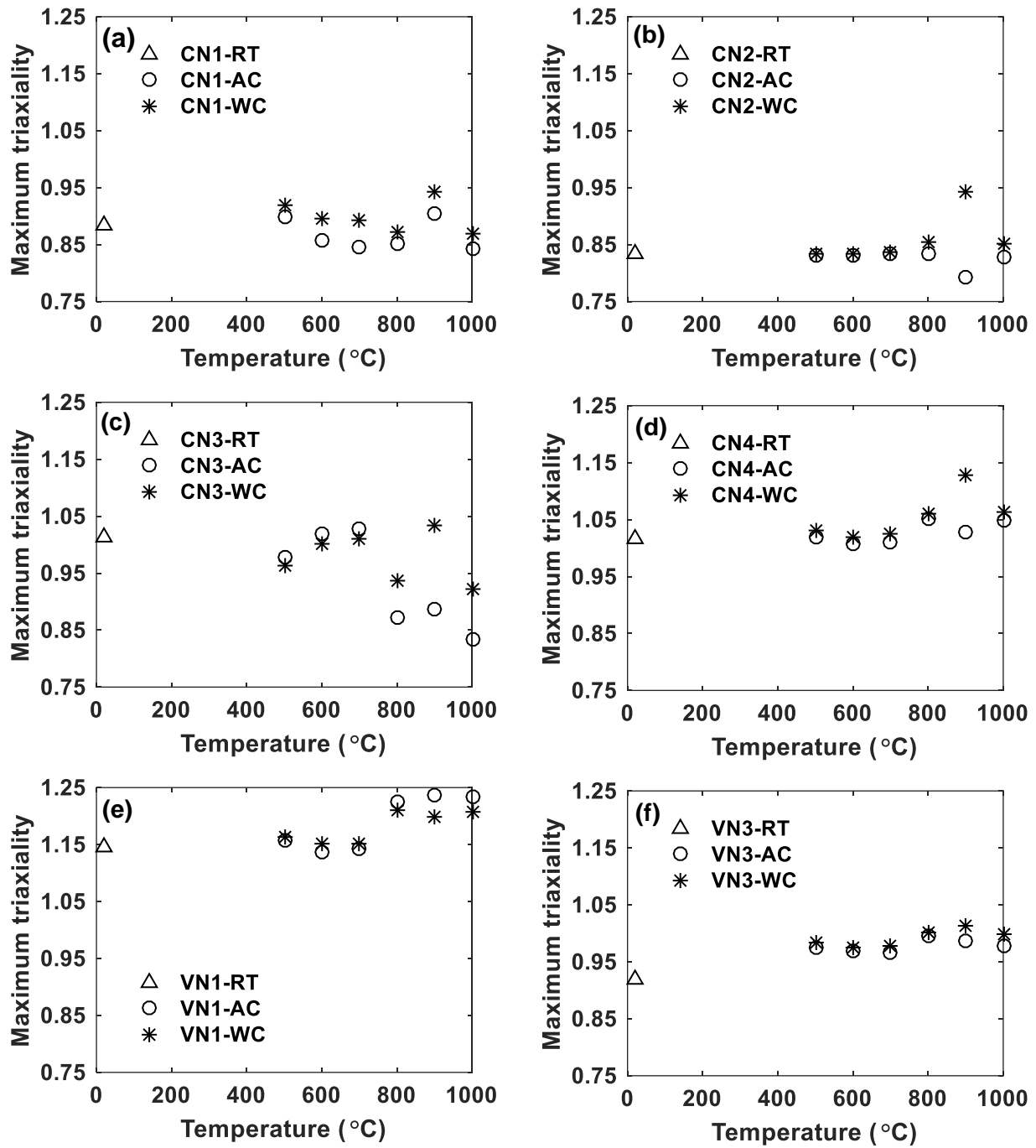


Figure 4.23. Maximum stress triaxialities of post-fire test specimens at $1.35 \pm 0.05\%$ strain: a) CN1, b) CN2, c) CN3, d) UN1, e) VN1, and f) VN2.

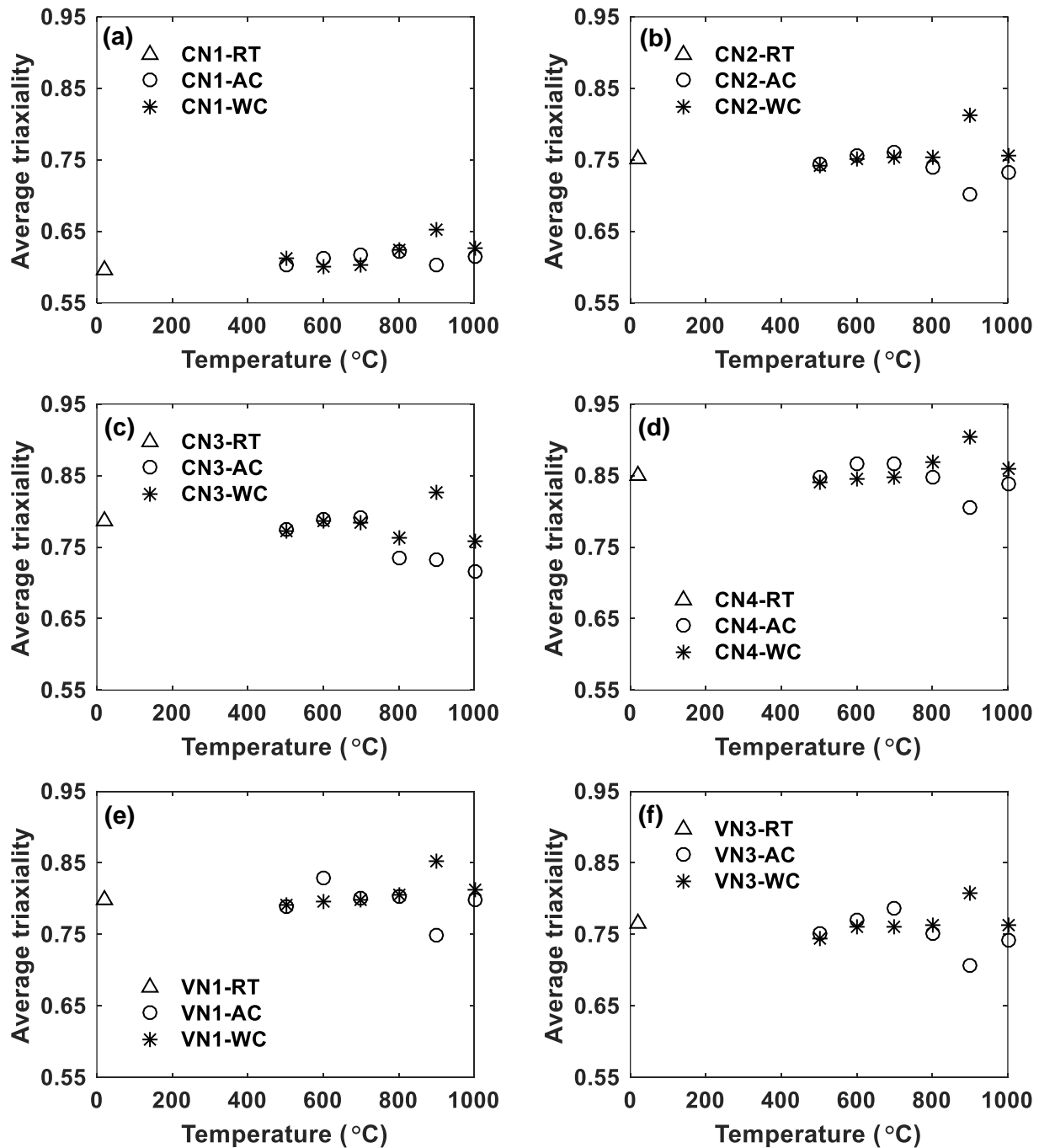


Figure 4.24. Average stress triaxialities of post-fire test specimens at $1.35 \pm 0.05\%$ strain: a) CN1, b) CN2, c) CN3, d) UN1, e) VN1, and f) VN2.

4.3.4. Elastic Modulus

Elastic modulus is defined as the slope of the engineering stress-strain curve in the elastic region [64]. Post-fire elastic moduli of both un-notched and notched test specimens are provided

in Table 4.5. To quantify the change observed in the elastic modulus as a result of triaxiality and cooling from elevated temperatures, post-fire elastic modulus residual factors are determined for each specimen. Post-fire elastic modulus residual factor is defined as the ratio of elastic modulus of test specimen evaluated at a target temperature (e.g. $E_{T,CN2}$) to the elastic modulus of un-notched RT (SPR-RT) specimen ($E_{20,SPR}$). Post-fire elastic modulus residual factors of un-notched and notched test specimens are presented in Figure 4.25(a) and Figure 4.26, respectively. The influence of elevated temperatures and cooling methods on the elastic modulus of ASTM A572 steels is determined by comparing the elastic moduli of un-notched AC and WC specimens with the elastic modulus of un-notched RT (SPR-RT) specimen. As observed in Table 4.5 and Figure 4.25(a), the elastic moduli of un-notched (SPR) specimens remained relatively unaffected after exposure to temperatures up to 1000 °C, for both cooling methods. This can be attributed to the fact that elastic modulus is a microstructure-insensitive property of structural steel and remains unaffected at room temperatures despite the temperature-induced microstructure changes in steel [64, 65]. To quantify the effect of high stress triaxiality on the elastic modulus of ASTM A572 steels, the elastic moduli of notched RT specimens are compared with the elastic modulus of un-notched RT (SPR-RT) specimen. The presence of high stress triaxiality is observed to increase the elastic modulus of notched RT specimens by up to 116% when compared to the un-notched RT specimen (see Figure 4.26). As a material property, the elastic modulus is not expected to exhibit a change in the case of notched specimens. However, the increase observed in the elastic modulus of notched specimens can be attributed to the definition of elastic modulus employed in this study, which is taken as the slope of the elastic portion of stress versus longitudinal strain. Evaluating the slope of stress versus diametric strain is more appropriate when evaluating the elastic modulus of notch specimens. However, in this

study, the elastic moduli of all test specimens are determined based on the stress versus longitudinal strain, in accordance with the procedures recommended by ASTM E111 [66]. The combined influence of high stress triaxiality and cooling methods on the post-fire elastic modulus of ASTM A572 steel is inferred by comparing the elastic moduli of notched AC and WC specimens with the elastic modulus of un-notched RT (SPR-RT) specimen. As observed in Figure 4.26, elastic moduli of notched AC specimens experienced a slight reduction after exposure to high temperatures, when compared to the elastic modulus of the corresponding notched RT specimen. Notwithstanding this, the elastic moduli of notched AC specimens remained higher than the elastic modulus of un-notched RT (SPR-RT) specimen. On the other hand, with the exception of a few specimens, no considerable change is observed in the elastic modulus of notched WC specimens when compared to the corresponding notched RT specimen. These results suggest that cooling from elevated temperatures does not affect the elastic modulus of ASTM A572 steels.

Table 4.5. Post-fire elastic modulus of test specimens.

Temperature (°C)	Cooling method	Elastic modulus (MPa)						
		SPR	CN1	CN2	CN3	UN1	VN1	VN2
20	-	208.88	305.51	378.73	451.88	385.32	387.08	380.98
500	AC	219.12	330.06	395.15	468.47	463.69	381.96	367.67
	WC	232.44	325.55	375.63	477.92	410.95	398.45	393.35
600	AC	206.01	320.48	387.53	398.29	370.69	366.82	383.02
	WC	200.95	296.62	387.81	425.02	352.83	407.79	377.52
700	AC	206.38	308.13	353.33	364.18	363.28	375.02	369.31
	WC	203.11	323.63	400.01	414.57	387.01	385.45	390.51
800	AC	203.53	253.68	225.57	247.54	242.73	264.10	310.44
	WC	198.78	252.51	315.42	321.58	333.62	342.29	292.23
900	AC	194.41	319.26	330.97	423.03	341.57	365.71	360.99
	WC	204.73	278.18	340.62	365.56	347.36	406.21	396.24
1000	AC	195.89	259.99	318.96	358.76	338.59	342.38	358.98
	WC	200.37	328.45	313.93	314.70	321.58	331.10	340.65

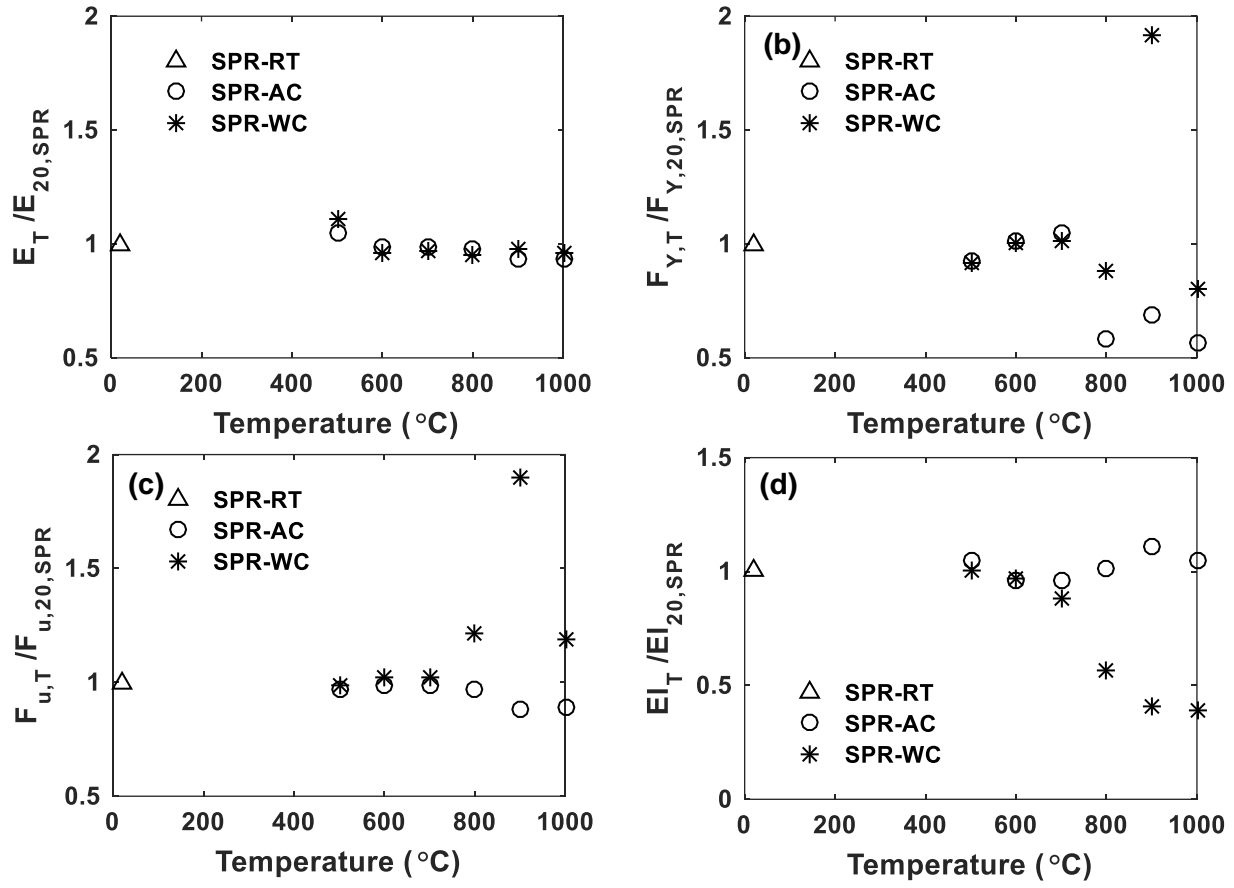


Figure 4.25. Residual factors of specimen SPR under different cooling regimes: a) elastic modulus, b) yield strength, c) ultimate tensile strength, and d) ductility.

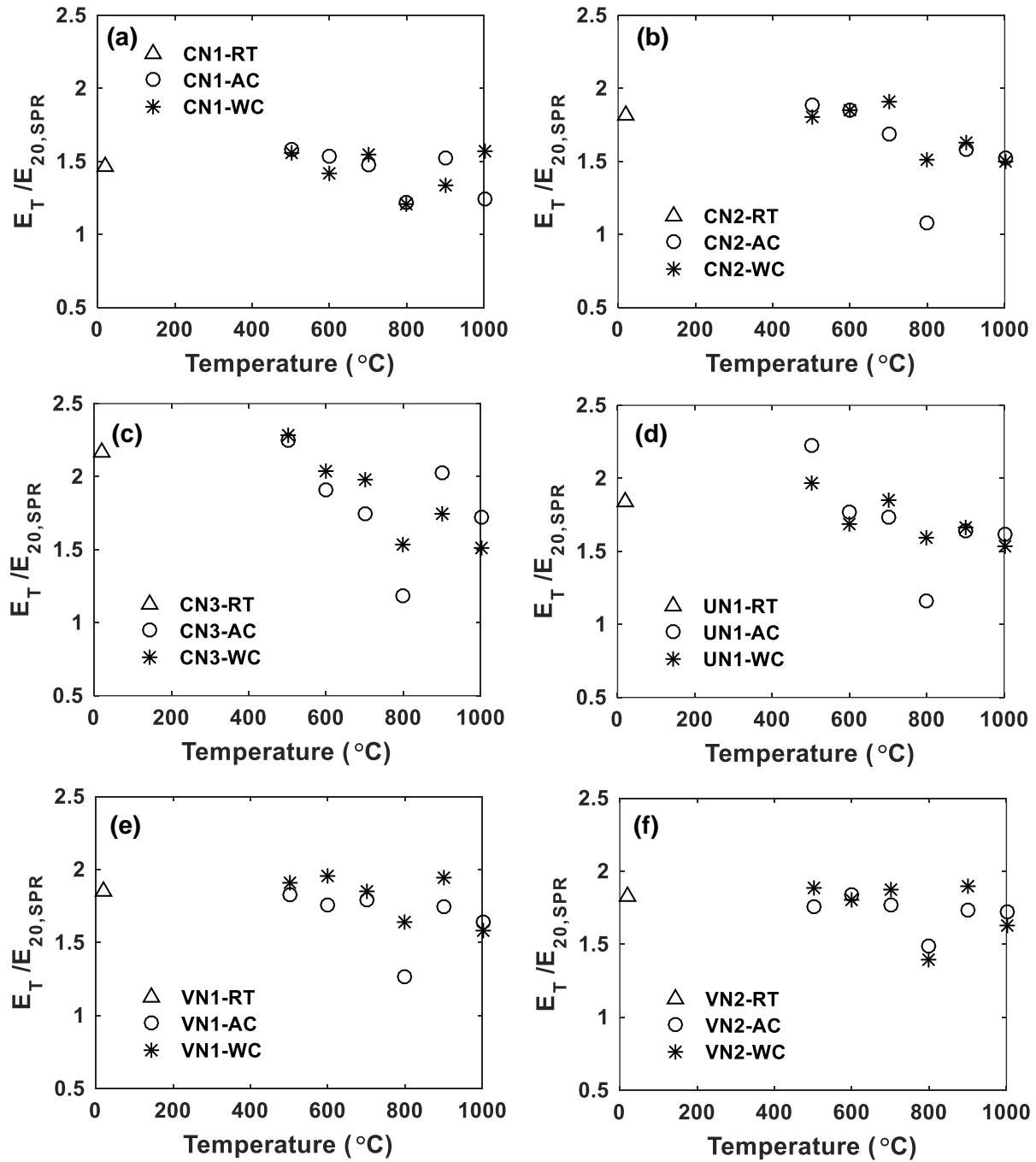


Figure 4.26. Elastic modulus residual factors of post-fire test specimens: a) CN1, b) CN2, c) CN3, d) UN1, e) VN1, and f) VN2.

4.3.5. Yield Strength

The yield strength of test specimens is determined using the 0.2% strain offset method [65]. Post-fire yield strengths of both un-notched and notched test specimens are provided in

Table 4.6. The change observed in yield strength of test specimens is quantified in terms of yield strength residual factor, which is defined as the ratio of the yield strength of a test specimen that is cooled after exposure to elevated temperature (e.g. $F_{y,T,CN2}$) to yield strength of un-notched specimen (SPR) at room temperature ($F_{y,20,SPR}$). Post-fire yield strength residual factors of un-notched and notched test specimens are provided in Figure 4.25(b) and Figure 4.27, respectively. Moreover, post-fire yield strength residual factors are provided in Table 4.7. To quantify the effect of elevated temperatures and cooling method on the yield strength of ASTM A572 steels, post-fire yield strengths of un-notched (SPR) AC and WC specimens are compared with the yield strength of un-notched RT (SPR-RT) specimen. As observed in Table 4.6 and Figure 25(b), un-notched specimens do not exhibit a considerable change in yield strength when cooled from temperatures up to 700 °C, irrespective of the cooling method. However, when exposed to temperatures beyond 700 °C, un-notched AC specimens exhibited up to 44% reduction in yield strength. Almost a similar amount of degradation (40%) in yield strength was reported in a previous study when ASTM A572 Gr. 50 steels were air-cooled after exposure to 800 °C [36]. This decrease in the yield strength can be attributed to the loss of precipitation hardening strength that is imparted by the micro-alloying elements in ASTM A572 Gr. 50 steels [67-69]. Un-notched specimens experienced up to 20% reduction in yield strength when water-cooled from 800 °C and 1000 °C temperatures. However, a significant increase of 91% is observed in the yield strength of un-notched specimens that are water-cooled from 900 °C. To investigate this significant increase in yield strength, microstructures of test specimens are obtained RT (see Figure 4.28), 900-AC (see Figure 4.29), and 900-WC (see Figure 4.30) conditions using standard metallographic techniques [70]. As observed in Figure 28, ASTM A572 Gr. 50 steels consist of ferrite and pearlite phases. At 900-WC condition, the austenite phase, which formed at 900 °C,

transformed back to ferrite and a stronger martensite phase, as shown by needle-like structure in Figure 4.30. Hence, a significant increase in yield strength observed in specimens that are water-cooled from 900 °C can be attributed to the formation of stronger martensite phase in ASTM A572 steels [71], as revealed by the microstructure of SPR-900-WC specimen (see Figure 4.30). To summarize, both air-cooling and water-cooling from high temperatures are found to adversely affect the yield strength of un-notched RT specimens, with the exception of the 900-WC specimen, where a significant increase in yield strength is observed due to the formation of stronger martensite phase in steel microstructure.

To determine the influence of stress triaxiality on the yield strength of A572 steels, the yield strengths of notched RT specimens are compared with the yield strength of the un-notched RT (SPR-RT) specimen. As evident from Table 4.6 and Figure 4.27, notched RT specimens exhibited up to 55% (VN1-RT specimen) higher yield strength when compared to un-notched RT (SPR-RT) specimen, which can be attributed to the presence of high stress triaxiality in notched RT specimens [45]. The combined effect of high stress triaxiality and cooling methods on the yield strength of A572 Gr. 50 steels is evaluated by comparing post-fire yield strengths of notched AC and notched WC specimens with the yield strength of un-notched RT (SPR-RT) specimen. It can be observed from Figure 27 that notched AC specimens that are exposed to temperatures up to 700 °C exhibited an almost similar increase in yield strength as observed in notched RT specimens (up to 55%) when compared to yield strength of un-notched RT specimen. However, when exposed to 800 °C, notched AC specimens experienced a reduction in yield strength (up to 17%) when compared to un-notched RT specimen (SPR-RT). Beyond 800 °C, notched AC specimens with relatively low stress triaxiality (CN1-AC) exhibited up to 27% reduction in yield strength whereas a majority of notched AC specimens exhibited slightly higher

yield strength when compared to un-notched RT (SPR-RT) specimen. In the case of notched WC specimens that are cooled from temperatures up to 700 °C experienced an almost similar increase in yield strength as observed in notched RT (up to 55%) when compared to the yield strength of un-notched RT specimen. When water-cooled from 800 °C, notched specimens exhibited up to 44% higher yield strength than the yield strength of un-notched RT specimen. Notched specimens that are water-cooled after exposure to 900 °C, exhibited a significant increase of up to 158% (VN1-900-WC) in yield strength when compared to un-notched RT (SPR-RT) specimen. The significant increase in yield strength of 900-WC specimens can be attributed to two factors: a) the formation of stronger martensite microstructure (as seen in Figure 30) in 900-WC specimens, and b) a slight increase in stress triaxiality of 900-WC specimens (as discussed in Section 4.3.3). Interestingly, notched WC specimens that are cooled from 1000 °C exhibited a decrease in yield strength when compared to the corresponding notched RT specimen but had yield strength greater than the un-notched RT (SPR-RT) specimen. These results once again highlight the positive influence of high stress triaxiality and negative influence of high temperature except in cases where martensite is formed on the yield strength of ASTM A572 Gr. 50 steels.

Table 4.6. Post-fire yield strength of test specimens.

Temperature (°C)	Cooling method	Yield strength (MPa)						
		SPR	CN1	CN2	CN3	UN1	VN1	VN2
20	-	392.64	513.56	561.00	570.79	610.04	608.54	579.02
500	AC	364.72	488.54	539.49	545.55	585.19	604.87	572.89
	WC	360.78	497.61	536.52	573.22	553.75	593.76	558.59
600	AC	397.98	522.19	594.74	581.45	616.04	639.05	604.02
	WC	395.41	501.49	568.31	620.47	597.49	601.89	579.24
700	AC	410.13	534.51	600.21	594.58	632.11	657.88	603.30
	WC	396.12	518.82	586.72	586.01	617.34	628.17	592.20
800	AC	229.13	326.41	371.24	381.06	369.50	376.17	365.12
	WC	346.35	463.48	528.89	547.08	565.17	567.21	547.47
900	AC	272.05	375.46	432.82	395.71	400.78	442.56	392.34
	WC	751.17	944.29	919.77	906.41	1015.01	887.02	996.35
1000	AC	220.56	285.92	391.03	398.62	440.96	448.01	413.53
	WC	316.29	380.95	488.10	508.40	492.71	528.60	505.14

Table 4.7. Post-fire yield strength residual factors of test specimens.

Temperature (°C)	Cooling method	Yield strength residual factor ($F_{y,T}/F_{y,20}$)						
		SPR	CN1	CN2	CN3	UN1	VN1	VN2
20	-	1.00	1.31	1.43	1.45	1.55	1.55	1.47
500	AC	0.93	1.24	1.37	1.39	1.49	1.54	1.46
	WC	0.92	1.27	1.37	1.46	1.41	1.51	1.42
600	AC	1.01	1.33	1.51	1.48	1.57	1.63	1.54
	WC	1.01	1.28	1.45	1.58	1.52	1.53	1.48
700	AC	1.04	1.36	1.53	1.51	1.61	1.68	1.54
	WC	1.01	1.32	1.49	1.49	1.57	1.60	1.51
800	AC	0.58	0.83	0.95	0.97	0.94	0.96	0.93
	WC	0.88	1.18	1.35	1.39	1.44	1.44	1.39
900	AC	0.69	0.96	1.10	1.01	1.02	1.13	1.00
	WC	1.91	2.40	2.34	2.31	2.59	2.26	2.54
1000	AC	0.56	0.73	1.00	1.02	1.12	1.14	1.05
	WC	0.81	0.97	1.24	1.29	1.25	1.35	1.29

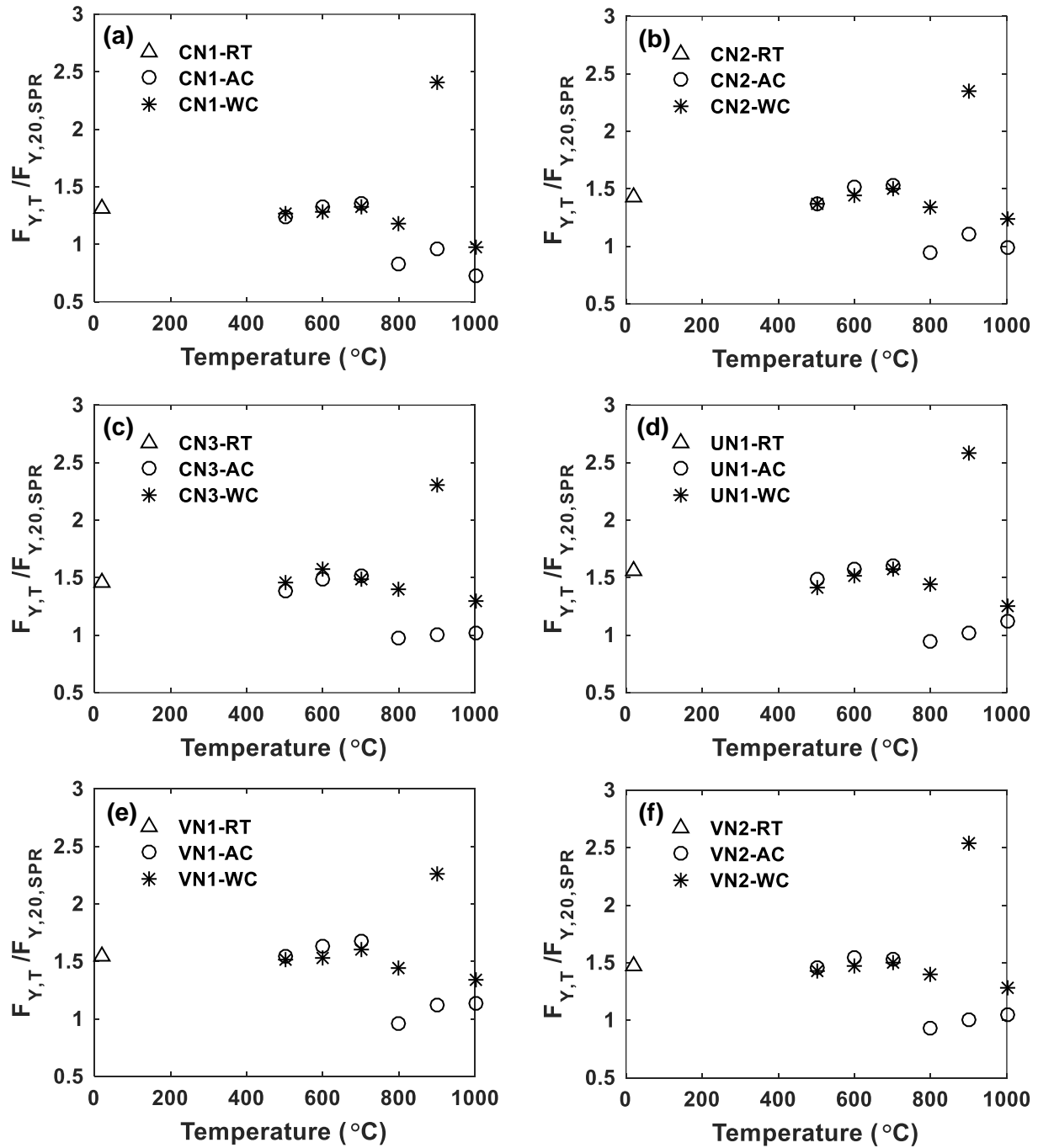


Figure 4.27. Yield strength residual factors of post-fire test specimens: a) CN1, b) CN2, c) CN3, d) UN1, e) VN1, and f) VN2.

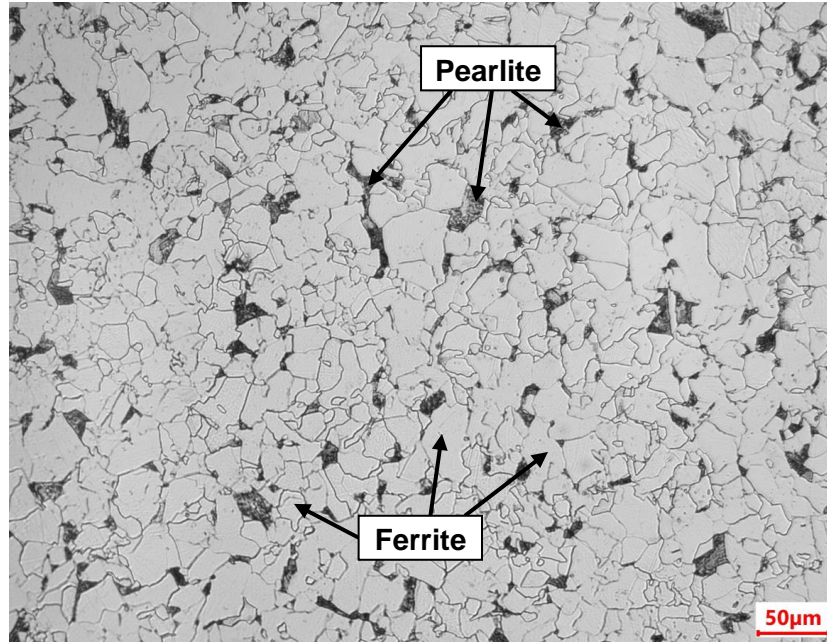


Figure 4.28. Microstructure of ASTM A572 Gr. 50 steel at room temperature.

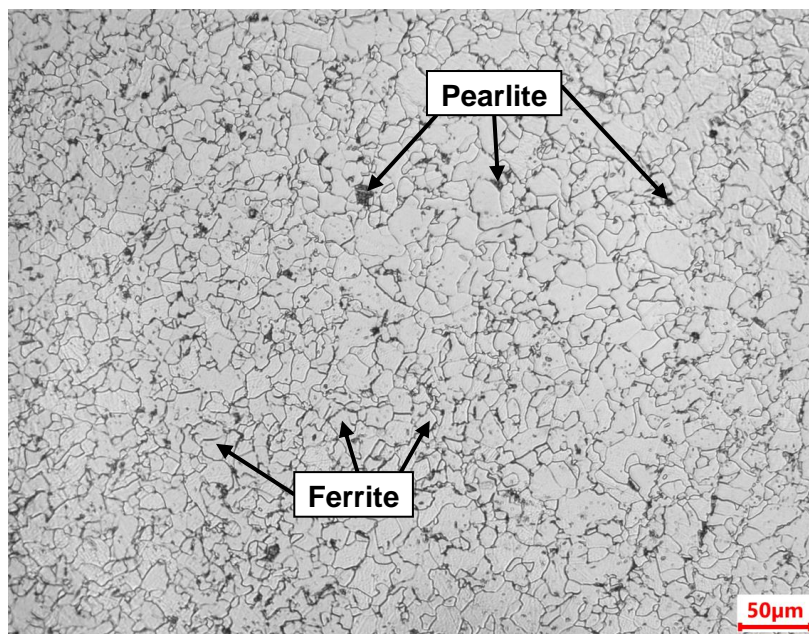


Figure 4.29. Microstructure of ASTM A572 gr. 50 steel after air-cooling from 900 °C to room temperature.

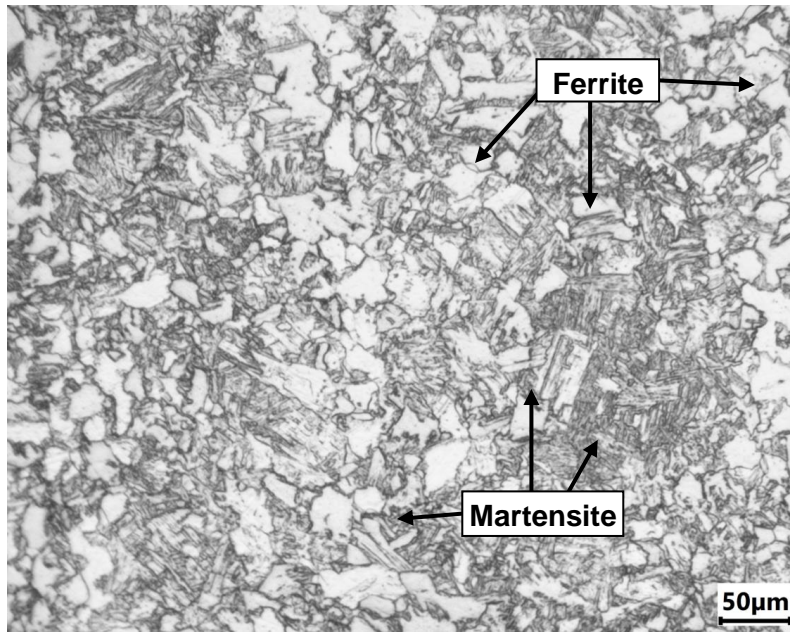


Figure 4.30. Microstructure of ASTM A572 Gr. 50 steel after water-cooling from 900 °C to room temperature.

4.3.6. Ultimate Tensile Strength

Ultimate tensile strength is defined as the maximum stress obtained from the engineering stress-strain curve of a test specimen [64]. Post-fire ultimate tensile strengths of both un-notched and notched test specimens are provided in Table 4.8. The variation in ultimate tensile strength of test specimens is quantified in terms of the ultimate tensile strength residual factor, which is defined as the ratio of ultimate tensile strength of a test specimen that is cooled from an elevated temperature (e.g. $F_{u,T,CN2}$) to the ultimate tensile strength of un-notched specimen (SPR) at room temperature ($F_{u,20,SPR}$). Post-fire ultimate tensile strength residual factors of un-notched and notched test specimens are provided in Figure 4.25(c) and Figure 4.31, respectively. Moreover, post-fire ultimate tensile strength residual factors are provided in Table 4.9. To quantify the influence of the cooling method on the ultimate tensile strength of A572 Gr. 50 steels, post-fire ultimate tensile strengths of un-notched AC and WC (SPR-AC and SPR-WC) specimens are compared with ultimate tensile strength of un-notched RT (SPR-RT) specimen. As observed in

Table 4.8 and Figure 4.25(c), the ultimate tensile strength of un-notched specimens almost remain unaffected when specimens are either air-cooled or water-cooled from temperatures up to 700 °C. Beyond 700 °C, un-notched AC specimens experienced a modest reduction of up to 12% in ultimate tensile strength in spite of grain refinement as the strength due to precipitation hardening mechanism of microalloying elements in A572 steels is lost when exposed to these temperatures [67-69]. However, un-notched specimens that are water-cooled from temperatures beyond 700 °C, exhibited up to 90% increase in ultimate tensile strength (SPR-900-WC), due to the formation of stronger martensite microstructure (see Figure 4.30).

To understand the effect of high stress triaxiality on the ultimate tensile strength of A572 Gr. 50 steels the ultimate tensile strengths of notched RT specimens are compared with the ultimate tensile strength of un-notched RT (SPR-RT) specimen. As observed in Table 4.8 and Figure 4.31, notched RT specimens experienced up to 55% higher ultimate tensile strength (VN1-RT) when compared to un-notched RT (SPR-RT). A similar amount of increase was also observed in yield strength of notched RT specimens and it can be attributed to the high stress triaxiality of notched RT specimens [45]. To determine the combined influence of high stress triaxiality and cooling methods on the ultimate tensile strength of ASTM A572 Gr. 50 steels, the ultimate tensile strengths of notched AC and notched WC specimens are compared with the ultimate tensile strength of un-notched RT (SPR-RT) specimen. As observed in Table 4.8 and Figure 4.31, notched AC specimens that are exposed to temperatures up to 800 °C, exhibited up to 46% higher ultimate tensile strength when compared to the ultimate tensile strength of un-notched RT specimen. Beyond 800 °C, notched AC specimens exhibited up to 33% higher ultimate tensile strength than that of un-notched RT specimen. This indicates that while the ultimate tensile strength of notched AC specimens remained higher than un-notched RT

specimen, the ultimate tensile strength of notched AC specimens decreased when compared to corresponding notched RT specimen. The higher yield strength of notched AC specimens can be attributed to the presence of high stress triaxiality. In the case of water-cooling method, no noticeable change is observed in ultimate tensile strength when notched specimens are exposed to temperatures up to 700 °C when compared to the corresponding notched RT specimen. However, notched WC specimens exhibited an increase in ultimate tensile strength after exposure to temperatures beyond 700 °C. Notched specimens that are water-cooled from 900 °C exhibited up to 172% higher ultimate tensile strength (VN1-900-WC) than un-notched RT specimen, which can be attributed to the formation of stronger martensite phase (see Figure 4.30) in ASTM A572 steels [71] in addition to the presence of high stress triaxiality in notched WC specimens, as previously discussed in Section 4.3.3. These results highlight the combined positive effect of formation of martensite and the presence of high triaxiality on the ultimate tensile strength of water-cooled ASTM A572 steels.

Table 4.8. Post-fire ultimate tensile strength of test specimens.

Temperature (°C)	Cooling method	Ultimate tensile strength (MPa)						
		SPR	CN1	CN2	CN3	UN1	VN1	VN2
20	-	505.88	670.21	711.23	715.00	760.07	782.39	740.49
500	AC	491.82	647.99	695.14	703.63	743.01	757.89	721.40
	WC	499.36	670.84	716.31	724.40	758.27	770.46	728.73
600	AC	500.32	651.97	702.42	703.04	746.01	765.63	726.72
	WC	516.68	672.31	724.83	763.60	765.54	781.79	751.33
700	AC	500.77	655.27	700.02	707.74	740.66	737.85	715.70
	WC	517.49	676.05	735.37	733.76	776.22	796.44	759.90
800	AC	489.12	649.83	675.59	652.35	711.16	725.84	694.67
	WC	612.58	788.36	848.03	839.91	925.57	937.29	892.02
900	AC	444.47	582.88	610.47	612.61	659.87	675.48	645.61
	WC	962.21	1248.68	1272.52	1171.16	1375.77	1282.82	1374.45
1000	AC	449.96	586.98	619.58	611.66	641.41	673.40	639.86
	WC	599.15	755.88	825.40	807.61	871.77	918.97	859.40

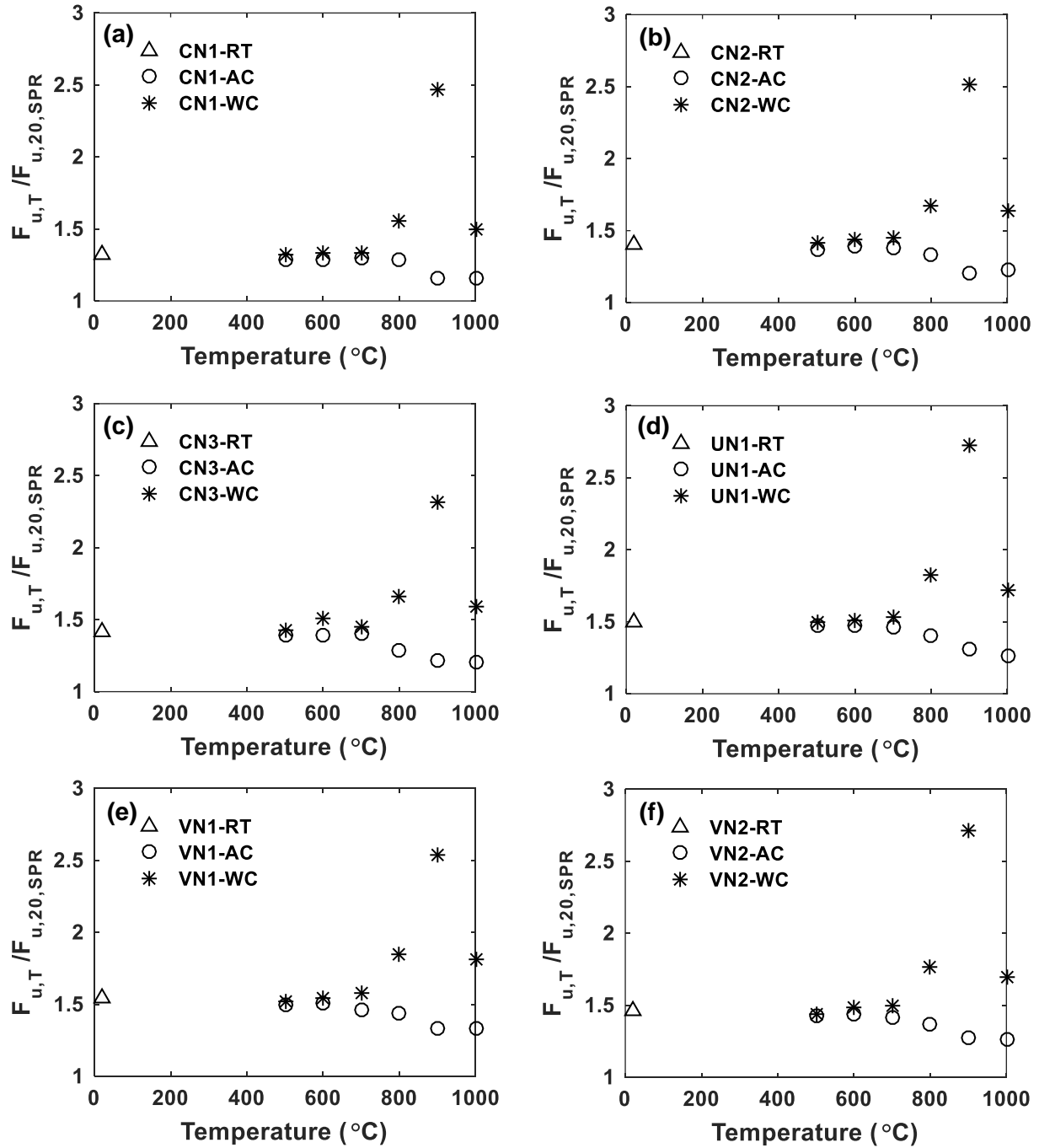


Figure 4.31. Ultimate tensile strength residual factors of post-fire test specimens: a) CN1, b) CN2, c) CN3, d) UN1, e) VN1, and f) VN2.

Table 4.9. Post-fire ultimate tensile strength residual factors of test specimens.

Temperature (°C)	Cooling method	Ultimate tensile strength residual factor ($F_{u,T}/F_{u,20}$)						
		SPR	CN1	CN2	CN3	UN1	VN1	VN2
20	-	1.00	1.32	1.41	1.41	1.50	1.55	1.46
500	AC	0.97	1.28	1.37	1.39	1.47	1.50	1.43
	WC	0.99	1.33	1.42	1.43	1.50	1.52	1.44
600	AC	0.99	1.29	1.39	1.39	1.47	1.51	1.44
	WC	1.02	1.33	1.43	1.51	1.51	1.55	1.49
700	AC	0.99	1.30	1.38	1.40	1.46	1.46	1.41
	WC	1.02	1.34	1.45	1.45	1.53	1.57	1.50
800	AC	0.97	1.28	1.34	1.29	1.41	1.43	1.37
	WC	1.21	1.56	1.68	1.66	1.83	1.85	1.76
900	AC	0.88	1.15	1.21	1.21	1.30	1.34	1.28
	WC	1.90	2.47	2.52	2.32	2.72	2.54	2.72
1000	AC	0.89	1.16	1.22	1.21	1.27	1.33	1.26
	WC	1.18	1.49	1.63	1.60	1.72	1.82	1.70

4.3.7. Ductility

In this study, the ductility of test specimens is defined as the percent elongation (El) observed at fracture of uniaxial tension test specimen [64]. Post-fire ductilities of un-notched and notched test specimens are provided in Table 4.10. The influence of high stress triaxiality and cooling methods on the ductility of ASTM A572 steels is quantified in terms of post-fire ductility residual factor, which is defined as the ratio of ductility of a test specimen that is cooled after exposure to elevated temperature (e.g. $El_{T,CN2}$) to the ductility of un-notched specimen (SPR) at room temperature ($El_{20,SPR}$). Post-fire ductility residual factors of un-notched and notched specimens corresponding to different target temperatures and cooling methods are presented in Figure 4.25(d) and Figure 4.32, respectively. Moreover, post-fire ductility residual factors are provided in Table 4.11. To determine the influence of cooling methods on post-fire ductility of ASTM A572 Gr. 50 steels, the ductility of un-notched AC and WC specimens are compared with the ductility of un-notched RT (SPR-RT) specimen. As evident from Table 4.10

and Figure 4.25(d), the ductilities of un-notched (SPR) specimens almost remain unchanged after exposure to temperatures up to 600 °C, regardless of the cooling method. Beyond 600 °C, un-notched AC specimens exhibited modest increase (up to 12%) in ductility. On the other hand, un-notched WC specimens experienced up to 61% reduction in ductility when water-cooled from temperatures beyond 600 °C, due to the formation of brittle martensite phase in ASTM A572 steel microstructure [71], as shown in Figure 4.30. To summarize, air-cooling leads to a modest increase in ductility whereas water-cooling from high temperatures lead to a major reduction in ductility of A572 Gr. 50 steels.

To evaluate the effect of high stress triaxiality on the ductility of ASTM A572 Gr. 50 steels, ductilities of notched RT specimens are compared with ductility of un-notched RT (SPR) specimen. As observed in Table 4.10 and Figure 4.32, the ductility of notched RT specimens decreased by up to 75% when compared to un-notched RT (SPR-RT) specimen. This major reduction in ductility of notched specimens can be attributed to the presence of high stress triaxiality in notched RT specimens [47, 48, 72]. To understand the influence of high stress triaxiality and cooling methods on post-fire ductility of ASTM A572 Gr. 50 steels, the ductilities of notched AC and notched WC specimens are compared with ductility of un-notched RT (SPR-RT) specimen. As observed from the results presented in Table 4.10 and Figure 4.32, notched AC specimens that are exposed to temperatures up to 1000 °C experienced up to 65% reduction in ductility when compared to the ductility of un-notched RT specimen, which is slightly less than the reduction in ductility observed in case of notched RT specimens. On the other hand, the ductility of notched WC decreased further with the increase in temperature. A maximum reduction of 89% is observed when notched specimens are water-cooled from 900 °C, due to the formation of brittle martensite phase in ASTM A572 steel microstructure and a slight increase in

stress triaxiality of WC specimens (as discussed in Section 4.3.3). To summarize, the combined influence of triaxiality and exposure to high temperatures is found to adversely influence the ductility of AC specimens and this can be mostly attributed to the presence of high triaxiality. On the other hand, the combined influence of stress triaxiality and water-cooling resulted in significant loss of ductility in WC specimens and this can be attributed to the formation of brittle martensite and a combined increase in stress triaxiality due to the notch and formation of martensite.

Table 4.10. Post-fire ductility of test specimens.

Temperature (°C)	Cooling method	Ductility (%)						
		SPR	CN1	CN2	CN3	UN1	VN1	VN2
20	-	45.06	21.67	12.26	11.10	13.19	13.66	14.19
500	AC	47.41	21.40	12.92	10.95	12.51	14.59	14.80
	WC	45.29	21.29	12.02	10.94	12.82	14.18	14.51
600	AC	43.10	22.27	13.98	12.15	14.37	14.15	14.23
	WC	43.61	21.78	13.65	10.69	13.91	13.85	9.53
700	AC	43.35	22.59	13.69	12.20	13.79	14.46	14.93
	WC	39.90	22.03	13.62	12.07	14.08	13.94	13.96
800	AC	45.57	20.20	13.71	12.79	14.66	14.80	14.88
	WC	25.53	14.32	9.28	7.77	9.40	7.28	9.46
900	AC	50.05	25.40	17.41	15.51	17.03	18.13	18.09
	WC	18.33	8.81	5.48	5.03	5.27	5.92	5.93
1000	AC	47.07	24.47	17.24	14.35	17.22	18.31	19.00
	WC	17.60	14.17	10.21	7.58	10.97	7.81	9.51

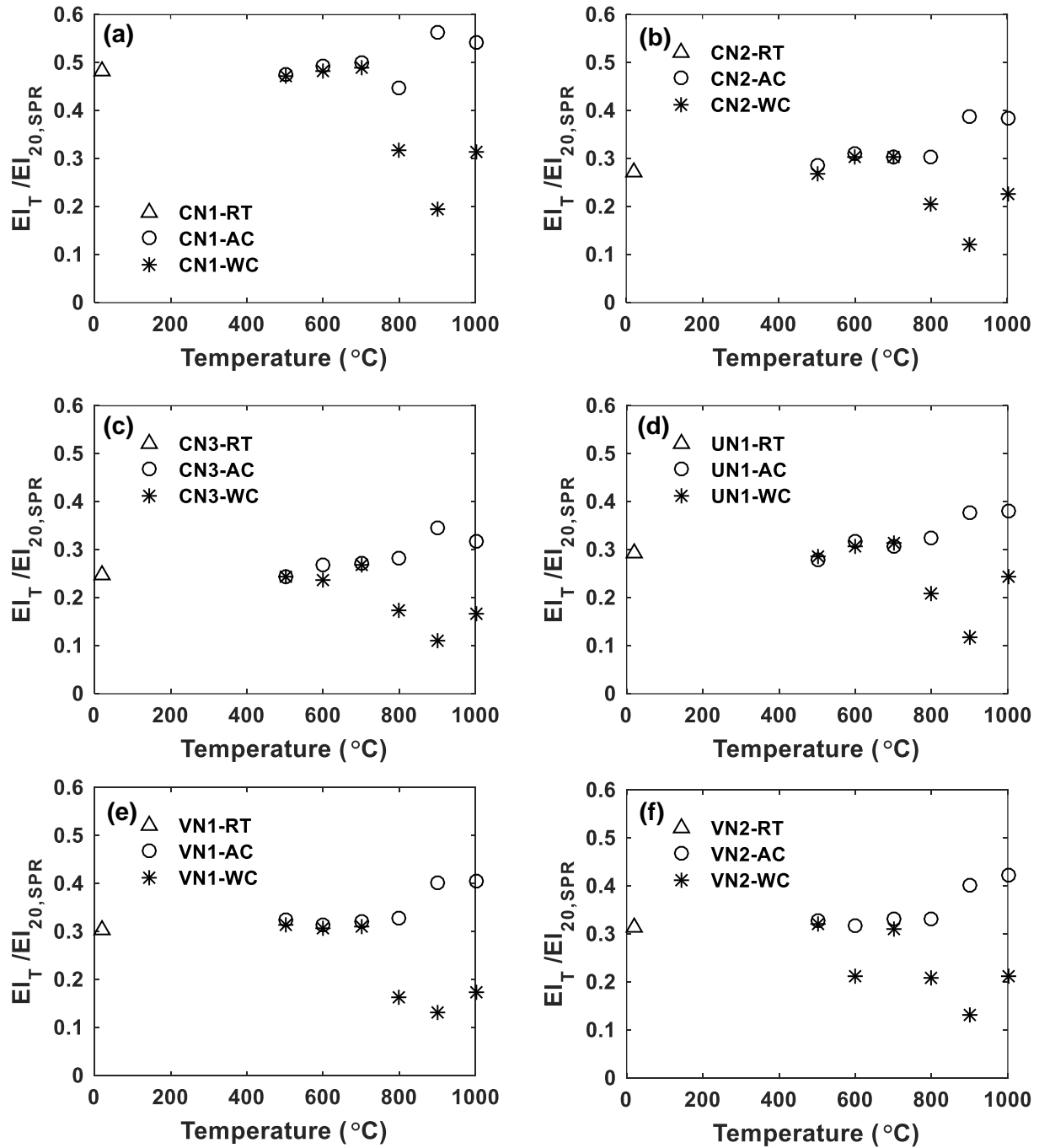


Figure 4.32. Ductility residual factors of post-fire test specimens: a) CN1, b) CN2, c) CN3, d) UN1, e) VN1, and f) VN2.

Table 4.11. Post-fire ductility residual factors of test specimens.

Temperature (°C)	Cooling method	Ductility residual factor (El_T/El_{20})						
		SPR	CN1	CN2	CN3	UN1	VN1	VN2
20	-	1.00	0.48	0.27	0.25	0.29	0.30	0.31
500	AC	1.05	0.47	0.29	0.24	0.28	0.32	0.33
	WC	1.01	0.47	0.27	0.24	0.28	0.31	0.32
600	AC	0.96	0.49	0.31	0.27	0.32	0.31	0.32
	WC	0.97	0.48	0.30	0.24	0.31	0.31	0.21
700	AC	0.96	0.50	0.30	0.27	0.31	0.32	0.33
	WC	0.89	0.49	0.30	0.27	0.31	0.31	0.31
800	AC	1.01	0.45	0.30	0.28	0.33	0.33	0.33
	WC	0.57	0.32	0.21	0.17	0.21	0.16	0.21
900	AC	1.11	0.56	0.39	0.34	0.38	0.40	0.40
	WC	0.41	0.20	0.12	0.11	0.12	0.13	0.13
1000	AC	1.04	0.54	0.38	0.32	0.38	0.41	0.42
	WC	0.39	0.31	0.23	0.17	0.24	0.17	0.21

4.3.8. Discussion on Residual Strength Factors for Structural Steels

In the post-fire investigations of structural steels, residual strength factors are commonly proposed which can be used to predict the post-fire residual strength of fire affected structural steels if the temperatures reached during fire exposure are known. Apart from experimental residual strength factors, simplified equations have also been proposed in various post-fire studies for evaluating the residual yield strength and ultimate tensile strength of steel after fire exposure. While various researchers have proposed different predictive models for determining residual strength of fire-affected steels, current design codes do not provide information on residual strength factors. When determining post-fire mechanical properties, British code (BS5950) suggests up to 10% strength reduction in mild structural steels that are exposed to temperatures beyond 600 °C and cooled naturally [73]. However, this reduction is not applicable for high strength low alloy steels or steels that are cooled using different cooling rates. The residual strength factors of ASTM A572 steels specimens that were previously discussed in

Section 4.3.5 and Section 4.3.6 are compared with the residual strength factors from predictive models that are proposed for hot-rolled structural steels in the literature. The predictive models are summarized in Table 4.12. Since the post-fire behavior of steel is also dependent on the chemical composition and steel grade type of as-received steel (such as mild steel, high strength low alloy steel, very high strength steel, and ultra high strength steels), only those predictive models are selected for comparison wherein the mechanical properties and chemical compositions of as-received steels are relatively similar to ASTM A572 steels. Existing predictive models for residual strength factors do not incorporate the influence of stress triaxiality and hence only the ASTM A572 residual strength factors obtained from un-notched specimens in this study are compared with the residual strength factors obtained from existing predictive models in the literature. All predictive models that are summarized in Table 4.12 provide residual strength factors for air-cooled steels whereas only a few of these models provide residual strength factors for water-cooled steels. The yield strength residual factors and ultimate tensile strength residual factors obtained in this study and from the existing predictive models are plotted in Figure 4.33 and Figure 4.34, respectively. As observed in these figures, the residual strength factors obtained in the study are within the post-fire residual factors limits that are predicted by other studies. It is clear from Figure 4.33 and Figure 4.34 that the residual strength factors remained relatively unaffected when structural steels are either air-cooled or water-cooled after exposure to 600 °C. Beyond 600 °C, high variation is observed in the yield strength residual factors and ultimate tensile strength residual factors of different air-cooled and water-cooled structural steels. This variation can be attributed to the difference in steel grade, the rolling directions in which steel specimens are extracted, the chemical compositions of as-received steels, and slight variation in cooling rates adopted in these studies. From the above discussion, it

can be inferred that the predictive models that are currently available in the literature can be used for predicting strength reduction or increase in post-fire steels. However, given the variation in the results, the predictive models should be used carefully when assessing the residual strength of fire-affected steel structures. While estimating residual mechanical properties of fire-affected structural steels, microstructural analysis should be conducted to identify the phases changes that the steel may have experienced and their subsequent effects on post-fire mechanical properties.

Table 4.12. Predictive models for strength residual strength factors for different structural steels.

Reference	Residual strength factor	
	Yield strength	Ultimate tensile strength
Aziz and Kodur 2016 [3]	AC: $20\text{ }^{\circ}\text{C} \leq T < 400\text{ }^{\circ}\text{C}$: $\frac{F_{y,T}}{F_{y,20}} = 1.0$	AC: $20\text{ }^{\circ}\text{C} \leq T < 400\text{ }^{\circ}\text{C}$: $\frac{F_{u,T}}{F_{u,20}} = 1.0$
	AC: $400\text{ }^{\circ}\text{C} \leq T \leq 1000\text{ }^{\circ}\text{C}$: $\frac{F_{y,T}}{F_{y,20}} = (10^{-8})T^3 - (2.12 \times 10^{-5})T^2 + (1.31 \times 10^{-2})T - 1.43$	AC: $400\text{ }^{\circ}\text{C} \leq T \leq 1000\text{ }^{\circ}\text{C}$: $\frac{F_{u,T}}{F_{u,20}} = (7.64 \times 10^{-9})T^3 - (1.68 \times 10^{-5})T^2 + (1.1 \times 10^{-2})T - 1.26$
	WC: $20\text{ }^{\circ}\text{C} \leq T \leq 1000\text{ }^{\circ}\text{C}$: $\frac{F_{y,T}}{F_{y,20}} = (5.94 \times 10^{-12})T^4 - (9.71 \times 10^{-9})T^3 + (4.04 \times 10^{-6})T^2 - (3.6 \times 10^{-4})T + 1.0$	WC: $20\text{ }^{\circ}\text{C} \leq T \leq 1000\text{ }^{\circ}\text{C}$: $\frac{F_{u,T}}{F_{u,20}} = 0.95$
Qiang et al. 2012 [4]	AC: $20\text{ }^{\circ}\text{C} \leq T < 1000\text{ }^{\circ}\text{C}$: $\frac{F_{y,T}}{F_{y,20}} = (-3.24 \times 10^{-10})T^3 + (4.98 \times 10^{-8})T^2 + (4.52 \times 10^{-5})T + 0.998$	AC: $20\text{ }^{\circ}\text{C} \leq T < 1000\text{ }^{\circ}\text{C}$: $\frac{F_{u,T}}{F_{u,20}} = (-2.79 \times 10^{-7})T^2 + (1.08 \times 10^{-4})T + 0.996$
Tao et al. 2013 [5]	AC: $T \leq 500\text{ }^{\circ}\text{C}$: $\frac{F_{y,T}}{F_{y,20}} = 1.0$	AC: $T \leq 500\text{ }^{\circ}\text{C}$: $\frac{F_{u,T}}{F_{u,20}} = 1.0$
	AC: $T > 500\text{ }^{\circ}\text{C}$: $\frac{F_{y,T}}{F_{y,20}} = 1 - 2.33 \times 10^{-4}(T - 500) - 3.88 \times 10^{-7}(T - 500)^2$	AC: $T > 500\text{ }^{\circ}\text{C}$: $\frac{F_{u,T}}{F_{u,20}} = 1 - 1.95 \times 10^{-4}(T - 500)$
Wang et al. 2015 [6]	AC: $20\text{ }^{\circ}\text{C} \leq T \leq 900\text{ }^{\circ}\text{C}$: $\frac{F_{y,T}}{F_{y,20}} = (-1.17 \times 10^{-9})T^3 + (5.54 \times 10^{-7})T^2 + (1.33 \times 10^{-4})T + 1.0$	AC: $20\text{ }^{\circ}\text{C} \leq T \leq 900\text{ }^{\circ}\text{C}$: $\frac{F_{u,T}}{F_{u,20}} = (-3.81 \times 10^{-10})T^3 - (6.36 \times 10^{-8})T^2 + (1.79 \times 10^{-4})T + 1.0$
	WC: $20\text{ }^{\circ}\text{C} \leq T \leq 900\text{ }^{\circ}\text{C}$: $\frac{F_{y,T}}{F_{y,20}} = (-1.73 \times 10^{-9})T^3 + (1.25 \times 10^{-6})T^2 - (8.05 \times 10^{-5})T + 1.0$	WC: $20\text{ }^{\circ}\text{C} \leq T \leq 900\text{ }^{\circ}\text{C}$: $\frac{F_{u,T}}{F_{u,20}} = (8.11 \times 10^{-10})T^3 - (7.03 \times 10^{-7})T^2 + (1.93 \times 10^{-4})T + 1.0$
Lu et al. 2016 [7]	AC: $20\text{ }^{\circ}\text{C} \leq T \leq 700\text{ }^{\circ}\text{C}$: $\frac{F_{y,T}}{F_{y,20}} = 1.0$	AC: $20\text{ }^{\circ}\text{C} \leq T \leq 1000\text{ }^{\circ}\text{C}$: $\frac{F_{u,T}}{F_{u,20}} = 0.999 + (1.59 \times 10^{-4})T - (2.89 \times 10^{-7})T^2$
	AC: $700\text{ }^{\circ}\text{C} < T \leq 1000\text{ }^{\circ}\text{C}$: $\frac{F_{y,T}}{F_{y,20}} = 1.6 - (8.88 \times 10^{-4})T$	WC: $20\text{ }^{\circ}\text{C} \leq T \leq 1000\text{ }^{\circ}\text{C}$: $\frac{F_{u,T}}{F_{u,20}} = 0.990 + (2.57 \times 10^{-4})T - (5.91 \times 10^{-7})T^2 + (3.16 \times 10^{-10})T^3$
	WC: $20\text{ }^{\circ}\text{C} \leq T \leq 600\text{ }^{\circ}\text{C}$: $\frac{F_{y,T}}{F_{y,20}} = 1.007 + (2.17 \times 10^{-5})T$	
	WC: $600\text{ }^{\circ}\text{C} < T \leq 1000\text{ }^{\circ}\text{C}$: $\frac{F_{y,T}}{F_{y,20}} = 1.313 - (4.75 \times 10^{-4})T$	
Li et al. 2017 [8]	AC: $20\text{ }^{\circ}\text{C} \leq T \leq 500\text{ }^{\circ}\text{C}$: $\frac{F_{y,T}}{F_{y,20}} = 1.0$	AC: For $20\text{ }^{\circ}\text{C} \leq T \leq 400\text{ }^{\circ}\text{C}$: $\frac{F_{u,T}}{F_{u,20}} = 1.0$
	AC: $500\text{ }^{\circ}\text{C} < T \leq 900\text{ }^{\circ}\text{C}$: $\frac{F_{y,T}}{F_{y,20}} = 2.42 - (3.687 \times 10^{-3})T + (1.693 \times 10^{-6})T^2$	AC: For $400\text{ }^{\circ}\text{C} < T \leq 900\text{ }^{\circ}\text{C}$: $\frac{F_{u,T}}{F_{u,20}} = 1.477 - (1.356 \times 10^{-3})T + (4.102 \times 10^{-7})T^2$
	WC: $20\text{ }^{\circ}\text{C} \leq T \leq 500\text{ }^{\circ}\text{C}$: $\frac{F_{y,T}}{F_{y,20}} = 1.0$	WC: $20\text{ }^{\circ}\text{C} \leq T \leq 500\text{ }^{\circ}\text{C}$: $\frac{F_{u,T}}{F_{u,20}} = 1.0$
	WC: $500\text{ }^{\circ}\text{C} < T \leq 900\text{ }^{\circ}\text{C}$: $\frac{F_{y,T}}{F_{y,20}} = -12.11 + (6.651 \times 10^{-2})T - (1.095 \times 10^{-4})T^2 + (5.78 \times 10^{-8})T^3$	WC: For $500\text{ }^{\circ}\text{C} < T \leq 900\text{ }^{\circ}\text{C}$: $\frac{F_{u,T}}{F_{u,20}} = 1.366 + (4.909 \times 10^{-3})T - (1.89 \times 10^{-5})T^2 + (1.524 \times 10^{-8})T^3$
Maraveas et al. 2017 [9]	AC: $T \leq 600\text{ }^{\circ}\text{C}$: $\frac{F_{y,T}}{F_{y,20}} = 1.0$	AC: $T \leq 600\text{ }^{\circ}\text{C}$: $\frac{F_{u,T}}{F_{u,20}} = 1.0$
	AC: $600\text{ }^{\circ}\text{C} < T < 800\text{ }^{\circ}\text{C}$: $\frac{F_{y,T}}{F_{y,20}} = 1.756 - T/800$	AC: $600\text{ }^{\circ}\text{C} < T < 800\text{ }^{\circ}\text{C}$: $\frac{F_{u,T}}{F_{u,20}} = 1.655 - T/920$
	AC: $T \geq 800\text{ }^{\circ}\text{C}$: $\frac{F_{y,T}}{F_{y,20}} = 0.748$	AC: $T \geq 800\text{ }^{\circ}\text{C}$: $\frac{F_{u,T}}{F_{y,20}} = 0.82$

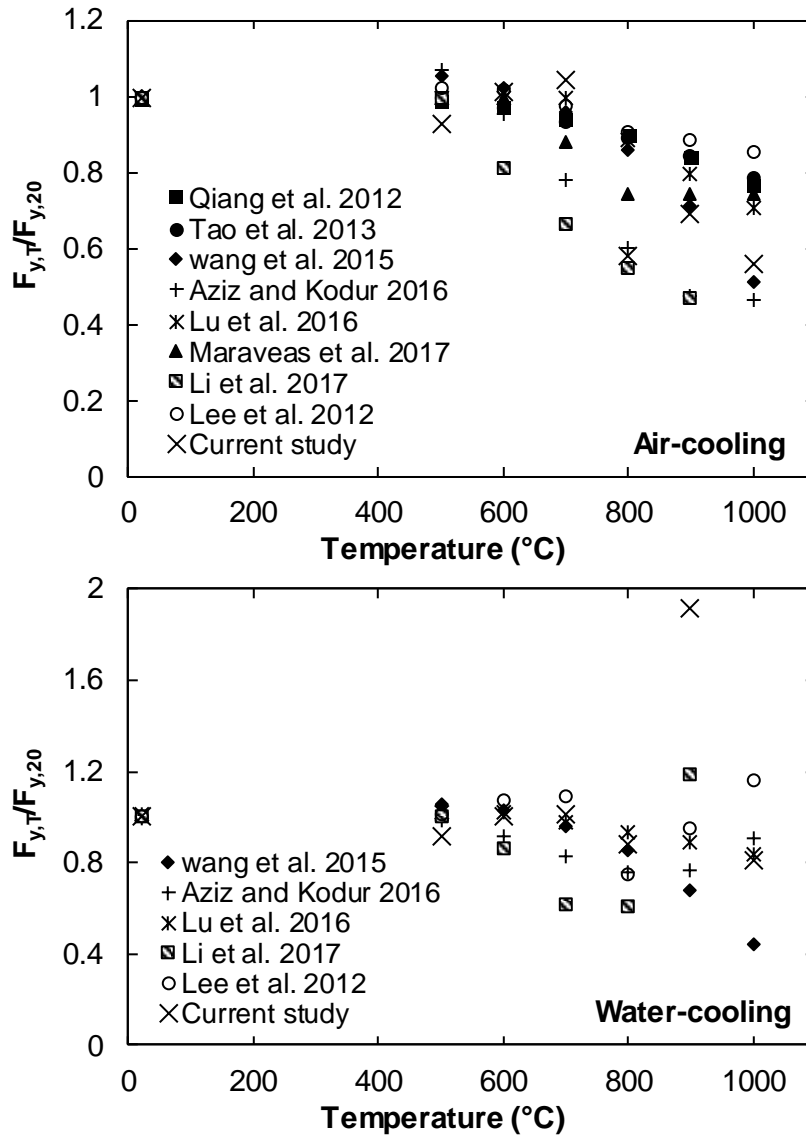


Figure 4.33. Comparison of yield strength residual factors of structural steels.

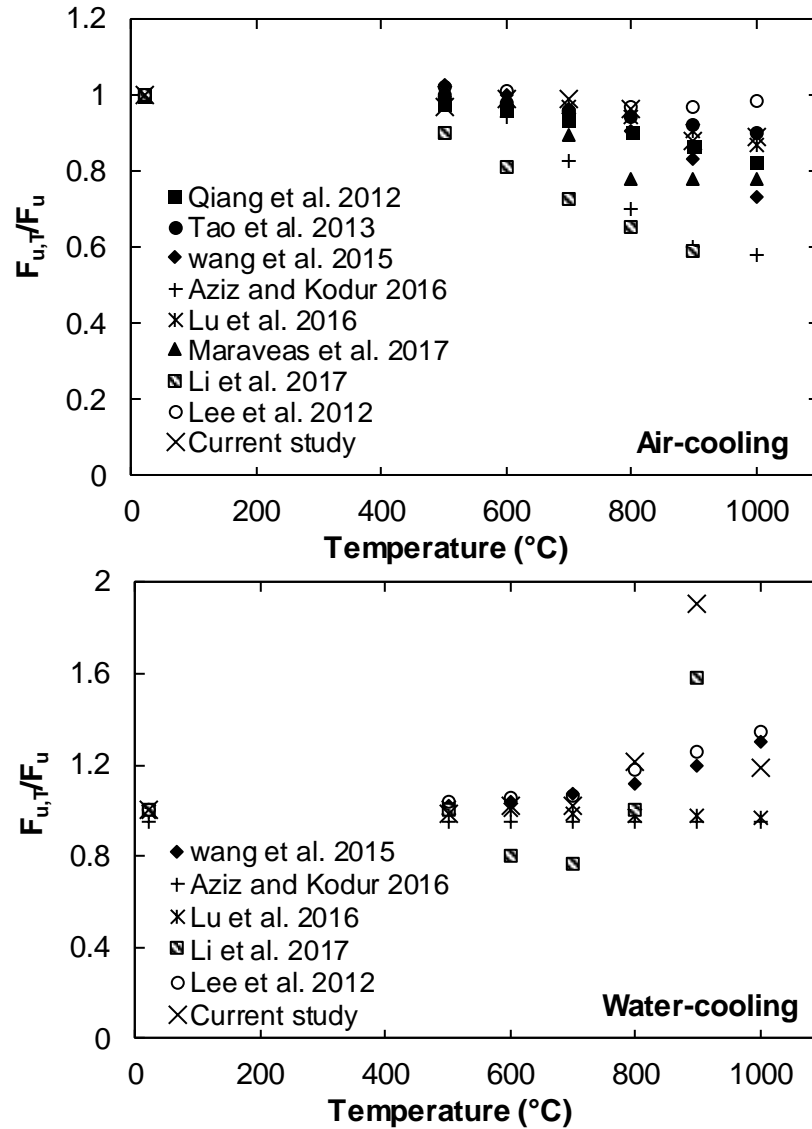


Figure 4.34. Comparison of ultimate tensile strength residual factors of structural steels.

4.4. Conclusions

Following are important conclusions drawn from this study:

1. In the absence of high stress triaxiality, post-fire mechanical properties of ASTM A572 Gr. 50 steels almost remained unaffected after exposure to temperatures up to 600 °C, irrespective of the cooling method.
2. ASTM A572 Gr. 50 steels do not exhibit a considerable change in elastic modulus when air-cooled or water-cooled from temperatures up to 1000 °C.

3. Air-cooling from temperatures beyond 700 °C lead to a decrease in yield strength (up to 44%) and ultimate tensile strength (up to 12%) of un-notched specimens.
4. Water-cooling from temperatures beyond 700 °C resulted in up to 19% decrease in yield strength except for 900-WC specimen, which exhibited a 91% increase in yield strength due to the formation of martensite microstructure. On the other hand, water-cooling from temperatures beyond 700 °C resulted in up to 90% increase in ultimate tensile strength of ASTM A572 Gr. 50 steels.
5. The combined effect of high stress triaxiality and water-cooling from temperatures beyond 700 °C resulted in a significant increase in yield strength and ultimate tensile strength of notched specimens. The yield strength and ultimate strength of notched WC specimens are observed to increase by up to 158% and 172%, respectively when compared to un-notched RT specimen.
6. Air-cooling resulted in a reduction of yield strength (up to 27%) in some notched AC specimens that are air-cooled from temperatures beyond 700 °C when compared to un-notched RT specimen. However, the ultimate tensile strength and ductility of notched AC specimens that are exposed to temperatures in excess of 700 °C did not exhibit considerable reduction and remained higher than the un-notched RT specimen.
7. Air-cooling from temperatures beyond 700 °C resulted in a modest increase (12%) in ductility of un-notched AC specimens. On the other hand, water-cooling resulted in a major decrease of 61% in ductility of un-notched WC specimen due to the formation of brittle martensite.

8. Presence of high stress triaxiality and water-cooling resulted in significant decrease of up to 89% in ductility of notched WC specimens when compared to un-notched RT specimen.

Existing post-fire investigations and current post-fire predictive models do not incorporate the influence of stress triaxiality on post-fire mechanical properties of structural steels. However, high stress triaxiality is observed to have significant influence on post-fire yield strength, ultimate tensile strength and ductility of ASTM A572 steels, as discussed in detail in Sections 4.3.5, 4.3.6 and 4.3.7. Hence, in case of structural members wherein stress triaxiality may arise due to the presence of corrosion pits, welds, sharp corners and other geometric discontinuities, the influence of stress triaxiality should be considered when evaluating residual mechanical properties. While the existing predictive models give conservative estimate of residual yield strength and ultimate tensile strength, by not accounting the increase in strength due to stress triaxiality, it is important to note that the high stress triaxiality results in significant loss in ductility in both air-cooled and water-cooled steels. Therefore, the influence of high stress triaxiality should be considered when evaluating ductility of fire-affected steels considering the fact that post-fire steels lose 65% and 89% ductility in air-cooled and water-cooled scenarios, respectively, under high stress triaxialities.

4.5. References

- [1] M. Garlock, I. Paya-Zaforteza, V. Kodur, L. Gu, Fire hazard in bridges: Review, assessment and repair strategies, *Engineering Structures*, 35 (2012) 89-98.
- [2] V. Kodur, L. Gu, M. Garlock, Review and assessment of fire hazard in bridges, *Transportation Research Record: Journal of the Transportation Research Board*, (2010) 23-29.

- [3] G. Peris-Sayol, I. Paya-Zaforteza, S. Balasch-Parisi, J. Alós-Moya, Detailed Analysis of the Causes of Bridge Fires and Their Associated Damage Levels, *Journal of Performance of Constructed Facilities*, 31 (2017) 04016108.
- [4] V. Kodur, L. Gu, M.E.M. Garlock, Review and Assessment of Fire Hazard in Bridges, *Transportation Research Record*, 2172 (2010) 23-29.
- [5] Fire Protection of Steel Bridges and the Case of the MacArthur Maze Fire Collapse, in: TCLEE 2009.
- [6] I. Payá-Zaforteza, M.E.M. Garlock, A numerical investigation on the fire response of a steel girder bridge, *Journal of Constructional Steel Research*, 75 (2012) 93-103.
- [7] W.J. Wright, Steel bridge design handbook: Bridge steels and their mechanical properties, in, Federal Highway Administration, Report # FHWA-IF-12-052 - Vol. 1, 2012.
- [8] ASTM International, ASTM A709/A709M Standard Specification for Structural Steel for Bridges, in, ASTM International, West Conshohocken, PA, 2017.
- [9] ASTM International, Standard Specification for High-Strength Low-Alloy Columbium-Vanadium Structural Steel, in, ASTM International, West Conshohocken, PA, 2015.
- [10] B. Jansen, Atlanta bridge collapse shows how fire defeats concrete, steel, in: USA Today, March 31, 2017.
- [11] L. Blest, Fire continues to burn on Enola Low Grade Trail bridge; Cause still under investigation, in: LancasterOnline, April 13, 2018.
- [12] E.M. Aziz, Response of fire exposed steel bridge girders, in, Michigan State University, Ann Arbor, 2015, pp. 321.

- [13] V. Kodur, M. Dwaikat, R. Fike, High-Temperature Properties of Steel for Fire Resistance Modeling of Structures, *Journal of Materials in Civil Engineering*, 22 (2010) 423-434.
- [14] V. Kodur, E. Aziz, M. Dwaikat, Evaluating Fire Resistance of Steel Girders in Bridges, *Journal of Bridge Engineering*, 18 (2013) 633-643.
- [15] G. Hu, M.A. Morovat, J. Lee, E. Schell, Elevated Temperature Properties of ASTM A992 Steel, in: *Structures Congress 2009*, American Society of Civil Engineers, 2009, pp. 1067-1076.
- [16] W. Cai, M.A. Morovat, M.D. Engelhardt, True stress-strain curves for ASTM A992 steel for fracture simulation at elevated temperatures, *Journal of Constructional Steel Research*, 139 (2017) 272-279.
- [17] J. Lee, M.A. Morovat, G. Hu, M.D. Engelhardt, E.M. Taleff, Experimental investigation of mechanical properties of ASTM A992 steel at elevated temperatures, *Engineering Journal-American Institute of Steel Construction*, 50 (2013) 249-272.
- [18] M.A. Morovat, A.H.E. Ghor, E.G. Hantouche, Time-Dependent Response of Flush Endplate Connections to Fire Temperatures, *Journal of Structural Engineering*, 144 (2018) 04018023.
- [19] M. Memari, H. Mahmoud, B. Ellingwood, Stability of Steel Columns Subjected to Earthquake and Fire Loads, *Journal of Structural Engineering*, 144 (2018) 04017173.
- [20] J. Outinen, P. Mäkeläinen, Mechanical properties of structural steel at elevated temperatures and after cooling down, *Fire and materials*, 28 (2004) 237-251.
- [21] S. Chiew, M. Zhao, C. Lee, Mechanical properties of heat-treated high strength steel under fire/post-fire conditions, *Journal of Constructional Steel Research*, 98 (2014) 12-19.

- [22] American Society of Civil Engineers (ASCE), Structural Fire Protection, ASCE committee on fire protection, Manual No. 78, (1992).
- [23] European Committee for Standardization, EN 1993-1-2, Eurocode 3: Design of Steel Structures-Part 1-2: General rules structural fire design, in, Bruxelles, Bélgica, 2005.
- [24] Standards Australia, AS4100: Steel structures, Standards Australia, NSW, Australia, (1998).
- [25] British Standards Institute (BSI), Structural use of steelwork in building, Part 8: Code of practice for fire resistant design, British Standard Institution, (1990).
- [26] American Institute of Steel Construction (AISC), AISC 360-05-specification for structural steel buildings, ANSI/AISC, Chicago, (2005).
- [27] D. Glassman Jonathan, E.M. Garlock Maria, Post-Fire Strength Assessment of Steel Bridges Based on Residual Out-of-Plane Web Deformations, Structures Congress 2014.
- [28] R.H. Tide, Integrity of structural steel after exposure to fire, Engineering Journal-American Institute of Steel Construction, 35 (1998) 26-38.
- [29] J. Lu, H. Liu, Z. Chen, X. Liao, Experimental investigation into the post-fire mechanical properties of hot-rolled and cold-formed steels, Journal of Constructional Steel Research, 121 (2016) 291-310.
- [30] H.U. Sajid, R. Kiran, Influence of stress concentration and cooling methods on post-fire mechanical behavior of ASTM A36 steels, Construction and Building Materials, 186 (2018) 920-945.
- [31] C.I. Smith, B.R. Kirby, D.G. Lapwood, K.J. Cole, A.P. Cunningham, R.R. Preston, The reinstatement of fire damaged steel framed structures, Fire Safety Journal, 4 (1981) 21-62.

- [32] W. Wang, T. Liu, J. Liu, Experimental study on post-fire mechanical properties of high strength Q460 steel, *Journal of Constructional Steel Research*, 114 (2015) 100-109.
- [33] G.-Q. Li, H. Lyu, C. Zhang, Post-fire mechanical properties of high strength Q690 structural steel, *Journal of Constructional Steel Research*, 132 (2017) 108-116.
- [34] X. Qiang, F.S. Bijlaard, H. Kolstein, Post-fire mechanical properties of high strength structural steels S460 and S690, *Engineering Structures*, 35 (2012) 1-10.
- [35] J. Lee, M.D. Engelhardt, E.M. Taleff, Mechanical Properties of ASTM A 992 Steel After Fire, *Engineering Journal (Chicago)*, 49 (2012) 33-44.
- [36] E.M. Aziz, V.K. Kodur, Effect of temperature and cooling regime on mechanical properties of high-strength low-alloy steel, *Fire and Materials*, 40 (2016) 926-939.
- [37] Z. Chen, J. Lu, H. Liu, X. Liao, Experimental study on the post-fire mechanical properties of high-strength steel tie rods, *Journal of Constructional Steel Research*, 121 (2016) 311-329.
- [38] F. Azhari, A. Heidarpour, X.-L. Zhao, C.R. Hutchinson, Mechanical properties of ultra-high strength (Grade 1200) steel tubes under cooling phase of a fire: an experimental investigation, *Construction and Building Materials*, 93 (2015) 841-850.
- [39] X. Qiang, F.S. Bijlaard, H. Kolstein, Post-fire performance of very high strength steel S960, *Journal of Constructional Steel Research*, 80 (2013) 235-242.
- [40] J. Lu, H. Liu, Z. Chen, L. Bisby, Experimental investigation of the residual mechanical properties of cast steels after exposure to elevated temperature, *Construction and Building Materials*, 143 (2017) 259-271.
- [41] S. Gunalan, M. Mahendran, Experimental investigation of post-fire mechanical properties of cold-formed steels, *Thin-Walled Structures*, 84 (2014) 241-254.

- [42] Z. Tao, X.-Q. Wang, M.K. Hassan, T.-Y. Song, L.-A. Xie, Behaviour of three types of stainless steel after exposure to elevated temperatures, *Journal of Constructional Steel Research*, (2018).
- [43] R. Wang, R. Ajit Sheno, A. Sobey, Ultimate strength assessment of plated steel structures with random pitting corrosion damage, *Journal of Constructional Steel Research*, 143 (2018) 331-342.
- [44] S. Xu, H. Wang, A. Li, Y. Wang, L. Su, Effects of corrosion on surface characterization and mechanical properties of butt-welded joints, *Journal of Constructional Steel Research*, 126 (2016) 50-62.
- [45] H.U. Sajid, R. Kiran, Influence of high stress triaxiality on mechanical strength of ASTM A36, ASTM A572 and ASTM A992 steels, *Construction and Building Materials*, 176 (2018) 129-134.
- [46] R. Kiran, K. Khandelwal, A micromechanical model for ductile fracture prediction in ASTM A992 steels, *Engineering Fracture Mechanics*, 102 (2013) 101-117.
- [47] R. Kiran, K. Khandelwal, Experimental studies and models for ductile fracture in ASTM A992 steels at high triaxiality, *Journal of Structural Engineering*, 140 (2013) 04013044.
- [48] R. Kiran, K. Khandelwal, A triaxiality and Lode parameter dependent ductile fracture criterion, *Engineering Fracture Mechanics*, 128 (2014) 121-138.
- [49] ASTM International, ASTM E83 Standard Practice for Verification and Classification of Extensometer Systems, in, West Conshohocken, PA, 2016.
- [50] J.F. Bell, The Portevin-le Chatelier Effect, in: J.F. Bell (Ed.) *The Physics of Large Deformation of Crystalline Solids*, Springer Berlin Heidelberg, Berlin, Heidelberg, 1968, pp. 174-193.

- [51] G. Krauss, Martensite in steel: strength and structure, *Materials Science and Engineering: A*, 273-275 (1999) 40-57.
- [52] A. Yilmaz, The Portevin–Le Chatelier effect: a review of experimental findings, *Science and Technology of Advanced Materials*, 12 (2011) 063001.
- [53] M. Abbadi, P. Hähner, A. Zeghloul, On the characteristics of Portevin–Le Chatelier bands in aluminum alloy 5182 under stress-controlled and strain-controlled tensile testing, *Materials Science and Engineering: A*, 337 (2002) 194-201.
- [54] A. van den Beukel, Theory of the effect of dynamic strain aging on mechanical properties, *physica status solidi (a)*, 30 (1975) 197--206.
- [55] Dassault-Systèmes, ABAQUS/standard analysis user's manual, Dassault Systèmes Simulia, Providence, RI., 2016.
- [56] R. Kiran, K. Khandelwal, A coupled microvoid elongation and dilation based ductile fracture model for structural steels, *Engineering Fracture Mechanics*, 145 (2015) 15-42.
- [57] K. Poh, Stress-strain-temperature relationship for structural steel, *Journal of materials in civil engineering*, 13 (2001) 371-379.
- [58] J. Lee, M.D. Engelhardt, B.J. Choi, Constitutive model for ASTM A992 steel at elevated temperature, *International Journal of Steel Structures*, 15 (2015) 733-741.
- [59] W.E. Luecke, J.D. McColskey, C.N. McCowan, S.W. Banovic, R.J. Fields, T. Foecke, T.A. Siewert, Mechanical properties of structural steels, Federal Building and Fire Safety Investigation of the World Trade Center Disaster, National institute of Standards and Technology, (2005).
- [60] M. Seif, L. Choe, J. Gross, W. Luecke, J. Main, D. McColskey, F. Sadek, J. Weigand, C. Zhang, Temperature-dependent material modeling for structural steels: formulation and

- application, US Department of Commerce, National Institute of Standards and Technology, 2016.
- [61] Z. Tao, X.-Q. Wang, B. Uy, Stress-Strain Curves of Structural and Reinforcing Steels after Exposure to Elevated Temperatures, *Journal of Materials in Civil Engineering*, 25 (2013) 1306-1316.
- [62] J.W. Hancock, A.C. Mackenzie, On the mechanisms of ductile failure in high-strength steels subjected to multi-axial stress-states, *Journal of the Mechanics and Physics of Solids*, 24 (1976) 147-160.
- [63] W. Li, F. Liao, T. Zhou, H. Askes, Ductile fracture of Q460 steel: Effects of stress triaxiality and Lode angle, *Journal of Constructional Steel Research*, 123 (2016) 1-17.
- [64] D.R. Askeland, P.P. Fulay, W.J. Wright, *The Science and Engineering of Materials*, SI Edition, CL-Engineering, 2011.
- [65] K.K. Chawla, M. Meyers, *Mechanical behavior of materials*, Prentice Hall, 1999.
- [66] ASTM International, ASTM E111-17 Standard Test Method for Young's Modulus, Tangent Modulus, and Chord Modulus, in, ASTM International, West Conshohocken, PA, 2017.
- [67] T. Pan, X.-y. Chai, J.-g. Wang, H. Su, C.-f. Yang, Precipitation Behavior of V-N Microalloyed Steels during Normalizing, *Journal of Iron and Steel Research, International*, 22 (2015) 1037-1042.
- [68] R.C. Cochrane, 6 - Phase transformations in microalloyed high strength low alloy (HSLA) steels, in: E. Pereloma, D.V. Edmonds (Eds.) *Phase Transformations in Steels*, Woodhead Publishing, 2012, pp. 153-212.

- [69] J. Baird, R. Preston, Processing and properties of low carbon steel, Mechanical Working of Steel I, Metallurgical Society of AIME, New York, (1973) 1-46.
- [70] G.F. Vander Voort, ASM Handbook Volume 9: Metallography and microstructures, ASM International, Materials Park, OH, 2004.
- [71] W.D. Callister, D.G. Rethwisch, Materials Science and Engineering: An Introduction, Wiley, 2010.
- [72] A.M. Agogino, Notch effects, stress state, and ductility, Journal of Engineering Materials and Technology, 100 (1978) 348-355.
- [73] R. Lawson, G. Newman, Fire Resistant Design of Steel Structures: A Handbook to BS 5950, Steel Construction Institute, 1990.
- [74] F.-x. Ding, Z.-w. Yu, H.-l. Wen, Experimental research on mechanical properties of Q235 steel after high temperature treatment, Journal of building materials, 2 (2006) 023.
- [75] I.-R. Choi, K.-S. Chung, Residual strength of structural steels: SN400, SM520 AND SM570, Applications of Structural Fire Engineering, (2016).
- [76] F. Azhari, A. Heidarpour, X.-L. Zhao, C.R. Hutchinson, Post-fire mechanical response of ultra-high strength (Grade 1200) steel under high temperatures: Linking thermal stability and microstructure, Thin-Walled Structures, 119 (2017) 114-125.
- [77] F. Azhari, A.-A.H. Apon, A. Heidarpour, X.-L. Zhao, C.R. Hutchinson, Mechanical response of ultra-high strength (Grade 1200) steel under extreme cooling conditions, Construction and Building Materials, 175 (2018) 790-803.
- [78] C. Maraveas, Z. Fasoulakis, K.D. Tsavdaridis, Post-fire assessment and reinstatement of steel structures, Journal of structural fire engineering, 8 (2017) 181-201.

5. MICROSTRUCTURE-MECHANICAL PROPERTY RELATIONSHIPS FOR POST-FIRE STRUCTURAL STEELS⁴

This chapter discusses the post-fire microstructure behavior and microstructure-mechanical property relationships for ASTM A36, ASTM A572, and ASTM A992 structural steels.. The contents of this chapter have been published in Sajid, H.U., Naik, D.L. and Kiran, R., 2020. Microstructure–Mechanical Property Relationships for Post-Fire Structural Steels. *Journal of Materials in Civil Engineering*, 32(6), p.04020133.

5.1. Introduction

Post-fire mechanical properties refer to the macroscopic mechanical properties of a material that are determined after their exposure to fire accidents. Owing to the importance of these properties in evaluating the performance of steel structures after the fire, extensive research has been carried out on structural steels (e.g. ASTM A36 etc.) that are used in the United States, European and Chinese construction industry [1-18]. As a result of these investigations, it has become possible to conveniently predict the mechanical properties of structural steels that are subjected to fire accidents as a function of elevated temperature. However, the temperatures developed during a fire accident are seldom known. Therefore, the post-fire mechanical properties predicted as a function of temperature may be inaccurate if the temperatures estimated are not correct. To overcome this limitation, a microstructural approach is developed in this study. This approach considers the microstructural characteristics of structural steel instead of temperature to predict the post-fire mechanical properties and does not require prior knowledge of temperature experienced by steel in fire accidents. The rationale behind this approach is based

⁴ This chapter was co-authored by H.U. Sajid, D.L. Naik, and R. Kiran. H.U. Sajid had the primary responsibility of preparing the specimens, conducting all tests, and drafting this chapter. R. Kiran supervised the research and revised this chapter.

on the fact that the structural steels undergo microstructural changes when exposed to high temperatures which consequently alters their mechanical properties. These microstructural changes primarily include the evolution of different metallurgical phases, their volume fractions, and altered grain sizes. While metallurgical phase refers to a physically homogeneous state of matter consisting of certain chemical composition and a distinct type of atomic bonding and arrangement of elements, grain size refers to the linear dimensions of the grain, in which the atomic arrangement is nearly identical [19]. In this study, the microstructure of structural steel is characterized by quantifying the volume fraction of each phase and determining the average grain/colony size of each phase in the steel microstructure.

Carbon content, the presence of various alloying elements, and different heat treatment methods during manufacturing, process and operation period are the major factors that govern the above mentioned microstructural features in structural steel. In this study following three structural steels – ASTM A36 [20], ASTM A572 [21] and ASTM A992 [22] are considered and their microstructural changes as a function of elevated temperature to which steels are exposed are investigated. Details of the chemical composition of these three structural steels are provided in Table 5.1. These structural steels are also referred to as low carbon steels as carbon content in them are generally reported to vary from 0.05 to 0.2% by weight. In general, the carbon content in steels intended for structural applications is restricted to 0.30% [23]. Apart from carbon content, manganese and silicon are the other two alloying elements that are commonly found in all three structural steels. However, in ASTM A572 and ASTM A992 structural steels (also referred to as high strength low alloy (HSLA) steels [24, 25]), additional alloying elements such as nickel, molybdenum, vanadium, titanium, aluminum, and niobium are found in small quantities (typically less 0.1%). These chemical compositions of structural steels along with

different types of heat treatments (heating to high temperature and subsequent cooling) result in the change of microstructure features like phase volume and grain sizes and consequently alters the macroscopic mechanical properties of structural steels. To interpret the metallurgical phases in the microstructure, iron-iron carbide ($Fe-Fe_3C$) phase diagrams are used [23, 26]. This diagram can aid in identifying the metallurgical phases at a given temperature and carbon content of steel. The $Fe-Fe_3C$ constitutional phase diagram is a result of extensive metallurgical analyses of different types of steels that was carried out over decades. Adapting the $Fe-Fe_3C$ constitutional phase diagram two distinct metallurgical phases are identified in the above mentioned structural steels: ferrite (also referred to as $\alpha-Fe$) and pearlite. Ferrite is a single-phase constituent which does not contain carbides or contains only traces of carbide in solid solution and has a body-centered cubic (bcc) crystal structure, as illustrated in Figure 5.1(a) [26]. Ferrite essentially constitutes the major portion of as-received structural steel microstructure at room temperature (RT). Pearlite is a two-phased micro constituent that has a lamellar form and consists of alternating layers of ferrite phase and cementite ($Fe-Fe_3C$) phase. Unlike ferrite, cementite is harder constituent of steel microstructure and has an orthorhombic crystal structure (see Figure 5.1(b)) [27, 28]. Hence, the presence of cementite makes pearlite hard and strong compared to ferrite phase.

Table 5.1. Chemical composition of ASTM A36, A572, and A992 structural steels.

Chemical composition (%)	ASTM A36	ASTM A572 Gr. 50	ASTM A992
Carbon (C)	0.15	0.05	0.10
Manganese (Mn)	0.69	1.34	0.93
Phosphorous (P)	0.018	0.011	0.016
Sulphur (S)	0.004	0.004	0.044
Silicon (Si)	0.18	0.15	0.19
Copper (Cu)	0.24	0.28	0.25
Chromium (Cr)	0.15	0.19	0.14
Nickle (Ni)	0.088	0.13	0.09
Molybdenum (Mo)	0.0195	0.04	0.020
Vanadium (V)	0.0048	0.083	0.001
Titanium (Ti)	0.0012	0.001	—
Niobium (Nb)	0.0024	0.003	0.021
Iron (Fe)	98.4521	97.718	98.198

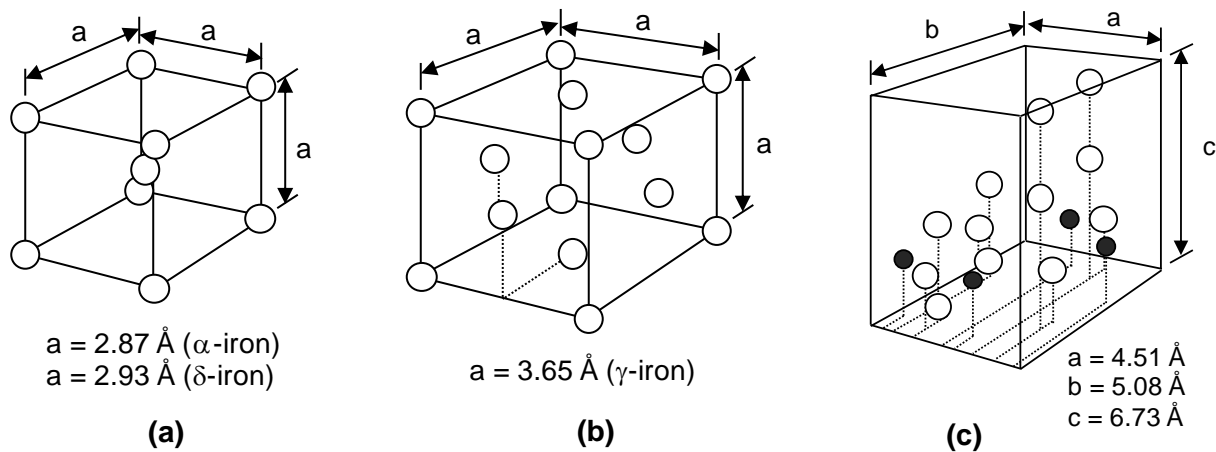


Figure 5.1. The crystal structures of (a) ferrite (body-centered cubic), (b) austenite (face-centered cubic, and (c) cementite (orthorhombic). Adapted from (Vander Voort 2004).

Although the metallurgical phases for these structural steels can be interpreted from the constitutional diagram, quantification of the grain sizes and their relationship with macroscopic mechanical properties for the above mentioned structural steels is not available in the literature. Therefore, the current study aims to quantify the microstructural changes that structural steels undergo after being exposed to fire accidents and develop a relationship between the microstructural parameters and post-fire macroscopic mechanical properties of structural steels. The microstructure in this study is quantified by determining the volume fraction of each

microstructural constituent (ferrite and pearlite) present in the steel microstructure and evaluating ferrite grain size and pearlite colony size. The details of test specimens, heating and cooling process, tensile testing and microstructural analysis are provided in Section 5.2. The microstructural analysis, tensile test results and the multi-linear regression relationships developed in this study are discussed in Section 5.3. In the end, the conclusions obtained from this study and their potential application in forensic investigations of fire-affected steel structures are discussed in Section 5.4.

5.2. Experimental Procedure

5.2.1. Test Specimens

In this study, post-fire microstructure-mechanical property relationships are investigated for three different structural steels: ASTM A36, ASTM A572 Gr. 50 and ASTM A992 steels. The chemical composition of these structural steels (as specified by the manufacturer) is summarized in Table 5.1. Test specimens for uniaxial tension tests are prepared in accordance with ASTM E8. Each tensile test specimen has a 50 mm reduced section length and reduced cross-section diameter of 10 mm, as shown in Figure 5.2. ASTM A36 steel specimens are machined from a 19-mm bar stock steel. ASTM A572 steel specimens are cut from ASTM A572 Gr. 50 steel sheets whereas ASTM A992 specimens were extracted from a wide flange beam. The test specimens are subjected to target elevated temperatures of 500 °C, 600 °C, 700 °C, 800 °C, 900 °C and 1000 °C. Temperatures below 500 °C are not explored in this study as previous research conducted on structural steels reported that mechanical properties of structural steels remain almost unaffected when steels are air-cooled from temperatures up to 500 °C [2, 4, 14]. The uniaxial test specimens are heated to target temperatures inside an electric furnace at an average heating rate of 10 °C/min. The specimens are left at the target temperatures for a period

of 1 hour to ensure uniform temperature distribution across the specimens. The heated test specimens are subsequently removed from the furnace and are left to air-cool in an open tray. The air-cooled specimens are then subjected to uniaxial tension tests. All specimens are tested using a servo-hydraulic MTS 798 machine at a displacement rate of 0.02 mm/sec. An epsilon contact extensometer is used to measure the extension within the 25-mm gauge section of the uniaxial tension test specimen, as shown in Figure 5.2. In total, 24 tension tests are conducted herein, which include 18 air-cooled tests (1 test for each steel type for each temperature condition) and 6 room temperature tests (two tests for each steel type at room temperature). Variation in mechanical properties is observed when samples are cut from different batches or along different directions (rolling or transverse) from the same batch of steel plates or I-beams [29]. Near perfect repeatability of mechanical properties is observed in specimens cut from the same batch of plates or I-beams along a certain direction [30]. Hence, only one test per steel for a given elevated temperature is conducted in case of air-cooled specimens.

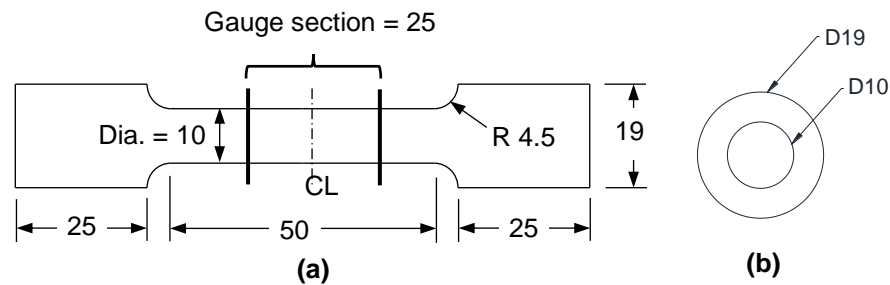


Figure 5.2. Geometric details of a typical cylindrical test specimen's (a) gauge section, and (b) cross-section. (all dimensions are in mm.).

5.2.2. Characterization of Microstructure of Post-fire Test Specimens

The microstructural parameters like volume fractions of ferrite and pearlite, ferrite grain size and pearlite colony size of post-fire steels are characterized from the metallographic specimens that are prepared using standard metallography techniques [31]. Disc-shaped specimens are cut from air-cooled specimens and are mounted in epoxy resin. These specimens

are then grinded and polished using experimental protocols specified in ASM metallography handbook [31]. All specimens are first grinded using coarser and finer Silicon Carbide (SiC) papers in the following grit size sequence: 60, 120, 400, 800 and 1200. These specimens are then further polished using 6 microns, 3 microns, 0.5 micron, and 0.03 micron alumina suspension. Light Microscopy, Scanning Electron Microscopy, Auger Electron Spectroscopy, Transmission Electron Microscopy, Electron Backscatter Diffraction, and Atom Probe Tomography are among popular techniques that are currently in use to characterize the composition of phases and grain sizes that include [23]. In this study, Light Microscopy is adapted to determine the volume fractions of ferrite and pearlite, ferrite grain size and pearlite colony size in the steel microstructure. To reveal the microstructure of post-fire steels, polished metallographic steel specimens are etched using 2% Nital solution, which is a commonly used etchant for low-carbon steels. Using an optical microscope, 8 micrographs are acquired from various locations of the etched metallographic specimen (periphery and central portions), as shown in Figure 5.3. These micrographs are used to evaluate the volume fractions of ferrite and pearlite, ferrite grain size and pearlite colony size in the steel microstructure. The phases themselves are identified indirectly using reference Iron-Iron Carbide ($Fe-Fe_3C$) constitutional diagrams, as shown in Figure 5.4. To quantify the volume fractions and grain sizes, micrographs obtained for each test specimen are processed using MIP Cloud software, which uses pixel intensity approach to determine the volume fraction of phases and these results are cross-verified by employing machine learning-based texture recognition algorithms co-developed by second and third authors of this manuscript [32]. The average grain size in each phase is calculated in accordance with ASTM E112 [33].

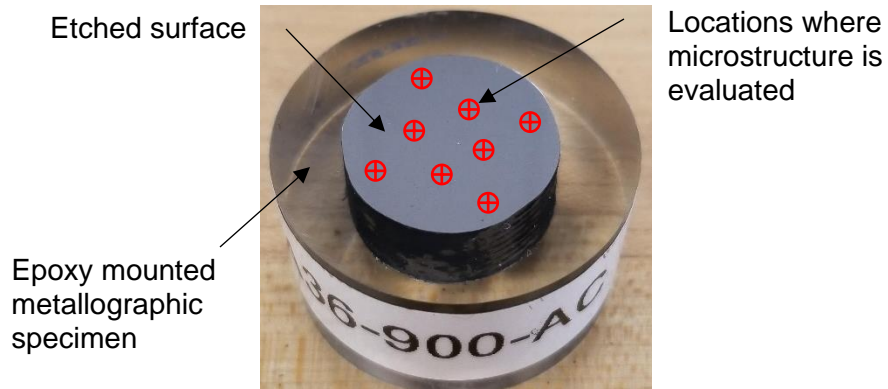


Figure 5.3. Typical epoxy mounted metallographic specimen with locations where micrographs are extracted for microstructural analysis.

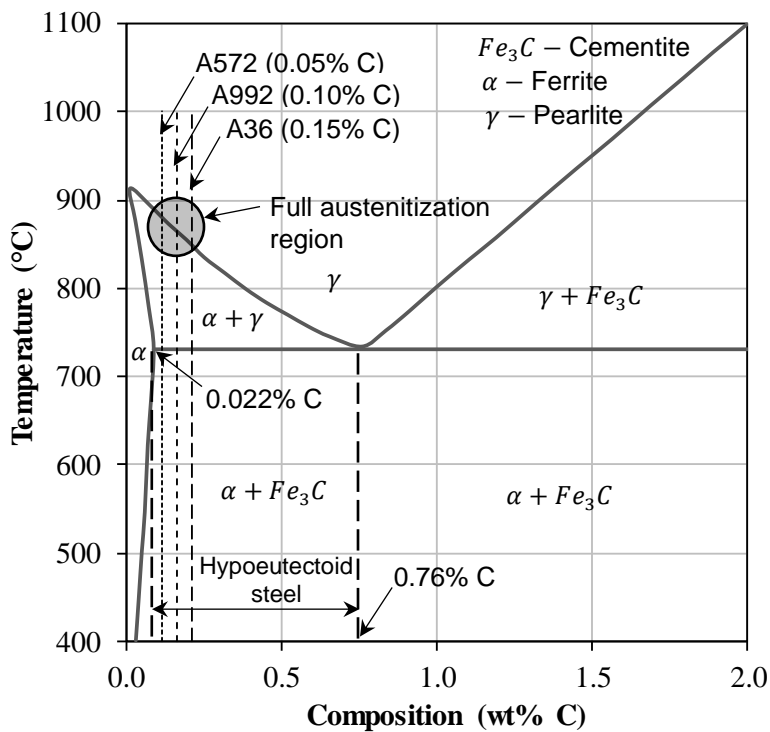


Figure 5.4. Iron-Iron Carbide phase diagram for hypoeutectoid steels (0.022-0.76% C).

5.3. Results and Discussion

In this section, the results obtained from post-fire mechanical tests and microstructural analyses are presented.

5.3.1. Post-Fire Microstructure

In this study, the post-fire microstructure of test specimens is examined under an optical microscope using the procedure discussed in Section 5.2.2. Representative microstructures of room temperature steel specimens (RT specimens) and post-fire air-cooled test specimens are provided in Figure 5.5, Figure 5.6 and Figure 5.7, respectively. As observed in these figures, the microstructure of all three types of steels consists of ferrite and pearlite. However, the grain size and volume fractions of ferrite and pearlite are observed to vary. To evaluate the area fractions of ferrite and pearlite, ferrite grain size and pearlite colony size, 8 separate micrographs were acquired from each metallographic specimen from various locations (see Figure 5.3). These micrographs were obtained at 20X magnification to ensure enough number of grains/colonies of each microstructural constituent (ferrite and pearlite) is present in the micrograph. The area fractions of ferrite and pearlite, ferrite grain size and pearlite colony size obtained from these micrographs corresponding to different temperature exposure conditions are shown in Figure 5.8 and Figure 5.9. As observed in Figure 5.8, ferrite and pearlite area fractions experience only minor change (up to 5%) when metallographic specimens are air-cooled from temperatures up to 1000 °C, for all three structural steels that are investigated in this study. ASTM A36 steels are observed to possess on average $77\pm 2\%$ ferrite and $22\pm 2\%$ pearlite whereas ASTM A572 and ASTM A992 steels are composed of $82\pm 2\%$ ferrite and $18\pm 2\%$ pearlite. Unlike area fractions of ferrite and pearlite, the grain size of ferrite exhibited slightly higher change when specimens are air-cooled from different target temperatures (see Figure 5.9). The changes that occurred in all three steels are as follows: (i) Ferrite grain size in ASTM A36 steel specimens did not exhibit considerable change when air-cooled from temperatures up to 600 °C (see Figure 5.9(a)). For 600-800 °C temperatures, ASTM A36 air-cooled specimens exhibited a slight increase in ferrite

grain size whereas pearlite colony size remained the same. Beyond 800 °C, both ferrite and pearlite experienced an increase in grain/colony size. (ii) In the case of ASTM A572 steels, ferrite and pearlite phases do not experience a considerable change in grain size when air-cooled from temperatures up to 700 °C (see Figure 5.9(b)). At 800 °C, ASTM A572 air-cooled specimens experienced a reduction in ferrite grain size and pearlite colony size. Beyond 800 °C, ASTM A572 air-cooled specimens did not experience a further reduction in ferrite grain size and pearlite colony size (see Figure 5.9(b)). (iii) In the case of ASTM A992 steels, ferrite grain size and pearlite colony size almost remained the same when specimens are air-cooled from temperatures up to 700 °C (see Figure 5.9(c)). Both ferrite grain size and pearlite colony size exhibited a decreasing trend when ASTM A992 steels are air-cooled after exposure to temperatures beyond 700 °C.

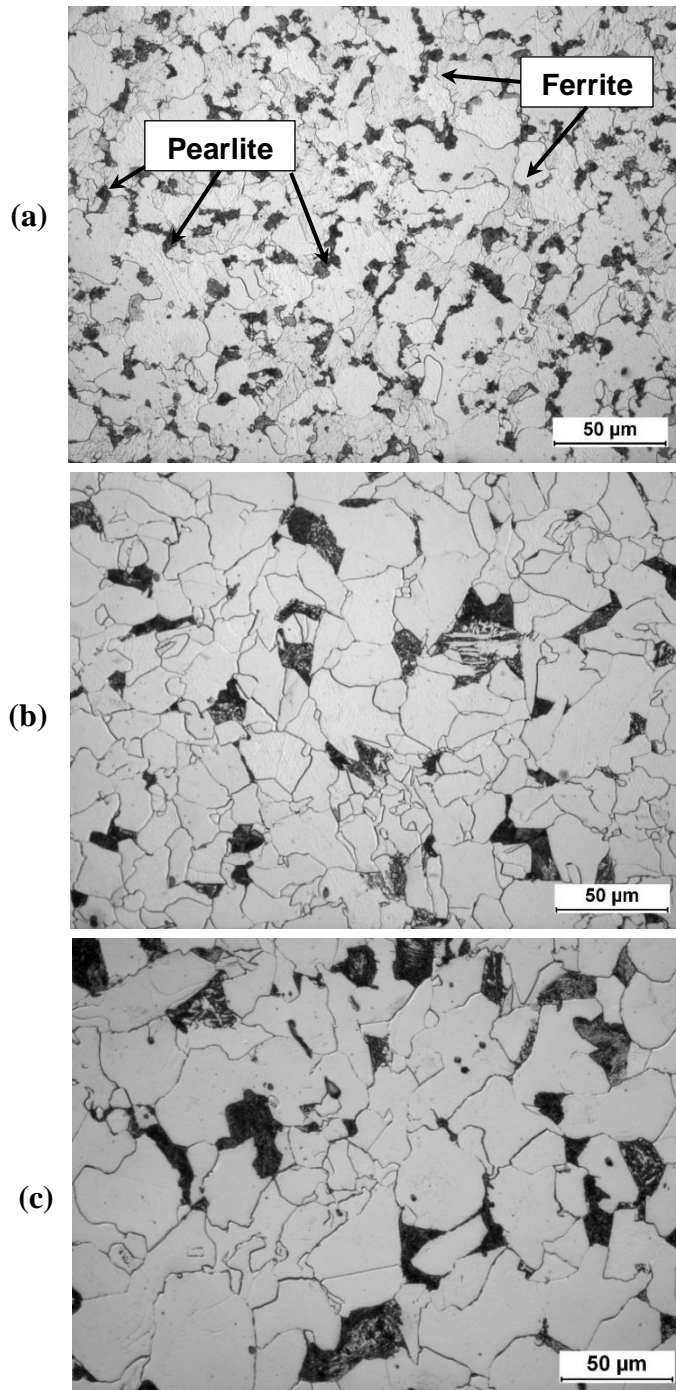


Figure 5.5. Microstructure of reference steel specimens evaluated at room temperature: (a) ASTM A36, (b) ASTM A572 Gr. 50, and (c) ASTM A992.

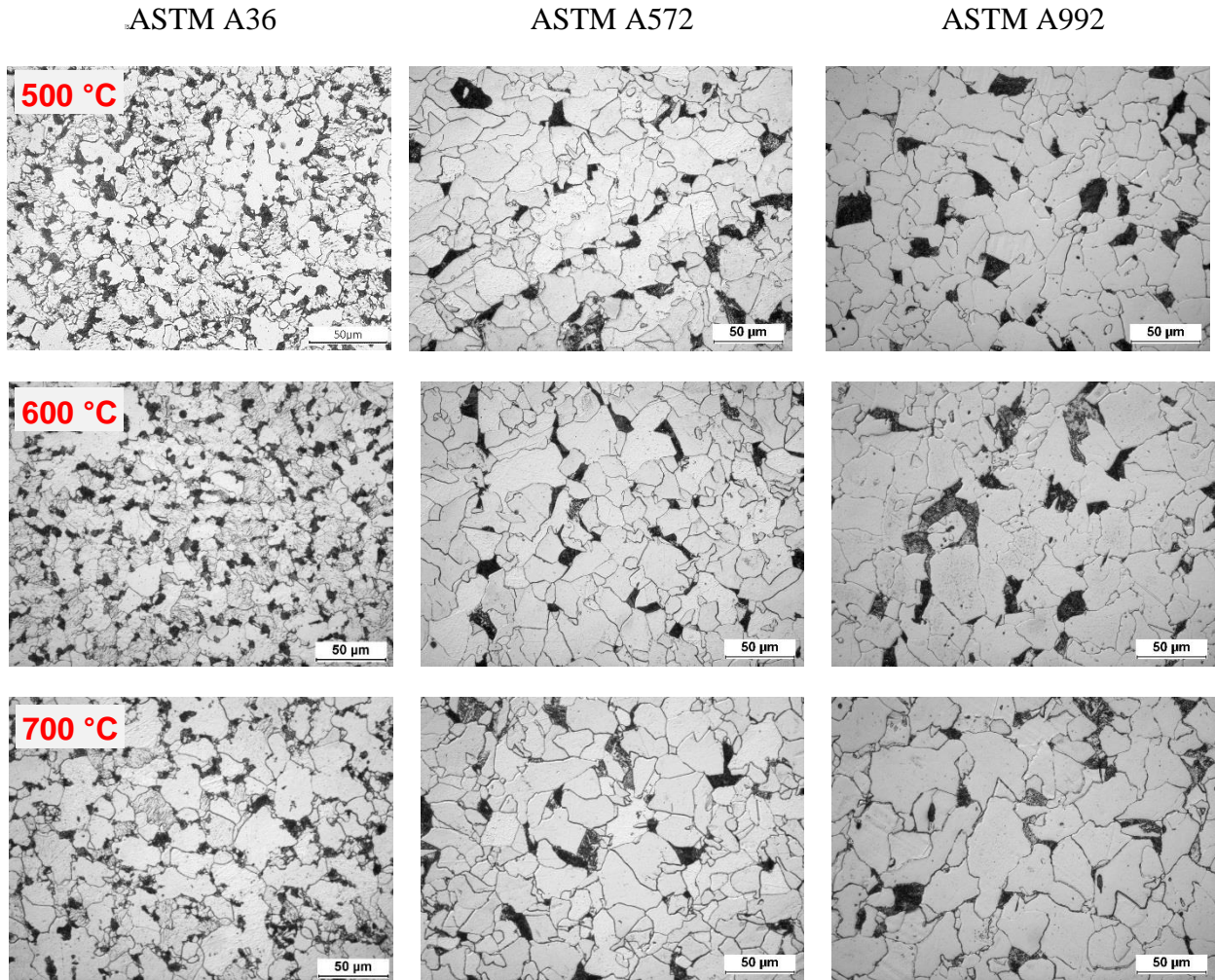


Figure 5.6. Post-fire air-cooled microstructures of structural steel specimens corresponding to different target temperatures (500-700 °C).

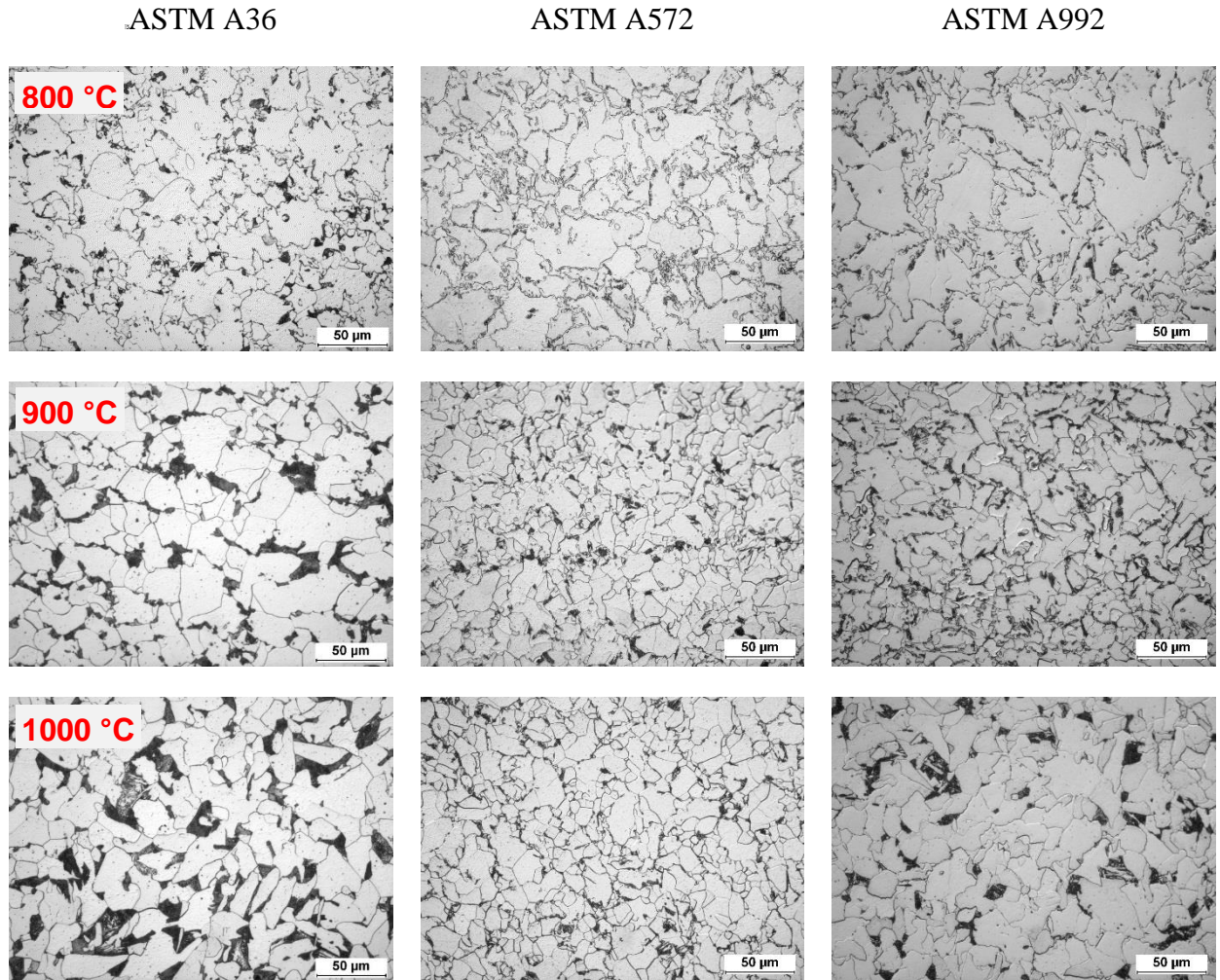


Figure 5.7. Post-fire air-cooled microstructures of structural steel specimens corresponding to different target temperatures (800-1000 °C).

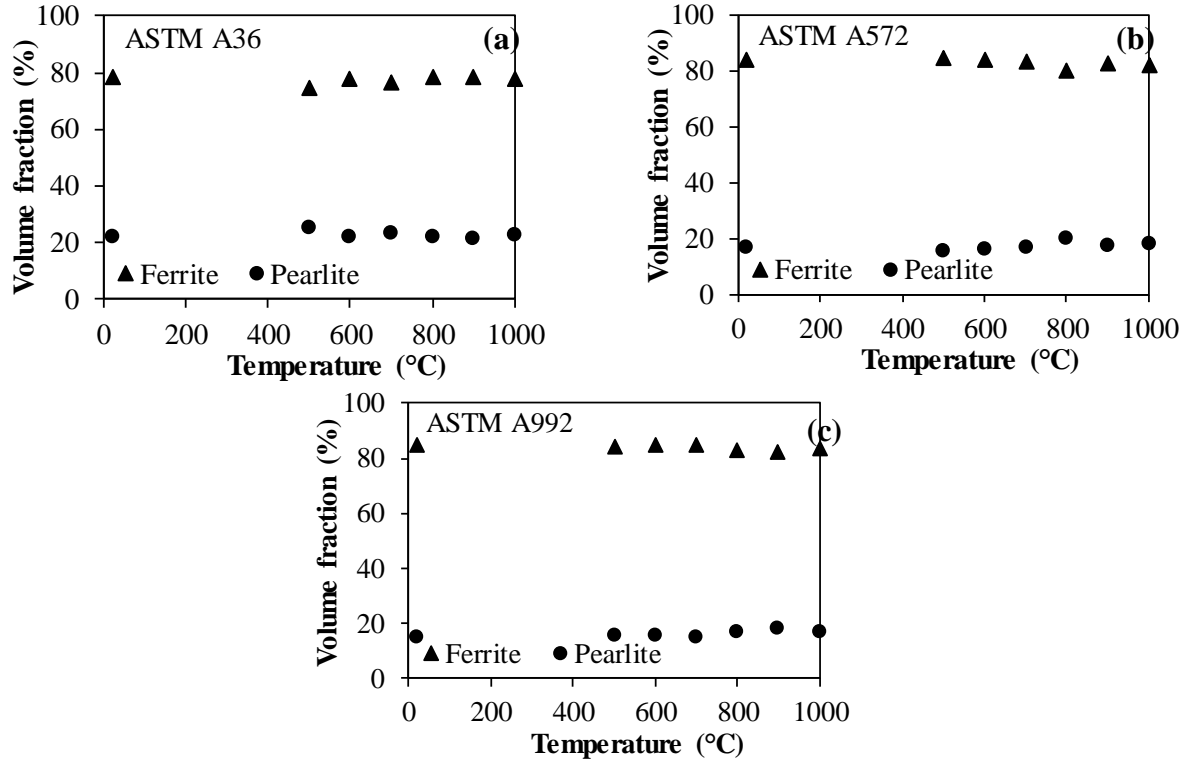


Figure 5.8. Fractions of ferrite and pearlite in AC steels: (a) A36, (b) A572, and (c) A992.

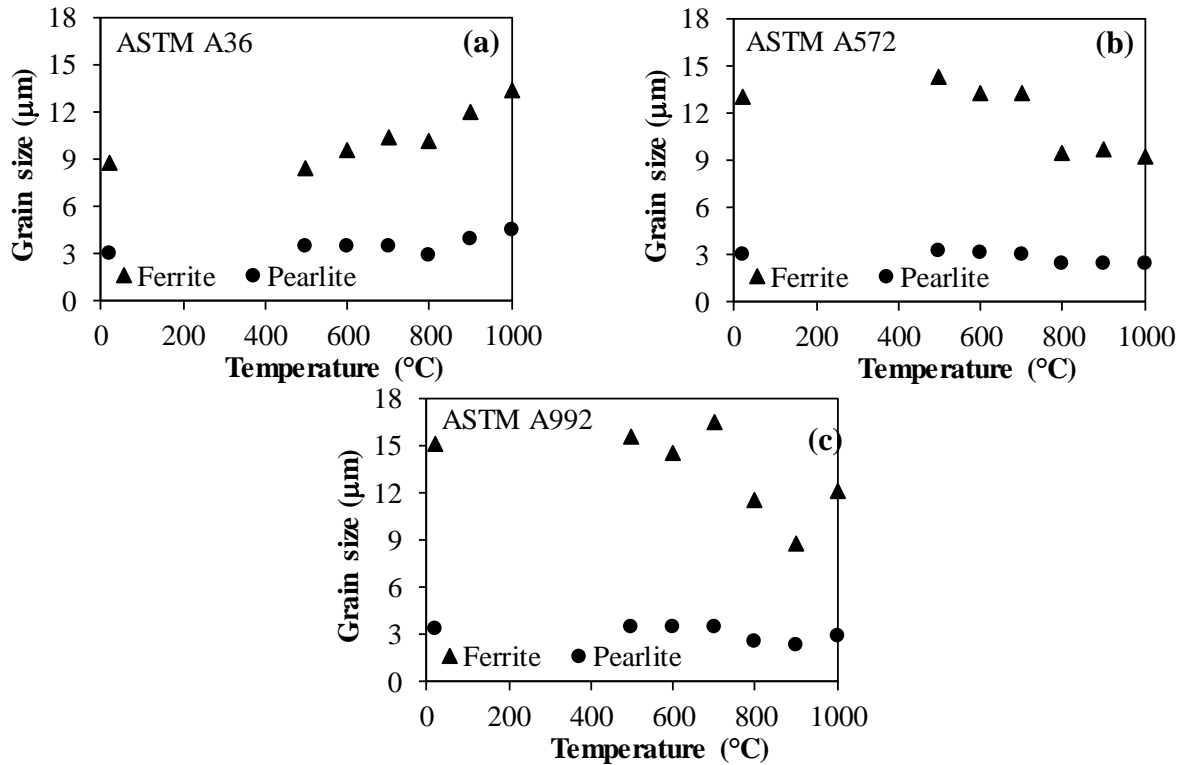


Figure 5.9. Ferrite grain and pearlite colony size in AC steels: (a) A36, (b) A572, and (c) A992.

The grain size trends observed in different steel specimens, as discussed above, occur as a result of phase transformation and consequent changes in the crystal structure experienced by the microstructure of steel specimens during heating and air-cooling from different target temperatures. Based on the carbon content of structural steels, it can be inferred from the $Fe-Fe_3C$ constitutional diagram (see Figure 5.4) that steels are primarily composed of ferrite and pearlite phases. As shown in Figure 5.5, the ferrite phase is represented by grey regions whereas the dark regions indicate the pearlite colonies in the microstructure. As discussed in Section 5.1, ferrite has a body-centered cubic structure (bcc) and is also referred to as alpha-Iron ($\alpha-Fe$). When steel specimens are heated to temperatures close to 727 °C (also referred to as eutectoid transformation temperature), ferrite and pearlite phases start transforming to austenite phase (austenitizing) which is a metastable phase. Austenite, which is also referred to as gamma-Iron ($\gamma-Fe$), has a face-centered cubic (fcc) crystal structure (see Figure 5.1(b)) and is stable above 727 °C. Austenite is stable at room temperature only if the steel has high concentrations of manganese and nickel, which is not the case in structural steels investigated in this study. Ferrite and pearlite do not experience a change in their crystal structures and grain sizes prior to the eutectoid transformation temperature. Hence, the grain size of ferrite and pearlite colony size are not expected to exhibit considerable change prior to this temperature (727 °C), as witnessed in grain size results that were discussed in the previous paragraph. For the steels studied herein, complete austenitization can be achieved when the temperature is raised to about 860 °C. Austenitizing is both temperature and time-dependent and hence sufficient time is needed for complete austenitization [26]. The austenite phase starts transforming back to ferrite once the temperature drops below 860 °C during the cooling phase of steel specimens. Ferrite starts to nucleate and continue to grow at the austenite grain boundaries. Below 727 °C, the

transformation of austenite to ferrite is completed and the remaining untransformed austenite is surrounded by ferrite. Subsequent cooling below 727 °C results in the transformation of remaining austenite to pearlite (ferrite phase + cementite phase) by eutectoid reaction [34]. The resulting microstructure comprises of ferrite and pearlite. The ferrite grain size and pearlite structure in the resulting microstructure depend on the cooling rate and carbon content [34]. In this study, all metallographic specimens were naturally cooled (air-cooled). However, two distinct trends are observed in ferrite grain size in this study when compared to RT grain size. In the case of ASTM A36 steel (mild steel), the ferrite grain size increased after A36 specimens are air-cooled after exposure to temperatures beyond 700 °C (see Figure 5.9(a)). However, in the case of ASTM A572 and ASTM A992 steels, ferrite grain refinement is observed when specimens are subjected to temperatures beyond 700 °C (see Figure 5.9(a)). These contrasting trends can be attributed to the varying chemical composition of these structural steels. When ASTM A36 steel specimens are heated to temperatures beyond 700 °C, austenite grains start forming and continue to coarsen as the temperature increases beyond 860 °C [5]. Upon air-cooling, the austenite transforms back to ferrite and pearlite, as discussed above, while retaining the coarser grain size. However, in case of ASTM A572 and ASTM A992 steels, the coarsening of austenite grains during heating and the resulting transformation to ferrite grains during cooling is restricted by the carbides of microalloying elements (such as vanadium carbide and niobium carbide) [5, 35]. The austenite grain boundaries are pinned by the carbides as they dissolve in the austenite phase during austenitization and hence the resulting ferrite grains are relatively fine-grained. The consequences of these transformations, grain size changes and precipitation of carbides of microalloying elements (in case of ASTM A36 and ASTM A572 HSLA steels) on mechanical properties of structural specimens will be discussed in the next section.

5.3.2. Post-Fire Microstructure and Mechanical Properties

5.3.2.1. Yield Strength

Post-fire yield strength values of uniaxial tension test specimens are obtained from the engineering stress-strain curve using 0.2% stain offset method [36] and are summarized in Table 5.2. Post-fire yield strength, volume fractions of ferrite and pearlite, ferrite grain size and pearlite colony size observed after exposure to different elevated temperatures are shown in Figure 5.10 through Figure 5.12. As observed in Figure 10, the post-fire yield strength of ASTM A36 steel specimens remained almost unaffected when specimens are air-cooled from temperatures up to 600 °C. Similarly, ASTM A572 and ASTM A992 steel specimens do not experience a considerable reduction in yield strength when specimens are air-cooled from temperatures up to 700 °C (see Figure 5.11 and Figure 5.12). This is expected since volume fractions of ferrite and pearlite, ferrite grain size and pearlite colony size do not experience considerable change when metallographic specimens are air-cooled from temperatures up to 600 °C for ASTM A36 and 700 °C for ASTM A572 and ASTM A992, as shown in Figure 5.8 and Figure 5.9, respectively. The decrease in yield strength of ASTM A36 specimens corresponding to 700 °C may be the consequence of partial spheroidization of pearlite phase, which occurs at a temperature close to 727 °C [5]. During spheroidization, the cementite layers in the pearlite structure progressively break up and shrink into sphere-like structures and as a result, cementite exists as sphere-like structures in the ferrite matrix [27]. When air-cooled from temperatures beyond 600 °C, ASTM A36 exhibited 22% reduction in yield strength. The degradation in yield strength of ASTM A36 steel specimens can be attributed to a slight increase in ferrite volume fraction and a corresponding decrease in pearlite volume fraction as well as the increase in ferrite grain size. ASTM A572 and ASTM A992 exhibited 42% and 28% reduction in yield strength, respectively,

when air-cooled from 800 °C. This reduction in yield strength of ASTM A572 and ASTM A992 steels can be attributed to the loss of strength contributed by precipitation hardening mechanism in these steels when steel specimens are air-cooled after exposure to 800 °C. With the exception of A572 steel specimen air-cooled from 1000 °C, both ASTM A572 and ASTM A992 steels exhibited an increase in yield strength (when compared to 800-AC yield strength) when air-cooled from temperatures beyond 800 °C. This recovery in yield strength can be attributed to the reduction in ferrite grain size as well as regaining of strength contributed by precipitation hardening mechanism [5, 34].

Table 5.2. Post-fire yield strength of structural steel specimens (R = residual factor).

Temperature (°C)	Yield strength, σ_y (MPa)					
	ASTM A36	ASTM A36 (R_{σ_y})	ASTM A572	ASTM A572 (R_{σ_y})	ASTM A992	ASTM A992 (R_{σ_y})
20 (RT)	383.92	1.00	392.64	1.00	350.42	1.00
500	389.41	1.01	364.72	0.93	340.20	0.97
600	380.72	0.99	397.98	1.01	362.52	1.03
700	319.35	0.83	410.13	1.04	372.53	1.06
800	300.79	0.78	229.13	0.58	256.61	0.73
900	306.42	0.80	272.05	0.69	274.20	0.78
1000	303.82	0.79	220.56	0.56	343.34	0.98

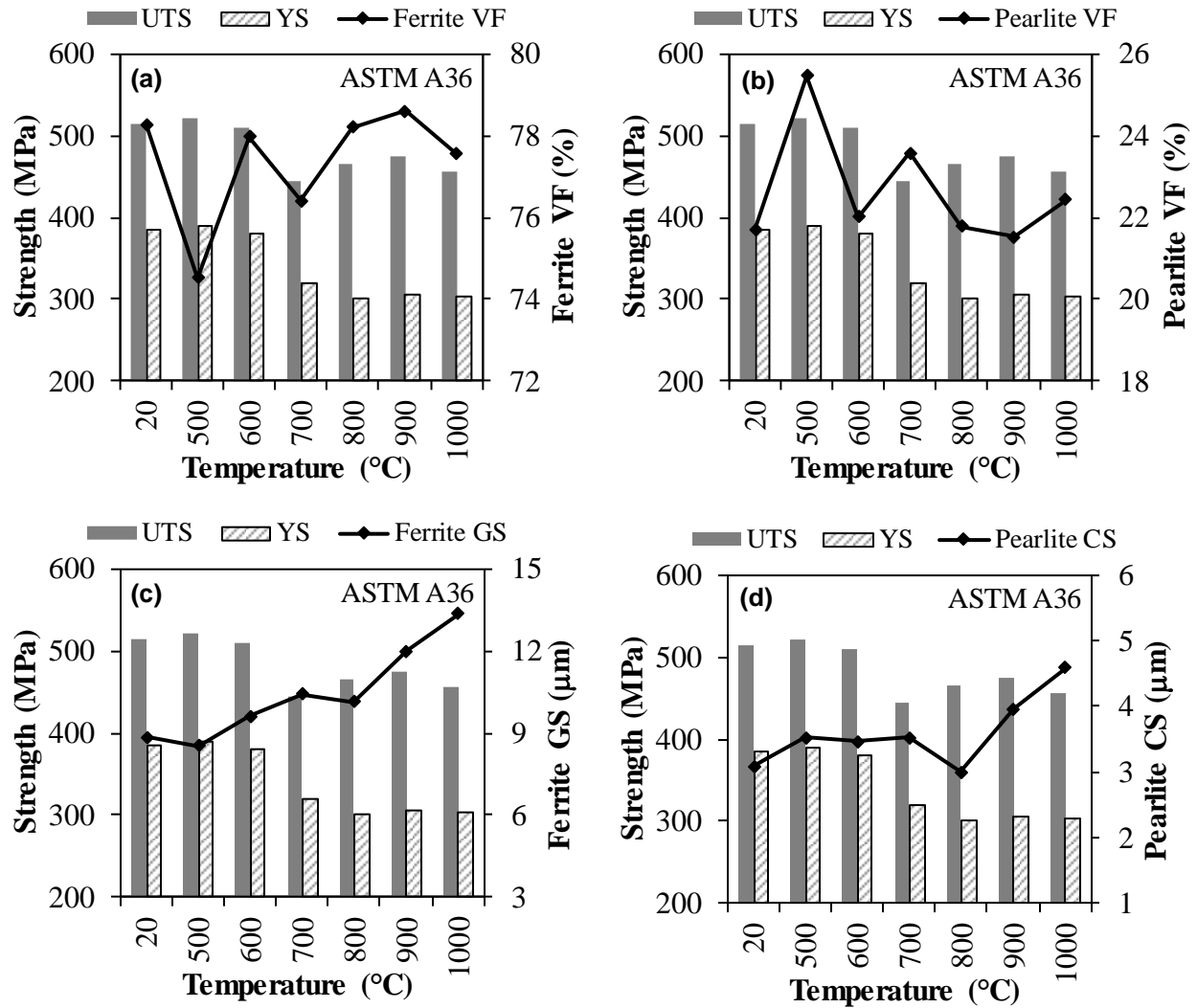


Figure 5.10. Post-fire yield strength (YS), ultimate tensile strength (UTS) and evolution of (a) ferrite volume fraction (VF), (b) pearlite VF, (c) ferrite grain size (GS) and (d) pearlite colony size (CS) of ASTM A36 steel specimens corresponding to different target temperatures.

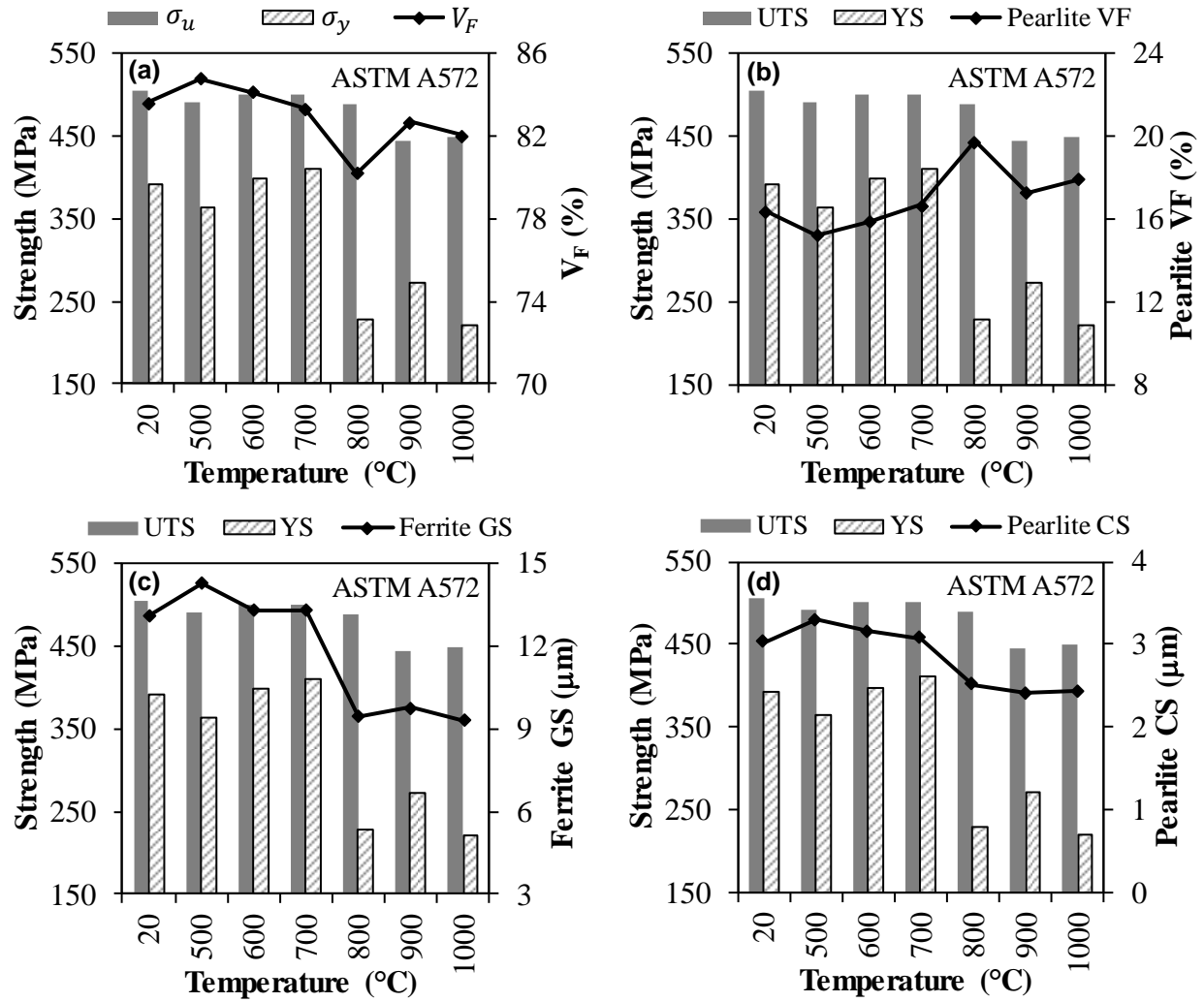


Figure 5.11. Post-fire yield strength (YS), ultimate tensile strength (UTS) and evolution of (a) ferrite volume fraction (VF), (b) pearlite VF, (c) ferrite grain size (GS) and (d) pearlite colony size (CS) of ASTM A572 steel specimens corresponding to different target temperatures.

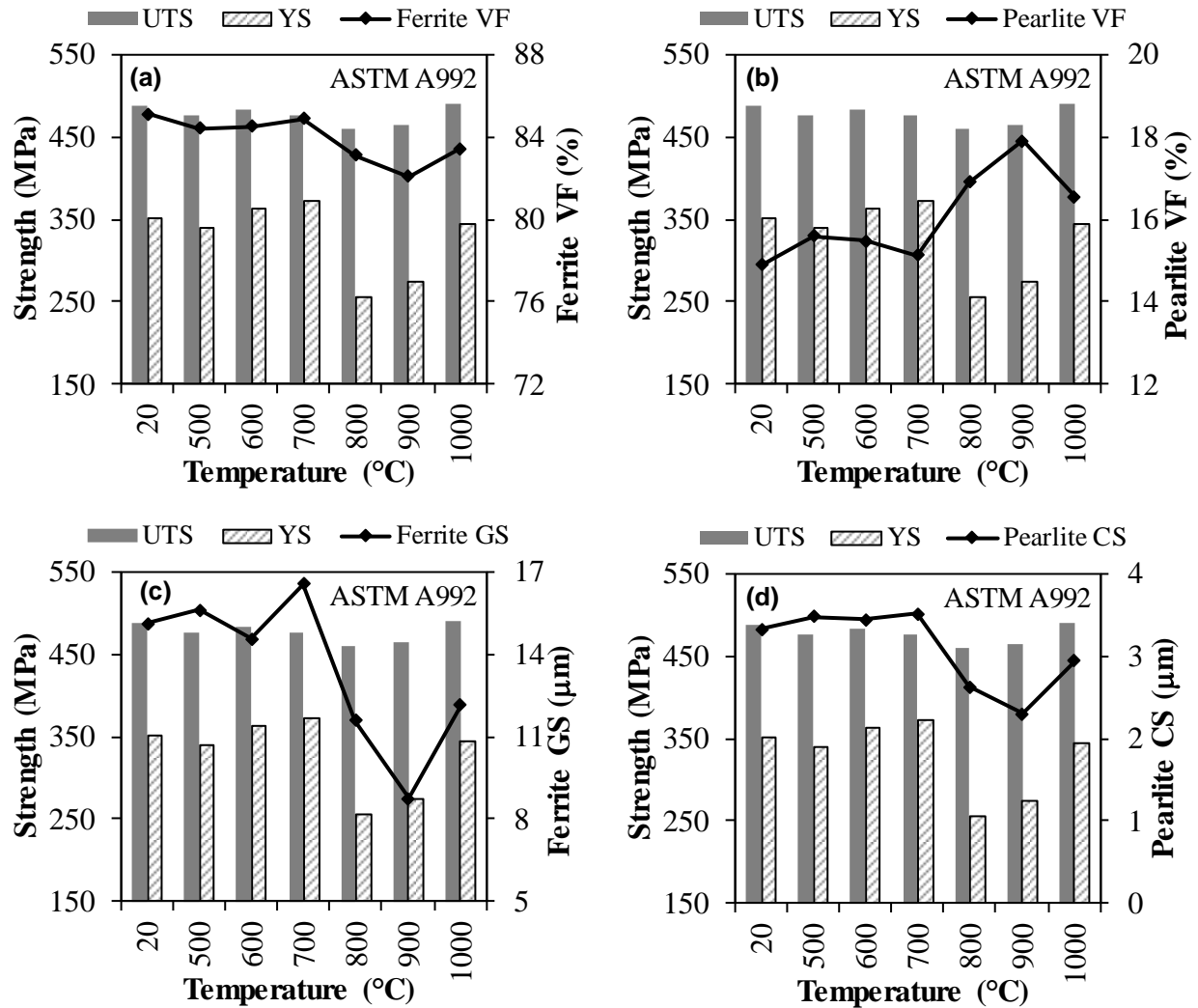


Figure 5.12. Post-fire yield strength (YS), ultimate tensile strength (UTS) and evolution of (a) ferrite volume fraction (VF), (b) pearlite VF, (c) ferrite grain size (GS) and (d) pearlite colony size (CS) of ASTM A992 steel specimens corresponding to different target temperatures.

5.3.2.2. Ultimate Tensile Strength

Post-fire ultimate tensile strength is defined as the maximum stress obtained from the engineering stress-strain curve [34]. The post-fire ultimate tensile strength of all steels are summarized in Table 5.3. Post-fire ultimate tensile strengths corresponding to different elevated temperatures are shown in Figure 5.10 through Figure 5.12. Also, volume fractions of ferrite and pearlite, ferrite grain size and pearlite colony size are also plotted in Figure 5.10 through Figure 5.12 to illustrate the microstructural changes after exposure to different elevated temperatures.

As observed in Figure 5.10 through Figure 5.12, post-fire ultimate tensile strengths of ASTM A36 and ASTM A572 Gr. 50 steels decreased by up to 14% when air-cooled from temperatures up to 1000 °C whereas ASTM A992 air-cooled steel specimens exhibited a minimal reduction in post-fire ultimate tensile strength (up to 6%). ASTM A992 steels almost completely recover their room temperature ultimate tensile strength when air-cooled from 1000 °C (see Figure 5.12). The decreasing trend in ultimate tensile strengths of ASTM A36 steels and ASTM A572 and ASTM A992 HSLA steels can be attributed to different types of strengthening mechanisms in these steels [37], as discussed in Section 5.3.1. ASTM A36 steel derives its strength mainly from dislocation motion, which is affected by the grain size and morphology of grain boundaries. In the context of this study, which focuses on the grain size, it can be observed that as the ferrite grain size increases in case of ASTM A36 air-cooled specimens, the hindrance offered by the grain boundaries to the dislocation motion decreases, which result in a reduction in ultimate tensile strength. On the other hand, ASTM A572 and ASTM A992 steels acquire their strength from both dislocation motion and precipitation hardening due to the presence of alloying elements [25]. When ASTM A572 and ASTM A992 steels are heated to 800 °C, which is above the eutectoid transformation temperature, the carbides within these steels begin dissolving in the austenite phase. Upon air-cooling, the austenite phase transforms back to ferrite and pearlite and there is a reduction in re-precipitation of carbides and nitrides, which leads to loss of strength contributed by precipitation hardening mechanism that existed in steels prior to exposure to elevated temperatures [5]. Hence, a net reduction in ultimate tensile strength is noticed in HSLA steels. ASTM A572 and ASTM A992 regain ultimate tensile strength upon cooling from 900 °C and 1000 °C due to re-precipitation of carbides and nitrides and formation of fine-grained ferrite and pearlite microstructure (see Figure 5.7), as discussed in Section 5.3.1. At this juncture, it is

very important to note that the factors like the initiation of necking in the test specimens also have a significant influence on the ultimate tensile strength. The initiation of necking depends on strain hardening properties of phases and geometrical imperfections [38, 39]. The influence of necking on the ultimate tensile strength of steels falls outside the scope of the current study.

Table 5.3. Post-fire ultimate tensile strength of structural steel specimens (R = residual factor).

Temperature (°C)	Ultimate tensile strength, σ_u (MPa)					
	ASTM A36	ASTM A36 (R_{σ_u})	ASTM A572	ASTM A572 (R_{σ_u})	ASTM A992	ASTM A992 (R_{σ_u})
20 (RT)	514.59	1.00	505.88	1.00	488.27	1.00
500	520.63	1.01	491.82	0.97	476.77	0.98
600	510.82	0.99	500.32	0.99	482.75	0.99
700	443.49	0.86	500.77	0.99	476.78	0.98
800	465.00	0.90	489.12	0.97	460.36	0.94
900	474.18	0.92	444.47	0.88	465.64	0.95
1000	455.33	0.88	449.96	0.89	490.89	1.01

5.3.2.3. Ductility

Post-fire ductility is defined as the engineering strain at fracture in this study [34]. Post-fire ductility values obtained from uniaxial tension tests are summarized in Table 5.4. Post-fire ductility of uniaxial tension test specimens and volume fractions of ferrite and pearlite, ferrite grain size and pearlite colony size obtained from metallographic specimens after exposure to different elevated temperatures are shown in Figure 5.13 through Figure 5.15. As observed in Figure 5.13, the ductility of ASTM A36 steels increased by 22% when compared to reference RT ductility when air-cooled after exposure to 700 °C. When air-cooled from temperatures beyond 800 °C, ASTM A36 steel experienced up to 11% increase in ductility when compared to the ductility of RT specimen. The ductility of ASTM A572 steel remained almost unaffected when air-cooled after exposure to temperatures up to 600 °C. ASTM A572 steels experienced up to 11% increase in their RT ductility when air-cooled from temperatures beyond 600 °C. On the

other hand, ASTM A992 steels exhibited a reduction in post-fire ductility for almost all temperatures and a maximum reduction of 23% is observed when compared to the ductility of reference RT specimen when air-cooled from 1000 °C. It is observed that both ASTM A572 and ASTM A992 steels exhibited a decrease in ferrite grain size, as discussed in Section 5.3.1. However, the ductility of ASTM A572 steels increased after exposure to temperatures beyond 800 °C whereas the ductility of ASTM A992 steels decreased for the same temperature exposure conditions. It is important to note that the ductility is strongly influenced by the initial defects and stress concentrations [30, 40-44]. The influence of initial defects and stress concentrations on the ductility of post-fire structural steels falls outside the scope of this work.

Table 5.4. Post-fire ductility of structural steel specimens (R = residual factor).

Temperature (°C)	Ductility, El (%)					
	ASTM A36	ASTM A36 (R_{El})	ASTM A572	ASTM A572 (R_{El})	ASTM A992	ASTM A992 (R_{El})
20 (RT)	40.31	1.00	45.06	1.00	43.43	1.00
500	40.86	1.01	47.41	1.05	41.76	0.96
600	44.13	1.09	43.10	0.96	42.77	0.98
700	49.22	1.22	43.35	0.96	39.30	0.90
800	38.77	0.96	45.57	1.01	40.39	0.93
900	44.85	1.11	50.05	1.11	44.02	1.01
1000	44.83	1.11	47.07	1.04	33.41	0.77

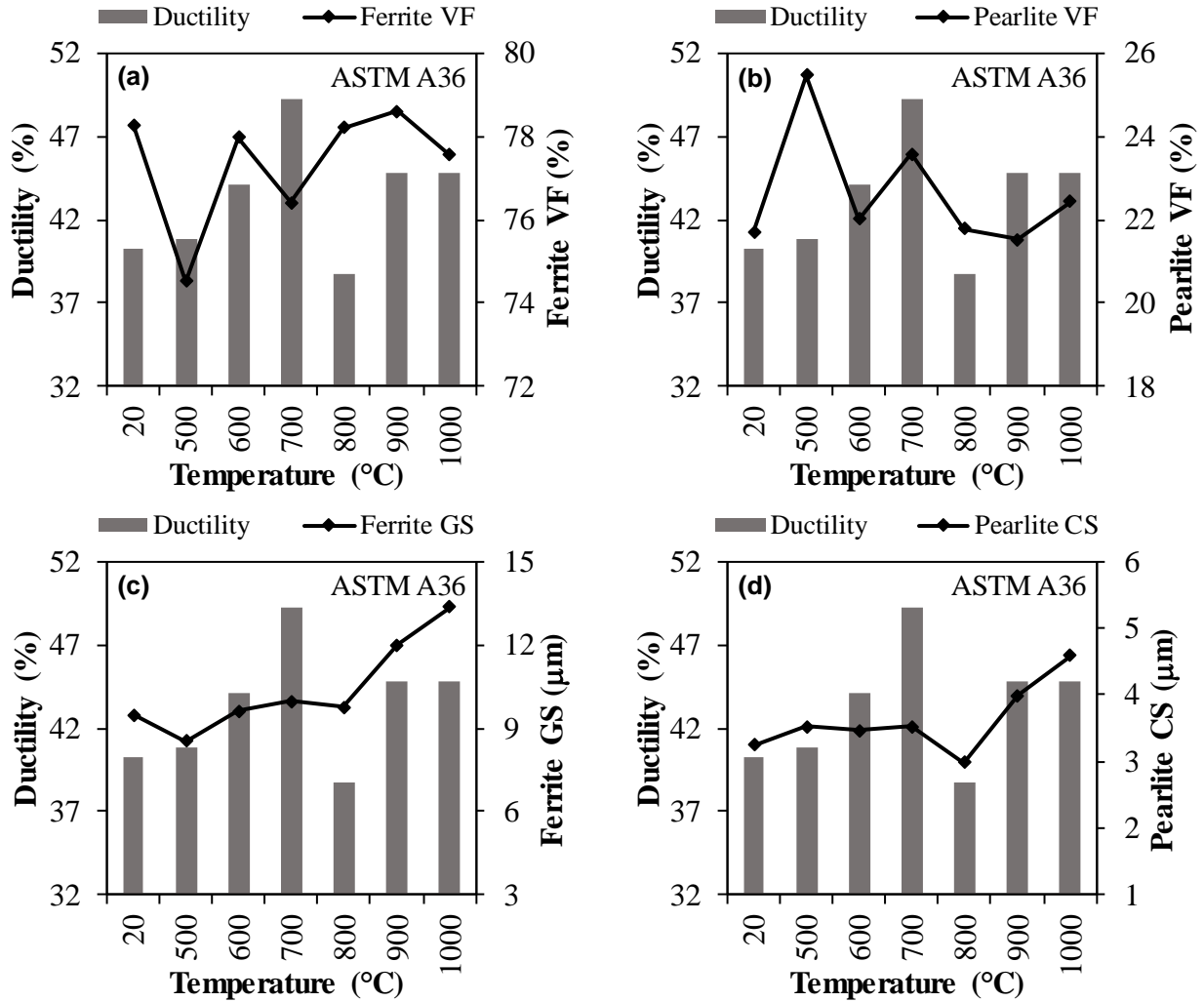


Figure 5.13. Post-fire ductility and evolution of (a) ferrite volume fraction (VF), (b) pearlite VF, (c) ferrite grain size (GS) and (d) pearlite colony size (CS) of ASTM A36 steel specimens corresponding to different target temperatures.

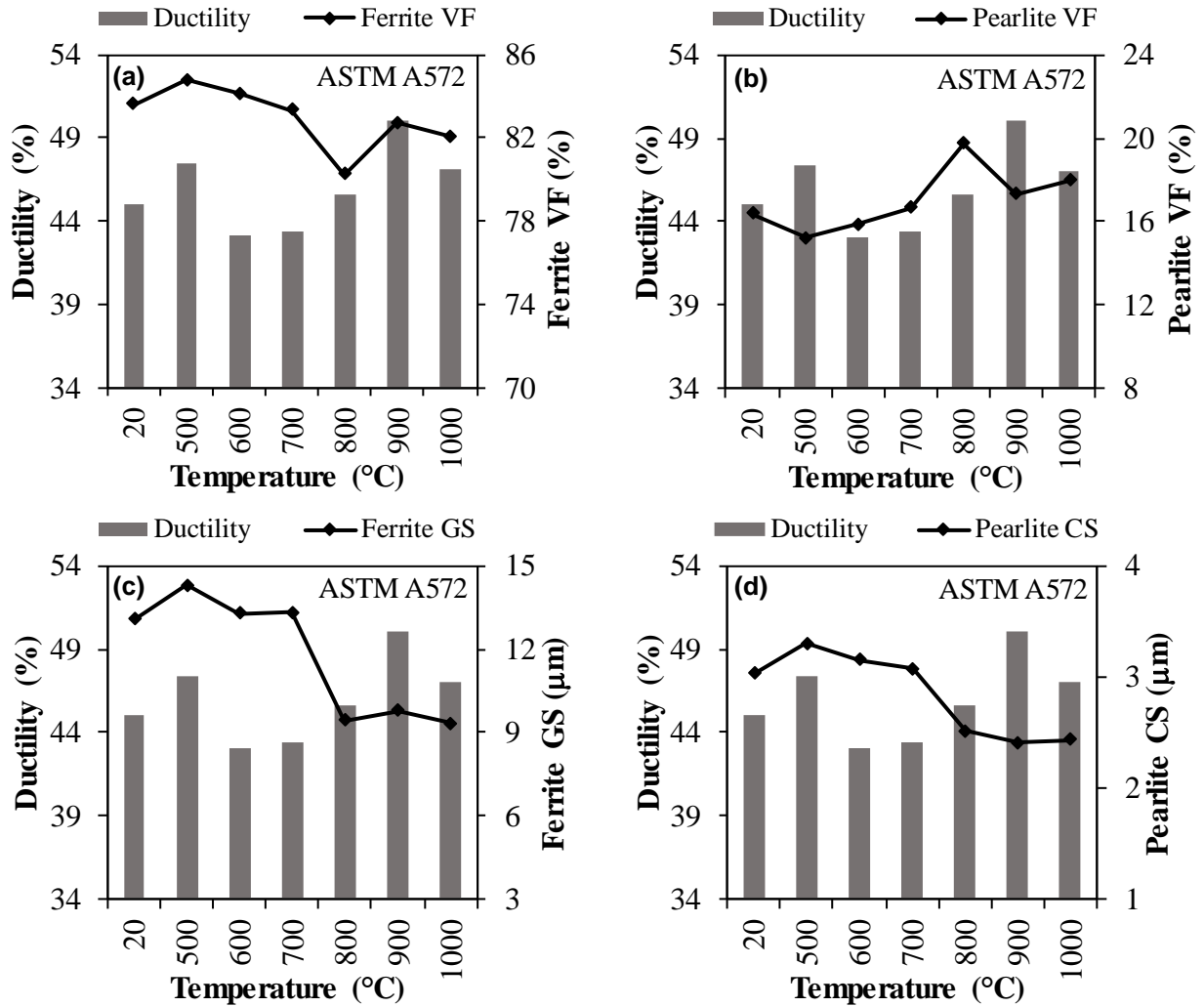


Figure 5.14. Post-fire ductility and evolution of (a) ferrite volume fraction (VF), (b) pearlite VF, (c) ferrite grain size (GS) and (d) pearlite colony size (CS) of ASTM A572 steel specimens corresponding to different target temperatures.

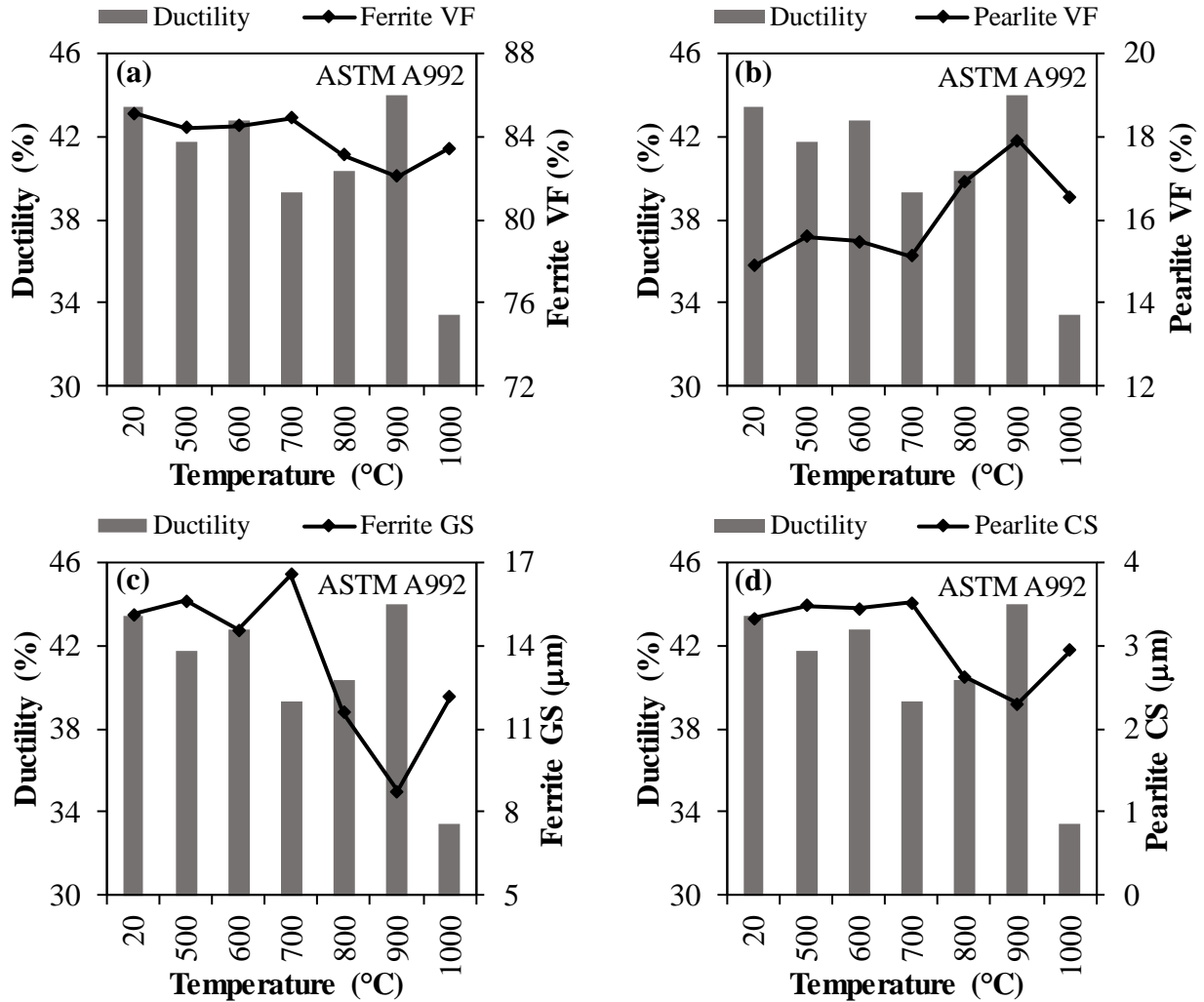


Figure 5.15. Post-fire ductility and evolution of (a) ferrite volume fraction (VF), (b) pearlite VF, (c) ferrite grain size (GS) and (d) pearlite colony size (CS) of ASTM A992 steel specimens corresponding to different target temperatures.

5.3.3. Predictive Models

Multivariate linear regression equations are proposed to predict the yield strength of structural steel specimens that are air-cooled after exposure to elevated temperatures. To this end, the experimental data is imported into MATLAB® environment and a multivariate linear regression code developed based on the theory and assumptions provided in ref. [45] is used. The calibrated equations are provided below.

ASTM A36:

$$\sigma_y = 459.57 - 35.52 g_F + 69.18 c_P \quad (5.1)$$

ASTM A572:

$$\sigma_y = 82.09 + 63.04 g_F - 175.93 c_P \quad (5.2)$$

ASTM A992:

$$\sigma_y = 78.32 - 13.91 g_F + 141.88 c_P \quad (5.3)$$

where, σ_y = yield strength corresponding to 0.2% strain offset (MPa), g_F = ferrite grain size (μm) ($8.00 \mu\text{m} \leq g_F \leq 16.00 \mu\text{m}$), and c_P = pearlite colony size (μm) ($2.30 \mu\text{m} \leq c_P \leq 4.60 \mu\text{m}$).

The post-fire yield strengths obtained from the multivariate linear regression equations and the experiments are provided in Figure 5.16. The yield strengths obtained from the experiments and the regression models are compared with the yield strengths obtained from the microstructure-property relationships that are available in the existing literature for ferrite-pearlite steels with carbon content less than 0.25% by weight in Figure 5.17 through Figure 5.19. The existing microstructure-property models are summarized in Table 5.5. The existing relationships include both the elemental compositions and microstructural features (grain sizes and volume fractions of phases) when determining the yield strengths. As observed in Figure 5.17 and Figure 5.19, the existing microstructure-property relationships predict a conservative estimate of yield strengths for ASTM A36 and ASTM A572 steels that are air-cooled from temperatures up to 700 °C. For ASTM A36 and ASTM A992 steels that are air-cooled from temperatures beyond 700 °C, the existing relationships are able to predict reasonably close yield strengths. On the other hand, the proposed regression models are able to predict the yield strength of air-cooled ASTM A36 and ASTM A992 steels with reasonable accuracy for the entire range of temperatures that are studied herein (see Figure 5.17 and Figure 5.19). In the case

of ASTM A572 steels, the existing models underestimate the yield strength of specimens that are air-cooled from temperatures up to 700 °C and overestimate the yield strength of specimens that are subjected to temperatures beyond 700 °C (see Figure 5.18). On the other hand, the proposed regression model is able to predict the yield strength with reasonable accuracy for temperatures up to 1000 °C. The existing models are able to give reasonable estimates of the yield strengths of the three structural steels that are air-cooled from temperatures beyond 700 °C. This implies that these models are suitable for yield strength prediction for only a limited range of temperatures. Furthermore, since the elemental composition and the strengthening mechanisms vary in different steels, it is more appropriate to calibrate microstructure-property models that are applicable for a particular steel type or steels with identical properties.

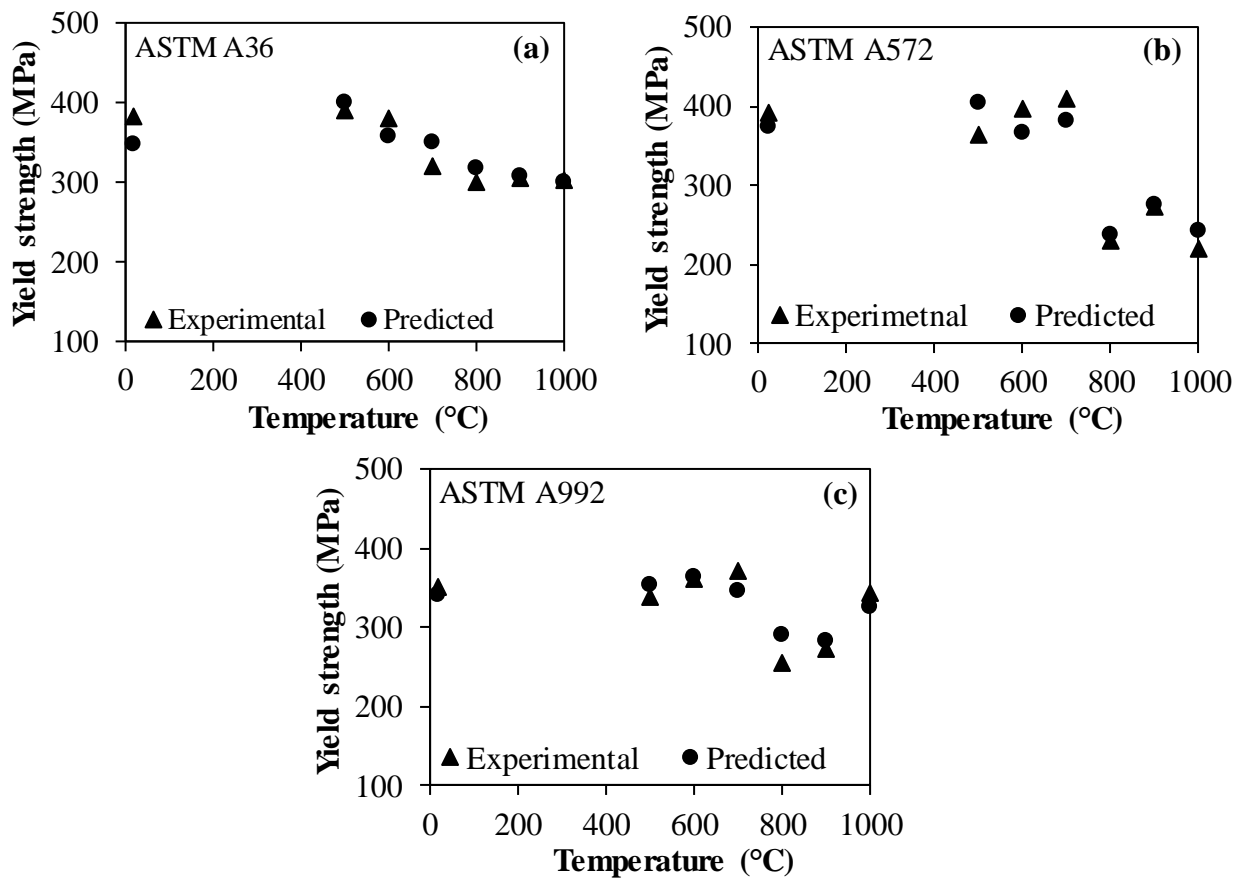


Figure 5.16. Yield strengths of test specimens obtained from experiments and multivariate linear regression-based models for (a) ASTM A36, (b) ASTM A572, and (c) ASTM A992.

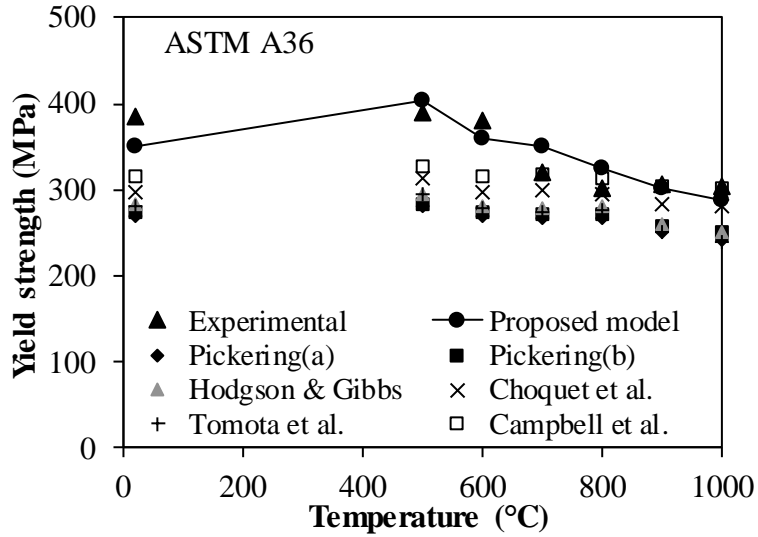


Figure 5.17. Comparison of the proposed model for ASTM A36 steel with the existing microstructure-property relationship for yield strength.

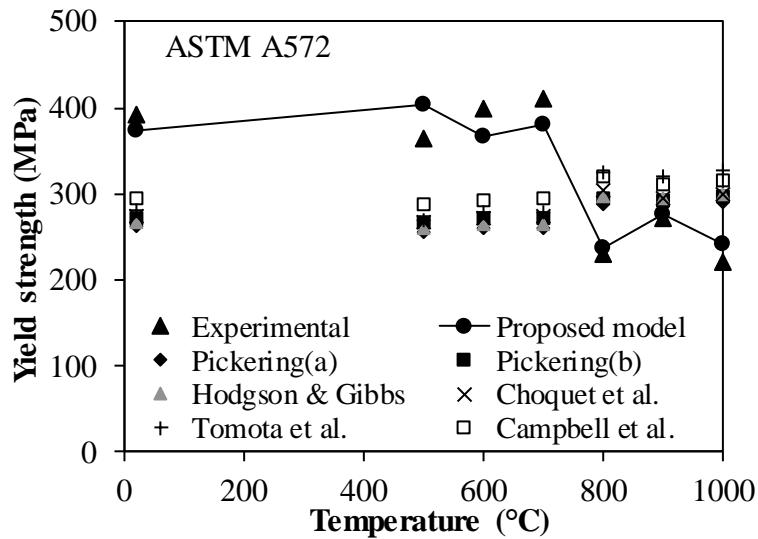


Figure 5.18. Comparison of the proposed model for ASTM A572 Gr. 50 steel with the existing microstructure-property relationship for yield strength.

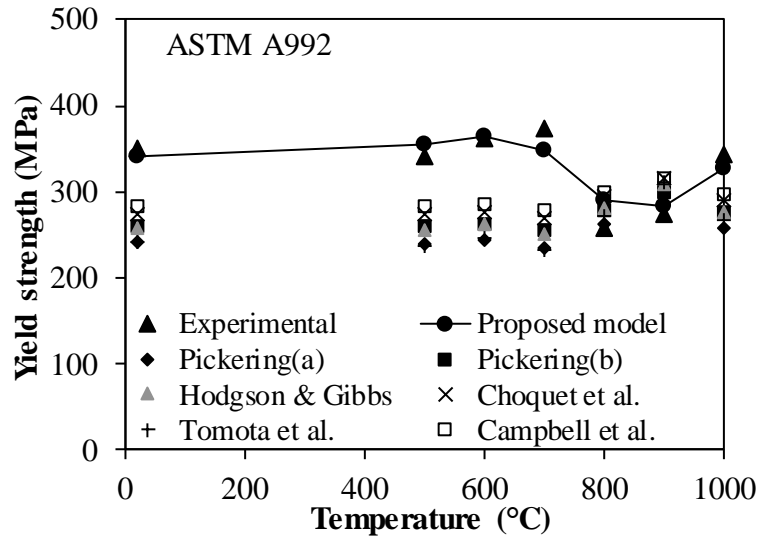


Figure 5.19. Comparison of the proposed model for ASTM A992 steel with the existing microstructure-property relationship for yield strength.

Table 5.5. Existing microstructure-property relationship models for yield strength.

Ref.	Metallurgical composition - microstructure-property relationships for yield strength
[46] (a)	$\sigma_y = 53.9 + 32.34(Mn) + 83.2(Si) + 354.3(N_f) + 17.4d^{-\frac{1}{2}}$
[47] (b)	$\sigma_y = 88 + 37(Mn) + 83(Si) + 2918[(N) - 3.42(Ti)] + 15.1d^{-\frac{1}{2}}$
[48]	$\sigma_y = 62.2 + 26.1(Mn) + 60.2(Si) + 3286[(N) - 3.42(Ti)] + 19.7d^{-\frac{1}{2}}$
[49]	$\sigma_y = 63 + [23(Mn) + 53(Si) + 700(P) + 5000[(N) - 3.42(Ti)]] + [15.4 - 30(C) + \frac{6.094}{0.8+(Mn)}] f_\alpha d_\alpha^{-\frac{1}{2}} + (360 + 2600(C)^2)(1 - f_\alpha)$
[50]	$\sigma_y = \left(373 + 62.7(Mn) + 109(Si) + 10.8d_\alpha^{-\frac{1}{2}} \right) \left(0.002 + \frac{5.35}{\varepsilon_p^{10+d_\alpha^{-\frac{1}{2}}}} - 0.024(Mn) - 0.037(Si) - 0.12 \right)$
[51]	$\sigma_y = f_\alpha \left(132 + 11.8d_\alpha^{-\frac{1}{2}} \right) + (1 - f_\alpha) \left(408 + 92.2(Mn) + 0.400S_p^{-\frac{1}{2}} \right) + 79.7(Si)$

where,

σ_y = yield strength at 0.2% strain offset in MPa.

Mn, Si, N, Ti, P, C = elemental composition of manganese, silicon, nitrogen, titanium, phosphorus, and carbon, respectively, in % weight.

N_f = free Nitrogen content in % weight.

d and d_α = ferrite grain size in millimeters.

f_α = ferrite fraction in the microstructure.

S_p = pearlite spacing in micrometers.

It should be noted that except for only one specimen in which case of 14% reduction is observed in ultimate tensile strength (ASTM A36-700 °C), the majority of steel specimens that are air-cooled after exposure to high temperatures exhibited a modest decrease of around 10% or less. In fact, ASTM A992 steels exhibited a maximum reduction of 6% in ultimate tensile strength when air-cooled from temperatures up to 1000 °C. In addition, the ultimate tensile strength is also influenced by the onset of necking apart from the microstructure. Similarly, ductility which is defined as the engineering fracture strain in this study is also strongly

dependent on post-necking stress states [30, 40-44] along with microstructure. The relationships between microstructural parameters and ultimate tensile strength and ductility are not pursued in this study as these mechanical properties also depend on non-microstructural parameters.

5.4. Conclusions

A detailed microstructure study was conducted to investigate the relationship between post-fire microstructure and mechanical properties of ASTM A36, ASTM A572, and ASTM A992 steels. Based on the results obtained from uniaxial tension tests and microstructural analysis, multivariate regression equations are proposed to predict yield strength of structural steels as a function of post-fire microstructural parameters that include volume fraction and grain size of ferrite and pearlite colony size. Based on the results obtained in this study, the following conclusions are drawn:

1. Volume fractions of ferrite and pearlite phases remain relatively unaffected when steel specimens are air-cooled from after exposure to temperatures up to 1000 °C.
2. ASTM A36 steels exhibited up to 41% increase in ferrite and pearlite grain sizes when air-cooled from temperatures beyond 700 °C. On the other hand, ASTM A572 and ASTM A992 steels experienced a reduction in ferrite grain size (up to 29% and 42%, respectively) and pearlite colony size (up to 21% and 32%, respectively) upon air-cooling from temperatures beyond 700 °C.
3. ASTM A36, ASTM A572, and ASTM A992 steels do not exhibit a considerable change in yield strength and ultimate tensile strength when air-cooled from temperatures up to 600 °C.

4. ASTM A36 steels that are air-cooled from temperatures beyond 700 °C exhibited up to a 22% decrease in yield strength, which can be attributed to the increase in ferrite grain size.
5. ASTM A572 and ASTM A992 steels exhibited a reduction in yield strength, 42% and 28%, respectively when air-cooled from 800°C, which can be attributed to the loss of strength contributed by precipitation hardening mechanism. Beyond 800 °C, both types of HSLA steels exhibited recovery in yield strength due to grain size refinement and regaining of strength from precipitation hardening.
6. ASTM A36 and ASTM A572 steels exhibited up to 14% reduction in post-fire ultimate tensile strength whereas a modest decrease of 6% was observed in the case of ASTM A992 steels.

Based on results obtained in this study, multivariate linear regression equations are proposed for estimating post-fire yield strength of structural steels (ASTM A36, ASTM A572, and ASTM A992) as a function of ferrite grain size and pearlite colony size with reasonable accuracy.

The results obtained from microstructural analyses and post-fire mechanical tests and the subsequent regression equations developed in this study can play an important role in the estimation of mechanical properties of structural steels that are exposed to fire accidents. These results also establish a convenient microstructure approach to understand and quantify the deterioration that occurs in structural steels as a result of fire and subsequent cooling especially when temperature information is not available.

5.5. References

- [1] J. Lee, M.D. Engelhardt, E.M. Taleff, Mechanical Properties of ASTM A 992 Steel After Fire, *Engineering Journal (Chicago)*, 49 (2012) 33-44.
- [2] E.M. Aziz, V.K. Kodur, Effect of temperature and cooling regime on mechanical properties of high-strength low-alloy steel, *Fire and Materials*, 40 (2016) 926-939.
- [3] M. Garlock, I. Paya-Zaforteza, V. Kodur, L. Gu, Fire hazard in bridges: Review, assessment and repair strategies, *Engineering Structures*, 35 (2012) 89-98.
- [4] Z. Tao, X.-Q. Wang, B. Uy, Stress-Strain Curves of Structural and Reinforcing Steels after Exposure to Elevated Temperatures, *Journal of Materials in Civil Engineering*, 25 (2013) 1306-1316.
- [5] C.I. Smith, B.R. Kirby, D.G. Lapwood, K.J. Cole, A.P. Cunningham, R.R. Preston, The reinstatement of fire damaged steel framed structures, *Fire Safety Journal*, 4 (1981) 21-62.
- [6] J.-H. Chi, P.-C. Peng, Using the microstructure and mechanical behavior of steel materials to develop a new fire investigation technology, *Fire and Materials*, 41 (2017) 864-870.
- [7] H.U. Sajid, R. Kiran, Influence of stress concentration and cooling methods on post-fire mechanical behavior of ASTM A36 steels, *Construction and Building Materials*, 186 (2018) 920-945.
- [8] H.U. Sajid, R. Kiran, Post-fire mechanical behavior of ASTM A572 steels subjected to high stress triaxialities, *Engineering Structures*, 191 (2019) 323-342.
- [9] J. Outinen, P. Mäkeläinen, Mechanical properties of structural steel at elevated temperatures and after cooling down, *Fire and materials*, 28 (2004) 237-251.

- [10] S. Gunalan, M. Mahendran, Experimental investigation of post-fire mechanical properties of cold-formed steels, *Thin-Walled Structures*, 84 (2014) 241-254.
- [11] G.-Q. Li, H. Lyu, C. Zhang, Post-fire mechanical properties of high strength Q690 structural steel, *Journal of Constructional Steel Research*, 132 (2017) 108-116.
- [12] X. Qiang, F.S. Bijlaard, H. Kolstein, Post-fire mechanical properties of high strength structural steels S460 and S690, *Engineering Structures*, 35 (2012) 1-10.
- [13] W. Wang, T. Liu, J. Liu, Experimental study on post-fire mechanical properties of high strength Q460 steel, *Journal of Constructional Steel Research*, 114 (2015) 100-109.
- [14] J. Lu, H. Liu, Z. Chen, X. Liao, Experimental investigation into the post-fire mechanical properties of hot-rolled and cold-formed steels, *Journal of Constructional Steel Research*, 121 (2016) 291-310.
- [15] C. Maraveas, Z. Fasoulakis, K.D. Tsavdaridis, Post-fire assessment and reinstatement of steel structures, *Journal of structural fire engineering*, 8 (2017) 181-201.
- [16] C. Maraveas, Z.C. Fasoulakis, K.D. Tsavdaridis, Mechanical properties of High and Very High Steel at elevated temperatures and after cooling down, *Fire Science Reviews*, 6 (2017) 3.
- [17] Z. Tao, X.-Q. Wang, M.K. Hassan, T.-Y. Song, L.-A. Xie, Behaviour of three types of stainless steel after exposure to elevated temperatures, *Journal of Constructional Steel Research*, (2018).
- [18] Y. Yu, L. Lan, F. Ding, L. Wang, Mechanical properties of hot-rolled and cold-formed steels after exposure to elevated temperature: A review, *Construction and Building Materials*, 213 (2019) 360-376.

- [19] B.W. Roberts, C.P. Thornton, *Archaeometallurgy in global perspective: methods and syntheses*, Springer, 2014.
- [20] ASTM, ASTM A36/A36M-14 Standard Specification for Carbon Structural Steel., in, ASTM International, West Conshohocken, PA, 2014.
- [21] ASTM, ASTM A572/A572M-18 Standard Specification for High-Strength Low-Alloy Columbium-Vanadium Structural Steel., in, ASTM International, West Conshohocken, PA, 2018.
- [22] ASTM, ASTM A992/A992M-11(2015) Standard Specification for Structural Steel Shapes., in, West Conshohocken, PA, 2015.
- [23] G. Krauss, *Steels: Processing, Structure, and Performance*, ASM International, Materials Park, Ohio, 2015.
- [24] J.R. Davis, *Alloying : understanding the basics*, ASM International, Materials Park, OH, 2001.
- [25] M.S. Rashid, High-Strength, Low-Alloy Steels, *Science*, 208 (1980) 862.
- [26] W.D. Callister, D.G. Rethwisch, *Materials Science and Engineering: An Introduction*, Wiley, 2010.
- [27] L.E. Samuels, *Light microscopy of carbon steels*, ASM International, 1999.
- [28] H.K.D.H. Bhadeshia, Cementite, *International Materials Reviews*, (2019) 1-27.
- [29] R. Pała, S. Lipiec, I. Dzioba, Influence of the steel rolling direction on the mechanical properties and distribution of the local stress in front crack, in: *IOP Conference Series: Materials Science and Engineering*, IOP Publishing, 2018, pp. 012064.

- [30] H.U. Sajid, R. Kiran, Influence of high stress triaxiality on mechanical strength of ASTM A36, ASTM A572 and ASTM A992 steels, *Construction and Building Materials*, 176 (2018) 129-134.
- [31] G.F. Vander Voort, *ASM Handbook Volume 9: Metallography and microstructures*, ASM International, Materials Park, OH, 2004.
- [32] D.L. Naik, H.U. Sajid, R. Kiran, Texture-Based Metallurgical Phase Identification in Structural Steels: A Supervised Machine Learning Approach, *Metals*, 9 (2019) 546.
- [33] ASTM, ASTM E112-13 Standard Test Methods for Determining Average Grain Size., in, West Conshohocken, PA, 2013.
- [34] D.R. Askeland, P.P. Fulay, W.J. Wright, *The Science and Engineering of Materials*, SI Edition, CL-Engineering, 2011.
- [35] L. Cuddy, J. Raley, Austenite grain coarsening in microalloyed steels, *Metallurgical Transactions A*, 14 (1983) 1989-1995.
- [36] K.K. Chawla, M. Meyers, *Mechanical behavior of materials*, Prentice Hall, 1999.
- [37] H. Clemens, S. Mayer, C. Scheu, *Microstructure and Properties of Engineering Materials, Neutrons and Synchrotron Radiation in Engineering Materials Science: From Fundamentals to Applications*, (2017) 1-20.
- [38] K.E. N'souglo, A. Srivastava, S. Osovski, J.A. Rodríguez-Martínez, Random distributions of initial porosity trigger regular necking patterns at high strain rates, *Proceedings of the Royal Society A: Mathematical, Physical and Engineering Sciences*, 474 (2018) 20170575.

- [39] A. Srivastava, L. Ponson, S. Osovski, E. Bouchaud, V. Tvergaard, A. Needleman, Effect of inclusion density on ductile fracture toughness and roughness, *Journal of the Mechanics and Physics of Solids*, 63 (2014) 62-79.
- [40] R. Kiran, K. Khandelwal, A triaxiality and Lode parameter dependent ductile fracture criterion, *Engineering Fracture Mechanics*, 128 (2014) 121-138.
- [41] R. Kiran, K. Khandelwal, A coupled microvoid elongation and dilation based ductile fracture model for structural steels, *Engineering Fracture Mechanics*, 145 (2015) 15-42.
- [42] H. Wen, H. Mahmoud, New model for ductile fracture of metal alloys. I: Monotonic loading, *Journal of engineering mechanics*, 142 (2015) 04015088.
- [43] A. Kanvinde, G. Deierlein, The void growth model and the stress modified critical strain model to predict ductile fracture in structural steels, *Journal of Structural Engineering*, 132 (2006) 1907-1918.
- [44] Y. Zhu, M.D. Engelhardt, R. Kiran, Combined effects of triaxiality, Lode parameter and shear stress on void growth and coalescence, *Engineering Fracture Mechanics*, 199 (2018) 410-437.
- [45] D.L. Naik, R. Kiran, Naïve Bayes classifier, multivariate linear regression and experimental testing for classification and characterization of wheat straw based on mechanical properties, *Industrial Crops and Products*, 112 (2018) 434-448.
- [46] F.B. Pickering, Towards Improved Ductility and Toughness, in: *Climax Molybdenum Company Symposium*, Kyoto, 1971, pp. 9.
- [47] F.B. Pickering, *Physical metallurgy and the design of steels*, Applied Science Publishers, London, 1978.

- [48] P.D. Hodgson, R.K. Gibbs, A Mathematical Model to Predict the Mechanical Properties of Hot Rolled C-Mn and Microalloyed Steels, *ISIJ International*, 32 (1992) 1329-1338.
- [49] P. Choquet, P. Fabregue, J. Giusti, B. Chamont, in: S. Yue (Ed.) *International Symposium on Mathematical Modeling of Hot-rolling of Steel*, Canadian Institute of Mining and Metallurgy, Montréal, Qubec, 1990, pp. 34-43.
- [50] Y. Tomota, M. Umemoto, N. Komatsubara, A. Hiramatsu, N. Nakajima, A. Moriya, T. Watanabe, S. Nanba, G. Anan, K. Kunishige, Prediction of mechanical properties of multi-phase steels based on stress-strain curves, *ISIJ international*, 32 (1992) 343-349.
- [51] P. Campbell, E. Hawbolt, J. Brimacombe, Microstructural engineering applied to the controlled cooling of steel wire rod: Part II. Microstructural evolution and mechanical properties correlations, *Metallurgical Transactions A*, 22 (1991) 2779-2790.

6. INFLUENCE OF CORROSION AND SURFACE ROUGHNESS ON WETTABILITY OF ASTM A36 STEELS⁵

This chapter discusses the influence of corrosion and surface roughness on wettability of ASTM A36 steel and it further describes the influence of surface roughness and wettability on corrosion damage in ASTM A36 steel. The contents of this chapter have been published in Sajid, H.U. and Kiran, R., 2018. Influence of corrosion and surface roughness on wettability of ASTM A36 steels. *Journal of Constructional Steel Research*, 144, pp.310-326.

6.1. Introduction

Corrosion is widely regarded as one of the most common forms of deterioration experienced by steel structures in their service life. Corrosion induced damage poses a significant threat to the safety and integrity of both inland and offshore infrastructure. Maintenance of structures to limit or prevent the damage due to corrosion is a significant issue in United States and other parts of the world [1–3]. In the past, damage due to corrosion has resulted in severe damage and even collapse of both inland and offshore structures causing huge loss of life and property [4–7]. Failure of structures due to corrosion can also adversely affect the environment. For instance, a 2003 offshore hydrocarbon release report attributed approximately 45% of hydrocarbon leaks to corrosion related failures [8,9]. Also, according to Pipeline and Hazardous Materials Safety Administration (PHMSA) statistics, about 17% of pipeline accidents that occurred in the United States in the past 20 years are caused by corrosion induced failures [10]. Corrosion is recognized as one of the primary contributing factors in 20% of all refinery accidents that occurred in European Union countries in the past 30 years [5]. In aviation industry,

⁵ This chapter was co-authored by H.U. Sajid and R. Kiran. H.U. Sajid had the primary responsibility of preparing the specimens, conducting all tests, and drafting this chapter. R. Kiran supervised the research and revised this chapter.

over 20% of accidents that resulted in a human injury are caused by corrosion failures [11]. The total cost of corrosion related damages in 2016 is estimated to be 2.5 trillion USD globally [12]. The United States [13] and other major economies [11] regularly spend huge amounts of money for repairs and maintenance associated with corrosion damages.

The amount of corrosion induced in structural steel is determined by the presence of oxygen, salt and water in the exposure environment. Corrosion results in loss of material, reduction in section and formation of corrosion products [1]. These factors cause reduction in load carrying capacity of steel members and lead to subsequent failures [14]. Two most frequent corrosion modes with varying implications are observed in steel structures. They are uniform corrosion and localized corrosion [1,15–17]. Uniform corrosion is reported as the most common form of corrosion in steels [15,17]. This type of corrosion occurs uniformly over the entire surface of steel, resulting in thinning of steel section and hence reduction in load carrying capacity of steel members. Localized corrosion occurs locally and does not affect the entire surface area of the steel member [16]. Pitting corrosion, galvanic corrosion, crevice corrosion and stress corrosion among others are some examples of localized corrosion [17]. Pitting corrosion is considered highly critical as it results in stress concentration which in turn serves as crack initiation site reducing the ductility and fatigue life of structural steel members [6,18–21]. Recently, researchers have reported effects of local corrosion on behavior and performance of structural steel using different corrosion models [22–25]. Early detection of corrosion can reduce the associated maintenance costs and improve the service life of steel structures.

To improve the corrosion resistance and service life of structural steels, various coating technologies have been developed [26–33]. In addition to this, weathering steels that do not need coating to prevent damage due to corrosion have been developed using different alloy

compositions [34]. However, despite this progress, corrosion remains as one of the significant deterioration processes in many steel structures. Corrosion in structural steel is a surface phenomenon. Therefore, it is imperative to understand the underlying phenomena that affect the amount of corrosion incurred on the surface of steel. The corrosion incurred in structural steels is strongly influenced by water wettability and water wettability of structural steels is not completely understood in the literature.

The interaction between air, water and surface of steel is important in evaluating the wettability and corrosion induced on the surface of steel. Wettability or degree of wetness is the tendency of a liquid to maintain contact with a solid surface [35–37]. Generally, wettability of a surface is influenced by surface chemistry, free energy, surface morphology and properties of the liquid [38–40]. Wettability of a liquid is generally defined in terms of contact angle of the liquid drop [41]. Contact angle (θ_c) is defined as the angle that liquid-vapor interface makes with solid-liquid interface during wetting process, and is illustrated in Figure 6.1(b) [37]. Therefore, a high contact angle corresponds to a lower wettability and vice versa. Surfaces that possess a contact angle greater than 90° are referred to as hydrophobic surfaces whereas surfaces with contact angle less than 90° are referred to as hydrophilic surfaces [42,43]. In other words, hydrophobic surfaces have lower affinity for water whereas hydrophilic surfaces have high affinity for water [44]. It is evident that hydrophobicity or hydrophilicity of a surface will affect the water presence and hence will influence the degree of corrosion on the surface of steel.

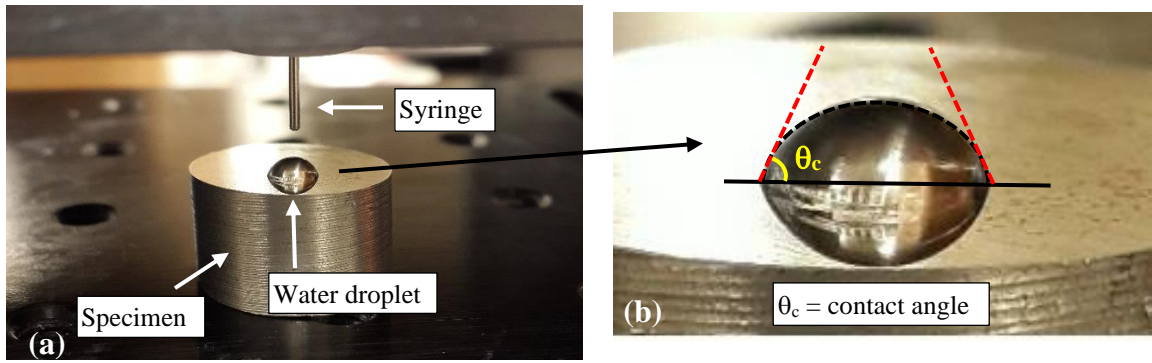


Figure 6.1. (a) Typical specimen during contact angle test, (b) Contact angle measurement.

Owing to several technological applications, hydrophobic and hydrophilic behavior of surfaces are extensively studied in the past few decades. To improve and optimize the behavior of surfaces, various surface treatments are developed. The objective of such surface treatment mainly involves altering the hydrophobic or hydrophilic nature of the surface to make it more efficient in its intended application. Extensive research in the recent past is conducted to develop superhydrophobic and superhydrophilic surfaces for different applications [40,42,44–55]. More recent research is directed towards developing surfaces with switchable wettability [56–59]. Many of these surfaces with tunable wettability are achieved by mimicking biological phenomena [45,59–61].

Structural steel is intrinsically a hydrophilic material. Surface tension of water is less than the surface energy of a clean steel surface, which results in spreading of water over steel surface [62,63]. However, steel surface is usually categorized as weakly hydrophilic [44] as it develops considerable contact angle in service conditions. This weak hydrophilic behavior of steel surface can be attributed to the formation of oxide layer either in monolayer form or thick oxide form due to its exposure to atmospheric moisture and oxygen [62]. The bonding interactions between these oxide layers and hydrogen of water avoid complete spreading of water on steel surface. Apart from surface chemistry, morphology of surface is another factor that affects the wettability

of steel surface. In particular, surface roughness is observed to influence the wettability of steel surface. Surface roughness acts as a porous medium for the liquid, as represented by roughness grooves in Figure 6.2. The apparent contact angle of the liquid on such a rough surface is affected by the relative surface energies of both solid and liquid phases. Depending on the interfacial tension between the rough surface and liquid, the liquid drop either follows the grooves and completely fills them up or the liquid drop get pinned to the groove edges due to entrapped air pockets in the grooves caused by surface roughness. The former case, also referred to as Wenzel state [64], is commonly observed in hydrophilic surfaces. The latter case, also referred to as Cassie-Baxter state [65], is typically observed in hydrophobic surfaces. Both Wenzel state and Cassie-Baxter state are illustrated in Figure 6.2(a) and Figure 6.2(b), respectively. In Wenzel state, the contact line between liquid and solid is completely characterized by liquid/solid surface tension. In Cassie-Baxter state, a composite interface comprising of both liquid/air and liquid/solid interfaces exist at the contact line between solid and liquid due to the entrapped air. The stability of both these states is affected by the geometry and homogeneity of roughness as well as the surface chemistries. It is observed that increase in roughness makes an intrinsically hydrophobic surface more hydrophobic and an intrinsically hydrophilic surface more hydrophilic [66,67]. Due to high surface energy of hydrophilic solid, surface/liquid interface follows the roughness of surface, thereby making the surface more wettable. Extensive research on wettability of rough surfaces, in general, has confirmed the role of roughness in altering the wettability of surfaces [42,66,68–70]. Recent research efforts have focused on investigating the effects of surface roughness on wettability of mild steel and low alloy steels [71–73].

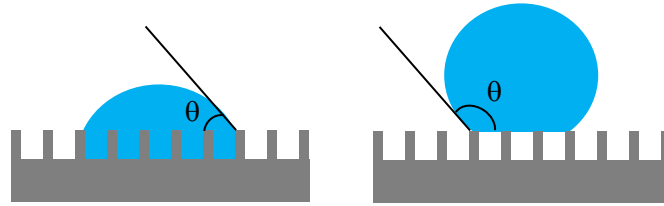


Figure 6.2. Illustration of wetting on rough surfaces (a) Wenzel state, (b) Cassie-Baxter state.

Controlling water wettability of steel surface is of primary interest due to its role in corrosion. To this end, researchers have studied the relationship between wettability and corrosion for steel subjected to different surface treatments [74–76]. Studies carried out on different types of stainless steels have concluded that improved corrosion resistance can be obtained by reducing the surface roughness [77–80]. However, the relationship between corrosion, surface roughness and water wettability is not fully explored for structural steels. The detrimental effects of corrosion in structural steels highlight the necessity to quantify the surface phenomena that play crucial role in corrosion. The current study aims to investigate the relation between surface roughness and corrosion with wettability of ASTM A36 steel.

6.2. Experimental Procedure

The procedures adopted for specimen preparation, contact angle tests, accelerated corrosion tests and surface roughness tests are elaborated in this section.

6.2.1. Specimen Preparation

The experimental specimens are machined from ASTM A36 cylindrical bar steel with diameters 19 mm and 10 mm. The cylindrical bar steel is cut to several specimens with a length of 10 mm each using low speed high precision cutting machine. In total, 24 number of such specimens are acquired from the cutting process. These specimens are further divided into two sets: set-A and set-B. Set-A comprises of 10 specimens and these specimens are used for investigating the influence of corrosion on wettability of ASTM A36 steel. Set-B comprises of

14 specimens and these specimens are used for investigating the influence of surface roughness on wettability of ASTM A36 steel. Followed by cutting, all these specimens have been degreased using abrasive paper, and then rinsed thoroughly with water and dried in hot air, in accordance with the cleaning procedures specified by ASTM G1 standard [81]. Each set-A specimen is prepared by successively grinding the surface using 120 and 400 grit silicon carbide (SiC) papers. Unlike set-A specimens, set-B specimens are grinded and polished to achieve different surface roughness levels. The smoothest specimen among set-B specimens (S0.5) is prepared by grinding the surface with 120, 400, 600, 800 and 1200 grit SiC papers (larger grit corresponds to finer surface roughness) successively followed by polishing with 5, 2.5 and 0.5 microns diamond paste. A typical set-B specimen, which is grinded beyond 120 grit SiC paper, has first been grinded using coarser SiC paper in the above mentioned order.

6.2.2. Contact Angle Test

Contact angle test is commonly used to characterize the wettability of a surface. The measurement of contact angle of a surface, as explained in Section 6.1, is illustrated in Figure 6.1. To measure the water wettability, the specimens prepared from the previous step are subjected to contact angle tests using a goniometer that is based on direct optical method. The experimental setup of goniometer is provided in Figure 6.3. A typical optical goniometer consists of a horizontal stage for mounting the specimen, a micrometer pipette and syringe for squirting a water droplet and an integrated camera for analyzing water droplet and measuring the contact angle. During the test, the horizontal stage with the mounted specimen is levelled and the syringe is brought close enough to the specimen surface using the knob provided on the equipment. The water drop is then impinged on to the specimen surface through the syringe and the contact angle is measured using the integrated camera. An average droplet volume of $16 \mu\text{l} \pm 1 \mu\text{l}$ is used in

this study. The contact angles have been measured for both set-A and set-B specimens at three distinct locations on surface of each specimen and the average of these three readings is evaluated. Afterwards, set-A specimens are subjected to accelerated corrosion and again the contact angles are measured following the same procedure, as explained above. A typical contact angle measuring test is shown in Figure 6.1(a). Contact angle test results are utilized to determine surface free energies of specimens using procedure that will be discussed in Section 6.3.5.

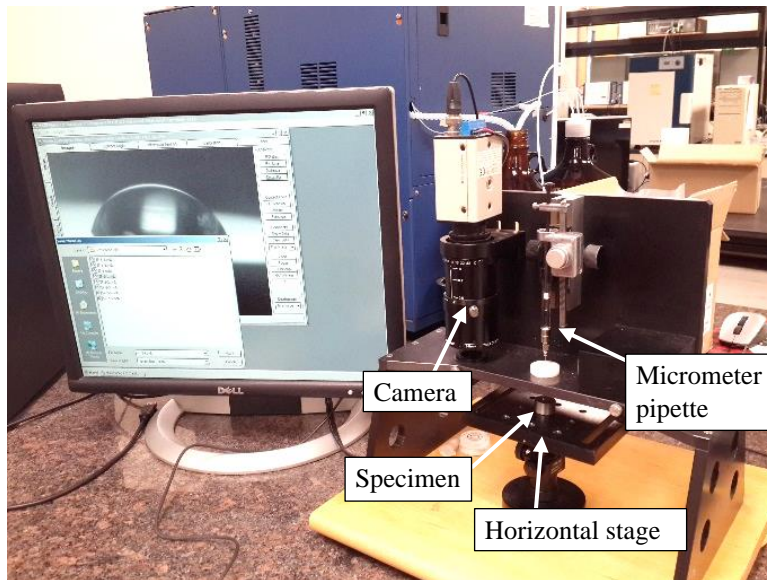


Figure 6.3. Optical goniometer for contact angle test.

6.2.3. Accelerated Corrosion Test

To evaluate the influence of corrosion on wettability of ASTM A36 steel, set-A specimens are subjected to accelerated corrosive environment. The accelerated corrosion test is carried out in accordance with ISO 14993 specifications [82]. ISO 14993 corrosion test is chosen in this study as this procedure effectively simulates corrosion that occurs in outdoor environments. In addition to this, ISO 14993 test can be conveniently conducted on smaller specimens that are used in the current study. This test method involves exposure of test

specimens to a cycle of salt solution mist (50 g/l NaCl solution), drying conditions, and periods of high humidity that are maintained inside a salt spray chamber. The test setup consists of a salt spray chamber with provisions for spraying salt solution and adjusting temperature and humidity. A typical cycle in the salt spray chamber consists of 2 hours of salt mist spray, 4 hours of dry conditions and 2 hours of wet conditions. Prior to the implementation of this procedure, the set-A specimens are cleaned using the procedures specified in Section 6.2.1 to remove any contaminants. Furthermore, mass and surface area of each specimen is determined. The specimens are then glued to panels and placed in the salt spray chamber such that the panels make an angle of 20° to the vertical, as shown in Figure 6.4. In accordance with the specifications provided in ISO 14993 [81] and ASTM B117 [83], adequate amount of salt solution is maintained in the salt reservoir to ensure constant supply of salt spray throughout the test period. In this study, exposure to corrosive environment ranged from 4 hours to 76 hours. The details of various testing conditions adopted in this study are summarized in Table 6.1. Moreover, the corrosion initiation and propagation mechanism is also discussed. To characterize the morphology of corrosion products, scanning electron microscopy (SEM) and energy-dispersive X-ray spectroscopy (EDS) analysis are carried out. After subjecting specimens to target corrosion exposure, the specimens are removed from the salt spray chamber, cleaned gently with warm water (with temperature of 35 °C) to remove traces of salt and then are used to evaluate the amount of corrosion, in accordance with ASTM G1 [81] and ASTM B117 [83] specifications.

Table 6.1. Testing conditions for ISO 14993 accelerated corrosion test.

<u>Salt mist conditions</u>	Temperature = 35°C, salt solution = NaCl (50 g/l)
<u>Dry conditions</u>	Temperature = 60°C, relative humidity < 30%
<u>Wet conditions</u>	Temperature = 50°C, relative humidity > 95%

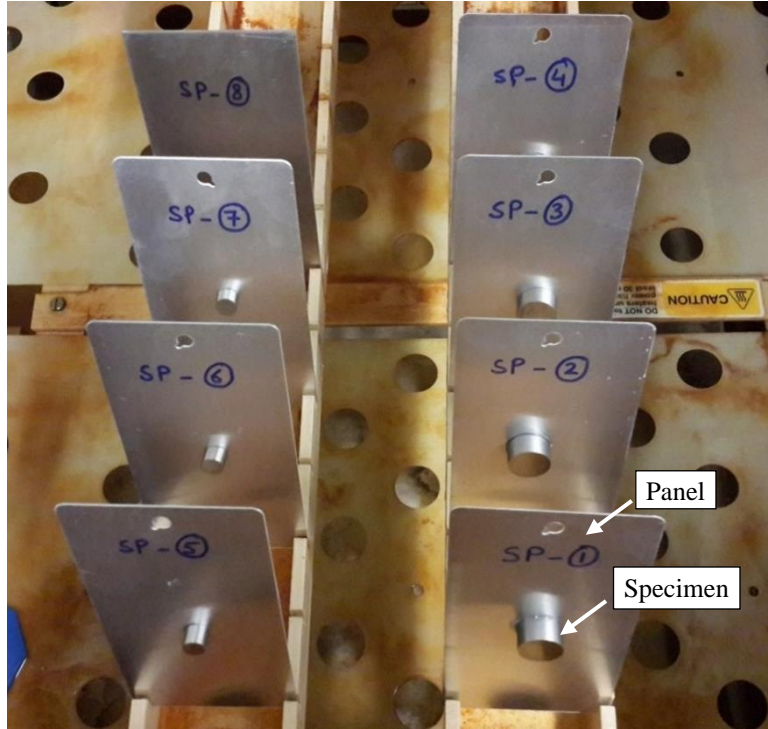


Figure 6.4. Specimens placed at 20° angle inside salt spray chamber.

6.2.4. Surface Roughness Test

To investigate the relationship between surface roughness induced by either corrosion or plain grinding and polishing, and wettability, surface roughness evaluation is carried out for both set-A and set-B specimens. Surface roughness of specimens is expressed in the form of roughness average parameter (R_a) herein. Roughness average (R_a) is commonly used to characterize overall roughness of a surface [84–86]. Roughness average (R_a) is defined as the arithmetic average of the absolute values over roughness profile ordinates and is calculated as follows [87]:

$$R_a = \frac{1}{l} \int_0^l |Z(x)| dx \quad (6.1)$$

where, l is the sampling length and Z is the profile height. The choice of R_a in this study is adopted for technical reasons as well as convenience of application. Among other commonly used surface roughness parameters (root mean square roughness (R_q), mean surface depth (R_z))

and maximum peak to valley height (R_t), R_a is well suited to quantify the influence of surface roughness on water wettability. Water contact angle is influenced by the interfacial tension which coincide with entire surface profile rather than locations of mean depth and maximum peak valley heights. Hence, it is imperative to take into account the average roughness variation of the entire surface profile. The choice of R_a fulfills this requirement. Secondly, R_a provides a more convenient description of height variations in the surface and is particularly suitable for surfaces that are machined or grinded, using a consistent technique. Keeping these advantages in mind, R_a surface parameter is chosen in this study. Apart from R_a , other surface roughness parameters were also calculated as part of this study that include root mean square roughness (R_q), mean surface depth (R_z) and maximum peak to valley height (R_t). However, only R_a is reported due to its importance and utility in the context of this study. For set-A specimens (subjected to different corrosion durations), 2D profiles and roughness average (R_a) values are evaluated using KLA-Tencor's P-15 Longscan Contact Stylus Profiler, as shown in Figure 6.5. Stylus profiler consists of an adjustable horizontal stage for mounting specimen, an optical assembly and stylus. The stylus moves along a scan length to acquire surface height variations. To minimize the errors that may arise due to non-uniform nature of corrosion on specimen's surface, a sufficiently high scanning length of 8.00 mm is selected. For each specimen, scans are taken at three distinct locations. Scanning locations are selected across the centerline of the specimens and between centerline and periphery of the specimens. These scanning locations approximately cover the locations contact angles are recorded for test specimens. Moreover, median smoothing filter was applied on scan data to minimize errors that may arise due to noise and spikes in data. For set-B specimens (uncorroded grinded and polished specimens), both 3D and 2D surface profiles and roughness average (R_a) values are evaluated using interferometry

based WykoTM NT3300 Non-Contact Optical Profiler, as shown in Figure 6.6. The roughness average for set-B specimen is calculated using a relation in accordance with ASME B46.1 [88]:

$$R_a = \frac{1}{MN} \sum_{i=1}^M \sum_{j=1}^N |Z_{ji}| \quad (6.2)$$

where, M and N are number of data points in X and Y directions, respectively and Z_{ji} is the surface height at a point relative to the mean plane. The optical profiler consists of adjustable horizontal stage for mounting specimen, optical assembly containing objective, reference mirror and beam splitter, and control interface for adjusting the stage and objective positions and focus. Contrary to corroded specimens, un-corroded specimens that are grinded and polished have relatively uniform roughness. Due to good repeatability of surface roughness in grinded and polished test specimens, a scanning area of $600 \mu\text{m} \times 600 \mu\text{m}$ is selected. Roughness values are calculated at three different locations on a typical specimen and average roughness values are then evaluated. To characterize the surface roughness of set-A specimens (corroded specimens), stylus profile is used as surfaces of set-A specimens are highly non-uniform due to corrosion. For set-B specimens (uncorroded specimens) the non-contact optical profiler is preferred, as these surfaces have relatively smooth and uniform roughness when compared to set-A specimens.

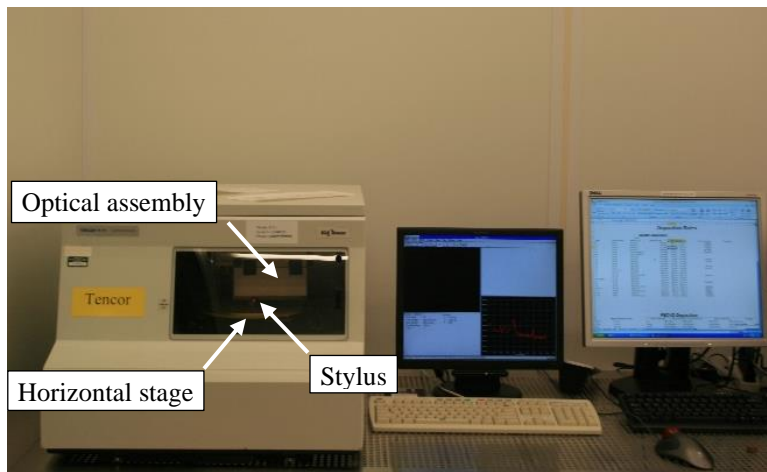


Figure 6.5. Stylus profiler for measuring surface roughness of corroded specimens.

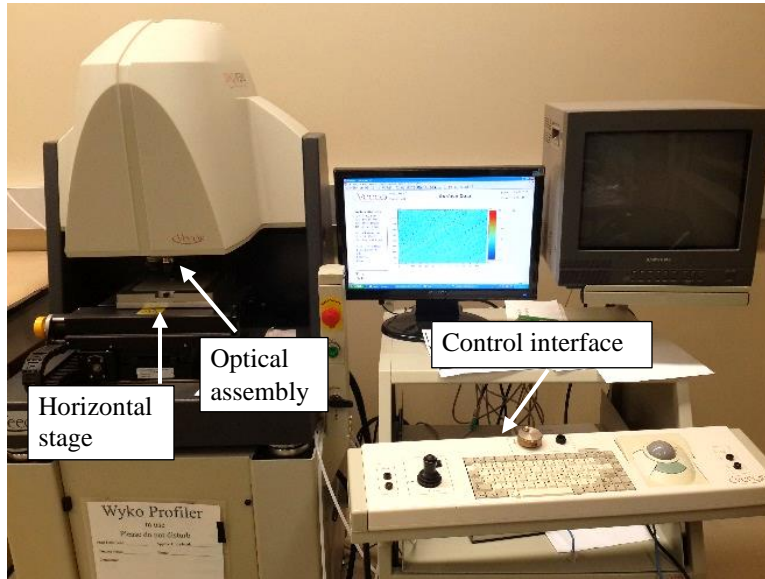


Figure 6.6. Non-contact optical profiler for measuring surface roughness of uncorroded specimens.

6.3. Results and Discussions

6.3.1. Contact Angle and Corrosion

In this section, the influence of corrosion on contact angle is investigated for ASTM A36 steel. This study is conducted on 10 set-A specimens that are pre-grounded using grit 400 SiC paper according to the grinding and polishing procedure provided in Section 6.2.1. The 10 set-A specimens are regrouped in to five sets of two specimens each and are designated as follows: S*-# where * represents the corrosion exposure time in hours and # designates the specimen number. For example, S16-2 represents the second specimen out of the two specimens that are exposed to corrosive environment for 16 hours. The contact angle is measured at three different locations for all set-A specimens using the procedure described in Section 6.2.2. The average of these three contact angle values is considered as the contact angle of a specimen. Typical images of water droplets on the surface of each specimen before corrosion exposure are shown in Figure 6.7. The contact angles for each set-A specimen prior to subjecting them to corrosion are

provided in Table 6.2. The average contact angles for set-A specimens ranged from 74.06° to 79.35° with an average contact angle of 76.71°. The maximum and minimum contact angles are observed to be within 3.44 % of the mean contact angle. For specimen S48-1, a relatively lower contact angle of 71.91° is observed at location 1. Similarly, for specimen S76-1, a relatively higher contact angle of 81.89° is observed. These variations in contact angles at different locations and in different specimens can be attributed to slight local variation in the surface roughness of these specimens. All contact angles are evaluated based on spherical fit of sessile drop at initial stage. Initial stage herein refers to first 5 seconds after impingement of water droplets on the surface of specimen.

Table 6.2. Contact angles of set-A test specimens before corrosion exposure.

Specimen ID	Polishing protocol	Contact angle (degrees)			Average contact angle (degrees)
		Location 1	Location 2	Location 3	
S4-1	Grit 400	77.14	75.72	73.95	75.60
S4-2	Grit 400	75.5	74.17	73.69	74.45
S16-1	Grit 400	79.50	77.29	76.72	77.84
S16-2	Grit 400	77.36	74.51	76.49	76.12
S32-1	Grit 400	76.23	77.96	78.08	77.42
S32-2	Grit 400	74.25	74.36	81.08	76.55
S48-1	Grit 400	71.91	77.69	72.58	74.06
S48-2	Grit 400	77.29	79.71	78.48	78.49
S76-1	Grit 400	78.09	81.89	78.06	79.35
S76-2	Grit 400	76.86	77.11	77.09	77.02

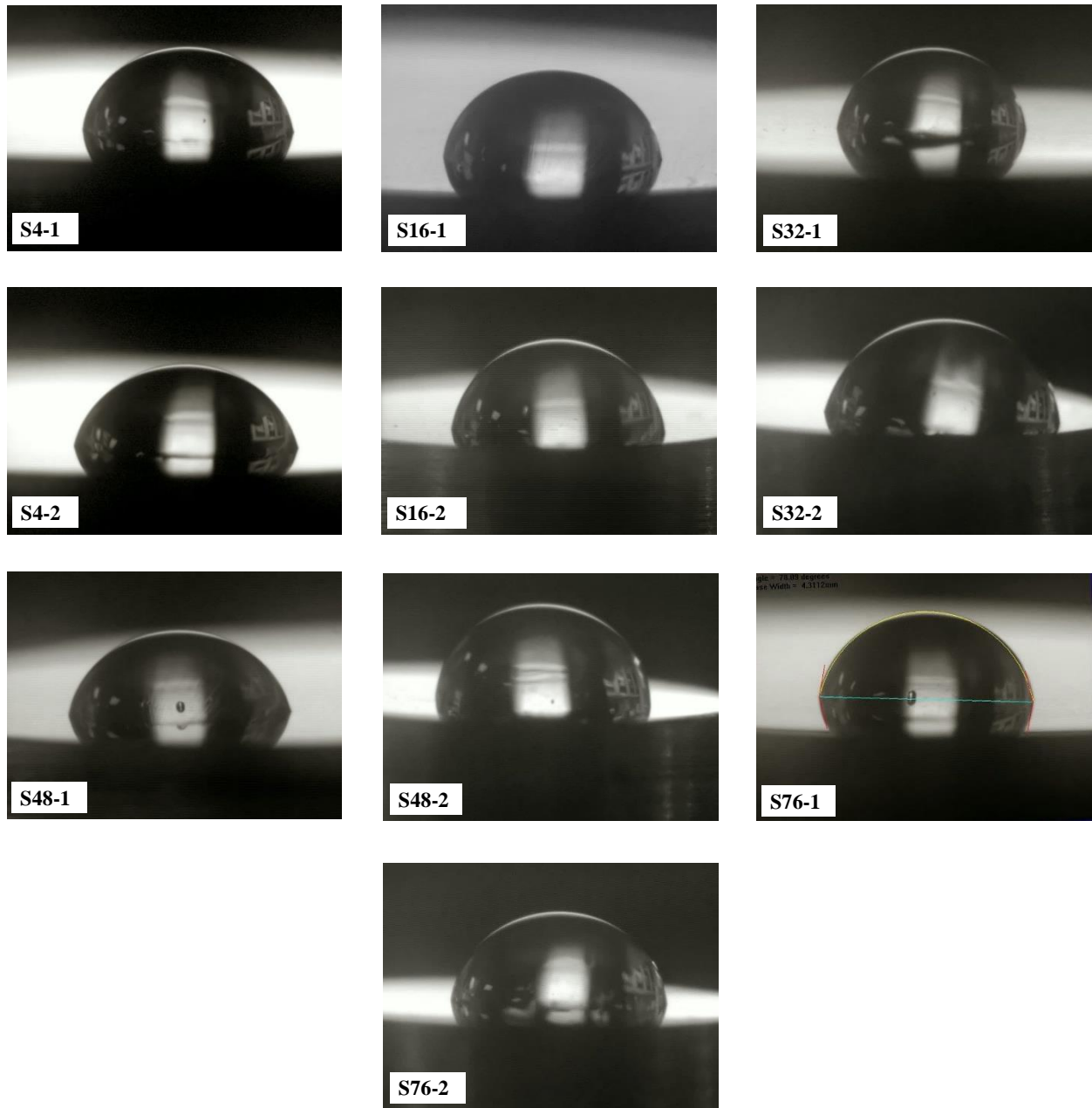


Figure 6.7. Typical images of water droplets on surfaces of specimens before corrosion.

The contact angles are measured again for each set-A specimen, after subjecting them to accelerated corrosion using accelerated corrosion test procedure described in Section 6.2.3.

During initial phases of corrosion, concentration cells (cathodic spots surrounding anodic spots)

are formed on the specimen's surface in the presence of water. The steel starts to corrode through anodic dissolution of iron (Eq. 6.3) and cathodic reduction of oxygen (Eq. 6.4):



The hydroxide ions formed during cathodic reaction then react with iron ions at anodic spots and result in iron (II) hydroxide (Eq. 5):



The oxidation and subsequent precipitation of iron (II) hydroxide lead to the formation of γ -FeOOH (also called lepidocrocite [89]). Further oxidation of γ -FeOOH results in the formation of a more stable α -FeOOH which is also referred to as goethite [89]. Optical micrographs of initial phase of corrosion in test specimens are shown in Figure 6.8. In Figure 6.8, initial corrosion is manifested in the form of pitting corrosion and uniform corrosion. The morphology and chemical composition of these rust layers are further discussed in Section 6.3.6.

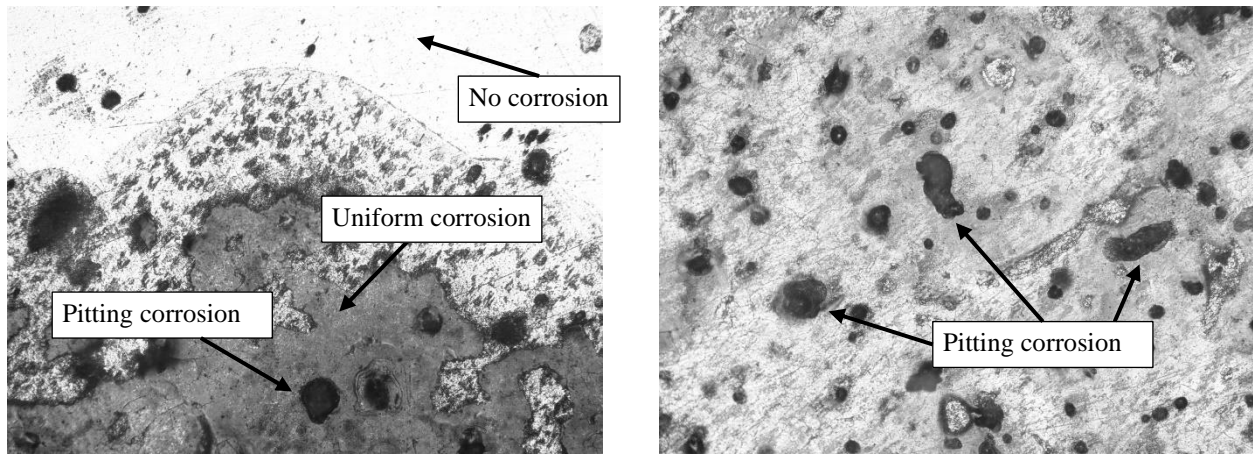


Figure 6.8. Optical micrographs for specimens during initial phase of corrosion.

After corrosion, the specimens are cleaned gently with warm water to remove salt traces and contact angles are then evaluated at three different locations. The corresponding contact angles are provided in Table 6.3. Typical images of water droplets on the surface of each

specimen after corrosion exposure are shown in Figure 6.9. An average contact angle of 45.56° is observed for S4-1 and S4-2 specimens with least corrosion exposure (4 hours). For specimens S76-1 and S76-2, that are subjected to highest corrosion exposure of 76 hours, an average contact angle of 14.73° is observed. Corrosion exposure of 76 hours results in 80% decrease in the initial contact angle. Contact angles are found to decrease by 40% of initial contact angle after the specimens are subjected to corrosion exposure of just 4 hours. Contact angles are plotted as a function of corrosion exposure time in Figure 6.10. The increase in corrosion exposure results in decrease in contact angle and hence increase in the hydrophilic nature of A36 steel. It can be observed that significant decrease in contact angle occurs during initial phase of corrosion (i.e. first 16 hours of corrosion exposure). Beyond 16 hours of exposure, the contact angles continue to decrease with a relatively slower rate as compared to initial phase of exposure. The decrease in contact angle can be visually observed in Figure 6.9. Shape of water droplets on surface of test specimens before corrosion is largely uniform. However, with increase in corrosion exposure, the uniformity of water droplets shapes changes substantially. The specimens that are exposed to higher corrosion rates developed pitting corrosion, which leads to increase in non-uniformity of water droplet shape across the surface of specimen.

Table 6.3. Contact angles of set-A test specimens after corrosion exposure.

Specimen ID	Corrosion exposure (h)	Contact angle (degrees)			Average contact angle (degrees)
		Location 1	Location 2	Location 3	
S4-1	4	49.04	43.72	44.21	45.66
S4-2	4	43.72	48.23	44.74	45.46
S16-1	16	34.37	31.54	32.66	32.86
S16-2	16	31.12	33.31	29.13	31.19
S32-1	32	29.96	28.58	29.15	29.23
S32-2	32	23.66	28.47	29.68	27.27
S48-1	48	21.95	19.85	23.19	21.66
S48-2	48	23.58	17.32	24.38	21.76
S76-1	76	16.24	14.27	14.99	15.17
S76-2	76	14.16	13.45	15.26	14.29

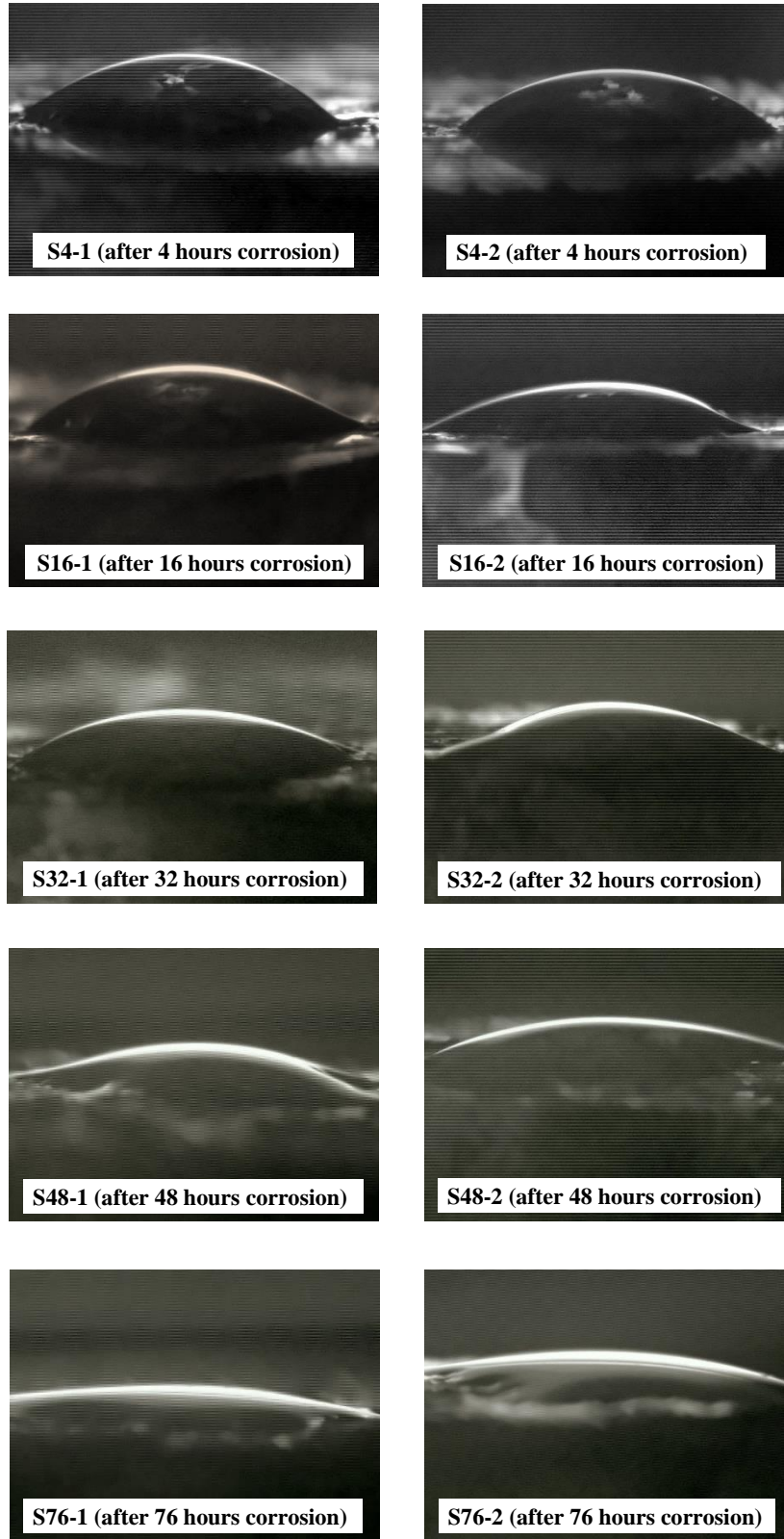


Figure 6.9. Variation in contact angle of specimens subjected to different corrosion durations.

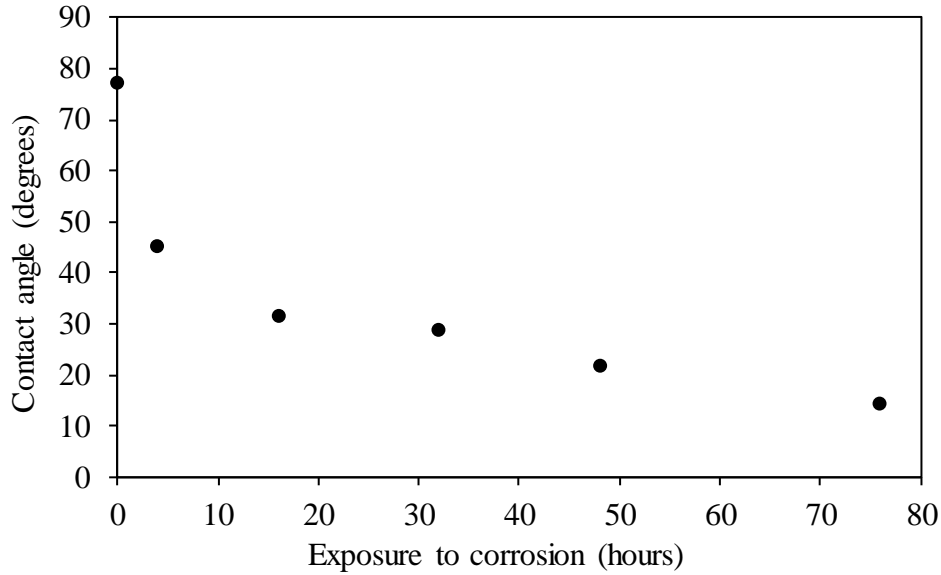


Figure 6.10. Corrosion exposure time in hours versus contact angle in degrees.

To evaluate the relationship between rate of corrosion and contact angle, rate of corrosion incurred in each set-A specimen is evaluated. To this end, rust is removed from specimens by placing them in an acidic solution for 10 minutes. The acidic solution is prepared using 500 ml of hydrochloric acid (HCl), 3.5 g of hexamethylene tetramine and reagent water to make a 1000 ml solution, in accordance with the chemical cleaning procedure specified in ASTM G1 standard. The specimens are then thoroughly rinsed with warm water and air-dried. Mass loss in each specimen is determined after removal of rust. There are number of methods to determine the amount of corrosion in carbon steels. Corrosion can be evaluated in the form of reduction in thickness using empirical equations proposed in [1,91,92]. The generic form of such empirical relations is as follows:

$$T = At^B \quad (6.6)$$

where, T is thickness reduction in μm , t is corrosion exposure time, and A and B are constants.

The amount of corrosion can also be expressed in the form of corrosion mass loss ratio [19,21].

To be consistent with the ASTM protocols, the rates of corrosion in this study are evaluated using the following relation specified in ASTM G1:

$$\text{Corrosion Rate} = \frac{K \times W}{A \times T \times D} \quad (6.7)$$

where, K is a constant, that depends on units of corrosion rate (for mm/y, $K = 8.76 \times 10^4$), T = time of exposure in hours, A is the area in cm^2 , W is the mass loss in grams, and D is the density of ASTM A36 steel in g/cm^3 (7.85 g/cm^3). Eq. (6.7) gives a reasonable estimate of corrosion rates for corrosion that is mostly uniform in nature. However, it should be noted the corrosion rates obtained from the above equation cannot be compared with corrosion rates obtained using regression based empirical relations and corrosion mass loss ratios, as discussed above. Details of corrosion test protocols and subsequent rate of corrosion in each set-A specimens are presented in Table 6.4. Specimens S76-1 and S76-2 with highest corrosion exposure (76 hours) have highest average corrosion rates of 1.76 mm/y and 1.40 mm/y, respectively. Specimens S4-1 and S4-2 with least corrosion exposure (4 hours) have lowest average corrosion rates of 0.19 mm/y and 0.13 mm/y, respectively. Rate of corrosion of specimens with similar corrosion exposure are averaged and plotted as function of time, as shown in Figure 6.11. From Figure 6.11, rate of corrosion is observed to increase linearly with increase in corrosion exposure time. Contact angles are observed to decrease with increase in the rate of corrosion in steel. Significant decrease in contact angle occurs till 0.5 mm/y corrosion rate. Initiation of corrosion is therefore of high importance due to its vital role in drastically increasing the wettability of steel. Specimens with high corrosion exposure have highly non-uniform and rough surfaces as compared to specimens with less corrosion exposure. In this study, it is hypothesized that the increase in wettability of specimens with high corrosion exposure can be attributed to their high

surface roughness based on literature review [66,68,69]. This hypothesis is verified in the next section.

Table 6.4. Rate of corrosion in different set-A test specimens.

Specimen ID	Corrosion exposure (h)	Area (cm ²)	Weight before corrosion (g)	Weight after corrosion (g)	Weight loss (g)	Rate of corrosion (mm/year)
S4-1	4	8.1906	19.9134	19.9128	0.0006	0.20
S4-2	4	8.3129	19.7872	19.7868	0.0004	0.13
S16-1	16	8.3174	20.2859	20.2809	0.0050	0.42
S16-2	16	3.1603	4.6298	4.6287	0.0011	0.24
S32-1	32	8.3614	20.4297	20.409	0.0207	0.86
S32-2	32	3.1994	4.7338	4.7292	0.0046	0.50
S48-1	48	8.5928	21.2256	21.1816	0.0440	1.19
S48-2	48	3.1996	4.7319	4.7190	0.0129	0.94
S76-1	76	8.8101	22.0672	21.9618	0.1054	1.76
S76-2	76	3.4885	5.1830	5.1498	0.0332	1.40

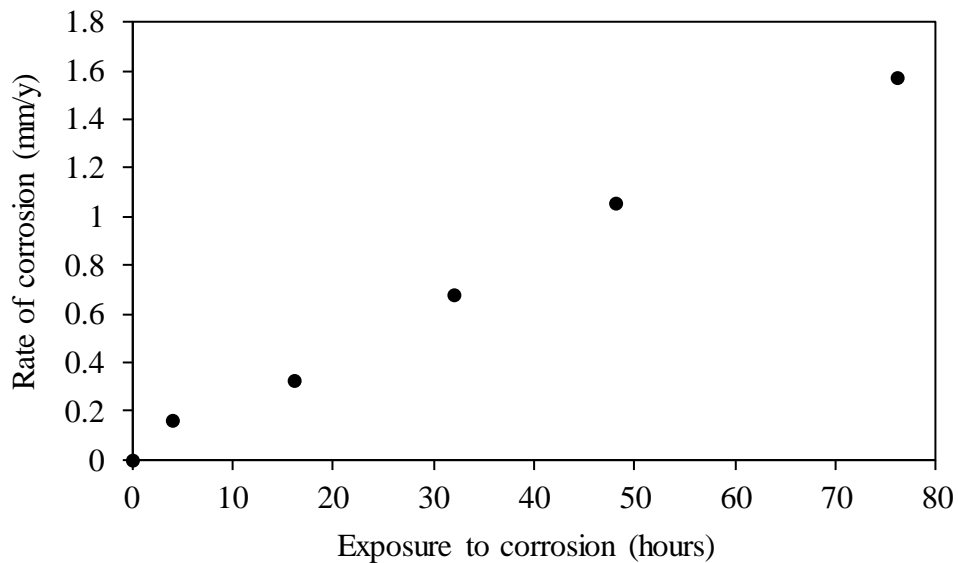


Figure 6.11. Corrosion exposure versus rate of corrosion.

6.3.2. Contact Angle and Surface Roughness Due to Corrosion

Surface roughness of set-A specimens subjected to different corrosion durations are determined to quantify the effects of surface roughness due to corrosion on wettability of steel.

To this end, 2D surface profiles and roughness average parameters (R_a) are evaluated for each

set-A specimen using the procedure described in Section 6.2.4. 2D surface profiles measured for each representative set-A specimens subjected to different corrosion durations are shown in Figure 6.12. As seen in Figure 6.12, variability in surface roughness of specimens becomes more prominent as exposure to corrosion increases. This increase in surface roughness variability can be attributed to the formation of pitting corrosion on surface of the specimens exposed to longer corrosion exposures. These surface profiles further explain the increase in non-uniformity of water droplets with increase in corrosion exposure as noticed in Figure 6.9. Average roughness values (R_a) of test specimens, calculated using Eq. (6.1), in accordance with the ASME B46.1 [88] and [87], are provided in Table 6.5. R_a values are calculated based on 2D surface roughness profiles evaluated at three different locations on surface of specimen. Average contact angles after corrosion exposure are plotted against corresponding surface roughness, as shown in Figure 6.13. From Figure 6.13, contact angles are observed to decrease with increase in surface roughness of corroded specimens. It is observed that increase in corrosion has led to increase in surface roughness, which in turn leads to decrease in contact angle. Therefore, the increase in hydrophilic nature of steel upon exposure to corrosion can be attributed to increase in surface roughness of steel specimens. The roughness caused by initial corrosion increase the wettability further with expedition of corrosion. These results confirm that wettability of ASTM A36 steel is improved by formation of rust which resulted in high surface roughness. However, these results do not quantify the effect of surface roughness on the wettability of steel in absence of rust. Therefore, further assessment is required to investigate the effects of surface roughness of uncorroded (bare) steel on wettability.

Table 6.5. Surface roughness of representative set-A test specimens after corrosion exposure.

Specimen ID	Corrosion exposure (h)	Roughness average, R_a (μm)			Average, R_a (μm)
		Location 1	Location 2	Location 3	
S4	4	2.03	3.60	2.81	2.81
S16	16	8.75	8.63	10.70	9.36
S32	32	9.88	19.09	17.20	15.39
S48	48	25.69	25.15	30.43	27.09
S76	76	67.36	55.40	55.87	59.54

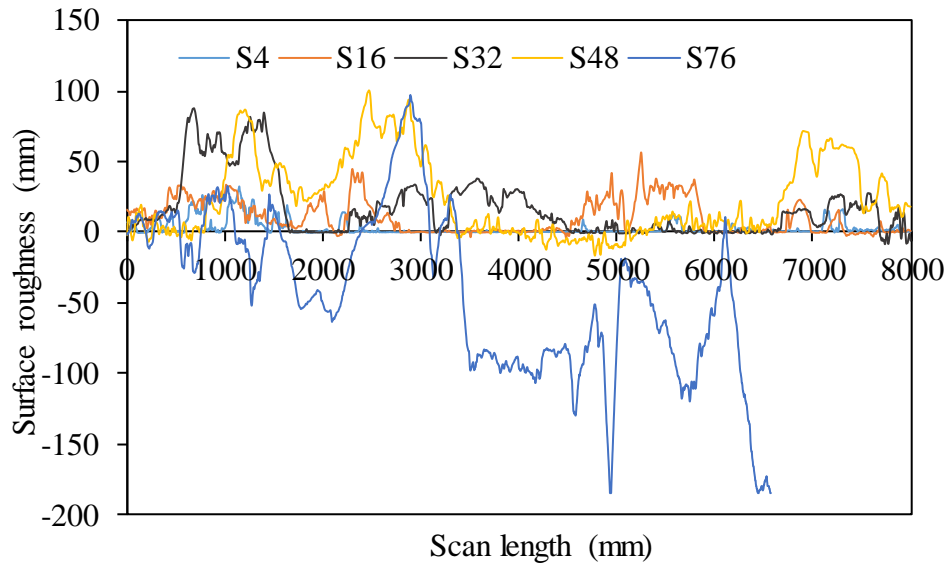


Figure 6.12. Surface roughness profiles of specimens subjected to different corrosion durations.

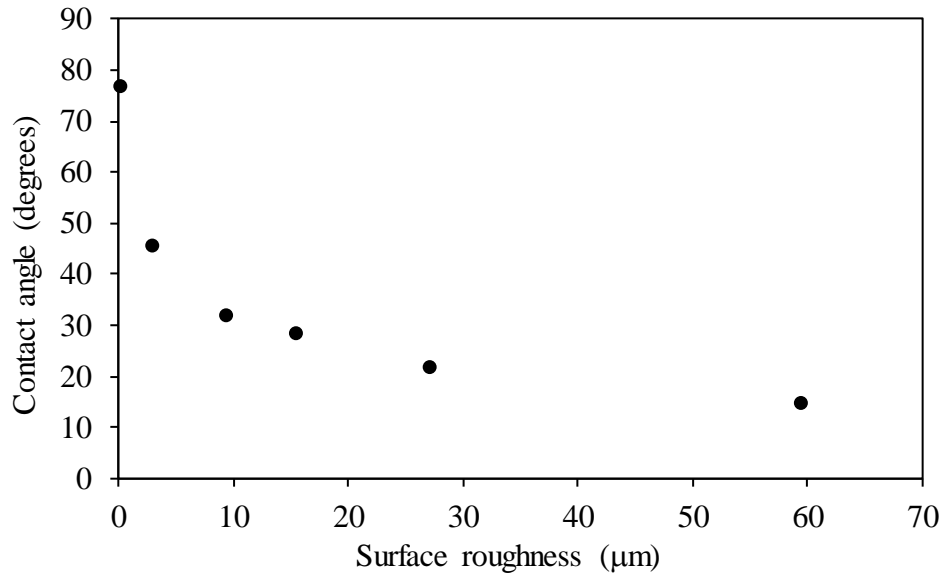


Figure 6.13. Surface roughness versus contact angle of test specimens subjected to corrosion.

6.3.3. Contact Angle and Surface Roughness of Bare Steel

In this section, the influence of surface roughness of un-corroded bare steel on contact angle is investigated for ASTM A36 steel. This study is conducted on 14 set-B specimens. The grinding and polishing protocols adopted for each specimen, as discussed in Section 6.2.1, are provided in Table 6.6 and Table 6.7. These 14 set-B specimens are regrouped in to seven sets of two specimens each and are designated as follows: S*-# where * represents the grit or diamond paste size up to which the specimen is grinded and polished and # designates the specimen number. In other words, S0.5-2 represents the second specimen out of the two specimens that is polished using successive finer grit SiC papers in the following order: 120, 400, 800, 1200 grit and 5 micron, 2.5 micron and 0.5 micron diamond pastes. 2D and 3D surface profiles of these specimens are extracted as described in Section 6.2.4, and are provided in Figure 6.14, Figure 6.15 and Figure 16. The average roughness values calculated for each set-B specimen, using Eq. (2), are given in Table 6.6. Roughness average values ranged from 495.78 nm for the specimen S120-2 to 12.40 nm for specimen S0.5. Contact angles measured at three different locations for each set-B specimen using the procedure discussed in Section 6.2.2 are given in Table 6.7. Typical images of water droplets on surface of the specimen during contact angle testing are given in Figure 6.17. An average contact angle of 71.19° is observed for S120-1 and S120-2 specimens with highest roughness average ($R_a = 495.78$ nm). For specimens S0.5-1 and S0.5-2, having lowest roughness average ($R_a = 12.40$ nm), an average contact angle of 88.98° is observed. From Table 6.7, contact angles are observed to increase with decrease in roughness. The rate of increase in contact angle is more in case of specimens polished below 50 nm. For quantifying the relationship between surface roughness and contact angle, the roughness average parameter, R_a , is plotted against contact angle, as shown in Figure 6.18. From Figure 6.18,

contact angles are observed to decrease with increase in surface roughness. Similarly, decreasing trend in contact angle is observed for surface roughness occurring due to corrosion, as shown in

Figure 6.13.

Table 6.6. Surface roughness of representative set-B test specimens polished to different grit sizes.

Specimen ID	Polishing protocol	Roughness average, R_a (nm)			Average R_a (nm)
		Location 1	Location 2	Location 3	
S120-2	Grit 120	427.12	630.00	430.22	495.78
S400-2	Grit 400	138.88	132.20	144.22	138.43
S800-2	Grit 800	41.40	33.13	34.38	36.30
S1200-2	Grit 1200	27.14	22.16	31.93	27.08
S5-2	5 Microns	25.99	20.31	21.24	22.51
S2.5-2	2.5 Microns	14.62	18.00	14.59	15.74
S0.5-2	0.5 Microns	10.90	15.12	11.19	12.40

Table 6.7. Contact angles of set-B test specimens polished to different grit sizes.

Specimen ID	Polishing protocols	Contact angle (degrees)			Average contact angle (degrees)
		Location 1	Location 2	Location 3	
S120-1	Grit 120	68.85	68.87	66.97	68.23
S120-2	Grit 120	72.99	74.44	75	74.14
S400-1	Grit 400	77.14	75.72	73.95	75.60
S400-2	Grit 400	75.5	74.17	73.69	74.45
S800-1	Grit 800	77.02	78.93	74.84	76.93
S800-2	Grit 800	74.78	76.43	78.47	76.56
S1200-1	Grit 1200	79.23	78.27	79.46	78.99
S1200-2	Grit 1200	79.79	76.86	79.2	78.62
S5-1	5 Microns	80.8	80.17	81.83	80.93
S5-2	5 Microns	79.78	81.67	79.46	80.30
S2.5-1	2.5 Microns	85.14	83.24	85.49	84.62
S2.5-2	2.5 Microns	85.99	87.3	86.3	86.53
S0.5-1	0.5 Microns	90.45	89.64	90.14	90.08
S0.5-2	0.5 Microns	88.91	87.05	87.67	87.88

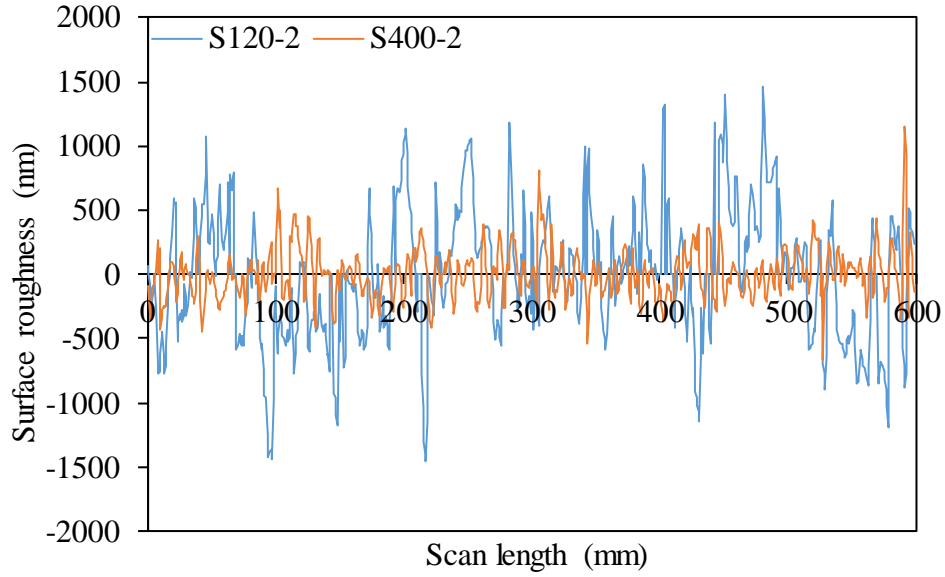


Figure 6.14. Surface roughness profiles of test specimens polished using 120 and 400 grit sizes.

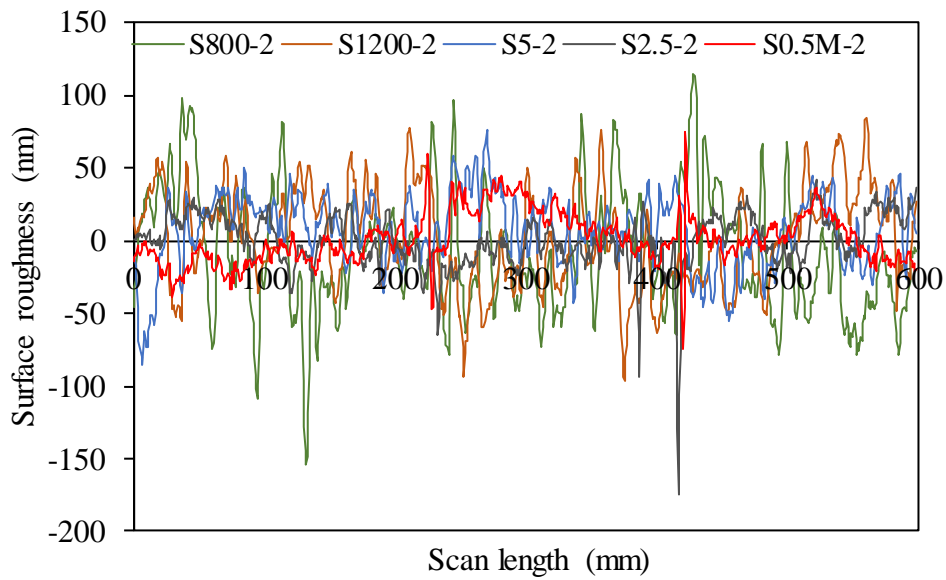


Figure 6.15. Surface roughness profiles of test specimens polished to grit sizes equal to or finer than 800 grit size.

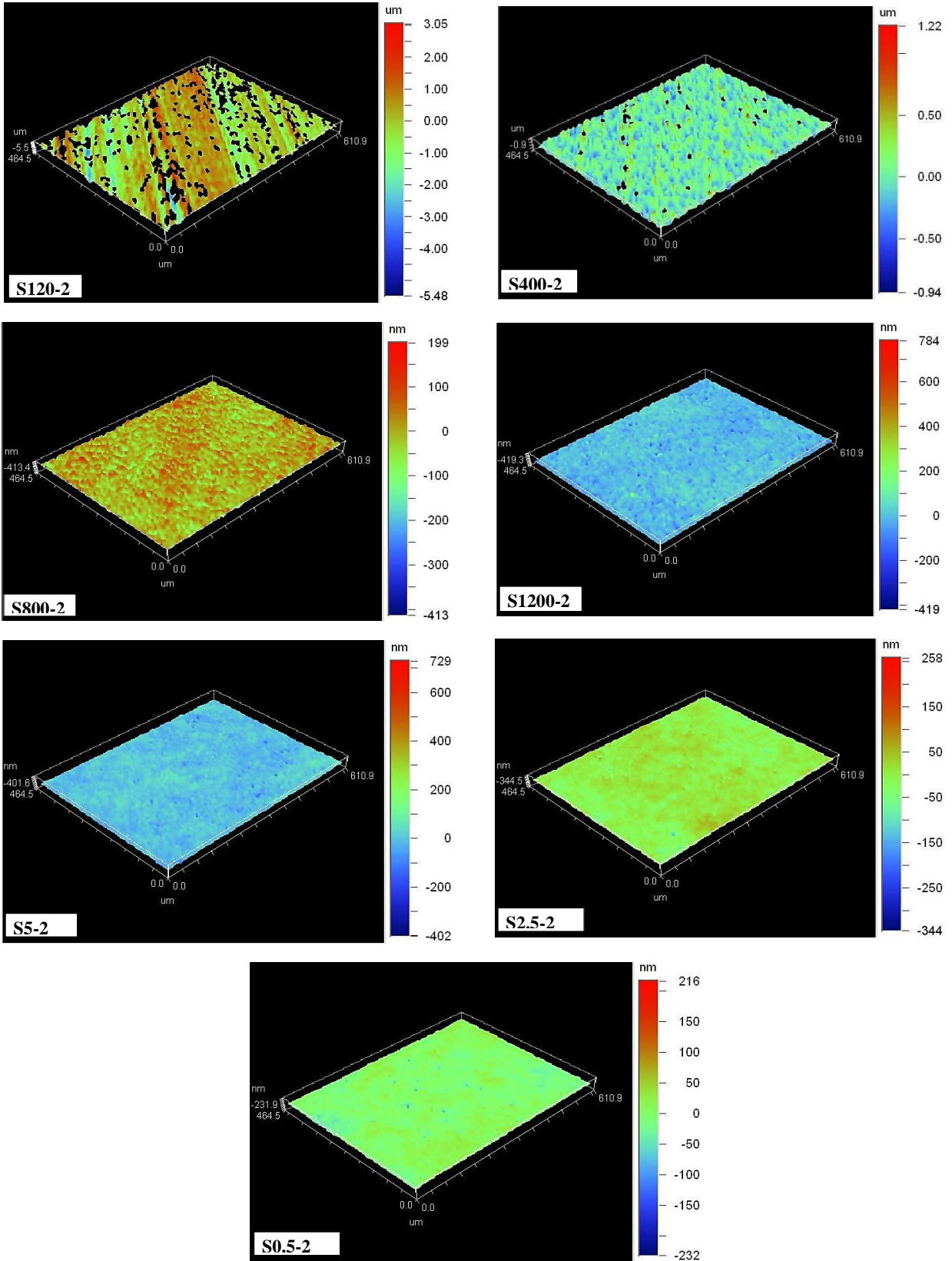


Figure 6.16. 3D surface profiles of test specimens polished to different grit sizes.

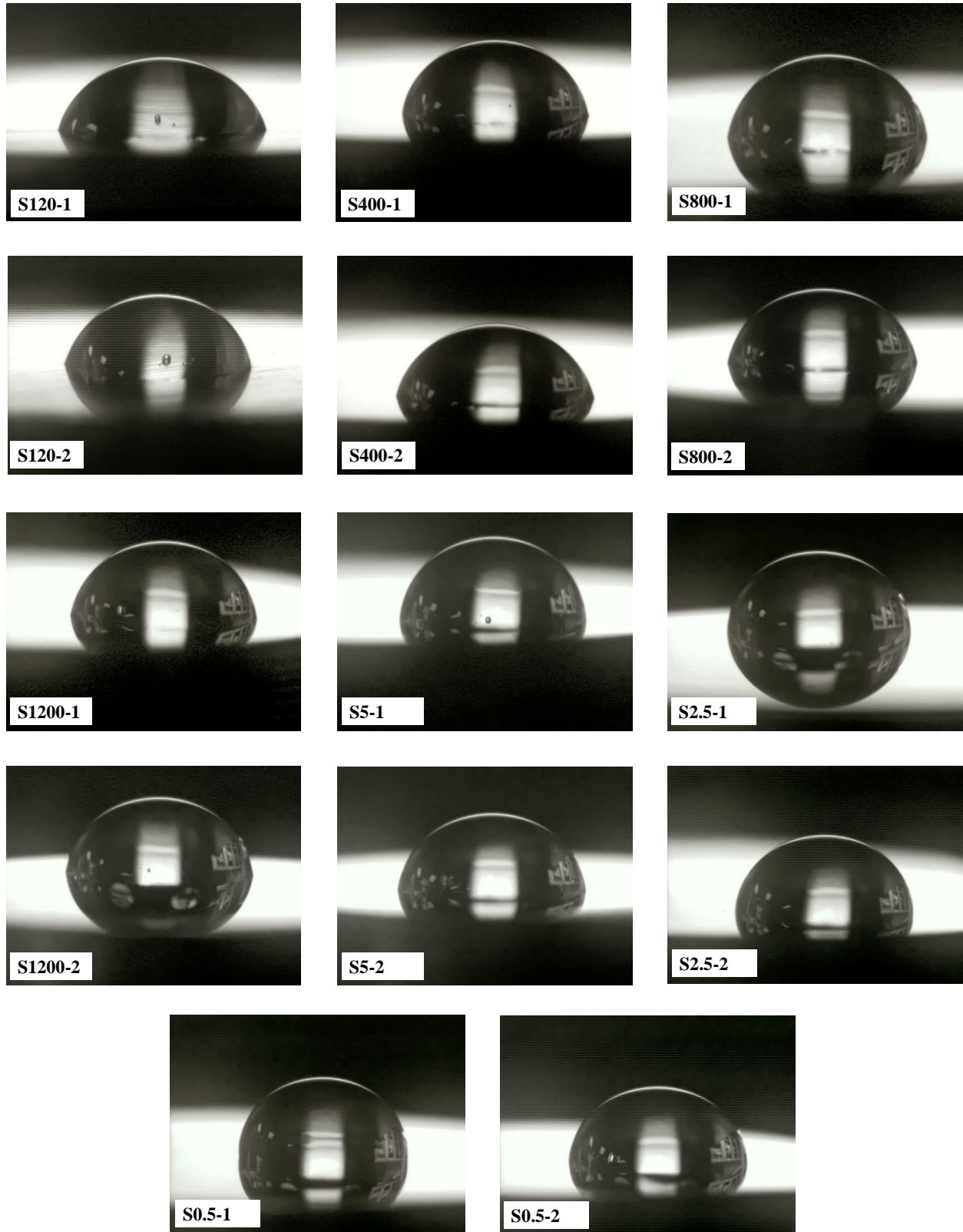


Figure 6.17. Typical images of water droplets on specimen's surfaces polished to different grit sizes.

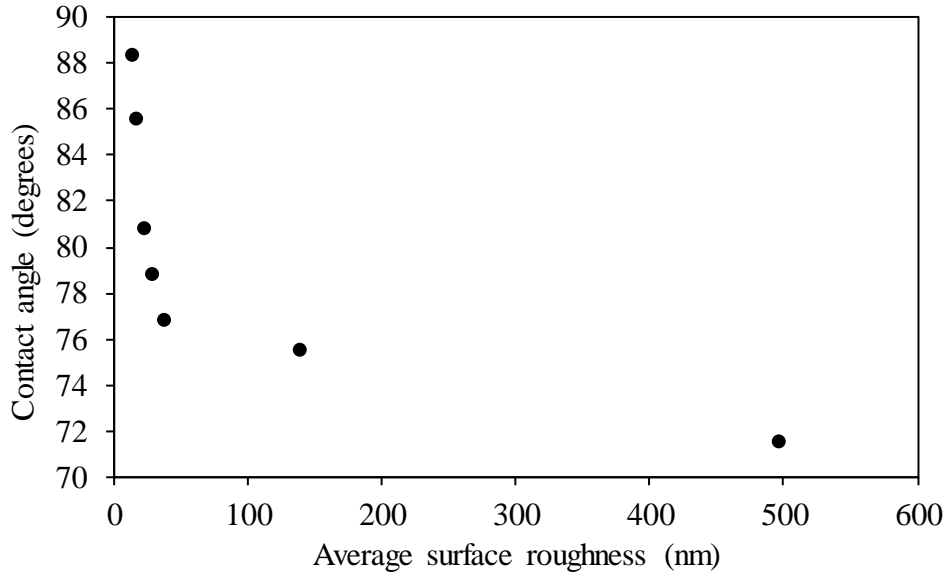


Figure 6.18. Surface roughness versus contact angle of test specimens polished to different grit sizes.

6.3.4. Surface Roughness and Corrosion

Results from previous sections indicate that increase in corrosion in ASTM A36 steel results in increase in surface roughness. Increase in surface roughness in turn increases the wettability of steel as concluded in Section 6.3.3. Hence, corrosion in ASTM A36 steel is influenced by surface roughness. To investigate the effect of surface roughness on corrosion, 3 uncorroded set-B specimens are subjected to 4 hours of accelerated corrosion using the procedure discussed in Section 6.2.3. These include specimen S120-2 (with highest surface roughness among all the set-B specimens) and specimens S2.5-2 and S0.5-2 (with lowest surface roughness among all set-A and set-B specimens). A small corrosion exposure duration of 4 hours is considered adequate for incurring visually differentiable corrosion rates in specimens studied herein. Figure 6.19 shows visual observation of these specimens after 4 hours of accelerated corrosion. It is observed that specimen S120-2 with high surface roughness value ($R_a = 495.78$ nm) experienced higher corrosion whereas specimens S2.5-2 and S0.5-2 with low surface roughness ($R_a = 15.74$ nm and $R_a = 12.40$ nm, respectively) experienced lower corrosion. These

results are in agreement with the results reported in the literature for Type 301, AISI 316 and AISI 304 stainless steels wherein decrease in surface roughness is observed to improve the corrosion resistance of these metals [77–79].

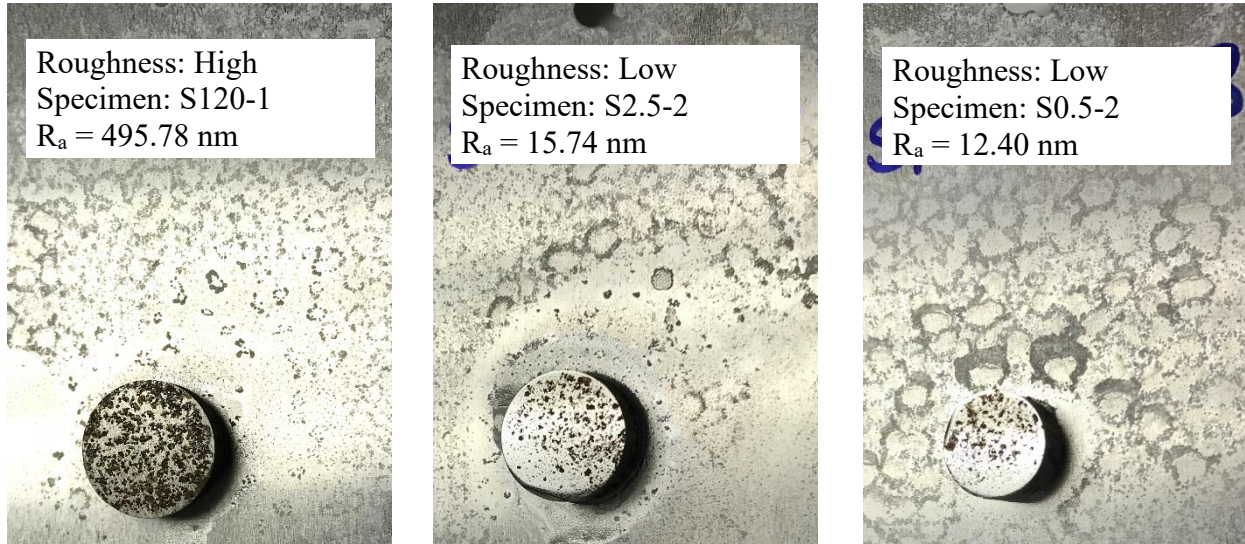


Figure 6.19. Visual comparison of corrosion on surfaces of most and least polished test specimens after 4 hours corrosion exposure (figure not to scale).

6.3.5. Surface Roughness, Wettability and Surface Energies

To understand the influence of surface roughness on surface energy and subsequent wetting potential of ASTM A36 steels, surface free energies of test specimens are determined using contact angle test results. Surface free energy of solid surfaces manifest the potential intermolecular interaction and the spreading potential of liquids on the solid surfaces. Numerous theoretical models are reported in the literature that are routinely used to determine the surface free energy and interfacial energy between liquid and solid surfaces using contact angle measurements [93–95]. These theoretical models require the use of contact angles measured using one or more liquids to characterize the surface free energy of a solid surface. In this study, the surface free energies of test specimens are determined using the following equation:

$$\gamma_s = \gamma_l(1 + \cos\theta)/2 \quad (6.8)$$

where γ_s = surface free energy of solids, γ_l = surface tension of the liquid (for water $\gamma_l = 72.8$ mJ/m²), and θ = contact angle formed by the liquid. Eq. 6.8 is derived by substituting the Antonov's rule (Eq. 6.10) into Young equation (Eq. 6.9) [96]:

Young equation:

$$\gamma_s = \gamma_{ls} + \gamma_l \cos\theta \quad (6.9)$$

Antonov rule:

$$\gamma_{ls} = \gamma_l - \gamma_s \quad (6.10)$$

where γ_{ls} = interfacial tension between the liquid and solid surface.

This approach facilitates the determination of surface free energy based on contact angles measured for a single liquid. The experimental validity of this method hinges on the assumption that dispersion forces hold significance in dictating the surface tension and the interfacial tension which holds true for the specimens studied herein. Surface free energies are determined for individual specimens and presented in Table 6.8. Moreover, average surface free energies corresponding to different surface roughness values are presented in Figure 6.20. As observed in Figure 6.20, surface free energy increases with increase in surface roughness. A sharp decrease in surface free energy is observed when surface roughness R_a of specimens decreases below 50 nm. The low surface energy increases the hydrophobic character of steel specimens as manifested by high contact angles for test specimens with $R_a < 50$ nm. Surface energy results of ASTM A36 steels are consistent with surface free energies that are reported for other type of steels that include AISI 52100 steel and AISI 304 stainless steel [97,98].

Table 6.8. Surface free energies of test specimens.

Specimen ID	Polishing protocols	Surface free energy (mj/m ²)			Average surface energy (mj/m ²)
		Location 1	Location 2	Location 3	
S120-1	Grit 120	49.53	49.52	50.64	49.90
S120-2	Grit 120	47.05	46.16	45.82	46.34
S400-1	Grit 400	44.50	45.38	46.46	45.45
S400-2	Grit 400	45.51	46.33	46.62	46.16
S800-1	Grit 800	44.58	43.39	45.92	44.63
S800-2	Grit 800	45.96	44.94	43.68	44.86
S1200-1	Grit 1200	43.20	43.80	43.06	43.35
S1200-2	Grit 1200	42.85	44.67	43.22	43.58
S5-1	5 Microns	42.22	42.61	41.57	42.14
S5-2	5 Microns	42.86	41.67	43.06	42.53
S2.5-1	2.5 Microns	39.48	40.68	39.26	39.81
S2.5-2	2.5 Microns	38.95	38.11	38.75	38.60
S0.5-1	0.5 Microns	36.11	36.63	36.31	36.35
S0.5-2	0.5 Microns	37.09	38.27	37.88	37.75

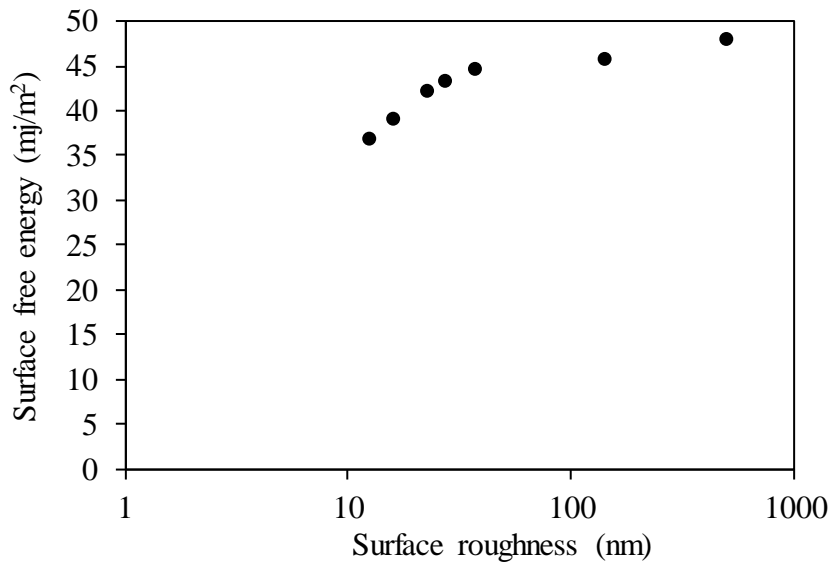


Figure 6.20. Surface free energy of test specimens at different surface roughness.

6.3.6. SEM and EDS Analysis

To characterize the corrosion morphology and determine the relationship between surface roughness and corrosion, scanning electron microscopy (SEM) and energy-dispersive X-ray

spectroscopy (EDS) analysis is conducted for test specimens that are subjected to 4 hours and 16 hours of accelerated corrosion (S4 and S16). Detailed micrographs of specimens S2 and S14 acquired at different magnification levels are provided in Figure 6.21 and Figure 6.22, respectively. Initial corrosion in steel surfaces is characterized by the presence of an amorphous mix of different ferrous oxides with high proportions of γ -FeOOH [89,99,100]. As observed from Figure 6.21(a), initial corrosion layer in test specimen S2 consists of amorphous mix with a layered structure. With continued corrosion, amorphous forms of α -FeOOH and γ -FeOOH emerge at the surface of amorphous rust layer, as shown in Figure 6.21(b). Initially, goethite is in the form of cotton balls (see Figure 6.21(c)), which later transforms into a semi-crystalline form with needle-shaped features, as shown in Figure 6.21(d). Upon continuous corrosion, goethite and lepidocrocite transform to crystalline form [89]. Figure 6.22(b) depicts goethite almost fully transformed into crystalline form. For the corrosion exposure range evaluated in these specimens, goethite is observed to be the dominant corrosion product during the later stages of corrosion. To determine the atomic composition of different corrosion morphologies, EDS analysis was conducted for both S4 and S16 specimens. EDS results of specimen S4 and S16 are presented in Figure 6.23 through Figure 6.25. As observed in Figure 6.23 and Figure 6.24, upon increase in corrosion exposure duration, the amount of oxygen increases whereas the amount of iron decreases. As expected, the crystalline form of α -FeOOH (goethite) formed duration later stages of corrosion is observed to have relatively higher content of oxygen as compared to amorphous and semi-crystalline goethite that are formed during initial and intermediate stages of corrosion, as shown in Figure 6.25.

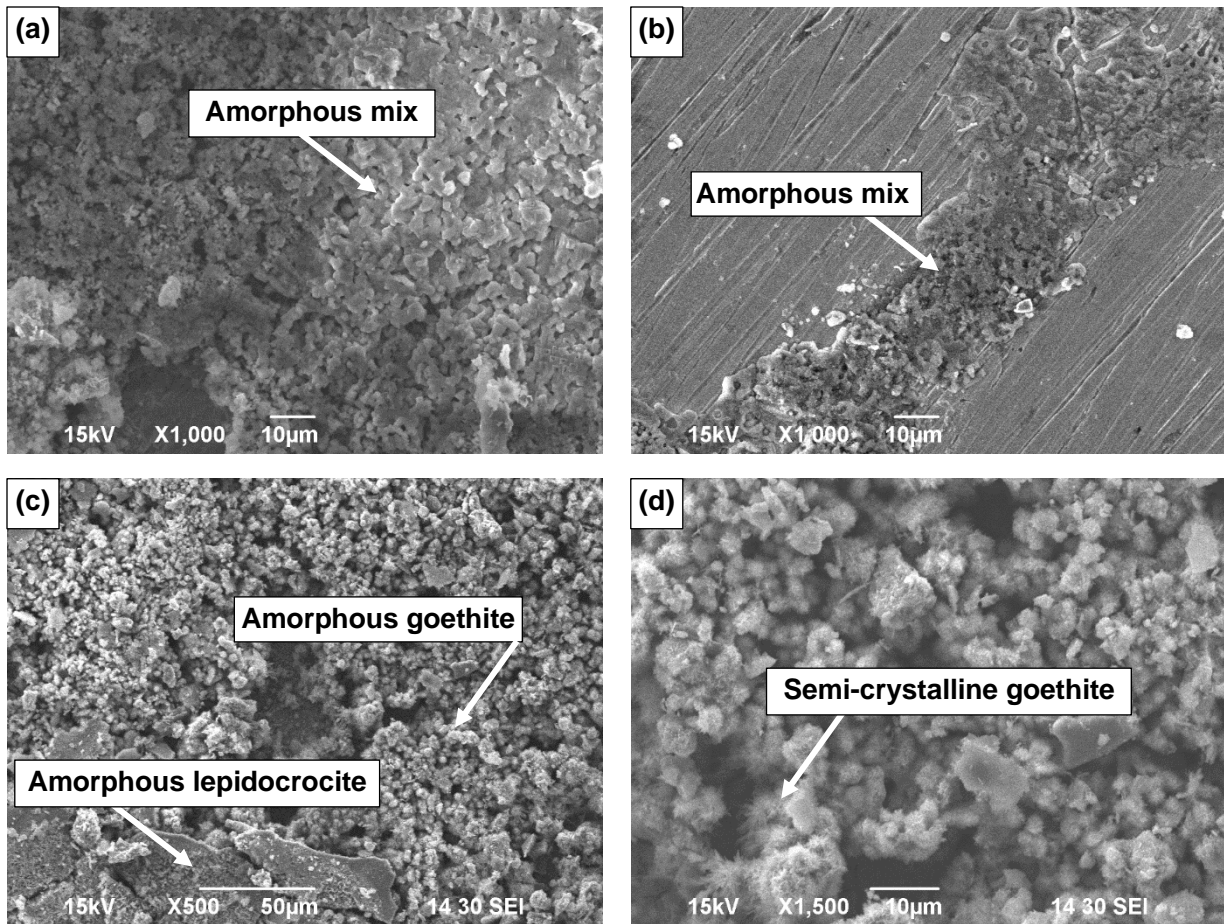


Figure 6.21. SEM micrographs of test specimen S4 (subjected to 4 hours corrosion).

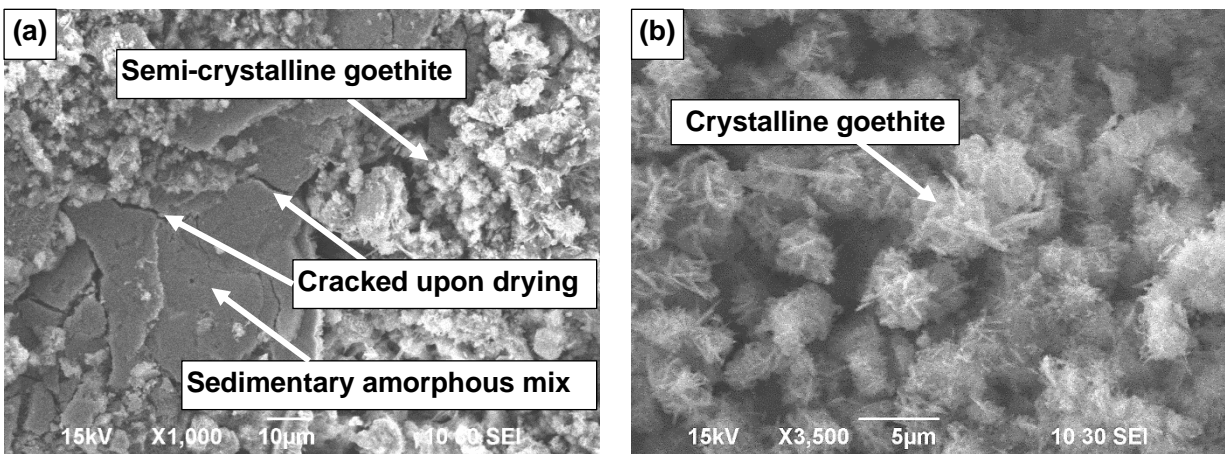


Figure 6.22. SEM micrographs of test specimen S16 (subjected to 16 hours corrosion).

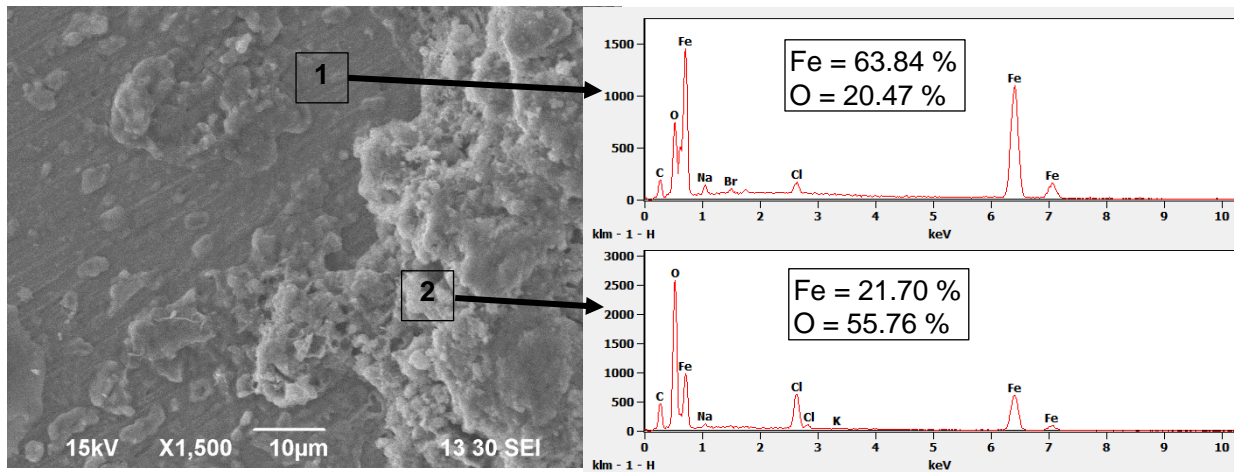


Figure 6.23. EDS analysis of specimen S4 (subjected to 4 hours corrosion).

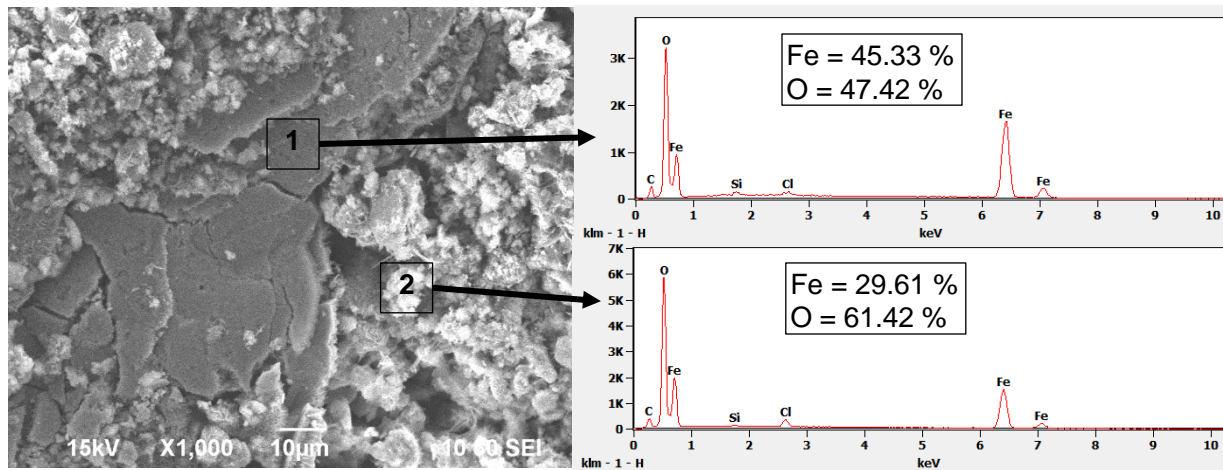


Figure 6.24. EDS analysis of specimen S16 (subjected to 16 hours corrosion).

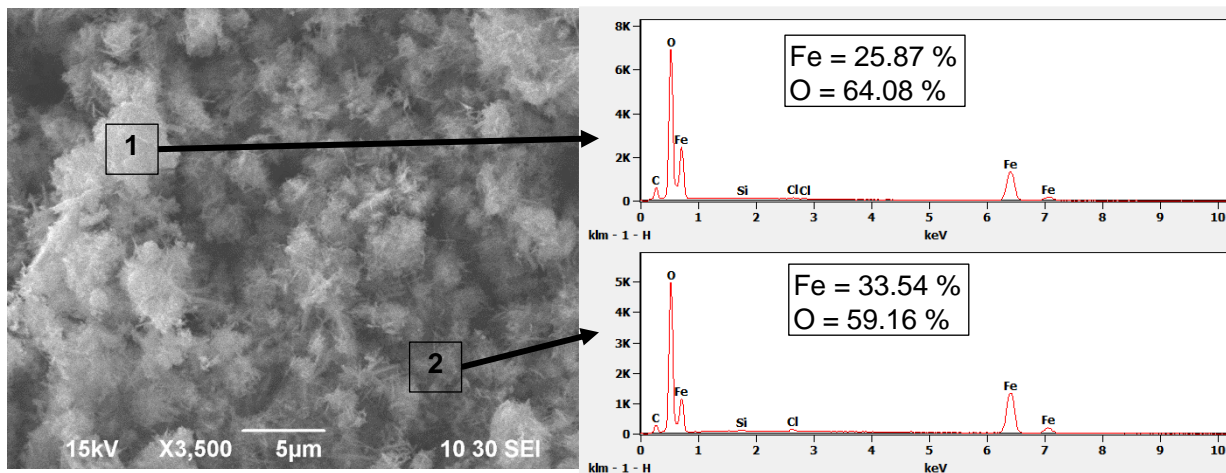


Figure 6.25. EDS analysis of specimen S16 at goethite location.

Both SEM and EDS analysis conducted in this study provided valuable insight into the morphology and atomic composition of corrosion products, respectively that are formed during different stages of corrosion. However, both of these analyses are of limited use while establishing a relationship between surface roughness and corrosion, which is the central point of the current work. Hence, SEM and EDS analysis are confined only to two specimens (S4 and S16) and are not explored for other specimens.

6.4. Predictive Equations

Analysis of test results obtained in this study indicate that increase in surface roughness caused by either corrosion or surface grinding and polishing leads to increase in wettability of ASTM A36 steel by water. Based on experimental results, three predictive equations are proposed to estimate contact angle of ASTM A36 steel for three roughness ranges. These equations, corresponding to three roughness average (R_a) ranges, are as follows

For ASTM A36 steel surfaces with low surface roughness, $R_a < 50$ nm

$$\theta_c = -0.4852R_a + 93.16 \quad (6.11)$$

For ASTM A36 steel surfaces with medium surface roughness, $50 \text{ nm} \leq R_a < 3000$ nm

$$\theta_c = -0.0114R_a + 77.19 \quad (6.12)$$

For ASTM A36 steel surfaces with high surface roughness, $R_a > 3000$ nm

$$\theta_c = -0.0003R_a + 33.32 \quad (6.13)$$

where, θ_c is the contact angle at initial stage based on spherical fit of water droplet, in degrees and R_a is the roughness average of surface of specimen, in nm. The predictive equations along with the experimental results corresponding to low, medium and high surface roughness are illustrated in Figure 6.26, Figure 6.27 and Figure 6.28, respectively.

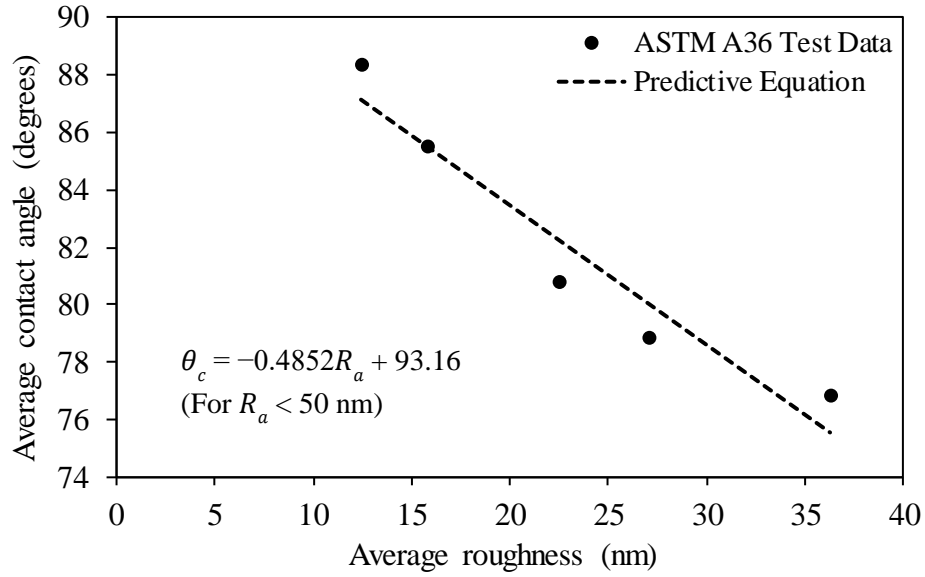


Figure 6.26. Comparison of proposed equations for low surface roughness with test data.

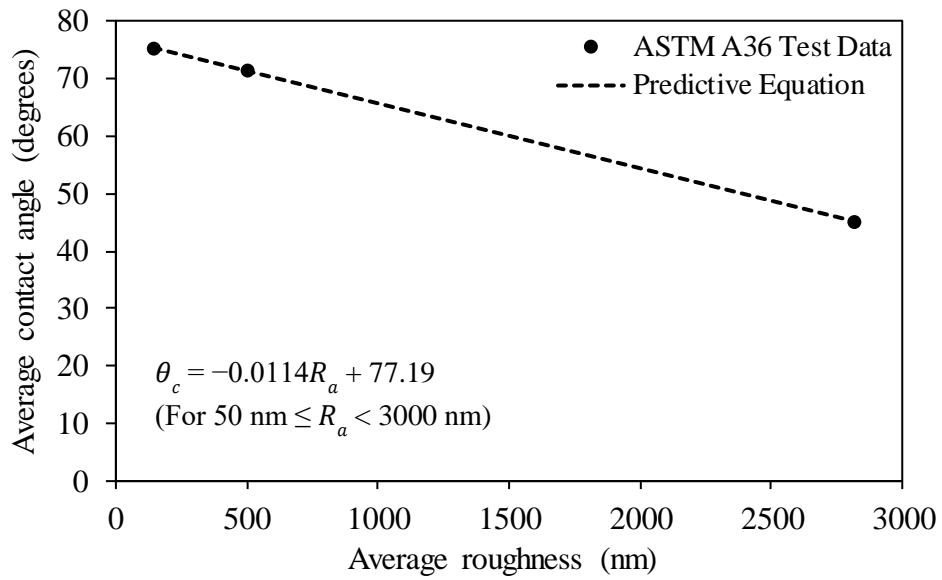


Figure 6.27. Comparison of proposed equations for medium surface roughness with test data.

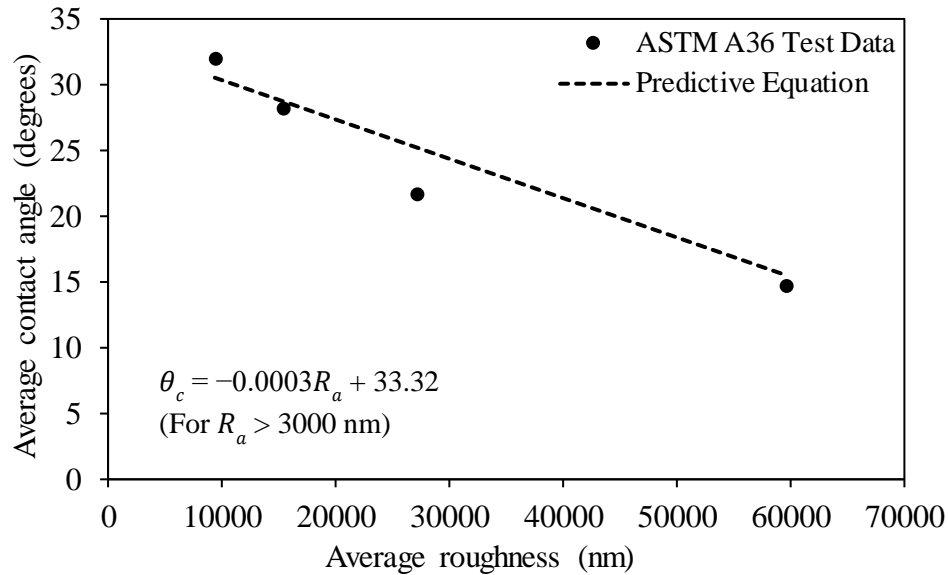


Figure 6.28. Comparison of proposed equations for high surface roughness with test data.

6.5. Conclusions

The following are some important conclusions that can be drawn from this study:

1. Corrosion exposure of 76 hours results in 80% decrease in the initial contact angle of ASTM A36 steel. Hence, increase in corrosion exposure increases the water wettability of ASTM A36 steel thereby making it more hydrophilic.
2. Contact angles are observed to decrease by 40% of initial contact angle after the specimens are subjected to just 4 hours of corrosion exposure. Hence, early stage corrosion in ASTM A36 steel is important as wettability of steel increases significantly in the early stages of corrosion.
3. Contact angles are observed to decrease from 88° to 15° as the average roughness of specimens increased from 12 nm to $59 \mu\text{m}$. This corresponds to a significant 83% decrease in the contact angle. With this, it can be concluded that surface roughness, caused either by corrosion process or grinding and polishing process, greatly influences the wettability of steel. Increase in surface roughness increases the wettability of ASTM

A36 steel, as manifested by decrease in the contact angle values. On the contrary, decrease in surface roughness increases the contact angle and this rate of increase in contact angle is more in case of specimens with average surface roughness below 50 nm.

4. High surface roughness caused by non-uniform surface corrosion is found to be more critical in influencing the wettability of steel as compared to surface roughness caused by a relatively uniform process resulting from grinding and polishing. Furthermore, the wettability of steel is found to be more sensitive to initial increase in surface roughness. The rate of increase in wettability is more when roughness average (R_a) value increases up to 2 μm . Beyond 2 μm roughness average, the rate of increase in wettability decreases.
5. Visual examination of specimens with a higher surface roughness ($R_a = 495.78 \text{ nm}$) and lower surface roughness ($R_a = 15.74 \text{ nm}$ and 12.40 nm) subjected to 4 hours of accelerated corrosion shows that specimen with lower surface roughness experienced less corrosion when compared to the specimens with higher surface roughness values. Further experiments are needed to quantify the influence of surface roughness on corrosion behavior of structural steel members.
6. Increase in surface roughness of ASTM A36 steels leads to increase in surface free energy and improve its hydrophilic behavior. When surface roughness of specimens is decreased below 50 nm, the surface free energy decreases rapidly and specimens approach a hydrophobic behavior.

6.6. References

- [1] J.R. Kayser, A.S. Nowak, Capacity Loss Due to Corrosion in Steel-Girder Bridges, *Journal of Structural Engineering*, 115(6), 1525-1537.

- [2] R. Rahgozar, Remaining capacity assessment of corrosion damaged beams using minimum curves, *Journal of Constructional Steel Research*, 65(2), 299-307.
- [3] E. Yamaguchi, T. Akagi, H. Tsuji, Influence of corrosion on load-carrying capacities of steel I-section main-girder end and steel end cross-girder, *International Journal of Steel Structures*, 14(4), 831-841.
- [4] P.R. Roberge, *Corrosion Engineering*, McGraw-Hill New York, NY, USA., 2008.
- [5] M.H. Wood, A.V. Arellano, L. Van Wij, *Corrosion-Related Accidents in Petroleum Refineries: Lessons learned from accidents in EU and OECD countries*, JRC Sci. Policy Reports, EUR. 26331 (2013).
- [6] J. Bhandari, F. Khan, R. Abbassi, V. Garaniya, R. Ojeda, Modelling of pitting corrosion in marine and offshore steel structures—A technical review, *J. Loss Prev. Process Ind.* 37 (2015) 39–62.
- [7] R.W. Poston, J.S. West, *Investigation of the Charlotte Motor Speedway Bridge Collapse*, in: *Struct. Congr.*, ASCE, 2005.
- [8] HSR, *Offshore Hydrocarbon Releases Statistics and Analysis*, 2002, 2002.
- [9] F. Khan, R. Howard, Statistical approach to inspection planning and integrity assessment, *Insight-Non-Destructive Test. Cond. Monit.* 49 (2007) 26–36.
- [10] L. Naik, Dayakar, R. Kiran, *Data Mining and Equi-Accident Zones for US Pipeline Accidents*, *J. Loss Prev. Process Ind.* (Manuscript under Rev. (2017)).
- [11] S. Lv, Q. Mu, X. Gao, T.S. Srivatsan, Influence of morphology of corrosion on fracture initiation in an aluminum alloy, *Mater. Des.* 45 (2013) 96–102.

- [12] G. Koch, J. Varney, N. Thompson, O. Moghissi, M. Gould, J. Payer, International Measures of Prevention, Application, and Economics of Corrosion Technologies Study, NACE Int. IMPACT Rep. (2016).
- [13] E. Ghali, V.S. Sastri, M. Elboudjaini, Corrosion prevention and protection: practical solutions, John Wiley and Sons, 2007.
- [14] J.-H. Ahn, I.-T. Kim, S. Kainuma, M.-J. Lee, Residual shear strength of steel plate girder due to web local corrosion, *J. Constr. Steel Res.* 89 (2013) 198–212.
- [15] R.E. Melchers, Probabilistic model for marine corrosion of steel for structural reliability assessment, *J. Struct. Eng.* 129 (2003) 1484–1493.
- [16] H.H. Uhlig, *Uhlig's Corrosion Handbook*, John Wiley & Sons, 2011.
- [17] P.P. Milella, *Fatigue and corrosion in metals*, Springer Science & Business Media, 2012.
- [18] R. Rahgozar, Y. Sharifi, Remaining fatigue life of corroded steel structural members, *Adv. Struct. Eng.* 14 (2011) 881–890.
- [19] S. Xu, B. Qiu, Experimental study on fatigue behavior of corroded steel, *Mater. Sci. Eng. A.* 584 (2013) 163–169.
- [20] S. Xu, Estimating the effects of corrosion pits on the fatigue life of steel plate based on the 3D profile, *Int. J. Fatigue.* 72 (2015) 27–41.
- [21] G. Qin, S. Xu, D. Yao, Z. Zhang, Study on the degradation of mechanical properties of corroded steel plates based on surface topography, *J. Constr. Steel Res.* 125 (2016) 205–217.
- [22] C. Liu, T. Miyashita, M. Nagai, Analytical study on shear capacity of steel I-girders with local corrosion nearby supports, *Procedia Eng.* 14 (2011) 2276–2284.

- [23] I.-T. Kim, M.-J. Lee, J.-H. Ahn, S. Kainuma, Experimental evaluation of shear buckling behaviors and strength of locally corroded web, *J. Constr. Steel Res.* 83 (2013) 75–89.
- [24] J.-H. Ahn, J.-H. Cheung, W.-H. Lee, H. Oh, I.-T. Kim, Shear buckling experiments of web panel with pitting and through-thickness corrosion damage, *J. Constr. Steel Res.* 115 (2015) 290–302.
- [25] B. Wu, J.-L. Cao, L. Kang, Influence of local corrosion on behavior of steel I-beams subjected to end patch loading: Experiments, *J. Constr. Steel Res.* 135 (2017) 150–161.
- [26] P. Jayaweera, D.M. Lowe, A. Sanjurjo, K.H. Lau, L. Jiang, Corrosion-resistant metallic coatings on low carbon steel, *Surf. Coatings Technol.* 86 (1996) 522–525.
- [27] N. Priyantha, P. Jayaweera, A. Sanjurjo, K. Lau, F. Lu, K. Krist, Corrosion-resistant metallic coatings for applications in highly aggressive environments, *Surf. Coatings Technol.* 163 (2003) 31–36.
- [28] W.-M. Zhao, Y. Wang, T. Han, K.-Y. Wu, J. Xue, Electrochemical evaluation of corrosion resistance of NiCrBSi coatings deposited by HVOF, *Surf. Coatings Technol.* 183 (2004) 118–125.
- [29] G. Gunasekaran, L.R. Chauhan, Eco friendly inhibitor for corrosion inhibition of mild steel in phosphoric acid medium, *Electrochim. Acta.* 49 (2004) 4387–4395.
- [30] J.J. Myers, W. Zheng, Modern Protection Systems to Prevent Corrosion of Structural Steel Elements Due to Deicing and Roadway Salts, in: *Des. Constr. Rehabil. Maint. Bridg.*, 2011: pp. 121–128.
- [31] P.B. Raja, A.K. Qureshi, A.A. Rahim, H. Osman, K. Awang, Neolamarckia cadamba alkaloids as eco-friendly corrosion inhibitors for mild steel in 1M HCl media, *Corros. Sci.* 69 (2013) 292–301.

- [32] E.A. Toubia, S. Emami, Experimental Evaluation of Structural Steel Coating Systems, *J. Mater. Civ. Eng.* 28 (2016) 4016147.
- [33] S.M. Daghash, O.E. Ozbulut, Mechanical Evaluation of Corrosion-Resistant Steel Plates for Bridge Girder Fabrication, in: *Struct. Congr. 2017*, 2017: pp. 494–505.
- [34] H.E. Townsend, Effects of alloying elements on the corrosion of steel in industrial atmospheres, *Corrosion*. 57 (2001) 497–501.
- [35] J.W. Amyx, D.M. Bass, R.L. Whiting, *Petroleum reservoir engineering: physical properties*, McGraw-Hill College, 1960.
- [36] P.-G. De Gennes, F. Brochard-Wyart, D. Quéré, *Capillarity and wetting phenomena: drops, bubbles, pearls, waves*, Springer Science & Business Media, 2013.
- [37] A. Datta, S. Mukherjee, *Structural and morphological evolution in metal-organic films and multilayers*, CRC Press, 2015.
- [38] Y. Lai, X. Gao, H. Zhuang, J. Huang, C. Lin, L. Jiang, Designing superhydrophobic porous nanostructures with tunable water adhesion, *Adv. Mater.* 21 (2009) 3799–3803.
- [39] K. Liu, M. Cao, A. Fujishima, L. Jiang, Bio-inspired titanium dioxide materials with special wettability and their applications, *Chem. Rev.* 114 (2014) 10044–10094.
- [40] T.A. Otitoju, A.L. Ahmad, B.S. Ooi, Superhydrophilic (superwetting) surfaces: A review on fabrication and application, *J. Ind. Eng. Chem.* 47 (2017) 19–40.
- [41] E. Matijevic, R.J. Good, *Surface and colloid science*, Springer Science & Business Media, 2012.
- [42] D. Quéré, Wetting and roughness, *Annu. Rev. Mater. Res.* 38 (2008) 71–99.
- [43] Y. Yuan, T.R. Lee, Contact angle and wetting properties, in: *Surf. Sci. Tech.*, Springer, 2013: pp. 3–34.

- [44] J. Drelich, E. Chibowski, D.D. Meng, K. Terpilowski, Hydrophilic and superhydrophilic surfaces and materials, *Soft Matter*. 7 (2011) 9804–9828.
- [45] L. Feng, S. Li, Y. Li, H. Li, L. Zhang, J. Zhai, Y. Song, B. Liu, L. Jiang, D. Zhu, Superhydrophobic surfaces: from natural to artificial, *Adv. Mater.* 14 (2002) 1857–1860.
- [46] H.Y. Erbil, A.L. Demirel, Y. Avci, O. Mert, Transformation of a simple plastic into a superhydrophobic surface, *Science* (80-.). 299 (2003) 1377–1380.
- [47] N.A. Patankar, On the modeling of hydrophobic contact angles on rough surfaces, *Langmuir*. 19 (2003) 1249–1253.
- [48] L. Jiang, Y. Zhao, J. Zhai, A lotus-leaf-like superhydrophobic surface: a porous microsphere/nanofiber composite film prepared by electrohydrodynamics, *Angew. Chemie*. 116 (2004) 4438–4441.
- [49] S. Michielsen, H.J. Lee, Design of a superhydrophobic surface using woven structures, *Langmuir*. 23 (2007) 6004–6010.
- [50] X.-M. Li, D. Reinhoudt, M. Crego-Calama, What do we need for a superhydrophobic surface? A review on the recent progress in the preparation of superhydrophobic surfaces, *Chem. Soc. Rev.* 36 (2007) 1350–1368.
- [51] P. Roach, N.J. Shirtcliffe, M.I. Newton, Progress in superhydrophobic surface development, *Soft Matter*. 4 (2008) 224–240.
- [52] H. Teisala, M. Tuominen, M. Aromaa, J.M. Mäkelä, M. Stepien, J.J. Saarinen, M. Toivakka, J. Kuusipalo, Development of superhydrophobic coating on paperboard surface using the liquid flame spray, *Surf. Coatings Technol.* 205 (2010) 436–445.
- [53] K. Liu, Y. Tian, L. Jiang, Bio-inspired superoleophobic and smart materials: design, fabrication, and application, *Prog. Mater. Sci.* 58 (2013) 503–564.

- [54] X. Zhou, Z. Zhang, X. Xu, F. Guo, X. Zhu, X. Men, B. Ge, Robust and durable superhydrophobic cotton fabrics for oil/water separation, *ACS Appl. Mater. Interfaces*. 5 (2013) 7208–7214.
- [55] X. Tian, T. Verho, R.H.A. Ras, Moving superhydrophobic surfaces toward real-world applications, *Science* (80-.). 352 (2016) 142–143.
- [56] Y. Guo, F. Xia, L. Xu, J. Li, W. Yang, L. Jiang, Switchable wettability on cooperative dual-responsive poly-L-lysine surface, *Langmuir*. 26 (2009) 1024–1028.
- [57] B. Xin, J. Hao, Reversibly switchable wettability, *Chem. Soc. Rev.* 39 (2010) 769–782.
- [58] Z. Hua, J. Yang, T. Wang, G. Liu, G. Zhang, Transparent surface with reversibly switchable wettability between superhydrophobicity and superhydrophilicity, *Langmuir*. 29 (2013) 10307–10312.
- [59] J. Yong, F. Chen, Q. Yang, Y. Fang, J. Huo, X. Hou, Femtosecond laser induced hierarchical ZnO superhydrophobic surfaces with switchable wettability, *Chem. Commun.* 51 (2015) 9813–9816.
- [60] H. Lee, B.P. Lee, P.B. Messersmith, A reversible wet/dry adhesive inspired by mussels and geckos, *Nature*. 448 (2007) 338.
- [61] T. Darmanin, F. Guittard, Recent advances in the potential applications of bioinspired superhydrophobic materials, *J. Mater. Chem. A*. 2 (2014) 16319–16359.
- [62] M.E. Schrader, Wettability of clean metal surfaces, *J. Colloid Interface Sci.* 100 (1984) 372–380.
- [63] M. Mantel, J.P. Wightman, Influence of the surface chemistry on the wettability of stainless steel, *Surf. Interface Anal.* 21 (1994) 595–605.

- [64] R.N. Wenzel, Resistance of solid surfaces to wetting by water, *Ind. Eng. Chem.* 28 (1936) 988–994.
- [65] A.B.D. Cassie, S. Baxter, Wettability of porous surfaces, *Trans. Faraday Soc.* 40 (1944) 546.
- [66] J. Bico, U. Thiele, D. Quéré, Wetting of textured surfaces, *Colloids Surfaces A Physicochem. Eng. Asp.* 206 (2002) 41–46.
- [67] K.-Y. Law, H. Zhao, *Surface wetting: characterization, contact angle, and fundamentals*, Springer, 2015.
- [68] H. Nakae, R. Inui, Y. Hirata, H. Saito, Effects of surface roughness on wettability, *Acta Mater.* 46 (1998) 2313–2318.
- [69] G. Palasantzas, J.T.M. De Hosson, Wetting on rough surfaces, *Acta Mater.* 49 (2001) 3533–3538.
- [70] D.M. Spori, T. Drobek, S. Zürcher, M. Ochsner, C. Sprecher, A. Mühlebach, N.D. Spencer, Beyond the lotus effect: roughness influences on wetting over a wide surface-energy range, *Langmuir.* 24 (2008) 5411–5417.
- [71] X. Tang, S. Richter, S. Nestic, Study of wettability of different mild steel surfaces, in: *17th Int. Corros. Congr., NACE International, 2009*: p. 1298.
- [72] K.J. Kubiak, T.G. Mathia, M.C.T. Wilson, Methodology for metrology of wettability versus roughness of engineering surfaces, in: *Proc. Fourteenth Int. Congr. Metrol. Paris, Fr., 2009*.
- [73] K.J. Kubiak, M.C.T. Wilson, T.G. Mathia, P. Carval, Wettability versus roughness of engineering surfaces, *Wear.* 271 (2011) 523–528.

- [74] W. Lu, D.D.L. Chung, Effect of rust on the wettability of steel by water, *Cem. Concr. Res.* 28 (1998) 477–480.
- [75] X.-F. Zhang, R.-J. Chen, J.-M. Hu, Superhydrophobic surface constructed on electrodeposited silica films by two-step method for corrosion protection of mild steel, *Corros. Sci.* 104 (2016) 336–343.
- [76] U. Trdan, M. Hočevnar, P. Gregorčič, Transition from superhydrophilic to superhydrophobic state of laser textured stainless steel surface and its effect on corrosion resistance, *Corros. Sci.* 123 (2017) 21–26.
- [77] T. Hong, M. Nagumo, Effect of surface roughness on early stages of pitting corrosion of type 301 stainless steel, *Corros. Sci.* 39 (1997) 1665–1672.
- [78] L.R. Hilbert, D. Bagge-Ravn, J. Kold, L. Gram, Influence of surface roughness of stainless steel on microbial adhesion and corrosion resistance, *Int. Biodeterior. Biodegradation.* 52 (2003) 175–185.
- [79] H. Lee, D. Kim, J. Jung, Y. Pyoun, K. Shin, Influence of peening on the corrosion properties of AISI 304 stainless steel, *Corros. Sci.* 51 (2009) 2826–2830.
- [80] T. Yuming, L.I.N. Bing, Z. Xuhui, Z.U.O. Yu, Effect of Surface Roughness on Early Stage of Pitting Corrosion of 316LSS, *Corros. Sci. Protection Technol.* 26 (2014) 505–510.
- [81] ASTM G1-03, Standard Practice for Preparing, Cleaning, and Evaluating Corrosion Test Specimens, ASTM International, West Conshohocken, PA, 2011.
- [82] ISO 14993:2001, Corrosion of metals and alloys - Accelerated testing involving cyclic exposure to salt mist, dry and wet conditions, (2001).

- [83] ASTM B117, tandard Practice for Operating Salt Spray (Fog) Apparatus, ASTM International, West Conshohocken, PA, 2016.
- [84] A.K. Bewoor, V.A. Kulkarni, Metrology and measurement, McGraw-Hill Education, 2009.
- [85] R.R.L. De Oliveira, D. a. C. Albuquerque, T.G.S. Cruz, F.M.Y. and F.L. Leite, Measurement of the Nanoscale Roughness by Atomic Force Microscopy: Basic Principles and Applications, At. Force Microsc. - Imaging, Meas. Manip. Surfaces At. Scale. (2012) 256.
- [86] D. Landolt, Corrosion and surface chemistry of metals, CRC press, 2007.
- [87] D.J. Whitehouse, Handbook of surface and nanometrology, CRC press, 2010.
- [88] ASME B46.1, Surface Texture - Surface Roughness, Waviness, and Lay, American Society of Mechanical Engineers, New York, 2009.
- [89] A. Raman, S. Nasrazadani, L. Sharma, Morphology of rust phases formed on weathering steels in various laboratory corrosion tests, Metallography. 22 (1989) 79–96.
- [90] D. De La Fuente, I. Díaz, J. Alcántara, B. Chico, J. Simancas, I. Llorente, A. García-Delgado, J.A. Jiménez, P. Adeva, M. Morcillo, Corrosion mechanisms of mild steel in chloride-rich atmospheres, Mater. Corros. 67 (2016) 227–238.
- [91] Y. Ma, Y. Li, F. Wang, The atmospheric corrosion kinetics of low carbon steel in a tropical marine environment, Corros. Sci. 52 (2010) 1796–1800.
- [92] F. Iwei, Atmospheric corrosion of carbon steels and weathering steels in Taiwan, Br. Corros. J. 26 (1991) 209–214.
- [93] R.J. Good, Contact Angle, Wetting, and Adhesion: A Critical Review, J. Adhes. Sci. Technol. 6 (1992) 1269–1302.

- [94] M. Gindl, G. Sinn, W. Gindl, A. Reiterer, S. Tschegg, A comparison of different methods to calculate the surface free energy of wood using contact angle measurements, *Colloids Surfaces A Physicochem. Eng. Asp.* 181 (2001) 279–287.
- [95] F. Hejda, P. Solar, J. Kousal, Surface Free Energy Determination by Contact Angle Measurements – A Comparison of Various Approaches, *WDS'10 Proc. Contrib. Pap.* (2010) 25–30.
- [96] H.E. Garrett, *Surface Active Chemicals*, Pergamon Press, New York, 1972.
- [97] Y. Hedberg, M.E. Karlsson, E. Blomberg, I. Odnevall Wallinder, J. Hedberg, Correlation between surface physicochemical properties and the release of iron from stainless steel AISI 304 in biological media, *Colloids Surfaces B Biointerfaces.* 122 (2014) 216–222.
- [98] M. Kalin, M. Polajnar, The correlation between the surface energy, the contact angle and the spreading parameter, and their relevance for the wetting behaviour of DLC with lubricating oils, *Tribol. Int.* 66 (2013) 225–233.
- [99] R.A. Antunes, R.U. Ichikawa, L.G. Martinez, I. Costa, Characterization of corrosion products on carbon steel exposed to natural weathering and to accelerated corrosion tests, *Int. J. Corros.* 2014 (2014) 9.
- [100] K. Xiao, C. Dong, X. Li, F. Wang, Corrosion Products and Formation Mechanism During Initial Stage of Atmospheric Corrosion of Carbon Steel, *J. Iron Steel Res. Int.* 15 (2008) 42–48.

7. EMPLOYING CORN DERIVED PRODUCTS TO REDUCE THE CORROSIVITY OF PAVEMENT DEICING MATERIALS⁶

This chapter discusses the efficacy of corn-derived products in reducing the corrosivity traditional pavement deicing materials and corrosion inhibition mechanism in ASTM A57 steel. The contents of this chapter have been published in Sajid, H.U., Kiran, R., Qi, X., Bajwa, D.S. and Battocchi, D., 2020. Employing corn derived products to reduce the corrosivity of pavement deicing materials. *Construction and Building Materials*, 263, p.120662.

7.1. Introduction

The application of large quantities of deicers on pavements is an essential practice in snow and ice removal operations to ensure public safety and continuous mobility in the winter season. The United States consumes about 24 million metric tons of road salt every year in the winter season which primarily consists of sodium chloride (NaCl) salt [1-3]. Deicers are used in both granular form and salt brine form. In a typical winter season, the state Department of Transportations (DoTs) in the United States apply as much as 44,000 pounds of deicing salt per lane mile, and some DoTs use salt brine in the range of 4 million gallons in the winter season [4, 5]. The annual consumption trends of sodium chloride deicers for roadway operations in the US are shown in Figure 7.1. The large scale application of deicers is essential since 70% of roadways in the US are located in the snowy regions. While deicers are essential in ice and snow removal operations, their extensive application leads to significant corrosion-induced deterioration in the transportation infrastructure and automobiles and has detrimental effects on the environment [2, 6-10]. Sodium chloride-based deicers provide an endless supply of chloride

⁶ This chapter was co-authored by H.U. Sajid, R. Kiran., X. Qi, D.S. Bajwa, and D. Battocchi. H.U. Sajid had the primary responsibility of preparing the specimens, conducting all tests, and drafting this chapter. R. Kiran supervised the research and revised this chapter.

ions that lead to corrosion in steel rebars. The chloride ion attack degrades and compromises the protective passive layer present on the embedded steel rebars and causes severe corrosion in steel rebars which reduces their functionality and causes expensive repairs and delays. Americans lost 6.9 billion hours and 3.1 billion gallons of fuel due to traffic delays resulting in a cumulative loss of \$160 billion in 2014 alone [11]. The steel structures present along the pavements and the automobiles undergo higher corrosion in the presence of chloride ions in the surrounding environment. In 2010, the annual cost of automobile corrosion due to deicing salt alone was estimated to be \$11.7 billion [4]. Every ton of deicing salt applied on pavements is estimated to cost damages ranging from \$803 to \$3,341/ton to transportation infrastructure, automobiles, and environment [12].

In addition to the corrosion damage, road salt deicers also cause salt-scaling as a result of the chemical reaction between the deicing salts and concrete, an increase in the quantity of the alkaline pore solution, the inclusion of free moisture on the concrete surface, and promotion of osmotic pressure in the concrete [13]. The freeze-thaw cycles of the deicing solution lead to superficial damage of the concrete surface, and thus cement paste materials and aggregates get exposed to the external loading and environment. Salt-scaling as a result of deicing salt application has been investigated in many recent studies wherein both physical and chemical interactions between the deicing salts and the concrete materials were noticed [14-16]. The ions present in the deicing salts can chemically react with calcium hydroxide in the pore solution, and some cement hydration products (e.g., Portlandite) and thus form oxychloride compounds [17]. The continued formation and growth of oxychloride crystals cause damage in the cement paste. In addition to the oxychloride product formation, the presence of magnesium ions can replace the calcium in CSH (calcium-silicate-hydrate) and thus form MSH (magnesium-silicate-hydrate)

[13, 18]. MSH has significantly lower bond strength when compared to CHS, and it has been observed to cause cracks and crumbling in concrete [19]. Finally, chloride-based deicers are known to aggravate the alkali-silica reaction in concrete by increasing the supply of alkali and pH level in the concrete [20, 21]. From the above discussion, it is clear that the application of deicing salts on concrete pavements causes numerous physical and chemical damages apart from the steel and rebar corrosion. The current study focuses on the corrosion mitigation aspect of the sodium chloride deicing salt.

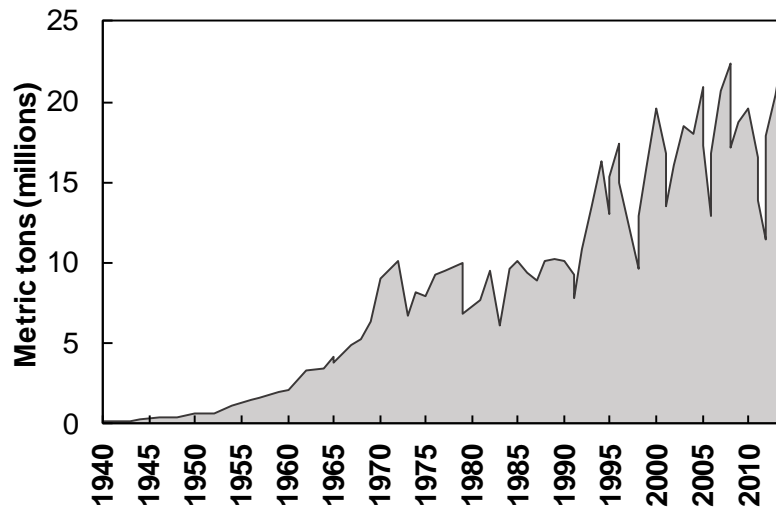


Figure 7.1. Annual salt ($NaCl$) consumption in the US for roadway deicing during the 1940-2014 period (data source: US Geological Survey).

Corrosion initiation in steel requires the steel surface to be covered with water or moisture, which can serve as an electrolyte and facilitate the migration of ions [22]. The moisture content that is needed to complete the corrosion reactions can be supplied by rain, fog, or relative humidity of the environment [23]. Even in the absence of deicers, the corrosion reactions can proceed at a slow rate given the above requirements are fulfilled and there is a certain critical level of humidity in the environment [24]. When deicers are applied on the pavements, the salt particles get deposited on steel structures such as bridges that are present in the vicinity. These

salt particles affect the rate of corrosion in steels in numerous ways. Firstly, due to the hygroscopic nature of salts, they absorb moisture from the air and hence the corrosion reactions proceed even at relatively lower humidity levels. Secondly, the presence of chloride ions increases the conductivity of water and hence results in faster corrosion rates. Thirdly, chloride ions can deteriorate the protective oxide layer that might be present on the surface of some steels [24]. All these factors lead to an increase in the rate of corrosion and hence faster deterioration of steels. When compared to granular salt deicers, salt brines are observed to be even more corrosive [25]. The application of pavement deicers typically causes corrosion in bridge decks, steel bridges, and automobiles, as illustrated in Figure 7.2.

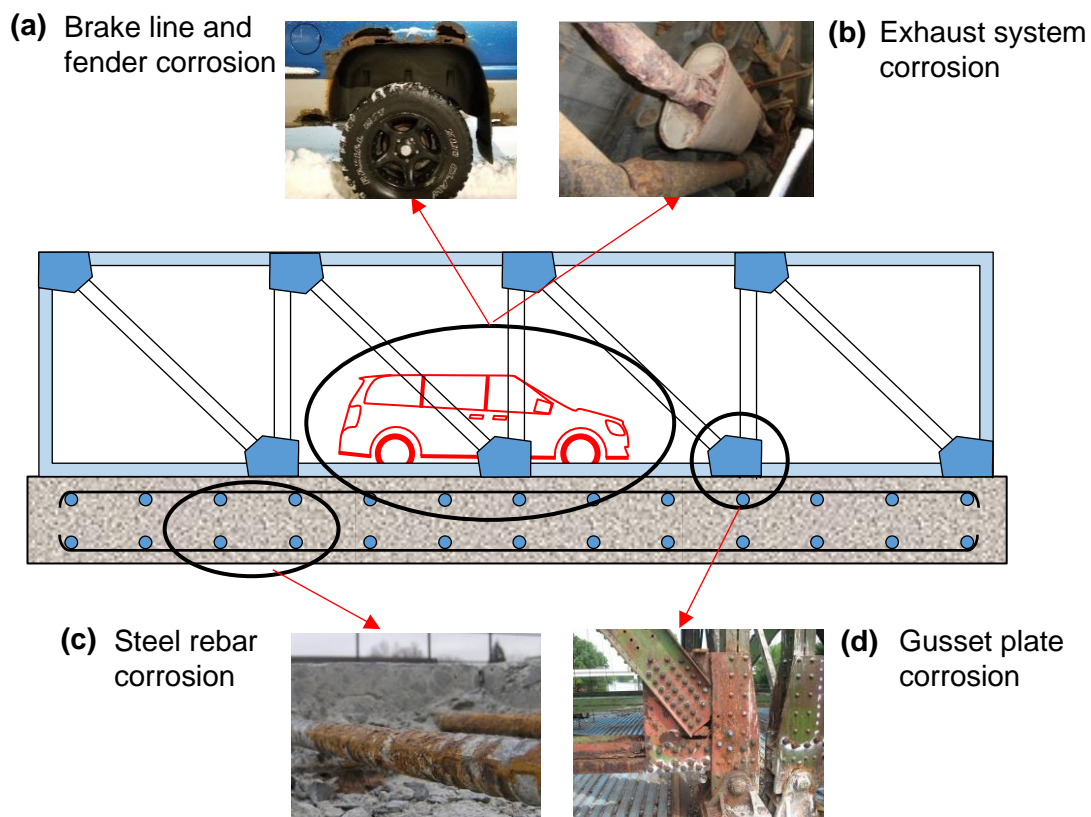


Figure 7.2. Typical corrosion damages observed in the transportation infrastructure: (a) brake line and fender corrosion, (b) exhaust system corrosion [78] (c) steel rebar corrosion [79], and (d) gusset plate corrosion [80].

It is worth mentioning that deicing salts do not only induce corrosion in the steel structures in the immediate vicinity of the deicer applied roads but they can also affect any steel infrastructure that is present in about 1.9 km of major highways wherein deicing salt deposits can accumulate over a period of time [26]. Automobiles traveling on the roadways with deicing salts can form salt mists or aerosols. Aerosols are formed due to the moving vehicle tires and are present in the form of saltwater or salt particles in the air. These particles can travel far away from roadways due to moving vehicles and wind. The most affected zone with a higher density of salt particles or droplets also referred to as the splash zone, is usually within 15 m of highways [27].

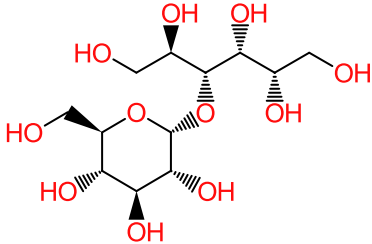
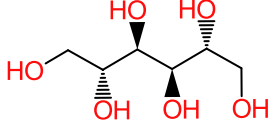
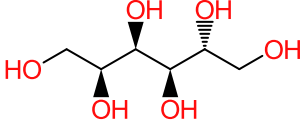
To mitigate the corrosion problems that occur due to chloride-based deicers ($NaCl$, $MgCl_2$, and $CaCl_2$), several alternatives are being pursued by the highway maintenance agencies. To this end, either chloride-based deicers are replaced with relatively non-corrosive deicers or the corrosiveness of chloride-based deicers is minimized by using different corrosion inhibitors or additives. In recent years, acetate and formate based deicers (potassium acetate (CH_3COOK), sodium acetate (CH_3COONa)), calcium magnesium acetate ($CaMg_2(CH_3COO)_6$), potassium formate ($KHCO_2$) have been used as a non-corrosive alternative to the chloride-based deicers. They are particularly used in airport pavements [28]. However, acetate and formate based deicers are expensive when compared to the chloride-based deicers. Moreover, acetate and formate based deicers have selective corrosion affinity towards different metals. For instance, acetate-based deicers are non-corrosive towards mild steel, however, they have been observed to be just as corrosive towards galvanized steels as chloride-based deicers [2]. Another approach to reducing the corrosivity of chloride-based deicers is to add corrosion inhibitors to the deicers, particularly to the salt brines. The corrosion inhibitors usually inhibit corrosion through the

following mechanisms: 1) adsorbing either physically or chemically on the steel surface and forming a thin protective film, 2) forming an oxide film on the steel surface, and 3) passivating the steel surface by reacting with the corrosive elements and forming insoluble precipitates on the surface [29]. Corrosion inhibitors are commonly categorized as 1) inorganic inhibitors (or passivators), 2) organic inhibitors, and 3) vapor-phase inhibitors [30]. Most of the inorganic inhibitors passivate the steel surface and shift the corrosion potential in the noble direction (anodic inhibitors) or delay the cathodic reaction by forming insoluble precipitates on the cathodic sites (cathodic inhibitors). The organic inhibitors usually delay both cathodic and anodic reaction (mixed type inhibitors) by adsorbing either physically or chemically on the steel surface or forming a thin film that serves as a protective barrier against corrosive species. The choice of using either organic or inorganic inhibitors is influenced by many factors such as the cost of inhibitor, toxicity, efficiency, etc. While many inorganic and organic inhibitors effectively inhibit corrosion of steel in corrosive media, their toxicity and cost limit their practical application. Many inorganic inhibitors have compounds (such as chromates and phosphates, etc.) that are toxic and are declared carcinogenic by the environmental protection agencies [31, 32]. In recent years, research efforts have intensified to develop low-cost environment-friendly organic inhibitors. To this end, various compounds have been developed and tested for their corrosion inhibition performance which includes agriculture-based products, plant extracts, and different ionic liquids among other compounds [33-37]. However, many of these products are either too expensive or cannot be produced in bulk scale for pavement deicing applications. Hence, there is a need to develop alternative NaCl deicers that are less corrosive, non-toxic, and effective in deicing operations.

The current work aims to reduce the corrosivity of conventional deicers (23% wt. NaCl salt brine) by incorporating low-cost, non-toxic, and environment-friendly corn-derived polyols namely sorbitol, mannitol, and maltitol. These polyols (also referred to as sugar alcohols), are derived from corn via catalytic hydrogenation [38] and are commonly used as sweeteners and as feedback material in the chemical industry. All the three polyols are commonly available in granular or powder form and can be produced in bulk scale. The molecular structure and chemical properties of these polyols are provided in Table 7.1. As observed in Table 7.1, sorbitol is an isomer of mannitol. The difference in sorbitol and mannitol only comes from the orientation of the hydroxyl group on the 2nd carbon. The choice of using these polyol compounds in the current study stems from three reasons. First, these polyols contain heteroatoms that are known to serve as centers of adsorption [39, 40] and thus these compounds can adsorb on the steel surface and block active corrosion sites. Secondly, the addition of these polyols significantly lower the freezing point of the salt brine deicers [41]. Finally, the addition of these polyol compounds in salt brine deicers improves the ice melting capacity of the salt brine deicers without compromising the skid resistance of the concrete pavements [42]. While these polyols have many interesting characteristics and are hence treated as high-value compounds, only a few studies have investigated their corrosion inhibitor potential when used as a standalone corrosion inhibitor in a pavement deicer-based corrosive media [43, 44]. In the current study, the corrosion inhibition potential of these polyols is quantified for ASTM A572 Gr. 50 steel in the traditional deicing solution (23% wt. NaCl brine). The aim is to decrease the corrosivity of salt brine deicers that are used in the snow removal operation in the transportation industry. This manuscript is organized as follows: Section 7.2 discusses the experimental procedure which includes the preparation of ASTM A572 steel specimens and corrosion tests, Section 7.3 discusses important

results obtained from the corrosion studies and proposed corrosion inhibition mechanism, and Section 7.4 presents important conclusions derived from this work.

Table 7.1. Chemical and physical properties of maltitol, mannitol, and sorbitol.

	Maltitol	Mannitol	Sorbitol
Chemical structure			
Chemical formula	$C_{12}H_{24}O_{11}$	$C_6H_{14}O_6$	$C_6H_{14}O_6$
Molar mass (g/mol)	344.31	182.17	182.17

7.2. Experimental Procedure

This section provides details about the preparation of ASTM A572 steel specimens for corrosion tests and the test protocols adopted for accelerated corrosion tests and potentiodynamic polarization tests conducted in this study.

7.2.1. Test Specimens

In this study, the corrosion inhibition performance of polyols is investigated for ASTM A572 Gr. 50 [45] high strength low alloy steel. ASTM A572 Gr. 50 steel is commonly used in the US construction industry particularly in bridges [46, 47], and has properties that are similar to Q460 [48], Q345B and S355JR steel grades that are used in Chinese and European construction industry. To determine the corrosion behavior, two sets of A572 steels specimens are prepared in this study. The first set of specimens that are used for accelerated corrosion tests are disc-shaped whereas square-shaped steel plates (3" × 3" × 5/16") are prepared for potentiodynamic (PD) polarization tests, as shown in Figure 7.3(a) and Figure 7.3(b), respectively. The chemical composition of A572 steels that are used in this study is provided in

Table 7.2. The microstructure of A572 steel used herein is primarily composed of ferrite and pearlite phases with an average ferrite grain size of 13 μm and an average pearlite colony size of 3 μm [49]. To avoid the influence of surface roughness on corrosion behavior [50, 51], the surfaces of both sets of steel specimens are prepared through successive grinding using Silicon Carbide (SiC) papers in the following grit order: #60, #120, #220, #400, #600 and #800. After grinding, the specimens are thoroughly cleaned using warm water and acetone to remove any residue present on the surface of specimens. In total, 13 disc-shaped specimens are prepared for accelerated corrosion tests whereas 20 steel plates are prepared for potentiodynamic polarization tests. The test procedures for both accelerated corrosion tests and potentiodynamic polarization tests are discussed in the next section.

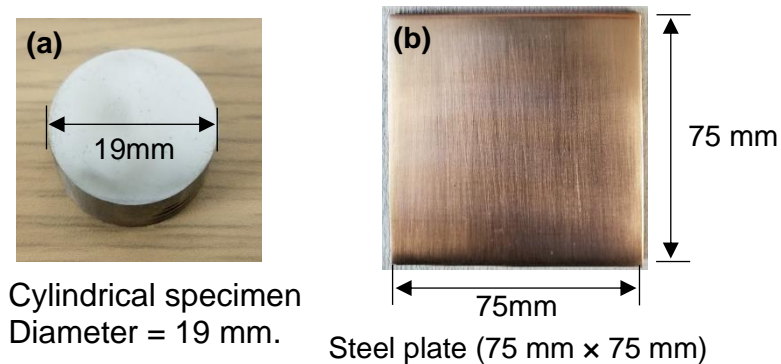


Figure 7.3. Specimens for corrosion tests: (a) cylindrical specimens for visually observing corrosion in a highly corrosive environment, and (b) steel plates for PD tests.

Table 7.2. Chemical composition of ASTM A572 steel.

Element	Composition (%)
Carbon (C)	0.0500
Manganese (Mn)	1.3400
Phosphorous (P)	0.0110
Sulphur (S)	0.0040
Silicon (Si)	0.1500
Copper (Cu)	0.2800
Chromium (Cr)	0.1900
Nickel (Ni)	0.1300
Molybdenum (Mo)	0.0400
Vanadium (V)	0.0830
Titanium (Ti)	0.0010
Niobium (Nb)	0.0030
Iron (Fe)	97.7180

7.2.2. Corrosion Tests

In this study, the corrosion behavior of steel specimens in the presence of different concentrations of corn-derived polyols is evaluated using accelerated corrosion tests and potentiodynamic polarization tests. During accelerated corrosion tests, disc-shaped test specimens are subjected to a constant flow of traditional deicing solution (23% wt. NaCl brine) which contained corn-derived polyols (sorbitol, mannitol, and maltitol) in the following weight concentrations: 0%, 0.5%, 1.0%, 2.0%, and 3.0%. All accelerated corrosion tests are conducted in a highly corrosive environment inside an environmental chamber wherein the temperature and relative humidity levels are maintained at 30°C and 100%, respectively. The experimental setup consists of a feed reservoir, which contains the deicing solution, peristaltic pump for producing a recurring flow of deicing solution, and a disc-shaped test specimen placed on an inclined steel plate, in accordance with ASTM B117 [52] standard. The test setup employed for the accelerated corrosion tests is shown in Figure 7.4. The inclination of the plate allows the flow of deicing media on the grinded top surface of test specimens and inhibits the accumulation of deicing media on the specimen during the experiment. The test specimens are exposed to the deicing

media for 48 hours at an average flow rate of 0.5 mL/min and images are taken at regular intervals to visually monitor the corrosion damage in steel specimens. These images are visually examined to study the corrosion inhibition and will be discussed in Section 7.3.1.

To quantify the corrosion rates and corrosion inhibition mechanism of polyols in the deicing solution, potentiodynamic polarization tests are conducted on the grinded steel plates. For elucidating the corrosion behavior of metals and corrosion inhibition mechanisms, several electrochemical techniques can be used which include linear polarization resistance tests, potentiodynamic polarization tests, electrochemical impedance spectroscopy, etc. [53]. Among these tests, potentiodynamic polarization tests are very commonly used as they provide useful information regarding corrosion mechanisms, corrosion rates, passivation range, pitting potential, and susceptibility of metals to corrosion in a specific corrosive environment. Moreover, potentiodynamic polarization tests are quick and inexpensive to run and yield fairly reproducible results [54]. In potentiodynamic polarization tests, the potential of the working electrode is varied at a selected rate (typically expressed as mV/s) by applying current through the electrolyte. The potential of the working electrode can be varied in either anodic direction (anodic polarization), cathodic direction (cathodic polarization), or both the anodic and cathodic directions (cyclic polarization). The boundaries of the potential scan (initial potential and final potential) are usually selected based on the desired polarization (anodic or cathodic). In this study, the potentiodynamic polarization tests are carried out using Gamry's potentiostat Interface E1000. The potentiodynamic polarization tests are performed using a conventional 3-electrode electrochemical cell which employs ASTM A572 steel plates with an exposed area of 7.07 cm² as a working electrode (WE). All potentials are measured against a saturated calomel electrode (SCE) whereas a stainless steel wire mesh is used as a counter electrode (CE). The

potentiodynamic polarization test setup used in this study is provided in Figure 7.5. All potentiodynamic polarization tests are conducted at room temperature (25 °C). Before starting the electrochemical tests, the working electrode (steel plate) is kept immersed in the polyol-based deicing solution for an average period of 2 hours to achieve a steady-state potential. For each polyol concentration in the deicing solution, the potentiodynamic polarization tests are repeated thrice on separate steel plates. During potentiodynamic polarization tests, the potential of the working electrode (steel plates) is varied from cathodic to the anodic direction (anodic scan) within a range of ± 500 mV with reference to the steady-state potential at a scanning rate of 10 mV/s. A high potential window of ± 500 mV is adopted in this study to capture the passivation and pitting behavior of steel plates. The corrosion rates, corrosion inhibition efficiencies, and the corrosion inhibition mechanisms corresponding to each polyol are then determined using the electrochemical measurement procedures that are specified in ASTM G102 [55] and will be discussed in section 7.3.2.

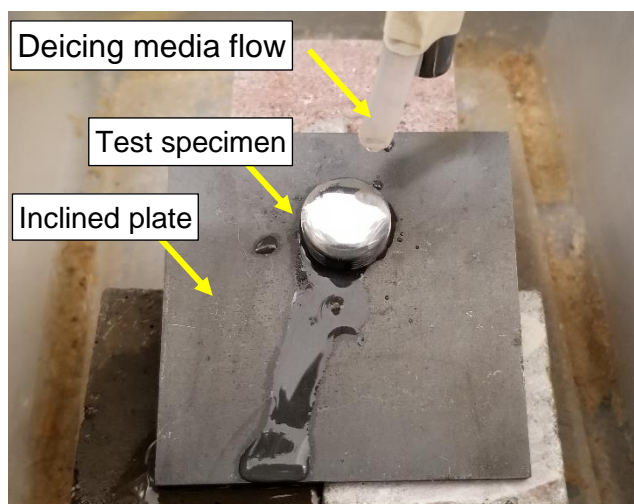


Figure 7.4. Typical cylindrical specimen subjected to flowing deicing media (23.0% *NaCl* brine + polyol) inside an environmental chamber at 30 °C temperature and 100% relative humidity conditions.

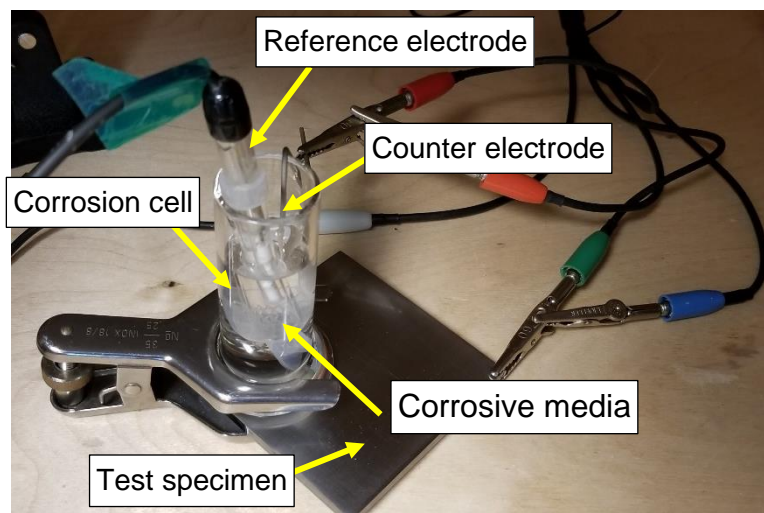


Figure 7.5. Typical corrosion cell with steel plate as working electrode (WE) (exposed area: 7.07 cm²), saturated calomel electrode as reference electrode (RE) and stainless steel wire mesh as counter electrode (CE).

7.2.3. Corrosion Products Characterization

To determine the types of corrosion products formed and to analyze the surface morphology of steel specimens with and without the presence of polyols in the sodium chloride deicing solution, various surface characterization techniques are employed herein. The morphology of corroded surfaces and the elemental composition of the corroded surface is obtained from Scanning Electron Microscopy (SEM) and Energy Dispersive X-ray Spectroscopy (EDS) analysis. Finally, the corrosion products formed at the surface are studied using X-ray Diffraction (XRD) technique. The results obtained from each surface characterization technique are discussed in Section 7.3.5.

7.3. Results and Discussion

In this section, the results obtained from both accelerated corrosion tests and potentiodynamic polarization tests corresponding to each polyol are discussed. Moreover, the corrosion inhibition mechanism is explained using adsorption isotherms.

7.3.1. Accelerated Corrosion Tests

Accelerated corrosion tests are carried out in this study for visually observing corrosion damage in the steel specimens. Specimens are subjected to a constant flow of traditional deicing media (23% wt. NaCl brine) in the absence and presence of different concentrations of polyols inside an environmental chamber for 48 hours. The corrosion damage is visually observed by taking images of specimens at regular intervals. These images are presented in Figure 7.6 through Figure 7.9. It should be noted that for 23% wt. NaCl brine solution and sorbitol+23% wt. NaCl brine solutions, images are taken at 8 hours interval. After confirming the lower corrosion damage in the specimens that are exposed to sorbitol+23% wt. NaCl brine solutions, the images for the remaining polyols (maltitol and mannitol) are obtained at longer time intervals. At the beginning of each test (time $t = 0$ hours), the disc-shaped steel specimens are observed to be free of any contamination or apparent corrosion distress. Varying amount of corrosion is observed in the specimens as the test progressed. As observed in Figure 7.6, the specimens subjected to the traditional deicing solution (23% wt. NaCl brine) exhibited noticeable corrosion damage after only 16 hours of exposure when compared to the deicing solutions which contain small quantities of polyols. In the case of deicing solutions containing 0.5% polyol, the corrosion damage is visually observed to initiate after 24 hours and the amount of corroded area increases with an increase in the exposure time (see Figure 7.7 through Figure 7.9). For higher concentrations of polyol in the brine solution (1.0% to 3.0%), the corrosion damage is noticed at 24 hours around the periphery of test specimens and there is no considerable increase in the corroded area during the remaining duration of the test. In summary, delayed corrosion initiation is observed in ASTM A572 steels that are exposed to the deicing solution containing a small weight concentration of polyols. Moreover, only a small amount of corrosion in these specimens

occurred during the exposure period. The accelerated corrosion tests are conducted to visually monitor the corrosion damage in steel specimens exposed to the deicing solutions containing polyols. To quantify the corrosion rates in steel specimens in the absence and presence of polyols in the salt deicing solutions and to elucidate the corrosion inhibition mechanism, potentiodynamic polarization tests are conducted and are discussed in the next section.



Figure 7.6. The visual appearance of ASTM A572 steel specimens exposed to the traditional deicing solution (23% *NaCl* brine).

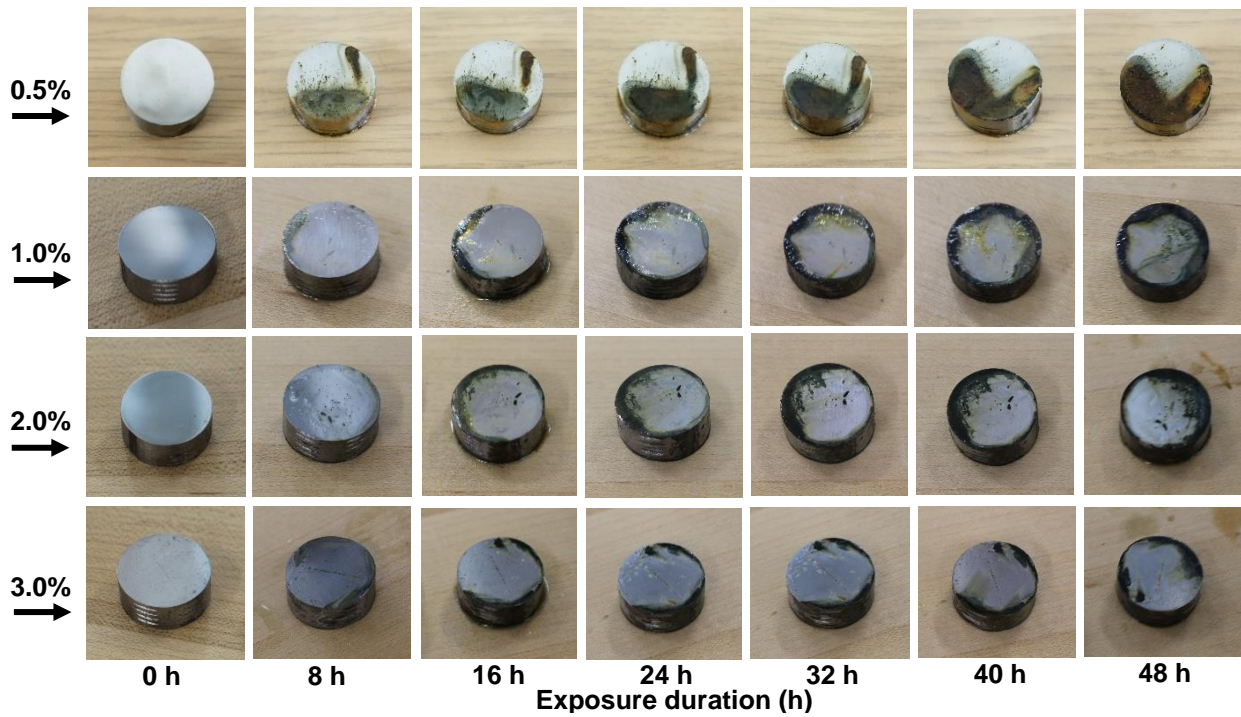


Figure 7.7. Visual appearance of ASTM A572 steel specimens exposed to deicing solution containing 0.5%, 1.0%, 2.0% and 3.0% sorbitol.

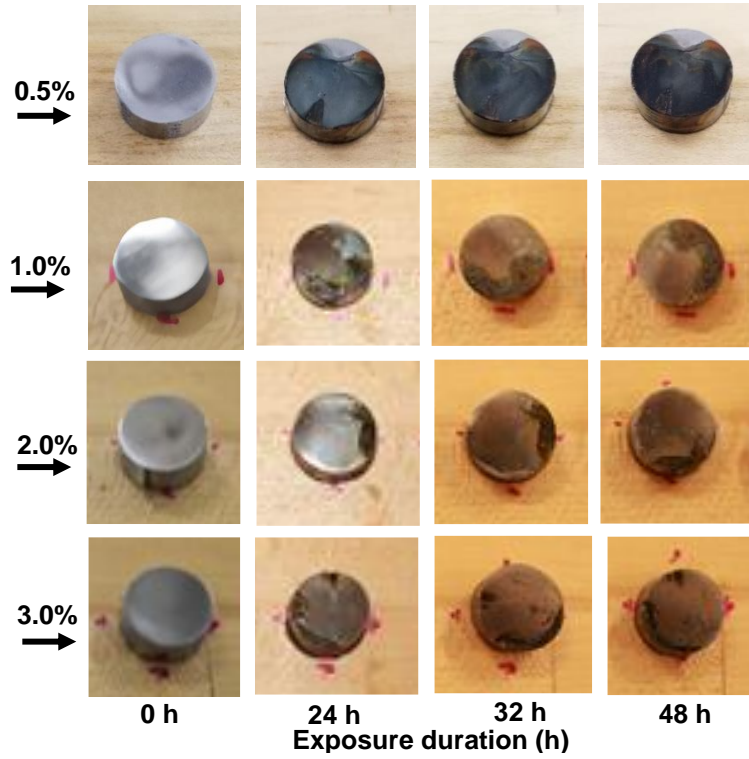


Figure 7.8. Visual appearance of ASTM A572 steel specimens exposed to deicing solution containing 0.5%, 1.0%, 2.0% and 3.0% mannitol.

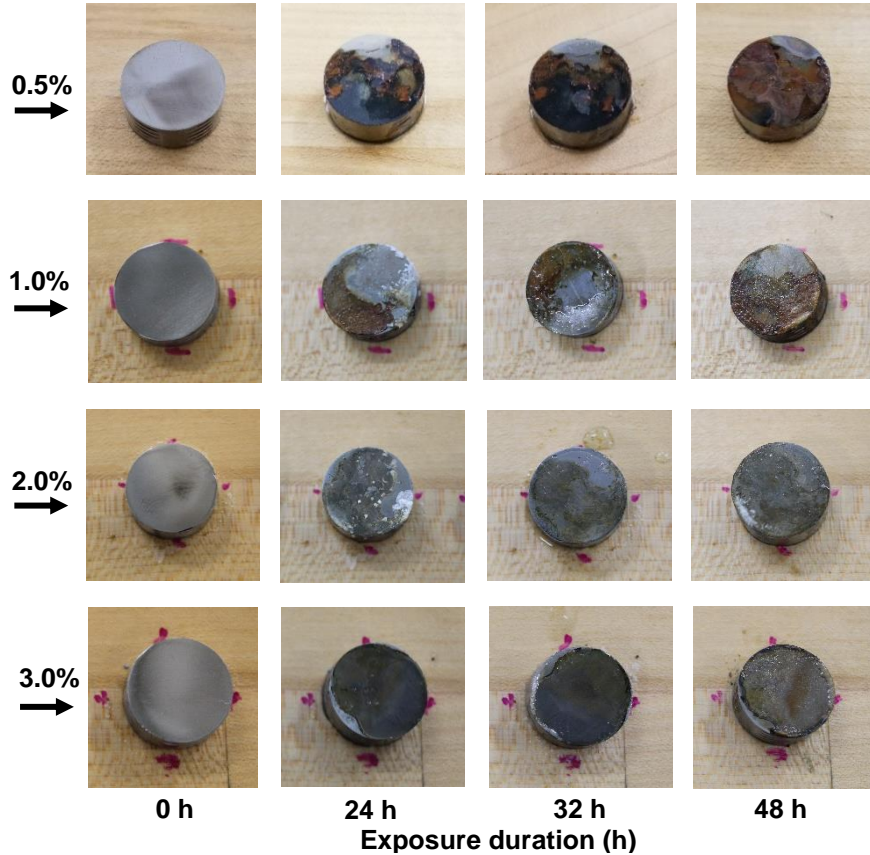


Figure 7.9. Visual appearance of ASTM A572 steel specimens exposed to deicing solution containing 0.5%, 1.0%, 2.0% and 3.0% maltitol.

7.3.2. Potentiodynamic Polarization Tests

The potentiodynamic polarization tests are conducted to evaluate the corrosion current densities, corrosion rates, and subsequent corrosion inhibition mechanism using the procedure discussed in Section 7.2.2. The polarization curves obtained from the potentiodynamic polarization tests usually provide insights on the important processes that occur at the anodic and cathodic sites. A schematic polarization curve that can be obtained for steels in the electrolytic environment simulated in this study is provided in Figure 7.10. As observed in Figure 7.10, the cathodic branch exhibits two regions: 1) hydrogen evolution, and 2) reduction of the passive film and dissolved oxygen [22]. On the other hand, the anodic branch exhibits an initial active corrosion region wherein the current density increases which is followed by the formation of a

passive region wherein the current density values remain almost constant and the potential decreases. The passive region represents the formation of the passivation layer. Finally, a marked increase in the current density is observed which reveals the breakdown of the passivation layer, active anodic dissolution, and the formation of pits. The potentiodynamic polarization curves of ASTM A572 steels in the deicing solution in the absence and presence of small concentrations of different polyols are presented in Figure 7.11. For each polyol concentration, three potentiodynamic polarization tests are conducted and only one curve is presented corresponding to each polyol concentration herein for the sake of clarity as the three curves almost overlapped. As observed in Figure 7.11, a typical Tafel behavior is observed in the cathodic branches for all polarization curves wherein the logarithmic current density varies linearly with the potential. Moreover, the shapes of cathodic and anodic branches remain the same for all cases. In most of the cases, the cathodic and anodic branches exhibited distinct regions that are illustrated in the schematic polarization diagram in Figure 7.10. The cathodic branches exhibited hydrogen evolution, and reduction of dissolved oxygen whereas the anodic branches exhibited an initial active corrosion region which is followed by the formation of a passive region and finally the breakdown of the passivation layer and the formation of pits. The polarization curves shifted towards lower current regions in the presence of the polyols (see Figure 7.11) which indicates corrosion inhibition. Moreover, in the presence of polyols, the corrosion potentials (E_{corr}) are observed to shift in the noble direction which indicates that the presence of polyols has a noticeable influence on retarding the electrochemical reactions (anodic dissolution of steel) happening at the anodic sites. The polarization curves are used to obtain necessary electrochemical parameters corresponding to each polyol concentration in the deicing solution and are discussed in the next section.

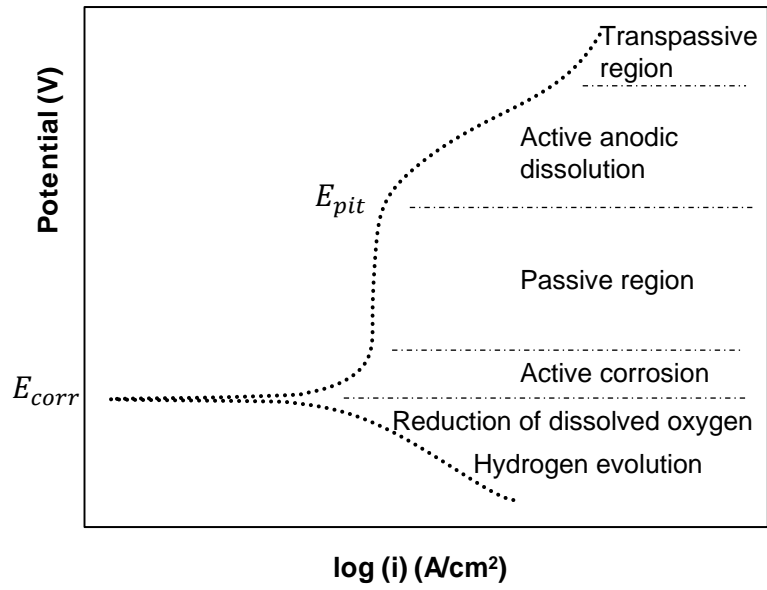


Figure 7.10. Schematic polarization curve of a typical test specimen.

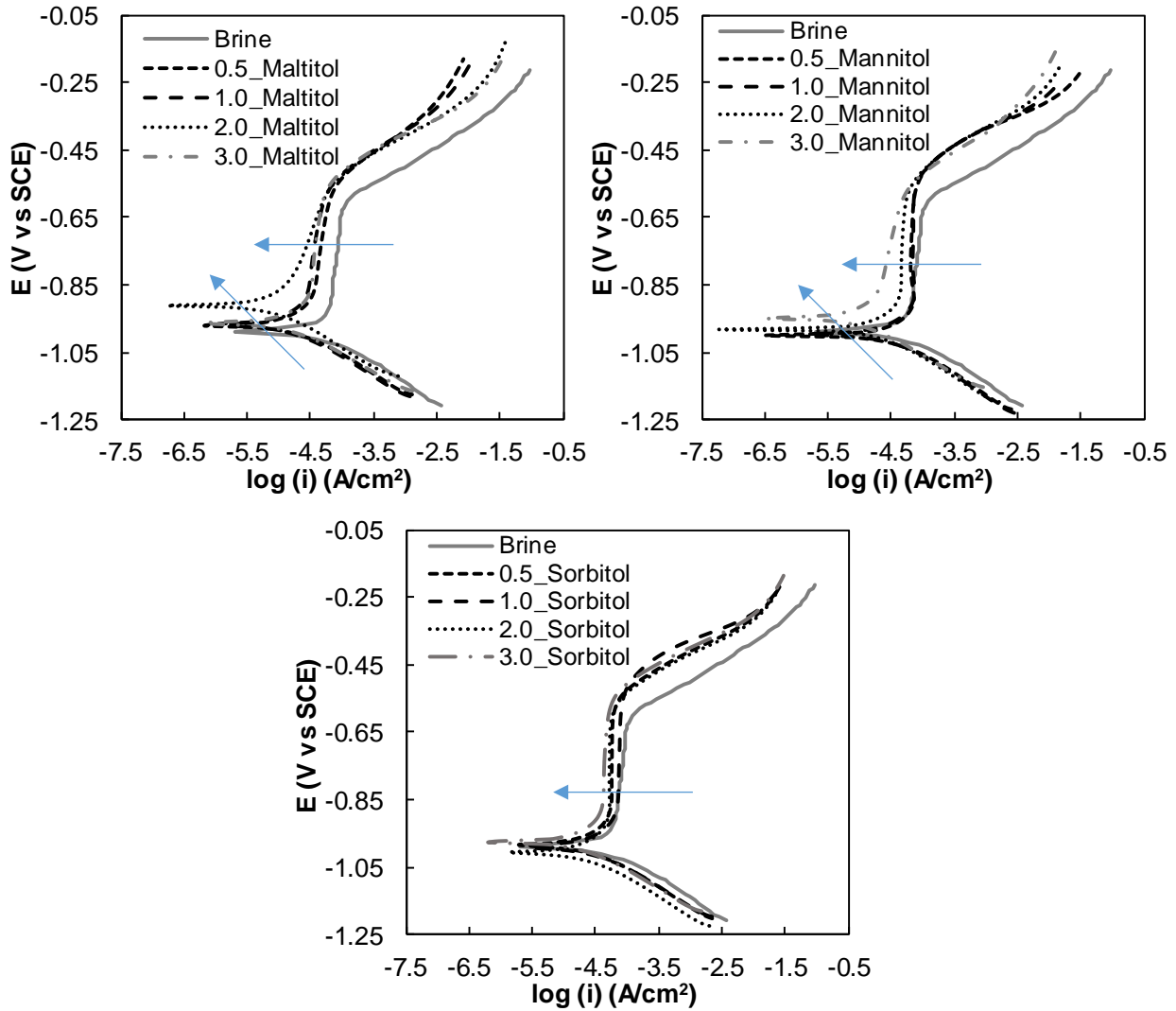


Figure 7.11. Potentiodynamic polarization curves of ASTM A572 steel specimens in deicing solution (23% NaCl brine) in the absence and presence of various polyols concentrations (0.5%, 1.0%, 2.0%, and 3.0%).

7.3.3. Tafel Extrapolation Results

Tafel extrapolation is performed to determine important electrochemical parameters that include corrosion potential (E_{corr}), corrosion current density (i_{corr}), anodic Tafel slope (β_a), and cathodic Tafel slope (β_c). For Tafel extrapolation, at least one branch (either cathodic or anodic) is required to exhibit Tafel behavior wherein the logarithmic current density varies linearly with the potential of the working electrode [56]. It is desirable to use both cathodic and anodic curves

in determining Tafel slopes. However, either cathodic or anodic branch can also be used in Tafel extrapolation to determine the Tafel slope and the subsequent corrosion current density. When using a single branch (cathode or anode) for Tafel extrapolation, the cathodic branch is generally preferred over the anodic branch for two reasons: 1) the cathodic branches usually exhibit a more pronounced Tafel region as compared to the anodic branch, and 2) the anodic branch usually exhibits passivation and pitting behavior, and roughening of the specimen surface, all of which can result in deviation of the anodic branch from the Tafel behavior [56]. It can be observed from Figure 7.11 that the polarization curves obtained for ASTM A572 steels exhibited a more pronounced Tafel behavior in the cathodic curves and relatively small Tafel region in the anodic curves. For these reasons, only cathodic curves are considered in Tafel extrapolation. To minimize the errors that are usually encountered in Tafel extrapolation due to the logarithmic nature of the current density, the extrapolating region is selected at least 50 mV away from the corrosion potential (E_{corr}) and the Tafel region extends at least over one decade of the corrosion current density [57]. The polarization parameters obtained after following the above procedure are provided in Table 7.3. The corrosion current densities are presented in Figure 7.12. From Figure 7.12 and Table 7.3, it is clear that the corrosion current densities decrease substantially when small quantities of polyols are added to the salt brine which confirms their corrosion inhibition potential. In the absence of polyols, an average corrosion current density of $70 \mu\text{A}/\text{cm}^2$ is observed for steel specimens. When small amounts of polyols are added to the deicing solution the average corrosion current density is observed to be in the range of $6\text{-}20 \mu\text{A}/\text{cm}^2$. The corrosion inhibition performance corresponding to different concentrations of each polyol is quantified by evaluating the corrosion inhibition efficiency (IE) which is defined as the relative reduction in the corrosion current density and is determined by using the following equation

$$IE (\%) = \frac{i_{corr}^0 - i_{corr}^{inh}}{i_{corr}^0} \times 100 \quad (7.1)$$

where, IE = inhibition efficiency corresponding to a particular concentration of polyol in the deicing solution (in %), i_{corr}^0 and i_{corr}^{inh} are corrosion current densities in the absence and presence of polyols in the deicing solutions, respectively (in $\mu\text{A}/\text{cm}^2$). The average inhibition efficiencies determined using the above equations are provided in Figure 7.13. It is clear from Figure 7.13 that the addition of even a small amount (0.5% wt.) of polyols that are investigated in this study result in an average corrosion inhibition efficiency of 71%. When the concentration of polyols is increased up to 3.0% wt., the average inhibition efficiencies reached 92%. These results indicate that a pronounced effect on corrosion rates is observed at 0.5% wt. concentration of polyols and a small but steady increase in corrosion inhibition efficiencies is observed when the weight concentrations of polyols are increased from 0.5% to up to 3.0% wt. The corrosion rates in ASTM A572 steel specimens in the absence and presence of polyols in the deicing solution are determined by using the following equations in accordance with the ASTM G102 procedure [55]

$$R = K_1 \frac{i_{corr}}{\rho} EW \quad (7.2)$$

where, CR = corrosion rate in mm/yr, $K_1 = 3.27 \times 10^{-3}$, i_{corr} = corrosion current density in $\mu\text{A}/\text{cm}^2$, ρ = density of steel in g/cm^3 , and EW = equivalent alloy weight which is a dimensionless parameter and is determined from the mass percent of each alloy component in the steel using the following equation

$$EW = \left(\sum \frac{n_i f_i}{W_i} \right)^{-1} \quad (7.3)$$

where, n_i = valence of the i th element of the steel alloy, f_i = mass fraction of the i th element of the steel, and W_i = atomic weight of the i th element in the steel. The average corrosion rates

determined using Eq. (7.2) are plotted in Figure 7.14. As observed in Figure 7.14, ASTM A572 steel specimens exhibited a higher average corrosion rate (0.83 mm/yr on average) in the absence of polyols in the deicing solution. The corrosion rates decreased substantially (up to 92%) in the presence of polyols. The lowest corrosion rate is noticed in the case of 2.0% maltitol in the deicing solution (0.062 mm/yr) and 3.0% sorbitol in the deicing solution (0.069 mm/yr). The mechanisms that led to the reduction of corrosion rate in the presence of polyols in the deicing solutions are discussed in the next section.

Table 7.3. Polarization parameters obtained from Tafel extrapolation.

Corrosion inhibitor	Concentration (%)	E_{corr} (V)	$-i_{corr}$ ($\mu\text{A}/\text{cm}^2$)	$-\beta_c$ (V/dec)	Corrosion rate (mm/yr)
None (23% NaCl salt brine only)	----	-1.002	71.189	0.137	0.829
Maltitol	0.5	-0.961	12.045	0.111	0.140
	1.0	-0.936	8.738	0.110	0.102
	2.0	-0.907	5.334	0.103	0.062
	3.0	-0.978	10.734	0.094	0.125
Mannitol	0.5	-0.993	20.378	0.105	0.237
	1.0	-0.975	11.597	0.095	0.135
	2.0	-0.988	11.311	0.085	0.132
	3.0	-0.956	7.654	0.096	0.089
Sorbitol	0.5	-0.953	15.230	0.099	0.177
	1.0	-0.954	15.409	0.126	0.179
	2.0	-0.975	11.564	0.090	0.135
	3.0	-0.933	5.979	0.092	0.069

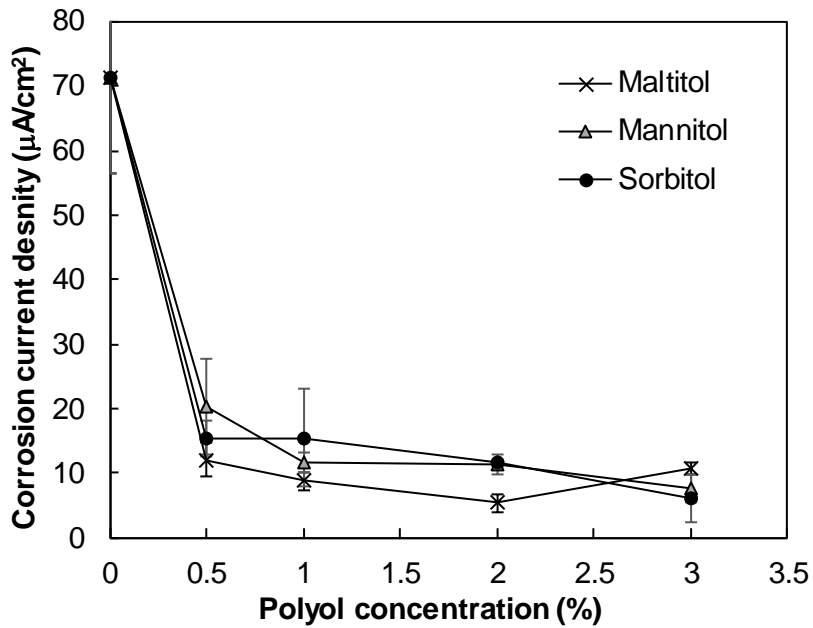


Figure 7.12. Corrosion current densities of ASTM A572 steel specimens as a function of polyols concentration in deicing solution.

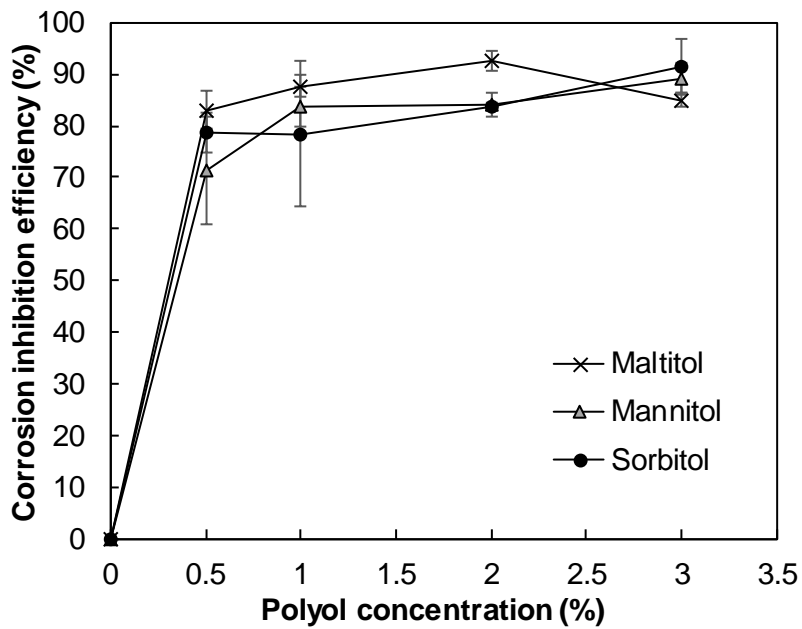


Figure 7.13. Corrosion inhibition efficiencies of polyols as a function of polyols concentration in deicing solution.

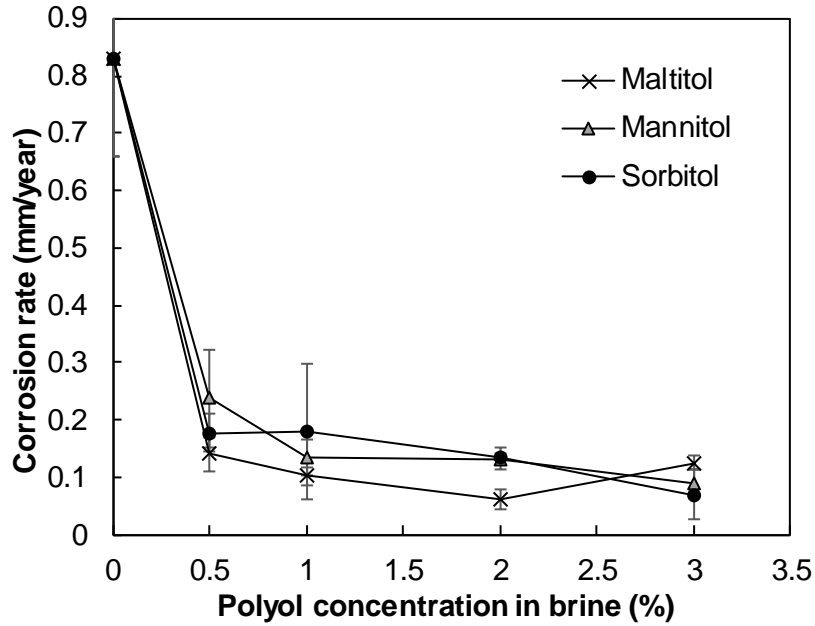


Figure 7.14. Corrosion rates in ASTM A572 steels as a function of polyols concentrations in deicing solution.

7.3.4. Corrosion Inhibition Mechanism of Polyols

In the aqueous solution, the loss of iron at anodic sites (also referred to as anodic dissolution of iron) is given by Eq. (7.4).



The reactions at the cathodic sites are usually governed by the pH level of the solution. In the case of acidic solution, the reduction of hydrogen ions occurs (Eq. (7.5)) whereas reduction of dissolved oxygen is usually noticed in neutral or basic solutions (Eq. (7.6)).



The hydroxyl ions formed as a result of reduction of dissolved oxygen can migrate to anodic sites and react with the iron ions thus leading to initial corrosion products formation in the form of ferrous hydroxide ($Fe(OH)_2$). Brine solution has substantially less solubility of dissolved oxygen due to the high concentration of sodium ions (Na^{+}) and chloride ions (Cl^{-}) [30]. As a

result, the reduction of dissolved oxygen can be less prominent when compared to the hydrogen evolution reaction. In such a case, the hydrogen evolution can also occur by direct reduction of water (Eq. (7.7)) [58, 59].



The presence of abundant sodium ions (Na^+) and chloride ions (Cl^-) in the traditional deicing solution (23% wt. NaCl) notably increases the conductivity of the electrolyte and hence the rate of anodic and cathodic reactions increases. In addition, in the presence of these ions, ferrous chloride ($FeCl_2$) can also be formed apart from the formation of ferrous hydroxide and sodium hydroxide ($NaOH$). Ferrous chloride can hydrolyze and form hydrochloric acid (Eq. (7.8)) which increases the acidity and subsequent corrosivity of the solution [30, 60].



With the addition of polyols in the deicing solution, the polyol molecules compete with the hydroxyl ions and oxygen atoms for attaching with the iron ions via physical and/or chemical adsorption. Polyols are known to have a chelating affinity for metal [61, 62]. In neutral or alkaline media, polyol molecules can provide anionic regions that are known to bind multivalent metal ions [61]. In addition, sugar-derived molecules can provide nucleophilic atoms that tend to bind metal ions more readily as compared to oxygen [61]. Both of these phenomena result in the formation of stable complexes of iron and thereby block active sites for anodic and/or cathodic reactions.

The electrochemical parameters obtained from potentiodynamic polarization tests are used to further elucidate the corrosion inhibition mechanism of the polyols that are studied herein. The Tafel plots are observed to shift towards the lower current region and slightly shift towards positive potential in the presence of polyols. However, the shape of the Tafel curves remained the same. The average change in the corrosion potential observed in the case of

maltitol is 56.5 mV whereas an average shift of 24 mV and 48.2 mV in the anodic direction is observed in the case of mannitol and sorbitol, respectively. The average corrosion potential shift for all three polyols is less than 85 mV which is usually considered as a benchmark potential value for categorizing a corrosion inhibitor either as cathodic or anodic [63, 64]. From these observations, it can be inferred that the polyols acted as mixed-type corrosion inhibitors. The slightly positive potential shift in the polarization curves reflects that the anodic inhibition is more dominant. The corrosion inhibition mechanism of mixed-type inhibitors is achieved via either physisorption or chemisorption of corrosion inhibitor molecules on the steel surface [65].

The adsorption behavior of the polyols corrosion inhibitors on the steel surface can be quantified with the help of adsorption isotherms. An adsorption isotherm is a graphical plot between the amount of adsorbate (corrosion inhibitor molecules) on the adsorbent (metal surface) and the concentration of the adsorbate and is usually determined experimentally [66]. Adsorption isotherms quantify the interaction between the metal surface and the corrosion inhibiting molecules [67, 68]. Adsorption isotherms describe the relationship between the surface coverage θ and the concentration of corrosion inhibitors. The surface coverage θ represents the thin layer of adsorbed inhibitors on the steel surface and it can be determined from the corrosion inhibition efficiency (IE) using Eq. (7.9).

$$\theta = \frac{IE(\%)}{100} \quad (7.9)$$

The most commonly used isotherms for studying the adsorption of corrosion inhibitors on the steel surfaces include Temkin isotherm, Langmuir isotherm, Frumkin isotherm, Flory–Huggins isotherm, and Freundlich isotherm [67, 69, 70]. The surface coverage θ and corrosion inhibition concentration data obtained in the current study can be fitted to Langmuir isotherm [70]. It is worth mentioning that most organic corrosion inhibitors studied in the literature

usually fit the Langmuir adsorption isotherm (straight-line model) [67] which is provided in Eq. (7.10).

$$\frac{C_{inh}}{\theta} = \frac{1}{K_{ads}} + C_{inh} \quad (7.10)$$

where, C_{inh} is the corrosion inhibitor concentration, θ is the surface coverage and K_{ads} is the standard adsorption equilibrium constant. The standard adsorption equilibrium constant is determined from the Langmuir isotherm model and is then used to evaluate the standard free energy of adsorption (ΔG_{ads}^0). The standard free energy of adsorption (ΔG_{ads}^0) quantifies the interaction between adsorbate and the metal surface [71]. The standard free energy of adsorption (ΔG_{ads}^0) and the standard adsorption constant (K_{ads}) are related by Eq. (7.11) [72].

$$\Delta G_{ads}^0 = -RT \ln(55.5 K_{ads}) \quad (7.11)$$

where, R = universal gas constant, T = absolute temperature and 55.5 is the molar concentration of water. The adsorption isotherms for ASTM A572 steels in the absence and presence of different polyols in the deicing media are provided in Figure 7.15, along with Langmuir model fitted equations. The linear behavior observed in Figure 7.15 confirms that the Langmuir model accurately represents the adsorption behavior. The adsorption parameters obtained from the adsorption isotherms are provided in Table 7.4. The negative value of ΔG_{ads}^0 indicates the spontaneity of the adsorption process and stability of the adsorbed film on the metal surface. Different studies have suggested that the analysis of ΔG_{ads}^0 helps establish the adsorption type between a metal and an inhibitor [67]. If the ΔG_{ads}^0 values are close to -20 kJ/mol or lower, the adsorption process is physical. On the other hand, if the values are close to -40 kJ/mol or higher, a chemisorption process takes [73]. In many recent studies, the ΔG_{ads}^0 value falling between -28 kJ/mol and -38 kJ/mol is linked to mixed adsorption [73-75]. The ΔG_{ads}^0 values corresponding to each polyol corrosion inhibitor are closer to -20 kJ/mol. This suggests that that polyols inhibited

the corrosion in ASTM A572 steels in deicing media via physical adsorption on the steel surface which prevented interaction between the steel and corrosive media. It is important to note that standard free energy of adsorption gives information regarding the likely adsorption mode of polyol corrosion inhibitors on the steel surface and the quantitative aspects of the adsorbed layer are not further pursued in the current study. The adsorption of polyol inhibitors on the steel surface and corrosion products formation is further studied by analyzing the steel surface which is discussed in details in the next section.

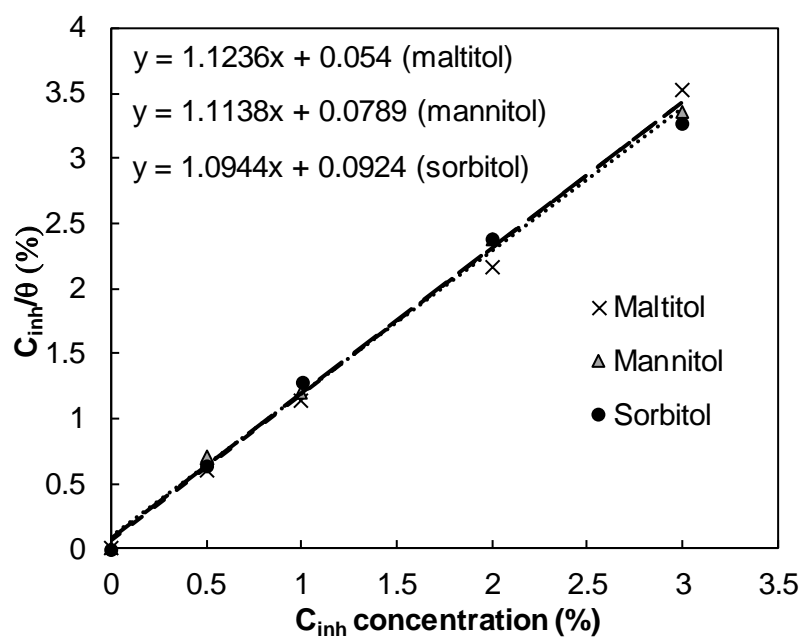


Figure 7.15. Langmuir adsorption isotherm plots for steel specimens in brine solution containing various concentrations of polyols in deicing solution.

Table 7.4. Calculated thermodynamic parameters from the Langmuir isotherm.

CI type	$1/K_{ads}$	ΔG_{ads}^0 (kJ.mol ⁻¹)
Maltitol	0.054	-25.95
Mannitol	0.0789	-23.43
Sorbitol	0.0924	-23.04

7.3.5. Surface Characterization Results

The surfaces of steel specimens after immersion and polarization tests in the absence and presence of different concentrations of polyols (sorbitol or mannitol or maltitol) in the traditional deicing solution (23% wt. NaCl) are analyzed to evaluate the morphology and type of corrosion products formed on the surfaces of the specimens. To this end, three different surface characterization techniques are employed that include SEM, EDS, and XRD. The SEM micrographs and EDS spectra of corroded steel surfaces are obtained using a JEOL JSM-6490LV scanning electron microscope. SEM micrographs obtained at 2000X magnification for representative specimens (reference specimen and specimens corresponding to 3.0% wt. polyol in the deicing solution) are provided in Figure 7.16. As observed in Figure 7.16(a), various products and rough surface morphology is noticed in the specimen that is subjected to the traditional deicing solution. The surface is mostly composed of semi-crystalline features that represent goethite (α -FeOOH) and lepidocrocite (γ -FeOOH) as well as amorphous forms of different ferrous hydroxides [50, 76, 77]. Moreover, sodium chloride salt crystals are also observed to be present on the surface. On the other hand, a thick oxide layer and few cotton ball-shaped features (goethite) and occasional sodium chloride crystals are observed in the specimens corresponding to polyol-salt deicing solutions (see Figure 7.16(b) through Figure 7.16(d)). The SEM micrographs corresponding to all three polyols exhibited an almost similar type of surface morphology and features. This clear distinction in the surface morphology of specimens in the absence and presence of polyols in the traditional deicing solution demonstrates the corrosion product formation slowed down due to the presence of a protective layer on the steel surface. To determine the elemental composition of the surface morphology and the products observed in SEM micrographs, EDS spectra are obtained for two different spots in the same SEM

micrographs. EDS spectra of the representative specimens are provided in Figure 7.17 and Figure 7.18. The EDS spectra of all four representative specimens featured four main elements that include iron (Fe), oxygen (O), sodium (Na), and chloride (Cl). The high-intensity peaks of iron and oxygen confirm the presence of corrosion products formation whereas the sodium and chloride peaks represent the presence of leftover sodium chloride salt from the deicing solution.

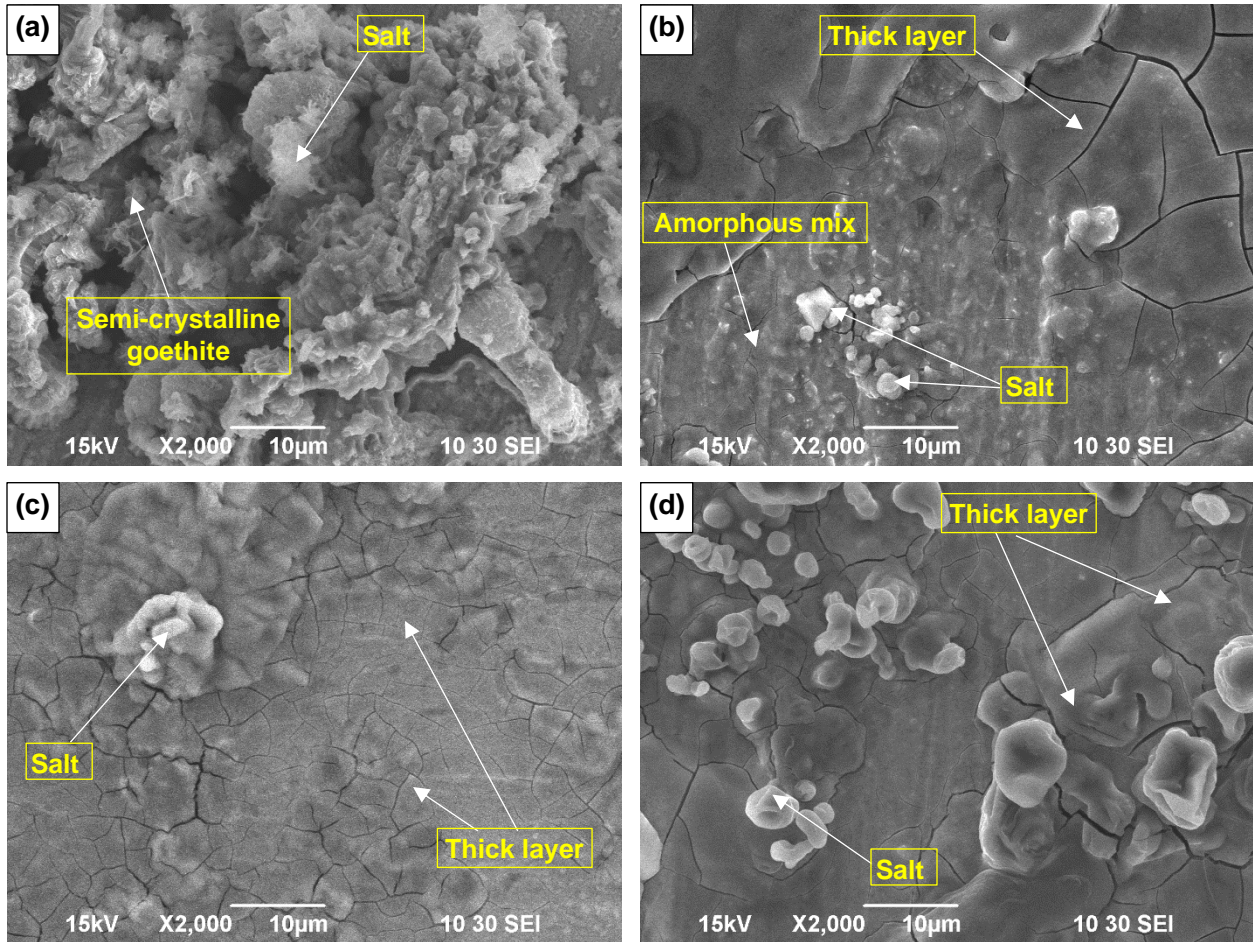


Figure 7.16. SEM micrographs of corroded steel surfaces corresponding to (a) 23% wt. sodium chloride deicing solution, (b) 3.0% wt. sorbitol in deicing solution, (c) 3.0% wt. mannitol in deicing solution, and (d) 3.0% wt. maltitol in deicing solution.

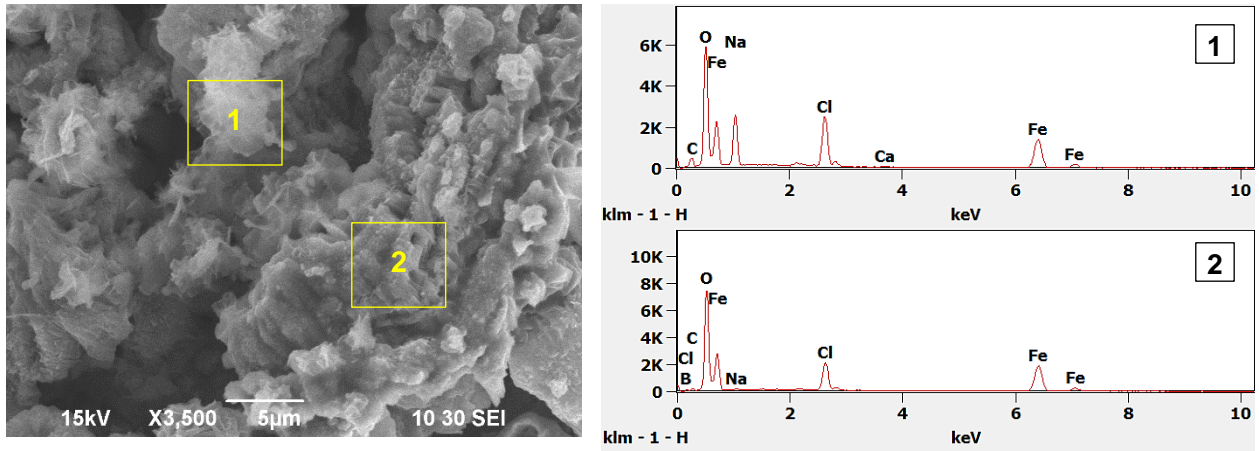


Figure 7.17. EDS analysis of corroded steel surfaces corresponding to 23% wt. sodium chloride deicing solution.

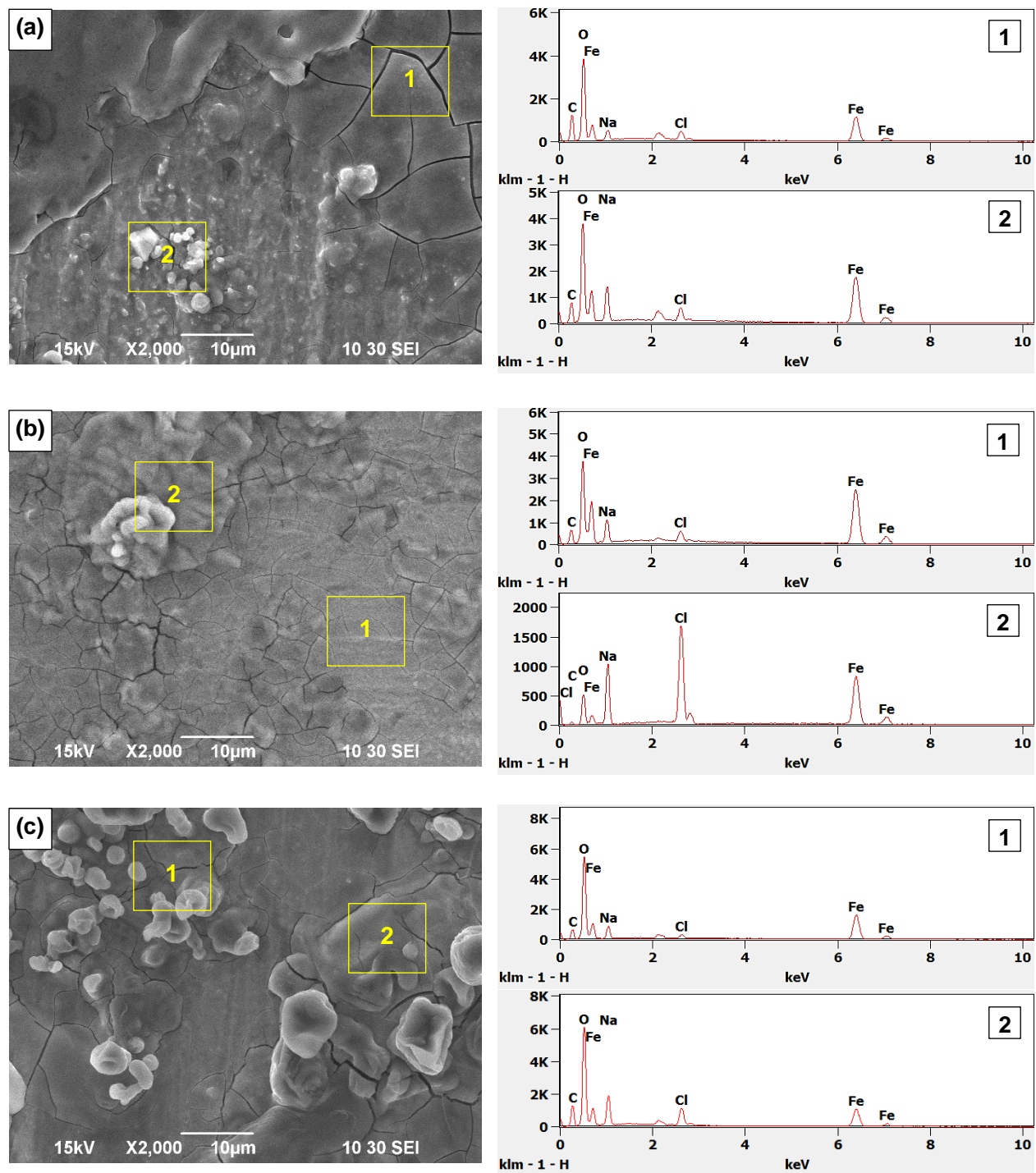


Figure 7.18. EDS analysis of corroded steel surfaces corresponding to (a) 3.0% wt. sorbitol in deicing solution, (b) 3.0% wt. mannitol in deicing solution, and (c) 3.0% wt. maltitol in deicing solution.

To further validate the composition of the products formed on the surface of the representative specimens, XRD patterns are obtained. The XRD patterns are directly obtained from the specimens surfaces using Bruker AXS' D8 Discover multipurpose X-Ray Diffractometer. To this end, steel specimens are fitted and the diffractometer laser is focused on a 100 μm diameter area on the specimen. The diffractograms of the representative specimens are then obtained over a 2-theta range of 10-100° and generator settings of 40 kV and 30 mA. The diffractograms (XRD patterns) obtained from XRD analysis are provided in Figure 7.19. As observed in Figure 7.19, 4 characteristics peaks are observed in each XRD pattern corresponding to $FeOOH$, Fe_2O_3 , Cl , and Fe that are typically noticed in low carbon steels [35, 36]. In the case of the traditional deicing salt specimen, the $FeOOH$ counts are more as compared to the specimens corresponding to polyol-salt deicing solutions. Moreover, in the case of polyol-salt deicing solutions, the peak corresponding to Fe_2O_3 almost vanishes. These results validate the formation of various corrosion products on steel surfaces that were previously noticed in SEM micrographs. Moreover, the vanishing of Fe_2O_3 peaks in some specimens corresponding to some polyol-salt deicing solution suggests a decrease and slowing down of corrosion product formation.

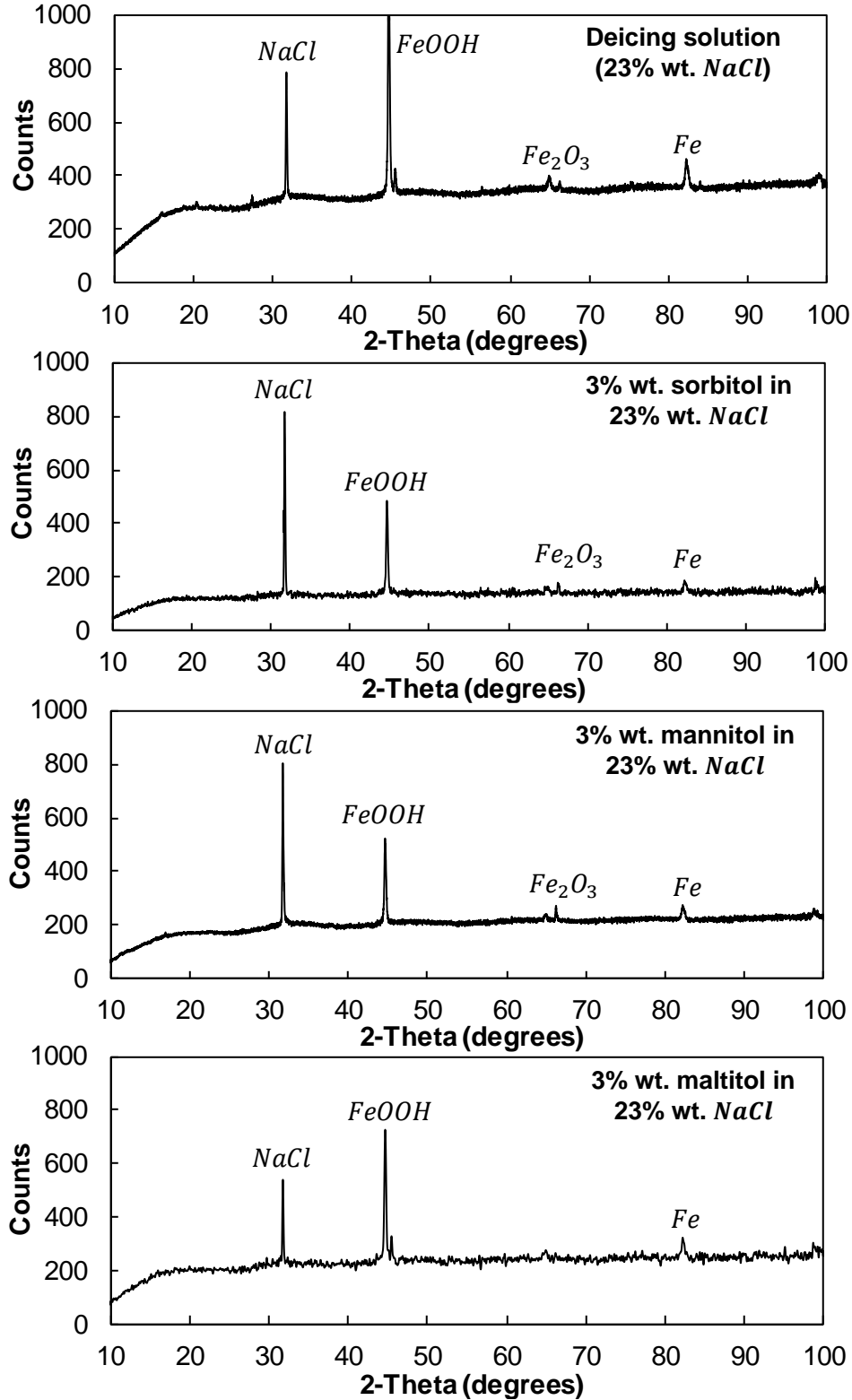


Figure 7.19. XRD patterns for phases present in the corrosion products formed on steel specimens in the absence and presence of 3.0% wt. polyol corrosion inhibitors in ref. deicing solution (23% wt. NaCl).

7.4. Conclusions

In this study, the corrosion inhibition performance is quantified for three corn-derived polyols, namely, maltitol, mannitol, and sorbitol in the traditional deicing solution (23% wt. NaCl brine). Following are the important conclusions that can be drawn from this work:

1. The visual observations from accelerated corrosion tests indicated delayed corrosion initiation and less corrosion damage in the steel specimens that are subjected to polyol-mixed deicing solutions (polyol+23% wt. NaCl) inside a corrosive environment.
2. The results obtained from the potentiodynamic polarization tests revealed that the presence of even small amounts of polyols (0.5% wt.) in the deicing media results in an average corrosion inhibition efficiency of up to 71%. When the concentration of polyols is increased up to 3.0% wt., the inhibition efficiencies reached up to 92%.
3. In the presence of 0.5% wt. sorbitol in the deicing solution, ASTM A572 steels exhibited a 79% reduction in the average corrosion rate (0.18 mm/yr) when compared to the average corrosion rate observed in the absence of sorbitol in the deicing solution (0.83 mm/yr). The average corrosion rate in steel specimens decreased by 92% (0.06 mm/yr) when the concentration of sorbitol in the deicing solution is increased from 0.5% to 3.0% wt.
4. The average corrosion rates in the steel specimens decreased by 83% after the addition of 0.5% wt. maltitol to the deicing solution (23% wt. NaCl). The lowest average corrosion rate in maltitol-mixed deicing solutions (0.06 mm/yr) is observed corresponding to 2.0% wt. concentration in the deicing solution.
5. The average corrosion rates in steel specimens decreased by 71% (0.24 mm/yr) in the presence of 0.5% wt. mannitol in the deicing solution. The average corrosion rate further

decreased (up to 89%, 0.09 mm/yr) when the concentration of mannitol in the deicing solution is increased up to 3.0% wt.

6. The corrosion inhibition, corrosion potentials, and corrosion rates obtained from the Tafel extrapolation revealed that the corn-derived polyols studied herein acted as mixed-type corrosion inhibitors in the deicing media. The corrosion inhibition is achieved via physisorption of polyols molecules on the steel surface.
7. Surface analysis results obtained from SEM, EDS, and XRD studies demonstrated the presence of different corrosion products formed on the steel surface and the formation of a protective oxide layer on specimens that are subjected to deicing solutions containing polyols.

7.5. References

- [1] K.R. Kolesar, C.N. Mattson, P.K. Peterson, N.W. May, R.K. Prendergast, K.A. Pratt, Increases in wintertime PM_{2.5} sodium and chloride linked to snowfall and road salt application, *Atmospheric environment*, 177 (2018) 195-202.
- [2] X. Shi, L. Fay, Z. Yang, T.A. Nguyen, Y. Liu, Corrosion of deicers to metals in transportation infrastructure: Introduction and recent developments, *Corrosion reviews*, 27 (2009) 23-52.
- [3] M. Fischel, Evaluation of selected deicers based on a review of the literature, Report No. CDOT-DTD-R-2001-15, Colorado Department of Transportation, (2001).
- [4] D.L. Kelting, Review of effects and costs of road de-icing with recommendations for winter road management in the Adirondack Park, Report No. AWI2010-01, Adirondack Watershed Institute, (2010).

- [5] P.C. Casey, C.W. Alwan, C.F. Kline, G.K. Landgraf, K.R. Linsenmayer, Impacts of using salt and salt brine for roadway deicing, Report No. FHWA-ID-14-231, Idaho Transportation Department, (2014).
- [6] T. Menzies, National Cost of Motor Vehicle Corrosion from Deicing Salt. Automotive Corrosion and Protection, in: Automotive Corrosion and Protection: Proceedings of the CORROSION/91 Symposium, NACE, Houston, Tex, 1997.
- [7] D.R. Buckler, G.E. Granato, Assessing biological effects from highway-runoff constituents, Report No. 99-240, U.S. Department of Transportation, (1999).
- [8] G.H. Koch, M.P. Brongers, N.G. Thompson, Y.P. Virmani, J.H. Payer, Corrosion cost and preventive strategies in the United States, in, United States Federal Highway Administration, 2002.
- [9] NCHRP, Guidelines for the selection of snow and ice control materials to mitigate environmental impacts, NCHRP Report 577, Transportation Research Board, 2007.
- [10] L. Fay, X. Shi, Environmental impacts of chemicals for snow and ice control: state of the knowledge, *Water, Air, & Soil Pollution*, 223 (2012) 2751-2770.
- [11] ASCE, America's Infrastructure Report Card 2017, American Society of Civil Engineers, (2019).
- [12] H.G. Stefan, E. Novotny, A. Sander, O. Mohseni, Study of Environmental Effects of De-icing Salt on Water Quality in the Twin Cities Metropolitan Area, Minnesota, Report No. MN/RC 2008-42, Minnesota Department of Transportation, (2008).
- [13] X. Shi, L. Fu, Sustainable winter road operations, Wiley Online Library, 2018.
- [14] C. Giebson, K. Seyfarth, J. Stark, Influence of acetate and formate-based deicers on ASR in airfield concrete pavements, *Cement and Concrete Research*, 40 (2010) 537-545.

- [15] Z. Liu, W. Hansen, Freezing characteristics of air-entrained concrete in the presence of deicing salt, *Cement and Concrete Research*, 74 (2015) 10-18.
- [16] J.M. Silva, S.M. Cramer, M.A. Anderson, M.I. Tejedor, J.F. Muñoz, Concrete microstructural responses to the interaction of natural microfines and potassium acetate based deicer, *Cement and concrete research*, 55 (2014) 69-78.
- [17] Y. Farnam, H. Todak, R. Spragg, J. Weiss, Electrical response of mortar with different degrees of saturation and deicing salt solutions during freezing and thawing, *Cement and Concrete Composites*, 59 (2015) 49-59.
- [18] H. Lee, R.D. Cody, A.M. Cody, P.G. Spry, Effects of various deicing chemicals on pavement concrete deterioration, in: Center for Transportation Research and Education (Ed.), *Mid-Continent Transportation Symposium Proceedings*, Iowa State University, Ames, USA, Citeseer, 2000, pp. 151-155.
- [19] W.S. Guthrie, C.D. Thomas, Deicer usage on concrete and asphalt pavements in Utah, Report No. UT-14.02, Utah Department of Transportation, (2014).
- [20] Y.-C. Chiu, J. Olek, Using Modified Mortar-Bar Test Method to Access the Effects of Deicers on Expansion of Mortars With and Without Reactive Aggregates, in: 4th International Conference on the Durability of Concrete Structures, Purdue University, West Lafayette, IN, USA, 2014, pp. 413-418.
- [21] X. Shi, M. Akin, T. Pan, L. Fay, Y. Liu, Z. Yang, Deicer impacts on pavement materials: Introduction and recent developments, *The Open Civil Engineering Journal*, 3 (2009).
- [22] E. McCafferty, *Introduction to Corrosion Science*, Springer Science & Business Media, 2010.

- [23] P.A. Schweitzer, Fundamentals of corrosion: mechanisms, causes, and preventative methods, CRC press, 2009.
- [24] Z. Ahmad, E. Institution of Chemical, Principles of corrosion engineering and corrosion control, (2006).
- [25] W.A. Nixon, J. Xiong, Investigation of materials for the reduction and prevention of corrosion on highway maintenance equipment, IIHR Technical Report No. 472, Iowa Highway Research Board, (2009).
- [26] A.L. Williams, G.J. Stensland, Atmospheric Dispersion Study of Deicing Salt Applied to Roads, Report No. FHWA/IL/HRC.2006-1, Illinois Department of Transportation, Bureau of Materials and Physical Research, (2006).
- [27] S. Lottes, C. Bojanowski, Computer Modeling and Analysis of Truck Generated Salt-Spray Transport Near Bridges, Report No. ANL/ESD/13-1, Argonne National Lab.(ANL), Argonne, IL (United States), (2013).
- [28] ACRP, Impact of Airport Pavement Deicing Products on Aircraft and Airfield Infrastructure, A Synthesis of Airport Practice. Transportation Research Board, Washington, DC, 2008.
- [29] C.G. Dariva, A.F. Galio, Corrosion inhibitors–principles, mechanisms and applications, Developments in corrosion protection, 16 (2014) 365-378.
- [30] R.W. Revie, H.H. Uhlig, Inhibitors and Passivators, in: Corrosion and Corrosion Control, 2008, pp. 303-316.
- [31] V.S. Sastri, Green corrosion inhibitors: theory and practice, John Wiley & Sons, 2012.

- [32] A.S.H. Makhoulf, 1 - Current and advanced coating technologies for industrial applications, in: A.S.H. Makhoulf, I. Tiginyanu (Eds.) *Nanocoatings and Ultra-Thin Films*, Woodhead Publishing, 2011, pp. 3-23.
- [33] O.S. Shehata, L.A. Korshed, A. Attia, *Green Corrosion Inhibitors, Past, Present, and Future*, in: *Corrosion Inhibitors, Principles and Recent Applications*, IntechOpen, 2017.
- [34] C. Verma, E.E. Ebenso, M. Quraishi, Ionic liquids as green and sustainable corrosion inhibitors for metals and alloys: an overview, *Journal of Molecular Liquids*, 233 (2017) 403-414.
- [35] M. Honarvar Nazari, M.S. Shihab, L. Cao, E.A. Havens, X. Shi, A peony-leaves-derived liquid corrosion inhibitor: protecting carbon steel from NaCl, *Green Chemistry Letters and Reviews*, 10 (2017) 359-379.
- [36] Y. Abboud, O. Tanane, A.E. Bouari, R. Salghi, B. Hammouti, A. Chetouani, S. Jodeh, Corrosion inhibition of carbon steel in hydrochloric acid solution using pomegranate leave extracts, *Corrosion Engineering, Science and Technology*, 51 (2016) 557-565.
- [37] M. Honarvar Nazari, E.A. Havens, A. Muthumani, X. Shi, Effects of processed agro-residues on the performance of sodium chloride brine anti-Icer, *ACS Sustainable Chemistry & Engineering*, 7 (2019) 13655-13667.
- [38] M. Grembecka, Sugar alcohols—their role in the modern world of sweeteners: a review, *European Food Research and Technology*, 241 (2015) 1-14.
- [39] K. Xhanari, M. Finšgar, Organic corrosion inhibitors for aluminium and its alloys in acid solutions: a review, *RSC Advances*, 6 (2016) 62833-62857.
- [40] B. Rani, B.B.J. Basu, Green inhibitors for corrosion protection of metals and alloys: an overview, *International Journal of corrosion*, 2012 (2012).

- [41] T. Abbas, D.L. Naik, R. Kiran, Exploring the Use of Polyols, Corn and Beet Juice for Decreasing the Freezing Point of Brine Solution for Deicing of Pavements, (Submitted to ASCE Journal of Cold Regions Engineering), (2019).
- [42] H.U. Sajid, D.L. Naik, R. Kiran, Improving the ice-melting capacity of traditional deicers, *Construction and Building Materials*, 271 (2021): 121527.
- [43] Y.H.-Y. Zhou Xin, Wang Fu-Hui, Corrosion Inhibition by Sorbitol/Diethylenetriamine Condensation Product for Carbon Steel in 3.5% NaCl Saturated Ca(OH)₂ Solution, *Acta Physico-Chimica Sinica*, 27 (2011) 647-654.
- [44] R. Ignash, I. Zarinya, B. Berge, Synthesis and study of polyol borates as corrosion inhibitors for steel and nonferrous metals, *Russian Journal of Applied Chemistry*, 82 (2009) 2146-2150.
- [45] ASTM, ASTM A572/A572M-18 Standard Specification for High-Strength Low-Alloy Columbium-Vanadium Structural Steel., in, ASTM International, West Conshohocken, PA, 2018.
- [46] H.U. Sajid, R. Kiran, Influence of high stress triaxiality on mechanical strength of ASTM A36, ASTM A572 and ASTM A992 steels, *Construction and Building Materials*, 176 (2018) 129-134.
- [47] H.U. Sajid, R. Kiran, Post-fire mechanical behavior of ASTM A572 steels subjected to high stress triaxialities, *Engineering Structures*, 191 (2019) 323-342.
- [48] W.-y. Wang, B. Liu, V. Kodur, Effect of temperature on strength and elastic modulus of high-strength steel, *Journal of materials in civil engineering*, 25 (2012) 174-182.
- [49] H.U. Sajid, D.L. Naik, R. Kiran, Microstructure-mechanical Property Relationships for Post-fire Structural Steels, *ASCE Journal of Materials in Civil Engineering*, (2020).

- [50] H.U. Sajid, R. Kiran, Influence of corrosion and surface roughness on wettability of ASTM A36 steels, *Journal of Constructional Steel Research*, 144 (2018) 310-326.
- [51] L. Ding, H. Torbati-Sarraf, A. Poursaee, The influence of the sandblasting as a surface mechanical attrition treatment on the electrochemical behavior of carbon steel in different pH solutions, *Surface and Coatings Technology*, 352 (2018) 112-119.
- [52] ASTM, International, ASTM B117-16 Standard Practice for Operating Salt Spray (Fog) Apparatus, in, ASTM International, West Conshohocken, PA, 2016.
- [53] P.R. Roberge, *Handbook of corrosion engineering*, McGraw-Hill, 2000.
- [54] R.I. Holland, Use of potentiodynamic polarization technique for corrosion testing of dental alloys, *European Journal of Oral Sciences*, 99 (1991) 75-85.
- [55] ASTM International. G102-89(2015)e1 Standard Practice for Calculation of Corrosion Rates and Related Information from Electrochemical Measurements . in, ASTM International, West Conshohocken, PA, 2015.
- [56] E. McCafferty, Validation of corrosion rates measured by the Tafel extrapolation method, *Corrosion Science*, 47 (2005) 3202-3215.
- [57] R.G. Kelly, J.R. Scully, D. Shoesmith, R.G. Buchheit, *Electrochemical techniques in corrosion science and engineering*, CRC Press, 2002.
- [58] D.A. Jones, *Principles and Prevention of Corrosion*, Prentice Hall, 1996.
- [59] Y.-S. Kim, J.-G. Kim, Corrosion behavior of pipeline carbon steel under different iron oxide deposits in the district heating system, *Metals*, 7 (2017) 182.
- [60] J. Alcántara, B. Chico, J. Simancas, I. Díaz, M. Morcillo, Marine atmospheric corrosion of carbon steel: A review, *Materials*, 10 (2017) 406.

- [61] J. Hodge, E. Nelson, B. Moy, Chelates in Agriculture, Metal Chelation by Glucose-Ammonia Derivatives, *Journal of Agricultural and Food Chemistry*, 11 (1963) 126-129.
- [62] F.P.J. Dwyer, D.P. Mellor, *Chelating agents and metal chelates*, Academic Press, New York, 1964.
- [63] M. Awad, A. Saad, M. Shaaban, B. Jahdaly, O.A. Hazazi, New insight into the mechanism of the inhibition of corrosion of mild steel by some amino acids, *Int. J. Electrochem. Sci*, 12 (2017) 1657-1669.
- [64] C. Lai, B. Xie, L. Zou, X. Zheng, X. Ma, S. Zhu, Adsorption and corrosion inhibition of mild steel in hydrochloric acid solution by S-allyl-O, O'-dialkyldithiophosphates, *Results in physics*, 7 (2017) 3434-3443.
- [65] B.E. Brycki, I.H. Kowalczyk, A. Szulc, O. Kaczerewska, M. Pakiet, *Organic Corrosion Inhibitors*, in: *Corrosion Inhibitors, Principles and Recent Applications*, IntechOpen.
- [66] H.-J. Butt, K. Graf, M. Kappl, *Physics and chemistry of interfaces*, John Wiley & Sons, 2013.
- [67] M. Christov, A. Popova, Adsorption characteristics of corrosion inhibitors from corrosion rate measurements, *Corrosion science*, 46 (2004) 1613-1620.
- [68] S. Marzorati, L. Verotta, S. Trasatti, Green corrosion inhibitors from natural sources and biomass wastes, *Molecules*, 24 (2019) 48.
- [69] H. Freundlich, Over the Adsorption in Solution, *Journal of Physical Chemistry*, 57 (1906) 385-471.
- [70] I. Langmuir, The constitution and fundamental properties of solids and liquids. Part I. Solids, *Journal of the American chemical society*, 38 (1916) 2221-2295.
- [71] G. Biresaw, K.L. Mittal, *Surfactants in Tribology*, 2 Volume Set, CRC Press, 2011.

- [72] Y. Liu, Is the Free Energy Change of Adsorption Correctly Calculated?, *Journal of Chemical & Engineering Data*, 54 (2009) 1981-1985.
- [73] M.H. Sliem, M. Afifi, A.B. Radwan, E.M. Fayyad, M.F. Shibl, F.E.-T. Heakal, A.M. Abdullah, AEO7 Surfactant as an Eco-Friendly Corrosion Inhibitor for Carbon Steel in HCl solution, *Scientific reports*, 9 (2019) 2319.
- [74] O. Kaczerewska, R. Leiva-Garcia, R. Akid, B. Brycki, I. Kowalczyk, T. Pospieszny, Effectiveness of O-bridged cationic gemini surfactants as corrosion inhibitors for stainless steel in 3 M HCl: Experimental and theoretical studies, *Journal of Molecular Liquids*, 249 (2018) 1113-1124.
- [75] H. Lgaz, R. Salghi, K.S. Bhat, A. Chaouiki, S. Jodeh, Correlated experimental and theoretical study on inhibition behavior of novel quinoline derivatives for the corrosion of mild steel in hydrochloric acid solution, *Journal of Molecular Liquids*, 244 (2017) 154-168.
- [76] A. Raman, S. Nasrazadani, L. Sharma, Morphology of rust phases formed on weathering steels in various laboratory corrosion tests, *Metallography*, 22 (1989) 79-96.
- [77] R.A. Antunes, R.U. Ichikawa, L.G. Martinez, I. Costa, Characterization of corrosion products on carbon steel exposed to natural weathering and to accelerated corrosion tests, *International Journal of Corrosion*, 2014 (2014).
- [78] X. Shi, Y. Li, S. Jungwirth, Y. Fang, N. Seeley, E. Jackson, Identification and laboratory assessment of best practices to protect DOT equipment from the corrosive effect of chemical deicers, in, *Washington State Department of Transportation*, 2012.

- [79] N. Gucunski, A. Maher, B. Basily, H. La, R. Lim, H. Parvardeh, S. Kee, Robotic platform robot for condition assessment of concrete bridge decks using multiple nde technologies, HDKBR INFO Magazin, 3 (2013) 5-12.
- [80] R.E. Mateega, Rehabilitation of Historic Holmes Street Bridge, in: STRUCTURE, STRUCTURE Magazine, 2013, pp. 3.

8. IMPROVING THE WETTABILITY OF STRUCTURAL STEELS BY EMPLOYING IONIC LIQUIDS⁷

This chapter discusses the effect of room temperature ionic liquids surface treatment on the wettability behavior of ASTM A57 steel. The contents of this chapter have been published in Sajid, H.U. and Kiran, R., 2021. Improving the wettability of structural steels by employing ionic liquids. *Journal of Molecular Liquids*, 324, p.115137.

8.1. Introduction

Support bearings are integral to a bridge system. They are vital for transferring loads from the superstructure to the substructure and accommodating thermal expansion and small rotations to ensure the functionality of a bridge system under all service conditions. While support bearings are meant to last throughout the life of a bridge, they often tend to have a lower service life as compared to bridges [1]. Steel bearings can trap dust and moisture and form an oxygen concentration cell that leads to corrosion and degradation of the bearings. Many studies, including a survey (see Figure 8.1), have pointed out corrosion as one of the main deterioration mechanisms that lead to a reduction in functionality and service life of metallic support bearings and other components, which result in frequent maintenance and repairs [1-5]. The corrosion problem in metallic support bearings is further exacerbated by exposure to deicing salts [6], rainwater, ineffective lubrication, excreted from animals, and leakages in the superstructure that allow the flow of deicing salts, dirt, and rainwater towards the bearings [4]. The direct maintenance and replacement cost of bearings accounts for about 7% of the entire bridge maintenance budget [2, 7]. To increase the service life and to counter the corrosion-related

⁷ This chapter was co-authored by H.U. Sajid and R. Kiran. H.U. Sajid had the primary responsibility of preparing the specimens, conducting all tests, and drafting this chapter. R. Kiran supervised the research and revised this chapter.

degradation of metallic bearings, different preventive maintenance measures are adopted that include cleaning of bearings (dust and debris removal, and washing), lubrication, and painting. The corrosion behavior, dust removal, and efficient lubrication are affected by the surface characteristics of the bearings, atmospheric conditions, lubricant characteristics, and frequency of cleaning and lubrication. Therefore, understanding the metallic surface characteristics, in particular, the surface wettability, can help improve the effectiveness of preventive measures via efficient lubrication, cleaning, and reduction of corrosion degradation, and thus lead towards improved service life of bearings.

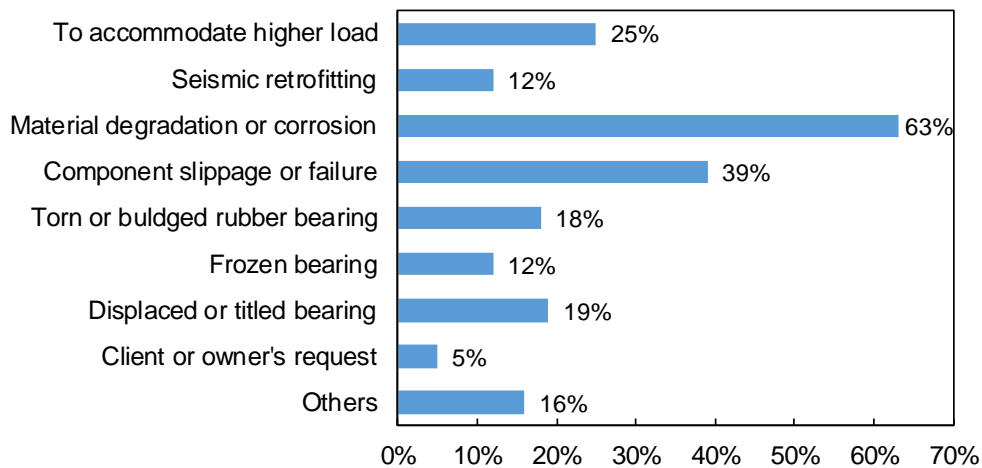


Figure 8.1. Reasons for bridge support bearing replacement (adopted from [4]).

Surface wettability of solid surfaces by liquids is an important parameter that influences many surface properties such as adhesion [8], corrosion resistance [9-21], anti-icing [22-30], self-cleaning and dust control [16, 23, 28, 31-34], lubrication [35-37], and heat transfer [30, 38-41], etc. Surface wettability can be defined as the tendency of a liquid to maintain contact with a solid surface [37] and it is commonly quantified in terms of contact angle (θ_c) of a probing liquid droplet [42]. The contact angle of the probing liquid is defined as the angle that the tangent of the liquid-vapor interface makes with the solid-liquid interface during the wetting process, as

illustrated in Figure 8.2. The wettability of a solid surface in terms of contact angle is typically evaluated by using probing liquids of known surface tension (e.g., water, diiodomethane, etc.). A high contact angle usually corresponds to a surface with low wettability, whereas a lower contact angle indicates a surface with high wettability. Apart from the contact angle of the probing liquid, the surface free energy of the solid surface is another important parameter that can be used to understand the wetting behavior of any liquid on the solid surface. The surface free energy of a solid surface quantifies the intermolecular forces that are present at the solid surface, which include polar interactions (e.g., hydrogen bonding and dipole-dipole interactions) and dispersive interactions (e.g., van der Waals interactions). This way, both polar and dispersive components of the surface free energy can be determined for a solid surface.

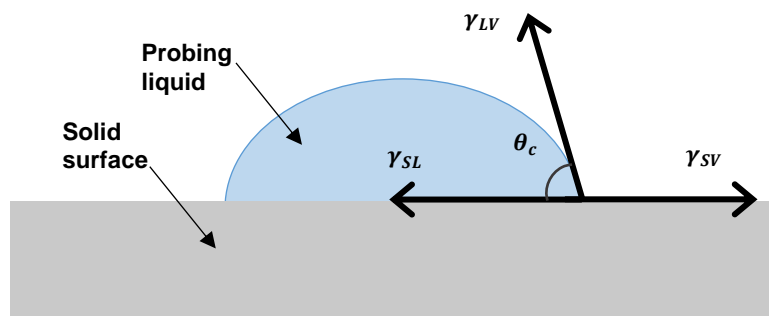


Figure 8.2. Illustration of contact angle (θ_c) of a probing liquid on a solid surface formed at the intersection of the three interfacial tensions (γ_{SL} , γ_{SV} , γ_{LV}).

For achieving desired performance (e.g., corrosion resistance, improved adhesion, lubrication, anti-icing, etc.), the wettability of metallic surfaces can be altered in several ways. For some applications, the surfaces are modified to become more hydrophobic, and in other cases, the surfaces are tuned towards a hydrophilic behavior. Such surfaces are commonly referred to as superhydrophobic ($\theta_c \gg 90^\circ$) or superhydrophilic ($\theta_c \ll 90^\circ$) surfaces [43]. Moreover, some surfaces are designed to serve dual purposes and are tuned to have switchable wettabilities, i.e., hydrophilic, or hydrophobic in the presence of different target media [44-47].

The wettability of surfaces can be changed by controlling the surface roughness [9, 48-52], chemical modification [46, 47, 53], low surface energy coatings [54, 55], microtexturing, and nanotexturing [11, 52, 56-59]. Many of these techniques involve biomimicking and are inspired by biological and natural phenomena that exhibit isotropic and anisotropic wettability. The variation in surface wettability primarily relies on surface chemistry, surface free energy, and surface morphology, and these characteristics can be tailored using different physical and chemical techniques. Superhydrophobic/superhydrophilic surfaces can be fabricated using a variety of techniques that include microtexturing and nanotexturing [11, 21, 52, 56-60], plasma treatment [28, 61-63], ultraviolet irradiation [64-66], ultrasonic spray pyrolysis [67-69], sol-gel process [70-74], etching and calcination [75-83], anodization [84-86], layer-by-layer assembly [87-89], phase inversion [90-92], hydrothermal treatment [19, 83, 93], solution immersion process [94-96], electrospinning [97-99], interfacial polymerization [100, 101], spray coating [102-106], spin coating [29, 107, 108], dip coating [109-112], pulsed laser deposition [113-115], and microwave irradiation [116, 117]. In recent years, texturing techniques, coatings, and etching processes have commonly been employed to change the wettability of metallic surfaces by changing the surface topography, building nanoscale topographical features, and employing low surface energy coatings.

While the above metal surface-altering techniques are yielding extremely promising results for tailoring surfaces for specific service requirements, they are often too costly for large-scale infrastructure applications and are limited by the availability of advanced equipment and the high cost of design. Hence, new avenues are constantly being pursued to tailor the wettability of metallic and non-metallic surfaces using alternative techniques. The current study explores the use of room-temperature ionic liquids (RTILs) for modulating the wetting behavior of the steel

surface to improve the preventive maintenance of bearings by facilitating efficient cleaning, lubrication, and corrosion resistance. RTILs are a relatively new class of materials that have found extensive applications in surface treatments and surface modulations. RTILs have many unique properties such as low toxicity, low vapor pressure, high thermal stability, high chemical stability, and are less hazardous towards the environment that render RTILs desirable for many applications [118, 119]. RTILs have also been explored as potential probing liquids in wettability tests [120]. The wettability and corrosion activity of ionic liquids has been investigated for steel and other metallic and non-metallic materials [121-124]. The ionic liquids investigated in these studies exhibited minimal corrosion activity and a contact angle, which steadily deteriorated with time. Moreover, RTILs have been successfully employed as green corrosion inhibitors for metallic materials, among other corrosion inhibitors [118, 125, 126]. In recent studies, the surface treatment of titanium-based implants with dicationic imidazolium-based ionic liquids led to improved corrosion and wear resistance [127-129]. Similarly, the Ionic liquid surface treatment enhanced the corrosion resistance of Mg-based biodegradable implants [130, 131]. Finally, one study also explored the effect of hydrophobic ionic liquid surface treatment on the water wettability of wood surfaces [132]. These results suggest that ionic liquids have immense potential to improve the corrosion and wear resistance of alloys. While the corrosion resistance of RTILs has been explored for some alloys, only limited investigations have been conducted to understand the role of RTIL surface treatment in regulating the wettability of metallic materials, particularly steels [133-135]. With this in mind, the current study aims to investigate the influence of RTIL surface treatment on the wetting behavior of structural steels. This study establishes the first attempt to alter the surface wetting behavior of a high strength low alloy structural steel by RTIL surface treatment and provides the results of a preliminary investigation

on wettability behavior of RTIL-treated high strength low alloy structural steels. The wettability of high strength low alloy steel surfaces that are pretreated with RTIL for different treatment durations is evaluated in terms of contact angle and surface free energy. To this end, the influence of surface treatment with seven different imidazolium-based RTILs that include 1-ethyl-3-methylimidazolium tetrachloroaluminate ([EMIM][AlCl₄]), 1-butyl-3-methylimidazolium hexafluorophosphate ([BMIM][PF₆]), 1-Ethyl-3-methylimidazolium tetrafluoroborate ([EMIM][BF₄]), 1-hexyl-3-methylimidazolium bromide ([HMIM][Br]), 1-hexyl-3-methylimidazolium hexafluorophosphate ([HMIM][PF₆]), 1-butyl-3-methylimidazolium bis(trifluoromethylsulfonyl)imide ([BMIM][NTf₂]) and 1,2-dimethyl-3-propylimidazolium bis(trifluoromethylsulfonyl)imide ([DMPIM][NTf₂]) on steel surface wettability is investigated. The experimental procedure and the results obtained from contact angle tests are provided in Section 8.2 and Section 8.3, respectively. The important conclusions of this study are summarized in Section 8.4.

8.2. Experimental Procedure

The preparation of RTIL solutions, surfaces of steel specimens, and treatment procedures for surfaces are described in this section. Furthermore, the contact angle tests and the surface free energy evaluation procedures used to quantify the surface wetting behavior of untreated and RTIL-treated steel surfaces are provided.

8.2.1. Preparation of Ionic Liquids Solutions

For this study, seven room-temperature imidazolium-based ionic liquids that include 1-ethyl-3-methylimidazolium tetrachloroaluminate ([EMIM][AlCl₄]), 1-butyl-3-methylimidazolium hexafluorophosphate ([BMIM][PF₆]), 1-Ethyl-3-methylimidazolium tetrafluoroborate ([EMIM][BF₄]), 1-hexyl-3-methylimidazolium bromide ([HMIM][Br]), 1-

hexyl-3-methylimidazolium hexafluorophosphate ([HMIM][PF₆]), 1-butyl-3-methylimidazolium bis(trifluoromethylsulfonyl)imide ([BMIM][NTf₂]), and 1,2-dimethyl-3-propylimidazolium bis(trifluoromethylsulfonyl)imide ([DMPIM][NTf₂]) are obtained from Ionic Liquid Technologies (IoLiTec), Inc. and Sigma-Aldrich. These RTILs have purities greater than 98% and are used in the study in as-received form without further purification. The purity of each IL and impurities present in each IL (as supplied by IoLiTech and Sigma-Aldrich) are provided in Table 8.1. Furthermore, the molecular structure of each IL is illustrated in Figure 8.3. Ethanolic solutions are prepared by mixing 1% w/w RTIL in ethanol. The steel surfaces are treated with these 1% w/w ethanolic RTIL solutions. The preparation procedure for steel surfaces is discussed in the next section.

Table 8.1. The purity and presence of impurities in the ILs.

RTIL	Purity (%)	Impurities (ppm)	
		Water	Halides
[EMIM][AlCl ₄]	>97	1500	–
[BMIM][PF ₆]	>99	133	<100
[BMIM][NTf ₂]	>99	56	<100
[HMIM][Br]	>99	149	–
[HMIM][PF ₆]	>99	62	<100
[EMIM][BF ₄]	>97	1950	–
[DMPIM][NTf ₂]	>99	70	<100

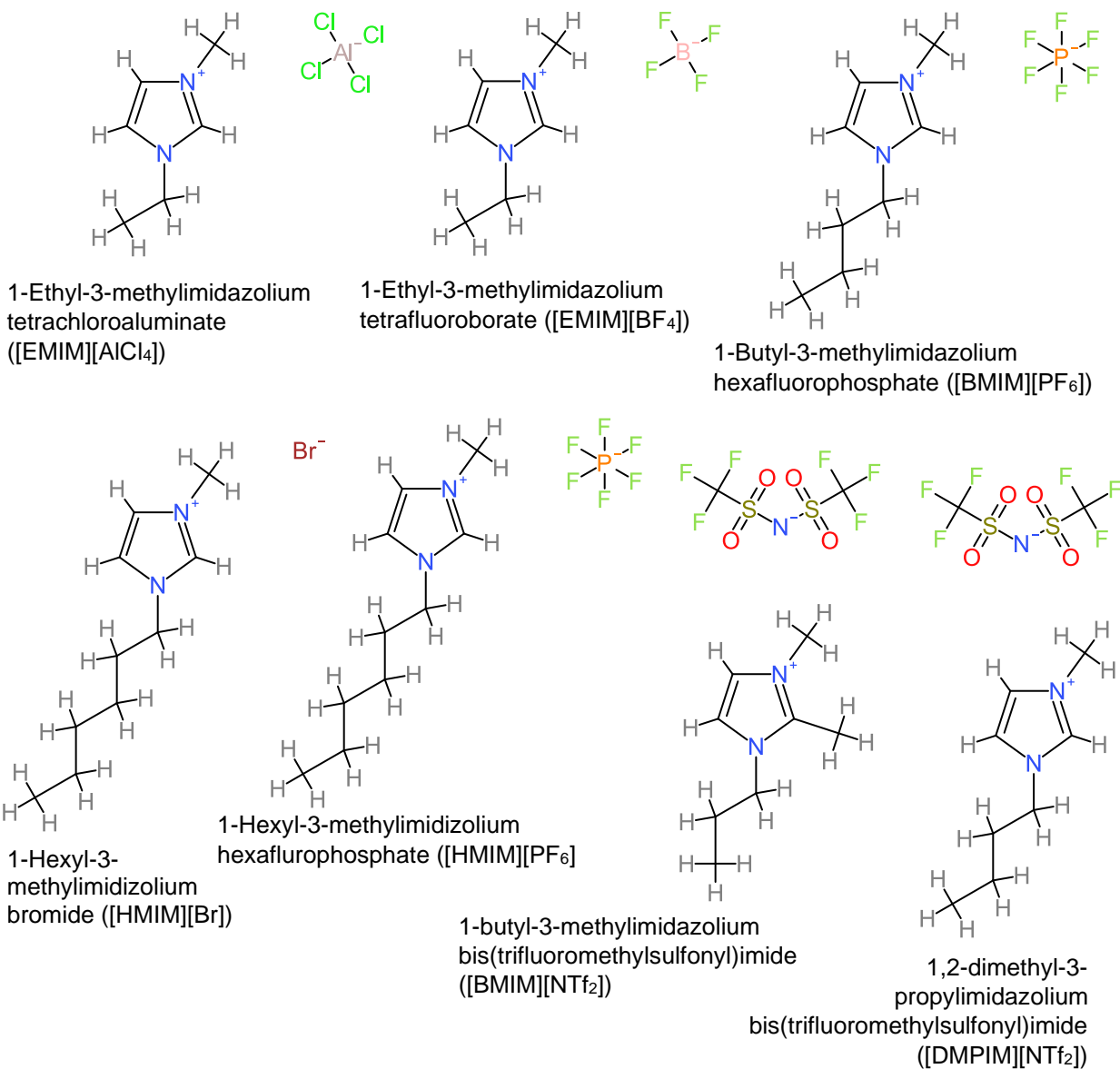


Figure 8.3. Molecular structures of ionic liquids used in this study.

8.2.2. Ionic Liquid Surface Treatment

Cylindrical steel specimens are prepared from a commercially available high strength low alloy ASTM A572 structural steel, which is commonly used in bridge construction in the United States [136, 137], to study the influence of RTIL treatment on surface wetting. The ASTM A572 steel used in this study has an average ferrite grain size of 13 μm and an average pearlite colony size of 3 μm [138], and the chemical composition as supplied by the manufacturer is provided in

Table 8.2. Each cylindrical specimen has an average diameter of 19 mm and a height of 15 mm. Steel specimens surfaces are ground using #60, #120, #320, and #400 silicon carbide papers, thoroughly washed with distilled water, rinsed, and air-dried before surface treatment with RTILs. The RTIL treatment of steel specimen surfaces is conducted using the dip-coating technique. Each specimen is slowly dipped in an ethanolic solution of 1% w/w RTIL, and the specimen is kept immersed in this solution for 0.5 or 4 hour(s). After the immersion period, the treated specimens are removed from the RTIL solution and are left to dry in an oven for 24 hours at 60°C to remove the excess ethanol [128, 139].

Table 8.2. Chemical composition of ASTM A572 high strength low alloy steel.

Element	Composition (%)
Carbon (C)	0.0500
Manganese (Mn)	1.3400
Phosphorous (P)	0.0110
Sulphur (S)	0.0040
Silicon (Si)	0.1500
Copper (Cu)	0.2800
Chromium (Cr)	0.1900
Nickle (Ni)	0.1300
Molybdenum (Mo)	0.0400
Vanadium (V)	0.0830
Titanium (Ti)	0.0010
Niobium (Nb)	0.0030
Iron (Fe)	97.7180

8.2.3. Contact Angle

The surface wetting behavior of RTIL-treated steel specimens is quantified in terms of contact angle and surface free energy. Contact angles of RTIL-treated steel specimens are determined using the sessile drop method using the DSA100 drop shape analyzer (Krüss Scientific) which employs an optical video camera-equipped goniometer. The contact angles of RTIL-treated steel surfaces are determined using polar (deionized water, Sigma-Aldrich,

conductivity: 4.3 $\mu\text{S}/\text{cm}$) and non-polar (diiodomethane, Sigma-Aldrich, purity >98%) probing liquids. The polar and dispersive components of the surface tension properties of both the probing liquids are provided in Table 8.3. For determining the contact angle using the sessile drop method, the probing liquid droplet with an average volume of 5 μL is gently deposited on the steel surface. The contact angle of the probing liquid droplet is then obtained from the drop shape analysis of the sessile drop at the specified time intervals. In this study, the contact angles are determined for both untreated and RTIL-treated steel surfaces after 5 seconds of the probing liquid droplet deposition on the specimen surface. After acquiring the contact angle at 5 seconds, the contact angles are then determined for the same liquid droplet in 15-second intervals until 140 seconds of total deposition time is achieved. Hence, a total of 10 contact angles are determined for each sessile drop at ten different time instances (5, 20, 35, 50, 65, 80, 95, 110, 125, 140 (seconds)). Acquiring initial contact angle and subsequent contact angles at different time ranges facilitate two goals. Firstly, the initial contact angle, which is obtained after 5 seconds of the probing liquid droplet deposition, provides the instantaneous wetting behavior of the RTIL-treated surfaces. Secondly, the contact angles obtained beyond 5 seconds can be used to understand the long-term interactions between the probing liquid and the RTIL-treated steel surfaces and any change in the wettability of the untreated and RTIL-treated steel surfaces. All contact angles are carefully determined using the contact angle test protocols outlined in Refs. [9, 140]. All contact angle tests are conducted at room temperature (22°C) and relative humidity of 55%. For each specimen and each RTIL exposure duration, ten contact angles are determined at three different locations on the specimens, and the average contact angle is reported herein. The contact angles are further used to determine the surface free energy of the untreated and RTIL-treated surfaces using the procedure described in the next section.

Table 8.3. Surface tension (polar and dispersive components) of the probing liquids (adapted from ref. [161]).

Probing liquid	Total surface tension, γ (mN/m)	Polar component, γ^P (mN/m)	Dispersive component, γ^D (mN/m)
Water	72.8	51.0	21.8
Diiodomethane	58.0	0	58.0

8.2.4. Surface Free Energy

The contact angle measurement indicates the wettability of a solid surface for a particular liquid that is used in contact angle measurement and does not provide information regarding the wettability of a solid surface by other liquids, and the interaction between the solid surface and the liquid. Surface free energy is an important indicator of surface wettability of solid surfaces, which can be used to gain insights into the interactions between the solid surface and the deposited liquids and to evaluate the wettability of a solid surface for different liquids. Surface free energy (SFE) can be defined as the work needed to increase the surface area of a solid phase. Surface free energy quantifies the intermolecular interactions between the solid and liquid phases and the spreading or wetting potential of a liquid on a solid surface. The surface free energy of a solid surface can be determined using the contact angle of either one or more than one probing liquid. In the latter case, usually, at least two probing liquids with one being polar and the other being non-polar (dispersive) are used to evaluate the surface free energy of a solid surface. Many thermodynamics-based theoretical approaches are available that can be used to determine the surface free energy of a solid from the contact angle of polar and non-polar liquids on a solid surface. These approaches include Zisman critical surface tension approach [141], Berthelot's combining rule [142], Antonow's rule [143], Good and Garifalco method [144], Neumann's equation of state approach [145], Fowkes approach [146, 147], Owens-Wendt-Rabel-Kaelble (OWRK) method [148], geometric-mean and harmonic-mean approach [148,

149], acid-base approach (van Oss-Good-Chaudhury method) [150], and Chibowski method [151]. Depending on the type of the solid and the probing liquids, these approaches can be used to determine either the total surface free energy or the polar and dispersive components of the surface free energy. In the current study, the surface free energy is determined using the OWRK model, which is most commonly used for determining the surface free energy from the contact angle. The OWRK model requires the contact angles obtained from both polar and dispersive probing liquids. The OWRK model is based on two fundamental assumptions. First, the surface free energy of the surface occurs as a result of polar and dispersive (non-polar) interactions (Eq. (8.1)).

$$\gamma_{sv} = \gamma_{sv}^d + \gamma_{sv}^p \quad (8.1)$$

where, γ_{sv} represents the surface free energy and the superscripts p and d denote polar and dispersive components of the surface free energy (γ_{sv}), respectively. Secondly, the OWRK model adopts the applicability of Berthelot's combining rule, which assumes that work of adhesion between a solid and a liquid is equivalent to the geometric mean of the work of cohesion of the solid and the liquid, which leads to Eq. (8.2).

$$W_{sl} = \sqrt{W_{ll}^d W_{ss}^d} + \sqrt{W_{ll}^p W_{ss}^p} \quad (8.2)$$

where, W_{sl} is the work of adhesion ($W_{sl} = \gamma_{lv} + \gamma_{sv} - \gamma_{sl}$, γ_{lv} is the surface tension of the liquid and γ_{sl} is the interfacial tension between the liquid and the solid), W_{ss} is the work of cohesion for the solid ($W_{ss} = 2\gamma_{sv}$), and W_{ll} is the work of cohesion for the liquid. The work of adhesion can be substituted by the Young-Dupre equation and can thus be represented by Eq. (8.3) as

$$W_{sl} = \gamma_{lv}(1 + \cos\theta) \quad (8.3)$$

Substituting Eq. (8.3) and the values of the work of cohesion of solid and liquid Eq. (8.2) leads to Eq. (8.4).

$$\frac{1}{2}[\gamma_{lv}(1 + \cos\theta)] = \sqrt{\gamma_{lv}^d \gamma_{sv}^d} + \sqrt{\gamma_{lv}^p \gamma_{sv}^p} \quad (8.4)$$

Since Eq. (8.4) has two unknowns (γ_{sv}^d and γ_{sv}^p), two probing liquids with known dispersive components are required to determine the unknown polar and dispersive components of the surface free energy and hence the total surface free energy of the solid surface. To achieve this, first, the contact angle (θ) is determined using diiodomethane probe liquid which only has a dispersive component of surface tension ($\gamma_{lv}^p = 0$). This reduces Eq. (8.4) to

$$\gamma_{sv}^d = \frac{\gamma_{lv}(1 + \cos\theta)^2}{4} \quad (8.5)$$

where, contact angle (θ) is determined using diiodomethane. The dispersive component of surface free energy (γ_{sv}^d) is determined using Eq. (8.5). Once γ_{sv}^d is determined, the polar component of the surface free energy (γ_{sv}^p) is determined from Eq. (8.4) using water as probe liquid, which has both polar and dispersive components of the surface tension. The total surface free energies of the untreated and RTIL-treated steel surfaces are then determined from Eq. (1). The surface free energies of test specimens are reported and discussed in Section 8.3.4.

8.3. Results and Discussion

The contact angle test results and the surface free energy evaluated for RTIL-treated steel specimens are discussed in this section.

8.3.1. Water Contact Angle

The contact angle of the untreated and RTIL-treated steel specimens are determined using the procedure discussed in Section 8.2.2. The contact angles of water (polar probing liquid) on steel specimens obtained at different time intervals (5 seconds to 140 seconds) after surface treatment of steel specimens with ethanolic RTIL solutions for 0.5 hours and 4 hours are provided in Figure 8.4 and Figure 8.5, respectively. The probing liquid drop images on untreated

and RTIL-treated surfaces are presented in Figure 8.6 and Figure 8.7. The probing liquid drop images obtained at certain time instances (5 sec, 35 sec, 65 sec, 95, and 125 sec) are presented for the sake of brevity. From Figure 4 and Figure 5, it is clear that untreated specimens exhibited the highest water contact angle (lowest wettability) when compared to the steel specimens that are surface-treated with ethanolic solutions of room temperature ionic liquids. The untreated steel specimens exhibited an average initial water contact angle of 77.12° . The average initial water contact angle of steel specimens decreased by 24-87% after ionic liquid treatment. The average initial water contact of the steel specimens that are treated with RTIL for 0.5 hours exhibited the following trends: $[\text{EMIM}][\text{AlCl}_4]$ (58.52°) > $[\text{HMIM}][\text{PF}_6]$ (38.81°) > $[\text{BMIM}][\text{PF}_6]$ (32.10°) > $[\text{DMPIM}][\text{NTf}_2]$ (28.04°) > $[\text{BMIM}][\text{NTf}_2]$ (24.99°) > $[\text{EMIM}][\text{BF}_4]$ (18.71°) > $[\text{HMIM}][\text{Br}]$ (9.53°). The average water contact angle of both untreated and RTIL-treated specimens decreased steadily with an increase in the elapsed time until an equilibrium is achieved (see Figure 8.4). For most of the specimens, the average water contact angle decreased continuously until 65 sec beyond which the average water contact angle remained relatively static. The average water contact angle of most of the RTIL-treated specimens deteriorated by 39-55% whereas the average water contact angle of the untreated specimen decreased only by 16%. That is, the RTIL treated samples became more wettable with time. In the case of the $[\text{HMIM}][\text{Br}]$ -treated specimens, complete spreading (water wetting) is observed after 20 seconds of water droplet deposition. An increase in the RTIL treatment time from 0.5 hours to 4 hours lead to a small reduction in the water contact angles of the RTIL-treated steel specimens (see Figure 8.7 and Figure 8.5). With this, there is no need for longer treatment time, especially for applications that require increased water wettability (for example, cleaning of bridge bearings).

The underlying mechanisms that lead to an increase in the water wettability of the RTIL-treated structural steels are discussed in the next section.

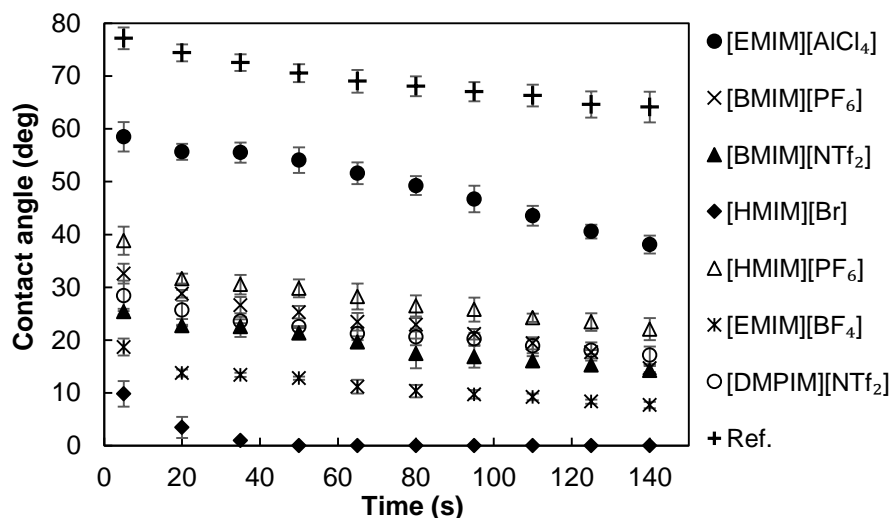


Figure 8.4. Water Contact angle results for 1%IL+Ethanol (exposure duration: 30 minutes) at different time intervals.

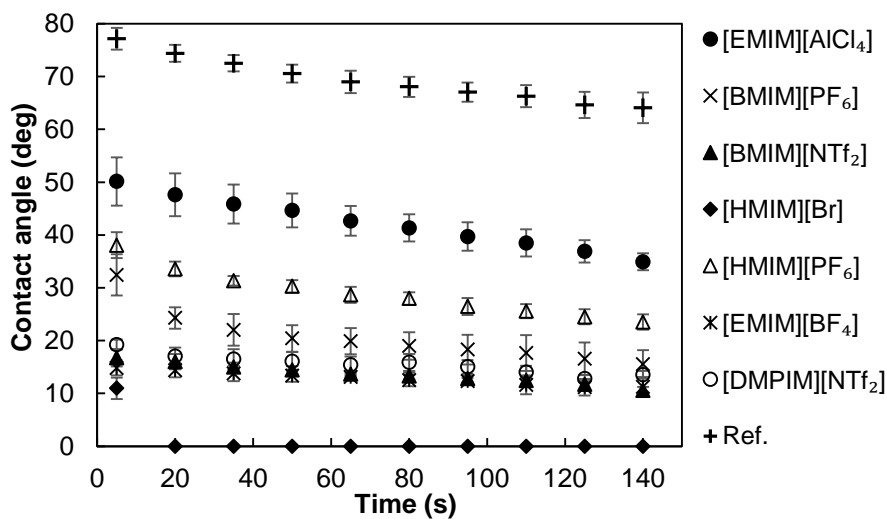


Figure 8.5. Water Contact angle results for 1%IL+Ethanol (exposure duration: 4 hours) at different time intervals.

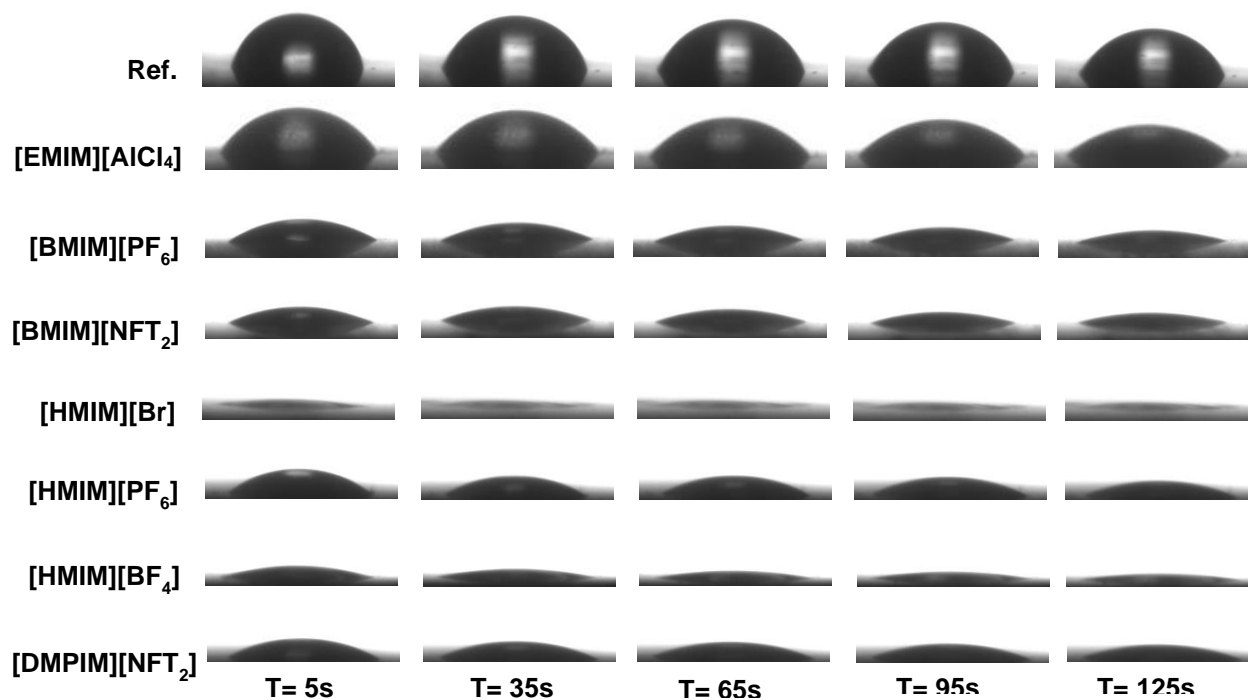


Figure 8.6. Water Contact angles for 1%IL+Ethanol (exposure duration: 30 minutes) at different time intervals.

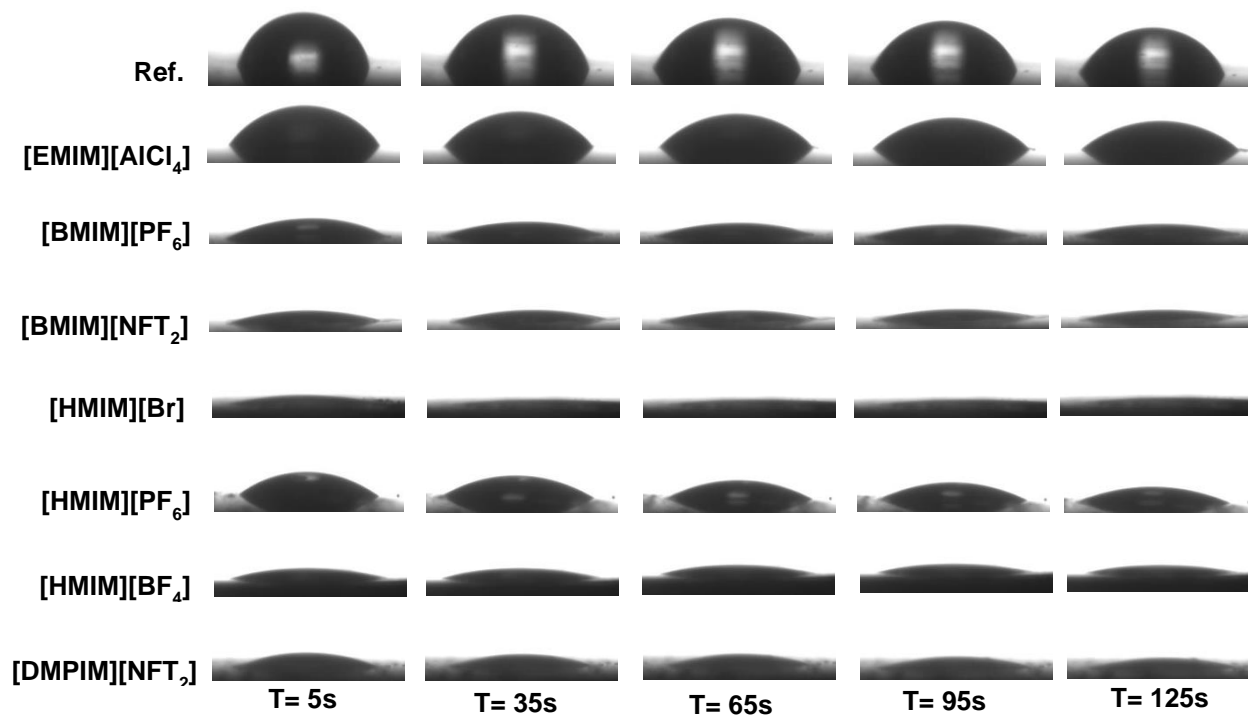


Figure 8.7. Water Contact angles for 1%IL+Ethanol (exposure duration: 4 hours) at different time intervals.

8.3.2. Discussion on Water Contact Angle of RTIL-treated Steel Surfaces

The water contact angle trends for both untreated and RTIL-treated specimens can be explained by the surface characteristics of both sets of steel specimens and the associated laws of contact angles for metallic surfaces. On a rigid, flat, and chemically homogenous surface (see Figure 2), the surface wetting contact angle follows Young's equation (Eq. (8.6))

$$\cos \theta_c = \frac{\gamma_{sv} - \gamma_{sl}}{\gamma_{lv}} \quad (8.6)$$

The contact angle observed on the polished untreated steel surfaces can be described by Eq. 8.6. For untreated steel specimens, the average initial water contact angle of 77.12° is reported in previous studies [9], which is usually the result of the oxide monolayer that spontaneously forms on the steel surface after exposure to the environment [9]. When steel surfaces are treated with RTILs, a thin film or coating of the RTIL can form on the surface [127, 128, 130], which is a function of the treatment time [130] and the type of RTIL. The presence of such a thin film or surface coating can, therefore, alter the wetting behavior of the RTIL-treated steel surfaces, as they are no more similar to the untreated steel surfaces. The wetting properties of the steel surfaces are thus dictated by the RTIL film, and the properties of the RTIL (anionic hydrophilicity or hydrophobicity). Consequently, the surface wettability of the RTIL-treated steel surfaces can be described by the modified form of Young's equation (Eq. 8.7), which can be described as

$$\cos \theta_o = \frac{\gamma_{ov} - \gamma_{ol}}{\gamma_{lv}} \quad (8.7)$$

where θ_o is the apparent contact angle of a water droplet on the RTIL-treated steel surface, γ_{ol} is the interfacial tension between the liquid (water) and the RTIL-treated surface, and γ_{ov} is the RTIL layer-air interfacial tension. The wettability of steel surface can be increased by virtue of the modified Young's equation (Eq. 8.7), if γ_{ov} is greater than γ_{ol} [152]. In the current study, the

average value of γ_{ov} (RTIL layer-air interfacial tension) is greater than the γ_{ol} (the interfacial tension between water and RTIL). The average γ_{ov} value of NTf₂-based ionic liquids reportedly ranges between 27 mN/m and 48 mN/m [153, 154] whereas the γ_{ov} value of [BF₄], [PF₆], [Br], and [Cl]based ionic liquids ranges between 35 mN/m and 70 mN/m, depending upon the number *n* in the alkyl chain length [155]. On the other hand, the average value of the room temperature γ_{ov} (RTIL layer-air interfacial tension) of these RTILs range between 10 mN/m and 19 mN/m [156]. Hence, the RTIL-treated surfaces are expected to higher wettability (since γ_{ov} is greater than γ_{ol}) and the wettability trends of the RTIL-treated steel surfaces discussed in the previous section confirmed the theoretical trends. Experimental characterization of the RTIL film formed on the steel surface is not pursued herein and falls outside the scope of the current study.

Among the RTIL-treated steel specimens, the RTILs with hydrophobic anions such as [PF₆] and [NTf₂] exhibited higher water contact angles, which can be attributed to the immiscibility of these anions with water. Previous studies conducted on the wettability of Au (gold) surfaces with ultra-thin ILs films with hydrophobic anion moieties (such as [PF₆] and [NTf₂]) also observed high water contact angles as compared to Au substrates that are treated with hydrophilic anions [135]. Apart from the anion dependency, the wettability of the metal substrate is also dependent on the fraction of the steel surface covered by the ionic liquid film formed after surface treatment [157]. A high surface fraction of ionic liquid film with hydrophilic anion (such as [HMIM][Br]) changes the thermodynamic nature of the steel surface as compared to the bulk steel and thus significant interaction can occur with water. For instance, the interaction energy of water is higher with [BF₄] anion (-32 kJ/mol) as compared to [PF₆] anion (-28 kJ/mol) for the same cation ([BMIM]) [158]. This, in turn, leads to higher IL-water interaction and thus higher wettability and complete spreading of the water droplet on the steel

surfaces that are treated with a hydrophilic ionic liquid (see Figure 8.4 and Figure 8.5). Finally, the increase in the alkyl chain length of the cations (HMIM compared to BMIM) reduces the water-cation interaction [158]. Moreover, for alkyl chain length with $n \leq 8$, the surface tension is observed to decrease with the increase in the alkyl chain length of the ionic liquid, which can be attributed to the weakening coulomb interactions in the case of longer alkyl chain lengths [153]. Hence, the steel specimens that are treated with ILs having the same anions (for instance [BMIM][PF₆] and [HMIM][PF₆]) but higher alkyl chain length ([HMIM][PF₆]) exhibited slightly higher water contact angle (lower water wettability).

8.3.3. Diiodomethane Contact Angle

The diiodomethane (non-polar liquid) contact angles are determined to evaluate the surface free energies of untreated and RTIL-treated steel surfaces and to understand the wetting behavior of RTIL-treated steel surfaces for non-polar liquids (such as lubricants). The contact angle of diiodomethane (non-polar probe liquid) on untreated and RTIL-treated steel specimens is determined at 5 seconds and then at 15-second intervals after the deposition of the probe liquid on the surface using the procedure discussed in Section 8.2.3. Moreover, the non-polar contact angles are obtained for specimens that are pretreated with ethanolic IL solutions for two different durations (0.5 hours and 4 hours). The deposited probe liquid at different elapsed times is shown in Figure 8.8 and Figure 8.9. The average contact angles obtained for both untreated and RTIL-treated steel specimens are provided in Figure 8.10 and Figure 8.11. As observed in Figure 8.10 and Figure 8.11, the diiodomethane contact angle remained relatively static and did not exhibit considerable deterioration throughout the elapsed time of 140 seconds. Moreover, no considerable influence of RTIL solutions immersion time is noticed. An average initial contact angle of 62.30° is observed for untreated steel specimens. On the other hand, the RTIL surface

treatment led to a reduction in the diiodomethane contact angle of steel surfaces. The average initial diiodomethane contact angle of the RTIL-treated steel surface decreased by 25-66% when compared to the untreated steel surface. The average initial diiodomethane contact of the steel specimens that are treated with RTIL for 0.5 hours exhibited the following trends:

[DMPIM][NTf₂] (49.56°) > [BMIM][NTf₂] (46.12°) > [BMIM][PF₆] (43.75°) > [HMIM][PF₆] (41.87°) > [EMIM][BF₄] (40.30°) > [EMIM][AlCl₄] (38.35°) > [HMIM][Br] (20.87°). These

values demonstrate that RTIL-treatment leads to increased wetting of steel surfaces by non-polar liquids, which can also help in improving the lubrication of steel surfaces for non-polar lubricants. The contact angle trends in the case of RTIL-treated steel specimens demonstrate that the steel specimens that are treated with ionic liquids with high alkyl chain lengths and hydrophobic and bulky anions result in high contact angles (low wettability). The diiodomethane contact angles along with the water contact angles are used to obtain surface free energies of steel specimens that are discussed in the next section.

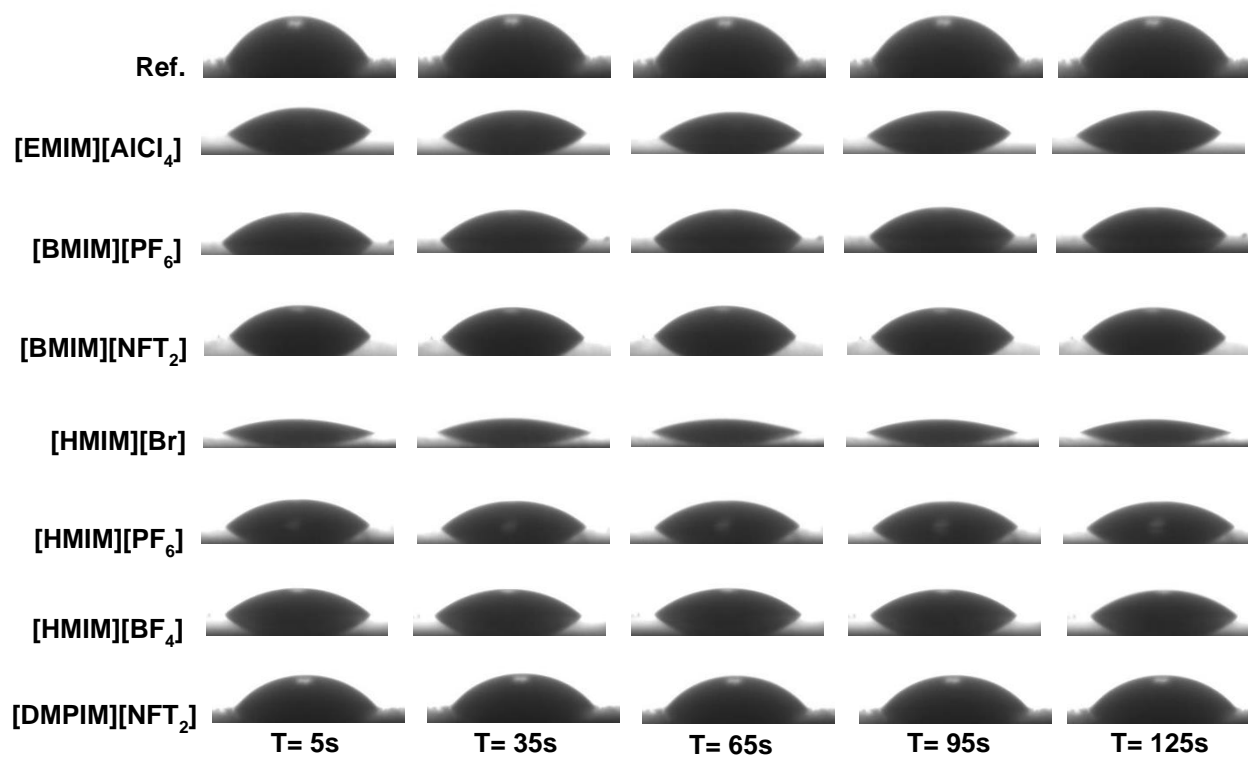


Figure 8.8. Diiodomethane contact angles for 1%IL+Ethanol (exposure duration: 30 minutes) at different time intervals.

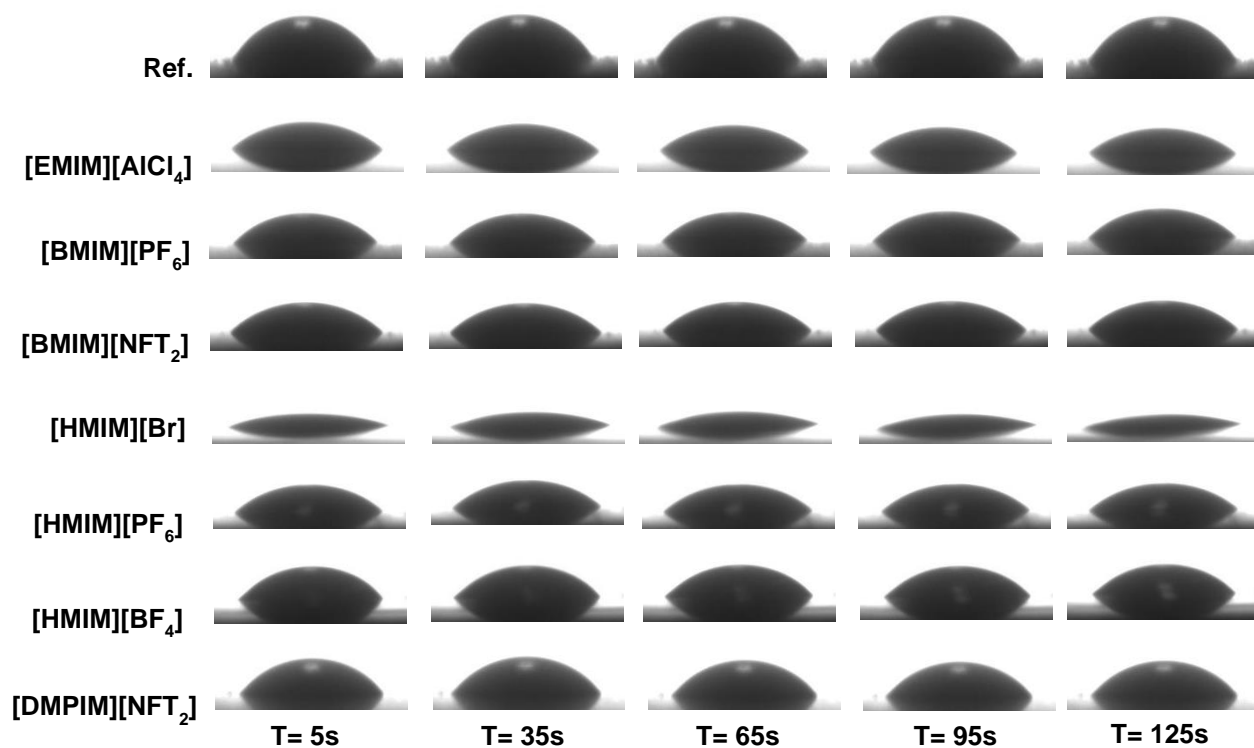


Figure 8.9. Diiodomethane contact angles for 1%IL+Ethanol (exposure duration: 4 hours) at different time intervals.

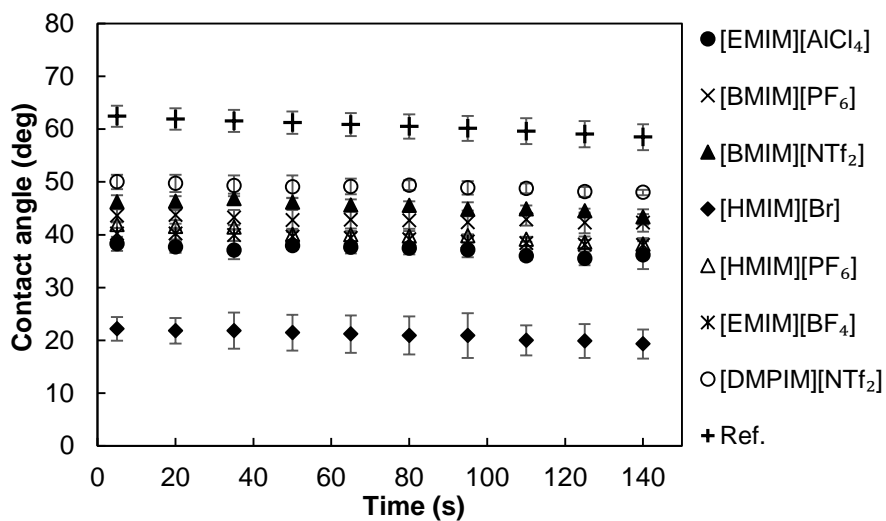


Figure 8.10. Diiodomethane Contact angle results for 1%IL+Ethanol (exposure duration: 30 minutes) at different time intervals.

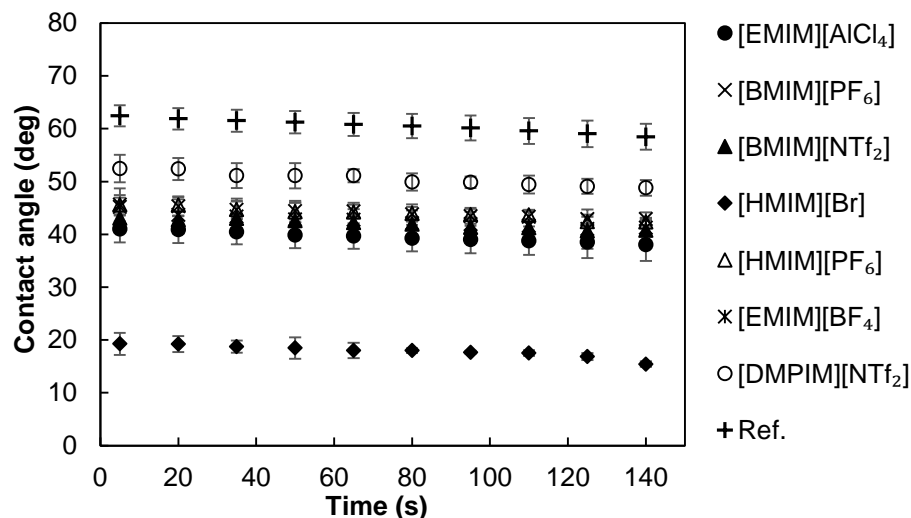


Figure 8.11. Diiodomethane Contact angle results for 1%IL+Ethanol (exposure duration: 4 hours).

8.3.4. Surface Free Energy

The surface free energies of untreated and RTIL-treated steel specimens are determined from the polar and non-polar probe liquid contact angles using the procedure discussed in Section 8.2.4. The average surface energies of test specimens are obtained by taking the average of individual contact angles at different time intervals (for 4 hours immersion time) and are provided in Figure 8.12. An average surface energy value of 38.77 mJ/m² is observed in the case of untreated specimens (see Figure 8.12), which is typical for a polished steel surface [9]. On the other hand, the IL surface treatment increased the surface free energy of steel surfaces. The average surface free energies of RTIL-treated steel specimens exhibited the following trends: [HMIM][Br] (77.67 mJ/m²) > [EMIM][BF₄] (73.57 mJ/m²) > [BMIM][NTf₂] (70.68 mJ/m²) > [BMIM][PF₆] (69.24 mJ/m²) > [DPMIM][NTf₂] (69.05 mJ/m²) > [HMIM][PF₆] (67.60 mJ/m²) > [EMIM][AlCl₄] (56.69 mJ/m²). From Figure 8.12, it can be inferred that the presence of ionic liquid film increased the surface free energy of steel specimens and thus render them more amenable to wetting by both polar and non-polar liquids. A similar observation was also noticed

in a recent study wherein the IL-modification of a commonly used polymer (poly(methyl methacrylate)) increased the surface free energy of the polymer [159]. Finally, among the RTIL-treated steel specimens, the increase in the alkyl chain length of the cation and increase in the anion size resulted in slightly lower surface free energy (e.g. [DPMIM][NTf₂] and [HMIM][PF₆]) when compared to the surface free energy obtained in the case of ILs with lower alkyl chain length and smaller anion size (e.g. [EMIM][BF₄]). This observation can be attributed to the dispersion of the ion charge in the case of RTILs with large anion size and longer alkyl chain lengths [159, 160].

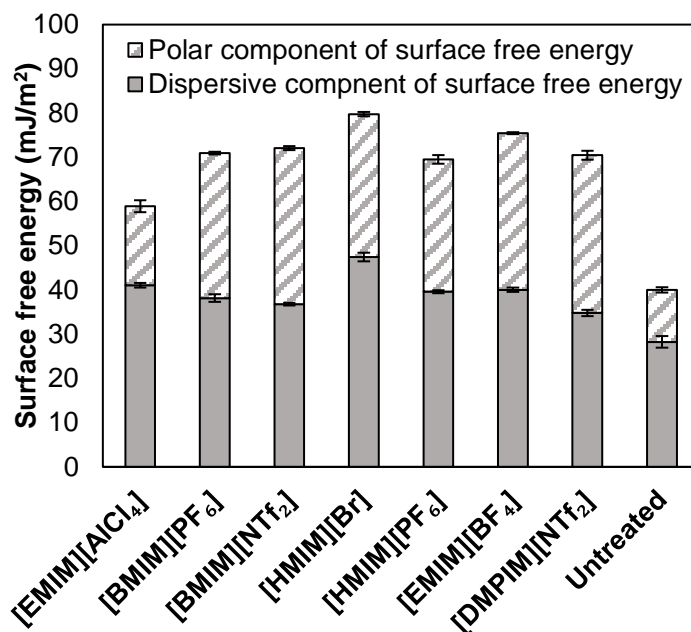


Figure 8.12. Average surface free energies (polar and dispersive components) of untreated and RTIL-treated steel specimens.

8.4. Conclusions

In this study, the wetting behavior of steel specimens that are treated with various room-temperature ionic liquids with different alkyl chain lengths and anions was investigated. The important conclusions that can be drawn from this study are as follows:

1. Ionic liquids surface treatment increased the water wettability and surface free energies of the steel surfaces and thus rendered them more amenable to water and non-polar liquid wetting.
2. Steel specimens that are treated with ionic liquids with long alkyl chain length and bulky and hydrophobic anions (e.g. [PF₆] and [NTf₂]) exhibited relatively lower wettability when compared to steel specimens that are treated with ionic liquids with lower alkyl chain lengths and hydrophilic anions (e.g. [Br] and [BF₄]).
3. The average initial water contact angle of steel specimens decreased by 24-87% after surface treatment with ionic liquids. The highest reduction in water contact angle is noticed in the case of ionic liquids with hydrophilic anion (such as [Br] and [BF₄]), which can be attributed to the stronger interaction between water and the hydrophilic anions.
4. The water contact angle steadily decreased and relatively stabilized 65 seconds after the deposition of the water droplet on the RTIL-treated surface. In contrast, the non-polar liquid contact angle remained almost static for the entire period.
5. Both polar and dispersive components of surface free energies of the RTIL-treated steel specimens increased, which demonstrated the stronger interactions (van der Waals, hydrogen bonding, and dipole-dipole interactions) among the water and ionic liquid films.

The wetting behavior of the room temperature ionic liquid treated steel surfaces reported herein for structural steels for the first time provides a unique perspective for engineers and staff involved in bridge bearing maintenance. These results can be used for improving the cleaning and lubrication efficiency of large and inaccessible structural steel components (such as bearings). As the bridge maintenance authorities are increasingly using a bearing-washing

routine to clean the bearings of any deleterious debris and dirt, the ionic liquid surface treatment can improve the water-based cleaning efficiency by improving the water wettability of steel surfaces. Moreover, the RTIL-treatment can also lead to improved spreading of non-polar lubricants and thus increase the efficiency of the bearing lubrication process. Finally, the room temperatures ionic liquids used in this study are previously observed to inhibit corrosion in different types of steels in corrosive media [118, 125]. Therefore, the presence of a room-temperature ionic liquid film on the steel bearing surface can help mitigate corrosion in steel bearing and associated components through direct corrosion inhibition and facilitation of effective cleaning of bearings. The influence of the weight percentage of RTILs in the ethanol and the choice of solvent is not investigated in this study and will be pursued in future studies.

8.5. References

- [1] L.M. Freire, J. De Brito, J.R. Correia, Management system for road bridge structural bearings, *Structure and Infrastructure Engineering*, 10 (2014) 1068-1086.
- [2] L.M. Freire, J. de Brito, J.R. Correia, Inspection survey of support bearings in road bridges, *Journal of Performance of Constructed Facilities*, 29 (2015) 04014098.
- [3] L. Lindquist, Corrosion of steel bridge girder anchor bolts, in, MS Thesis. Georgia Institute of Technology, 2008.
- [4] A.O. Fasheyi, Bridge Bearings: Merits, Demerits, Practical Issues, Maintenance and Extensive Surveys on Bridge Bearing, (2012).
- [5] D.L. Naik, H.U. Sajid, R. Kiran, G. Chen, Detection of Corrosion-Indicating Oxidation Product Colors in Steel Bridges under Varying Illuminations, Shadows, and Wetting Conditions, *Metals*, 10 (2020) 1439.

- [6] H.U. Sajid, D.L. Naik, R. Kiran, Improving the ice-melting capacity of traditional deicers, *Construction and Building Materials* 271 (2021): 121527.
- [7] M. Fragnet, J. Seantier, La structure de la Norme EN 1337. Les appareils d'appui structuraux: la mise en application des normes européennes, ENPC/SA Ponts Formation Edition, Paris (in French), (2005).
- [8] K.L. Mittal, Contact Angle, Wettability and Adhesion, Volume 3, CRC Press, 2003.
- [9] H.U. Sajid, R. Kiran, Influence of corrosion and surface roughness on wettability of ASTM A36 steels, *Journal of Constructional Steel Research*, 144 (2018) 310-326.
- [10] X.-F. Zhang, R.-J. Chen, J.-M. Hu, Superhydrophobic surface constructed on electrodeposited silica films by two-step method for corrosion protection of mild steel, *Corrosion Science*, 104 (2016) 336-343.
- [11] U. Trdan, M. Hočevár, P. Gregorčič, Transition from superhydrophilic to superhydrophobic state of laser textured stainless steel surface and its effect on corrosion resistance, *Corrosion Science*, (2017).
- [12] A.V. Anand, S. Gollakota, V. Hariprasad, Ashifkhan, N. Shunmugavelu, V. Arumugam, Role of micropatterns on wettability and corrosion characteristics of SS304 steel surface, in: *AIP Conference Proceedings*, AIP Publishing LLC, 2019, pp. 040006.
- [13] M. Conradi, T. Sever, P. Gregorčič, A. Kocijan, Short-and long-term wettability evolution and corrosion resistance of uncoated and polymer-coated laser-textured steel surface, *Coatings*, 9 (2019) 592.
- [14] L. Boinovich, S. Gnedenkov, D. Alpysbaeva, V. Egorkin, A. Emelyanenko, S. Sinebryukhov, A. Zaretskaya, Corrosion resistance of composite coatings on low-carbon

- steel containing hydrophobic and superhydrophobic layers in combination with oxide sublayers, *Corrosion science*, 55 (2012) 238-245.
- [15] J. Li, L. Pan, Q. Fu, Y. Zhou, N. Guo, Wettability and corrosion behavior of a Ni coating on 304 stainless steel surface, *Surface and Coatings Technology*, 357 (2019) 740-747.
- [16] X. Dong, J. Meng, Y. Hu, X. Wei, X. Luan, H. Zhou, Fabrication of Self-Cleaning Superhydrophobic Surfaces with Improved Corrosion Resistance on 6061 Aluminum Alloys, *Micromachines*, 11 (2020) 159.
- [17] E.A. de Souza Filho, E.F. Pieretti, R.T. Bento, M.F. Pillis, Effect of nitrogen-doping on the surface chemistry and corrosion stability of TiO₂ films, *Journal of Materials Research and Technology*, 9 (2020) 922-934.
- [18] J.A. Nardi, J.A. Strauss, F.M. Fardo, L.C. Ferreira, E.M. Martini, F. Horowitz, Wettability and anticorrosion of thin PTFE-like/alumina coatings on carbon steel, *Progress in Organic Coatings*, 148 (2020) 105823.
- [19] F. Zhang, C. Zhang, L. Song, R. Zeng, S. Li, H. Cui, Fabrication of the superhydrophobic surface on magnesium alloy and its corrosion resistance, *Journal of Materials Science & Technology*, 31 (2015) 1139-1143.
- [20] B. Lin, Y. Zuo, Inhibition of Q235 carbon steel by calcium lignosulfonate and sodium molybdate in carbonated concrete pore solution, *Molecules*, 24 (2019) 518.
- [21] U. Trdan, T. Sano, D. Klobčar, Y. Sano, J. Grum, R. Šturm, Improvement of corrosion resistance of AA2024-T3 using femtosecond laser peening without protective and confining medium, *Corrosion Science*, 143 (2018) 46-55.

- [22] Q. Fu, X. Wu, D. Kumar, J.W. Ho, P.D. Kanhere, N. Srikanth, E. Liu, P. Wilson, Z. Chen, Development of sol–gel icephobic coatings: effect of surface roughness and surface energy, *ACS applied materials & interfaces*, 6 (2014) 20685-20692.
- [23] L. Feng, Z. Yan, X. Shi, F. Sultonzoda, Anti-icing/frosting and self-cleaning performance of superhydrophobic aluminum alloys, *Applied Physics A*, 124 (2018) 142.
- [24] C. Wei, B. Jin, Q. Zhang, X. Zhan, F. Chen, Anti-icing performance of super-wetting surfaces from icing-resistance to ice-phobic aspects: Robust hydrophobic or slippery surfaces, *Journal of Alloys and Compounds*, 765 (2018) 721-730.
- [25] T. Bharathidasan, S.V. Kumar, M. Bobji, R. Chakradhar, B.J. Basu, Effect of wettability and surface roughness on ice-adhesion strength of hydrophilic, hydrophobic and superhydrophobic surfaces, *Applied surface science*, 314 (2014) 241-250.
- [26] H. Saito, K. Takai, G. Yamauchi, Water-and ice-repellent coatings, *Surface Coatings International*, 80 (1997) 168-171.
- [27] M. Ruan, W. Li, B. Wang, B. Deng, F. Ma, Z. Yu, Preparation and anti-icing behavior of superhydrophobic surfaces on aluminum alloy substrates, *Langmuir*, 29 (2013) 8482-8491.
- [28] B. Subeshan, A. Usta, R. Asmatulu, Deicing and self-cleaning of plasma-treated superhydrophobic coatings on the surface of aluminum alloy sheets, *Surfaces and Interfaces*, 18 (2020) 100429.
- [29] G. Momen, M. Farzaneh, Facile approach in the development of icephobic hierarchically textured coatings as corrosion barrier, *Applied surface science*, 299 (2014) 41-46.
- [30] S. Moghtadernejad, C. Lee, M. Jadidi, An Introduction of Droplet Impact Dynamics to Engineering Students, *Fluids*, 5 (2020) 107.

- [31] O.-U. Nimittrakoolchai, S. Supothina, Deposition of organic-based superhydrophobic films for anti-adhesion and self-cleaning applications, *Journal of the European Ceramic Society*, 28 (2008) 947-952.
- [32] Y.-Y. Quan, L.-Z. Zhang, R.-H. Qi, R.-R. Cai, Self-cleaning of surfaces: the role of surface wettability and dust types, *Scientific reports*, 6 (2016) 38239.
- [33] R. Fürstner, W. Barthlott, C. Neinhuis, P. Walzel, Wetting and self-cleaning properties of artificial superhydrophobic surfaces, *Langmuir*, 21 (2005) 956-961.
- [34] Z. He, Z. Zhang, J. He, CuO/Cu based superhydrophobic and self-cleaning surfaces, *Scripta Materialia*, 118 (2016) 60-64.
- [35] C. Liu, F. Guo, P. Wong, X. Li, Tribological behaviour of surfaces with stepped wettability under limited lubricant supply, *Tribology International*, 141 (2020) 105880.
- [36] X. Li, F. Guo, P. Wong, Y. Zhao, Regulation of lubricant supply by wettability gradient in rolling EHL contacts, *Tribology International*, 120 (2018) 565-574.
- [37] P.-G. De Gennes, F. Brochard-Wyart, D. Quéré, *Capillarity and wetting phenomena: drops, bubbles, pearls, waves*, Springer Science & Business Media, 2013.
- [38] H. Hu, Z. Lai, G. Ding, Influence of surface wettability on heat transfer and pressure drop characteristics of wet air in metal foam under dehumidifying conditions, *International Journal of Thermal Sciences*, 135 (2019) 331-343.
- [39] M. Moezzi, S. Kazemzadeh Hannani, B. Farhanieh, The role of surface wettability on the heat transfer in liquid-liquid two-phase flow in a microtube, *Physics of Fluids*, 31 (2019) 082004.
- [40] J. Cui, Y. Cui, Effects of surface wettability and roughness on the heat transfer performance of fluid flowing through microchannels, *Energies*, 8 (2015) 5704-5724.

- [41] H.M. Ali, M.A. Qasim, S. Malik, G. Murtaza, Techniques for the Fabrication of Super-Hydrophobic Surfaces and Their Heat Transfer Applications, *Heat Transfer: Models, Methods and Applications*, (2018) 283.
- [42] E. Matijevic, R.J. Good, *Surface and colloid science*, Springer Science & Business Media, 2012.
- [43] Y. Yuan, T.R. Lee, Contact angle and wetting properties, in: *Surface science techniques*, Springer, 2013, pp. 3-34.
- [44] Z. Hua, J. Yang, T. Wang, G. Liu, G. Zhang, Transparent surface with reversibly switchable wettability between superhydrophobicity and superhydrophilicity, *Langmuir*, 29 (2013) 10307-10312.
- [45] H. Gao, Y. Liu, G. Wang, S. Li, Z. Han, L. Ren, Biomimetic metal surfaces inspired by lotus and reed leaves for manipulation of microdroplets or fluids, *Applied Surface Science*, 519 (2020) 146052.
- [46] T.A. Otitoju, A.L. Ahmad, B.S. Ooi, Superhydrophilic (superwetting) surfaces: A review on fabrication and application, *Journal of Industrial and Engineering Chemistry*, 47 (2017) 19-40.
- [47] Y. Shi, W. Yang, X. Feng, L. Feng, G. Yue, Y. Wang, Bio-inspired fabrication of copper oxide nanowire films with switchable wettability via a facile thermal oxidation method, *RSC Advances*, 5 (2015) 26107-26113.
- [48] K. Kubiak, M. Wilson, T. Mathia, P. Carval, Wettability versus roughness of engineering surfaces, *Wear*, 271 (2011) 523-528.

- [49] S. Panda, A. Panzade, M. Sarangi, S. Roy Chowdhury, Spectral approach on multiscale roughness characterization of nominally rough surfaces, *Journal of Tribology*, 139 (2017).
- [50] A. Sari, N.S. Al Maskari, A. Saeedi, Q. Xie, Impact of surface roughness on wettability of oil-brine-calcite system at sub-pore scale, *Journal of Molecular Liquids*, 299 (2020) 112107.
- [51] N.S. Al Maskari, A. Sari, A. Saeedi, Q. Xie, Influence of surface roughness on the contact angle due to calcite dissolution in an oil–brine–calcite system: a nanoscale analysis using atomic force microscopy and geochemical modeling, *Energy & Fuels*, 33 (2019) 4219-4224.
- [52] S. Moghtadernejad, M. Jadidi, K.T. Ahmmed, C. Lee, A. Dolatabadi, A.-M. Kietzig, Experimental study of droplet shedding on laser-patterned substrates, *Physics of Fluids*, 31 (2019) 122107.
- [53] S. Taleb, T. Darmanin, F. Guittard, Switchable and reversible superhydrophobic surfaces: Part one, *Interdisciplinary Expansions in Engineering and Design With the Power of Biomimicry*, (2018) 123.
- [54] S. Srinivasan, S.S. Chhatre, J.M. Mabry, R.E. Cohen, G.H. McKinley, Solution spraying of poly (methyl methacrylate) blends to fabricate microtextured, superoleophobic surfaces, *Polymer*, 52 (2011) 3209-3218.
- [55] K. Liu, Y. Tian, L. Jiang, Bio-inspired superoleophobic and smart materials: design, fabrication, and application, *Progress in Materials Science*, 58 (2013) 503-564.

- [56] Y. Jiao, C. Li, S. Wu, Y. Hu, J. Li, L. Yang, D. Wu, J. Chu, Switchable underwater bubble wettability on laser-induced titanium multiscale micro-/nanostructures by vertically crossed scanning, *ACS applied materials & interfaces*, 10 (2018) 16867-16873.
- [57] V. Vercillo, S. Tonnichia, J.M. Romano, A. García-Girón, A.I. Aguilar-Morales, S. Alamri, S.S. Dimov, T. Kunze, A.F. Lasagni, E. Bonaccorso, Design Rules for Laser-Treated Icephobic Metallic Surfaces for Aeronautic Applications, *Advanced Functional Materials*, 30 (2020) 1910268.
- [58] O. Raimbault, S. Benayoun, K. Anselme, C. Mauclair, T. Bourgade, A.-M. Kietzig, P.-L. Girard-Lauriault, S. Valette, C. Donnet, The effects of femtosecond laser-textured Ti-6Al-4V on wettability and cell response, *Materials Science and Engineering: C*, 69 (2016) 311-320.
- [59] J. Bonse, S. Höhm, S.V. Kirner, A. Rosenfeld, J. Krüger, Laser-induced periodic surface structures—A scientific evergreen, *IEEE Journal of selected topics in quantum electronics*, 23 (2016).
- [60] T. Aizawa, T. Inohara, K. Wasa, Femtosecond Laser Micro-/nano-texturing of Stainless Steels for Surface Property Control, *Micromachines*, 10 (2019) 512.
- [61] Z.G. Guo, J. Fang, J.c. Hao, Y.m. Liang, W.m. Liu, A novel approach to stable superhydrophobic surfaces, *ChemPhysChem*, 7 (2006) 1674-1677.
- [62] A. Woodward, W. Schofield, V. Roucoules, J. Badyal, Super-hydrophobic surfaces produced by plasma fluorination of polybutadiene films, *Langmuir*, 19 (2003) 3432-3438.

- [63] J. Ryu, K. Kim, J. Park, B.G. Hwang, Y. Ko, H. Kim, J. Han, E. Seo, Y. Park, S.J. Lee, Nearly perfect durable superhydrophobic surfaces fabricated by a simple one-step plasma treatment, *Scientific reports*, 7 (2017) 1-8.
- [64] G.R. Chagas, D.E. Weibel, UV-induced switchable wettability between superhydrophobic and superhydrophilic polypropylene surfaces with an improvement of adhesion properties, *Polymer Bulletin*, 74 (2017) 1965-1978.
- [65] J. Li, Q. Sun, S. Han, J. Wang, Z. Wang, C. Jin, Reversibly light-switchable wettability between superhydrophobicity and superhydrophilicity of hybrid ZnO/bamboo surfaces via alternation of UV irradiation and dark storage, *Progress in Organic Coatings*, 87 (2015) 155-160.
- [66] N. Areid, A. Peltola, I. Kangasniemi, A. Ballo, T.O. Närhi, Effect of ultraviolet light treatment on surface hydrophilicity and human gingival fibroblast response on nanostructured titanium surfaces, *Clinical and Experimental Dental Research*, 4 (2018) 78-85.
- [67] C. Özgür, O. Şan, Fabrication of superhydrophilic membrane filters using spherical glass particles obtained by ultrasonic spray pyrolysis, *Ceramics International*, 37 (2011) 965-970.
- [68] A. Dundar, M. Krichevskaya, A. Katerski, I.O. Acik, TiO₂ thin films by ultrasonic spray pyrolysis as photocatalytic material for air purification, *Royal Society open science*, 6 (2019) 181578.
- [69] S.S. Lathe, P. Sudhagar, C. Ravidhas, A.J. Christy, D.D. Kirubakaran, R. Venkatesh, A. Devadoss, C. Terashima, K. Nakata, A. Fujishima, Self-cleaning and superhydrophobic

- CuO coating by jet-nebulizer spray pyrolysis technique, *CrystEngComm*, 17 (2015) 2624-2628.
- [70] S. Wang, C. Liu, G. Liu, M. Zhang, J. Li, C. Wang, Fabrication of superhydrophobic wood surface by a sol–gel process, *Applied Surface Science*, 258 (2011) 806-810.
- [71] R. Taurino, E. Fabbri, M. Messori, F. Pilati, D. Pospiech, A. Synytska, Facile preparation of superhydrophobic coatings by sol–gel processes, *Journal of colloid and interface science*, 325 (2008) 149-156.
- [72] L. Gu, Y. Wang, C. Xu, F. Zhang, Z. Wu, X. Zhang, Z. Shi, C. Peng, Construction of superhydrophobic surfaces by sol-gel techniques, in: 2017 IEEE International Conference on Manipulation, Manufacturing and Measurement on the Nanoscale (3M-NANO), IEEE, 2017, pp. 156-160.
- [73] K. Vidal, E. Gómez, A.M. Goitandia, A. Angulo-Ibáñez, E. Aranzabe, The Synthesis of a Superhydrophobic and Thermal Stable Silica Coating via Sol-Gel Process, *Coatings*, 9 (2019) 627.
- [74] H. Yang, P. Pi, Z.-Q. Cai, X. Wen, X. Wang, J. Cheng, Z.-r. Yang, Facile preparation of super-hydrophobic and super-oleophilic silica film on stainless steel mesh via sol–gel process, *Applied Surface Science*, 256 (2010) 4095-4102.
- [75] J.-H. Kim, A. Mirzaei, H.W. Kim, S.S. Kim, Facile fabrication of superhydrophobic surfaces from austenitic stainless steel (AISI 304) by chemical etching, *Applied Surface Science*, 439 (2018) 598-604.
- [76] A. Esmailirad, M.V. Rukosuyev, M.B. Jun, F.C. van Veggel, A cost-effective method to create physically and thermally stable and storable super-hydrophobic aluminum alloy surfaces, *Surface and Coatings Technology*, 285 (2016) 227-234.

- [77] Y. Qi, Z. Cui, B. Liang, R.S. Parnas, H. Lu, A fast method to fabricate superhydrophobic surfaces on zinc substrate with ion assisted chemical etching, *Applied Surface Science*, 305 (2014) 716-724.
- [78] C. Du, X. He, F. Tian, X. Bai, C. Yuan, Preparation of superhydrophobic steel surfaces with chemical stability and corrosion, *Coatings*, 9 (2019) 398.
- [79] L. Li, V. Breedveld, D.W. Hess, Creation of superhydrophobic stainless steel surfaces by acid treatments and hydrophobic film deposition, *ACS applied materials & interfaces*, 4 (2012) 4549-4556.
- [80] X. Qian, T. Tang, H. Wang, C. Chen, J. Luo, D. Luo, Fabrication of Hydrophobic Ni Surface by Chemical Etching, *Materials*, 12 (2019) 3546.
- [81] Y. Huang, D.K. Sarkar, X. Chen, Fabrication of corrosion resistance micro-nanostructured superhydrophobic anodized aluminum in a one-step electrodeposition process, *Metals*, 6 (2016) 47.
- [82] W. Liu, Q. Xu, J. Han, X. Chen, Y. Min, A novel combination approach for the preparation of superhydrophobic surface on copper and the consequent corrosion resistance, *Corrosion Science*, 110 (2016) 105-113.
- [83] X.-L. Wei, N. Li, J.-F. An, C.-F. Huo, H. Liu, R. Yang, X. Li, Z.-S. Chao, Synthesis of superhydrophobic flower-like ZnO on nickel foam, *CrystEngComm*, 22 (2020) 205-212.
- [84] J. Liang, K. Liu, D. Wang, H. Li, P. Li, S. Li, S. Su, S. Xu, Y. Luo, Facile fabrication of superhydrophilic/superhydrophobic surface on titanium substrate by single-step anodization and fluorination, *Applied Surface Science*, 338 (2015) 126-136.
- [85] C.N. Barbier, J.T. Simpson, B.R. D'Urso, E. Jenner, Superhydrophobic anodized metals and method of making same, in, United States, 2018.

- [86] S. Vanithakumari, R. George, U.K. Mudali, Influence of silanes on the wettability of anodized titanium, *Applied surface science*, 292 (2014) 650-657.
- [87] T.T. Isimjan, T. Wang, S. Rohani, A novel method to prepare superhydrophobic, UV resistance and anti-corrosion steel surface, *Chemical engineering journal*, 210 (2012) 182-187.
- [88] N. Zhao, F. Shi, Z. Wang, X. Zhang, Combining Layer-by-Layer Assembly with Electrodeposition of Silver Aggregates for Fabricating Superhydrophobic Surfaces, *Langmuir*, 21 (2005) 4713-4716.
- [89] L. Zhai, F.Ç. Cebeci, R.E. Cohen, M.F. Rubner, Stable Superhydrophobic Coatings from Polyelectrolyte Multilayers, *Nano Letters*, 4 (2004) 1349-1353.
- [90] J. Shi, N.M. Alves, J.F. Mano, Towards bioinspired superhydrophobic poly (L-lactic acid) surfaces using phase inversion-based methods, *Bioinspiration & Biomimetics*, 3 (2008) 034003.
- [91] C.-F. Wang, Y.-J. Tsai, S.-W. Kuo, K.-J. Lee, C.-C. Hu, J.-Y. Lai, Toward Superhydrophobic/Superoleophilic Materials for Separation of Oil/Water Mixtures and Water-in-Oil Emulsions Using Phase Inversion Methods, *Coatings*, 8 (2018) 396.
- [92] S. Munirasu, F. Banat, A.A. Durrani, M.A. Haija, Intrinsically superhydrophobic PVDF membrane by phase inversion for membrane distillation, *Desalination*, 417 (2017) 77-86.
- [93] F. Guo, X. Su, G. Hou, Z. Liu, Z. Mei, Fabrication of superhydrophobic TiO₂ surface with cactus-like structure by a facile hydrothermal approach, *Colloids and Surfaces A: Physicochemical and Engineering Aspects*, 395 (2012) 70-74.

- [94] J. Li, X. Liu, Y. Ye, H. Zhou, J. Chen, A simple solution-immersion process for the fabrication of superhydrophobic cupric stearate surface with easy repairable property, *Applied Surface Science*, 258 (2011) 1772-1775.
- [95] J. Li, X. Liu, Y. Ye, H. Zhou, J. Chen, A facile solution-immersion process for the fabrication of superhydrophobic surfaces with high water adhesion, *Materials Letters*, 66 (2012) 321-323.
- [96] J. Xu, J. Xu, Y. Cao, X. Ji, Y. Yan, Fabrication of non-flaking, superhydrophobic surfaces using a one-step solution-immersion process on copper foams, *Applied Surface Science*, 286 (2013) 220-227.
- [97] M. Kang, R. Jung, H.-S. Kim, H.-J. Jin, Preparation of superhydrophobic polystyrene membranes by electrospinning, *Colloids and Surfaces A: Physicochemical and Engineering Aspects*, 313 (2008) 411-414.
- [98] S. Papadopoulou, C. Tsiptsias, A. Pavlou, K. Kaderides, S. Sotiriou, C. Panayiotou, Superhydrophobic surfaces from hydrophobic or hydrophilic polymers via nanophase separation or electrospinning/electrospraying, *Colloids and Surfaces A: Physicochemical and Engineering Aspects*, 387 (2011) 71-78.
- [99] M. Megaraj, M. Keppannan, Fabrication of a Superhydrophobic Nanofibers by Electrospinning, in: *Electrospinning Method Used to Create Functional Nanocomposites Films*, IntechOpen, 2018.
- [100] S. Joshi, H. Kathuria, S. Verma, S. Valiyaveetil, Functional Catechol–Metal Polymers via Interfacial Polymerization for Applications in Water Purification, *ACS Applied Materials & Interfaces*, 12 (2020) 19044-19053.

- [101] G. Lai, W. Lau, P. Goh, Y. Tan, B. Ng, A. Ismail, A novel interfacial polymerization approach towards synthesis of graphene oxide-incorporated thin film nanocomposite membrane with improved surface properties, *Arabian journal of chemistry*, 12 (2019) 75-87.
- [102] S.M. Gateman, K. Page, I. Halimi, A.R.C. Nascimento, S. Savoie, R. Schulz, C. Moreau, I.P. Parkin, J. Mauzeroll, Corrosion of One-Step Superhydrophobic Stainless-Steel Thermal Spray Coatings, *ACS Applied Materials & Interfaces*, 12 (2019) 1523-1532.
- [103] W.I. El Dessouky, R. Abbas, W.A. Sadik, A.G.M. El Demerdash, A. Hefnawy, Improved adhesion of superhydrophobic layer on metal surfaces via one step spraying method, *Arabian Journal of Chemistry*, 10 (2017) 368-377.
- [104] H. Ye, L. Zhu, W. Li, H. Liu, H. Chen, Simple spray deposition of a water-based superhydrophobic coating with high stability for flexible applications, *Journal of Materials Chemistry A*, 5 (2017) 9882-9890.
- [105] X.H. Xu, Z.Z. Zhang, J. Yang, X. Zhu, Study of the corrosion resistance and loading capacity of superhydrophobic meshes fabricated by spraying method, *Colloids and Surfaces A: Physicochemical and Engineering Aspects*, 377 (2011) 70-75.
- [106] P.H.G. de Cademartori, W.H. Schreiner, W.L.E. Magalhães, Facile one-step fabrication of highly hydrophobic medium density fiberboard (MDF) surfaces via spray coating, *Progress in Organic Coatings*, 125 (2018) 153-159.
- [107] W.-F. Chen, P. Koshy, C.C. Sorrell, Effects of film topology and contamination as a function of thickness on the photo-induced hydrophilicity of transparent TiO₂ thin films deposited on glass substrates by spin coating, *Journal of materials science*, 51 (2016) 2465-2480.

- [108] G. Momen, R. Jafari, M. Farzaneh, Ice repellency behaviour of superhydrophobic surfaces: Effects of atmospheric icing conditions and surface roughness, *Applied Surface Science*, 349 (2015) 211-218.
- [109] C. Yeom, Y. Kim, Purification of oily seawater/wastewater using superhydrophobic nano-silica coated mesh and sponge, *Journal of industrial and engineering chemistry*, 40 (2016) 47-53.
- [110] L.-Y. Cui, R.-C. Zeng, S.-Q. Li, F. Zhang, E.-H. Han, Corrosion resistance of layer-by-layer assembled polyvinylpyrrolidone/polyacrylic acid and amorphous silica films on AZ31 magnesium alloys, *RSC advances*, 6 (2016) 63107-63116.
- [111] K. Maghsoudi, E. Vazirinasab, G. Momen, R. Jafari, Advances in the fabrication of superhydrophobic polymeric surfaces by polymer molding processes, *Industrial & Engineering Chemistry Research*, 59 (2020) 9343-9363.
- [112] Y. Wang, J. Xue, Q. Wang, Q. Chen, J. Ding, Verification of icephobic/anti-icing properties of a superhydrophobic surface, *ACS applied materials & interfaces*, 5 (2013) 3370-3381.
- [113] R.A. Alawajji, G.K. Kannarpady, A.S. Biris, Fabrication of transparent superhydrophobic polytetrafluoroethylene coating, *Applied Surface Science*, 444 (2018) 208-215.
- [114] H. Li, H. Lu, S. Liu, Q. Li, Q. Liu, SiO₂ shell on ZnO nanoflake arrays for UV-durable superhydrophobicity on Al substrate, *Materials Research Bulletin*, 114 (2019) 85-89.
- [115] H. Kwong, M. Wong, Y. Wong, K. Wong, Superhydrophobicity of polytetrafluoroethylene thin film fabricated by pulsed laser deposition, *Applied surface science*, 253 (2007) 8841-8845.

- [116] E. Lee, K.-H. Lee, Facile fabrication of superhydrophobic surfaces with hierarchical structures, *Scientific reports*, 8 (2018) 1-7.
- [117] Y.-P. Zhang, P.-P. Li, P.-F. Liu, W.-Q. Zhang, J.-C. Wang, C.-X. Cui, X.-J. Li, L.-B. Qu, Fast and simple fabrication of superhydrophobic coating by polymer induced phase separation, *Nanomaterials*, 9 (2019) 411.
- [118] C. Verma, E.E. Ebenso, M. Quraishi, Ionic liquids as green and sustainable corrosion inhibitors for metals and alloys: an overview, *Journal of Molecular Liquids*, 233 (2017) 403-414.
- [119] J. Hulsbosch, D.E. De Vos, K. Binnemans, R. Ameloot, Biobased Ionic Liquids: Solvents for a Green Processing Industry?, *ACS Sustainable Chemistry & Engineering*, 4 (2016) 2917-2931.
- [120] L. Gao, T.J. McCarthy, Ionic liquids are useful contact angle probe fluids, *Journal of the American Chemical Society*, 129 (2007) 3804-3805.
- [121] D. Blanco, J.L. Viesca, M.T. Mallada, B. Ramajo, R. González, A.H. Battez, Wettability and corrosion of [NTf₂] anion-based ionic liquids on steel and PVD (TiN, CrN, ZrN) coatings, *Surface and Coatings Technology*, 302 (2016) 13-21.
- [122] D. Blanco, N. Rivera, P. Oulego, M. Díaz, R. González, A.H. Battez, Novel fatty acid anion-based ionic liquids: Contact angle, surface tension, polarity fraction and spreading parameter, *Journal of Molecular Liquids*, 288 (2019) 110995.
- [123] M.M. Pereira, K.A. Kurnia, F.L. Sousa, N.J. Silva, J.A. Lopes-da-Silva, J.A. Coutinho, M.G. Freire, Contact angles and wettability of ionic liquids on polar and non-polar surfaces, *Physical Chemistry Chemical Physics*, 17 (2015) 31653-31661.

- [124] D. Blanco, M. Bartolomé, B. Ramajo, J.L. Viesca, R. González, A. Hernández Battez, Wetting Properties of Seven Phosphonium Cation-Based Ionic Liquids, *Industrial & Engineering Chemistry Research*, 55 (2016) 9594-9602.
- [125] M. Uerdingen, C. Treber, M. Balsler, G. Schmitt, C. Werner, Corrosion behaviour of ionic liquids, *Green Chemistry*, 7 (2005) 321-325.
- [126] H.U. Sajid, R. Kiran, X. Qi, D.S. Bajwa, D. Battocchi, Employing corn derived products to reduce the corrosivity of pavement deicing materials, *Construction and Building Materials*, 263 (2020) 120662.
- [127] I.M. Gindri, D.A. Siddiqui, C.P. Frizzo, M.A. Martins, D.C. Rodrigues, Improvement of tribological and anti-corrosive performance of titanium surfaces coated with dicationic imidazolium-based ionic liquids, *RSC advances*, 6 (2016) 78795-78802.
- [128] I.M. Gindri, D.A. Siddiqui, C.P. Frizzo, M.A. Martins, D.C. Rodrigues, Ionic liquid coatings for titanium surfaces: effect of IL structure on coating profile, *ACS applied materials & interfaces*, 7 (2015) 27421-27431.
- [129] D.A. Siddiqui, I.M. Gindri, D.C. Rodrigues, Corrosion and Wear Performance of Titanium and Cobalt Chromium Molybdenum Alloys Coated with Dicationic Imidazolium-Based Ionic Liquids, *Journal of Bio-and Tribo-Corrosion*, 2 (2016) 27.
- [130] Y. Zhang, X. Liu, S.S. Jamali, B.R. Hinton, S.E. Moulton, G.G. Wallace, M. Forsyth, The effect of treatment time on the ionic liquid surface film formation: Promising surface coating for Mg alloy AZ31, *Surface and Coatings Technology*, 296 (2016) 192-202.
- [131] H.H. Elsentriecy, H. Luo, H.M. Meyer, L.L. Grado, J. Qu, Effects of pretreatment and process temperature of a conversion coating produced by an aprotic ammonium-

- phosphate ionic liquid on magnesium corrosion protection, *Electrochimica Acta*, 123 (2014) 58-65.
- [132] D. Fuczek, J. Zabielska-Matejuk, J. Pernak, W. Przybylska, Wettability of wood surfaces treated with ionic liquids, *Drewno. Prace Naukowe. Doniesienia. Komunikaty*, 53 (2010).
- [133] B.S. Lee, Y.S. Chi, J.K. Lee, I.S. Choi, C.E. Song, S.K. Namgoong, S.-g. Lee, Imidazolium Ion-Terminated Self-Assembled Monolayers on Au: Effects of Counteranions on Surface Wettability, *Journal of the American Chemical Society*, 126 (2004) 480-481.
- [134] Njoroge, M.W. Matson, G.K. Jennings, Dynamic Anion-Adaptive Poly (ionic liquid) Films via Surface-Initiated Ring-Opening Metathesis Polymerization, *The Journal of Physical Chemistry C*, 121 (2017) 20323-20334.
- [135] Njoroge, B.W. Bout, M.W. Matson, P.E. Laibinis, G.K. Jennings, Co-Poly(ionic liquid) Films via Anion Exchange for the Continuous Tunability of Ion Transport and Wettability, *ACS Omega*, 3 (2018) 16158-16164.
- [136] H.U. Sajid, R. Kiran, Influence of high stress triaxiality on mechanical strength of ASTM A36, ASTM A572 and ASTM A992 steels, *Construction and Building Materials*, 176 (2018) 129-134.
- [137] H.U. Sajid, R. Kiran, Post-fire mechanical behavior of ASTM A572 steels subjected to high stress triaxialities, *Engineering Structures*, 191 (2019) 323-342.
- [138] H.U. Sajid, D.L. Naik, R. Kiran, Microstructure–Mechanical Property Relationships for Post-Fire Structural Steels, *Journal of Materials in Civil Engineering*, 32 (2020) 04020133.

- [139] A. Cione, Deposition Of Ionic Liquid Thin Films Onto Self-Assembled Monolayers, MS Thesis. Vanderbilt University., (2007).
- [140] T. Huhtamäki, X. Tian, J.T. Korhonen, R.H. Ras, Surface-wetting characterization using contact-angle measurements, *Nature protocols*, 13 (2018) 1521-1538.
- [141] W.A. Zisman, Relation of the Equilibrium Contact Angle to Liquid and Solid Constitution, in: *Contact Angle, Wettability, and Adhesion*, American Chemical Society, 1964, pp. 1-51.
- [142] D. Berthelot, Sur le mélange des gaz, *Compt. Rendus*, 126 (1898) 1703-1706.
- [143] G.N. Antonow, Sur la tension superficielle à la limite de deux couches, *J. Chim. Phys.*, 5 (1907) 372-385.
- [144] L. Girifalco, R.J. Good, A theory for the estimation of surface and interfacial energies. I. Derivation and application to interfacial tension, *The Journal of Physical Chemistry*, 61 (1957) 904-909.
- [145] D. Li, A. Neumann, Contact angles on hydrophobic solid surfaces and their interpretation, *Journal of colloid and interface science*, 148 (1992) 190-200.
- [146] F.M. Fowkes, Determination of interfacial tensions, contact angles, and dispersion forces in surfaces by assuming additivity of intermolecular interactions in surfaces, *The Journal of Physical Chemistry*, 66 (1962) 382-382.
- [147] F.M. Fowkes, Dispersion force contributions to surface and interfacial tensions, contact angles, and heats of immersion, in, ACS Publications.
- [148] D.K. Owens, R. Wendt, Estimation of the surface free energy of polymers, *Journal of applied polymer science*, 13 (1969) 1741-1747.

- [149] C. Ozcan, N. Hasirci, Evaluation of surface free energy for PMMA films, *Journal of applied polymer science*, 108 (2008) 438-446.
- [150] C. Van Oss, R. Good, M. Chaudhury, Additive and nonadditive surface tension components and the interpretation of contact angles, *Langmuir*, 4 (1988) 884-891.
- [151] E. Chibowski, Surface free energy of a solid from contact angle hysteresis, *Advances in colloid and interface science*, 103 (2003) 149-172.
- [152] X. Dai, N. Sun, S.O. Nielsen, B.B. Stogin, J. Wang, S. Yang, T.-S. Wong, Hydrophilic directional slippery rough surfaces for water harvesting, *Science advances*, 4 (2018) eaaq0919.
- [153] C. Kolbeck, J. Lehmann, K. Lovelock, T. Cremer, N. Paape, P. Wasserscheid, A. Froba, F. Maier, H.-P. Steinrück, Density and surface tension of ionic liquids, *The Journal of Physical Chemistry B*, 114 (2010) 17025-17036.
- [154] K. Shimizu, B.S. Heller, F. Maier, H.-P. Steinrück, J.N. Canongia Lopes, Probing the surface tension of ionic liquids using the langmuir principle, *Langmuir*, 34 (2018) 4408-4416.
- [155] G. Law, P.R. Watson, Surface tension measurements of N-alkylimidazolium ionic liquids, *Langmuir*, 17 (2001) 6138-6141.
- [156] R.L. Gardas, R. Ge, N. Ab Manan, D.W. Rooney, C. Hardacre, Interfacial tensions of imidazolium-based ionic liquids with water and n-alkanes, *Fluid phase equilibria*, 294 (2010) 139-147.
- [157] J.N. Israelachvili, *Intermolecular and surface forces*, Academic press, 2011.

- [158] M. Klähn, C. Stüber, A. Seduraman, P. Wu, What Determines the Miscibility of Ionic Liquids with Water? Identification of the Underlying Factors to Enable a Straightforward Prediction, *The Journal of Physical Chemistry B*, 114 (2010) 2856-2868.
- [159] C. Fedosse Zornio, S. Livi, J. Duchet-Rumeau, J.-F. Gerard, Ionic Liquid-Nanostructured Poly (Methyl Methacrylate), *Nanomaterials*, 9 (2019) 1376.
- [160] M.G. Freire, P.J. Carvalho, A.M. Fernandes, I.M. Marrucho, A.J. Queimada, J.A. Coutinho, Surface tensions of imidazolium based ionic liquids: anion, cation, temperature and water effect, *Journal of Colloid and Interface Science*, 314 (2007) 621-630.
- [161] F.M. Fowkes, Attractive forces at interfaces, *Industrial & Engineering Chemistry*, 56 (1964) 40-52.

9. IMPROVING THE ICE-MELTING CAPACITY OF TRADITIONAL DEICERS⁸

This chapter discusses the effect of corn-derived polyols on enhancing the ice melting capacity of the traditional salt brine deicer for pavement applications. The contents of this chapter have been published in Sajid, H.U., Naik, D.L. and Kiran, R., 2021. Improving the ice-melting capacity of traditional deicers. *Construction and Building Materials*, 271, p.121527.

9.1. Introduction

Various deicing products in the granular and solution forms are used to facilitate ice and snow removal operations in the winter season. The commonly used deicers include chloride-deicers (sodium chloride ($NaCl$), magnesium chloride ($MgCl_2$), and calcium chloride ($CaCl_2$)), potassium acetate (CH_3COOK), sodium acetate (CH_3COONa), calcium magnesium acetate ($CaMg_2(CH_3COO)_6$), potassium formate ($KHCO_2$), and various agriculture-based products such as glycerol, beet juice, and molasses. Among these deicers, sodium chloride-based deicers are popularly used for winter maintenance of roads [1, 2]. According to the USGS statistics, the United States consumes up to 24 million metric tons of deicing salt on an annual basis, which is primarily composed of sodium chloride and other chloride-based deicers [3]. The large-scale application of sodium chloride-based deicer is linked with corrosion-induced degradation in transportation infrastructure [1, 4-8] and automobiles [1, 5, 9-11] and is proven to have a negative impact on the environment [12-16].

To address the problems associated with the usage of traditional salt brine deicer and to improve the effectiveness of salt brine deicer, different additives are usually added to the salt brine deicer. In the process of developing novel and effective deicers, several researchers have

⁸ This chapter was co-authored by H.U. Sajid, D.L. Naik, and R. Kiran. H.U. Sajid had the primary responsibility of preparing the specimens, conducting all tests, and drafting this chapter. R. Kiran supervised the research and revised this chapter.

focused mainly on the freezing point depression of the modified salt brine deicer. Freezing point depression is the difference in the temperature between the freezing point of pure solvent (water) and that of solution (water + NaCl) and can be achieved by adding a non-volatile solute to the solvent [17]. To this end, several new deicers have been developed by adding different organic and inorganic additives to traditional salt solutions [18-23]. These additives act as freezing point depressants and thus lower the eutectic point of the salt brine deicers. However, as noted by Koefod 2008 [24], a lower eutectic point of a deicing chemical does not necessarily translate into a high ice melting capacity. Muthumani and Shi [20] investigated the freezing point depressions and snow melting capacities of four agro-based deicers and two complex chlorides/minerals (CCM) based deicers. All four agro-based deicers investigated in their study significantly lowered the freezing point of the salt brine deicer (23% wt. NaCl). However, no significant improvement in the snow melting capacity was observed in the case of agro-based salt brine deicers at 9.4°C. A recent study reported the ineffectiveness of rock-salt (NaCl) deicer to melt ice at temperatures below -10 °C [18], which is much warmer than the eutectic temperature of the 23.3% wt. salt brine (-21.2 °C) [18]. When magnesium and calcium nitrates are mixed in different proportions, a eutectic point as low as -30 °C can be obtained, but their ice melting capacity is not better when compared to NaCl until the eutectic point of NaCl is exceeded [25]. Similarly, sodium acetate, potassium acetate, magnesium acetate are observed to have lower ice melting capacity (up to -20 °C temperature) despite having lower eutectic points when compared to NaCl [26].]. Therefore, it is necessary to quantify the ice melting capacity of new deicers in addition to their ability to lower the freezing point.

Apart from the freezing point depression and ice melting capacity of the deicers, the viscosity of the deicing solutions is another important parameter of interest whenever developing

agro-based deicing products. While organic materials generally improve the ice melting performance of deicer, they are observed to be more viscous [19]. The viscosity of the deicing solutions affects the handling and transportation of the deicing solutions as well as the uniform placement of deicing solutions on the pavement surface. The addition of additives such as glycerol (organic product) has been found to increase the viscosity of the sodium chloride deicing solution [19]. Therefore, it is important to determine the viscosities of the agro-based deicers to ensure their convenient handling, transportation to the field, and uniform placement on the pavement surface.

The addition of organic additives in the deicing solutions can significantly alter the frictional properties of the pavement surface on which the deicing solutions are applied and hence understanding the effects of organic additives based deicers on the frictional behavior of pavement. The frictional behavior of pavement can be quantified in terms of skid resistance. The skid resistance of a pavement established the slipperiness of the pavement surface and it is important for the safe operation of vehicles on pavements. Skid resistance of pavements is affected by the pavement surface conditions, surface roughness, and the composition of pavement materials [27-29]. Previous studies conducted on chloride-based deicers, acetate-based deicers, and agro-based deicers revealed that agro-based with high concentrations of either $MgCl_2$ or $CaCl_2$ result in lower friction coefficients when compared to $NaCl$ -based deicers [30]. In the absence of additives, 23.3% $NaCl$ deicing solution improves the friction coefficient of an icy asphalt pavement by 67.3% [31]. The addition of additives such as sodium metasilicate, sodium formate, and glycerin in the salt brine solution is observed to decrease the friction coefficient of deiced asphalt pavement. Another study conducted on $NaCl$ and $CaCl_2$ solutions

and an agriculture-based deicer also observed a reduction in the skid resistance of pavements when agriculture-based deicing material is applied on the surface [32].

Lastly, the surface runoff of deicing chemicals (in solid deicer form or liquid deicer form) from pavements is known to adversely impact the levels of dissolved oxygen in the water bodies [12, 16]. Dissolved oxygen (DO) is a measure of the level of free, non-compound oxygen available in the water, i.e., the oxygen that is not bonded to any other element, and it is considered as an important preliminary parameter for water quality assessment. Dissolved oxygen is necessary to many forms of aquatic life and excessive or depleted levels of DO can harm aquatic life and affect water quality. The deicers that are applied on the pavements may reach the stagnant water bodies or river streams adjacent to roads through surface run-off or soil infiltration and may reduce their DO levels which can thus adversely impact the aquatic life and water quality [12, 16]. Therefore, it is important to consider the impacts of alternative deicers on aquatic life. In summary, when improving the ice melting capacity of the traditional deicers, it is important to investigate other parameters of interests that include their influence on the skid resistance of the pavements, their viscosity, and dissolved oxygen levels in the water where the deicers may end up after runoff from pavements. With this, the current study aims to investigate the ice melting capacity of 23.3% wt. NaCl brine deicer which contains bio-based additives. Three corn-derived polyols namely, maltitol, sorbitol, and mannitol are added to the conventional 23.3% wt. NaCl brine solution as additives. The freezing point depression of these bio-based additives is provided in Table 9.1. The ice melting capacity of these bio-based salt brine deicers at sub-freezing temperatures is not previously reported. In addition to the ice melting capacity, the viscosities of the polyol-modified deicing solutions, the skid resistance of the pavements with deicing solutions, and the dissolved oxygen values corresponding to

optimum polyol-modified deicing solutions are also investigated. The experimental setups and the results obtained from the ice melting tests, viscosity tests, skid resistance, and dissolved oxygen tests are discussed in Section 9.2 and Section 9.3, respectively. Important conclusions derived from this study are provided in Section 9.4.

Table 9.1. Freezing points of salt brine containing bio-based additives [33].

Additive	Concentration in 23.3% wt. salt brine (%)	Freezing point (°C)
Sorbitol	27.7	-38.1
Mannitol	13.3	-26.7
Maltitol	27.7	-35.6

9.2. Experimental Work

9.2.1. Ice Melting Capacity Tests

The ice melting capacity (IMC) of salt brine deicer after the addition of corn-derived polyols and juices is investigated by performing ice melting tests using an in-house built test setup, as shown in Figure 9.1. First, the deicing solutions are prepared by adding corn-derived polyols (sorbitol, mannitol, and maltitol) to the salt brine deicer in the following weight concentrations: 0%, 5%, 10%, 15%, and 27.7%. Different ice melting test setups and methods are currently used in ice melting tests of deicing chemicals such as SHRP H205.2 test [34], Shaker test [35], Mechanical Rocker test [36], and Ice Cube Titration test [37]. Some of these test methods involve insulated containers or thermos containing the deicing solution at various subfreezing temperatures and shaking of ice cubes in the deicing solutions [34, 35, 38]. In the current study, each deicing solution is kept at 10 °C to mimic the temperature of the deicer just before application on road. The ice melting behavior of each bio-based deicer (salt brine+maltitol, salt brine+mannitol, and salt brine+sorbitol) is evaluated for the following temperatures: 0 °C, -10 °C, -20 °C, and -30 °C. For this purpose, ice cubes with approximately 38 mm length are first formed in a commercially available freezer by setting the temperature

around $-5\text{ }^{\circ}\text{C}$. The ice cubes are then immersed in acetone solution which is preset to the target temperature by using dry ice. The ice cubes are kept immersed at the target temperatures for 2 minutes. After the ice cubes reach the target temperature, the ice cubes are removed from acetone and are placed in the vicinity of dry ice to maintain the target temperature. The temperature of the acetone solution and the ice cubes is constantly monitored using K-type thermocouples to ensure the target temperature is maintained. One ice cube is then immersed in a 70 ml test solution (salt brine+polyol or juice, set a $10\text{ }^{\circ}\text{C}$) for 2 minutes. The weights of the ice cube before and after immersion in the test solution are obtained which are used to quantify the ice melting potential of the test solution. In total, 52 different combinations of salt brine + polyols and temperatures are tested for ice melting capacity, and each test is repeated twice. The results obtained from ice melting capacity tests are discussed in Section 9.3.1.

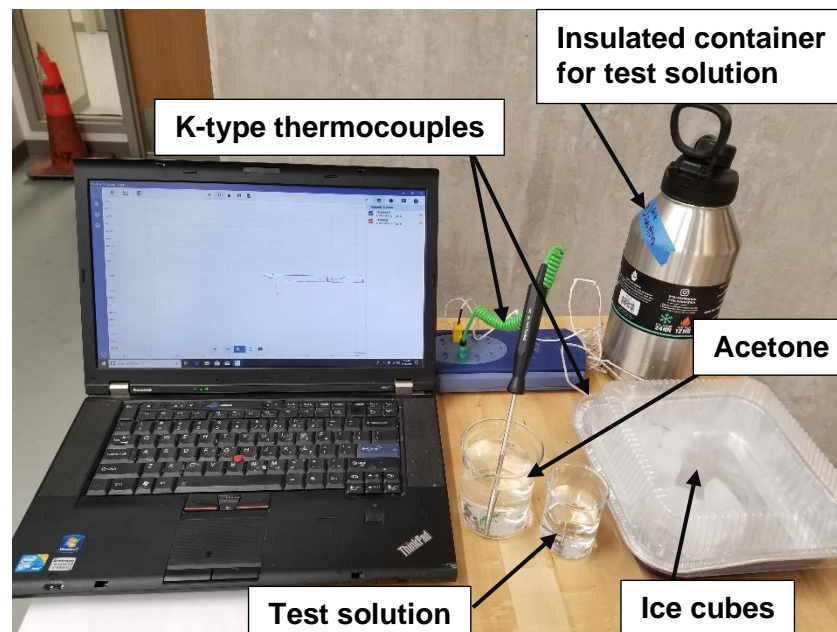


Figure 9.1. Test setup for conducting ice melting tests.

9.2.2. Skid Resistance Tests

Skid resistance is a measure of the frictional force that is generated when a tire slides on a wet pavement surface [39]. Skid resistance quantifies the slipperiness of a pavement surface and is considered a primary contributory factor to road accidents [27]. High skid resistance prevents skidding of the vehicle tires on the pavement surface and thus ensures adequate control for operating vehicles on highways. The skid resistance of pavements can be evaluated using field and laboratory testing methods that include Locked Wheel Tester (ASTM E274) [39, 40], Spin Up Tester [41], Side Force Method (e.g. MuMeter and the Sideway Force Coefficient Routine Investigation Machine (SCRIM)) [39, 42], Fixed Slip Method [39], Variable Slip Method (ASTM E1859) [43], British Pendulum Tester (ASTM E303) [44, 45], and Dynamic Friction Tester (ASTM E1911) [46]. In this study, the skid resistance of deiced pavement surfaces is determined using the British Pendulum Tester in accordance with the procedure specified in ASTM E303 (see Figure 9.2). The skid resistance of the pavement surfaces is determined for the reference deicing solution (23.3% wt. NaCl) and bio-based deicing solution combinations that led to higher ice melting (23.3% wt. NaCl + 27.7% wt. sorbitol, 23.3% wt. NaCl + 27.7% wt. maltitol, and 23.3% wt. NaCl + 27.7% wt. mannitol). The skid resistance tests are performed on a cleaned Portland cement concrete (PCC) pavement surface on the premises of the North Dakota State University. The test pavement used for the skid resistance tests conforms to the concrete pavement specifications of the city of Fargo, and the North Dakota Department of Transportation (NDDOT). The pavement is constructed using Portland Cement Type-1 (conforming to ASTM C-150), clean water (which is free from oils, alkalis, and acids), well-graded coarse and fine aggregates, and has an approximate air-entrainment of 6%. The relative humidity and temperature at the time of skid resistance tests were recorded to be 52% and 22°C,

respectively. The pavement surface is first cleaned then the deicing solution is applied and kept on the surface for 10 minutes. The British Pendulum Tester is then employed to obtain the skid resistance values in terms of British Pendulum Number (BPN). BPN is an indirect measure of skid resistance and higher BPN values indicate higher skid resistance of a road surface. For each deicing solution combination, different locations of PCC pavement surface are chosen and each test is repeated 5 times. The skid resistance of pavements results for both reference deicing solution and polyol-brine deicing solutions are discussed in Section 9.3.3.

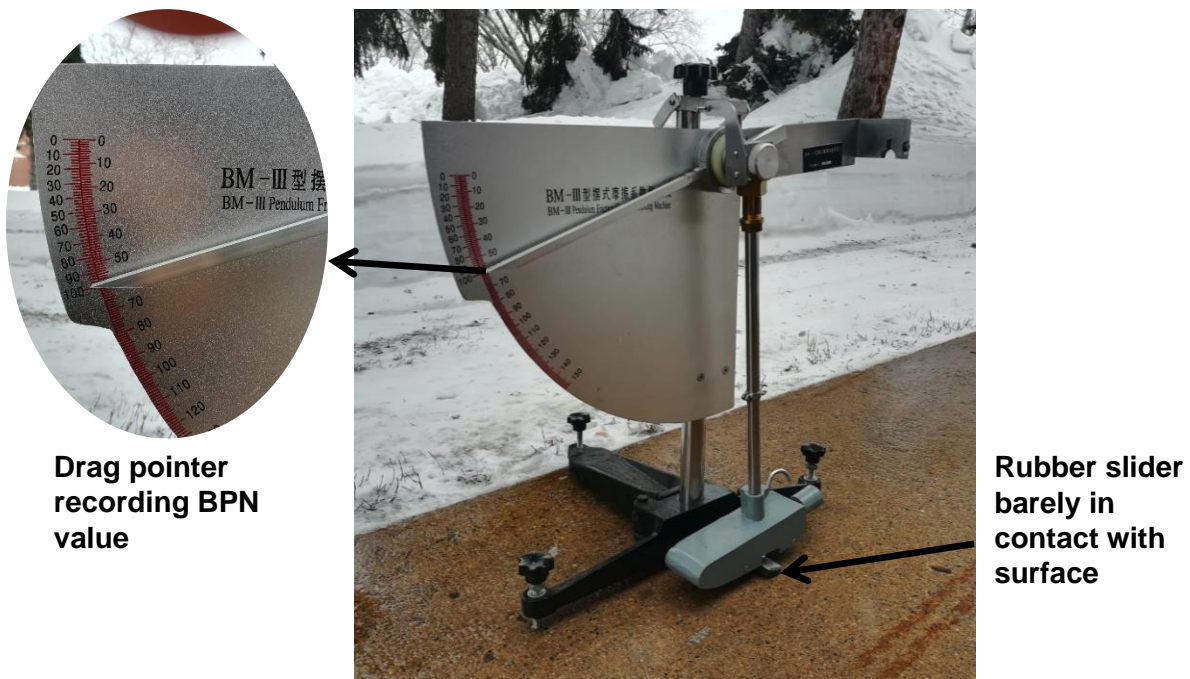


Figure 9.2. British Pendulum Tester for measuring skid resistance of pavement surface.

9.2.3. Viscosity Tests

The viscosity of a fluid is a measure of its resistance to the deformation at a given rate. The viscosity of the deicing solution affects the handling and transportation of deicing solutions to the field. It further affects the workability and uniform spreading of a deicing solution on the pavement surface. In this study, the viscosity of the bio-based deicing solutions and reference deicing solution is determined using HAAKE Viscotester® 550 (see Figure 9.3). HAAKE

viscotester® 500 consists of a standard cylindrical spindle and the data acquisition (DAQ) system that measures and records the shear stress and shear rate of a given fluid. The viscosity (η) is then evaluated using the following equation

$$\eta = \frac{\text{shear stress}}{\text{shear strain}} = \frac{M(R_a^2 - R_i^2)}{4\pi L R_a^2 R_i^2 \omega} \quad (9.1)$$

where, M (torque) = τ (Pa)/369.4 (Pa.N.cm), R_i = radius of the swindle, R_a = radius of the cylinder, L = length of the swindle, and ω = angular velocity. To perform the viscosity test, 50 ml of the deicing solution is filled in a 13.5 mm diameter centrifuge tube. The cylindrical spindle of the viscotester is then gradually lowered in the solution until a desired depth, as specified by the equipment manufacturer, is achieved. The spindle is then set to undergo rotations at a speed of 1032 rpm and the associated shear stress (Pa) magnitude is recorded. For each deicer solution, the test is repeated three times. All viscosity tests are conducted at a constant temperature of 20 °C. The viscosity tests are conducted for the salt brine deicer and the bio-based deicing solutions that resulted in higher ice melting capacity. The results obtained from the viscosity tests are discussed in Section 9.3.4.

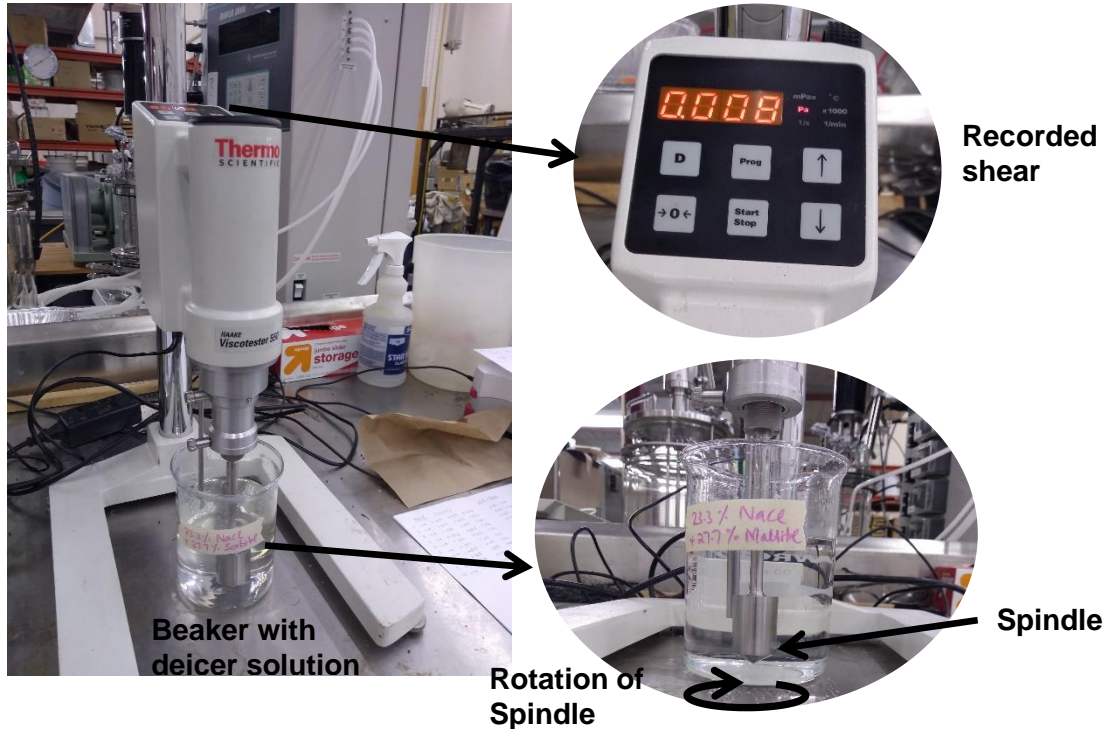


Figure 9.3. Viscosity test set up.

9.2.4. Dissolved Oxygen (DO) Tests

In this study, the influence of optimal combinations of corn-based polyol+brine solution on the change in the DO levels of the natural stream water (Red River) is investigated. Red River stream water is chosen for the reason that it runs parallel to a significant portion of road network in the city of Fargo, ND, and mimics the real-world scenario where the deicers can run-off into a nearby stream. For carrying out a DO experiment in the laboratory, about 45 ml of raw Red river water sample acquired from the Fargo water treatment plant is first filled in a centrifuge tube of 50 ml capacity. 2 μ l of the deicing solution is then added to the raw water sample to obtain a concentration of 45 mg/L. The DO level of the mix containing raw water and deicer solution is then measured using a Thermo Scientific Orion Star® benchtop DO meter (see Figure 9.4). The initial reading is referred to as ‘Day 0’ reading. The mix is then left undisturbed for the next 72 hours to obtain a ‘Day 3’ reading. The difference in the DO level indicates the amount of oxygen

consumed by the aquatic microorganisms in 72 hours. The test procedure is adapted for reference deicing solution and deicing solution corresponding to 27% polyol, namely, (1) 23.3 wt. % brine, (2) 23.3 wt. % brine + 27.7 wt.% sorbitol, (3) 23.3 wt.% brine + 27.7 wt.% maltitol, (4) 23.3 wt.% brine + 13.33 wt.% mannitol and were repeated in triplicates. The results obtained from DO tests are discussed in Section 9.3.5.



Figure 9.4. Benchtop Dissolved Oxygen Meter.

9.3. Results and Discussions

9.3.1. Ice Melting Capacity

The ice melting capacity corresponding to different concentrations of corn-derived polyols in the salt brine deicer is determined using the procedure discussed in Section 9.2.1. The percentage decrease in the weight of the ice cube immersed in the salt brine deicer (salt brine deicer) and corn-derived polyol solutions (salt brine+polyol) is provided in Figure 9.5. In addition, the percent change in the weight of ice cube polyols-based deicing solutions with respect to the salt brine deicer (salt brine deicer) is provided in Figure 9.6. As observed in Figure 9.5, the addition of polyols led to a higher decrease in the weight of ice cube at almost all target temperatures with the exception of -30 °C. The ice melting capacity of salt brine with 27.7% sorbitol increased by 43% at -10 °C (see Figure 9.6(a)). At -20 °C, the presence of 27.7% sorbitol in the salt brine led to a 13% increase in the ice melting capacity of the deicing solution.

At -30 °C, the sorbitol-based deicing solutions are observed to have similar ice melting capacity as that of salt brine. In the case of mannitol-based deicing solutions, the ice melting capacity is observed to increase by up to 93% and 112% at -10 °C and -20 °C, respectively (see Figure 9.6(b)). Moreover, at -30 °C, the presence of 27.7% mannitol in the salt brine led to an increase of 81% in the ice melting capacity. The higher increase in the ice melting capacity of mannitol-based deicing solutions can be attributed to the lower solubility of mannitol in the salt brine when compared to other polyols which lead to the presence of the undissolved mannitol solute particles in the salt brine. The undissolved mannitol particles in the salt brine can melt the ice and form a solution that can further contribute to the melting of ice. The ice melting capacity of salt brine increased by 17% at -10 °C and -20 °C when 27.7% maltitol is added to the salt brine deicer (see Figure 9.6(c)). However, beyond -20 °C, the ice melting capacity of maltitol-based deicing solutions is observed to decrease, which indicates that salt brine+maltitol solution is no more effective for ice melting at -30 °C (see Figure 9.6(c)). These results illustrate that the ice melting capacity of the salt brine deicer increased with the addition of various concentrations of corn-derived polyols. Among the polyols, mannitol and sorbitol resulted in higher ice melting even at lower temperatures (-20 °C and -30 °C). The maximum ice melting capacity is obtained when 27.7% wt. mannitol is added to 23.3% wt. brine solution for -20 °C target temperature wherein two times more ice melting is observed when compared to the 23.3% wt. NaCl brine.

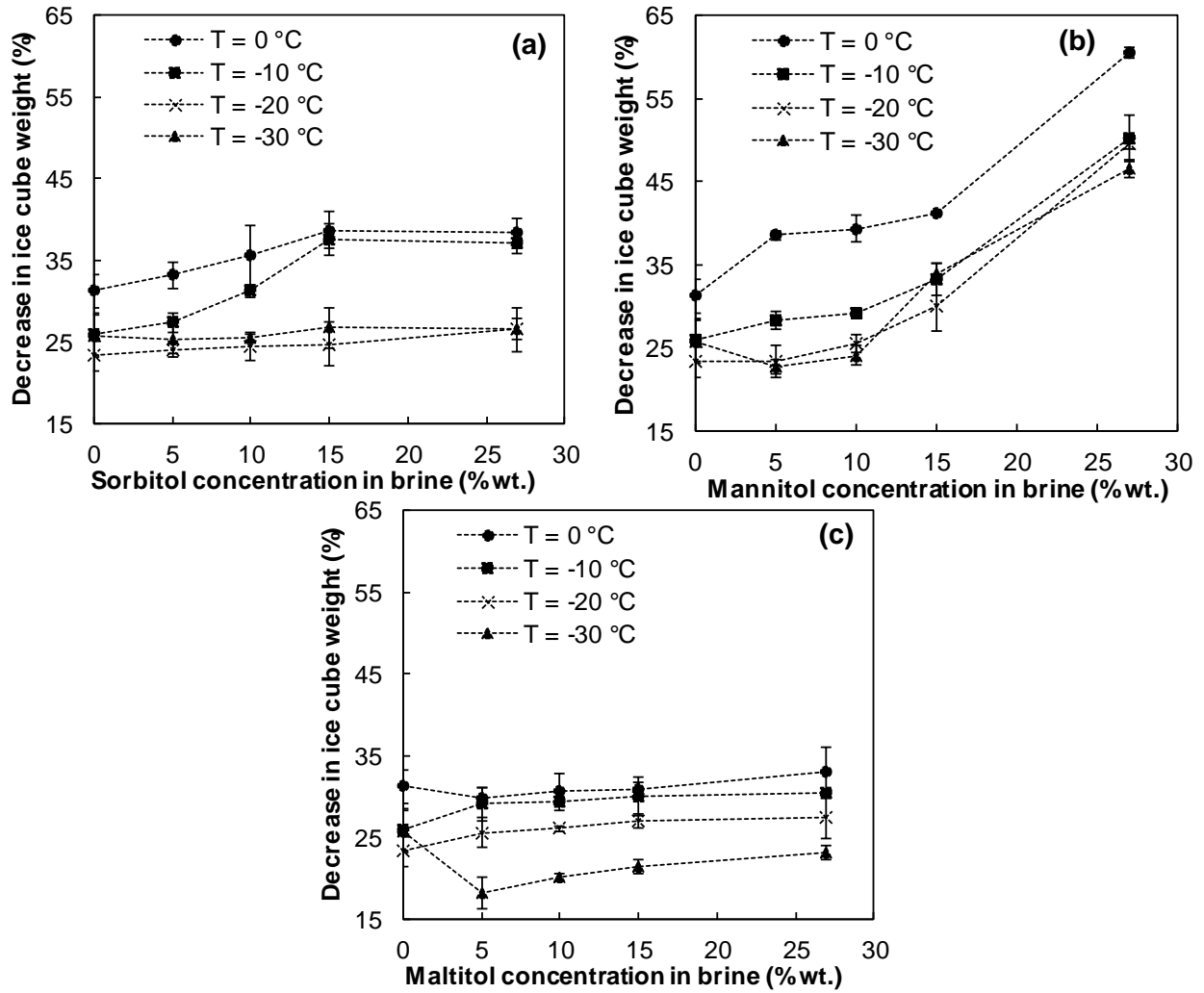


Figure 9.5. Percent decrease in weight of ice cube with an increase in the concentration of (a) sorbitol, (b) mannitol, and (c) maltitol, in the 23.3% wt. NaCl deicer at various low temperatures.

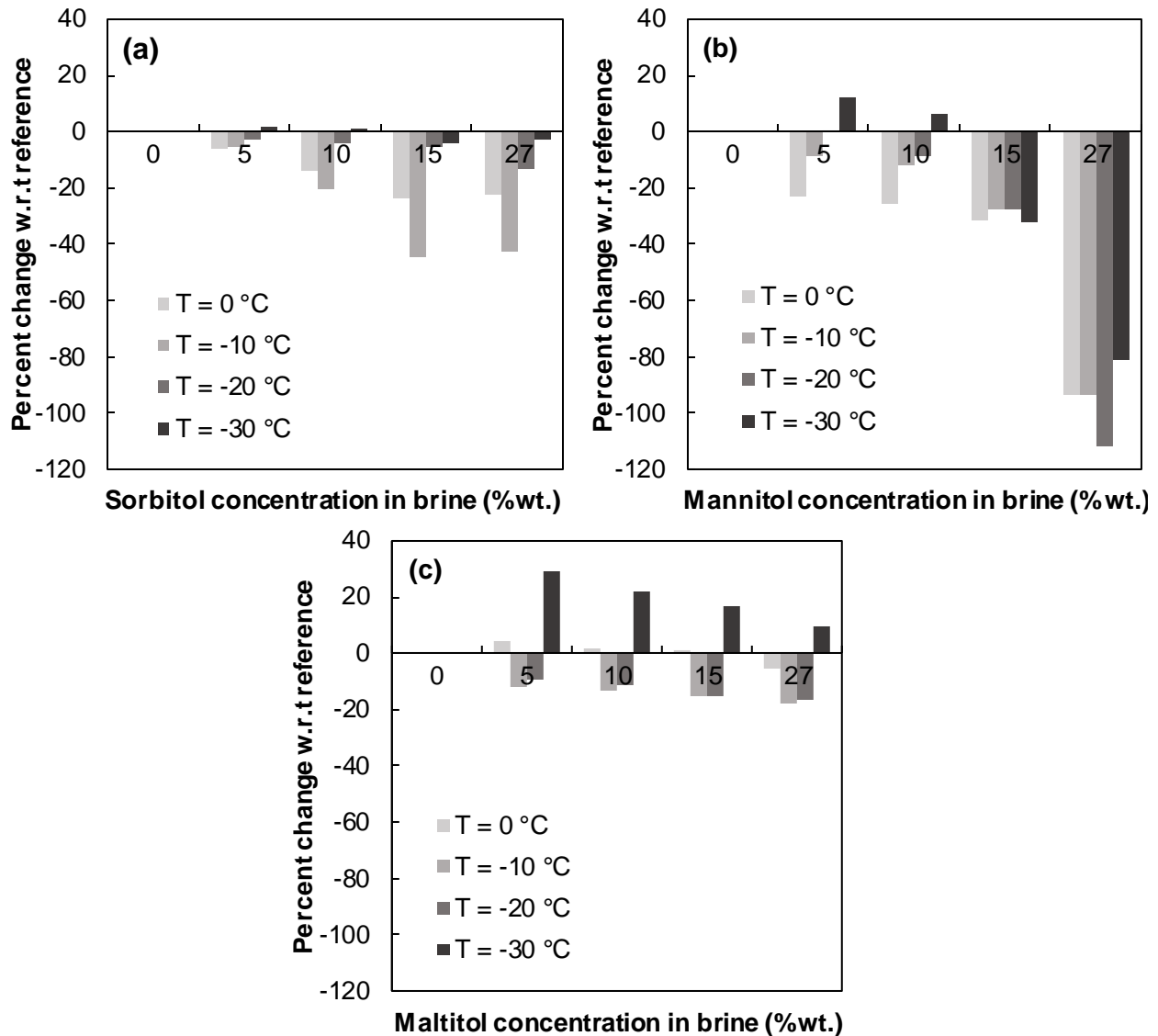


Figure 9.6. Percent decrease in the weight of ice cube immersed in (a) 23.3% wt. NaCl brine+sorbitol, (b) 23.3% wt. NaCl brine+mannitol, and (c) 23.3% wt. NaCl brine+maltitol solutions when compared to the traditional deicing solution (23.3% wt. NaCl brine), at different low temperatures.

The improvement in the ice melting capacity of the polyol-mixed salt brine deicing solution can be explained by analyzing the mechanism that leads to the melting of ice in the presence of traditional rock salt or salt brine deicers. The ice melting in the presence of salt happens in two stages. Firstly, the solid salt particles dissolve in the thin layer of water molecules that is present on the surface of the ice crystals. The ice melting thus starts by virtue of the

lowering the freezing point of the melted (salt-)water as compared to water. This process continues until all salt particles get dissolved in the melted water. Secondly, the melted water containing the dissolved salt particles continues to melt ice until the concentration of the salt particles becomes low enough that the freezing point of the salt-water becomes equal to the freezing point of water [38]. In the case of salt brine deicers, the ice melting follows only the second stage of ice melting as salt particles are already dissolved in the water. The ice melting capacity of the deicers thus depends on the amount of the solute particles in the salt-water. The polyol-mixed deicers have a higher concentration of solute particles when compared to salt brine deicer alone, and, therefore, higher ice melting occurred in the case of polyol-mixed deicers. Moreover, the highest ice melting observed in the case of mannitol-based deicers can be attributed to the presence of undissolved mannitol particles that can readily dissolve in the melted water. The ice melting capacities of the deicing solutions envisaged in this study are further compared with the ice melting capacities of the deicers that are commonly used in the pavement deicing operations, as discussed in the next section.

9.3.2. Comparison of Ice Melting Capacities of Liquid Deicers

The ice melting capacities of the polyol-mixed deicers envisaged in this study are compared with the commonly used deicing chemicals in the pavement deicing operations that include magnesium chloride, calcium chloride, potassium acetate, and beet juice. The ice melting capacities obtained at temperatures close to -10°C (-9.4°C and -12.2°C) and -20°C (-17.7°C) are compared due to the lack of data at other temperatures. Specifically, the ice melting capacity at -30°C is not available for comparison. Moreover, due to the different types of tests used in this current study and previous studies, for each case, the ice melting performance of a liquid deicer is obtained with respect to salt brine deicer in the corresponding study. The ice melting capacity

data obtained from the current study and refs. [20, 35] is provided in Figure 9.7 and Figure 9.8. The brackets (1) and (2) in Figure 9.7 represent 10 minutes and 60 minutes of shaking duration that was adopted in the ice melting tests conducted in these studies. Moreover, only the ice melting capacities corresponding to 25% deicer in 23% or 23.3% NaCl (e.g., KAcce_50% represent 50% potassium acetate solution that is mixed with 23% NaCl brine in 25/75 ratio) are considered. As observed in Figure 9.7, the liquid deicers investigated in the previous studies resulted in 16-51% higher ice melting when mixed with 23% NaCl brine in a 25/75 ratio. On the other hand, the polyol-based deicers (27% polyol in 23.3% wt. NaCl) resulted in 17-93% more melting when compared to 23.3% wt. NaCl brine. The ice melting capacity improvement observed in the case of 27% Sorbitol in salt brine deicing solution is comparable to potassium acetate based deicing solution (50% potassium solution that is mixed with 23% NaCl brine in 25/75 ratio) and magnesium chloride-based deicing solution (29% magnesium chloride solution that is mixed with 23% NaCl brine in 25/75 ratio), and it performed better when compared to beet juice-based deicer (15% beet juice that is mixed with 23% NaCl brine in 25/75 ratio). On the other hand, mannitol-based deicing solution (27% mannitol in 23.3% wt. NaCl) performed better among all the deicing solutions and both the temperatures that are considered in this study (see Figure 9.5 and Figure 9.6). These results demonstrate that polyol-based deicers investigated in this study can result in comparable or superior ice melting when compared to the traditional salt brine-based liquid deicers. However, it is important to note that the inferences from this comparison are affected by the differences in the composition of liquid deicers and different types of ice melting tests adopted in different studies.

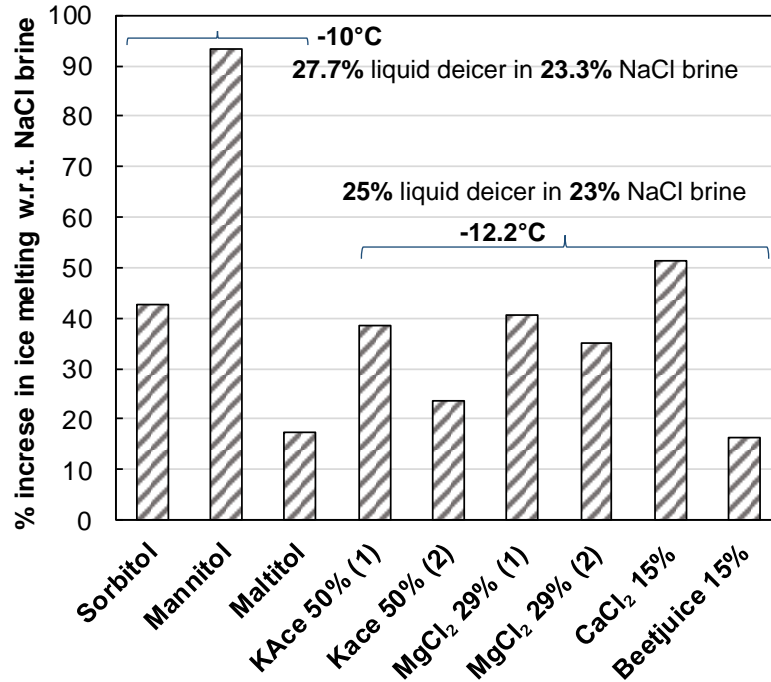


Figure 9.7. A comparison of the performance of the ice melting capacity of different deicers when compared to 23.3% NaCl salt brine deicer at -10°C and -12.2°C.

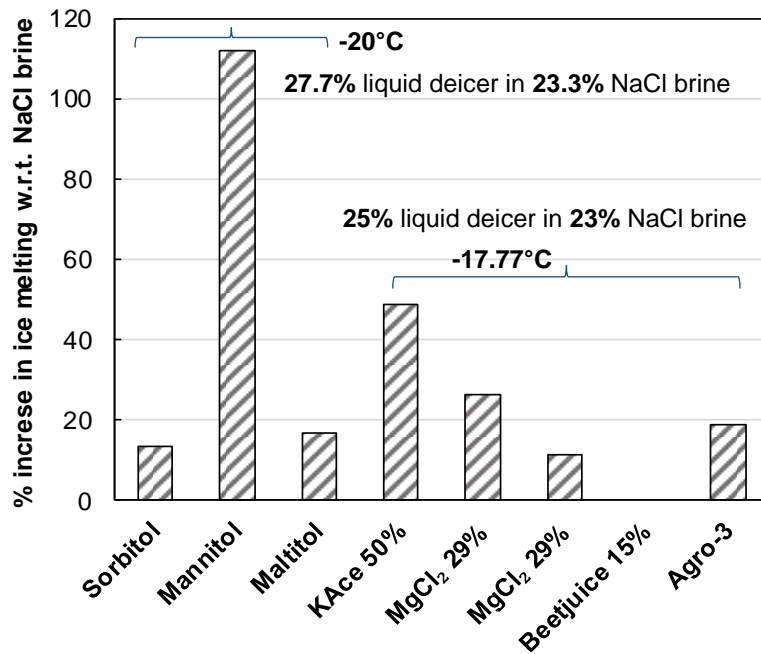


Figure 9.8. A comparison of the performance of the ice melting capacity of different deicers when compared to 23.3% NaCl salt brine deicer at -20°C and -17.77°C.

9.3.3. Skid Resistance

The skid resistance of PCC pavements after the application of (23.3% wt. NaCl) and bio-based deicing solutions (23.3% wt. NaCl + 27.7% wt. sorbitol, 23.3% wt. NaCl + 27.7% wt. maltitol, and 23.3% wt. NaCl + 27.7% wt. mannitol) is determined in terms of BPN values using the procedure described in Section 9.2.2. The skid resistance test conducted for the optimum deicing solution combinations is depicted in Figure 9.9. The BPN values of salt brine deicer and bio-based deicing solution are provided in Table 9.2. The reduction in the average BPN values corresponding to the reference and bio-based deicing solutions is provided in Figure 9.10. As observed from Figure 9.10 and Table 9.2, the BPN values of the pavement surface decreased after the application of salt brine deicer and bio-based deicing solutions. The application of reference brine deicing solution on test pavement surface resulted in a 17% reduction in the average BPN values (skid resistance). The bio-based deicing solutions resulted in a slightly higher reduction in the BPN values (skid resistance) when compared to the salt brine deicer. An almost similar reduction in the BPN values is noticed corresponding to the three bio-based deicing combinations tested herein. The average BPN values of the pavement surface decreased by 32-35% after the application of the bio-based deicing solution (23.3% wt. NaCl + 27.7% polyol) (see Figure 9.10). The skid resistance of the mannitol-based deicing solution is also determined for 13.3% mannitol in the brine solution as no undissolved particles are present at this concentration. The average BPN values of the pavement surface decreased by 24% after the application of 13.3% mannitol + 23.3% wt. brine solution. This also shows that increasing the concentration of polyols in the deicing solutions leads to a decrease in the skid resistance of the pavement surface.



Figure 9.9. Skid resistance test on the PCC surface for all four optimal combinations of polyol and brine.

Table 9.2. Average BPN values of the pavement surface before and after the treatment with deicer solution.

S. No.	Solution	BPN value											
		Before deicer application						After deicer application					
		1	2	3	4	5	Avg.	1	2	3	4	5	Avg.
1	23.3% Brine	112	115	115	115	115	114.4	95	95	94	95	94	94.6
2	23.3% Brine + 27.7% Sorbitol	116	113	113	113	114	113.8	84	75	75	75	75	76.8
3	23.3% Brine + 27.7% Maltitol	90	92	90	90	90	90.4	60	60	60	60	60	60
4	23.3% Brine + 27.7% Mannitol	103	100	100	98	100	100.2	70	68	68	68	68	68.4
5	23.3% Brine + 13.3% Mannitol	101	102	104	103	103	102.6	77	77	78	78	77	77.4

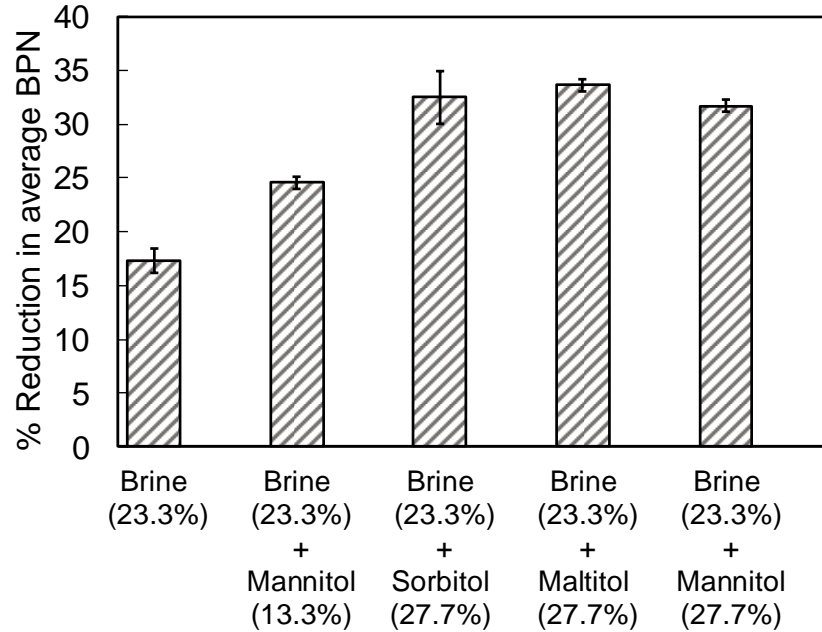


Figure 9.10. Reduction in average BPN value for various combinations of bio-based deicing solutions and salt brine deicer (brine).

9.3.4. Viscosity

The viscosity of the salt brine deicer (23.3% wt. NaCl) and bio-based deicing solutions (23.3% wt. NaCl + 27.7% wt. sorbitol, 23.3% wt. NaCl + 27.7% wt. maltitol, and 23.3% wt. NaCl + 13.3% mannitol) is determined using the procedure provided in Section 9.2.3. The viscosity of both reference and bio-based deicing solutions are provided in Table 9.3. From Table 9.3, it can be inferred that the viscosity of the salt brine deicer (23.3% wt. NaCl) increased with the addition of corn-based polyols (sorbitol or mannitol or maltitol). The addition of 27.7% wt. sorbitol and 27.7% wt. maltitol is observed to increase the viscosity of the salt brine deicer (23.3% wt. NaCl) by 50 % and 64% respectively. Similarly, the bio-based deicing solution with 13.3% wt. mannitol in 23.3% wt. NaCl exhibited a 21.4% increase in viscosity when compared to the viscosity of the salt brine deicer. The viscosity values obtained for the optimal polyol-based deicing solutions investigated in this study are further compared with the viscosities of NaCl-based deicer that continued agriculturally-derived organic product, namely, glycerol. The

viscosity values of 20% wt. NaCl deicers that contained 10-60% wt. of 80% glycerol are obtained from ref. [19] and are provided in Table 9.3. As observed in Table 9.3, the viscosities of 27% polyol-based deicing solutions (1.388-1.878 mPa.s) are relatively similar to 10-20% wt. 80% glycerol + 20% NaCl deicers (1.33-1.94 mPa.s). Moreover, increasing the concentration of agriculturally-derived products (80% glycerol) in 20% NaCl is observed to increase the viscosity of the deicing solution.

Table 9.3. The viscosity of deicer solutions (20.3°C). (S. No. 6-11 values are obtained from ref. [19].

S. No.	Solution	Viscosity (mPa.s)
1	23.3% Brine	1.143
2	23.3% Brine + 27.7% Sorbitol	1.714
3	23.3% Brine + 27.7% Maltitol	1.878
4	23.3% Brine + 13.3% Mannitol	1.388
*5	Tap water	0.979
6	10% (80% Glycerol + 20% NaCl)	1.33
7	20% (80% Glycerol + 20% NaCl)	1.94
8	30% (80% Glycerol + 20% NaCl)	2.41
9	40% (80% Glycerol + 20% NaCl)	3.82
10	50% (80% Glycerol + 20% NaCl)	6.66
11	60% (80% Glycerol + 20% NaCl)	10.68

Note: (*) indicates measurement performed for calibration in this study.

9.3.5. Dissolved Oxygen Test Results

The Dissolved Oxygen (DO) tests are conducted using the test protocol discussed in Section 9.2.4. The average of the three replicates and the reduction in DO levels after 3 days is summarized in Table 9.4. From Table 9.4, it can be observed that 23.3% salt brine deicer did not affect the DO levels of raw water after 3 days. However, the DO levels for the polyol-based deicing solutions are observed to drop. 27.7% sorbitol-based deicing solution recorded a 33% reduction in the DO level when compared to the salt brine deicing solution. Similarly, the 13.3% mannitol-based deicing solution and 27.7% maltitol-based deicing solution resulted in 4.67% and

24% reduction in the DO level when compared to the salt brine deicer. The DO test results indicate that polyol-based deicing solutions resulted in dissolved oxygen depletion when compared to the salt brine deicer. At this juncture, it is important to note that only DO tests are performed in this study to determine the depletion of DO when polyols are employed as deicers and the influence of the deicing solutions on the DO levels in the raw river water, and further detailed tests fall beyond the scope of the current study.

Table 9.4. Three-day Dissolved Oxygen test of river water mixed with various deicers.

S. No	Deicer Solution	Time	Dissolved Oxygen (mg/L)				Consumed DO
			1	2	3	Average	
1	The Control sample (River water)	<i>Day 0</i>	6.85	6.99	6.77	6.87	1.43
		<i>Day 3</i>	5.33	5.29	5.69	5.44	
2	23.3% Brine	<i>Day 0</i>	6.89	6.93	6.71	6.84	1.42
		<i>Day 3</i>	5.5	5.29	5.47	5.42	
3	23.3% Brine + 27.7% Sorbitol	<i>Day 0</i>	6.59	6.45	6.31	6.45	2.14
		<i>Day 3</i>	4.12	4.4	4.4	4.31	
4	23.3% Brine + 27.7% Maltitol	<i>Day 0</i>	6.5	6.6	6.2	6.43	1.89
		<i>Day 3</i>	4.48	4.75	4.4	4.54	
5	23.3% Brine + 13.3% Mannitol	<i>Day 0</i>	6.46	6.61	6.4	6.49	1.50
		<i>Day 3</i>	5.26	4.96	4.75	4.99	

Note: 'Day 0' indicates the reading obtained immediately after the addition of deicer solution, and 'Day 3' indicates the reading obtained after 72 hours of deicer addition.

9.4. Conclusions

Following are the important conclusions that can be drawn from this study:

1. The salt brine deicer mixed with bio-based additives exhibited superior ice melting capacity even at sub-freezing temperatures when compared to salt brine deicer alone.
2. When 27.7% wt. mannitol is added to the salt brine deicer, 93%, 112%, and 81% increase in the ice melting is observed at -10 °C, -20 °C, and -30 °C, respectively when compared to the reference 23.3% wt. salt brine deicer.

3. The addition of 27.7% wt. sorbitol resulted in a 43% and 13% increase in the ice melting capacity of the reference salt brine at -10 °C and -20 °C, respectively. However, at -30 °C, the addition of 27.7% wt. sorbitol to salt brine deicer did not improve the ice melting capacity.
4. When 27.7% wt. maltitol is added to salt brine deicer, the ice melting capacity of the deicing solution increased by 17% at both -10 °C and -20 °C. However, at -30 °C, the addition of 27.7% wt. maltitol to salt brine deicer did not improve the ice melting capacity of the traditional salt brine deicer.
5. A comparative analysis of the polyol-mixed deicers with commonly used salt brine-based liquid deicers indicated that sorbitol-based deicers result in comparable ice melting whereas mannitol-based deicers resulted in superior ice melting when compared to the salt brine-based liquid deicers.
6. The average skid resistance of PCC pavement decreased by 17% after the application of salt brine deicer. The application of polyol-based deicers led to an average reduction of 33% in the skid resistance of the PCC pavement surface when compared to the skid resistance of the dry surface.
7. The addition of 27.7% sorbitol and 27.7% maltitol in the salt brine deicer results in an average increase of 50% and 64%, respectively, in the viscosity of the salt brine deicer. Moreover, lower skid resistance is observed for PCC pavements with the application of viscous polyol-mixed deicers.
8. The addition of 27.7% polyol in the salt brine deicer resulted in up to 33% consumption of dissolved oxygen in river water when compared to the salt brine deicer.

9. The polyol-mixed deicing products introduced in this study can be directly sprayed on the pavement surface. Moreover, these products can also be used for pre-wetting of the pavement surface (anti-icing operations). We did not study the direct application of polyols on the road.

9.5. References

- [1] X. Shi, L. Fay, Z. Yang, T.A. Nguyen, Y. Liu, Corrosion of deicers to metals in transportation infrastructure: Introduction and recent developments, *Corrosion reviews*, 27 (2009) 23-52.
- [2] M. Fischel, Evaluation of selected deicers based on a review of the literature, Report No. CDOT-DTD-R-2001-15, Colorado Department of Transportation, (2001).
- [3] K.R. Kolesar, C.N. Mattson, P.K. Peterson, N.W. May, R.K. Prendergast, K.A. Pratt, Increases in wintertime PM_{2.5} sodium and chloride linked to snowfall and road salt application, *Atmospheric environment*, 177 (2018) 195-202.
- [4] X. Shi, Y. Liu, M. Mooney, M. Berry, B. Hubbard, L. Fay, A.B. Leonard, Effect of chloride-based deicers on reinforced concrete structures, Report No. WA-RD 741.1. Washington State Department of Transportation (WSDOT), (2010).
- [5] H.U. Sajid, R. Kiran, X. Qi, D.S. Bajwa, D. Battocchi, Employing corn derived products to reduce the corrosivity of pavement deicing materials, *Construction and Building Materials*, 263 (2020) 120662.
- [6] Á. Vega-Zamanillo, L. Juli-Gándara, M.Á. Calzada-Pérez, E. Teijón-López-Zuazo, Impact of Temperature Changes and Freeze—Thaw Cycles on the Behaviour of Asphalt Concrete Submerged in Water with Sodium Chloride, *Applied Sciences*, 10 (2020) 1241.

- [7] N. Xie, X. Shi, Y. Zhang, Impacts of Potassium Acetate and Sodium-Chloride Deicers on Concrete, *Journal of Materials in Civil Engineering*, 29 (2017) 04016229.
- [8] X. Shi, K. Fortune, R. Smithlin, M. Akin, L. Fay, Exploring the performance and corrosivity of chloride deicer solutions: Laboratory investigation and quantitative modeling, *Cold Regions Science and Technology*, 86 (2013) 36-44.
- [9] M.H. Nazari, X. Shi, Vehicle Risks of Winter Road Operations and Best Management Practices, *Sustainable Winter Road Operations*, (2018) 241-272.
- [10] M. Honarvar Nazari, D. Bergner, X. Shi, Managing Metallic Corrosion on Winter Maintenance Equipment Assets, *Environmental Sustainability in Transportation Infrastructure*, 61-76.
- [11] Y. Li, Y. Fang, N. Seeley, S. Jungwirth, E. Jackson, X. Shi, Corrosion by chloride deicers on highway maintenance equipment: Renewed perspective and laboratory investigation, *Transportation research record*, 2361 (2013) 106-113.
- [12] L. Fay, X. Shi, Environmental impacts of chemicals for snow and ice control: state of the knowledge, *Water, Air, & Soil Pollution*, 223 (2012) 2751-2770.
- [13] X. Shi, D. Veneziano, N. Xie, J. Gong, Use of chloride-based ice control products for sustainable winter maintenance: A balanced perspective, *Cold Regions Science and Technology*, 86 (2013) 104-112.
- [14] C.F. Mason, S.A. Norton, I.J. Fernandez, L.E. Katz, Deconstruction of the Chemical Effects of Road Salt on Stream Water Chemistry, *Journal of Environmental Quality*, 28 (1999) 82-91.
- [15] S.P. Jungwirth, Managing the environmental impacts of chemicals used for snow and ice control, Master's thesis. Montana State University, Bozeman Montana, (2014).

- [16] D.M. Ramakrishna, T. Viraraghavan, Environmental impact of chemical deicers—a review, *Water, Air, and Soil Pollution*, 166 (2005) 49-63.
- [17] D.D. Ebbing, S.D. Gammon, R. Wentworth, *General chemistry*, Houghton Mifflin Boston, 2005.
- [18] K. Nilssen, A. Klein-Paste, J. Wåhlin, The effect of additives on the low temperature ice-melting capacity of NaCl, *Transportation research record*, 2672 (2018) 158-166.
- [19] P. Taylor, J. Verkade, K. Gopalakrishnan, K. Wadhwa, S. Kim, Development of an Improved Agricultural-Based Deicing Product, Report No. IHRB Project TR-581. Iowa Highway Research Board, Iowa Department of Transportation (IDOT), (2010).
- [20] A. Muthumani, X. Shi, Effectiveness of Liquid Agricultural By-Products and Solid Complex Chlorides for Snow and Ice Control, *Journal of Cold Regions Engineering*, 31 (2017) 04016006.
- [21] W.A. Nixon, A.D. Williams, A guide for selecting anti-icing chemicals, version 1.0, IIHR Technical Report No. 420. IIHR-Hydroscience and Engineering. College of Engineering, The University of Iowa, Iowa City, IA., 420 (2001).
- [22] X. Shi, L. Fay, C. Gallaway, K. Volkening, M.M. Peterson, T. Pan, A. Creighton, C. Lawlor, S. Mumma, Y. Liu, Evaluation of alternative anti-icing and deicing compounds using sodium chloride and magnesium chloride as baseline deicers—Phase I, Report No. CDOT-2009-1. Colorado Department of Transportation (CDOT), (2009).
- [23] M. Honarvar Nazari, E.A. Havens, A. Muthumani, X. Shi, Effects of processed agro-residues on the performance of sodium chloride brine anti-Icer, *ACS Sustainable Chemistry & Engineering*, 7 (2019) 13655-13667.

- [24] Koefod, Eutectic Depressants: Relationship of Eutectic, Freezing Point, and Ice Melting Capacity in Liquid Deicers, *Surface Transportation Weather and Snow Removal and Ice Control Technology*, 73-84 (2008).
- [25] V. Danilov, E. Frolova, D. Kondakov, L. Avdyushkina, V. Orlova, Low-temperature anti-icing reagents in the Ca (NO₃)₂-Mg (NO₃)₂-CO (NH₂)₂-H₂O system and their properties, *Theoretical Foundations of Chemical Engineering*, 45 (2011) 697.
- [26] V. Danilov, E. Frolova, D. Kondakov, L. Avdyushkina, A. Bykov, V. Orlova, Low-temperature anti-icing reagents in aqueous salt systems containing acetates and formiates, *Theoretical Foundations of Chemical Engineering*, 46 (2012) 528-535.
- [27] A.G. Kokkalis, O.K. Panagouli, Fractal evaluation of pavement skid resistance variations. I: Surface Wetting, *Chaos, Solitons & Fractals*, 9 (1998) 1875-1890.
- [28] I.M. Asi, Evaluating skid resistance of different asphalt concrete mixes, *Building and Environment*, 42 (2007) 325-329.
- [29] A.B. Slimane, M. Khoudeir, J. Brochard, M.-T. Do, Characterization of road microtexture by means of image analysis, *Wear*, 264 (2008) 464-468.
- [30] L. Fay, X. Shi, Laboratory investigation of performance and impacts of snow and ice control chemicals for winter road service, *Journal of Cold Regions Engineering*, 25 (2011) 89-114.
- [31] M.H. Nazari, X. Shi, Developing Renewable Agro-Based Anti-Icers for Sustainable Winter Road Maintenance Operations, *Journal of Materials in Civil Engineering*, 31 (2019) 04019299.
- [32] J. Cao, A study of effects of a new agricultural-based deicer on the properties of pavement concrete, Master's thesis. Iowa State University, (2014).

- [33] T. Abbas, D.L. Naik, R. Kiran, Exploring the Use of Polyols, Corn and Beet Juice for Decreasing the Freezing Point of Brine Solution for Deicing of Pavements, (Submitted to ASCE Journal of Cold Regions Engineering), (2019).
- [34] C.C. Chappelow, A.D. McElroy, R.R. Blackburn, D. Darwin, F.G. de Noyelles, C.E. Locke Jr, Handbook of test methods for evaluating chemical deicers, in, Strategic Highway Research Program, 1992.
- [35] B. Gerbino-Bevins, C.Y. Tuan, M. Mattison, Evaluation of Ice-Melting Capacities of Deicing Chemicals, Journal of Testing and Evaluation, 40 (2012) 952-960.
- [36] C.Y. Tuan, I. Albers, Development of a mechanical rocker test procedure for ice melting capacity evaluation, Report No. NDOR Project: M322. Nebraska Department of Roads, Materials & Research, (2014).
- [37] S. Koefod, J. Adkins, M. Akin, Alternative Approaches to Measuring Deicer Ice-Melting Capacity, International Conference on Winter Maintenance and Surface Transportation Weather, Coralville, Iowa, United States., (2012) 432-442.
- [38] K. Nilssen, A. Klein-Paste, J. Wåhlin, Accuracy of Ice Melting Capacity Tests: Review of Melting Data for Sodium Chloride, Transportation Research Record, 2551 (2016) 1-9.
- [39] J.J. Henry, Evaluation of pavement friction characteristics, NCHRP Synthesis 291. Transportation Research Board, 291 (2000).
- [40] ASTM International, E274/E274M-15 Standard Test Method for Skid Resistance of Paved Surfaces Using a Full-Scale Tire, in, ASTM International, West Conshohocken, PA, 2015.

- [41] J.C. Wambold, W.E. Meyer, J.J. Henry, New-Generation Skid Testers for the 1990s, in: Surface Characteristics of Roadways: International Research and Technologies, ASTM International, 1990.
- [42] J. Hosking, G. Woodford, Measurement of skidding resistance. Part 1: guide to the use of SCRIM, Report No. 737. Transport and Road Research Laboratory, Department of Environment, Crowthorne, Berkshire, (1976).
- [43] ASTM International, E1859/E1859M-11 Standard Test Method for Friction Coefficient Measurements Between Tire and Pavement Using a Variable Slip Technique, in, ASTM International, West Conshohocken, PA, 2015.
- [44] Y. Liu, T. Fwa, Y. Choo, Effect of surface macrotexture on skid resistance measurements by the British Pendulum Test, Journal of Testing and Evaluation, 32 (2004) 304-309.
- [45] ASTM International, E303-93 Standard Test Method for Measuring Surface Frictional Properties Using the British Pendulum Tester, in, ASTM International, West Conshohocken, PA, 2018.
- [46] ASTM International. ASTM E1911-19 Standard Test Method for Measuring Surface Frictional Properties Using the Dynamic Friction Tester, in, ASTM International., West Conshohocken, PA, 2019.

10. A SURVEY ON THE EFFECTS OF DEICING MATERIALS ON PROPERTIES OF CEMENT-BASED MATERIALS⁹

This chapter presents a state-of-the-art review of the concrete deterioration mechanisms that are instigated by the large-scale usage of conventional and contemporary deicing chemicals on concrete pavements and sidewalks. The contents of this chapter have been published in Sajid, H.U., Jalal, A., Kiran, R., and Al-Rahim, A. 2021. A survey on the effects of deicing materials on properties of cement-based materials. *Construction and Building Materials*, (Accepted).

10.1. Introduction

Ice and snow accumulation on pavements reduces the pavement friction and can cause skidding of the vehicles and hamper the safety of roadway users [1]. During 2007-2016, approximately 18%, 13%, and 16% of weather-related car crashes in the U.S. were attributed to snow/sleet, icy pavement, and snow/slushy pavement, respectively [2]. The melted snow can fill the voids in concrete pavements and cause cracking in pavements upon freezing [3]. To mitigate the negative implications of ice and snow on concrete pavements and roadway users, various types of deicing chemicals are commonly employed in winter roadway operations. The application of deicing chemicals ensures the safety of roadway users and continuous mobility across the roadways and also protects concrete from harmful freezing in the concrete void structure. Despite these advantageous aspects of deicing chemicals, they are widely observed to cause infrastructure deterioration and hence lead to increased infrastructure maintenance costs. Deicing chemicals interact with concrete both physically and chemically, and the results of these interactions are manifested in the form of decreased strength and integrity of concrete, which can

⁹ This chapter was co-authored by H.U. Sajid, A. Jalal, R. Kiran, and A. Al-Rahim. H.U. Sajid had the primary responsibility of preparing the specimens, conducting all tests, and drafting this chapter. R. Kiran supervised the research and revised this chapter.

be attributed to 1) interaction with cement hydration products and formation of different expansive or non-cementitious products, and 2) interaction with the aggregates, 3) the physical damage and internal cracks formed by expansive product formation and crystallization of deicing salts. Apart from deterioration in the properties of concrete, chloride-based deicers are also linked with increased corrosion rates in rebars. The surface deterioration and void formation in concrete can facilitate the ingress of deleterious chemical species (such as chloride and sulfate ions) and moisture which affects the properties of concrete as well as rebars. Moreover, the use of deicing chemicals can increase the intensity of freeze-thaw-related deterioration in concrete. The deicer-induced deterioration in the concrete is commonly manifested in the form of scaling, spalling, cracking in the concrete, chloride contamination, ettringite formation, pore pressure, and rebar corrosion.

To mitigate the negative impacts of chloride-based deicers on concrete deterioration, various types of deicing chemicals have been developed or are in the process of development. These prevention strategies can be divided into three classes: 1) increasing the concrete resistance against deicers-induced deterioration through the incorporation of supplementary cementitious materials and better mix design, 2) adopting effective winter maintenance strategies that include decreasing the usage of deicers and encouraging the use of deicing solutions (e.g., NaCl brine), prewetting and anti-icing, updating equipment, and training, and 3) using topical treatments on concrete that primarily include the usage of concrete penetrating sealants and protective coatings (e.g., siloxanes). For achieving the objectives of these deicing-induced concrete deterioration strategies, it is important to understand the extent of deterioration and damage mechanism in concrete due to the application of commonly used deicers. The negative effects of deicers have been studied by different researchers. Most of these studies employed

wet-dry exposure cycles, freeze-thaw cycles, and continuous soaking regimes to simulate the deicer exposure and quantified the influence of deicing exposure on different properties of concrete. To this end, the negative implications of chloride-based deicers and acetate-based deicers are well-documented in different studies [4]. Moreover, the damaging effects of some agro-based deicers on concrete have also been investigated in the recent past [5]. Shi et al. [4] discussed the impacts of both traditional chloride-based deicers (NaCl, MgCl₂, and CaCl₂) and alternative deicers (acetate and format-based deicers) on cement and asphalt concrete and summarized some of the deicers-induced deterioration prevention strategies.

In the past decade, many studies have been conducted that explored the effects of incorporating supplementary cementitious materials on deicers-induced deterioration in concrete and the effects of deicing solutions, deicer blends, and agro-based deicers on the strength and integrity of the concrete. Many of these studies have used different methodologies to achieve their objectives and hence a comprehensive review of the existing research efforts is needed to combine and critically review the studies on the variation of the deicing salts, the additives that are added in cementitious mixtures, and experimental approaches and their significance in order to address the concerns of deicers and guide future research efforts in this direction. The objective of this paper is to discuss the effects of the recently developed laboratory-scale deicing formulations as well as the conventional deicing solutions on important properties of concrete that include scaling, mass loss, and compressive strength. Moreover, it also aims to discuss the performance of concrete incorporating supplementary cementitious materials and alternative mix design when subjected to different deicing solutions. In essence, this review article provides a comprehensive state-of-the-art review of the recent developments in the deicing-induced deterioration in concrete for both conventional and new deicing solutions and thus it can be used

as a guide when designing new laboratory-based deicers or evaluating the field applications of the existing deicers. This review article exclusively focuses on deicers impacts on cement concrete, and it is organized as follows: Section 10.2 discusses the physical and chemical deterioration mechanisms in concrete due to the application of deicers and their consequences for strength and other properties of concrete, Section 10.3 discusses the experimental techniques that are commonly employed for studying the physical and chemical deterioration in concrete, Section 10.4 presents a critical review of impacts of a wide range of deicing chemicals that have been investigated in the recent past, and Section 10.5 summarizes important conclusions and recommendations for future studies.

10.2. Deicers-induced Deterioration Mechanisms in Concrete

Deicer-induced deterioration in concrete is commonly exacerbated by different physical processes and chemical interactions between deicers and cement paste and deicers and aggregates. These deteriorations are manifested in the form of scaling damage, loss of compressive strength, mass change, expansion, and spalling. This section summarizes each of these physical deterioration mechanisms and discusses important factors that contribute to physical deterioration in concrete. Furthermore, it discusses the chemical interactions that occur between 1) deicers and cement hydration products, and 2) deicers and aggregates.

10.2.1. Physical Deterioration

10.2.1.1. Scaling

Scaling is the superficial damage (flaking or peeling) of the top surface of the concrete, which is initiated when the concrete is exposed to deicing chemical or freeze-thaw conditions. ASTM C672 provides guidance on determining scaling but some researchers showed some variation in the test [6]. In addition to deicing chemical exposure, scaling can also result from

insufficient curing and performing finishing operations while the bleed water is on the surface. The scaling can start as small patches, and it can extend to other areas. Several mechanisms of the scaling of concrete have been proposed in the literature to explain the deicing salt-induced scaling in concrete, and it is suggested to be similar to the scaling mechanism that is observed due to frost damage. Specifically, three different theories have been proposed to explain the scaling phenomena that include the hydraulic pressure theory, osmotic pressure theory, and glue-spalling theory.

Hydraulic pressure theory was one of the earliest proposed mechanisms which is based on the hydraulic pressure due to ice formation [1]. When concrete experiences freezing temperatures, the water in the voids solidifies. As the ice occupies around 9% higher volume compared to water and the volume change of cement paste is negligible, the capillary pores inside the concrete give the required extra room to the ice to some extent creating hydraulic pressure inside the concrete. A schematic of this mechanism is depicted in Figure 10.1. As observed in Figure 10.1(c), an escalation of hydraulic pressure causes scaling in the surface and result in the break-away of surface particles. If the temperature increases again, the ice becomes water and releases the hydraulic pressure. The process repeats, and more surface concrete particles are affected by scaling. Later, Powers [3] introduced an osmotic pressure mechanism for salt scaling. Cement-based material has two types of pores, namely gel pores, and capillary pores. Capillary pores are comparatively larger. According to the theory of osmotic pressure, the diffusion of water from the gel pores towards the capillary cavities creates a tensile pressure due to differences in concentration, as shown in Figure 10.2. Water in the gel pores is pure and stays through to the minute space even at very low temperatures. Capillary pore solutions, on the other hand, contain deicing agent ions that freeze at low temperatures. As soon as the water molecules

start to freeze in the pores, salt ions do not occupy the gel pore surface and therefore a gradient in salt concentration is formed. Because of this different concentration, water molecules with areas of low salt concentration (gel pores) diffuse into areas of higher salt concentration (capillary pores). This diffusion creates osmotic pressure in the higher concentrated surface area of the concrete which causes tensile stresses, a buildup of internal pressure, and mechanical damage in capillary voids and eventually leads to scaling. Apart from hydraulic and osmotic pressure theories, glue-spalling is another theory that was proposed by Valenza II and Scherer [7]. According to the glue-spalling theory, as the deicer melts the snow, the water forms a brine solution with the salt in deicers. Later, the temperature might drop again that will cause the ice to form again, and this ice penetrates into the pores of the concrete, thus adhering to concrete-like glue. With the subsequent fall in temperature, the ice begins to shrink (up to five times more than the concrete layer) which causes the underlying concrete to shrink together initiating cracks and scaling. Scaling can also result from salt crystallization. When the deicers are applied, the concentration of salt ions on the surface gets higher than that in the pores. Salt begins precipitating in the pores and thus forms crystals. The growth of crystals produce mechanical stresses within the pores which cause scaling in the long run [8].

The voids attribute and types are essential to determine their role regarding scaling caused by freezing weather. Normally, water and air voids are the two main types of pores in cement-based material. Water voids are irregular and detrimental in nature that can solidify with an increase in volume at low temperature that leads to internal hydraulic pressure. In contrast, air facilitates the release of pore pressure by providing extra room for expansion [9]. However, the size, number, shape, and spacing between voids are of key importance, otherwise, the same voids' counter action of reduction in compression strength becomes more considerable. Smaller

voids in larger numbers with minimum spacing are required to avoid scaling due to severe surrounding with a minimum decrease in mechanical strength. Similarly, some voids are irregular big air voids that are because of improper compaction of mortar or concrete. Some studies consider the overall surface area of voids of great importance. A larger surface area indicates more pores of smaller size with smaller vacant space in the specimen [10].

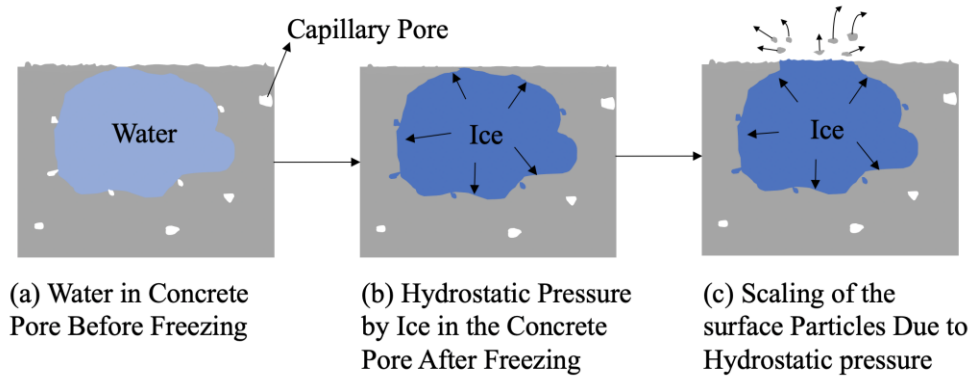


Figure 10.1. Mechanism of scaling due to hydrostatic pressure. (a) water in the concrete pore before freezing; (b) hydrostatic pressure by ice in the concrete pores after freezing where the capillary pores leave space to the increased ice volume (c) scaling of the surface particle due to hydrostatic pressure.

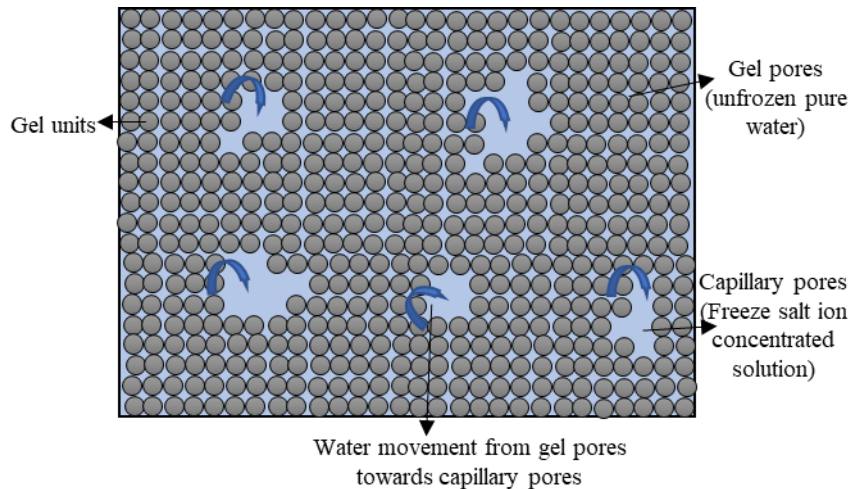


Figure 10.2. Mechanism of osmotic pressure development.

10.2.1.2. Mass Change

Mass change is also a common physical characteristic of the concrete exposed to a deicer solution. Portland cement-based material (concrete) can experience either mass loss or mass gain upon exposure to deicing chemicals. ASTM C666 can be used to determine the mass loss when specimen is exposed to a deicing solution [11]. The mass loss could occur due to surface scaling. At the same time, the mass gain is also possible due to salt crystallization and water absorption. Different deicers show different mass change characteristics throughout deicing exposure time. Typically, about 0.5-2.0%, mass change has been observed in concrete when it is exposed to common chloride and acetate-based deicing chemicals for an extended duration.

10.2.1.3. Expansion

Concrete and cement mortar can exhibit expansion upon exposure to deicing chemicals for an extended period. This expansion depends on various parameters of the experiment. Several deicers demonstrate different types of expansion characteristics. The deicing chemicals-induced expansion in concrete is commonly observed to be a function of the water to cement ratio, the concentration of deicing salts in the deicing solution, and the calcium-magnesium ratio of the deicers.

10.2.1.4. Spalling

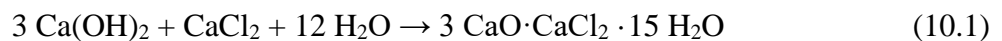
In addition to scaling, deicing chemicals can also result in spalling of concrete which refers to the breaking away of concrete surfaces. Spalling often extends to the top layer of the reinforcing bars and is commonly caused by the deicers-induced corrosion of rebars. Moreover, the factors that contribute to scaling are also observed to be responsible for spalling.

10.2.2. Chemical Deterioration

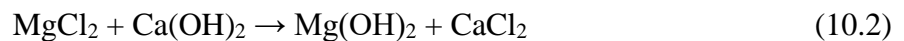
The chemical deterioration mechanism is different for different deicers based on their chemical compositions. Deicers may cause damaging effects to concrete by causing reactions with cement paste and aggregates. The chemical interactions between deicers and concrete (cement paste or aggregates) can be linked with some of the physical deteriorations. In the following sections, the chemical deterioration mechanisms in concrete are discussed for the commonly available deicers.

10.2.2.1. Reaction Between Cement Paste and Deicers

Ions in the deicers can react with the cement paste. For example, chloride ions in sodium chloride, calcium chloride, and other chloride-based deicers can cause calcium hydroxide leaching [5, 12, 13]. Calcium hydroxide can occupy more than 20 percent of the total volume of cement paste. Calcium hydroxide leaching can cause a significant deterioration in concrete and adversely affect the strength and durability of concrete. CaCl_2 based deicers can cause slow but severe deterioration in concrete. Calcium hydroxide in cement paste can react with CaCl_2 to form calcium oxychloride [14, 15].



MgCl_2 can stem from Mg-based deicers, which can react with calcium hydroxide to form CaCl_2 .



Calcium oxychloride can cause immense hydraulic pressures in concrete, which can lead to severe cracking. Sutter et al. [15] found radial cracking in the cylinders that were exposed to CaCl_2 and MgCl_2 solutions. In another study, affected areas of the cement paste were found to be more porous [16], and nearly no calcium hydroxide was found in that area. Besides, oxychloride formation also affects the strength and durability of the concrete.

Magnesium ions in MgCl_2 and other Mg-based deicers can react with C-S-H in cement paste and create M-S-H [12, 15, 17].



M-S-H is a non-cementitious product that is not associated with the strength of the cement. C-S-H is a significant contributor to the strength of concrete; thus, magnesium ions can reduce the compressive strength of the concrete [15, 18, 19]. Moreover, magnesium ions can form brucite ($\text{Mg}(\text{OH})_2$ crystal) that causes crystal growth pressure in concrete, which can cause concrete to expand and lose strength [15, 19-21]. The complex salt formation, e.g., brucite and calcium oxychloride, depends largely on the concentrations of the solution. Calcium oxychloride formation occurs at a temperature between 0°C to 50°C [22]. Deicers-induced chemical deterioration in concrete becomes a key factor when deicers are used in higher concentrations [16]. The formation of expansive products such as Friedel's salt, brucite, and calcium oxychloride can be obtained from SEM images (see Figure 10.3) and XRD spectra (see Figure 10.4) of cement mortar or concrete specimens that are constantly exposed to the deicing salts [23, 24].

The main interaction is the same with commonly used deicers such as calcium acetate, magnesium acetate, and CMA. The main cause of the deterioration is the formation of non-cementitious MSH, which leads to the peeling of aggregate and cement paste. The CSH gel is the product of cement hydration, which leads to a bond between aggregate and binding matrix. The penetration of CMA reaches CSH at the interference of aggregate and surface, resulting in MSH and expansive nature products, i.e. brucite. MSH has no binding capacity, which is why aggregates are detached from the binding matrix. The severe condition also brings shrinkage cracks in MSH. This whole process also leads to the precipitation of brucite and a calcite layer in the cavity area. Magnesium acetate also behaves the same, but calcium acetate has not shown

any new product production other than calcite. Overall, it was observed that magnesium is the main reason for the breakdown and formation of MSH and brucite, while the calcium contribution through the formation of calcite precipitates is low [25].

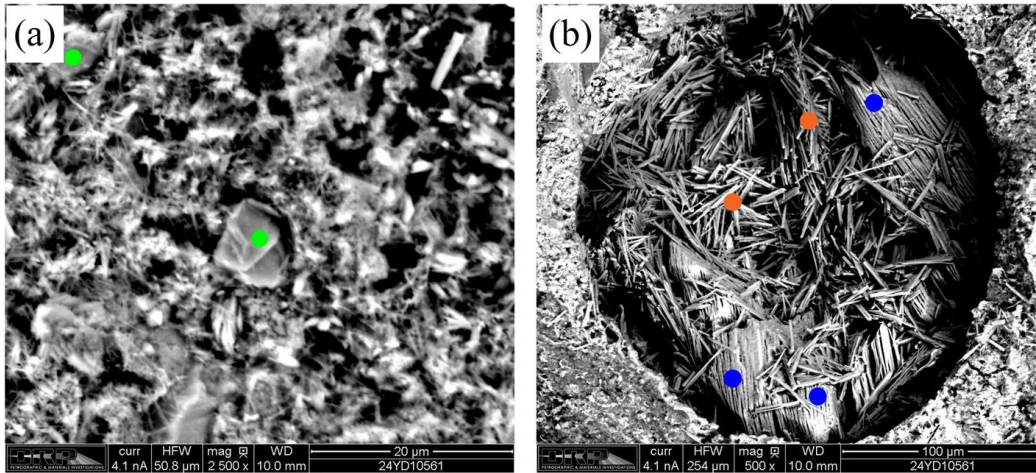


Figure 10.3. Backscattered electron images of (a) cement matrix (b) air void in cement paste matrix indicating the formation of crystals of Friedel's salt (shown by green circles), ettringite (shown by orange circles), and Ca-oxy (shown by blue circles). (adopted from Ref. [23]).

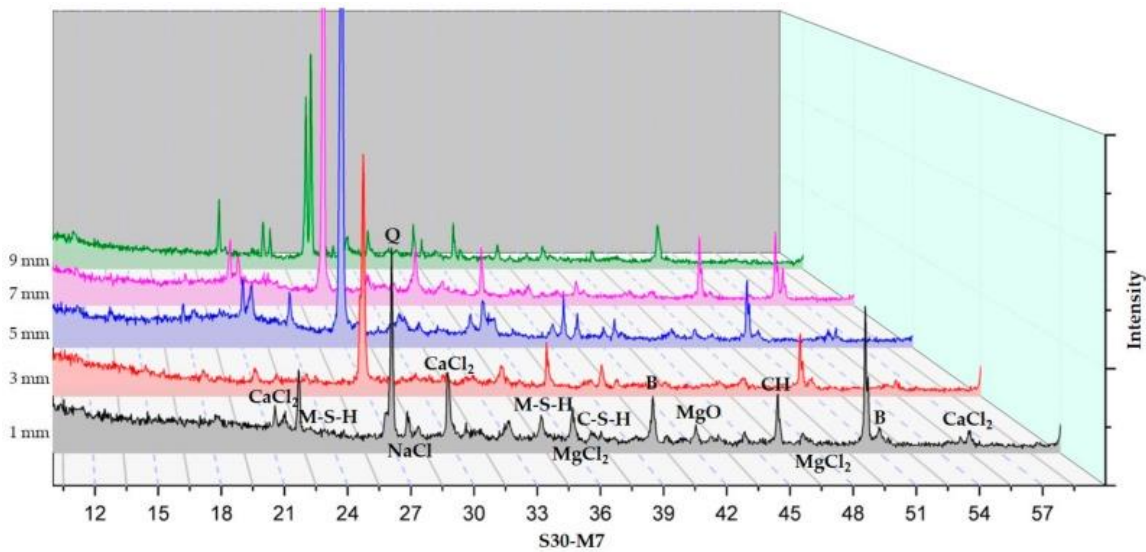


Figure 10.4. XRD spectra of concrete specimens after 180 days of deicing solution exposure indicate the formation of brucite (B, occurring at around 40° and 51.5°) and other products. (adopted from Ref. [24]).

10.2.2.2. Reaction Between Aggregates and Deicers

The two most common aggregate cement reactions are the alkali-silica reaction (ASR) and alkali-carbonate (ACR) reaction. Deicers can accelerate ASR in concrete with reactive aggregates [13, 26-28]. Deicers provide extra alkali to the pore solution, which forms N(K)-S-H gel. This gel swells as it attracts water from the cement paste. When absorbing pressure, this gel can cause internal pressure which can lead to expansion and cracking of the aggregate and cement paste.

CaCl₂ and MgCl₂ do not have any impact on ASR. From several studies, it is indicated that NaCl primarily causes the instigation of the ASR process [29-33]. The increase in pH in the pore solution is the potential cause of ASR. NaOH is formed by the reaction between NaCl and Ca(OH)₂. Chloride ions in deicing salts can accelerate ASR [29].



Dolomite (CaMg(CO₃)₂) aggregate can react with alkalis in cement paste, referred to as Alkali-Carbonate Reaction (ACR). Dolomite aggregate reacts with OH⁻ anion in the cement paste and creates Mg²⁺ and CO₃²⁻ cations [4]. CO₃²⁻ cations form CaCO₃ and OH⁻ by reacting with the portlandite, while brucite is formed from the precipitation of Mg²⁺ ions [4]. This formation of brucite and CaCO₃ crystals can cause crystal growth in the concrete, which eventually causes expansion and cracking in the cement paste [34].

10.3. Experimental Techniques for Characterizing Physical and Chemical Deterioration

This section describes the experimental techniques and specimen preparation procedures that have been adopted in the literature for investigating the deicers-induced physical and chemical deterioration in cement-based materials. Specifically, the mix design and materials that are used in the preparation of concrete specimens, the experimental procedures for simulating the

concrete deicing exposure, and the laboratory tests that are used for quantifying the deicer-induced deterioration in concrete are discussed in this section.

10.3.1. Materials Selection and Mix Design

The deicer-induced deterioration has been investigated for both ordinary Portland cement (OPC) concrete and concrete mixes that use supplementary cementitious materials. Many of the earlier studies focused on understanding the performance of air-entrained and non-air-entrained OPC and high-strength concrete when subjected to conventional chloride-based deicers. Recent research efforts have been dedicated to understanding the role of unconventional concrete mix design and supplementary cementitious materials in mitigating or accelerating the harmful effects of conventional deicers on concrete. Specifically, extensive investigations have been conducted to understand the deicers-induced deteriorations in concrete mixes wherein the cement is partially replaced by fly ash [20, 21, 34], blast furnace slag [20, 21, 35], and modified forms of blast furnace slag [21]. In most of the literature on the deicers' impact on concrete, a water-cement ratio of 0.35-0.5 is adopted. Moreover, a variety of admixtures are used in the concrete specimens used in the literature to simulate the concreting in cold regions or to improve the properties of concrete. Similarly, concrete specimens with and without air entrainment are used and their performance in deicing exposure tests is compared. For this purpose, a wide variety of commercially available entraining agents are utilized in different studies to achieve the desired air content in the hardened concrete specimens [5, 35-37].

10.3.2. Deicer Selection

For field applications, deicers are selected based on their effectiveness during the freezing temperatures, cost, availability, and ease of application on the pavement surface. The effectiveness of deicers in melting ice and snow is defined by their effective temperature, which

is the lowest temperature where a deicer can be practically used for ice melting, anti-icing, and other applications [30]. In highway deicing and anti-icing operations, chloride-based deicers are most commonly used due to their lower cost and ample availability [31]. Among the chloride-based deicers, NaCl is most commonly employed in the highways. The effective temperature for NaCl is 15°F [32]. Below this temperature, it cannot melt the snow, thereby making it inappropriate during extremely low freezing temperatures. However, it is often mixed with other deicers and corrosion inhibitors to make it applicable to a wide range of areas. Changing the concentration of NaCl deicers and mixing it with other deicers and additives is known to reduce the freezing point of NaCl solution and hence making them more effective in snow melting at temperatures below 15°F [33-35]. While NaCl does not cause serious deterioration in concrete, it is widely observed to corrode steel [31, 36] and is known to adversely affect the environment and aquatic life [30]. On the other hand, calcium chloride is also a chloride-based deicer which is effective at temperatures as low as -25° F, which makes it suitable for cool winter areas. It is relatively harmless to the environment. However, it causes significant deterioration in concrete [4, 10] and is more expensive as compared to sodium chloride [37]. Magnesium chloride is another chloride-based deicer that works at a relatively low temperature (-10°F) and it is widely used for deicing on highways and parking lots [38]. However, it is also observed to be corrosive, cause severe deterioration in concrete and may cause pollution to the environment [39, 40]. Calcium magnesium acetate (CMA) deicer is less corrosive when compared to chloride-based deicers [41]. It is also biodegradable, which makes it environmentally friendly to some extent. However, CMA is not as cost-effective as chloride-based deicers. Moreover, its application is limited to moderately cold temperatures. Potassium acetate is another acetate-based deicer that works at a very low temperature (-15°F) [42]. Like CMA, it is a less corrosive and more

environmentally friendly option. Hence, it is mostly employed in airport runways. In addition to the aforementioned deicers, potassium formate, calcium formate, and urea are also used as deicers in different applications [3].

Selecting deicers is an integral part of the experimental schemes adopted in the literature. Different deicers have different characteristics and lead to varying rates of deterioration in concrete. To this end, the most commonly tested deicers include chloride-based deicers (NaCl, CaCl₂, and MgCl₂), acetate-based (e.g. CMA), and formate-based deicers. The popularity of these deicers is evident from the number of peer-reviewed publications on different types of deicers in the past four decades, as shown in Figure 10.5. Additionally, agro-based and other propriety deicing chemicals have also been investigated for their deterioration impact in cement-based materials. Some researchers also added certain corrosion inhibitors to the deicing solutions while investigating the influence of deicing chemicals on concrete. The above-mentioned deicing solutions have been used in the deicing exposure experiments in concentrations that mostly ranged from 3% to 30%. Moreover, some studies used mixed deicers wherein NaCl and another chloride-based deicer are mixed in 50-50 or other ratios. As sodium chloride is the most commonly used deicer, it is used as a deicer in almost every study. Additionally, calcium chloride and magnesium chloride are also used in many experiments related to deicers, as they show the most severe deteriorations in concrete. Furthermore, several new deicing chemicals have been investigated in recent studies.

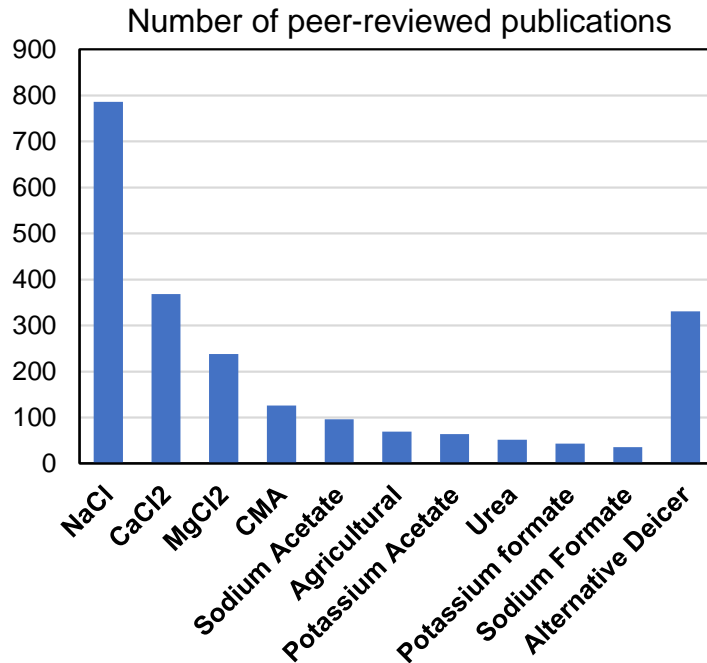


Figure 10.5. The number of peer-reviewed publications (journal articles, reports, and proceedings) on different types of deicers in the period 1980-2021. The data is obtained from the Scopus database using the following search query: deicing/deicer/anti-icing and “name of deicer”.

10.3.3. Deicer Exposure Methods

To investigate the physical and chemical deterioration of concrete due to deicer, it is essential to select the appropriate deicer exposure method. To this end, three deicer exposure techniques are commonly adopted in the experimental schemes that include continuous soaking, freeze-thaw exposure, and wet-dry exposure of deicing solutions. Each of these deicing exposure techniques are discussed in the subsequent sections.

10.3.3.1. Continuous Soaking

Continuous soaking of concrete samples in the deicer solution is a standard experimental technique for characterizing physical and chemical deterioration in concrete. Most of the researchers used or modified ASTM C1260 [51] test to examine the effect of continuous soaking in deicing solution. The continuous soaking exposure method has been used in different studies

[15, 19, 49, 52]. During the continuous soaking exposure method, the samples are immersed in a deicer solution or water solution for a certain period. This soaking period may vary in different experimental protocols depending upon the concentration of deicer solution or experimental goal. There is no standard temperature that is followed by the researchers. The temperature could be room temperature or temperature as low as 4°C. At the end of the soaking period, samples are taken off from the solution and different physical and chemical tests are conducted. This method does not show the frost effect or temperature-change effect of the deicer solution.

10.3.3.2. Freeze-Thaw Exposure

The freeze-thaw (F-T) test is used to elucidate the physical and chemical characteristics of concrete exposed to deicers. ASTM C666 [11] is the standard test to illustrate the resistance of concrete to rapid freezing and thawing. F-T test simulates the freeze-thaw scenario that most highways experience during the winter season in colder regions. During subzero temperatures, the water trapped in the concrete pores freezes. When the temperature rises, the ice in the concrete melts which is followed by freezing once the temperature drops to subzero level again. Roadways experience several such cycles during every winter season. Ice has around 9% more volume when compared to water and this extra volume exerts hydraulic pressure in pores in the absence of adequate pore space, which eventually leads to cracks and deterioration in concrete. F-T exposure tests mimic this process in the laboratory and are hence used to study the physical and chemical deterioration of concrete. During F-T exposure tests, the samples are submerged in a deicer solution in a container and are subjected to F-T cycles. A typical F-T cycle consists of a ‘freezing’ interval and a ‘thawing’ interval. During freezing intervals, the containers wherein concrete samples are fully submerged in the deicing solution are placed in a freezer and stored at freezing temperatures (i.e., -10 to -22° C) for a certain time period. This is followed by a thawing

interval during which the containers are taken out of the freezer and are placed at room temperature for thawing. The selection of the freezing and thawing period is dependent on the experimental procedure. One of the standard practices for the freeze-thaw test is to use a cycle time of 24 hours. The freezing interval varies between 12-18 hours, and the thawing interval varies between 6-12 hours. A high concentration of deicer is usually used in F-T tests due to their lower freezing point and the ability to get the required deterioration quickly. Some researchers adopted a longer cycle time using a less concentrated deicer solution. The cycle time can vary from two days to even one month. The physical and chemical deterioration in concrete is tracked at a specific number of F-T exposure cycles by conducting different laboratory tests.

10.3.3.3. Wet-Dry Exposure

Another widely used deicing exposure method is Wet-Dry (W-D) exposure test. Here, the samples are soaked in the deicing solution for a certain period (referred to as 'Wet' period). Which is followed by a 'Dry' period during which the samples are taken off from the solution and placed in an open space for drying. It is a common practice to keep the temperature around 0-4°C during the wet period and room temperature (20°-25° C) for dry period. This wetting and drying are continued for a certain number of cycles. The length of a cycle depends on the parameters of the experiments. After specific number of W-D exposure cycles, samples are subjected to different physical and chemical tests to evaluate the deicer-induced deterioration.

10.3.4. Deicer-induced Deterioration Tests

10.3.4.1. Visual Evaluation, Scaling, and Scaling Rating

Visual evaluation is a qualitative test wherein the specimens are visually examined for physical deterioration from the deicer exposure. Visual examination of concrete, mortar or cement paste specimens is carried out at the beginning of F-T and W-D exposure tests and after a

specific number of F-T or W-D exposure cycles. To this end, specimens are visually monitored and photographed and any change in the physical appearance of the specimen surface is noted. The physical deterioration is usually in the form of cosmetic cracks on the surface, surface scaling, and spalling. From visual evaluation, the extent of scaling in the specimens is identified. Moreover, a scaling rating is usually assigned to the specimens based on the visually observed scaling damage. The scaling rating ranges from 0 (no scaling damage) to 5 (severe scaling damage) [5].

10.3.4.2. Mass Change Evaluation

The change in the mass of the specimens is another parameter which is commonly used in the literature to track deicer-induced deterioration in the concrete, mortar, or cement paste specimens. The increase in the mass of the specimen usually indicates the accumulation, precipitation, and crystallization of deicing salts in the pores, which can lead to pressure buildup in the pores and eventual cracking. On the other hand, the decrease in the mass of the specimen usually indicates scaling and break-off of aggregates or hydration products, which is once again indicative of deicer-induced physical deterioration in the specimens. The mass change in the specimens is commonly evaluated after a specific number of F-T or W-D exposure cycles and at the end of F-T or W-D exposure tests.

10.3.4.3. Expansion Measurement

Determining volumetric expansion in the specimens is another method of evaluating deterioration in the specimens as a result of exposure to deicing solutions. For this purpose, the length, width, and height of the samples are recorded at the beginning, after a specific number of exposure cycles, and at the end of F-T or W-D test. Usually, the visual evaluation, mass change evaluation, and expansion measurement are conducted after similar but a specific number of F-T

or W-D exposure cycles and these parameters are compared with the measurements recorded at the beginning of F-T and W-D tests for determining the deicer-induced physical deterioration

10.3.4.4. Strength Evaluation

Strength is one of the most important parameters that indicates the extent of deterioration in the concrete, mortar, or cement as a result of exposure to deicing solutions. Compressive strength, split tensile strength, and flexural strength are the three strength parameters that can be used to evaluate the deicer-induced deterioration in concrete. Owing to its practical importance, most researchers have focused on determining the compressive strength of concrete, mortar, or cement paste specimens whereas only few studies determined the flexural and split tensile strength of concrete specimens after deicer exposure tests. Compressive strength tests are conducted at the beginning of F-T or W-D continuous soaking testing and after a specific number of F-T or W-D exposure cycles using ASTM C39 and AASHTO T22 specifications. Moreover, non-destructive testing techniques are also used to evaluate the compressive strength of the concrete specimens [53, 54].

10.3.4.5. Dynamic Modulus of Elasticity Evaluation

The dynamic modulus of elasticity is another durability parameter which can be used to determine the extent of deicer-induced deterioration in the concrete. The dynamic modulus of elasticity of concrete specimens after exposure to deicing solutions is usually determined using non-destructive testing such as resonance frequency test, impulse excitation test, and sonic resonance test [53-55].

10.3.4.6. Chemical Composition and Surface Characterization

Chemical composition analysis and surface characterization tests are commonly employed to evaluate the chemical interactions between the deicing chemicals, cement hydration

products, and aggregates. Specifically, chemical composition analysis and surface characterization tests indicate the harmful or beneficial products that are formed as a result of chemical interactions between the deicing chemicals, cement hydration products, cementitious materials, and aggregates. Moreover, the surface characterization techniques are also used to elucidate the presence of microcracks in the specimens as a result of exposure to the deicing solutions. In essence, these tests quantify the deicer-induced chemical deterioration in cement-based materials. The most common chemical composition analysis tests include X-ray Diffraction (XRD) and Energy Dispersive X-Ray (EDX) analysis whereas optical microscopy and Scanning Electron Microscopy (SEM) are frequently used for the characterization of surface and microcracks and morphological analysis (see Figure 10.3 and Figure 10.4). XRD and EDX analysis yield the crystalline compounds and elemental composition of the products formed due to chemical interaction between the deicing solution and cement hydration products. For performing XRD analysis, powder samples are obtained from surface layers at various depths. For SEM analysis, a section is cut from the concrete sample which is further polished and prepared for examining the presence of microcracks and any products. XRD, SEM, and EDX analyses are usually performed after a specific number of F-T or W-D exposure cycles.

10.3.4.7. Ion Penetration Test

Ion penetration test is commonly used to determine the extent of deicing chemical ions penetration in the concrete, mortar, or cement paste specimens after exposure to deicing chemicals. Ion penetration test gives a quantitative account of the presence of deicing chemical ions (such as chloride ion, sodium ion, and magnesium ion, etc.) at certain depths in the specimen. This information is very important since the presence and concentration of these ions have a direct impact on the extent of concrete deterioration due to the formation of expansive

products and rate of corrosion in rebars. The commonly available laboratory tests for determining the ion penetration in concrete include salt ponding test (AASHTO T259), bulk diffusion test (Nordtest NTBuild 443), Rapid Chloride Permeability Test, (AASHTO T277 and ASTM C1202), total chloride content test (ASTM C1152), electrical migration techniques, rapid migration test (CTH Test), resistivity techniques, pressure penetration techniques, indirect measurement techniques, and sorptivity analysis. Among these methods, ASTM C1152, AASHTO T259, AASHTO T277, and ASTM C1202 test methods are commonly adopted in the literature.

10.4. A Critical Review of Previous Literature

Numerous studies have been performed by different researchers to elucidate the deicer-induced physical and chemical deterioration in concrete. While many characterization tests are performed to evaluate the deicer-induced deterioration in concrete, this review article focuses only on the most important properties of concrete that are vital for ensuring the serviceability of concrete structures and this section summarizes the most common deicer-induced concrete deterioration parameters that include scaling damage, scaling rating, mass change, and compressive strength that have been reported in the literature for different types of concrete mixes and deicing chemicals. Moreover, the results are discussed for both F-T and W-D exposure tests.

10.4.1. Scaling

Many researchers characterized scaling as an indicator of deicer-induced physical deterioration in concrete in their studies [56-58]. Scaling tests and scaling rating assignments are conducted using visual evaluation procedures discussed in Section 10.3.4.1. The scaling damage results obtained from the literature corresponding to W-D and F-T exposure tests are

summarized in Table 10.1. As observed in Table 10.1, the scaling damage has been investigated for a variety of deicing chemicals using different deicing exposure conditions (F-T or W-D), cement types, usage of admixtures, and supplementary cementitious materials (e.g., fly ash and blast furnace slag), different water-cement ratios and aggregate types. In the subsequent subsections, the scaling behavior of deicers corresponding to F-T, W-D, and continuous soaking tests is discussed.

Table 10.1. Studies focused on scaling damages on concrete due to deicer exposure.

Ref.	Deicer used	Exposure method	Parameters	Findings
[59]	CaCl ₂	-	Concrete (field)	-Damage in concrete linked with the chemical reaction between calcium chloride and cement paste, and mechanical stress developed by load and F-T cycles.
[60]	NaCl	W-D	Concrete w/c: 0.3, 0.26, 0.2	-No significant deterioration was found after 150 cycles. -W/c ratio, air void spacing factor, and length of curing did not have any impact on HPC specimens exposed to deicers.
[36]	CaCl ₂	Soaking	Concrete (OPC, OPC with 15% SF, OPC with 30% FA)	-Concrete specimens with or without air-entrained agent showed severe damage when exposed to CaCl ₂ . -This damaging effect is attributed to the formation of oxychloride products.
[49]	NaCl, CMA	Soaking	Mortar w/c =0.45,0.6 time- 22 months	-Ca/Mg molar ratio had significant effects on the mortar. -Higher Mg ion concentration is linked with increased deterioration in specimens. -NaCl did not cause significant scaling in specimens.
[19]	NaCl, CaCl ₂ , MgCl ₂	W-D, F-T	Concrete w/c =0.45, 0.6 time: 22 months conc: 0.75,3(M)	-CaCl ₂ , MgCl ₂ , Mg-acetate and Mg-nitrate caused significant scaling in specimen as compared to NaCl. -Brucite formation was assumed to be the potential reason behind the deterioration.
[61]	NaCl with six Cis	Soaking	Concrete slab	-Formation of calcium phosphates, magnesium phosphates, gypsum, and other precipitates resulted in scaling damage.
[35]	CMA (25 wt%)	Soaking	Concrete (Type I, Type II, Portland clinker with 20% limestone and 40% BFS)	-The deterioration of the concrete appeared to be slightly greater in the case of immersion in solutions manufactured using a commercial CMA based deicer product rather than employing pure calcium and magnesium acetates.
[62]	NaCl, Na-formate, K-acetate, Urea	F-T	Aggregate, Concrete (field)	-Disintegration observed in aggregates exposed to F-T cycles. The limestone aggregate was found to have a higher resistance to disintegration as compared to quartzite. -Scaling damages observed in asphalt concrete samples, particularly in the case of urea.

Table 10.1. Studies focused on scaling damages on concrete due to deicer exposure (continued).

Ref.	Deicer used	Exposure method	Parameters	Findings
[63]	NaCl	Soaking	Concrete (laboratory, field)	-Scaling due to formation of chloroaluminate crystals cement paste and in the air voids near the surface. -pH decreased near the surface is attributed to anisotropic expansion and tension cracks near the surface.
[65]	NaCl (3 wt%)	F-T	Concrete (OPC, blast-furnace & limestone OPC)	-Severe scaling in F-T exposure regardless of air-entrainer. -Scaling is affected by the air-entrainer, second finishing treatment, cement content, w/c ratio, and curing conditions.
[15]	NaCl, CaCl ₂ , MgCl ₂	Soaking	Mortar w/c: 0.45, 0.5, 0.6 time (d): 7, 14, 28, 56, 84, 112	-MgCl ₂ and CaCl ₂ showed initial deterioration after days and severe deterioration after 84 days. -No significant deterioration observed in the case of NaCl. -Deterioration is attributed to the formation of brucite and calcium oxychloride, in the case of MgCl ₂ and CaCl ₂ .
[5]	NaCl, CaCl ₂ (with Cl), KAc, agro-deicer	W-D, F-T	Cement paste w/c =0.4 Concrete w/c =0.4 time (d): 60 (1 day cycle)	-CaCl ₂ exhibited the highest scaling (under both W-D and F-T conditions) which is linked with salt crystallization and precipitation, and leaching of cement hydration products. -KAc and agro deicer showed limited deterioration. -F-T exposure resulted in higher scaling damage as compared to W-D exposure.
[64]	KAc, NaAc, NaCl	Soaking	Concrete (low-alkali cement, high-alkali cement)	-KAc and NaAc caused ASR in the specimens containing reactive aggregates. -Extensive scaling is observed in all cases. Surface cracking was more serious in the case of KAc .
[55]	NaCl, CaCl ₂ , MgCl ₂ , CMA (6.04M & 1.06M)	W-D	Concrete w/c =0.4 time: 70 weeks (1-week cycle)	-At 6.04 molal ion concentration, CaCl ₂ , MgCl ₂ , and CMA cause significant changes in concrete. -At 1.06 molal ion concentration, all deicers exhibited relatively lower scaling damage. -Among all the used deicers, NaCl appeared to have lower negative impact on concrete in any concentrations.
[4]	NaCl, MgCl ₂ , CMA, K-formate, K-acetate	F-T	Concrete time: until significant deterioration (1 day cycle)	- CMA solid deicer and MgCl ₂ liquid deicer were observed to be less deleterious to concrete. -NaCl-based deicer (IceSlicer™), and KAc-based deicer (CF7™) caused higher deterioration in concrete.
[66]	NaCl, CaCl ₂ , MgCl ₂ (3,30wt%)	W-D	Mortar w/c =0.5 time 124 weeks (4 weeks cycle)	-With the increase in concentration, severe scaling is observed in the specimens exposed to CaCl ₂ . -The specimens exposed to MgCl ₂ had less damage, and no damage was observed in the case of NaCl.
[67]	MgCl ₂ , CaCl ₂ , NaCl	Soaking	Concrete Time (d): 338	From the results, it appeared that Mg ²⁺ cation has a more detrimental effect on concrete as compared to Ca ²⁺ cation.
[31]	K-acetate, K-formate	Soaking	Cement paste Concrete	-Scaling and microcracks observed in the specimens. -ESEM/EDS study confirmed the formation of ASR gel.

Table 10.1. Studies focused on scaling damages on concrete due to deicer exposure (continued).

Ref.	Deicer used	Exposure method	Parameters	Findings
[68]	NaCl, CaCl ₂ , MgCl ₂	Soaking, W-T, F-T	Concrete (Type I, Type I + 20% FA time (d): 336 (1 day cycle)	-CaCl ₂ showed the highest scaling damage among all the deicers. Specimens exposed to CaCl ₂ had a 15% reduction in RDME after 154 cycles. For MgCl ₂ , the same amount of reduction was found after 300 cycles. -Specimens with fly ash showed better result in all the tests.
[69]	NaCl, K-acetate	W-D, F-T	Concrete (field and laboratory) w/c: 0.4 (laboratory)	-Interfacial transition zone (ITZ) attack was observed. -EDS results suggested leaching of Ca from cement paste. -Scaling damage due to formation of precipitates as well as crystallization-induced volume expansion.
[20]	NaCl, CaCl ₂ , MgCl ₂ (5.5M)	F-T	Concrete (Type I, Type I+FA, Type I BF, Type I+FA+BF Time (d): 350 (1 day cycle)	-CaCl ₂ resulted in higher scaling than MgCl ₂ and NaCl. -The deterioration is attributed to the formation of brucite and magnesium silicate hydrate. -Formation of calcium hydride is observed to increase the concrete porosity and thus result in high deicer penetration in concrete matrix.
[70]	NaCl, CaCl ₂ , MgCl ₂ , CMA	F-T	Concrete (field) Concentration: 0.75M	-Ca-acetate was less detrimental, and Mg-acetate was more detrimental. -The authors recommended using CMA with a high Ca:Mg ratio.
[71]	CaCl ₂ (4 wt%)	F-T	Concrete (OPC, AAC)	-The concrete prepared with AAC showed lower deicing salt scaling resistance when compared to OPC concrete. -Air-entraining agents improved the deicer scaling resistance of AAC concrete specimens.

10.4.1.1. Scaling Damage Under F-T Tests

The measurement of scaling damage in terms of five scaling ratings as per ASTM C 672-98 under F-T exposure cycles is provided in Figure 10.6. The severity of each of these scaling ratings is described in Table 10.2. As observed in Figure 10.6, the scaling damage has been investigated for a variety of deicing chemicals and deicer blends, and the concrete samples used in these studies included different cement types, admixtures, supplementary cementitious materials, water-cement ratios, and aggregate types. Sahin et al. [72] conducted comprehensive investigations on the effect of NaCl deicer on concrete durability by subjecting concrete specimens to 50 F-T cycles. The concrete specimens incorporated different cement content, curing conditions, air entrainment percentage, and water to cement ratio. Some of the samples

showed a very high scaling (> 3) even with a comparatively low F-T cycle. For instance, normal concrete with no air-entraining agent was observed to deteriorate more quickly after exposure to NaCl deicing solution as compared to air-entrained concrete specimens (3.5 scaling rating after 5 F-T cycles). The researcher used basalt aggregates, which make the material porous, resulting in greater absorption of the deicing solution. Samples hardened in water also have a one-dimensional cooling system. The normal concrete with no air-entraining agent was observed to deteriorate more quickly after exposure to NaCl deicing solution as compared to air-entrained concrete specimens. The addition of 0.1% air entrainment considerably enhanced the scaling resistance of concrete. Similarly, air curing was observed to be more effective as compared to water curing. In addition, the increase in cement amount decreased the permeability that in turn led to lower chloride ion penetration and low surface peeling [5, 72]. Matalka and Parviz [71] investigated the effect of CaCl_2 deicer on OPC concrete and alkali aluminosilicate cement concrete with and without air entrainment. The authors observed that normal concrete incurs minor deterioration as early as 4 F-T cycles while the addition of an air-entraining agent significantly enhanced the scaling resistance and only minor scaling was observed after 6 F-T cycles. This scaling damage in the specimens can be attributed to the pressure developed by the formation of crystals of Friedel's salt and ettringite [73]. A recent study also observed the formation of Friedel's salt and ettringite formation in cement paste, as confirmed by the backscattered electron images of the cement matrix provided in Figure 10.3 [23]. The degradation is also attributed to the leaching of Calcium ions (Ca^{+2}) from the C-S-H structure [34, 74]. The use of alkali aluminosilicate cement reduced the scaling resistance. However, the inclusion of air-entraining agents increased the scaling resistance. The reduction in scaling resistance in the presence of alkali aluminosilicate cement is attributed to the presence of Cl^- and

H⁺ ions [75]. Though, some specimens based on alkali aluminosilicate cement showed a scaling of 4 after 8 cycles of F-T in 4% calcium chloride deicing solution. Alkali aluminosilicate cement concrete pores are rich in sodium that causes the formation of sodium chloride that disturbs the hydrates in the alkali aluminosilicates due to the low basicity of void solution [12, 13]. But the introduction of air entrainment provides the extra space for crystals to grow to reduce the pressure on the pore structure [73]. Similarly, the pozzolanic reaction of fly ash also contributes to countering the detrimental effect of calcium chloride deicing solution [68].

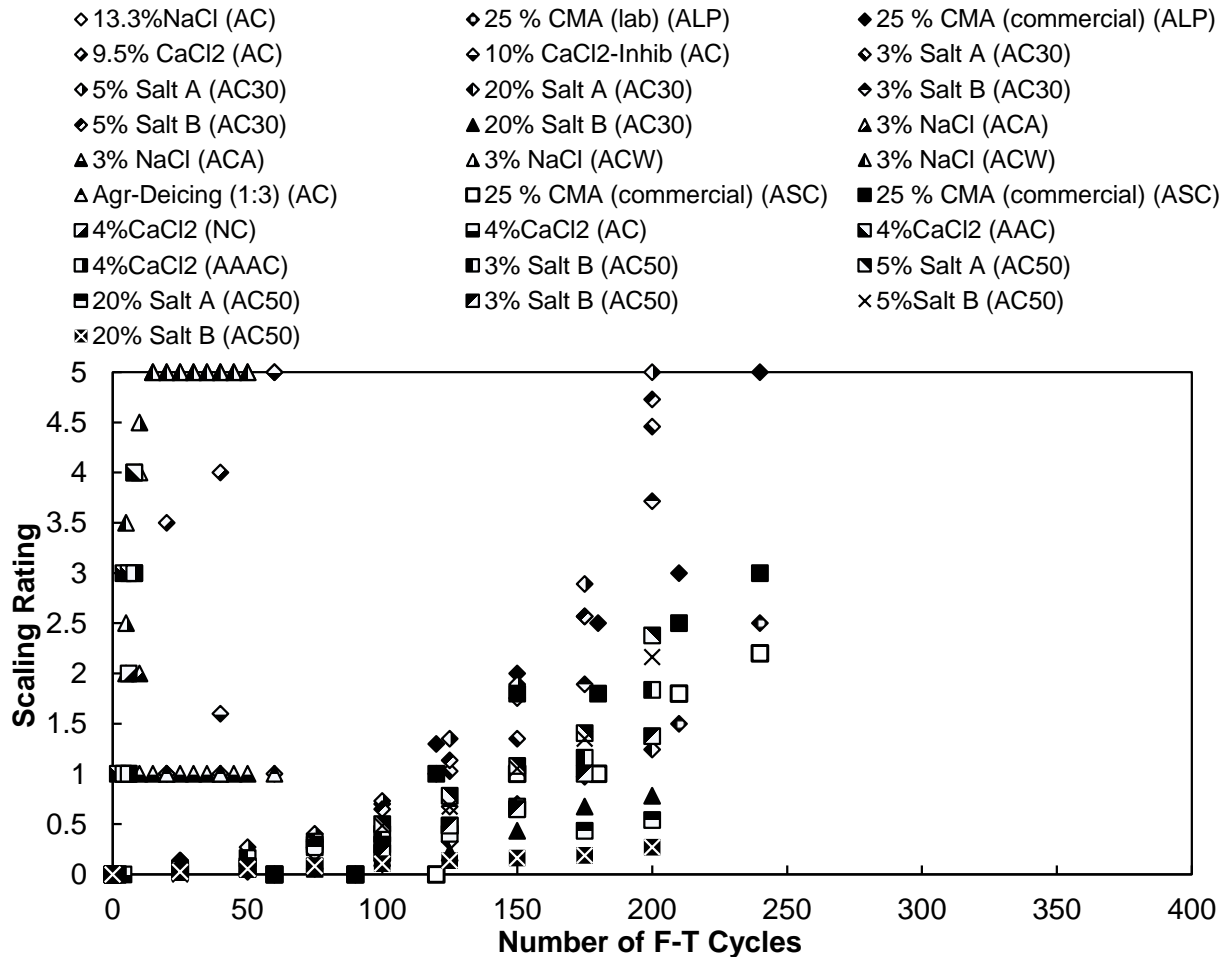


Figure 10.6. The variation of scaling rating with the number of F-T cycles for different studies ([5] [35] [49] [72] [71] [68] [76]).

Table 10.2. Scaling rating description.

Scaling Rating	Description
0	No scaling
1	Slight scaling (small flakes visible on sample surface)
2	Slight to moderate scaling (large flakes visible on the sample surface and sample edge damage noticeable)
3	Moderate scaling (sample edge damage and some fine aggregate visible)
4	Moderate to severe scaling
5	Severe scaling (chunks coming out of surfaces and edges, scaling depth >0.3 cm, and fine aggregate visible over the entire surface)

10.4.1.2. Scaling Behavior Under Continuous Soaking Tests

Santagata and Collepardi [35] investigated the effect of CMA deicer on limestone Portland and slag-based cement concrete and paste. The decay process started after 3 months of continuous soaking exposure. Overall, limestone-based cement composition revealed high scaling deterioration but the usage of laboratory-made CMA reduced the degradation process by half due to lack of impurities. The slag-based cement lowered the leaching of calcium hydroxide of cement.

10.4.1.3. Scaling Behavior Under W-D Tests

The effects of W-D exposure cycles of deicing solutions on the scaling damage of cement mortar and concrete specimens in terms of scaling ratings are presented in Figure 10.7. Figure 10.7 depicts the same overall trend of scaling damage in cement-based materials as that observed in the case of F-T tests (see Figure 10.6). However, the extent of scaling damage in the case of W-D tests is relatively less as compared to F-T tests which can be attributed to the lack of subzero temperatures during W-D tests. As observed in Figure 10.7, at a high number of W-D cycles, NaCl deicing solution resulted in slight to moderate scaling in concrete [55]. Wang et al. [5] study concluded that in the case of CaCl₂ the use of corrosion inhibitors reduced the scaling rate by half. Similarly, the investigations conducted by Drawin et al. [55] revealed that reducing

the concentration of CaCl_2 significantly reduced the scaling. In addition, the inclusion of fly ash decreases the permeability and thereby reduces the scaling deterioration [68]. Likewise, MgCl_2 also showed the same trend wherein low concentration and partial addition of fly ash significantly eradicated the trend of scaling. The use of CMA is observed to be detrimental both at low and high concentrations [49]. In contrast, the utilization of potassium acetate resulted in a slight or slight to moderate amount of scaling whereas agriculture-based acetate had constant scaling due to the presence of micropores [5]. Similarly, polyol-based deicing solution showed minute to moderate scaling and behave more similar to the NaCl solution effect. It is observed that the polyol hydrates and cement hydrates are chemically inert that do not cause the formation of any new product. This also avoids any leaching of calcium. Polyol-based deicing solutions mainly have 1% of sorbitol, maltitol, or mannitol in the 23% NaCl brine solution [77]. The potassium acetate expands lesser during the alkali-silica reaction due to the small diameter of the hydration product. Secondly, the potassium was only found on the surface and no deep penetration was observed which avoided the reaction with cement hydration products [5, 78].

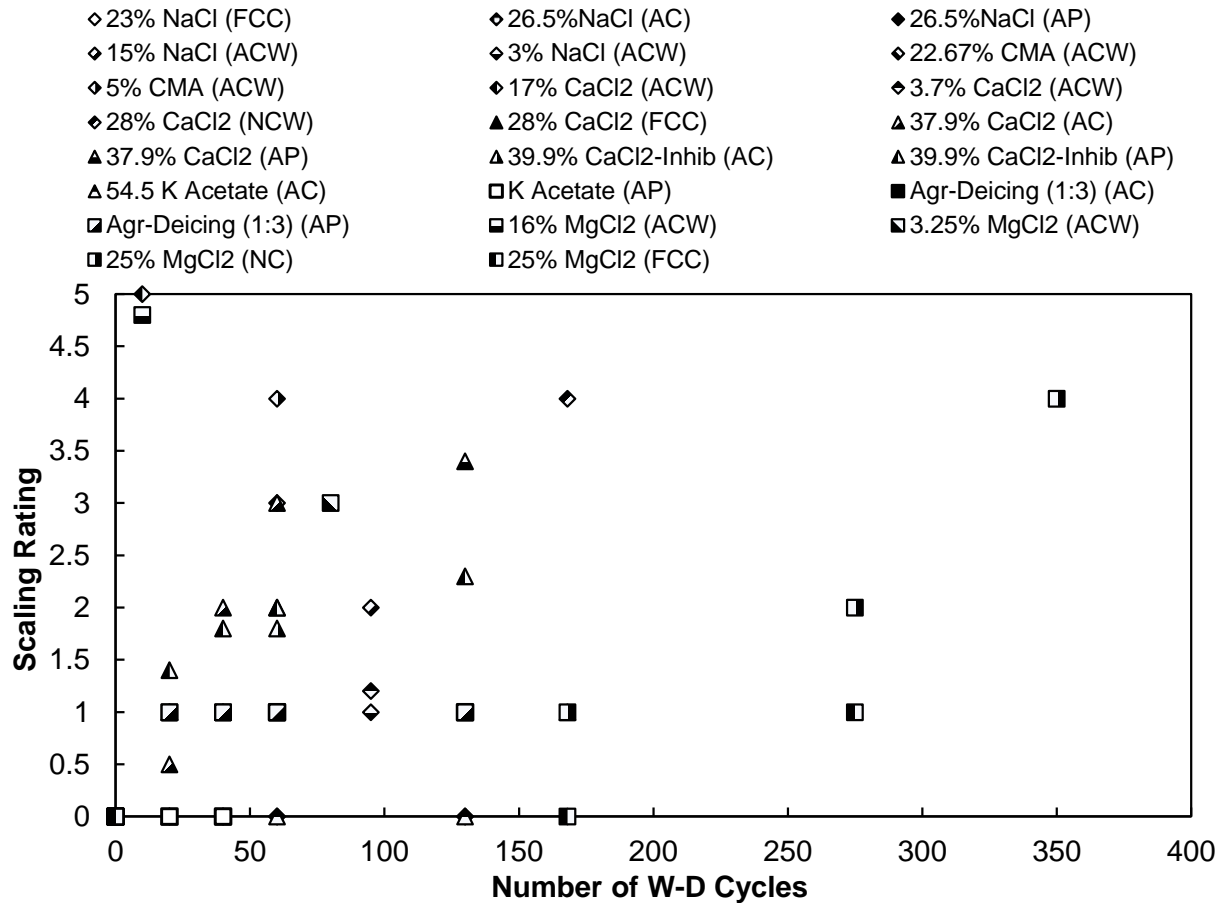


Figure 10.7. The variation of scaling rating with the number of W-D cycles for different studies.

The frost resistance of concrete also depends on the degree of saturation. If the moisture content exceeds the critical degree of saturation, the durability of the concrete is considerably reduced due to the high hydraulic pressure. A saturation level of 85% is regarded as a critical level of saturation. The deicing agent affects the saturation of the concrete or mortar sample. The deicing solution with 10% NaCl can increase the moisture retention level of a sample by 19% [79]. Similarly, air pores are designed to release the pressure developed by freezing the pore solution, but these pores can contain salts like MgCl₂ and CaCl₂ that attract moisture. These salts maintain moisture over time and increase the saturation level of the sample until the critical saturation level is reached [80]. Specimens are very prone to scaling at critical degree of saturation. In addition, salt deicing solutions reduce the absorption rate and thus the overall

absorption. Likewise, the release of water from samples soaked in saline solution is also very slow, which also leads to a high level of water retainment or a high degree of saturation.

Increasing the salt concentration decreases absorption and increases moisture retention.

According to a research study, a low concentration of NaCl solution behaves similarly to simple water submerge, while the effects of chlorides of calcium and magnesium are considerable.

MgCl₂ behaves worse among commercially available salt deicing agents [81].

10.4.1.4. Scaling Summary from Literature

From the existing studies, it can be seen that deicer-induced scaling in concrete is dependent on several parameters that include cement type, aggregate types, w/c ratio, type and concentration of a deicing chemical, presence of admixtures, and exposure conditions.

Considering all these parameters, a review of the existing literature suggests that all conventional chloride-based deicers (NaCl, CaCl₂, and MgCl₂) inflicted scaling damage in concrete mainly due to decalcification of cement paste and as well as osmotic and hydraulic pressure created by the formation of expansive oxychloride products and crystallization of these salts. A comparative review suggested that MgCl₂ and CaCl₂ caused significantly higher scaling damage as compared to NaCl. Chemical and morphological investigations (e.g., SEM and XRD) conducted in various research studies confirmed the formation of several new products in concrete specimens that are exposed to these deicing chemicals. The formation of calcium oxychloride in the case of CaCl₂ and the formation of brucite and M-S-H in the case of MgCl₂ are observed to contribute to scaling damage, deterioration, and loss of strength in concrete. Other deicers like CMA, Ca-acetate, Mg-acetate, etc. showed moderate scaling damage in concrete. Also, as far as the exposure mechanisms are concerned, the samples exposed to F-T exposure showed more deteriorations as compared to W-D or continuous soaking exposure which is primarily attributed

to the frost action in the case of F-T exposure. Air-entraining agents were used by several researchers to investigate the improvement of the scaling resistance of concrete and a positive impact on scaling resistance was observed. Thus it is recommended to use an air-entraining agent in the concrete mix. In some studies, corrosion inhibitors were used. The results showed the deicers to have a better performance in presence of certain corrosion inhibitors. But there is a lack of studies in this regard to reach a definite conclusion.

10.4.2. Compressive Strength

Compressive strength is an important indicator of the deterioration of concrete. When exposed to deicers, concrete shows a noticeable change in compressive strength. The change in compressive strength depends on several factors like deicer type, deicer exposure method, cycle time, w/c ratio, etc. Several researchers used compressive strength as the primary indicator of deicer-induced deterioration in concrete. In one of the earlier studies, Peterson [49] investigated the effect of CMA solutions with different Ca/Mg ratios and w/c ratios on the properties of concrete and adopted 22 months of continuous soaking of samples in the deicing solutions. The reduction in the compressive strength was observed to be higher in the case of CMA as compared to NaCl. Peterson [49] found that the compressive strength of concrete decreases with the increase in the concentrations of deicing solutions. When considering the Ca/Mg ratios during these experiments, Peterson [49] did not find any significant difference in the samples immersed in CMA solutions in similar conditions. Peterson [49] also measured flexural strength for the samples with different immersion parameters, w/c ratios, and Ca/Mg ratios. The results followed the same pattern as the results in compressive strength. In a later study, Santagata et al. [35] used both laboratory-made CMA and commercially bought CMA with the same Ca/Mg in their experiments. For comparison, they also immersed the samples in water. All the samples

immersed in water showed an increase in compressive strength during the 8-month study period. Samples immersed in CMA solutions showed an increase in compressive strength in the first 2-3 months period, no change for in the next 2-3 months, and a rapid deterioration in the subsequent months. The authors also observed a higher deterioration in the compressive strength corresponding to commercial-CMA deicer when compared to the laboratory-made CMA.

Santagata et al. [35] used two different concrete mixes (OPC Type II with limestone and OPC type III with slag) in their experiments. Wang et al. [5] conducted both W-D and F-T tests on cement paste and concrete samples and observed an increase in the compressive strength for the first 20-40 cycles which was attributed to the cement hydration. The samples immersed in distilled water and NaCl gained strength over the W-D and F-T cycles. While NaCl did not cause major deterioration in paste and concrete, the samples immersed in CaCl₂ suffered major deterioration. Strength loss was delayed when the inhibitor was used with CaCl₂. But eventually, it impacted negatively when the deterioration started. In another recent study, Shi et al. [44] compared the compressive strengths of two different concrete mixes subjected to NaCl, CaCl₂, and MgCl₂ deicers for 330-347 days. The bridge mix showed a better compressive strength compared to the pavement mix. The researchers used inhibitors to deicers to improve the corrosion resistance of the concrete, and it also resulted in a better compressive strength in the experiments. The researchers also indicated the positive role of Ca²⁺ compared to Mg²⁺, as inhibited CaCl₂ showed a better compressive strength when compared to MgCl₂. Cutler et al. [82] subjected Portland cement pervious concrete (PCPC) to F-T cycles of distilled water, NaCl, CaCl₂, and CMA solutions. All the samples exposed to different deicing solutions experienced strength loss over the time of 54 cycles. Samples exposed to CaCl₂ had the highest strength loss among the deicing solutions. Jain et al. [68] used Type I OPC and Type I OPC with 20% fly ash

concrete exposed to W-D and F-T cycles in distilled water, NaCl, MgCl₂, and CaCl₂. The researchers found that the samples subjected to CaCl₂ deicer had more negative impacts when compared to MgCl₂. Kim et al. [83] investigated the influence of waste glass sludge (WGS) on improving the F-T resistance of concrete. The concrete samples with WGS showed better compressive strength compared to the concrete with fly ash which was attributed to the high packing density and higher pozzolanic reactivity of WGS when compared to fly ash. Ning et al. [69] investigated the impact of NaCl and KAc deicers on on-field and laboratory-made concrete samples and observed a considerable reduction in the compressive strength after 15 F-T and W-D exposure cycles for both NaCl and KAc. Verian and Behnood [21] conducted W-D and F-T tests on concrete samples prepared using different percentage mixtures of Portland cement, fly ash, and slag cement. Overall, the samples immersed in CaCl₂ showed the highest strength loss (up to 19.61%) among the deicers investigated, which was attributed to the formation of calcium oxychloride. Recent studies conducted by Haselbach et al. [84] and Zheng et al. [85] noticed similar deterioration trends in normal and pervious concrete when calcium-based deicers were employed. Among all the deicers, NaCl showed less strength loss in the samples. The authors further inferred that samples prepared using dolomite aggregates showed better results compared to air-cooled blast furnace slag (ACBFS). The statistical analysis also suggested that F-T cycles resulted in higher deterioration in concrete when compared to W-D cycles.

In the subsequent subsections, the trends observed in the literature are presented in the form of normalized compressive strength for both F-T and W-D deicer exposure tests. Moreover, a summary of the most important conclusions from the literature corresponding to compressive strength is provided.

10.4.2.1. Compressive Strength Trends Under F-T Tests

The compressive strengths obtained from the literature are normalized by dividing each compressive strength with the compressive strength of control specimens to enable a comparison between different deicers (see Figure 10.8). The control specimens are exposed to simple water during F-T cycles. The horizontal straight line represents the reference line while the data points above that line had an increase in strength, and the data points below the reference line had a reduction in the compressive strength due to the deicing salts exposure. As observed in Figure 10.8, in most of the deicer F-T exposure tests, a reduction in the compressive strength of concrete occurs whereas an increase in the compressive strength is observed in some cases. For most of the deicing combinations, the compressive strength is observed to decrease by 30% when subjected to more than 50 F-T exposure cycles. However, for some deicers (for instance Salt B: 70% NaCl + 25% MgCl₂ + 5% CaCl₂), the compressive strength of air-entrained concrete decreased by more than 50%. The NaCl deicing solutions reduce the compressive strength of concrete by 8% unless the modification in the concrete mix ingredients is adopted. Moreover, the addition of an air-entrainment agent limits the compressive strength reduction to only 2-8% [5, 20, 69]. In contrast, the inclusion of fly ash and air-cooled blast furnace slag (ACBFS) increased the strength up to 7% [5, 20, 21, 82] even at 310 F-T cycles. The fly ash and ACBFS reduce porosity that decreases the penetration of chloride ions and hence ensures the completion of hydration processes to gain strength. In the case of calcium chloride, the reduction is more significant, especially at higher F-T cycles. This decline may go up to 73% [5, 21] which is mainly attributed to the formation of expansive calcium oxychloride [86]. Similarly, the reaction of calcium chloride with elements involved in the hydration process of cement results in calcium hydroxide and monosulfate that raise the porosity near the surface and thus reduces the concrete

durability [15, 21]. This detrimental effect can be resolved by the addition of air-entraining agents, fly ash, and slag. Similarly, the addition of corrosion inhibitors and latex modified fiber reinforced concrete initially increase the strength by up to 18% but decreased the strength at later stages [21, 82]. The decreasing trend in the concrete compressive strength when immersed in CaCl_2 and CaCl_2 -inhibitor can be associated with their scaling damage. In the case of samples immersed in K-acetate and agricultural-based deicing agents, the slight scaling does not interpret the change in strength, since the mild scaling is due to the formation of micropores [5]. On average, magnesium chloride performed better but showed no enhancement even upon the addition of air-entraining agents, slag, and fly ash. Potassium acetate initially exhibited a 17% decrease in compressive strength in the presence of air-entraining agent and low concentration but eventually resulted in up to 30% reduction in compressive strength in continuous F-T cycles [69]. The SEM images revealed the formation of rod-shaped precipitate crystals that caused the expansion in concrete that led to an increase in permeability and reduction in compressive strength [69]. The limited results that are available for agricultural deicing products exhibited better compressive strength results even at higher F-T cycles, in some cases.

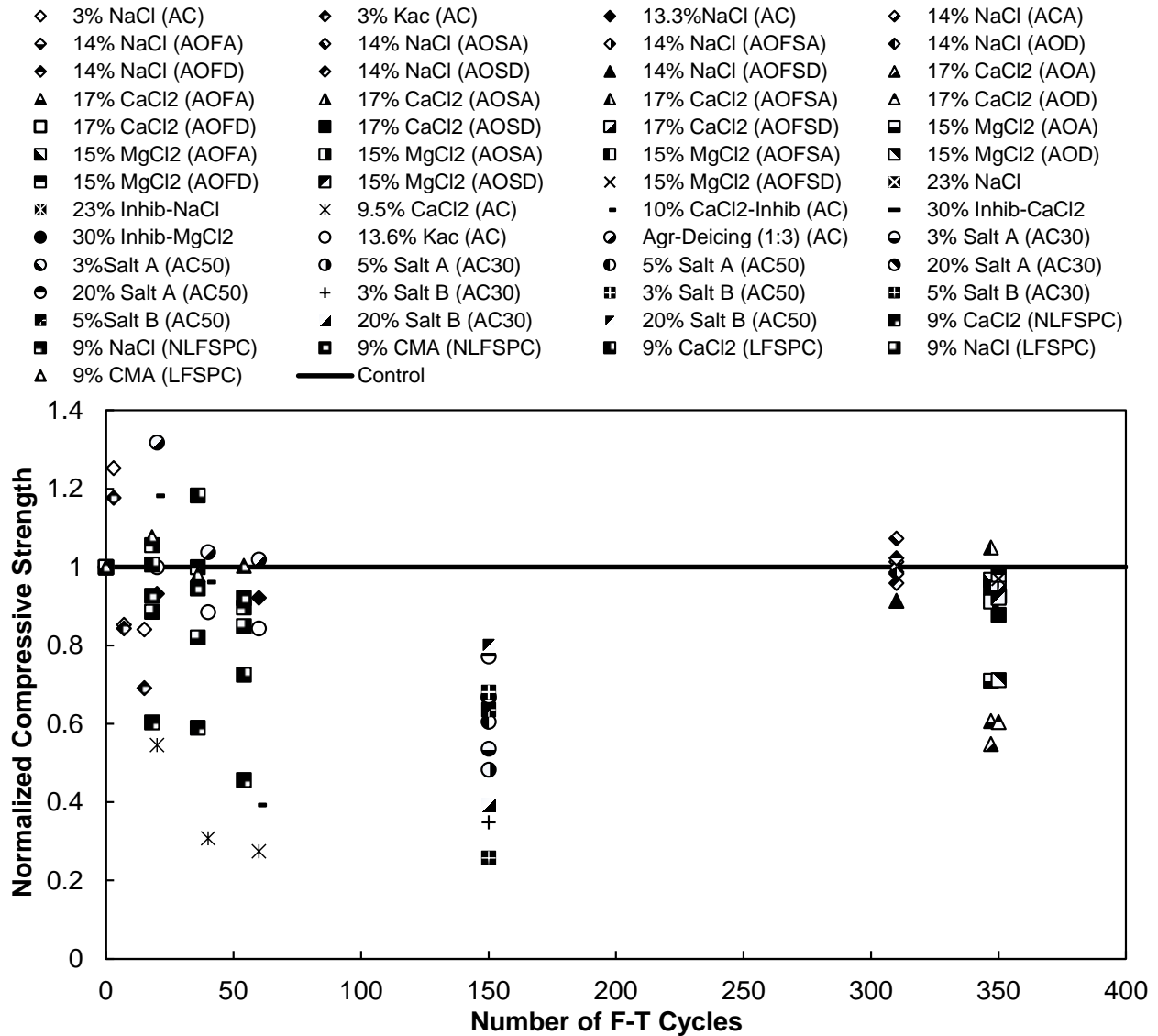


Figure 10.8. Change in concrete compressive strength under F-T cycles in deicing solution.

10.4.2.2. Compressive Strength Trends Under W-D Tests

Figure 10.9 illustrates the compressive strength trends observed in concrete when subjected to W-D cycles of different deicing chemicals. When compared to F-T exposure, relatively less variation in concrete compressive strength is observed in the case of W-D exposure cycles. Still, the majority of the deicing solutions are observed to decrease the compressive strength of concrete. Initially, NaCl showed no influence and even resulted in an improvement of up to 20% in compressive strength due to continuity of hydration process ([5],

[20], [68]). The comparative penetration of chloride ions is observed to be less in the case of NaCl [18]. However, the formation of chloroaluminate [21] and small precipitates of halite causes a reduction in the mechanical strength of concrete. The addition of fly ash as a partial replacement of cement marginally increased the compressive strength [68]. In contrast, the introduction of dolomite aggregate resulted in up to 21% higher compressive strength in the presence of fly ash and slag, respectively. The reduction in compressive strength is observed to be more pronounced in the case of calcium chloride [5]. Initially, the strength reduction is minute but after two months of W-D cycles, the compressive strength decreased dramatically by up to 45%. It was found that CaCl_2 solution reacts with constituents of concrete to produce calcium aluminum chloride sulfate hydrate (Ca-Al-Cl-S hydrate). In addition, leaching of CH and ettringite exacerbate the deterioration process. The use of corrosion inhibitors in calcium chloride deicing solution stabilizes the strength reduction during early W-D exposure cycles. The partial replacement of cement by fly ash or slag imparted better results. Similarly, magnesium chloride showed more stabilized behavior with simple improvement in concrete permeability, which results in substantial enhancement in compressive strength. In some cases, the addition of fly ash and slag increased strength by 3% and 14%, respectively [20]. Some of the researchers tried the saturated limewater that was found to be efficient only with fly ash concrete [68]. The potassium acetate exposure to concrete with air entrainment results in a minor reduction in compressive strength (5%) after 2 months of W-D cycles. Unlike chloride-based deicing solution, the potassium acetate has CH and no ettringite, but the economic factor hinders its application [5]. The agriculture-based deicing solutions lead to a relatively lower reduction in compressive strength which can be possibly attributed to limited penetration and absence of cement leaching [5]. The addition of 1% of polyol in NaCl solution as a deicing agent showed

better performance as compared to simple NaCl solution. Even after 90 W-D cycles samplers submerged in polyol-based deicing solution regain their strength. This may be because agriculture-based deicing blocks the pores that resist the penetration of chloride ions [77].

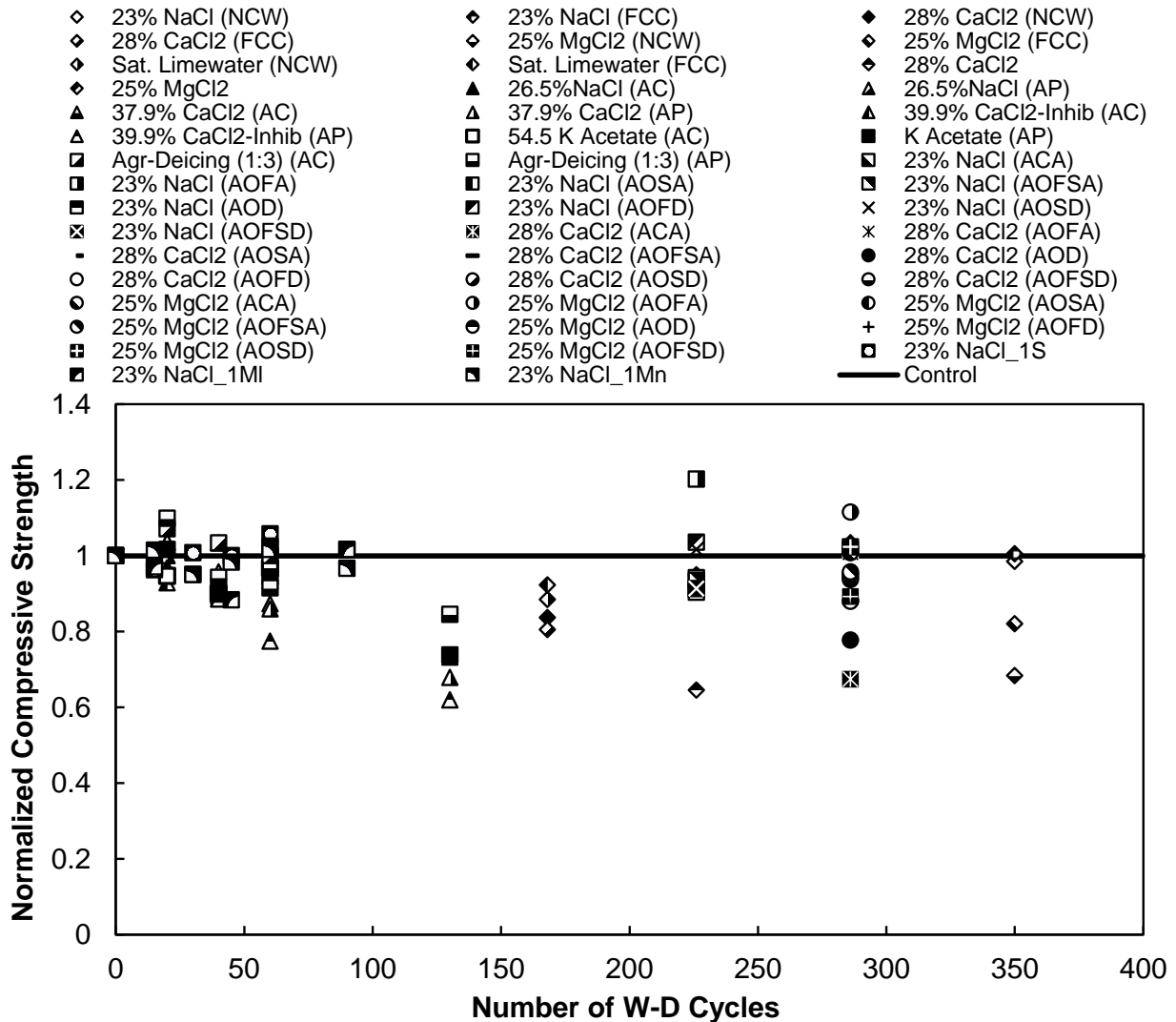


Figure 10.9. Concrete compressive strength trends observed under W-D cycles in deicing solution.

10.4.2.3. Compressive Strength Summary from Literature

Based on the existing research, it can be inferred that in most of the cases, concrete gained compressive strength during early exposure periods irrespective of deicers and concrete mix used, due to cement hydration. However, the compressive strength is observed to decrease at

higher W-D cycles. Among chloride-based deicers, NaCl showed a relatively lower reduction in compressive strength, whereas CaCl₂ and MgCl₂ lead to major deterioration in concrete compressive strength during W-D and F-T exposure cycles. Many of the studies indicated that CaCl₂ had the most detrimental effects on concrete, mainly due to the formation of calcium oxychloride. MgCl₂ also has some detrimental effects on concrete due to the formation of brucite and M-S-H.

10.4.3. Mass Change

Mass change is another sign of concrete deterioration, and many researchers used it as an indicator of deicer-induced concrete deterioration in their investigations. Peterson [49] in his experiments investigated the mass loss effect on concrete samples exposed to CMA solutions and observed that samples with higher w/c had more mass loss than the samples with lower w/c. It was further noticed that samples exposed to 20°C had more mass loss than the samples exposed to 5°C. Santagata et al. [35] found a similar pattern in the mass loss data as that observed in the case of compressive strength. The samples immersed in CMA solutions had mass gain for the first 3 months, which was followed by a significant mass loss. Wang et al. [5] observed that samples immersed in NaCl and water solution gained mass during the W-D period. For other deicers like CaCl₂, K-acetate, they found mass gain over the period which was attributed to the hydration of cement. Since a 7-day curing time was adopted, the cement hydration continued when the samples were immersed in deicer solutions, and it continued until the saturation period. The authors also assumed that the salt precipitation might be responsible for the mass gain on those samples whereas mass loss was attributed to the peeling of materials from the surface and increased surface area due to the formation of cracks. Contrary to previous studies, a significant amount of mass loss was found for NaCl in the study conducted by Shi et

al. [44]. Along with NaCl, K-acetate, Na-acetate also caused a significant amount of mass loss in concrete samples (up to 6%). The authors suggested that these deicing agents changed the chemical composition of the pore solution and created stress in the concrete. Also, Na⁺ and K⁺ cations increased the saltiness of the pore solution and increased the solubility of the cement hydrates. Moreover, only little mass gain/loss was observed in the case of CMA and MgCl₂. Cutler et al. [82] also found mass loss in the samples exposed to deicing solutions. The samples exposed to CaCl₂ experienced the highest mass loss while samples exposed to CMA had the least mass loss. Jain et al. [68] found mass gain in the samples exposed to W-D and F-T cycles immersed in NaCl and MgCl₂. The authors assumed that the mass gain was attributed to the concretion (compaction) of microstructure as well as water absorption in the microcracks. For CaCl₂, Type I samples had a mass loss, but cement mixed with fly ash gained mass during the W-D and F-T cycles. Ning et al. [69] found significant mass loss in the samples exposed to NaCl and KAc deicers compared to water. For NaCl exposure, the samples exhibited up to 6% loss in mass.

In the subsequent subsections, the mass change trends observed in the literature for both F-T and W-D deicer exposure tests are presented. Moreover, a summary of the most important conclusions from the literature corresponding to mass change is provided.

10.4.3.1. Mass Change Trends Under F-T Tests

Figure 10.10 illustrates the mass change trends observed in concrete after exposure to F-T cycles in deicing solution. Initially, most of the data points lie near to the original mass but later on mostly drops due to the involvement of the scaling that causes the surface particles to break away and thereby induces a reduction in mass. As observed in Figure 10.10, for most of the deicing solutions, the mass loss/gain is around 2%. However, in some cases (for instance Salt A:

80% NaCl + 20% CaCl₂ and Salt B: 70% NaCl + 25% MgCl₂ + 5% CaCl₂), the increase in mass can be as high as 15%. When concrete specimens are subjected to CaCl₂ deicing solution F-T cycles, up to a 5% decrease in the mass can occur which is mainly attributed to scaling [5]. However, the inclusion of fly ash in concrete is observed to lead to mass gain because the deterioration is restricted to micro-level cracks that invite the water to penetrate [68]. No significant mass loss is noticed in the case of concrete samples that are subjected to MgCl₂ which is linked with the restriction of deicer ingress once a permeable layer of brucite (Mg(OH)₂) is formed [17]. Similarly, potassium acetate solution is observed to increase the mass because of mass gain due to water absorption and the creation of crystals [5]. In contrast, some studies found dilute potassium acetate may cause a small reduction in mass due to surface scaling [69]. Wu et al. [76] tried to investigate the combination of commonly used deicing chemicals at different concentrations and concretes of two different strengths. The combination of sodium chloride and calcium chloride showed a high level of mass loss at low concentration and a high number of F-T cycles, besides lowering the compressive strength of concrete (see Salt-A in Figure 10.10 and Figure 10.8). A similar trend was also observed when chlorides of sodium, magnesium, and calcium were mixed (Salt B). The severity was comparably low due to the involvement of magnesium chloride. The dilute salt solution may partially freeze at very low temperature therefore glue-spall theory involves and large thermal expansion coefficients difference between ice and concrete leads to tensile pressure and subsequent scaling [7]. Similarly, high-strength concrete exhibited high resistance to the pressure created by crystals of salt and Friedel's salt [87].

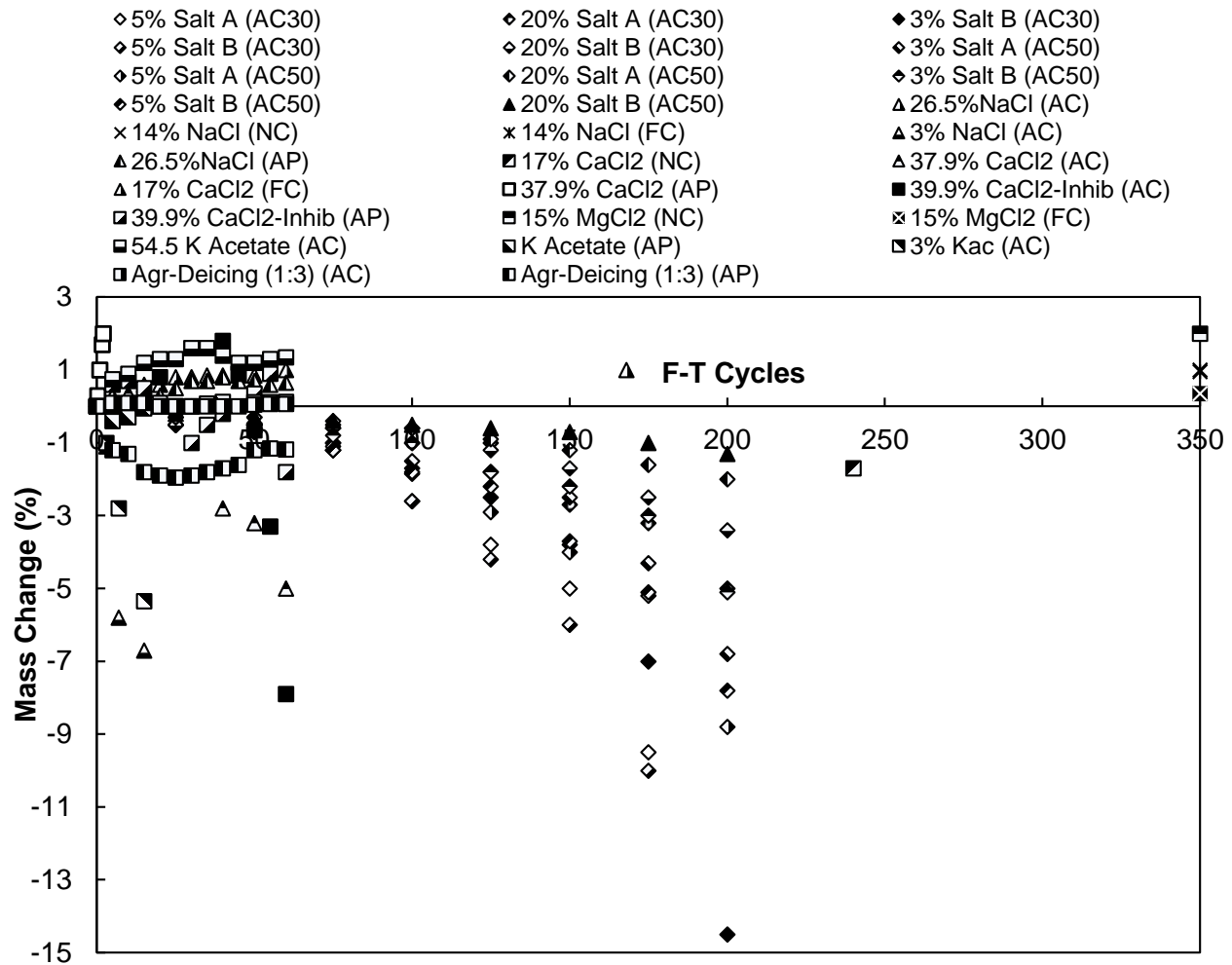


Figure 10.10. Mass variation with the increase in F-T cycles.

10.4.3.2. Compressive Strength Trends Under W-D Tests

Figure 10.11 summarizes the effect of the deicing solution on mass change in concrete under W-D cycles on concrete. Unlike F-T exposure cycles, limited studies were found that select the W-D cycles to check the effect of deicing chemicals on mass changes in concrete. When normal air-entrained concrete was exposed to NaCl deicer, its mass remained approximately constant [5]. Similarly, CaCl₂ also presented the same trend. The addition of corrosion inhibitor and fly ash was also found significant to reduce the concrete mass reduction [5]. Similarly, magnesium chloride also showed no reduction in mass due to limited scaling in

W-D exposure. Finally, the agri-based deicing solution led to around a 2% mass change in concrete. The W-D of concrete in polyol-based deicing solution showed a small increase in mass after 30 cycles due to deposition of salt precipitate in micro-cracks and surface [77].

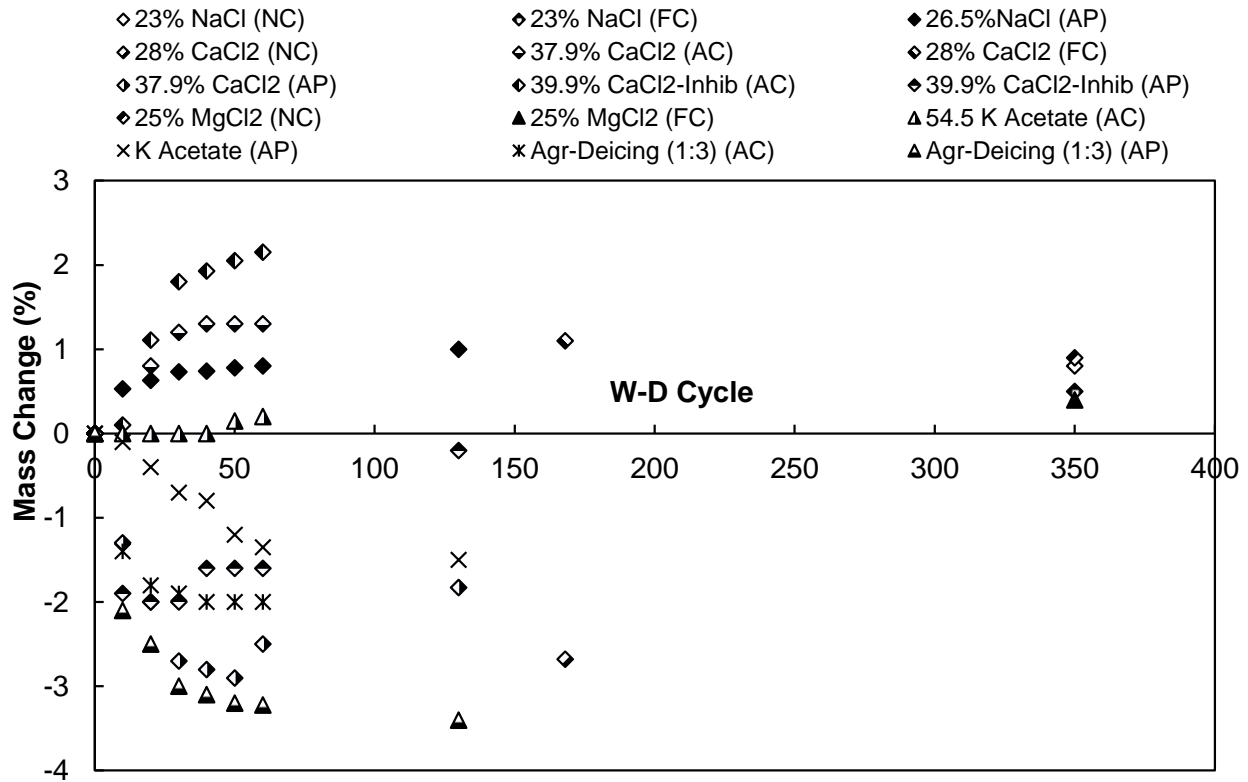


Figure 10.11. Mass variation with the increase in W-D cycles.

10.4.3.3. Mass Change Summary from Literature

From the existing studies, mixed results are observed for the mass loss. The samples exposed to NaCl had both mass loss and mass gain in several studies. This variation happened mainly because of the difference in the experimental setup and other factors. Salt crystallization and water absorption caused the samples to gain mass, while there could be other factors like solubility and sample handling that caused the mass loss. Without considering these, the samples seemed to gain mass during the immersion period. In most of the studies, the samples gained mass in the first few months for all the deicing solutions. For the deicers like CaCl₂, MgCl₂ the

samples tend to lose mass after a certain period. This mainly happens due to the scaling and peeling of materials from the samples. From the existing studies, no clear conclusion can be reached for mass loss or mass gain. But both the mass loss and mass gain could have a negative impact on the concrete.

10.5. Conclusions

The most important conclusions observed in the literature on the effect of the deicing chemicals on the properties of cement-based materials are summarized below.

1. The type and concentration of the deicing solution, the type of concrete, and the handling of the experimental procedure are among the major factors that dictate the influence of deicing chemicals on the physical and chemical properties of concrete.
2. The chemical interaction of the deicing solution with cementitious hydration products leads to different products that result in physical deterioration in the form of scaling and loss of compressive strength.
3. Chlorides of sodium, calcium, and magnesium, and acetates of magnesium and calcium and most commonly studied deicers. Similarly, continuous soaking, W-D, and F-T cycles with modification were used to study the effect of the deicing solutions on concrete. It has been found that F-T cycles are truly representative and serve as an adequate methodology for obtaining representative conclusions. Initially, concrete behaves normally under the influence of deicing solutions but later starts deterioration due to ion penetration that chemically reacts with cement hydration products.
4. Scaling is observed to be the most common indication of deterioration in concrete. Scaling occurs either due to pressure exerted by precipitates like Friedel's salt, calcium oxychloride, and ettringite in the case of chloride-based deicing solution or when the

products are expansive, creating stresses in the pores of the concrete. Similarly, the leaching of calcium ions due to the C-S-H structure and production of non-cementitious products like the M-S-H chain also contributes to structural degradation.

5. Among the commonly available deicing agents, magnesium chloride was found relatively better due to the formation of brucite ($\text{Mg}(\text{OH})_2$) at the surface of the concrete that can control the chloride ion penetration. However, the application of MgCl_2 is linked with the formation of M-S-H that results in a deterioration in concrete compressive strength.
6. The Agricultural derived deicing formulations are observed to perform better, but further investigations about their long-term performance are needed.
7. The most common remedy for mitigating the deicers-induced deterioration in concrete is to alter the microstructure and porosity of concrete which focuses on decreasing the size and volume of voids in concrete to inhibit penetration of detrimental deicing chemical ions. Researchers tried air entrainment, partial replacement of cement by a finer binding agent, and the use of different sources of aggregates. The air-entrainment and inclusion of fly ash or slag-type cement improved the freeze-thaw resistance of concrete, but the penetration of deleterious ions may still continue due to high porosity. Similarly, the ACBFS and dolomite type aggregates also enhanced the durability of concrete against the aggressive action of the deicing chemicals.

10.6. Recommendations and Future Research Directions

Based on the literature presented on physical and chemical deteriorations of concrete exposed to deicers, this section describes the major limitations of the existing literature and provides directions for future studies.

1. While the deicer-induced physical and chemical deterioration of concrete has been extensively investigated, many of the existing studies overlook the environmental concerns of the deicers. Many of the deicers which are used in practice have medium to severe environmental impacts.
2. In many cases, the deicers used by local municipal authorities have a mixture of different deicers. However, very few studies have investigated the effects of a combination of different deicing chemicals on concrete and hence further investigations are needed to understand the influence of various deicing blends on the properties of concrete.
3. Many popularly used deicers are corrosive to structural steels and rebars, and hence corrosion inhibitors are usually added to the deicer or concrete. There are only a handful of studies where the deicing chemicals included corrosion inhibitors. While many corrosion inhibitors have been investigated in the past decade for their intended performance, only a few studies have investigated the impacts of corrosion inhibitors-mixed deicers on concrete.
4. Whether it is physical, chemical, or environmental, the use of deicing chemicals for winter maintenance of concrete pavements and bridge decks has some negative impacts. Many researchers tried to find alternative methods of deicing without the use of deicing chemicals [88]. One of the methods is insulation underneath a bridge deck or highway pavements to prevent rapid heat loss leading to ice formation. Several insulation materials like plastic foam and urethane foam are used in those studies to prevent ice formation and accumulation and reduce the number of freeze-thaw cycles. However, further studies are needed in this direction to investigate the effect of differential cooling caused by insulation on the properties of concrete and their life cycle costs.

5. In the past, some studies tested pavement heating systems (e.g., electric heaters, cables with heated fluid, geothermal energy, carbon nanotubes, infrared heat lamps, etc. [89-100]) as an alternative technique of deicing. More investigations are needed to assess the efficacy of pavement heating systems in melting snow and their long-term impacts on the properties of concrete need to be investigated.
6. Conductive concrete is another alternative deicing technique wherein electrically conductive components (e.g. carbon fibers, graphite, steel shavings, etc.) are added to the concrete mix or surface concrete that result in consistent electric heating for melting ice [101-117]. However, more investigations are needed to validate the ice melting and skid resistance performance of such pavements and the impact of electrically conductive materials on the properties of fresh and hardened concrete.

10.7. References

- [1] T.C. Powers, The mechanism of frost action in concrete, in, University of Maryland, College Park, MD, 1965.
- [2] United States DOT. How do weather events impact roads?, in, United States DOT. https://ops.fhwa.dot.gov/weather/q1_roadimpact.htm. Accessed 11 November 2021, 2020.
- [3] T.C. Powers, Freezing Effects in Concrete, ACI Symposium Publication, 47 (1975).
- [4] X. Shi, M. Akin, T. Pan, L. Fay, Y. Liu, Z. Yang, Deicer impacts on pavement materials: Introduction and recent developments, *The Open Civil Engineering Journal*, 3 (2009).
- [5] K. Wang, D.E. Nelsen, W.A. Nixon, Damaging effects of deicing chemicals on concrete materials, *Cement and Concrete Composites*, 28 (2006) 173-188.

- [6] ASTM International. ASTM C672 / C672M-12, Standard Test Method for Scaling Resistance of Concrete Surfaces Exposed to Deicing Chemicals (Withdrawn 2021), in, ASTM International, West Conshohocken, PA, 2012.
- [7] J.J. Valenza, G.W. Scherer, A review of salt scaling: II. Mechanisms, Cement and Concrete Research, 37 (2007) 1022-1034.
- [8] J.M. Sayward, Salt Action on Concrete, in, Cold Regions Research and Engineering Lab Hanover NH, 1984.
- [9] M. Pigeon, J. Marchand, R. Pleau, Frost resistant concrete, Construction and Building Materials, 10 (1996) 339-348.
- [10] M.T. Hasholt, Air void structure and frost resistance: A challenge to Powers' spacing factor, Materials and structures, 47 (2014) 911-923.
- [11] ASTM International. ASTM C666/C666M Standard Test Method for Resistance of Concrete to Rapid Freezing and Thawing, in, ASTM International, West Conshohocken, PA, 2015.
- [12] C. Ftikos, G. Parissakis, The combined action of Mg^{2+} and Cl^{-} ions in cement pastes, Cement and Concrete Research, 15 (1985) 593-599.
- [13] S. Chatterji, Mechanism of the $CaCl_2$ attack on portland cement concrete, Cement and Concrete Research, 8 (1978) 461-467.
- [14] J. Monical, C. Villani, Y. Farnam, E. Unal, W. Weiss, Using low-temperature differential scanning calorimetry to quantify calcium oxychloride formation for cementitious materials in the presence of calcium chloride, Advances in Civil Engineering Materials, 5 (2016) 142-156.

- [15] L. Sutter, T. Van Dam, K.R. Peterson, D.P. Johnston, Long-term effects of magnesium chloride and other concentrated salt solutions on pavement and structural Portland cement concrete, *Transportation research record*, 1979 (2006) 60-68.
- [16] T.J. Van Dam, *Chemical Deicers and Concrete Pavement: Impacts and Mitigation:[techbrief]*, in, United States. Federal Highway Administration, 2018.
- [17] W. Kurdowski, The protective layer and decalcification of CSH in the mechanism of chloride corrosion of cement paste, *Cement and Concrete Research*, 34 (2004) 1555-1559.
- [18] G. Frigione, R. Sersale, The action of some aggressive solutions on Portland, pozzolanic and blast furnace slag cement mortars, *Cement and Concrete Research*, 19 (1989) 885-893.
- [19] R.D. Cody, A.M. Cody, P.G. Spry, G.-L. Gan, Experimental deterioration of highway concrete by chloride deicing salts, *Environmental & Engineering Geoscience*, 2 (1996) 575-588.
- [20] K.P. Verian, P. Panchmatia, J. Olek, T. Nantung, Pavement concrete with air-cooled blast furnace slag and dolomite as coarse aggregates: effects of deicers and freeze-thaw cycles, *Transportation Research Record*, 2508 (2015) 55-64.
- [21] K.P. Verian, A. Behnood, Effects of deicers on the performance of concrete pavements containing air-cooled blast furnace slag and supplementary cementitious materials, *Cement and Concrete Composites*, 90 (2018) 27-41.
- [22] W. Weiss, Y. Farnam, *Concrete Pavement Joint Deterioration: Recent Findings to Reduce the Potential for Damage*, in: *Moving Advancements into Practice (MAP) Brief, Concrete Pavement Research and Technology (CP Road Map)*, 2015.

- [23] C. Qiao, N. Hosseinzadeh, P. Suraneni, S. Wei, D. Rothstein, Petrographically quantifying the damage to field and lab-cast mortars subject to freeze-thaw cycles and deicer application, *Journal of Infrastructure Preservation and Resilience*, 2 (2021) 1-12.
- [24] J.-K. Jang, H.-G. Kim, J.-H. Kim, J.-S. Ryou, The evaluation of damage effects on MgO added concrete with slag cement exposed to calcium chloride deicing salt, *Materials*, 11 (2018) 793.
- [25] H. Lee, R.D. Cody, A.M. Cody, P.G. Spry, Effects of various deicing chemicals on pavement concrete deterioration, in: Center for Transportation Research and Education (Ed.), *Mid-Continent Transportation Symposium Proceedings*, Iowa State University, Ames, USA, Citeseer, 2000, pp. 151-155.
- [26] M. Kawamura, S. Komatsu, Behavior of various ions in pore solution in NaCl-bearing mortar with and without reactive aggregate at early ages, *Cement and concrete research*, 27 (1997) 29-36.
- [27] J. Duchesne, M.-A. Bérubé, Effect of the cement chemistry and the sample size on ASR expansion of concrete exposed to salt, *Cement and concrete research*, 33 (2003) 629-634.
- [28] E.S. Sumsion, W.S. Guthrie, Physical and chemical effects of deicers on concrete pavement: Literature review, in, Utah Department of Transportation, Salt Lake, UT, 2013.
- [29] M. Kawamura, K. Takeuchi, A. Sugiyama, Mechanisms of expansion of mortars containing reactive aggregate in NaCl solution, *Cement and concrete research*, 24 (1994) 621-632.
- [30] M. Kawamura, K. Takeuchi, Alkali-silica reaction and pore solution composition in mortars in sea water, *Cement and concrete research*, 26 (1996) 1809-1819.

- [31] C. Giebson, K. Seyfarth, J. Stark, Influence of acetate and formate-based deicers on ASR in airfield concrete pavements, *Cement and Concrete Research*, 40 (2010) 537-545.
- [32] C. Giebson, K. Seyfarth, H.-M. Ludwig, Influence of sodium chloride on ASR in highway pavement concrete, *Proceedings of the 15th ICAAR*. São Paulo, Brazil: Instituto Brasileiro do Concreto-IBRACON, (2016).
- [33] S. Chatterji, Chemistry of alkali–silica reaction and testing of aggregates, *Cement and Concrete Composites*, 27 (2005) 788-795.
- [34] S.H. Kosmatka, M.L. Wilson, A. Portland Cement, Design and control of concrete mixtures, Portland Cement Association, Skokie, Illinois, 2016.
- [35] M. Santagata, M. Collepardi, The effect of CMA deicers on concrete properties, *Cement and Concrete Research*, 30 (2000) 1389-1394.
- [36] L.C.a.C.P. M. Collepardi, Durability of Concrete Structures Exposed to CaCl₂ Based Deicing Salts, *ACI Symposium Publication*, 145.
- [37] C. Foy, M. Pigeon, N. Banthia, Freeze-thaw durability and deicer salt scaling resistance of a 0,25 water-cement ratio concrete, *Cement and Concrete Research*, 18 (1988) 604-614.
- [38] M. Fischel, Evaluation of selected deicers based on a review of the literature, Report No. CDOT-DTD-R-2001-15. Colorado Department of Transportation (CDOT) Research Division., (2001).
- [39] H.U. Sajid, R. Kiran, X. Qi, D.S. Bajwa, D. Battocchi, Employing corn derived products to reduce the corrosivity of pavement deicing materials, *Construction and Building Materials*, 263 (2020) 120662.

- [40] K. Nilssen, A. Klein-Paste, J. Wåhlin, The effect of additives on the low temperature ice-melting capacity of NaCl, *Transportation research record*, 2672 (2018) 158-166.
- [41] H.U. Sajid, D.L. Naik, R. Kiran, Improving the ice-melting capacity of traditional deicers, *Construction and Building Materials*, 271 (2021) 121527.
- [42] T. Abbas, D.N. Lavadiya, R. Kiran, Exploring the Use of Polyols, Corn, and Beet Juice for Decreasing the Freezing Point of Brine Solution for Deicing of Pavements, *Sustainability*, 13 (2021) 5765.
- [43] R. Kiran, D.L. Naik, H.U. Sajid, Corn-Based Deicers, IHRB Project TR-754. Iowa Highway Research Board, Iowa Department of Transportation, Ames, IA., (2020).
- [44] X. Shi, L. Fay, C. Gallaway, K. Volkening, M.M. Peterson, T. Pan, A. Creighton, C. Lawlor, S. Mumma, Y. Liu, Evaluation of alternative anti-icing and deicing compounds using sodium chloride and magnesium chloride as baseline deicers–Phase I, Report No. CDOT-2009-1. Colorado Department of Transportation (CDOT), (2009).
- [45] W.A. Nixon, Economics of Using Calcium Chloride vs. Sodium Chloride for Deicing/Anti-Icing, in, Project Report No. TR-488, Iowa Highway Research Board, Iowa Department of Transportation, Iowa City, IA, 2008.
- [46] X. Shi, L. Fay, C. Gallaway, K. Volkening, M.M. Peterson, T. Pan, A. Creighton, C. Lawlor, S. Mumma, Y. Liu, T.A. Nguyen, Evaluation of alternate anti-icing and deicing compounds using sodium chloride and magnesium chloride as baseline deicers, Report No. CDOT-2009-01. Colorado Department of Transportation. Denver, CO, (2009).
- [47] L. Fay, X. Shi, Environmental impacts of chemicals for snow and ice control: state of the knowledge, *Water, Air, & Soil Pollution*, 223 (2012) 2751-2770.

- [48] R.D. Cody, P.G. Spry, A.M. Cody, G.-L. Gan, The role of magnesium in concrete deterioration, Report No. HR-355. Iowa Highway Research Board. Iowa Department of Transportation, (1994).
- [49] O. Peterson, Chemical effects on cement mortar of calcium magnesium acetate as a deicing salt, *Cement and concrete research*, 25 (1995) 617-626.
- [50] Western Transportation Institute, Field Usage of Alternative Deicers for Snow and Ice Control, Report No. TRS 1706. Local Road Research Board. Minnesota Department of Transportation., (2017).
- [51] ASTM International. ASTM C1260 Standard Test Method for Potential Alkali Reactivity of Aggregates (Mortar-Bar Method), in, ASTM International, West Conshohocken, PA, 2021.
- [52] X. Shi, L. Fay, M.M. Peterson, M. Berry, M. Mooney, A FESEM/EDX investigation into how continuous deicer exposure affects the chemistry of Portland cement concrete, *Construction and building materials*, 25 (2011) 957-966.
- [53] S. Sajid, L. Chouinard, Impulse response test for condition assessment of concrete: A review, *Construction and Building Materials*, 211 (2019) 317-328.
- [54] S. Sajid, L. Chouinard, N. Carino, Robustness of Resonant Frequency Test for Strength Estimation of Concrete, *Advances in Civil Engineering Materials*, 8 (2019) 451-462.
- [55] D. Darwin, J. Browning, L. Gong, S.R. Hughes, Effects of Deicers on Concrete Deterioration, *ACI Materials Journal*, 105.
- [56] R. Gagne, M. Pigeon, P. Aitcin, Deicer salt scaling resistance of high strength concretes made with different cements, *Special Publication*, 126 (1991) 185-200.

- [57] H. Eguez Alava, N. De Belie, G. De Schutter, Proposed mechanism for the formation of oxychloride crystals during sodium chloride application as a deicer salt in carbonated concrete, *Construction and Building materials*, 109 (2016) 188-197.
- [58] P. Reiterman, M. Keppert, Effect of various de-icers containing chloride ions on scaling resistance and chloride penetration depth of highway concrete, *Roads and Bridges-Drogii Mosty*, 19 (2020) 51-64.
- [59] L. Berntsson, S. Chandra, Damage of concrete sleepers by calcium chloride, *Cement and Concrete Research*, 12 (1982) 87-92.
- [60] R. Gagne, M. Pigeon, Deicer salt scaling resistance of high-performance concrete, *Special Publication*, 122 (1990) 29-44.
- [61] J.-W. Jang, M.G. Hagen, G.M. Engstrom, I. Iwasaki, Cl⁻, SO₄²⁻, and PO₄³⁻ distribution in concrete slabs ponded by corrosion-inhibitor-added deicing salts, *Advanced Cement Based Materials*, 8 (1998) 101-107.
- [62] Y. Hassan, A. Abd El Halim, A. Razaqpur, W. Bekheet, M. Farha, Effects of runway deicers on pavement materials and mixes: comparison with road salt, *Journal of transportation engineering*, 128 (2002) 385-391.
- [63] M. Bérubé, J. Dorion, J. Duchesne, B. Fournier, D. Vézina, Laboratory and field investigations of the influence of sodium chloride on alkali-silica reactivity, *Cement and Concrete Research*, 33 (2003) 77-84.
- [64] P.R. Rangaraju, K.R. Sompura, J. Olek, Investigation into Potential of Alkali-Acetate-Based Deicers to Cause Alkali-Silica Reaction in Concrete, *Transportation research record*, 1979 (2006) 69-78.

- [65] G. Skripkiūnas, D. Nagrockienė, G. Girskas, M. Vaičienė, E. Barauskaitė, The cement type effect on freeze–thaw and deicing salt resistance of concrete, *Procedia engineering*, 57 (2013) 1045-1051.
- [66] A. Poursaei, A. Laurent, C. Hansson, Corrosion of steel bars in OPC mortar exposed to NaCl, MgCl₂ and CaCl₂: Macro-and micro-cell corrosion perspective, *Cement and Concrete Research*, 40 (2010) 426-430.
- [67] X. Shi, Y. Liu, M. Mooney, M. Berry, B. Hubbard, L. Fay, A.B. Leonard, Effect of chloride-based deicers on reinforced concrete structures, Report No. WA-RD 741.1. Washington State Department of Transportation (WSDOT), (2010).
- [68] J. Jain, J. Olek, A. Janusz, D. Jozwiak-Niedzwiedzka, Effects of deicing salt solutions on physical properties of pavement concretes, *Transportation research record*, 2290 (2012) 69-75.
- [69] N. Xie, X. Shi, Y. Zhang, Impacts of Potassium Acetate and Sodium-Chloride Deicers on Concrete, *Journal of Materials in Civil Engineering*, 29 (2017) 04016229.
- [70] B.D. Lee, Y.S. Choi, Y.G. Kim, I.S. Kim, E.I. Yang, A comparison study of performance and environmental impacts of chloride-based deicers and eco-label certified deicers in South Korea, *Cold Regions Science and Technology*, 143 (2017) 43-51.
- [71] F. Matalkah, P. Soroushian, Freeze thaw and deicer salt scaling resistance of concrete prepared with alkali aluminosilicate cement, *Construction and Building Materials*, 163 (2018) 200-213.
- [72] R. Şahin, M.A. Taşdemir, R. Gül, C. Çelik, Determination of the optimum conditions for de-icing salt scaling resistance of concrete by visual examination and surface scaling, *Construction and Building Materials*, 24 (2010) 353-360.

- [73] J.J. Valenza, G.W. Scherer, Mechanism for salt scaling of a cementitious surface, *Materials and structures*, 40 (2007) 259-268.
- [74] V. Alatyppö, J. Valtonen, Experiences on the effects of de-icing chemicals on bituminous airfield runways in Finland, in: 2007 Worldwide Airport Technology Transfer Conference Federal Aviation Administration American Association of Airport Executives, 2007.
- [75] J.L. Provis, J.S.J. Van Deventer, *Geopolymers: structures, processing, properties and industrial applications*, Elsevier, 2009.
- [76] Z. Wu, C. Shi, P. Gao, D. Wang, Z. Cao, Effects of deicing salts on the scaling resistance of concrete, *Journal of Materials in Civil Engineering*, 27 (2015) 04014160.
- [77] H.U. Sajid, R. Kiran, D.S. Bajwa, Effect of agro-derived corrosion inhibitors on the properties of Portland cement mortar, *Construction and Building Materials*, 310 (2021) 125236.
- [78] K. Shomglin, L. Turanli, H.-R. Wenk, P. Monteiro, G. Sposito, The effects of potassium and rubidium hydroxide on the alkali–silica reaction, *Cement and concrete research*, 33 (2003) 1825-1830.
- [79] C. MacInnis, J.D. Whiting, The frost resistance of concrete subjected to a deicing agent, *Cement and Concrete Research*, 9 (1979) 325-336.
- [80] L. Sutter, *Deicing Salts and Concrete Pavements, Moving Advancements into Practice (MAP) Brief August 2014*, (2014).
- [81] R.P. Spragg, J. Castro, W. Li, M. Pour-Ghaz, P.-T. Huang, J. Weiss, Wetting and drying of concrete using aqueous solutions containing deicing salts, *Cement and Concrete Composites*, 33 (2011) 535-542.

- [82] H.E. Cutler, K. Wang, V.R. Schaefer, J.T. Kevern, Resistance of Portland cement pervious concrete to deicing chemicals, *Transportation research record*, 2164 (2010) 98-104.
- [83] J. Kim, J.-H. Moon, J.W. Shim, J. Sim, H.-G. Lee, G. Zi, Durability properties of a concrete with waste glass sludge exposed to freeze-and-thaw condition and de-icing salt, *Construction and building materials*, 66 (2014) 398-402.
- [84] L. Haselbach, N. Almeida, M. Ross, Pervious Concrete Chemical Degradation by Calcium Chloride Deicer, *Journal of Cold Regions Engineering*, 35 (2021) 04020029.
- [85] K. Zheng, H. Liu, L. Feng, N. Xie, Effects of Calcium-Based Deicing Chemicals on the Durability of Concrete Products, *Journal of Materials in Civil Engineering*, 33 (2021) 04021321.
- [86] Y. Farnam, H. Todak, R. Spragg, J. Weiss, Electrical response of mortar with different degrees of saturation and deicing salt solutions during freezing and thawing, *Cement and Concrete Composites*, 59 (2015) 49-59.
- [87] S. Goni, A. Guerrero, Accelerated carbonation of Friedel's salt in calcium aluminate cement paste, *Cement and Concrete Research*, 33 (2003) 21-26.
- [88] L.G. Terry, K. Conaway, J. Rebar, A.J. Graettinger, Alternative Deicers for Winter Road Maintenance—A Review, *Water, Air, & Soil Pollution*, 231 (2020) 1-29.
- [89] J. Lai, J. Qiu, J. Chen, H. Fan, K. Wang, New technology and experimental study on snow-melting heated pavement system in tunnel portal, *Advances in Materials Science and Engineering*, 2015 (2015).

- [90] A.G. Mohammed, G. Ozgur, E. Sevkat, Electrical resistance heating for deicing and snow melting applications: Experimental study, *Cold Regions Science and Technology*, 160 (2019) 128-138.
- [91] R.C. Lee, J.T. Sackos, J.E. Nydahl, K.M. Pell, Bridge heating using ground-source heat pipes.
- [92] M. Cress, Heated bridge deck construction and operation in Lincoln, Nebraska, in: *IABSE Symposium*, 1995, pp. 449-454.
- [93] J.A. Zenewitz, Survey of alternatives to the use of chlorides for highway deicing, in, 1977.
- [94] S.A.-A. Yehia, Conductive concrete overlay for bridge deck deicing, *The University of Nebraska-Lincoln*, 1999.
- [95] S. Baumgärtel, J.A. Schweighofer, J. Rohn, J. Luo, The performance of geothermal passive heating and cooling for asphalt and concrete pavement, *Developments in the Built Environment*, (2021) 100051.
- [96] H.S. Kim, H. Ban, W.-J. Park, Deicing Concrete Pavements and Roads with Carbon Nanotubes (CNTs) as Heating Elements, *Materials*, 13 (2020) 2504.
- [97] G. Lei, X. Yu, T. Li, O. Habibzadeh-Bigdarvish, X. Wang, M. Mrinal, C. Luo, Feasibility study of a new attached multi-loop CO₂ heat pipe for bridge deck de-icing using geothermal energy, *Journal of Cleaner Production*, 275 (2020) 123160.
- [98] T. Li, X. Yu, O. Habibzadeh-Bigdarvish, G. Lei, A.J. Puppala, Heating performance of a novel externally-heated geothermal bridge de-icing system: field tests and numerical simulations, *Sustainable Energy Technologies and Assessments*, 46 (2021) 101280.

- [99] H. Liu, P. Maghoul, A. Bahari, M. Kavgic, Feasibility study of snow melting system for bridge decks using geothermal energy piles integrated with heat pump in Canada, *Renewable Energy*, 136 (2019) 1266-1280.
- [100] S. Baumgärtel, J. Rohn, J. Luo, Experimental study of road deicing by using the urban groundwater under the climatic condition of Nuremberg city, Germany, *SN Applied Sciences*, 2 (2020) 1-13.
- [101] A. Sassani, A. Arabzadeh, H. Ceylan, S. Kim, S.S. Sadati, K. Gopalakrishnan, P.C. Taylor, H. Abdulla, Carbon fiber-based electrically conductive concrete for salt-free deicing of pavements, *Journal of cleaner production*, 203 (2018) 799-809.
- [102] S.A. Yehia, C.Y. Tuan, Thin conductive concrete overlay for bridge deck deicing and anti-icing, *Transportation Research Record*, 1698 (2000) 45-53.
- [103] P. Maleki, B. Iranpour, G. Shafabakhsh, Investigation of de-icing of roads with conductive concrete pavement containing carbon fibre-reinforced polymer (CFRP), *International Journal of Pavement Engineering*, 20 (2019) 682-690.
- [104] H. Abdulla, H. Ceylan, S. Kim, K. Gopalakrishnan, P.C. Taylor, Y. Turkan, System requirements for electrically conductive concrete heated pavements, *Transportation Research Record*, 2569 (2016) 70-79.
- [105] A. Malakooti, W.S. Theh, S.S. Sadati, H. Ceylan, S. Kim, M. Mina, K. Cetin, P.C. Taylor, Design and full-scale implementation of the largest operational electrically conductive concrete heated pavement system, *Construction and Building Materials*, 255 (2020) 119229.
- [106] C.Y. Tuan, S. Yehia, Evaluation of electrically conductive concrete containing carbon products for deicing, *Materials Journal*, 101 (2004) 287-293.

- [107] A. Arabzadeh, A. Sassani, H. Ceylan, S. Kim, K. Gopalakrishnan, P.C. Taylor, Comparison between cement paste and asphalt mastic modified by carbonaceous materials: Electrical and thermal properties, *Construction and Building Materials*, 213 (2019) 121-130.
- [108] Z. Yan, W. Liu, J. Chen, D. Jin, Pavement conductive wearing surface with graphite heating film de-icing potential and performance experimental study, *International Journal of Pavement Research and Technology*, 14 (2021) 688-696.
- [109] W. Zhao, X. Chen, Y. Zhang, W. Su, F. Xu, B. Li, Deicing performances of a road unit driven by a hydronic heating system in severely cold regions of China, *Computers & Mathematics with Applications*, (2019).
- [110] A. Shishegaran, M.A. Naghsh, H. Taghavizade, M.H. Afsharmovahed, A. Shishegaran, M.B. Lavasani, Sustainability Evaluation of Conductive Concrete for Pavement Deicing: The Case Study of Parkway Bridge, Tehran, Iran, *Arabian Journal for Science and Engineering*, 46 (2021) 4543-4562.
- [111] H. Dehghanpour, K. Yilmaz, F. Afshari, M. Ipek, Electrically conductive concrete: A laboratory-based investigation and numerical analysis approach, *Construction and Building Materials*, 260 (2020) 119948.
- [112] R. Fulham-Lebrasseur, L. Sorelli, D. Conciatori, Development of electrically conductive concrete and mortars with hybrid conductive inclusions, *Construction and Building Materials*, 237 (2020) 117470.
- [113] A. Arabzadeh, M.A. Notani, A.K. Zadeh, A. Nahvi, A. Sassani, H. Ceylan, Electrically conductive asphalt concrete: an alternative for automating the winter maintenance

- operations of transportation infrastructure, *Composites Part B: Engineering*, 173 (2019) 106985.
- [114] D. Sun, G. Sun, X. Zhu, F. Xiao, Z. Dai, F. Liu, Electrical characteristics of conductive ultrathin bonded wearing course for active deicing and snow melting, *International Journal of Pavement Engineering*, 20 (2019) 1299-1308.
- [115] R. Rao, J. Fu, Y. Chan, C.Y. Tuan, C. Liu, Steel fiber confined graphite concrete for pavement deicing, *Composites Part B: Engineering*, 155 (2018) 187-196.
- [116] H. Abdulla, H. Ceylan, S. Kim, M. Mina, K.S. Cetin, P.C. Taylor, K. Gopalakrishnan, B. Cetin, S. Yang, A. Vidyadharan, Design and construction of the world's first full-scale electrically conductive concrete heated airport pavement system at a US airport, *Transportation Research Record*, 2672 (2018) 82-94.
- [117] Y.-h. Bai, W. Chen, B. Chen, R. Tu, Research on electrically conductive concrete with double-layered stainless steel fibers for pavement deicing, *ACI Materials Journal*, 114 (2017) 935-943.

11. EFFECT OF AGRO-DERIVED CORROSION INHIBITORS ON THE PROPERTIES OF PORTLAND CEMENT MORTAR¹⁰

This chapter discusses the effect of corn-derived polyol corrosion inhibitors on the physical and chemical properties of ordinary Portland cement mortar. The contents of this chapter have been published in Sajid, H.U., Kiran, R., and D.S. Bajwa. 2021. 11. Effect of agro-derived corrosion inhibitors on the properties of portland cement mortar. *Construction and Building Materials*, 310, p.125236.

11.1. Introduction

Pavement deicers are commonly used in snow removal operations in the winter season. While deicers effectively melt the snow and ensure the safety of traffic operations, they are widely observed to accelerate chloride-induced corrosion in rebars, steel bridges, and automobiles [1-3]. To mitigate chloride-induced corrosion in rebars, corrosion inhibitors are usually added to deicing solutions to reduce their corrosivity towards rebars and passenger vehicles. Alternatively, corrosion inhibitors can also be added to the fresh concrete as admixed corrosion inhibitors or applied on the surface of the hardened concrete as migratory corrosion inhibitors to protect rebars against corrosion. Currently, many commercial deicing chemicals are used for pavement deicing operations that mostly include chloride-based deicers, phosphate-based deicers, and acetate-based deicers. Moreover, several agro-based deicers have been investigated for their deicing potential and some of the agro-based deicing solutions (such as sugar beet juice and other propriety agro-based materials) are being used in snow melting operations by different state departments of transportation [4-7]. Among the currently available

¹⁰ This chapter was co-authored by H.U. Sajid, R. Kiran, and D.S. Bajwa. H.U. Sajid had the primary responsibility of preparing the specimens, conducting all tests, and drafting this chapter. R. Kiran supervised the research and revised this chapter.

deicers, sodium chloride (rock salt) in the solid or brine solution form is the most commonly used deicer on the roadways.

The most commonly used admixed and migratory corrosion inhibitors include nitrites (e.g. calcium nitrite, sodium nitrite, and potassium nitrite), alkanolamines (e.g., diethanolamine, dimethylpropanolamine, monoethanolamine, dimethylethanolamine, triethanolamine, and methyldiethanolamine), amines (e.g., methylamine, dimethylamine, ethylamine, propylamine, cyclohexylamine, triethyltetramine, and hexamethylenetetramine), carboxylic acids (e.g., sodium gluconate, D-Saccharic acid, monopotassium salt, calcium α -D eptagluconate, phthalic acid, monopotassium salt, lactic acid, maleic acid, suberic acid, adipic acid, and sodium benzoate), sodium monofluoro phosphate, nitrates, benzoates, zinc and magnesium salts, and chromates [8-14]. In addition to these corrosion inhibitors, several proprietary blends of different corrosion inhibitors are used in concrete that include Darex Corrosion Inhibitor (DCI® and DCI®-S from GCP Applied Technologies Inc.), POSTRITE® (from GCP Applied Technologies Inc.), MCI® 2000 (from Cortec), Ferrogard® 901 and 903 (from Sika), Catexol 1000 CI (from Axim Concrete Technologies) and Rheocrete® 222+ (from BASF). These commercial corrosion inhibitors are based on alkanolamines, amines, and their salts with organic and inorganic acids [8, 15-17]. Moreover, oil/water emulsions have also been utilized as corrosion inhibitors for concrete in the past. Recently eco-friendly and natural corrosion inhibitors have been proposed for usage in reinforced concrete [17-19]. The above-discussed corrosion inhibitors act as anodic, cathodic, or mixed inhibitors. Some of these corrosion inhibitors act as pore blockers [20-22] and thus restrict the ingress deleterious species (e.g., chlorides) in concrete whereas others displace the chloride ion and form a protective film on the rebar surface. The efficiency of both admixed and migrating corrosion inhibitors depend on their dosage [8, 10, 23]. At sufficiently high

dosage, nitrite (e.g. calcium nitrite) and other corrosion inhibitors are quite effective, however, a reduction in their dosage is linked with an increase in corrosion rate and appearance of cracks in concrete. Therefore, it is necessary to maintain a certain dosage of corrosion inhibitors in concrete to ensure desirable levels of corrosion inhibition.

While the increase in the dosage of corrosion inhibitors ensure sustained and higher corrosion inhibition efficiency, the higher dosage is observed to have a negative impact on the properties of fresh and hardened concrete (e.g., setting time, compressive strength, etc.) in the case of some corrosion inhibitors [10, 23]. Schutter and Luo [24] investigated the influence of four different types of corrosion-inhibiting admixtures on properties of normal strength concrete that utilized ordinary Portland cement (OPC) and blast furnace slag cement. They observed a decrease in both early age and long-term compressive strength of concrete regardless of the cement type. The usage of amino- and ester-based aqueous solution corrosion inhibitor resulted in about 14% decrease in the 28 days compressive strength of OPC-based concrete. Overall, a 7.5–20.5% decrease in compressive strength of concrete was noticed. A similar observation of a 10-20% reduction in the compressive strength was noticed in several other investigations that utilized amino and ester-based organic inhibitors in concrete [25-28]. Schutter and Luo [24] also used a blend of amino alcohols and organic and inorganic inhibitors and noticed a 10.5% and 16.5% decrease in the 28-days compressive strength of concrete specimens corresponding to OPC and blast furnace slag cement, respectively. Similarly, Heren and Ölmez [29] observed a reduction in compressive strength of cement paste when ethanolamine corrosion inhibitors (monoethanolamine, diethanolamine, and triethanolamine) are used at 1% (wt.% of cement) dosage. The authors observed a reduction of 2%, 21%, and 26% in the 90-day compressive strength of cement paste corresponding to monoethanolamine, diethanolamine, and

triethanolamine, respectively [29]. Saraswathy and Song [11] studied the impact of various anodic, cathodic, and mixed-type corrosion inhibitors on the properties of concrete namely sodium nitrite, zinc oxide, mixed inhibitor (NaNO_2+ZnO), monoethanolamine, diethanolamine, and triethanolamine. The authors used three types of dosages that include 1%, 2%, and 3% by weight of OPC. The dosage rate of 1% resulted in 6-24% decrease in the compressive strength of concrete specimens. On the other hand, a high dosage rate of 3% resulted in 12-39% decrease in the compressive strength of concrete specimens. This included a decrease of 12.25%, 13.52%, 17.09%, 30.36%, 35.71%, and 39.54% corresponding to sodium nitrite, zinc oxide, monoethanolamine, triethanolamine, diethanolamine, and mixed inhibitor, respectively. Interestingly, the authors observed an increase in the compressive strength in most corrosion inhibitors when using a dosage of 2% by weight of OPC. An earlier review conducted by Hansson et al. noted that sodium nitrite, sodium benzoate, potassium chromate, and an organic corrosion inhibitor (mixture of amines and esters in a water medium) reduced the compressive strength of concrete [22]. For certain corrosion inhibitors (e.g., calcium nitrite and a proprietary migrating corrosion inhibitor), some researchers reported around 15% increase in the compressive strength of concrete [24, 26]. Some conflicting results are also documented in the literature wherein some researchers reported up to a 20% increase in the compressive strength of concrete when aminoalcohol-based corrosion inhibitors are used [25, 26] whereas other researchers observed an increase in the compressive strength for a similar class of corrosion inhibitors [8, 10, 24, 30]. Furthermore, the negative impact of deicers on cementitious materials with and without corrosion inhibitors are well-documented in the literature [31-33]

From the above discussion, it can be inferred that a majority of corrosion inhibitors tend to decrease the compressive strength of concrete whereas some corrosion inhibitors can increase

the compressive strength of concrete, depending on their pore-blocking ability, chemical interaction with the cement hydration products, corrosion inhibitor dosage, age of concrete, mode of application (admixed or migrating), and type of cement. Therefore, when investigating the efficacy of new corrosion inhibitors, it is important to evaluate its impact on the strength and durability properties of concrete. In our previous study, we demonstrated the corrosion inhibition performance of three corn-derived polyol corrosion inhibitors namely sorbitol, mannitol, and maltitol in NaCl brine solution. A 0.5-3.0% wt. addition of these polyols in 23% wt. NaCl deicing solution reduced the corrosion rates by up to 92%. The addition of 1.0% wt. polyol in the NaCl deicer resulted in at least 80-85% reduction in corrosion rates. The polyol molecules acted as mixed corrosion inhibitors and protected the steel from corrosion via physisorption on the steel surface [1]. The current study aims to evaluate the impact of these corn-derived polyol corrosion inhibitors on the properties of OPC-based mortar. Specifically, the authors aim to investigate the effect of three types of polyol corrosion inhibitors namely sorbitol, mannitol, and maltitol that are previously observed to considerably reduce the corrosivity of traditional NaCl deicer [1]. Important properties of OPC mortar specimens (such as scaling, mass change, compressive strength, and chemical composition) are determined when OPC mortar specimens are exposed to traditional NaCl deicing solution containing 1.0% wt. polyol corrosion inhibitors. The experimental procedure adopted in this study is discussed in Section 11.2 of this manuscript and important results and conclusions obtained from this study are discussed in Section 11.3 and Section 11.4, respectively.

11.2. Experimental Procedure

This section discusses the preparation of OPC mortar specimens and deicing solutions that contain the optimum amount of polyol corrosion inhibitors. The deicer/corrosion inhibitor

exposure tests and physical and chemical characterization tests that are conducted to track any physical or chemical deterioration in the Portland cement mortar specimens are discussed. Moreover, the changes observed in the compressive strength and mass of specimens as well as the scaling ratings of the specimens are discussed in this section.

11.2.1. Test Specimens

For this study, Portland cement mortar specimens are prepared using ASTM specifications [34]. To this end, a total of 105 cement mortar cubes (specimen size: $5 \times 5 \times 5$ cm) are prepared using Type I ordinary Portland cement and a water-cement ratio of 0.485. All test specimens are cured in water for 28 days before exposure to deicing solutions.

11.2.2. Corrosion Inhibitors Included Deicers Exposure Conditions

The field deicing solution exposure conditions are simulated by subjecting the cement mortar specimens to wetting-drying cycles. The specimens are exposed to the deicing solution with the optimal amount of corrosion inhibitors in the wetting cycle and are left indoors for drying cycle. To this end, four types of deicing solutions are prepared. Exposure to the distilled water in the wetting cycle is also studied herein for comparison purposes. Furthermore, 23% NaCl deicing solution without corrosion inhibitors is used as the reference deicing solution. The polyol-based deicing solutions are prepared by adding 1.0 wt.% polyol corrosion inhibitor (sorbitol or maltitol or mannitol) in the 23% NaCl deicing solution. The dosage of the corrosion inhibiting molecules in the NaCl-based deicing solution is adopted from our previous study [1] wherein 1.0 wt% of corrosion inhibitors is observed to be an ideal corrosion- inhibitor concentration for reducing the corrosivity of traditional NaCl deicing solution by up to 80-85%.

To simulate the exposure of the cement-based materials to the deicers, the cement mortar samples are subjected to wet-dry cycles for 90 days wherein cement mortar samples are

completely immersed in the polyol-based deicing solution for 15 ± 1 hours at 0°C (wet period) and then dried for 9 ± 1 hours at room temperature (25°C , dry period). As illustrated in Figure 11.1, each wet-dry (W-D) exposure cycle took approximately 24 hours to complete. The deicing solutions in the containers are changed after every 20 W-D exposure cycles.

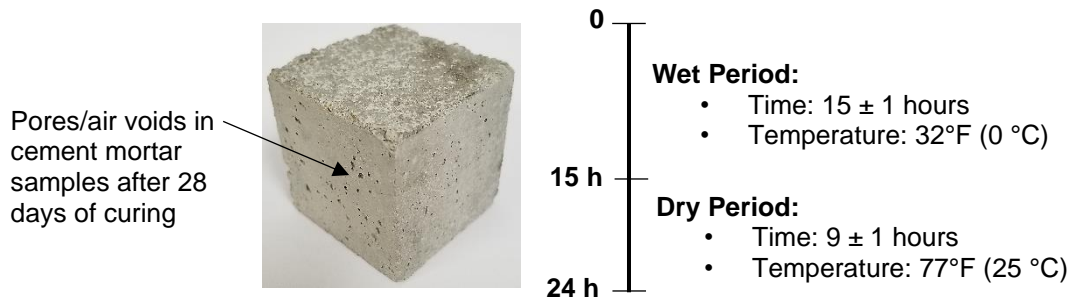


Figure 11.1. Experimental protocol for wet-dry exposure cycles and typical OPC mortar specimen after 28 days of curing.

11.2.3. Physical Characterization: Mass Change, Scaling, and Compressive Strength

Mass change, scaling, and compressive strength tests are conducted to determine the physical deterioration in the cement mortar specimens that are exposed to W-D cycles of deicing solutions in the absence and presence of polyol-based corrosion inhibitors. Cementitious materials may undergo mass gain or mass loss due to scaling damage or filling up of micropores with dried deicer particles. The mass changes and surface scaling damage in the cement mortar specimens are recorded after every 10 W-D exposure cycles. For observing scaling damage and mass changes, test specimens are taken out of the deicing solution containers and placed at room temperature for 5 hours to achieve adequate drying. Based on visual observation, a scaling rating of 1-5 is assigned to the specimen based on the extent of surface scaling. The description of scaling rating is adopted from the literature (see Table 11.2) [31]. The compressive strength tests of deicer-exposed cement mortar specimens are conducted using ASTM C109 specifications [34]. The compressive strength is one of the most important durability indicator that is used to

quantify the deicer and corrosion inhibitor-induced deterioration in cementitious materials. The experimental scheme with information about the deicing solutions, exposure conditions, and number of cycles after which each test is conducted is summarized in Table 11.1. The results obtained from scaling, mass change, and compressive strength tests for reference deicing solution, polyol corrosion inhibitor-based deicing solution, and tap water are discussed in Section 11.3.1, 11.3.2, 11.3.3, respectively.

Table 11.1. Experimental scheme.

Deicing chemical	Exposure condition	No. of samples	Testing performed after following W-D cycles			
			Mass change	Scaling	Compressive strength	XRD, SEM, EDS analysis
NaCl	Wet-Dry (W-D) cycles	3 per test per cycle	0, 10,	0, 10,	0, 15, 30, 45, 60, 90	0, 60
NaCl + Sorbitol			20, 30,	20, 30,		
NaCl + Maltitol			40, 50,	40, 50,		
NaCl + Mannitol			70, 90	70, 90		

11.2.4. Chemical Characterization: XRD and SEM, and EDS Analysis

Three types of chemical/surface characterization tests are performed to determine the chemical composition of the products formed in the specimens as a result of cement hydration and exposure to deicing solutions in the absence and presence of small concentrations of polyol-based corrosion inhibitors. This includes X-ray diffraction (XRD), scanning electron microscopy (SEM), and energy-dispersive X-ray spectroscopy (EDS) analysis. XRD, SEM, and EDS analyses are conducted at the beginning of the study and after 60 W-D exposure cycles. For XRD analysis, a powder cement sample is extracted from the surface layer of the specimen. Bruker AXS' D8 Discover multipurpose X-Ray Diffractometer is employed for XRD tests. The XRD patterns of the cement mortar specimens are then obtained over a 2-theta range of 5-70° and generator settings of 40 kV and 30 mA. SEM and EDS analysis are conducted at a location

of 1 cm from the surface of the specimens. The purpose of the SEM and EDS studies is to locate the presence of voids and microcracks in the specimens. Moreover, the EDS studies are aimed to identify the penetration of deicing salt ions near the surface of the specimens. The XRD analysis is conducted to determine the composition of any distinct compounds that are formed in cement mortar after exposure to the deicing solutions. The SEM micrographs and EDS spectra of cement mortar specimens are obtained using a JEOL JSM-6490LV scanning electron microscope. The results obtained from SEM, EDS, and XRD analysis are discussed in Section 11.3.4.

11.3. Results and Discussions

In this section, the physical and chemical deteriorations observed in the cement mortar specimens as a result of exposure to the traditional NaCl deicing solution in the absence and presence of the polyol corrosion inhibitors (sorbitol, maltitol, and mannitol) are discussed in terms of scaling damage, scaling ratings, mass loss or mass gain, compressive strength, and chemical changes. Moreover, the results obtained from this study are also compared with the results available in the literature for the most common deicers and corrosion inhibitors.

11.3.1. Scaling

Scaling can be defined as the superficial damage (flaking or peeling) of the top surface of the cementitious materials after exposure to deicing chemicals or freeze-thaw conditions [35]. Scaling is a commonly used indicator of deicer-induced deterioration in cement-based materials [31, 36-39]. The surface scaling phenomena observed in the reference deicing solution (Sol-A: 23% wt. NaCl) and polyol-based deicing solutions (23% wt. NaCl + 1% wt. sorbitol: Sol-B, 23% wt. NaCl + 1% wt. maltitol: Sol-C, and 23% wt. NaCl + 1% wt. mannitol: Sol-D), for the 90 cycles exposure, are provided in Figure 11.2 and Figure 11.3, respectively. As observed in Figure 11.2, after 20 wet-dry exposure cycles, cement mortar specimens corresponding to all

four types of deicing solutions exhibited a similar extent of surface scaling damage. In all specimens, small flakes are visible at the edges of the specimens. With further increase in the W-D exposure cycles, more flakes and buildup of deicer precipitates became visible at the surface and pores (see Figure 3). Moreover, the visual observation of specimens suggests that cement mortar specimens that are subjected to Sol-A and Sol-D suffered slightly higher scaling damage (both at the edges and interior surfaces) when compared to the cement mortar specimens that are Sol-B and Sol-C. The scaling damage observed in the specimens is typically observed in commonly used chloride-based deicing solutions (NaCl , CaCl_2 , and MgCl_2) in both W-D and Freeze-Thaw (F-T) exposure tests [31]. The scaling damage observed herein can be attributed to the excessive ingress of deicing solution into the cement mortar and subsequent accumulation, precipitation, and crystallization of deicing salts upon drying. These mechanisms are known to exert pressure and cause mechanical stresses within the cement mortar pores and thus cause scaling damage [35, 40, 41]. Furthermore, the chloride ions from the deicing solution can cause decalcification and form oxychloride crystals that can cause damage in the cement paste particularly when a high concentration of NaCl (e.g. 23 wt.%) is used as a deicer [35, 39, 42, 43].

Based on visual observations of each specimen after different W-D exposure cycles, a visual scaling rating is assigned to the cement mortar specimens. The visual scaling rating of specimens ranges from 0 (no scaling) to 5 (severe scaling) and the description of each scaling rating, as adopted from Wang et al. [31], is summarized in Table 11.2. The visual observation-based scaling ratings of cement mortar specimens after exposure to the W-D exposure cycles of the salt brine deicing solution in the absence and presence of polyol corrosion inhibitors are provided in Figure 11.4. For comparison, Figure 4 also includes the scaling rating of cement mortar specimens that are exposed to W-D exposure cycles of tap water. Based on the visual

observation of surface images of the cement mortar specimens after 20 wet-dry exposure cycles, all specimens are assigned a scaling rating of 1 which corresponds to slight scaling damage (see Figure 11.2 and Figure 11.4). At 40 W-D exposure cycles, the specimens exhibited a scaling rating of 2 (slight to moderate scaling), and beyond 45 W-D exposure cycles, the specimens are assigned a scaling rating of 2.5 or 3 (slight to moderate or moderate scaling). These results show that polyol-based deicing solutions cause slight to moderate and moderate scaling damage in cement-based materials and are no different from the scaling damage observed in the case of the specimens exposed to salt brine deicer without polyols. In essence, the addition of 1.0 wt.% polyol corrosion inhibitors does not cause any additional scaling damage than that is observed in the specimens exposed to 23% wt. NaCl solution.

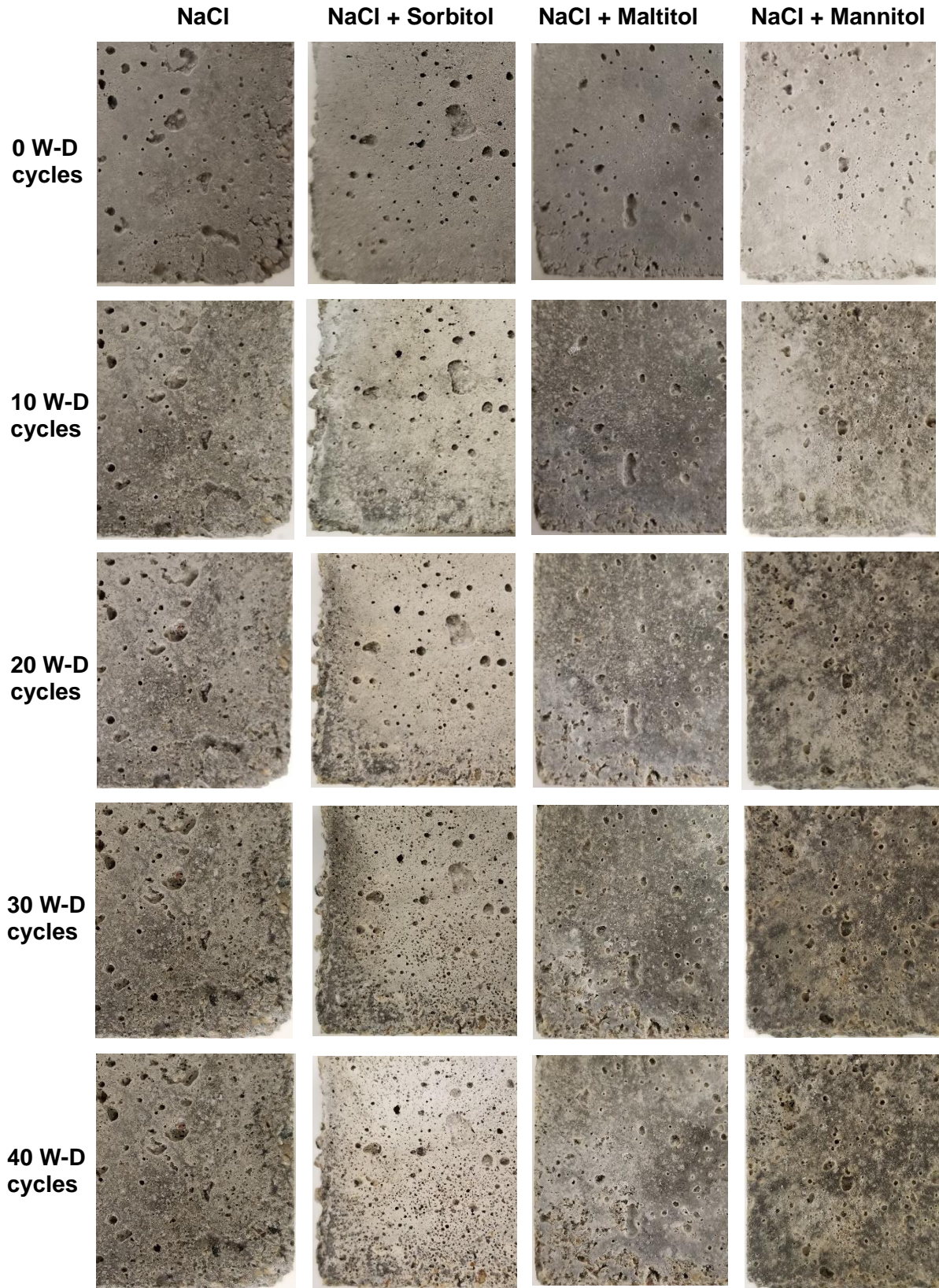


Figure 11.2. Visual appearance of cement mortar specimens after 0-40 W-D exposure cycles.

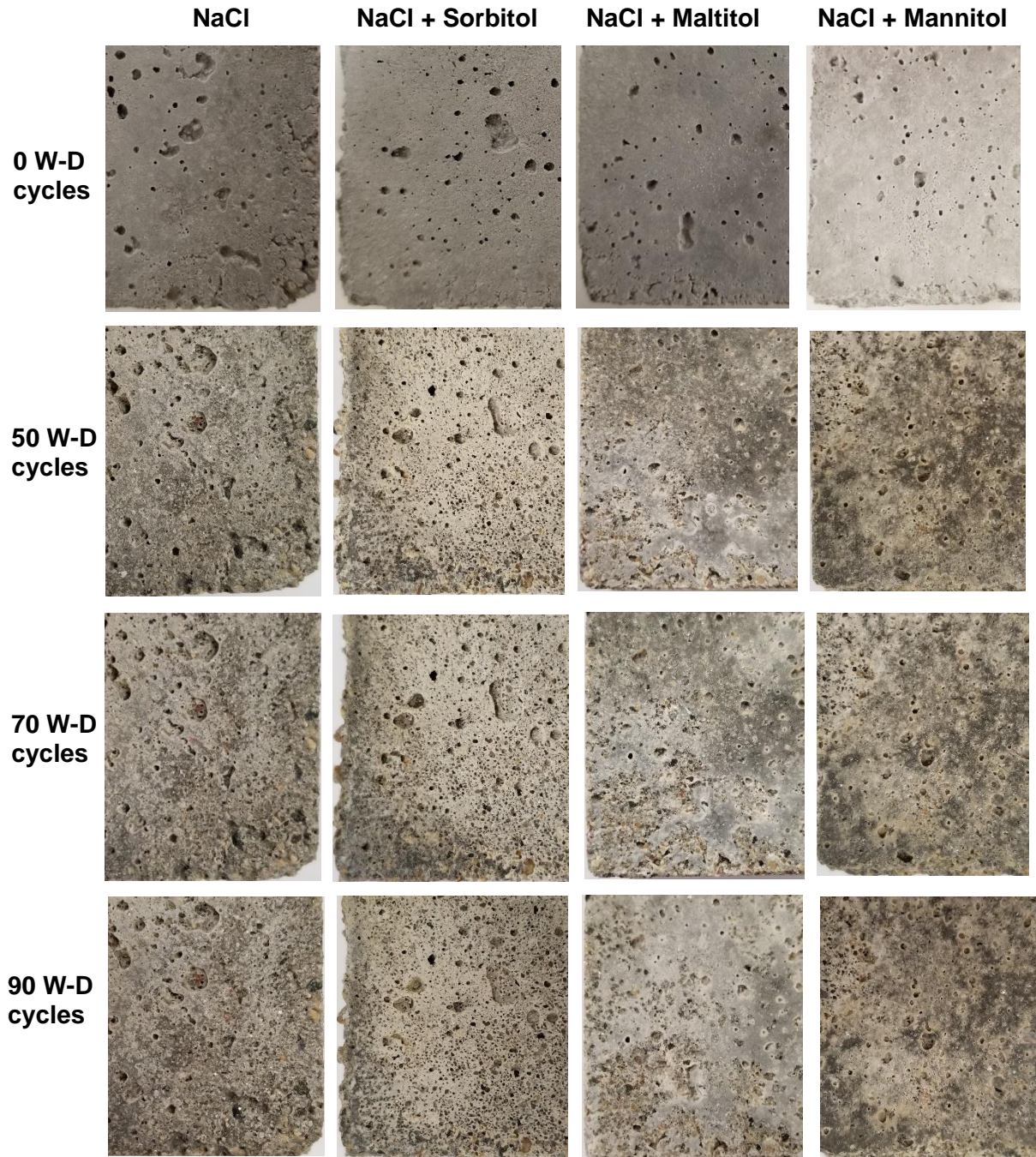


Figure 11.3. Visual appearance of cement mortar specimens after 0, 50-90 W-D exposure cycles.

Table 11.2. Description of the visual rating of scaling damage in cement mortar specimens.

Rating	Description
0	No scaling
1	Slight scaling (small flakes visible on sample surface)
2	Slight to moderate scaling (large flakes visible on the sample surface and sample edge damage noticeable)
3	Moderate scaling (sample edge damage and some fine aggregate visible)
4	Moderate to severe scaling
5	Severe scaling (chunks coming out of surfaces and edges, scaling depth > 0.3 cm, and fine aggregate visible over the entire surface)

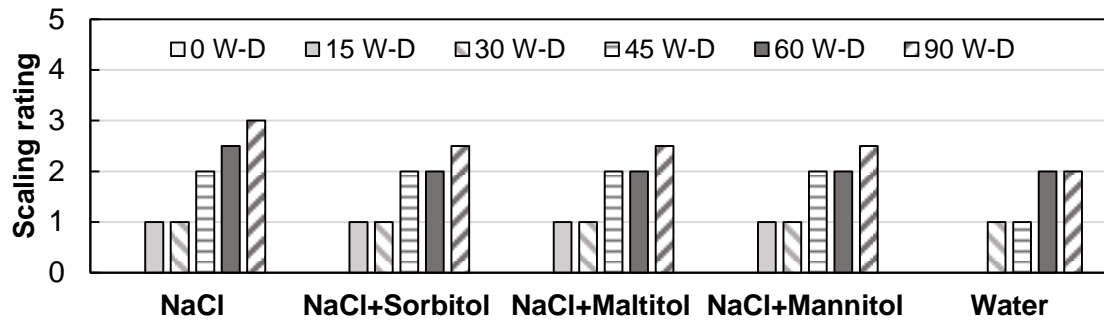


Figure 11.4. Visual observation-based scaling rating assigned to the OPC mortar specimens after exposure to W-D cycles of NaCl salt brine deicer with and without polyol corrosion inhibitors.

11.3.2. Mass Change

Mass change of specimens after exposure to a deicing solution is commonly used to characterize the deicer-induced damage in cement-based materials [31, 44]. The mass change indicates physical and chemical mechanisms that occur in cement mortar specimens after exposure to deicing solutions. An increase in the mass of cement mortar can be attributed to the continuous cement hydration, precipitation of deicing salts, and formation of micropores or increased surface area due to cracking absorbing available liquid or solid particles. Surface scaling can cause micro-cracks and increased surface area which can lead to high retention of the deicers upon drying, and thus mass gain is observed. On the other hand, mass loss is usually

indicative of breaking off of aggregates and cement hydration products from the surface which is usually driven by scaling-induced disintegration of particles on the surface. The mass change in specimens is determined after every 10 W-D exposure cycles and the average mass change observed in the cement mortar specimens is plotted in Figure 11.5. The negative mass change denotes an increase in the mass whereas the positive mass change indicates a mass loss in the cement mortar specimens. As observed in Figure 11.5, most of the specimens did not exhibit any considerable change in the mass when exposed to 30 W-D cycles which can be attributed to the lesser extent of the scaling damage that was noticed in Figure 11.2. Further exposure to W-D cycles caused up to a 0.4% increase in the mass of cement mortar specimens. This minor increase in the mass of cement mortar specimens can be attributed to the buildup of salt particles in the pore as well as an increase in the surface area of specimens due to microcracks formation at the surface. The increased surface area can retain more deicing solution and thus leads to mass gain [31]. The investigations conducted by Wang et al. [31] observed a similar mass gain in the case of W-D exposure tests for cement paste and concrete specimens. It is important to note that during the first 28 days of curing, the cement hydration also contributes to an increase in the mass. However, beyond 28 days, the contribution of cement hydration to mass gain can be expected to decrease, and hence that is the reason only a minor mass gain of 0.4% is observed in the current study as compared to other studies [31] and this mass gain can be primarily attributed to the precipitation of deicing salt and corrosion inhibitors. The mass change results suggest that polyol-based deicing solutions do not cause considerable change in the mass when applied on cementitious materials.

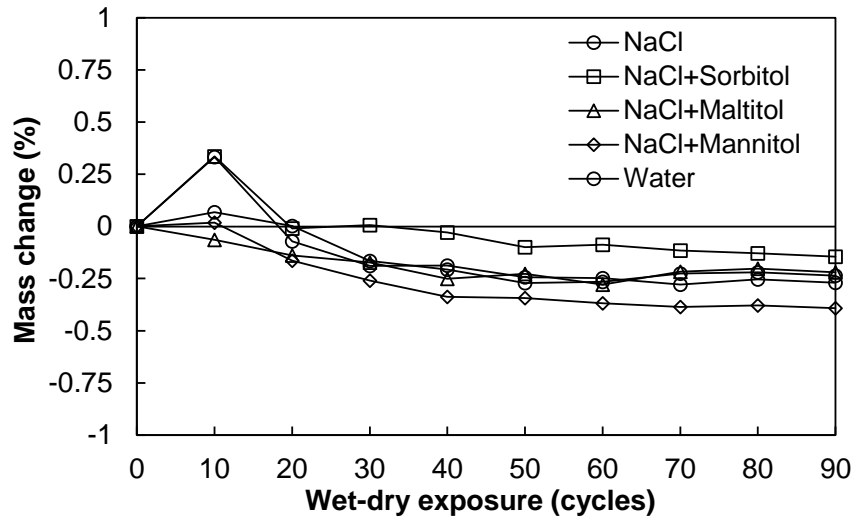


Figure 11.5. Mass change observed in the cement mortar specimens with respect to the number of W-D cycles of NaCl salt brine deicer with and without polyol corrosion inhibitors (note: negative mass change means mass gain).

11.3.3. Compressive Strength

The compressive strength of the cement mortar specimens can either decrease or increase, depending on the type of deicer and concentration of corrosion inhibitors. As discussed in Section 11.1, a higher concentration of corrosion inhibitors is linked with a reduction in the compressive strength of cementitious materials. It is also important to note that the deicing solution in itself can lead to a reduction in the compressive strength of cementitious materials due to the physical and chemical interactions between the deicing solution ions and cement hydration products. To elucidate the impact of polyol corrosion inhibitors, the compressive strengths of cement mortar specimens are determined after the 15th, 30th, 45th, 60th, and 90th W-D exposure cycles using the procedure discussed in Section 11.2.3. The compressive strength results corresponding to the reference deicing solution, polyol-based deicing solution, and tap water after a specific number of W-D exposure cycles are provided in Figure 11.6. As observed in Figure 11.6, both reference cement mortar specimens corresponding to NaCl deicer and cement mortar specimens that are subjected to polyol-based deicing solution exhibited almost

similar compressive strength (65 MPa on average) after 15 W-D cycles. Beyond 15 W-D exposure cycles, the compressive strength of cement mortar specimens is observed to decrease until 60 W-D exposure cycles. The specimens that are subjected to NaCl brine deicer suffered approximately an 18% decrease in the compressive strength. On the other hand, most of the polyol-based deicing solutions experienced approximately 10% decrease in compressive strength. Interestingly, at 90 W-D exposure cycles, most polyol-based deicing solutions are observed to regain their original strength (compressive strength observed at the onset of W-D exposure tests). The smaller decrease in the compressive strength of cement mortar in the case of polyol-based deicing solutions can be attributed to the smaller chloride penetration into the specimens due to the pore-blocking ability of agro-based deicers that was also observed in a previous study [31]. These results show that polyol-based deicing solutions cause either same or relatively less decrease in compressive strength of cement-based materials when compared to the traditional salt brine deicers.

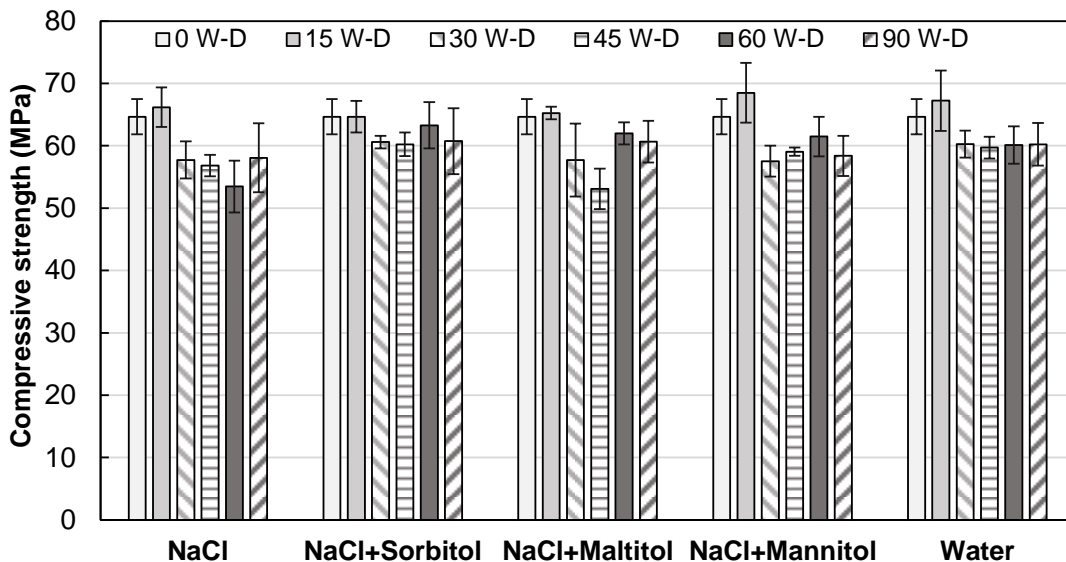


Figure 11.6. Compressive strength of cement mortar after exposure to W-D exposure cycles of NaCl salt brine deicer with and without polyol corrosion inhibitors.

11.3.4. Chemical Characterization: XRD, SEM, and EDS Analysis

Chemical composition analysis and morphological evaluation techniques are employed to evaluate the formation of any new products and cement hydration products when cement mortar specimens are subjected to W-D exposure cycles of salt brine deicing solution in the absence and presence of polyol corrosion inhibitors. Specifically, three types of chemical and surface characterization tests are conducted that include XRD analysis, determination of SEM micrographs, and EDS spectra. The sample preparation and testing procedure of each of these tests are discussed in Section 11.2.4. XRD analysis is conducted to assess the formation of any distinct chemical phases in the specimens after exposure to deicers W-D exposure cycles. XRD analysis is conducted at the beginning of the study (labeled as “No deicer exposure”) and after 60 W-D exposure cycles for both cement mortar specimens corresponding to both reference and polyol-based deicing solutions. The XRD spectra of cement mortar specimens are provided in Figure 11.7. As observed in Figure 11.7, the XRD spectra of test specimens show the presence of quartz, calcite, and hydration products such as calcium hydroxide and C-S-H that are typically observed in the OPC mortar that is exposed to NaCl-based deicing solution [31, 39, 45, 46]. In all the spectra, the intensity of quartz dominated the other compounds which can be linked with the relatively low penetration of NaCl deicer [31]. The presence of NaCl in cement mortar specimens can be attributed to the precipitation of the deicing solution in the voids. In the case of a polyol-based deicing solution, hydrated forms of sorbitol, mannitol, or maltitol are observed in the corresponding solutions in addition to the products that are observed in the reference NaCl only deicing solution. However, no new product formation or leaching of calcium is observed in the spectra which suggests that the lack of chemical interaction between the polyol hydrates and cement hydration products and hence they do not have a negative impact on cement paste.

Consequently, on slight to moderate scaling damage and relatively lesser deterioration in the compressive strength in the cement mortar specimens that are subjected to polyol-based deicers.

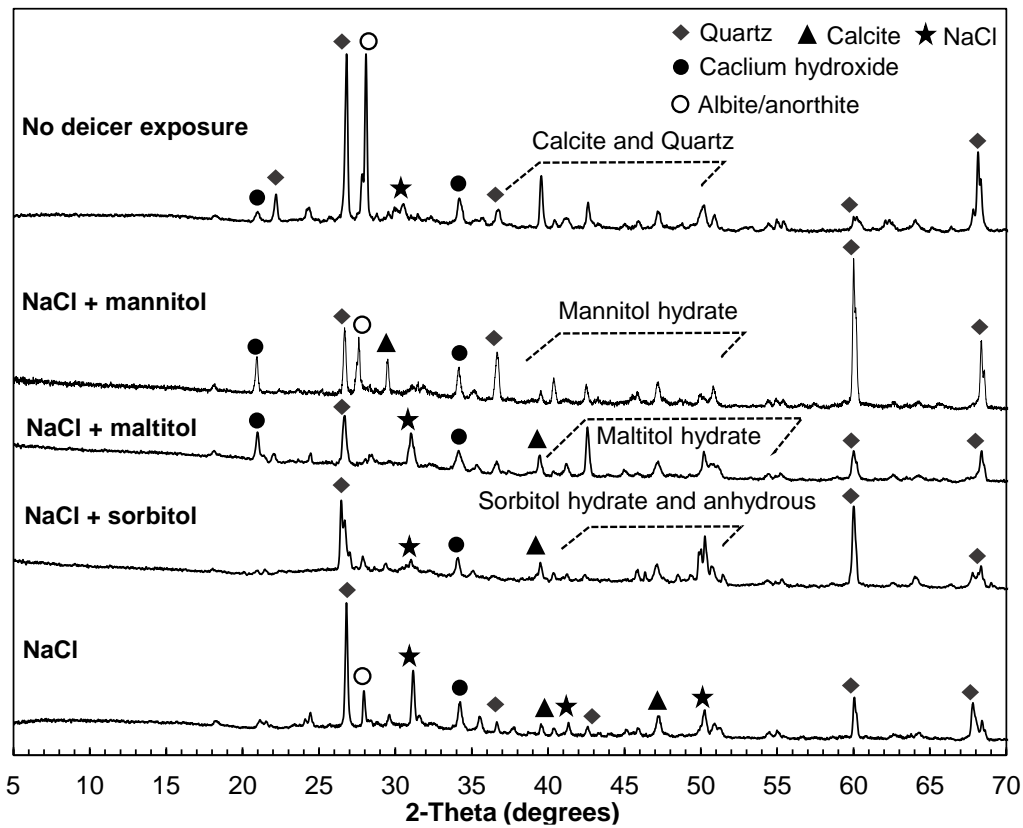


Figure 11.7. XRD spectra of cement mortar specimens after exposure to 60 W-D cycles of NaCl deicing solution in the absence and presence of polyol corrosion inhibitors.

To further assess the formation of any microcracks, micropores, or any new products, SEM micrographs are obtained for the cement mortar specimens after 60 W-D exposure cycles of the salt deicing solution and polyol corrosion inhibitor based deicing solutions using the procedure specified in Section 11.2.4. Moreover, the corresponding EDS spectra are also obtained to assess the elemental composition of the morphology observed in the SEM micrographs. The SEM micrographs and EDS spectra of test specimens obtained after 60 W-D cycles are provided in Figure 11.8 and Figure 11.10, respectively. Moreover, the SEM micrograph and XRD spectra of cement mortar specimens after exposure to 60 W-D cycles of

tap water are also obtained and are provided in Figure 11.9 for comparison purpose. As observed in Figure 11.8, the SEM micrographs of the cement mortar specimens corresponding to the reference deicing solution exhibit the formation of cracks in the cement matrix as well as some pores. Some precipitation of the deicing salts can also be noticed in the micrographs. The SEM micrographs of the cement mortar specimens that are subjected to 60 W-D exposure cycles of the NaCl deicer containing polyol corrosion inhibitors exhibited similar formation of cracks and pores. However, the extent of cracks and pores is observed to be relatively lower when compared to the cement mortar specimens that are exposed to the reference salt brine deicing solution. The EDS spectra of specific points in these micrographs are further obtained and presented in Figure 11. It can be noticed that in most cases, the EDS spectra show high peaks corresponding to calcium and oxygen which represent the cement hydration products. Similarly, the spots in the vicinity of the cracks showed peaks of Na and Cl elements which points towards the presence of the deicing salts precipitates, an observation consistent with the XRD spectra (see Figure 11.7). On the other hand, the EDS spectra obtained in the case of specimens that are exposed to tap water exhibited that formation of typical hydration products (see Figure 11.9) whereas microcracks are also observed in the SEM micrograph corresponding to the tap water specimen. However, no deposits or products are observed along the crack. The microcracks observed in the SEM micrographs could result from 1) the formation of expansive oxychloride products due to the penetration of chloride ions and precipitation/crystallization of deicing salt or polyols. Such microcracks can also be triggered by the preparation of specimens for SEM analysis due to the brittleness of the cement matrix. Moreover, cracks of similar nature were also observed in a recent study by Cheng et al. [46] wherein OPC cement mortar specimens were subjected to wetting and drying exposure cycles of multiple corrosive ions including NaCl. Overall, relatively

the specimens that are subjected to NaCl deicer exhibited similar morphology and similar elemental composition regardless of the presence of polyol corrosion inhibitors.

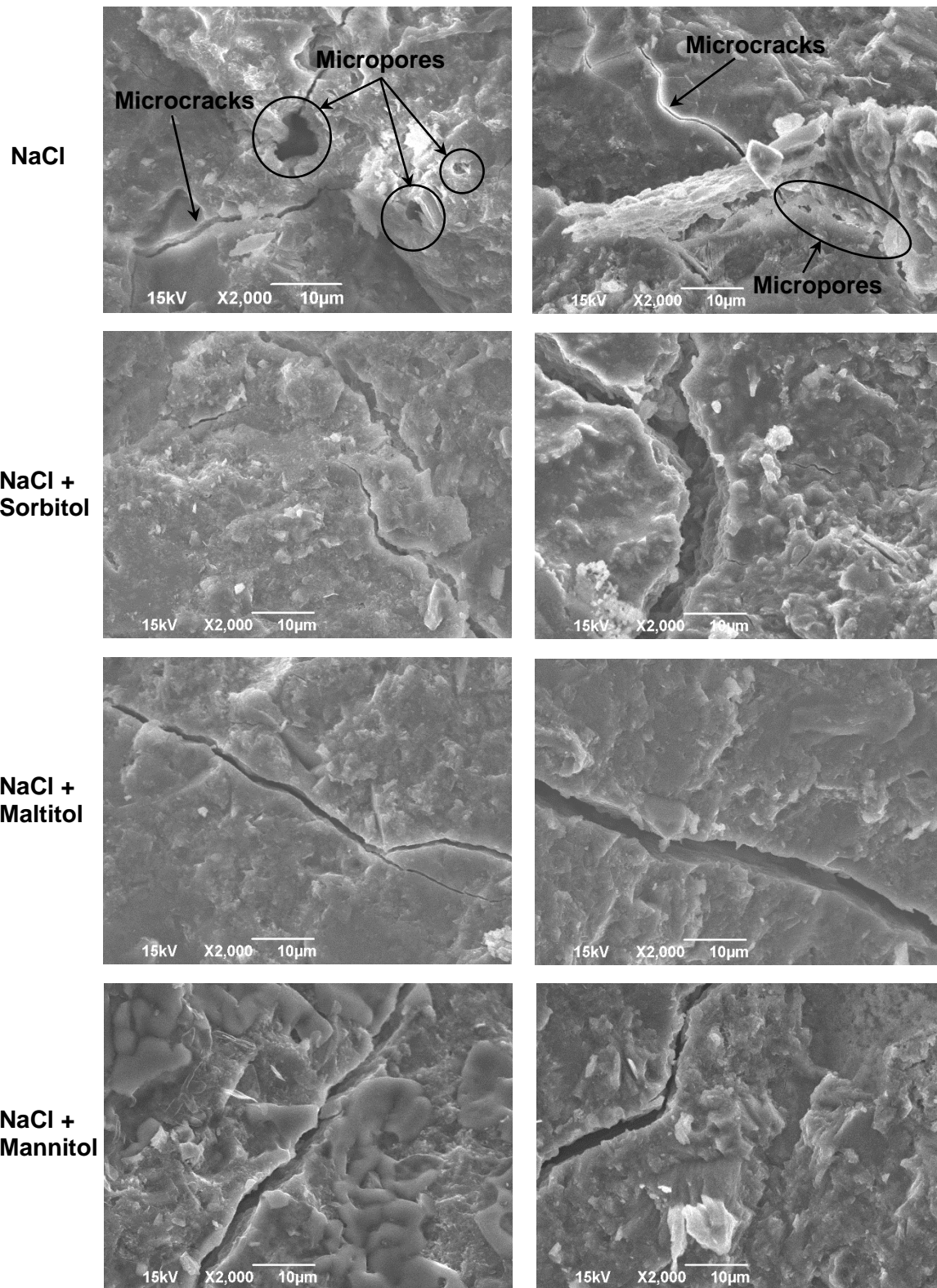


Figure 11.8. SEM micrographs of cement mortar specimens after exposure to 60 W-D cycles of NaCl deicing solution in the absence and presence of polyol corrosion inhibitors.

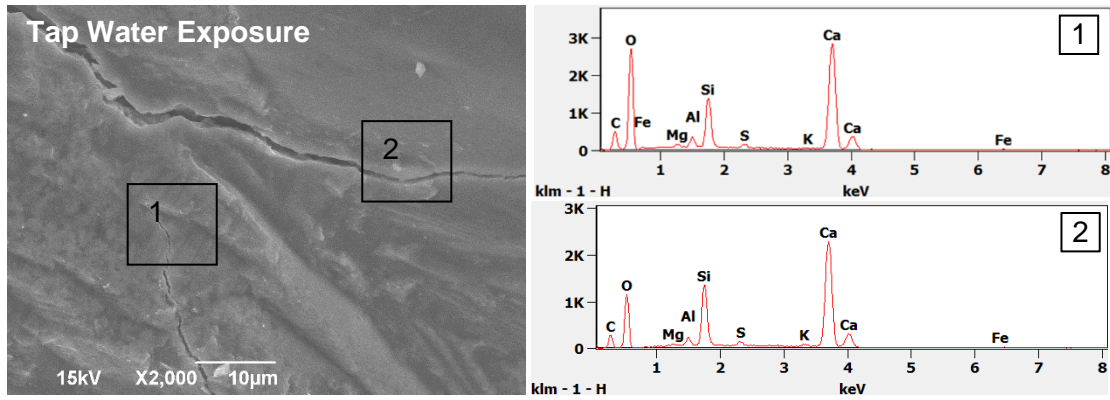


Figure 11.9. SEM micrograph and EDS spectra of cement mortar specimens after exposure to 60 W-D cycles of tap water.

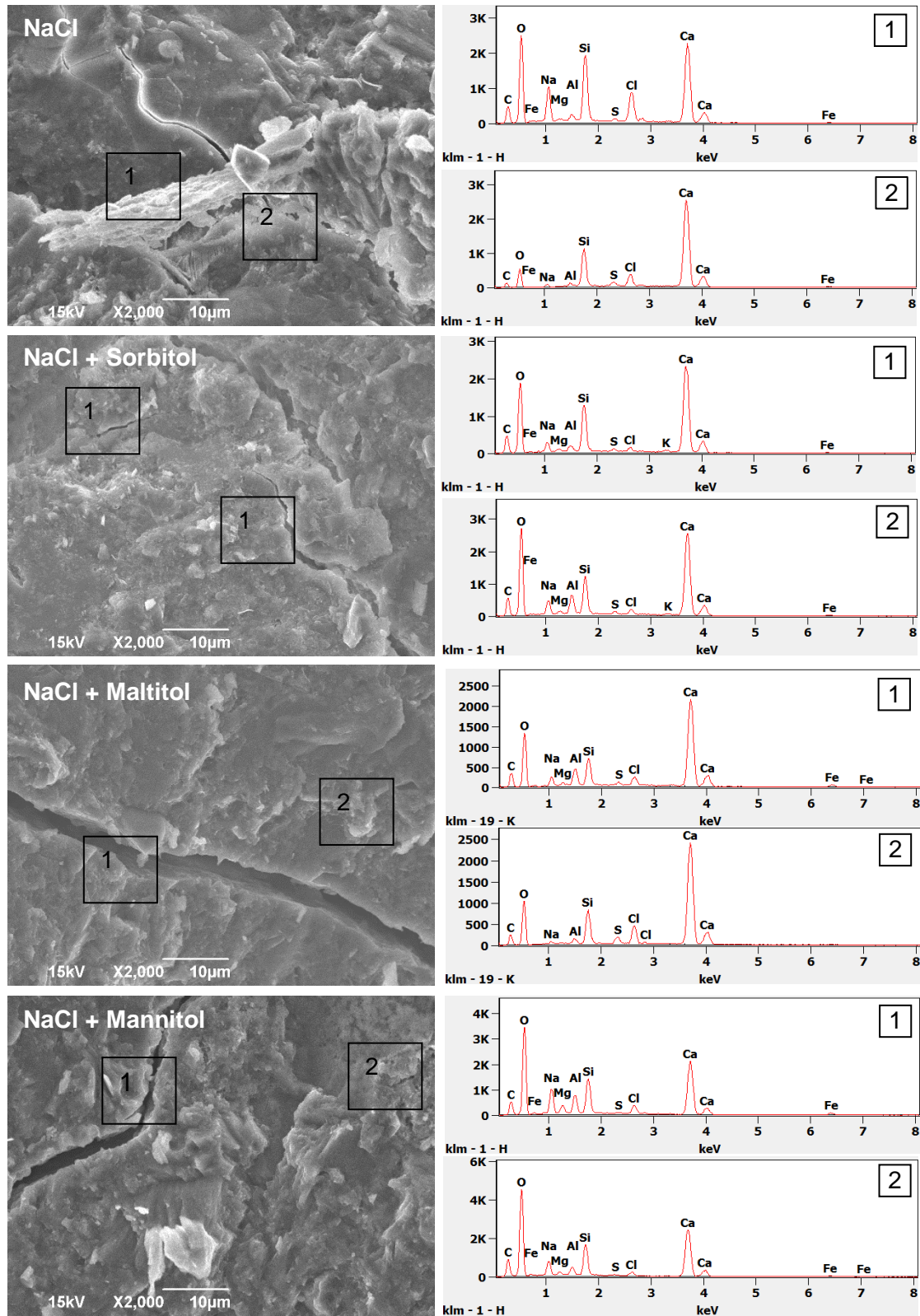


Figure 11.10. EDS spectra of cement mortar specimens after exposure to 60 W-D cycles of NaCl deicing solution in the absence and presence of polyol corrosion inhibitors.

11.3.5. Performance Comparison with the Literature and Discussion

The percentage decrease in the compressive strength of cement mortar specimens obtained in this study (60 W-D cycles) is compared with the percent decrease in the compressive strength of cement mortar or concrete specimens that are reported in the literature for different types of corrosion inhibitors and agro-based deicers. The results of this study and those obtained from the literature are provided in Figure 11.11. A comparison of compressive strengths revealed that for most corrosion inhibitors, the compressive strength of OPC materials decreases by 10-16% whereas for some corrosion inhibitors, the compressive strength can decrease as high as 39%. It is also observed that surface-applied deicing solutions containing corrosion inhibitors and migrating corrosion inhibitors result in lesser deterioration in concrete compressive strength as compared to admixed corrosion inhibitors. The polyol corrosion inhibitors investigated herein resulted in less than 10% reduction in compressive strength of cement mortar and thus performs relatively better when compared to many commonly used admixed corrosion inhibitors in concrete.

The mass changes and scaling damage results are not widely reported for many corrosion inhibitors. However, for common deicers the mass change and scaling damage results are available. Previous studies conducted on NaCl and CaCl₂ deicers as well as CaCl₂ deicers with corrosion inhibitors also resulted in slight to moderate scaling damage (i.e., scaling rating of 2 to 3) in the case of W-D exposure cycles in cement paste and concrete [31]. Similarly, the mass change was less than 1% for the specimens beyond 28 days of W-D cycles. To summarize, the polyol corrosion inhibitors do not cause further deterioration in the properties of cement-based materials and have a relatively less negative impact on the compressive strength (see Figure

11.11) and other durability properties of cement mortar and cement concrete when compared to other corrosion inhibitors.

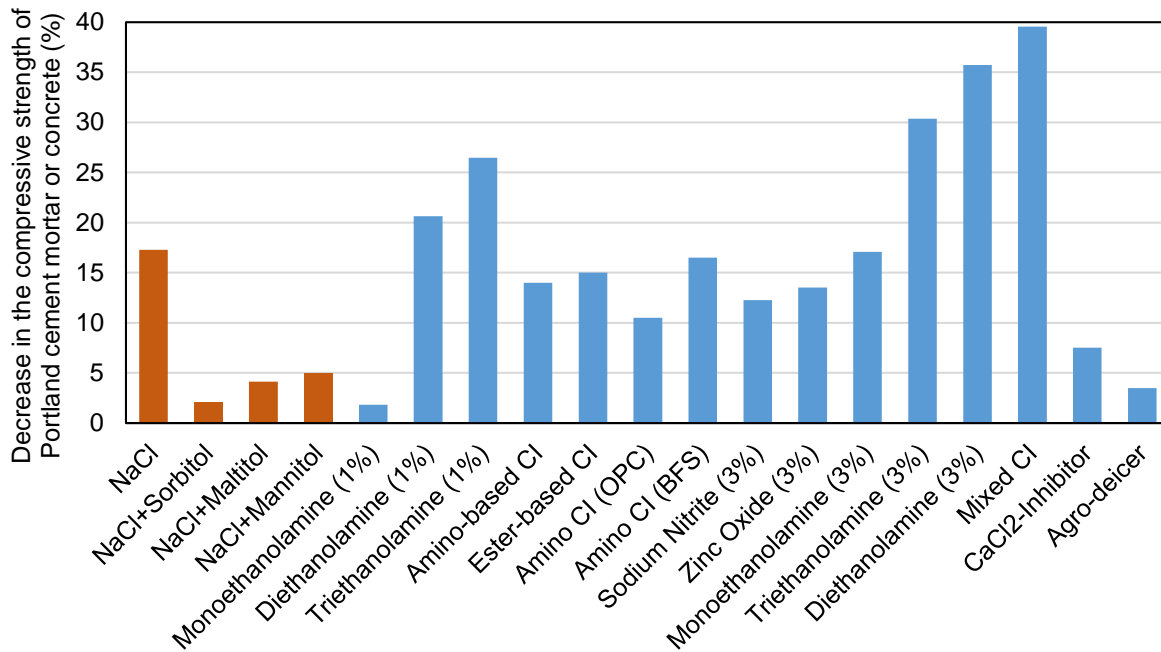


Figure 11.11. A comparison of compressive strength deterioration of cement mortar and concrete caused by different corrosion inhibitors and deicers.

11.4. Conclusions

The present study evaluated the impact of polyol corrosion inhibitor added deicing solutions on the compressive strength, scaling resistance, mass change, and chemical properties of ordinary Portland cement mortar. The important conclusions obtained from this investigation are:

1. NaCl deicing solution causes slight to moderate scaling damage in cement mortar specimens which can be attributed to the penetration and precipitation of deicing molecules in the cement mortar. The addition of polyol corrosion inhibitors in the NaCl deicer did not result in any further scaling damage.
2. The addition of polyol corrosion inhibitors in the NaCl deicing solution (1.0 wt.% sorbitol, mannitol, or maltitol) does not cause a significant mass change in the cement

mortar specimens and hence it will not have a further negative impact on properties of cement mortar when compared to NaCl deicing solution. This is reflected by the lower surface scaling and spalling of cement mortar.

3. Exposure to the reference salt brine deicing solution results in a 12-17% reduction in the compressive strength of concrete after exposure to more than 60 W-D cycles. For the same number of exposure cycles, a relatively lower deterioration in the compressive strength of cement mortar is observed (2-8%) when 1.0 wt.% corn-derived polyols are added to the NaCl deicing solution. The relatively lower reduction in the compressive strength of cement mortar can be attributed to the relatively lower scaling damage and lack of significant chemical interaction between the corrosion inhibitors and cement hydration products due to the pore clogging effect of polyols.
4. The chemical composition analysis (XRD and EDS) revealed the presence of NaCl deicing salt precipitates as well as the presence of cement hydration products. However, no considerable decalcification is observed when the deicing solutions are applied on the hardened cement mortar surface regardless of the presence of corrosion inhibitors. This demonstrates that the addition of polyol corrosion inhibitors does not alter the chemical composition of the hardened cement matrix and does not result in the formation of deleterious products and thus does not cause further damage in cement mortar when compared to NaCl deicing solution.
5. The morphological analysis conducted using SEM revealed the formation of microcracks and some micropores in the specimens that are subjected to NaCl deicing solution both during the absence and presence of polyol corrosion inhibitors. The morphological pattern is similar in all specimens which demonstrates that the addition of polyol

corrosion inhibitors in the NaCl deicing solution did not cause any further microcracking or form any superficial products. The microcracks observed in the SEM micrographs may be linked with the formation of expansive oxychloride crystals and deicer precipitates.

A comparative analysis of the type and dosage of polyol corrosion inhibitors investigated herein shows that the addition of polyol corrosion inhibitors does not cause further deterioration in the cement mortar when compared to the traditional salt brine deicer. Moreover, polyol corrosion inhibitors resulted in a relatively lower reduction in the cement mortar compressive strength when compared to the majority of the commonly used concrete corrosion inhibitors. The results obtained from this study further demonstrate that at an optimum amount (1.0% wt.) of corn-derived polyols namely sorbitol, mannitol, and maltitol can be added to the 23.0% wt. NaCl deicing solution without any concern for the deterioration in the properties of hardened concrete. Moreover, the addition of similar or higher amount of these corn-derived polyols in the traditional NaCl deicing solution has been demonstrated to significantly reduce the corrosivity of the NaCl deicing solution without compromising the snow melting capacity of the NaCl deicing solution [1, 2].

11.5. References

- [1] H.U. Sajid, R. Kiran, X. Qi, D.S. Bajwa, D. Battocchi, Employing corn derived products to reduce the corrosivity of pavement deicing materials, *Construction and Building Materials*, 263 (2020) 120662.
- [2] H.U. Sajid, D.L. Naik, R. Kiran, Improving the ice-melting capacity of traditional deicers, *Construction and Building Materials*, 271 (2021) 121527.

- [3] X. Shi, L. Fay, Z. Yang, T.A. Nguyen, Y. Liu, Corrosion of deicers to metals in transportation infrastructure: Introduction and recent developments, *Corrosion reviews*, 27 (2009) 23-52.
- [4] J. Barrett, Brine With a Dash of Beet Juice—A Pungent Cocktail for Icy Roads, in: *Wall Street Journal*, March 15, 2020.
- [5] A. Mannette, KDOT using beet juice to clear ice on roadways, in: *The Ottawa Herald*, Dec 27, 2019.
- [6] M. Honarvar Nazari, E.A. Havens, A. Muthumani, X. Shi, Effects of processed agro-residues on the performance of sodium chloride brine anti-Icer, *ACS Sustainable Chemistry & Engineering*, 7 (2019) 13655-13667.
- [7] M.H. Nazari, X. Shi, Developing Renewable Agro-Based Anti-Icers for Sustainable Winter Road Maintenance Operations, *Journal of Materials in Civil Engineering*, 31 (2019) 04019299.
- [8] B. Elsener, U. Angst, 14 - Corrosion inhibitors for reinforced concrete, in: P.-C. Aïtcin, R.J. Flatt (Eds.) *Science and Technology of Concrete Admixtures*, Woodhead Publishing, 2016, pp. 321-339.
- [9] C. Page, V. Ngala, M. Page, Corrosion inhibitors in concrete repair systems, *Magazine of Concrete Research*, 52 (2000) 25-37.
- [10] H.-S. Lee, V. Saraswathy, S.-J. Kwon, S. Karthick, Corrosion inhibitors for reinforced concrete: A review, *Corrosion inhibitors, principles and recent applications*, (2018) 95-120.
- [11] V. Saraswathy, H.-W. Song, Improving the durability of concrete by using inhibitors, *Building and environment*, 42 (2007) 464-472.

- [12] H.-W. Song, V. Saraswathy, Analysis of corrosion resistance behavior of inhibitors in concrete using electrochemical techniques, *Metals and Materials International*, 12 (2006) 323-329.
- [13] M. Ormellese, L. Lazzari, S. Goidanich, G. Fumagalli, A. Brenna, A study of organic substances as inhibitors for chloride-induced corrosion in concrete, *Corrosion Science*, 51 (2009) 2959-2968.
- [14] M.I. Prieto, A. Cobo, Á. Rodríguez, M. de las Nieves González, The efficiency of surface-applied corrosion inhibitors as a method for the repassivation of corroded reinforcement bars embedded in ladle furnace slag mortars, *Construction and Building Materials*, 54 (2014) 70-77.
- [15] A. Poursaeed, Corrosion protection methods of steel in concrete, in: *Corrosion of Steel in Concrete Structures*, Elsevier, 2016, pp. 241-248.
- [16] D.R. Lankard, N.G. Thompson, M. Yunovich, Procedures for evaluating corrosion-inhibiting admixtures for structural concrete, (2000).
- [17] C. Venkatesh, S.K. Mohiddin, N. Ruben, Corrosion Inhibitors Behaviour on Reinforced Concrete—A Review, in: B.B. Das, N. Neithalath (Eds.) *Sustainable Construction and Building Materials*, Springer Singapore, Singapore, 2019, pp. 127-134.
- [18] A. Zomorodian, R. Bagonyi, A. Al-Tabbaa, The efficiency of eco-friendly corrosion inhibitors in protecting steel reinforcement, *Journal of Building Engineering*, 38 (2021) 102171.
- [19] M.L.S. Rivetti, J. Netto, M.A. Junior, D.V. Ribeiro, Corrosion inhibitors for reinforced concrete, in: *Corrosion inhibitors, principles and recent application*, IntechOpen, 2018, pp. 1-25.

- [20] M. Büchler, 7 - Corrosion inhibitors for reinforced concrete, in: H. Böhni (Ed.) Corrosion in Reinforced Concrete Structures, Woodhead Publishing, 2005, pp. 190-214.
- [21] H. Böhni, Corrosion in reinforced concrete structures, Woodhead Publishing, Cambridge, England, 2005.
- [22] C. Hansson, L. Mammoliti, B. Hope, Corrosion inhibitors in concrete—part I: the principles, Cement and concrete research, 28 (1998) 1775-1781.
- [23] K.-Y. Ann, H. Jung, H. Kim, S. Kim, H.Y. Moon, Effect of calcium nitrite-based corrosion inhibitor in preventing corrosion of embedded steel in concrete, Cement and concrete research, 36 (2006) 530-535.
- [24] G. De Schutter, L. Luo, Effect of corrosion inhibiting admixtures on concrete properties, Construction and Building Materials, 18 (2004) 483-489.
- [25] M.C. Brown, Assessment of commercial corrosion inhibiting admixtures for reinforced concrete, in, Virginia Tech, 1999.
- [26] M.C. Brown, R.E. Weyers, M.M. Sprinkel, Effect of corrosion-inhibiting admixtures on material properties of concrete, Materials Journal, 98 (2001) 240-250.
- [27] C.K. Nmai, S.A. Farrington, G. Bobroski, Organic-based corrosion-inhibiting admixture for reinforced concrete, Concrete International, 14 (1992) 45-51.
- [28] M. Allyn, G.C. Frantz, Corrosion tests with concrete containing salts of alkenyl-substituted succinic acid, Materials Journal, 98 (2001) 224-232.
- [29] Z. Heren, H. Ölmez, The influence of ethanolamines on the hydration and mechanical properties of Portland cement, Cement and Concrete Research, 26 (1996) 701-705.
- [30] T.A. Söylev, M. Richardson, Corrosion inhibitors for steel in concrete: State-of-the-art report, Construction and Building Materials, 22 (2008) 609-622.

- [31] K. Wang, D.E. Nelsen, W.A. Nixon, Damaging effects of deicing chemicals on concrete materials, *Cement and Concrete Composites*, 28 (2006) 173-188.
- [32] X. Shi, M. Akin, T. Pan, L. Fay, Y. Liu, Z. Yang, Deicer impacts on pavement materials: Introduction and recent developments, *The Open Civil Engineering Journal*, 3 (2009).
- [33] H.U. Sajid, A. Jalal, M. Abdullah-Al-Rahim, R. Kiran, A Survey of Effects of Deicing Materials on Properties of Cement-based Materials, in, (Manuscript Under Review), 2021.
- [34] ASTM International, ASTM C109/C109M-16a Standard Test Method for Compressive Strength of Hydraulic Cement Mortars (Using 2-in. or [50-mm] Cube Specimens), in, ASTM International, West Conshohocken, PA, 2016.
- [35] X. Shi, L. Fu, Sustainable winter road operations, Wiley Online Library, 2018.
- [36] C. Giebson, K. Seyfarth, J. Stark, Influence of acetate and formate-based deicers on ASR in airfield concrete pavements, *Cement and Concrete Research*, 40 (2010) 537-545.
- [37] J.M. Silva, S.M. Cramer, M.A. Anderson, M.I. Tejedor, J.F. Muñoz, Concrete microstructural responses to the interaction of natural microfines and potassium acetate based deicer, *Cement and concrete research*, 55 (2014) 69-78.
- [38] Z. Liu, W. Hansen, Freezing characteristics of air-entrained concrete in the presence of deicing salt, *Cement and Concrete Research*, 74 (2015) 10-18.
- [39] H. Lee, R.D. Cody, A.M. Cody, P.G. Spry, Effects of various deicing chemicals on pavement concrete deterioration, in: Center for Transportation Research and Education (Ed.), *Mid-Continent Transportation Symposium Proceedings*, Iowa State University, Ames, USA, Citeseer, 2000, pp. 151-155.

- [40] Z. Liu, Frost Deterioration in Concrete Due to Deicing Salt Exposure: Mechanism, Mitigation and Conceptual Surface Scaling Model, in, 2014.
- [41] J. Cao, A study of effects of a new agricultural-based deicer on the properties of pavement concrete, Master's thesis. Iowa State University, (2014).
- [42] Y. Farnam, H. Todak, R. Spragg, J. Weiss, Electrical response of mortar with different degrees of saturation and deicing salt solutions during freezing and thawing, *Cement and Concrete Composites*, 59 (2015) 49-59.
- [43] R.D. Cody, A.M. Cody, P.G. Spry, G.-L. Gan, Experimental deterioration of highway concrete by chloride deicing salts, *Environmental & Engineering Geoscience*, 2 (1996) 575-588.
- [44] M. Santagata, M. Collepardi, The effect of CMA deicers on concrete properties, *Cement and Concrete Research*, 30 (2000) 1389-1394.
- [45] Y. Lee, S. Lim, H. Lee, Chloride Resistance of Portland Cement-Based Mortar Incorporating High Aluminate Cement and Calcium Carbonate, *Materials*, 13 (2020) 359.
- [46] S. Cheng, Z. Shui, X. Gao, J. Lu, T. Sun, R. Yu, Degradation progress of Portland cement mortar under the coupled effects of multiple corrosive ions and drying-wetting cycles, *Cement and Concrete Composites*, 111 (2020) 103629.

12. SOY-PROTEIN AND POLYOL-BASED COATINGS FOR MITIGATING CORROSION IN REINFORCED CONCRETE STRUCTURES¹¹

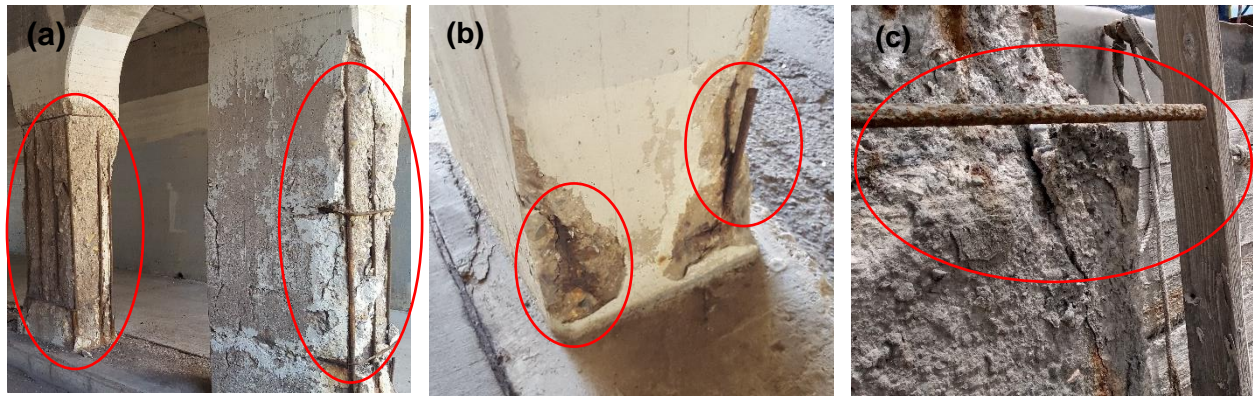
This chapter discusses the synthesis and corrosion performance characterization of soy protein-based coatings for mitigating corrosion in RC structures. The contents of this chapter have been published in Sajid, H.U., Kiran, R., and D.S. Bajwa. 2021. 11. Soy-protein and polyol-based coatings for mitigating corrosion in reinforced concrete structures. *Construction and Building Materials*, (Accepted).

12.1. Introduction

Chloride-induced corrosion serves as a significant hazard that can hamper the functionality, serviceability, and lifespan of reinforced concrete structures. The alkalinity in the concrete environment promotes the formation of a passive protective layer on steel rebars in concrete that protects the rebar from corrosion. However, the loss of alkalinity or the penetration of chloride ions from chloride-based deicers damages the passive layer and accelerates corrosion in the rebars. Chloride-induced corrosion, which is primarily driven by the usage of chloride-based deicers [1-3], thus leads to the deterioration of the reinforced concrete structures (e.g., reinforced concrete pavements, bridge decks, piers, etc.). The corrosion-induced deterioration in RC structures is manifested in the form of concrete spalling, delamination, cracking, and eventual reduction in the serviceability and load-carrying capacity of the RC structures. Typical corrosion-induced distress observed in the RC structures in the Midwest region of the U.S. is depicted in Figure 12.11 for different types of RC structures. Figure 12.1(a) shows the columns of an RC railroad bridge that suffered extensive steel rebar corrosion that led to spalling and

¹¹ This chapter was co-authored by H.U. Sajid, R. Kiran, and D.S. Bajwa. H.U. Sajid had the primary responsibility of preparing the specimens, conducting all tests, and drafting this chapter. R. Kiran supervised the research and revised this chapter.

delamination. Similar corrosion-induced deterioration (corroded rebars, spalling, and delamination) is noticed in the RC column and RC wall in Figure 12.1(b) and Figure 12.1(c), respectively. While RC structures typically have decades of service life, signs of active corrosion are usually noticed in RC bridges after 5-10 years of construction. The RC bridge decks located in the U.S. snow-belt states with a 1.5-inch concrete cover usually exhibit signs of active corrosion (rust stains and concrete spalling) in around 7-10 years after construction [4]. Such bridge decks usually require repair and rehabilitation around 20 years after their construction [4]. Some surveys show that in 70-90% of cases, the premature deterioration in RC structures is linked with corrosion [5]. Old RC bridge decks and pavements may become more vulnerable to chloride-induced corrosion due to the presence of minor cracks and formation of initial corrosion sites that lead to cracking and spalling and thus promote the ingress of chloride ions that can accelerate the corrosion in steel rebars. The corrosion vulnerability of older RC bridges is further exacerbated by the fact that 42% of all bridges in the U.S. (617,000 bridges) are at least 50 years old [6]. Chloride-induced corrosion, which is primarily driven by the usage of deicing salts, remains a major financial burden for bridge owners and departments of transportation as expensive and frequent repairs are usually required to protect the reinforced concrete bridge decks and pavements from corrosion and subsequent deterioration. The annual direct cost of highway bridge corrosion in the U.S. is estimated to be \$13.6 billion [7].



Railroad Bridge, Minnesota

Railroad Bridge, Minnesota

Pump House, Wyoming

(Excessive corrosion and corrosion-induced deterioration in RC structures)

Figure 12.1. Examples of corroded reinforced concrete structures in the U.S. Midwest region: (a,b) corroded rebars, excessive delamination, and spalling in the RC columns of a railroad bridge (MN, USA), and (c) delamination, spalling and corroded rebar in a pump house in a powerhouse (WY, USA).

To mitigate corrosion and its deleterious effects in RC structures, different prevention strategies are employed. The corrosion prevention measures in RC structures are guided by two basic principles: (1) prevent the reaction between the chloride ions and steel rebar by forming a barrier between the chloride ions and steel surface, and (2) prolong the time needed for the chloride ions to penetrate the concrete and thus delay the initiation of corrosion reaction in RC structures. The most common corrosion prevention measures in the RC industry include the use of coatings [4, 8-11] (e.g. epoxy coatings, galvanizing, copper cladding, etc.), surface treatment [12-14] (e.g. sandblasting, water immersion, etc.), corrosion-inhibitor based deicers [1, 15-17] (e.g. agro-based deicers), admixed and migratory corrosion inhibitors for concrete [18-25] (e.g. nitrites, amines, alkanolamines, and propriety blends, etc.), cathodic protection [26-28], corrosion-resistant rebars [29-31], and using concrete with supplementary cementitious materials [29, 32] (e.g. silica fume, fly ash, and blast furnace slag, etc.). Among, these corrosion prevention techniques, the coatings for rebars and the use of corrosion inhibitors are among the

popular techniques in RC structures due to their effectiveness and ease of usage. The commonly employed coatings in steel rebars are discussed in the next section.

12.2. Coatings for Steel Rebars and the Potential of Soybean-Based Coating Material

The rebar coating industry currently uses four types of coating technologies that are recognized by ASTM International and Concrete Reinforcing Steel Institute (CRSI). These include epoxy-coated rebars (ASTM A775, A884, A934) rebars, galvanized rebars (ASTM A767), dual-coated rebars (ASTM A1055), and vinyl-coated (ASTM A933) [9]. Among these coatings, epoxy-coating is the most widely used coating in North America. Approximately 10% of all reinforcing bars in North America are estimated to be coated. As per the 2011 National Bridge Inventory, more than 74,097 bridge decks in the U.S. are constructed using epoxy-coated rebars. Epoxy-coated rebars commonly employ fusion-bonded epoxy (FBE) coating. The epoxy coatings provide a barrier system that insulates the steel rebars from the chloride ions and water molecules and thus ensures a significant delay in the initiation of corrosion in rebars. The FBE coatings are linked with the improved corrosion resistance of steel rebars and lead to an overall increase in delaying the initiation of corrosion in rebars [4, 9, 11]. Many field observations of bridges with epoxy-coated rebars showed delayed initiation of corrosion. Despite their largely satisfactory performance, there have been instances of premature corrosion in the FBE coated rebars in bridges as early as 7 years after construction [4, 9, 11]. The premature corrosion in epoxy-coated rebars is commonly attributed to the defects in the coating that occur during fabrication, handling, and transportation of rebars, and vibration during concreting. The presence of defects and their ability to trigger localized corrosion and subsequent pitting is one of the main disadvantages of the epoxy coatings apart from their additional development requirement for rebars in concrete. Rebar epoxy coatings (such as FBE) are made of constituents that are

declared carcinogenic by environmental protection agencies and many such types of coatings are being banned in many countries. To prevent the early defects in the epoxy coating rebars, different researchers have investigated the performance of the epoxy coatings that are modified with different nano and micro materials such as graphene [33], carbon nanotubes [34], silica [35], and nano clay [36]. While these modifications improved corrosion resistance and integrity of the epoxy coatings, the high cost of the modified epoxy coatings remains a barrier to their large-scale commercial usage. Moreover, the toxicity and environmental concerns of the modified epoxy coatings remain at large. In this regard, coatings synthesized from plant-based materials present an effective and sustainable solution to overcome the problems associated with epoxy coatings. While many plant-derived materials have been investigated for their corrosion inhibition performance in corrosive media [36], only a few studies have explored the potential of plant-derived materials in the preparation of bio-based coatings for steels [37-39]. While the plant extracts-based coatings exhibited promising anticorrosion performance, their large-scale availability remains a major barrier in their application in infrastructure. For successful implementation of a bio-based coating in infrastructural applications, the based material needs to be abundantly available and they must exhibit desirable anticorrosion performance. In this regard, soybean, an abundantly available agricultural commodity in the U.S., presents an attractive alternative for preparing bio-based coatings. Soy-based products (specifically, the products derived from soybean oil) have shown promising corrosion inhibition in the recently conducted investigations. Moreover, soy protein has excellent adhesion properties and have been used as a wood adhesive by partially or fully replacing the formaldehyde-based wood adhesives [40, 41]. The current study is focused on investigating the corrosion protection of soy protein-based coatings. Specifically, soy protein coatings are synthesized from the soy protein isolate,

the protein-rich component of the soybean. The objective of this study is the synthesize and characterize the physical and chemical properties, and corrosion prevention performance of the soy protein coatings that can be used for in-situ application in old RC structures to fix the damaged epoxy coated rebars and thus improve the corrosion resistance of the rebars. The detailed experimental procedure and the characterization techniques employed for understanding the chemical and physical characteristics and corrosion prevention performance of the proposed soy protein coatings are discussed in the subsequent sections.

12.3. Experimental Procedure

This section describes the synthesis process of soy protein coatings and the experimental techniques that are employed for characterizing the physical and chemical characteristics of the soy protein coatings. This section further describes the corrosion performance evaluation of the soy protein coatings.

12.3.1. Soy Protein Isolate

Soy protein isolate is obtained from a commercial supplier and has 90% protein content as per the supplier-provided product sheet. SPI is a mixture of different proteins that are categorized into four protein classes based on their sedimentation coefficients 2S (polypeptides), 7S (β -conglycinin), 11S (glycinin), and 15S (dimer of glycinin) [41, 42]. Among these categories, 7S (β -conglycinin) and 11S (glycinin) constitute 35% and 52% of the SPI protein content, respectively [41, 42]. Thus, together these protein categories account for more than 80 wt% of SPI protein. 7S and 11S components are further composed of about 20 different amino acids combinations each of which has functional groups (such as -OH, -COOH, etc.) attached to the polypeptide chains of the protein molecule. Unfolding protein chains and exposing these

functional groups via chemical modification dictate the mechanical and chemical properties of the SPI-based coatings.

12.3.2. Synthesis of Soy-Based Coatings

Soy protein coatings are prepared by using soy protein isolate (SPI, the protein-rich component of soybean with 90% protein content) as a base material and food-grade sorbitol as a plasticizing agent. Both the ingredients are obtained from a commercial supplier. Additionally, 1N NaOH solution is prepared for denaturing the SPI mixture. The SPI concentrations in the soy protein coating formulations ranged from 5% to 15% (%wt. of deionized water). Moreover, each soy protein coating formulation further included 10%, 20%, or 30% of sorbitol (%wt. of SPI). Generally, protein-based films and coatings are brittle and the addition of plasticizers becomes necessary to impart reasonable ductility to the film/coating. To this end, additives with hydrophilic groups (e.g. glycol, sorbitol, etc.) are commonly used as plasticizers in edible coatings [43, 44]. In this study, sorbitol is used as a plasticizer as it is agro-derived and has corrosion inhibiting properties [1]. The sorbitol plasticizer is limited to 30% as a higher plasticizer content may increase the permeability and decrease the mechanical strength of the resulting SPI coatings.

Soy protein coatings are prepared by mixing SPI in deionized water and stirring for 10 minutes to achieve uniform dispersion of soy protein in water. Sorbitol plasticizer is then added to the aqueous soy protein mixture in varying concentrations (10%, 20%, 30% wt. of soy protein isolate) and stirred for further 20 minutes. The pH level of the resulting soy protein mixture is then adjusted to 12 by adding 1N NaOH solution to achieve denaturing of soy protein. Denaturing helps unfold the protein chains and expose the functional groups that can lead to improved adhesion and higher water resistance (improved barrier properties) [40, 41] The soy

protein mixture with adjusted pH level is then placed on an orbital shaker set at 210 rpm and 45 °C for 4 hours. The high-temperature treatment can aid the denaturing process. The coatings are cured at a temperature of 40 °C for 48 hours. The resulting soy protein coating material is stored at 5 °C before application on rebars. The soy protein coating synthesis process is depicted in Figure 12.2. In total, 12 soy protein coating formulations are prepared that include 4 combination each (0%, 10%, 20%, 30% Sorbitol) for 5%, 10%, and 15% SPI coatings. The synthesized coatings are labeled as S-#-*\$ where S refers to Soy Protein, # refers to wt.% of SPI isolate in deionized water, * refers to the pH level (alkalinity) of the soy protein suspension, and \$ denotes the sorbitol weight in the mixture as a function of SPI. For instance, specimen S-5-12-20 has 5% SPI, a pH level of 12, and 20% wt. (% SPI) of sorbitol.

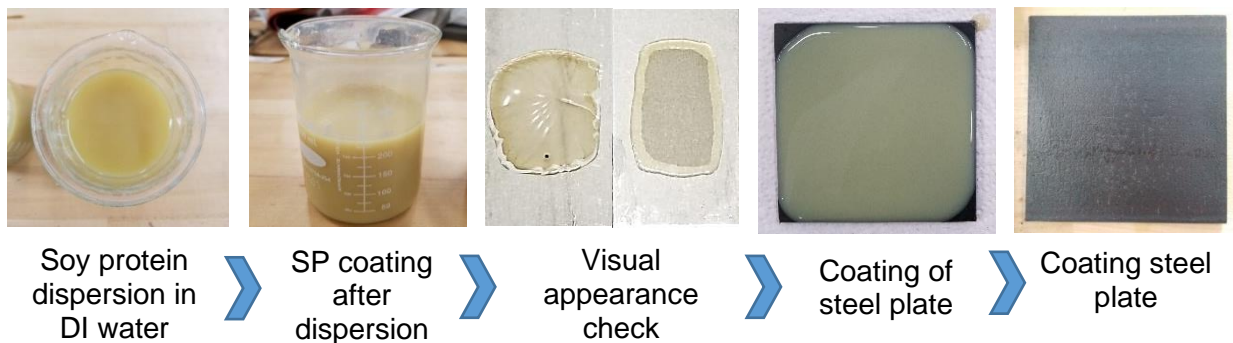


Figure 12.2. Typical workflow for each soy protein coating formulation trial.

12.3.3. Physical and Chemical Characterization Tests

Physical and chemical characteristics of each class of soy protein coatings are determined by conducting visual brittleness tests, viscosity tests, abrasion resistance tests, and Fourier transform infrared (FTIR) spectroscopy. The visual brittleness tests are conducted to evaluate the apparent brittleness or ductility of the cured soy protein coatings. For this purpose, soy protein coatings are applied on steel plates and are kept at 30°C for 48 hours for drying. The surface of the dried coating is then visually monitored for determining the apparent brittleness of the cured

soy protein coatings. For determining the abrasion resistance of the cured coatings, abrasion resistance tests are conducted using Falling Sand Abrasion Tester using the procedure specified in ASTM D968 [45]. The Falling Sand Abrasion Tester is shown in Figure 12.3. For determining the abrasion resistance of the soy protein coatings, soy protein-coated steel panels are subjected to silica abrasants from an 8-inch diameter sand reservoir via a guide tube. The soy protein-coated steel panels are placed at 45°. Silica particles are continuously pinged on the coated steel panel until 4-mm diameter of the substrate becomes visible as the coating worn off the steel substrate. The viscosity tests are performed to determine the consistency and workability of the soy protein coatings containing varying amounts of SPI and Sorbitol plasticizer. The viscosities of soy protein coatings are determined using HAAKE Viscotester® 550. HAAKE viscotester® 500 consists of a standard cylindrical spindle and the data acquisition (DAQ) system that measures and records the shear stress and shear rate of a given fluid (see Figure 12.4). The detailed procedure for viscosity determination can be found elsewhere [3]. Finally, the chemical bonds and functional groups that are present in the cured soy protein coatings are determined using FTIR tests. The FTIR spectra of each coating formulation are determined using Thermo Scientific Nicolet 8700 Fourier Transform Infrared Spectrometer. A spectral range of 4000-600 cm^{-1} is adopted in the FTIR tests.

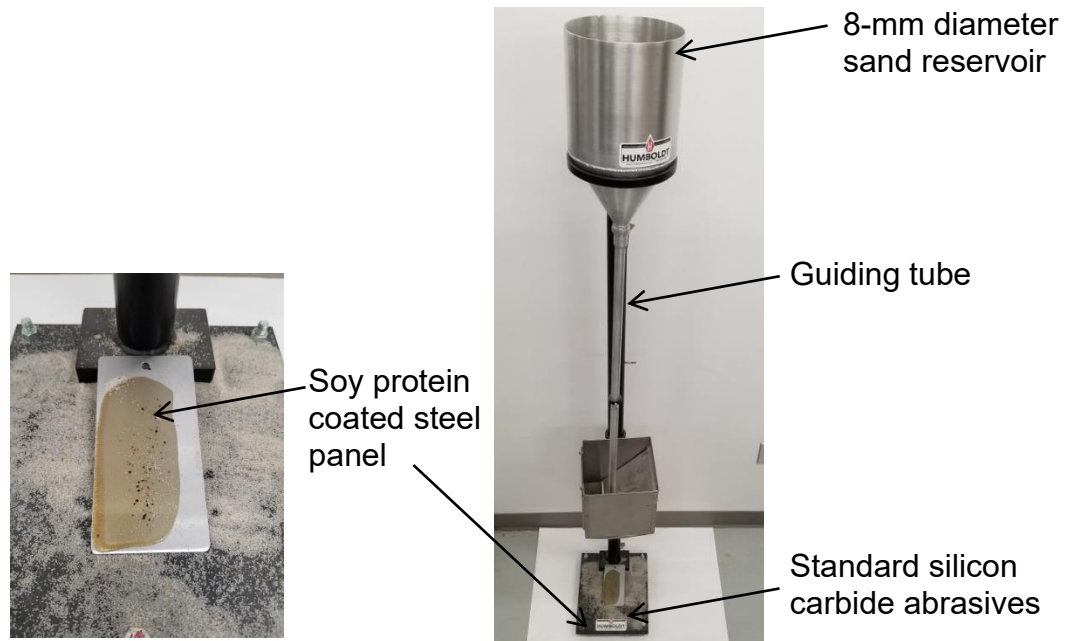


Figure 12.3. Falling Sand Abrasion Tester for determining the abrasion resistance of the soy protein-coated steel panels.

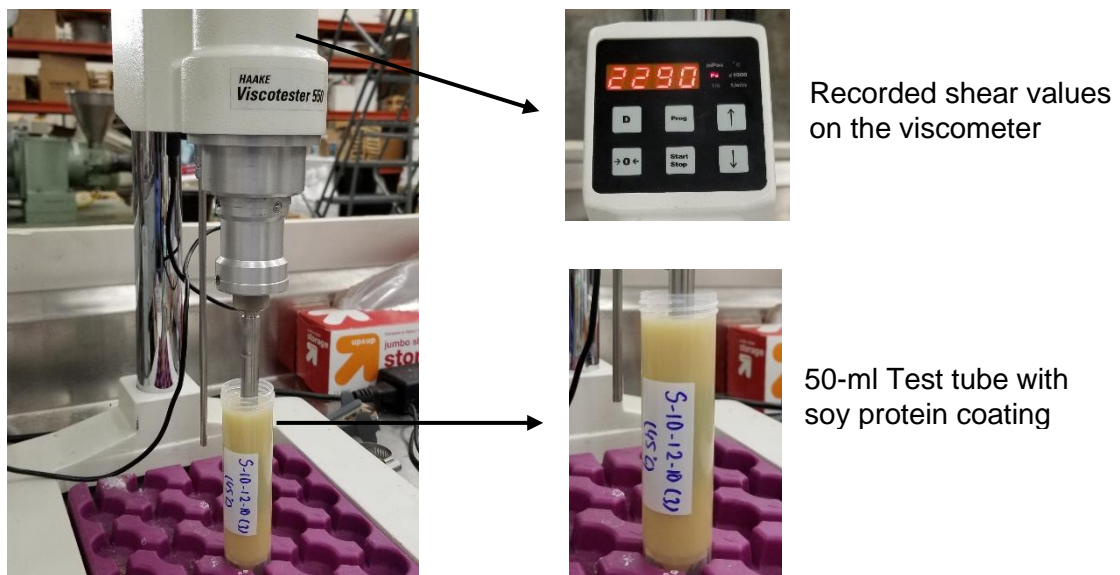


Figure 12.4. Viscosity test setup.

12.3.4. Corrosion Performance Characterization

The corrosion potential and corrosion rates of embedded rebars that are coated with polyol-based coatings are determined using rapid macrocell tests. For this purpose, a rapid

macrocell test setup is built using the procedures specified in the Strategic Highway Research Program (SHRP) manual. The rapid macrocell test setup consists of two containers with concrete pore solutions and the presence of sodium chloride (NaCl) in one solution, one rebar sample in one of the containers which act as an anode, two rebar samples immersed in the second container that acts as a cathode, and an electrical pathway between the anode and the cathode. The test setup is illustrated in Figure 12.5. Concrete pore solution for anodic and cathodic containers is prepared by mixing 974.8 g of distilled water, 18.81 g of potassium hydroxide (KOH), and 17.87 g of sodium hydroxide (NaOH) for preparing 1 L solution. Moreover, 15% of sodium chloride is added to the anodic container. Before immersing rebar specimens in the containers, specimens are thoroughly cleaned and degreased using acetone solution and air-dried. The rebar samples are then dip-coated with two coats of polyol-based soy protein coatings for 48 hours (see Figure 12.6). A period of 24 hours is adopted per coat for curing at 45°C. The coated rebar specimens are then embedded in 1:4 ordinary Portland cement mortar that is prepared using a 0.4 w/c ratio and about 6% air entrainment in the mix (see Figure 12.7). After curing for 14 days, the mortar-cladded rebar samples are dried for 24 hours and immersed in the containers (3-inch immersion depth for rebars). The voltage drop and subsequent corrosion rates across the embedded rebar specimens are then monitored for 120 days.

In addition to rapid macrocell corrosion tests, potentiodynamic polarization tests are also conducted herein to determine the corrosion current densities and corrosion rates. For this purpose, double-coated rebar specimens and coated panels are prepared using each of the coating formulations. Potentiodynamic polarization tests are then formed on the specimens using a standard 3-electrode electrochemical cell which included the coated specimens as working electrode, saturated calomel as reference electrode, stainless steel wire mesh as a counter

electrode. During potentiodynamic polarization tests, the potential of the working electrode (coated specimen) is varied from cathodic to the anodic direction (anodic scan) within a range of ± 500 mV with reference to the steady-state potential at a scanning rate of 2 mV/s. Tafel analysis is then performed on the polarization curves to obtain corrosion current densities and corrosion rates.

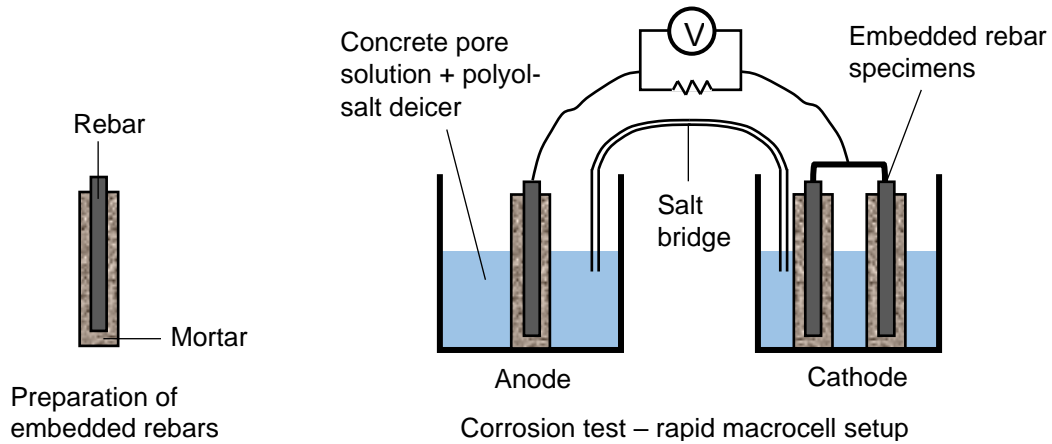


Figure 12.5. Schematic of macrocell corrosion test setup.

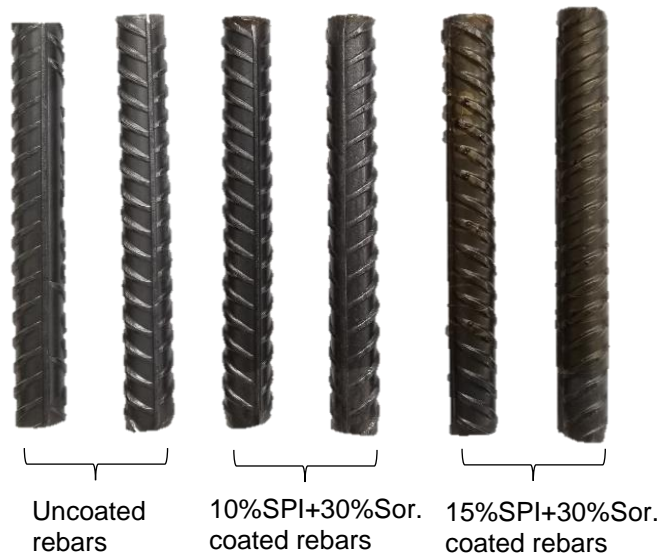


Figure 12.6. Uncoated (control) rebars and 10% and 15% soy protein-coated rebar specimens.

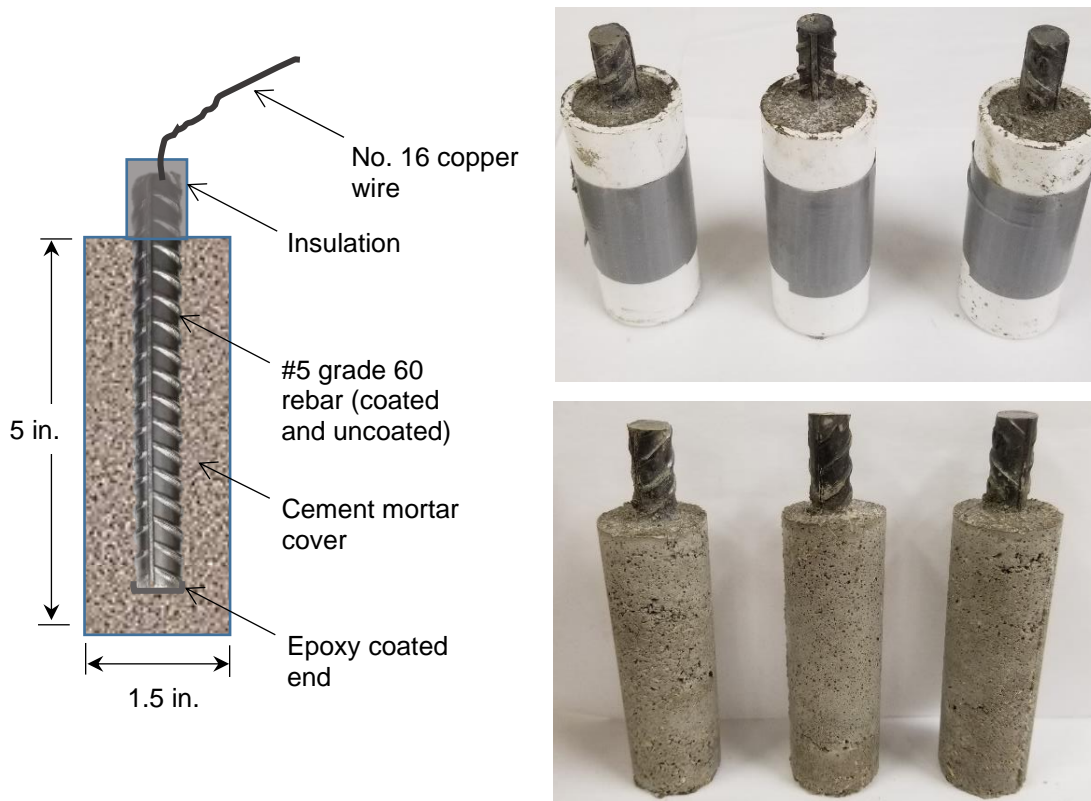


Figure 12.7. Rapid macrocell corrosion test specimens preparation (uncoated and coated rebars embedded in cement mortar).

12.4. Results and Discussion

This section discusses the physical and chemical characteristics of the soy protein coatings that are synthesized in this study. Moreover, the corrosion protection performance of the coatings, which is obtained from potentiodynamic polarization tests and rapid macrocell tests, is further discussed in this section.

12.4.1. Visual Brittleness of Cured Soy Protein Coatings

The brittleness of the hardened soy protein coating is qualitatively assessed based on visual observation of the specimens. For this purpose, the soy protein coatings corresponding to each coating formulation (wt.% of SPI and wt.% of Sorbitol) are spread on mild steel plates and then cured for 48 hours, as discussed in Section 12.3.2. The cured coatings are then observed visually and the photograph of each coating is provided in Figure 12.8. As observed in Figure

12.8, the coatings with 0% Sorbitol plasticizer is visibly brittle regardless of the wt.% of SPI in the coating. However, the addition of Sorbitol plasticizer is observed to significantly decrease the brittleness in the coatings. The highest improvement in the integrity (non-brittleness) is noted in the coatings corresponding to 30% Sorbitol content.

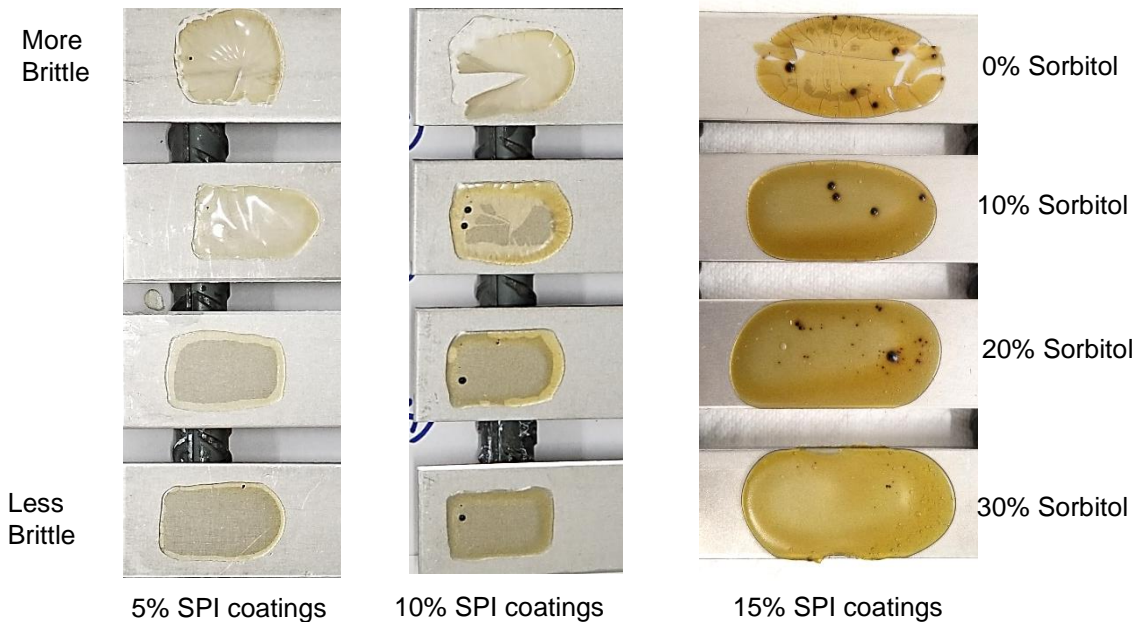


Figure 12.8. Visual brittleness of soy protein coatings with different concentrations of sorbitol.

12.4.2. Viscosities of Soy Protein Coatings

The viscosity tests are performed to determine the consistency and workability of the soy protein coatings containing varying amounts of SPI and Sorbitol plasticizer. The results obtained from the viscosity tests are provided in Figure 12.9. As observed in Figure 12.9, the viscosities for 5% SPI coatings ranged from 1.15 m.Pa.s (corresponding to 30% sorbitol) to 1.43 m.Pa.s (corresponding to 0% Sorbitol in coating). The increase in the concentration of SPI in the coatings is observed to increase the viscosities of the coating formulations. In the case of 10% SPI coatings, the viscosities are observed to be in the range of 6.00-6.80 m.Pa.s. Similarly, the viscosities are observed to further increase in the case of 15% SPI coatings wherein viscosities

are observed to be 24.8-26.4 m.Pa.s. It is further observed that the increase in the concentration of Sorbitol plasticizer in the coatings resulted in a minor reduction in their viscosities. These results showed that the 5% and 10% SPI coatings can be directly applied on the cracked concrete surface and hence can reach the rebar by virtue of their low viscosity. However, the 15% SPI coatings formulations need to be applied on the rebar surface directly for achieving desirable corrosion protection.

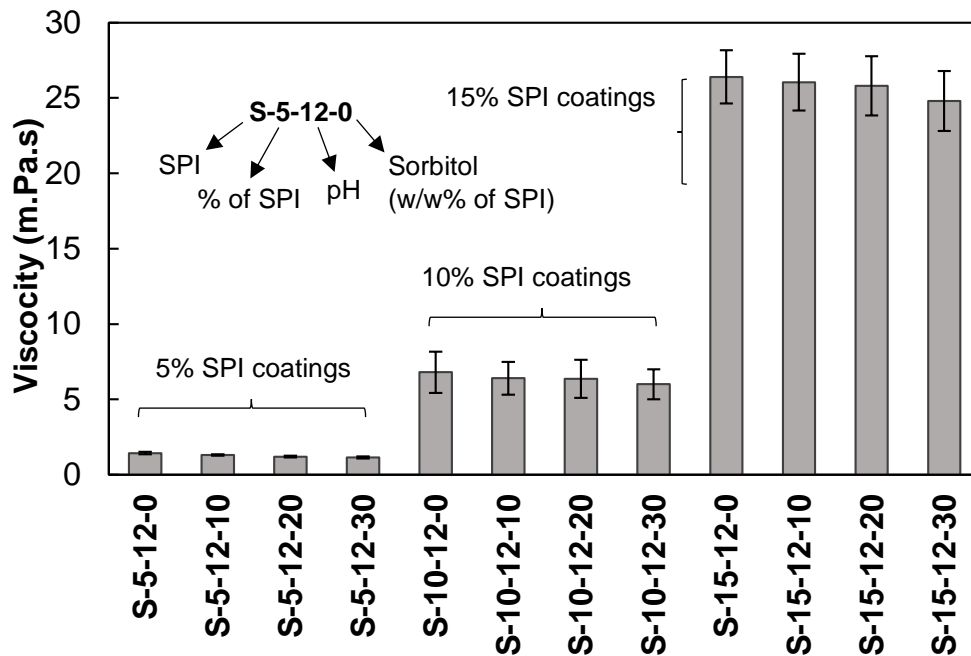


Figure 12.9. Viscosities of soy protein coatings with different concentrations of sorbitol.

12.4.3. Abrasion Resistance of Soy Protein Coatings

The abrasion resistance of the soy protein coatings is determined using the Falling Sand Abrasion Test method that was previously discussed in Section 12.3.3. The abrasion resistance of the coatings, reported in terms of volume of sand per mil of coating (L/min), is provided in Figure 12.10. As observed in Figure 12.10, the soy protein coatings with 5% SPI content have the least abrasion resistance, and the coating detached from the steel substrate during the initial impingement of sand abrasives. On the other hand, coatings with 10% and 15% SPI content

exhibited substantial abrasion resistance. The abrasion resistance of the soy protein coatings studied herein ranged between 6-142 L/mil. In the absence of sorbitol plasticizer, the coatings had poor abrasion resistance regardless of the SPI content. However, the addition of sorbitol plasticizer substantially increased the abrasion resistance of the coatings. The highest abrasion resistance is noted in the case of 10% and 15% SPI coatings with 30% sorbitol content. This shows that soy protein coatings with an appropriate amount of sorbitol coatings have adequate abrasion resistance for in-situ application.

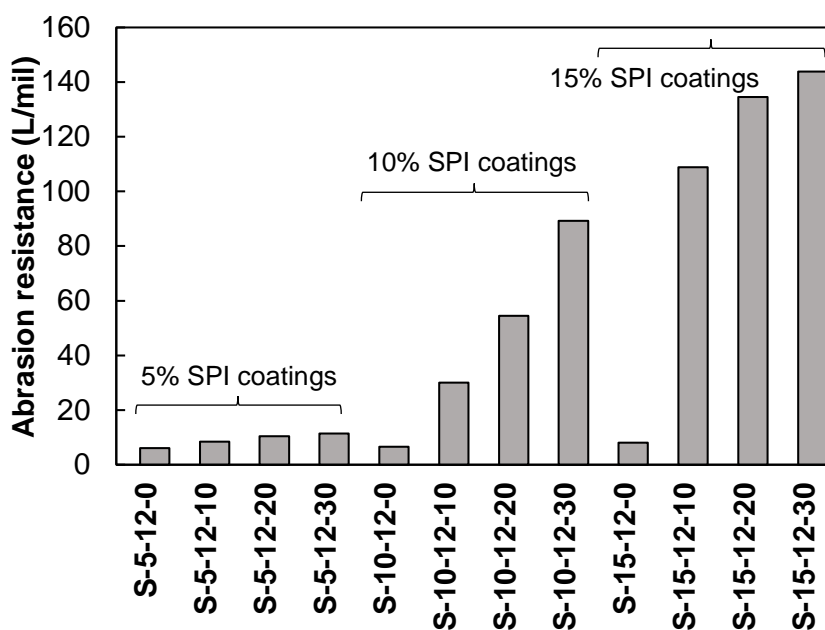


Figure 12.10. Abrasion resistance of soy protein coatings with different concentrations of sorbitol.

12.4.4. FTIR Results

The functional groups present in the cured soy protein coating materials are determined using Fourier transform infrared spectroscopy (FTIR). The FTIR spectra for the cured polyol soy protein coatings are provided in Figure 12.11. As shown in Figure 12.11, peaks corresponding to various stretching vibrations (such as O-H, N-H, C-H, C-O, C=O) are observed that indicate the presence of different functional groups (hydroxyl, amid, methyl, methylene, secondary amide,

and carboxyl group). Almost identical functional groups are observed in all coatings. The FTIR spectra at the medium range show peaks corresponding to Amide I ($1720\text{-}1600\text{ cm}^{-1}$) and Amide III ($1400\text{-}1200\text{ cm}^{-1}$) band patterns which show the unfolding of secondary structures in the soy protein. Moreover, it is observed that the -OH functional group almost vanished in the case of 15% SPI coatings. The presence of the observed functional groups in the FTIR spectra of the coatings exhibits the successful alkali modification of the soy protein mixture. Moreover, the disappearance of the hydrophilic groups (such as hydroxyl and carboxyl) in the spectra corresponding to the 15% SPI coatings shows that the addition of high sorbitol content improved the water-resistance of the cured soy protein coatings besides imparting ductility.

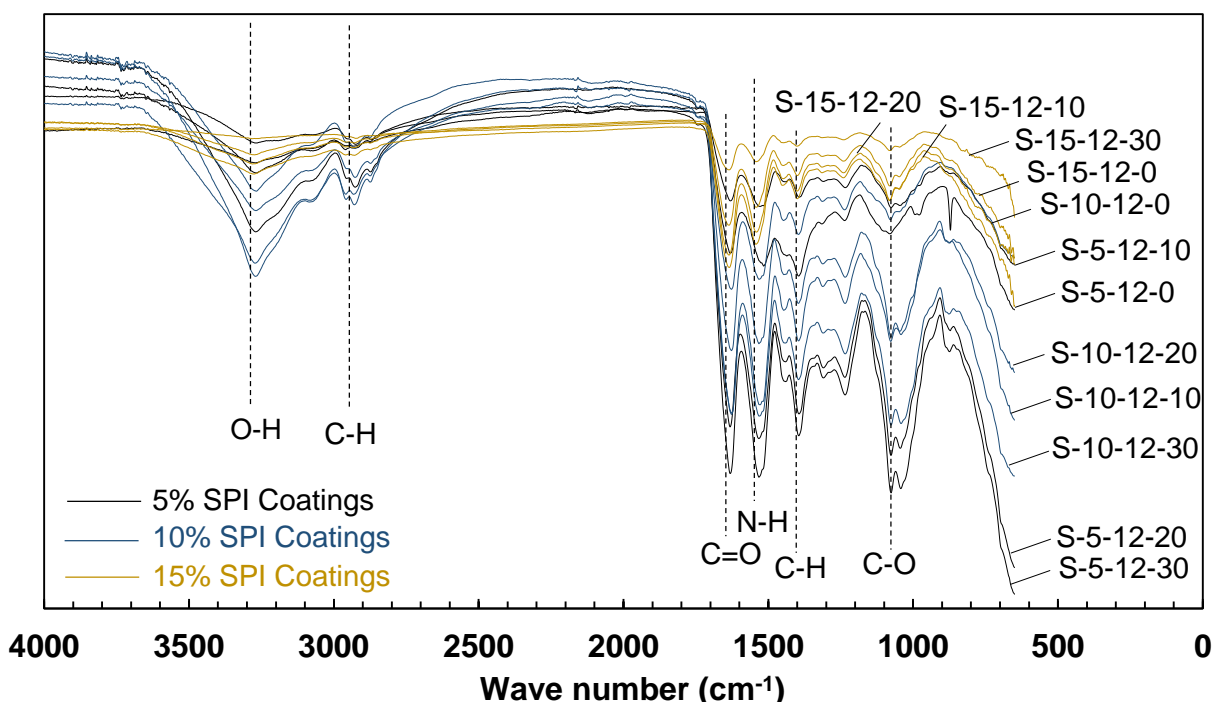


Figure 12.11. FTIR spectra of soy protein coatings with different concentrations of sorbitol.

12.4.5. Corrosion Performance Characterization

The results obtained from physical and chemical characterization tests showed that coating formulations with 5% and 10% SPI content and 30% sorbitol exhibited adequate

ductility and abrasion resistance besides reasonable viscosities and FTIR spectra. Therefore, corrosion performance is evaluated only for two types of coating formulations (S-10-12-30 and S-15-12-30) and bare rebars. The polarization curves obtained from the potentiodynamic polarization tests are provided in Figure 12.12. The Tafel analysis performance on these polarization curves showed that the application of 10% and 15% SPI coatings with 30% Sorbitol plasticizer content can reduce the corrosion current densities and corrosion current rates by 95% when compared to the corrosion current density and corrosion rate of bare steel specimens. To determine the long-term corrosion behavior of the soy protein coatings in the concrete environment, rapid macrocell corrosion tests are conducted for coated rebars. To this end, rapid macrocell corrosion tests are conducted using the procedure discussed in Section 12.3.4. The macrocell tests are run for 120 days and the corrosion rates incurred in the anodic rebar specimen are evaluated by monitoring the voltage drop between the anodic rebar and cathodic rebar across a 10-ohm resistor (see Figure 12.5). The corrosion rates are determined from the voltage drop values using Faraday's equation which is provided below.

$$\text{Corrosion rate } \left(\frac{\mu\text{m}}{\text{yr}} \right) = K \frac{V \cdot m}{n \cdot F \cdot D \cdot R \cdot A} \quad (12.1)$$

where, K = conversion factor (31.5×10^4), V = voltage drop across the resistor (mV), m = atomic weight of iron (55.8 g/g.atom), n = number of ion equivalents exchanged (for iron, $n = 2$), F = Faraday's constant (96485 coulombs/equivalent), D = density of iron (7.87 g/cm^3), R = resistance of the resistor (10 ohms), A = surface area of the immersed anodic rebar (approximately 39.9 cm^2). The corrosion rates obtained from rapid macrocell corrosion tests are provided in Figure 12.13. As shown in Figure 12.13, cement mortar embedded coated rebar specimens have considerably less corrosion rates as compared to cement mortar embedded bare rebar specimens. In the case of uncoated rebar, the average corrosion rate remained in the

vicinity of 0.25 $\mu\text{m}/\text{yr}$. The application of 10%SPI+ 30% Sorbitol coating on the rebar decreased the average corrosion rates to the range of 0.16 $\mu\text{m}/\text{yr}$. The lowest corrosion rate is observed in the case of 15%SPI+30% Sorbitol coated rebar specimens wherein the corrosion rates mainly hover around 0.12 $\mu\text{m}/\text{yr}$, which is 50% less than the uncoated rebar. These results together with the results obtained from the potentiodynamic polarization tests validate the effectiveness of the soy protein coatings in mitigating corrosion in rebars.

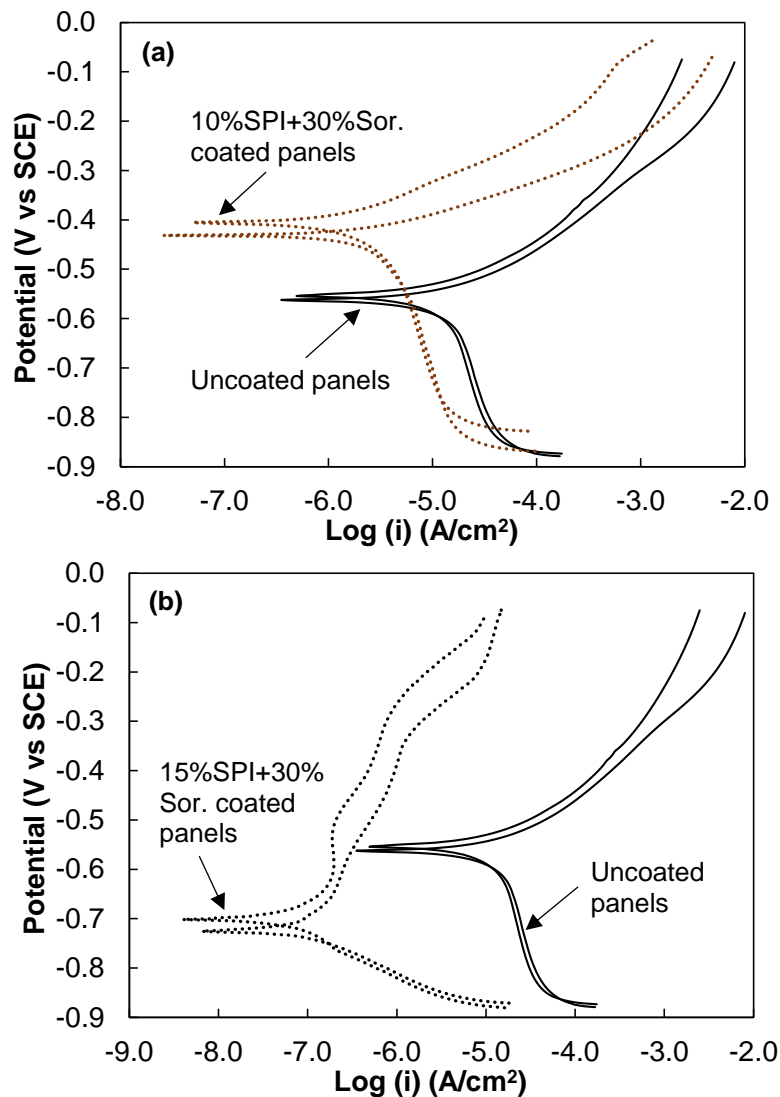


Figure 12.12. Potentiodynamic polarization curves of (a) 10% SPI coated steel panels and (b) 15% SPI coated steel panels, with 30% (w/w% of SPI) sorbitol as a plasticizer.

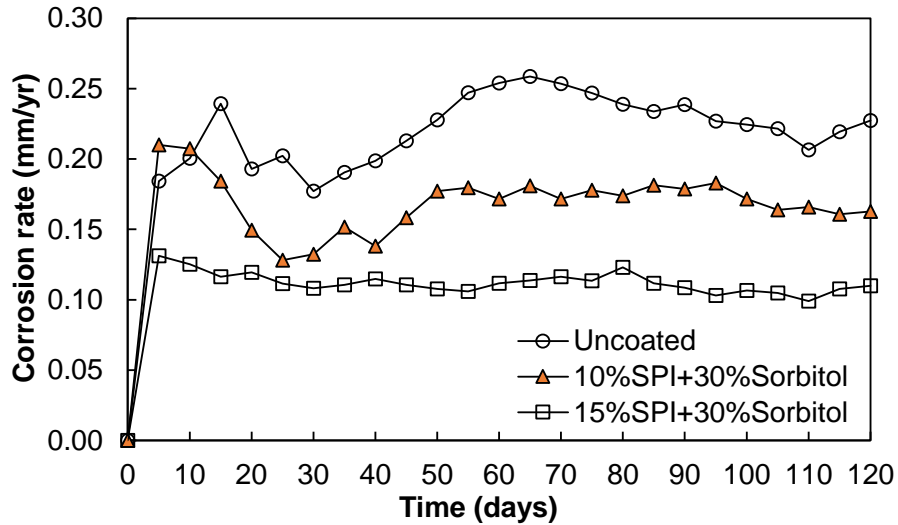


Figure 12.13. Corrosion rates obtained from rapid macrocell corrosion tests for uncoated rebars and soy protein-coated rebars that are embedded in Portland cement mortar.

12.5. Conclusions

The most important conclusion obtained from this study are as follows:

1. Soy protein coatings with 10-15% (% wt. of deionized water) SPI content and 10-30% (% wt. of SPI) Sorbitol content render adequate chemical properties for usage as anticorrosion coating material.
2. The FTIR results showed that heat treatment (45°C for 4 hours) and pH modification via NaOH successfully denatured soy protein dispersion and exposed the functional groups in the soy protein chains that imparted necessary properties for coating adhesion on the surface.
3. The increase in the SPI content in the soy protein coating decreased the viscosity of the soy protein coatings. The average viscosities of soy protein coatings ranged between 2.5-27 m.Pa.s. The addition of sorbitol plasticizer leads to a slight decrease in the viscosities of the soy protein coatings.

4. Soy protein coatings without the inclusion of plasticizers remained highly brittle upon drying regardless of SPI content. The addition of 10-30% sorbitol significantly reduced the visual brittleness in the cured and dried soy protein coatings. The highest decrease in the brittleness is observed corresponding to the soy protein coatings with 10% and 15% SPI content, and 30% Sorbitol.
5. The increase in the concentration of SPI and Sorbitol significantly enhanced the abrasion resistance of the soy protein coatings. The highest abrasion resistance is observed in the case of soy protein coating with 15% SPI and 30% Sorbitol (142 L/mil).
6. The potentiodynamic polarization tests showed that soy protein coatings with 10% or 15% SPI and 30% Sorbitol decreases the corrosion rates by more than 90%. The long-term corrosion rates obtained from the rapid macrocell corrosion rates showed cement mortar embedded rebars that are coated with soy protein coating (15% SPI+30% Sorbitol) incurred 50% less corrosion as compared to uncoated rebar specimens.

These results demonstrated that soy protein coatings have adequate physical and chemical characteristics for use as a supplementary protective coating material in mitigating corrosion in rebars. The proposed coating formulations can be applied in-situ to repair the damaged epoxy-coated rebars and can be used as supplementary coatings for old rebars.

12.6. References

- [1] H.U. Sajid, R. Kiran, X. Qi, D.S. Bajwa, D. Battocchi, Employing corn derived products to reduce the corrosivity of pavement deicing materials, *Construction and Building Materials*, 263 (2020) 120662.
- [2] K. Nilssen, A. Klein-Paste, J. Wåhlin, The effect of additives on the low temperature ice-melting capacity of NaCl, *Transportation research record*, 2672 (2018) 158-166.

- [3] H.U. Sajid, D.L. Naik, R. Kiran, Improving the ice-melting capacity of traditional deicers, *Construction and Building Materials*, 271 (2021) 121527.
- [4] J. Smith, Y.P. Virmani, Materials and methods for corrosion control of reinforced and prestressed concrete structures in new construction, Report No. FHWA-RD-00-081. United States Federal Highway Administration, (2000).
- [5] U.M. Angst, Challenges and opportunities in corrosion of steel in concrete, *Materials and Structures*, 51 (2018) 4.
- [6] ASCE, America's Infrastructure Report Card 2021, American Society of Civil Engineers, (2021).
- [7] NACE International. Highways and Bridges, in, NACE International.
<https://www.nace.org/resources/industries-nace-serves/highways-bridges>. Accessed on June 28, 2021.
- [8] D. Chung, Corrosion control of steel-reinforced concrete, *Journal of Materials Engineering and Performance*, 9 (2000) 585-588.
- [9] D. McDonald, Current Status of Coated Reinforcing Steel, in, *Structure Magazine*.
<https://www.structuremag.org/?p=7545>. Accessed on July 7th, 2021., 2014.
- [10] D.G. Manning, Corrosion performance of epoxy-coated reinforcing steel: North American experience, *Construction and Building Materials*, 10 (1996) 349-365.
- [11] F. Tang, Steel Rebar Coatings for Concrete Structures, in: *Structure Magazine*.
<https://www.structuremag.org/?p=10047>. Accessed on July 7th, 2021., 2016.
- [12] J. Hou, X. Fu, D.D.L. Chung, Improving both bond strength and corrosion resistance of steel rebar in concrete by water immersion or sand blasting of rebar, *Cement and Concrete Research*, 27 (1997) 679-684.

- [13] H.U. Sajid, R. Kiran, Influence of corrosion and surface roughness on wettability of ASTM A36 steels, *Journal of Constructional Steel Research*, 144 (2018) 310-326.
- [14] H.U. Sajid, R. Kiran, Improving the wettability of structural steels by employing ionic liquids, *Journal of Molecular Liquids*, 324 (2021) 115137.
- [15] M. Honarvar Nazari, M.S. Shihab, L. Cao, E.A. Havens, X. Shi, A peony-leaves-derived liquid corrosion inhibitor: protecting carbon steel from NaCl, *Green Chemistry Letters and Reviews*, 10 (2017) 359-379.
- [16] M. Honarvar Nazari, E.A. Havens, A. Muthumani, X. Shi, Effects of processed agro-residues on the performance of sodium chloride brine anti-Icer, *ACS Sustainable Chemistry & Engineering*, 7 (2019) 13655-13667.
- [17] M.H. Nazari, X. Shi, Developing Renewable Agro-Based Anti-Icers for Sustainable Winter Road Maintenance Operations, *Journal of Materials in Civil Engineering*, 31 (2019) 04019299.
- [18] B. Elsener, U. Angst, 14 - Corrosion inhibitors for reinforced concrete, in: P.-C. Aïtcin, R.J. Flatt (Eds.) *Science and Technology of Concrete Admixtures*, Woodhead Publishing, 2016, pp. 321-339.
- [19] C. Page, V. Ngala, M. Page, Corrosion inhibitors in concrete repair systems, *Magazine of Concrete Research*, 52 (2000) 25-37.
- [20] H.-S. Lee, V. Saraswathy, S.-J. Kwon, S. Karthick, Corrosion inhibitors for reinforced concrete: A review, *Corrosion inhibitors, principles and recent applications*, (2018) 95-120.
- [21] V. Saraswathy, H.-W. Song, Improving the durability of concrete by using inhibitors, *Building and environment*, 42 (2007) 464-472.

- [22] H.-W. Song, V. Saraswathy, Analysis of corrosion resistance behavior of inhibitors in concrete using electrochemical techniques, *Metals and Materials International*, 12 (2006) 323-329.
- [23] M. Ormellese, L. Lazzari, S. Goidanich, G. Fumagalli, A. Brenna, A study of organic substances as inhibitors for chloride-induced corrosion in concrete, *Corrosion Science*, 51 (2009) 2959-2968.
- [24] M.I. Prieto, A. Cobo, Á. Rodríguez, M. de las Nieves González, The efficiency of surface-applied corrosion inhibitors as a method for the repassivation of corroded reinforcement bars embedded in ladle furnace slag mortars, *Construction and Building Materials*, 54 (2014) 70-77.
- [25] A. Poursaeed, Corrosion protection methods of steel in concrete, in: *Corrosion of Steel in Concrete Structures*, Elsevier, 2016, pp. 241-248.
- [26] M.M. Cheung, C. Cao, Application of cathodic protection for controlling macrocell corrosion in chloride contaminated RC structures, *Construction and Building Materials*, 45 (2013) 199-207.
- [27] M.-n. Su, L. Wei, J.-H. Zhu, T. Ueda, G.-p. Guo, F. Xing, Combined impressed current cathodic protection and FRCM strengthening for corrosion-prone concrete structures, *Journal of Composites for Construction*, 23 (2019) 04019021.
- [28] N. Krishnan, D.K. Kamde, Z.D. Veedu, R.G. Pillai, D. Shah, R. Velayudham, Long-term performance and life-cycle-cost benefits of cathodic protection of concrete structures using galvanic anodes, *Journal of Building Engineering*, 42 (2021) 102467.
- [29] C. Zhang, F. Zhang, Incorporation of Silicon Fume and Fly Ash as Partial Replacement of Portland Cement in Reinforced Concrete: Electrochemical study on corrosion behavior

- of 316LN stainless steel rebar, *International Journal of Electrochemical Science*, 15 (2020) 3740-3749.
- [30] R. Duarte, A. Castela, R. Neves, L. Freire, M. Montemor, Corrosion behavior of stainless steel rebars embedded in concrete: an electrochemical impedance spectroscopy study, *Electrochimica Acta*, 124 (2014) 218-224.
- [31] G. Ping, S. Elliott, J. Beaudoin, B. Arsenault, Corrosion resistance of stainless steel in chloride contaminated concrete, *Cement and Concrete Research*, 26 (1996) 1151-1156.
- [32] M. Criado, D. Bastidas, S. Fajardo, A. Fernández-Jiménez, J. Bastidas, Corrosion behaviour of a new low-nickel stainless steel embedded in activated fly ash mortars, *Cement and Concrete Composites*, 33 (2011) 644-652.
- [33] S. Nandhini, M. Devasena, Review on graphene oxide composites, *International Journal of Nanomaterials and Nanostructures*, 2 (2016) 24-30.
- [34] Y. Cubides, H. Castaneda, Corrosion protection mechanisms of carbon nanotube and zinc-rich epoxy primers on carbon steel in simulated concrete pore solutions in the presence of chloride ions, *Corrosion Science*, 109 (2016) 145-161.
- [35] A. Afshar, S. Jahandari, H. Rasekh, M. Shariati, A. Afshar, A. Shokrgozar, Corrosion resistance evaluation of rebars with various primers and coatings in concrete modified with different additives, *Construction and Building Materials*, 262 (2020) 120034.
- [36] N. Sharma, S. Sharma, S.K. Sharma, R. Mehta, Evaluation of corrosion inhibition and self healing capabilities of nanoclay and tung oil microencapsulated epoxy coatings on rebars in concrete, *Construction and Building Materials*, 259 (2020) 120278.

- [37] K. Karattu Veedu, T. Peringattu Kalarikkal, N. Jayakumar, N.K. Gopalan, Anticorrosive performance of *Mangifera indica* L. Leaf extract-based hybrid coating on steel, *ACS Omega*, 4 (2019) 10176-10184.
- [38] L. Montoya, D. Contreras, A. Jaramillo, C. Carrasco, K. Fernández, B. Schwederski, D. Rojas, M. Melendrez, Study of anticorrosive coatings based on high and low molecular weight polyphenols extracted from the *Pine radiata* bark, *Progress in Organic Coatings*, 127 (2019) 100-109.
- [39] R.S. Peres, A.V. Zmozinski, F.R. Brust, A.J. Macedo, E. Armelin, C. Aleman, C.A. Ferreira, Multifunctional coatings based on silicone matrix and propolis extract, *Progress in Organic Coatings*, 123 (2018) 223-231.
- [40] X. Zhang, Y. Zhu, Y. Yu, J. Song, Improve performance of soy flour-based adhesive with a lignin-based resin, *Polymers*, 9 (2017) 261.
- [41] X. Ren, M. Soucek, Soya-based coatings and adhesives, in: *Soy-Based Chemicals and Materials*, ACS Publications, 2014, pp. 207-254.
- [42] K. Saio, M. Kamiya, T. Watanabe, Food Processing Characteristics of Soybean 11S and 7S Proteins, *Agricultural and Biological Chemistry*, 33 (1969) 1301-1308.
- [43] N.H. Ullsten, M. Gällstedt, M.S. Hedenqvist, Plasticizers for protein-based materials, *Viscoelastic and Viscoplastic Materials*; El-Amin, M., Ed.; IntechOpen: London, UK, (2016) 81-101.
- [44] N. Shaw, F. Monahan, E. O'riordan, M. O'sullivan, Physical properties of WPI films plasticized with glycerol, xylitol, or sorbitol, *Journal of Food Science*, 67 (2002) 164-167.

[45] ASTM International, ASTM D968 Standard Test Methods for Abrasion Resistance of Organic Coatings by Falling Abrasive, in, ASTM International, West Conshohocken, PA, 2017.

13. SUMMARY, OUTCOMES, AND FUTURE DIRECTIONS

13.1. Summary and Outcomes

This dissertation aimed to characterize and predict the post-fire damage in structural steels in terms of post-fire mechanical properties and to characterize and mitigate corrosion damage in steel and RC structures by coming up with low-cost, non-toxic, and environment-friendly corrosion mitigation techniques. The objectives of this dissertation are accomplished in two phases. The first phase of this dissertation focused on characterizing post-fire damage in structural steels by incorporating important parameters that include stress triaxialities, cooling rates encountered during fire extinguishing, and fire temperature. Moreover, the post-fire damage characterization in this dissertation included the microstructural changes that occur in structural steels after the fire has been extinguished. The post-fire damage in structural steels was quantified in terms of change in the mechanical properties of structural steels that include elastic modulus, yield strength, ultimate tensile strength, ductility (elongation at fracture strain), and uniform strain (elongation at ultimate tensile strength). Furthermore, the fracture surface characteristics of post-fire structural steels were also investigated.

The second phase of this dissertation proposed and validated three non-toxic, low-cost, environment-friendly solutions for mitigating corrosion in steel and RC structures that included 1) surface and wettability alteration of steels for increasing hydrophobicity of exposed steel surfaces and promoting cleaning and lubrication of inaccessible steel surfaces, 2) modification of traditional deicing solution with agro-based corrosion inhibitors that can mitigate corrosion without compromising the ice melting capacity of the deicer, and the properties of Portland cement mortar, and 3) synthesis of soy protein-based coatings for steel rebars that can be used

for in-situ application and repair of damaged coated rebars. The most important outcomes and scientific contributions of this dissertation are summarized below.

1. Post-fire residual factors are obtained for the two most commonly used structural steels (ASTM A36 and ASTM 572) that included the influence of stress concentrations, fire temperatures, and cooling methods.
2. Post-fire mechanical behavior investigations revealed that stress concentration and rapid cooling methods are the two critical parameters that have the highest influence on the post-fire mechanical behavior of commonly employed structural steels.
3. A set of strength-microstructure relationships are proposed for predicting the post-fire mechanical behavior of ASTM A36, ASTM A572, and ASTM A992 structural. These relationships can be used to predict the post-fire tensile strengths of these structural steels when fire temperatures are not known.
4. The results obtained from post-fire microstructural investigations and the proposed microstructural-mechanical property relationships contribute to reliable forensic analysis of collapsed or severely damaged post-fire steel structures.
5. The results obtained from the post-fire damage characterization and prediction investigation improve our current understanding of the mechanical behavior of fire-affected steel structures and have the potential to change the current code provisions relevant to the post-fire appraisal of steel structures and performance-based fire engineering of steel structures.
6. A new surface treatment-based corrosion mitigation technique that does not require the use of toxic chemicals was proposed. The surface roughness alteration successfully

imparted hydrophobicity in the steel surface and hence improved the corrosion resistance of the steel surface.

7. The ionic-liquid surface treatment was employed for the first time for structural steels and the results obtained from the wettability investigations demonstrated that RTIL-treatment can lead to improved surface cleaning and lubrication of inaccessible steel bridge components (such as steel bearings) and thus protect them from corrosion caused by deicing salts and deleterious debris and dirt.
8. New agriculturally derived, abundantly available, non-toxic corn-derived polyol corrosion inhibitors are successfully employed in decreasing the corrosivity of the traditional salt-based deicer without impacting the ice melting capacity of the traditional salt brine deicer.
9. The corn-derived polyol corrosion inhibitors investigated in this dissertation do not have a negative impact on the properties of Portland cement mortar when used in the specified concentrations. When used in slightly higher concentrations, the corn-derived polyols showed significant improvement in ice melting capacity without impacting the skid resistance of PCC pavement and do not lead to depletion of dissolved oxygen levels in the river water.
10. The polyol-mixed deicing products introduced in this dissertation can be directly sprayed on the pavement surface. Moreover, these products can also be used for pre-wetting of the pavement surface (anti-icing operations).
11. New soy protein-based coatings were synthesized and their corrosion protection performance was demonstrated for steel rebars. The results indicated that soy protein coatings provided adequate protection to rebars against corrosion. The soy protein

coatings studied herein have the potential for use as in-situ corrosion protection coating for repairing damaged rebar epoxy coatings.

13.2. Future Recommendation

Future recommendations and research directions for post-fire damage characterization and prevention, and corrosion prevention are discussed in the following subsections.

13.2.1. Post-Fire Damage Characterization and Multi-Scale Modeling

The results obtained from this dissertation can be further expanded to develop multi-scale models for predicting post-fire damage at material and structure levels. Specifically, future research efforts should focus on determining the shear and flexural capacities of fire-damaged components (girders, columns, connections) by incorporating multi-scale material models that can accommodate the change in microstructural and mechanical properties of structural steels as a result of fire exposure and subsequent extinguishing. In this regard, both physics-based and data-informed AI models can be developed. To this end, the data reported in this dissertation can be used to calibrate the post-fire material damage models. Moreover, reduced-scale structural components (e.g. connections) can be experimentally evaluated for post-fire damage and model validation. Importantly, such an experimental scheme should also include various levels of geometric discontinuities to reflect the stress triaxialities that are encountered in steel structures.

13.2.2. Post-Fire Damage Models for Inclusion in Building Standards

While many standards such as AISC and BS5950 have recommended high-temperature residual factors for determining the mechanical properties of structural steels corresponding to different fire temperatures and these residual factors are used in structural design when following the performance-based fire engineering design of structures, most of the standards do not provide any recommendation on the post-fire residual factors for determining the post-fire mechanical

properties of structural steels. While AISC recommends using a fire-affected steel structure when there is no obvious distortion in the steel members, nevertheless, post-fire capacity assessment of fire-affect steel structures becomes necessary to ensure the safety of the inhabitants. In such a case, the overestimation or underestimation of post-fire residual mechanical properties can affect the safety and economy of the structures. Therefore, it is necessary to develop uniform predicting equations that can be used for predicting post-fire residual mechanical properties of structural steels that can be subsequently used in determining the structural capacities of fire-affected steel structures. This dissertation provides important data for developing such uniform models and residual factors (in conjunction with the results from other investigations) for further inclusion in the building codes.

13.2.3. Residual Mechanical Properties Prediction for Steels with Variable Grain Sizes

This dissertation utilized three kinds of structural steels (ASTM A36, ASTM A572, and ASTM A992) for post-fire damage characterization and prediction of mechanical strength in the absence of fire temperatures. The ferrite grain sizes in the steels used in this dissertation ranged from 3 to 17 microns and thus the post-fire yield strength models proposed herein are calibrated for the microstructure grain sizes in this range. While this grain size range can be applicable for other types of structural steels with similar ferrite grain size ranges, future research efforts should focus on calibrating similar predictive models for structural steels with finer or coarser ferrite grain size than the steels investigated in this dissertation. Moreover, future research investigations can also include non-conventional structural steels that can become more mainstream in the coming decades. This includes structural stainless steels (for which the AISC standard specifications are currently being developed), high strength steels, and ultra high strength steels (such as U800 and U1200). Finally, the predictive equations for such steels shall

also need the incorporation of other metallurgical phases that are present in the modern high strength steels (e.g. Martensite phase) apart from the ferrite and pearlite phases.

13.2.4. Long-Term Field Performance of Polyol-Mixed Salt Brine Deicers

This dissertation demonstrated that corn-derived polyol corrosion inhibitors can reduce the corrosivity of traditional salt brine deicers (NaCl-based salt brine) in laboratory investigations. Future research efforts are recommended to evaluate the long-term field performance of corn-derived poly corrosion inhibitor mixed NaCl salt brine deicers. To this end, the corrosion inhibition performance should be evaluated for both steel and RC structures. Moreover, the vehicular corrosion can also be monitored on highways that are used for determining the long-term field performance of corn-derived polyol corrosion inhibitor mixed NaCl brine deicers. While this dissertation demonstrated that the addition of corn-derived polyols does not have much impact on the skid resistance of PCC surfaces, future research efforts should also include asphalt concrete surfaces. If future research utilizes a higher dosage of polyols for ice melting improvement than the dosage used in this dissertation, it is recommended that the influence of such dosage rates on dissolved oxygen levels in water bodies are evaluated to ensure that higher dosage rates do not affect the aquatic life and water quality.

13.2.5. Mixing Polyol Additives in Other Deicers

The investigation conducted in the current dissertation only used the traditional salt brine deicers as it is the most commonly used deicing product in North America. The future research investigation can expand the similar research methodology for determining the ice melting and corrosion inhibition performance of polyol corrosion inhibitors in other types of deicers or combination of deicers (e.g. NaCl mixed with $MgCl_2$ or $CaCl_2$) that are being used for anti-icing operations in highways. This dissertation used three types of food-grade corn-derived polyols

that included sorbitol, mannitol, and maltitol. Future research efforts are recommended to include other types of polyols in their research investigations.

13.2.6. Inclusion of Traditional and Novel Materials in Bio-Based Coatings

The soy protein coatings that are developed in this study are effective in mitigating steel rebar corrosion. The corrosion prevention performance and water resistance of soy protein coatings can be further improved by adopting three paths in future research efforts. The first pathway includes partial addition of constituents such as Bisphenol for improving the strength and water-resistance of the soy protein coatings. However, following this path will come at the cost of adding toxic material to the coating. Secondly, the cooking chemistry of the existing coating formulations can be further tweaked to further improve the unfolding of protein molecules and thus exposing the desired functional groups in the denatured soy protein coatings that can have higher strength and high resistance to water penetration. The third pathway includes the addition of traditional materials such as silica abrasives to the coating formulations that can act as reinforcement in the cured hardened coatings. It can further include the addition of novel materials such graphene oxide or nano clay that have previously been demonstrated to increase the corrosion resistance of traditional epoxy coatings. Lastly, the addition of toxic additives could be replaced by lignin-based materials and the antifoaming agents could also be introduced in the coating formulation to decrease the air bubbles that may get trapped during the high-temperature stirring and curing process. This will ensure that the resulting coating is largely pore-free and plant-based.